LIÈGE université
GIGA institute

Faculty of Medicine
GIGA Neurosciences/GIGA Stem-Cells

Laboratory of the *Molecular Regulation of Neurogenesis*
Pr. Laurent Nguyen

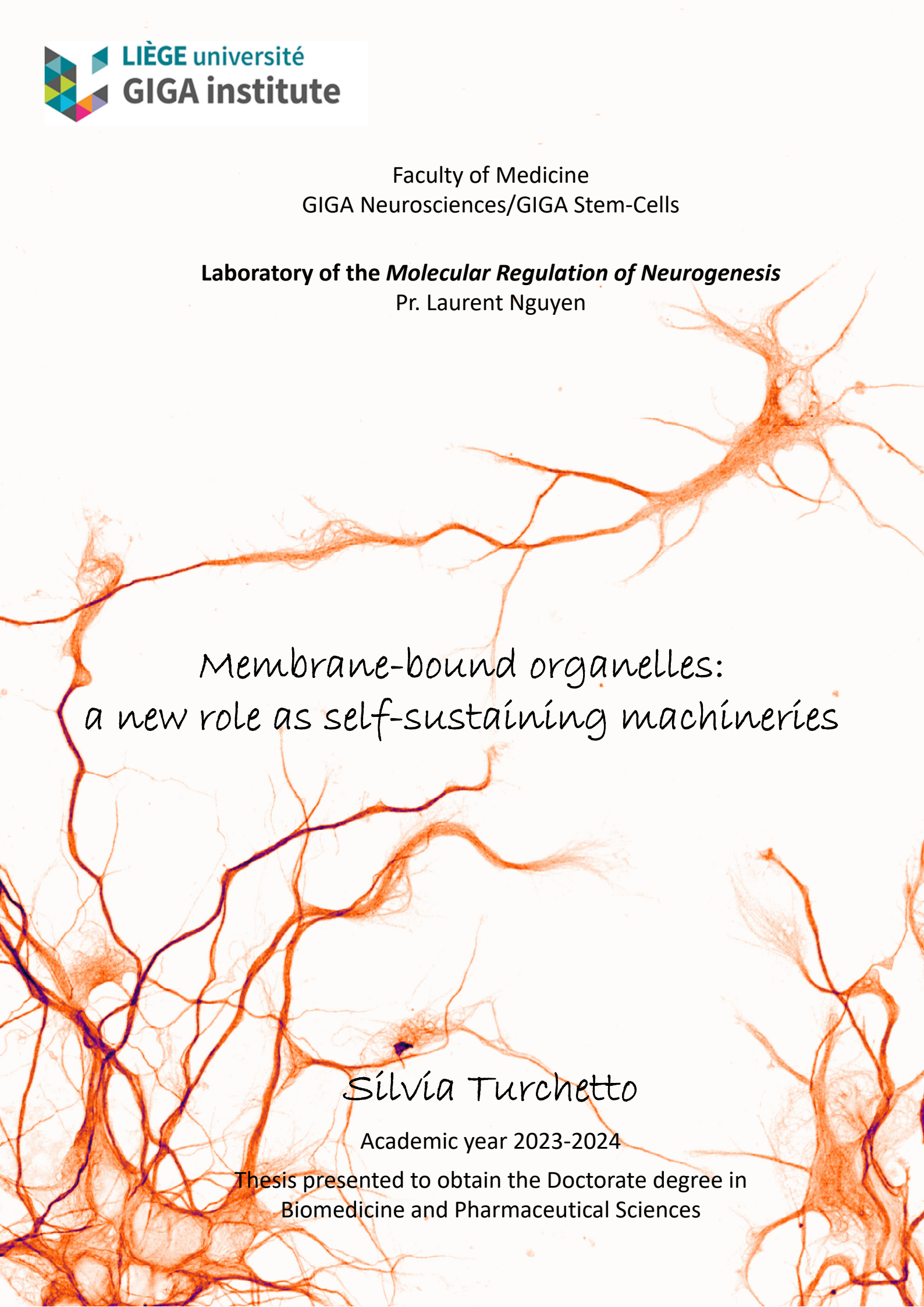

Membrane-bound organelles: a new role as self-sustaining machineries

Silvia Turchetto

Academic year 2023-2024

Thesis presented to obtain the Doctorate degree in
Biomedicine and Pharmaceutical Sciences

Abstract

Neurons are highly polarized cells with a very complex morphology, characterized by long dendritic and axonal extensions. Their architecture confers them the ability to receive information and relay it to neighboring or even distantly-located cells, supporting cell-to-cell communication within neuronal networks. The structural integrity and proper functioning of neurons highly relies on the coordination between two intracellular processes, namely axonal transport and local translation.

Axonal transport is the process used by neurons to distribute organelles, proteins, and mRNAs to their peripheral compartments to ensure homeostasis. Cargoes are transported by the molecular motors along the microtubule (MT) network and alterations in this process are often linked to neurological disorders. Through the activity of specialized enzymes, MTs are decorated with post-translational modifications (PTMs) such as acetylation, which are key regulators of the trafficking dynamics of motors. However, the mechanisms regulating MT acetylation and its contribution to transport dynamics, therefore to neuronal homeostasis, have yet to be fully elucidated.

Neurons also developed the ability to translate proteins in peripheral compartments, to respond efficiently to environmental stimuli and promptly sustain their energetic needs. Although recent evidence show that organelles can serve as platforms for the transport and translation of mRNAs, the mechanisms regulating this process are still largely unknown.

During my doctoral studies, I used the mouse as an experimental model to investigate, first, the role of tubulin acetylation in the regulation of axonal trafficking and, secondly, the functional correlation between the transport and translation machinery. I therefore contributed to two research projects that together characterized the enzymatic cascade leading to tubulin acetylation. Furthermore, I developed the toolbox to interrogate translation events on motile organelles.

We show that ATAT1, the enzyme catalyzing the acetylation of MTs, is essential for the regulation of axonal transport dynamics. We identify a vesicular pool of ATAT1 and unfold its displacement along MTs as essential to sustain its acetylation activity. Additionally, we characterized the enzymatic cascade upstream of ATAT1 that regulates MT acetylation. In this enzymatic cascade, Acly, whose stability is regulated by the Elongator complex, catalyzes the conversion of citrate into Acetyl-CoA, the substrate used by ATAT1 for its acetylating activity.

Additionally, we describe a new methodology to isolate motile cargos from mouse neurons and characterize their proteome and associated transcriptome. Additionally, we set-up a differentiation protocol to generate neuron-like cells that recapitulate key intracellular processes found in primary neurons. The cells were used to express the SunTag system to study the translation dynamics of candidate mRNAs. These two methodologies will enable the characterization of the transcripts associated with motile cargos and the study of their translation dynamics.

Résumé

Les neurones sont des cellules polarisées qui présente une morphologie complexe, caractérisée par de longues extensions dendritiques et axonales. Cette architecture confère aux neurones la capacité de recevoir des informations et de les transmettre aux cellules voisines ou même éloignées, assurant la communication cellulaire au sein du réseau neuronal. L'intégrité structurale et le bon fonctionnement des neurones dépendent fortement de la coordination entre deux processus intracellulaires, à savoir le transport axonal et la traduction locale.

Le transport axonal est le processus utilisé par les neurones pour distribuer leurs organites, des protéines et des ARNm aux compartiments périphériques afin d'assurer l'homéostasie. Les cargos sont transportés par des moteurs moléculaires le long du réseau de microtubules (MT) et des altérations dans ce processus sont souvent liées à des troubles neurologiques. Par l'activité d'enzymes spécialisées, les MT sont décorées de modifications post-traductionnelles (PTM) telles que l'acétylation, qui sont des régulateurs clés de la dynamique de trafic des moteurs. Cependant, les mécanismes régulant l'acétylation des MT et sa contribution à la dynamique de transport, et donc à l'homéostasie neuronale, restent peu compris.

Les neurones ont également développé la capacité de traduire des protéines dans des compartiments périphériques, pour répondre efficacement aux stimuli environnementaux et soutenir rapidement leurs besoins énergétiques. Bien que des preuves récentes montrent que les organites peuvent servir de plates-formes pour le transport et la traduction des ARNm, les mécanismes régulant ce processus sont encore largement inconnus.

Pendant mes études doctorales, j'ai utilisé la souris comme modèle expérimental pour étudier, d'une part, le rôle de l'acétylation de la tubuline dans la régulation du trafic axonal et, d'autre part, la corrélation fonctionnelle entre le système de transport et de traduction. J'ai ainsi contribué à deux projets de recherche qui ont caractérisé ensemble la cascade enzymatique conduisant à l'acétylation de la tubuline. De plus, j'ai développé un ensemble d'outils pour interroger les événements de traduction sur les organelles motiles.

Tout d'abord, nous montrons qu'ATAT1, l'enzyme catalysant l'acétylation des MT, est essentiel à la régulation de la dynamique du transport axonal. Nous identifions un pool vésiculaire d'ATAT1 et dévoilons son déplacement le long des MT comme essentiel pour

soutenir son activité d'acétylation. De plus, nous caractérisons la cascade enzymatique en amont d'ATAT1 qui régule l'acétylation des MT, où Acly, dont la stabilité est régulée par le complexe Elongator, catalyse la conversion du citrate en Acétyl-CoA, le substrat utilisé par ATAT1 pour son activité d'acétylation.

Ensuite, nous décrivons une nouvelle méthodologie pour isoler les cargos mobiles et associés aux MT dans les neurones de souris et caractériser leurs protéome et transcriptome associés. De plus, nous décrivons un nouveau protocole de différenciation pour générer des cellules de type neuronal qui reproduisent largement les processus intracellulaires présents dans les neurones primaires. Au sein de ces cellules, nous avons exprimé le système SunTag pour étudier la dynamique de traduction d'ARNm candidats. Ces deux méthodologies permettront la caractérisation des transcrits associés aux cargos mobiles et l'étude de leur dynamique de traduction.

Acknowledgements

I would like to thank all the members of my internal jury, **Prof. Brigitte Malgrange and Drs. Laurence Delacroix, Pierre Close and Christophe Desmet,** for accompanying me throughout my PhD, for their feedback and suggestions throughout the years, for the encouragements and appreciations given at every yearly assessment. I would equally like to thank the external members of my jury panel, **Prof. Ludo Van Den Bosch** and **Dr. Caroline Medioni**, for accepting our invitation to review this manuscript and for their constructive and attentive feedback.

Laurent, thank you for welcoming me in your lab and for your unconditional support throughout these five years. Thank you for your trust and for all the possibilities offered along the way, from the multiple projects I could join and the freedom to explore new methods and ideas, to the enriching and inspiring conferences I could attend. Looking back at this long marathon, you made me understand that giving up on something that hasn't been successful for quite some time doesn't mean failing but looking for brighter alternatives. That sometimes I have to stop doing what I am doing and look at the bigger picture, to refocus and not lose sight of the general purpose. Thank you for all the advices and encouragements, and above all for giving me the possibility to develop my confidence and independence.

Thank you, **Loïc**, for being my mentor during my first two years of PhD. You welcomed me in your running project and while teaching me about the art of multi-tasking you introduced me to the field of translation and the beauty behind its mechanisms. Thank you for trusting me all along, giving me the possibility to develop my independence while working on our shared projects. Thank you for always being ready to share your knowledge and experience. Your example showed me not to be scared about unknown methods but to be open minded in the search for alternatives and in the setting-up of new tools.

I am so glad I could share the office with you, **Sylvia**! In these past two years, you have been my fan number one, always ready to cheer for me and my experiments, to listen (very patiently) to my complaints, to cheer me up when failures would come, and to brainstorm with me when I needed to get back on my feet. Thank you for all the laughs, the relaxing chats at the end of the day and for being there when I most needed it. Thank you for spending all those days and the FACS with me, for teaching me all the FACS magic I know and for always believing in my vesicles. You are an extraordinary scientist full of ideas and determination, and with a big heart, and I wish you the very best of luck with your future career☺.

Thanks to you, **Bernard L.**, for all the help and support you gave me just by being next door! I admire the infinite dedication you have for your work but especially for all the possible existing cloning strategies. Thank you for helping with all my crazy SunTag clonings, for the patience and time invested and for always being willing to help. You always supported me throughout the years, trying to motivate me when things were not going in the right direction, and showing me your appreciation for my work.

A special thanks goes to **Prof. Marc Thiry** and **Patricia**, for their precious help with the electron microscopy, for their enthusiasm towards new challenges and their always ready availability to try new set ups even with a last-minute notice. I am truly grateful for your professionality and resilience. Thank you, **Dominique** and **Sofian**, for making our collaboration the best experience I could have ever had at the end of my lab time! Thank you for putting your trust in our ideas and investing your electrophy skills, rigorous commitment and working ethic in a new set of experiments. I truly enjoyed our insightful discussions and all your technical explanations, and I am happy your exemplary efforts rewarded us with a beautiful set of data.

Even though you joined the lab only recently, I am truly grateful that our lab paths crossed each other, **Fang-Shin**! I am happy you decided to join me in this "vesicular adventure". Thanks to your precious help I could better balance out the to-do list of the last months and I really appreciated your insights and tips that helped us succeed in our last goals. I really enjoyed working with you, I only wished it would have been for longer! Our motile vesicles are in good hands with you, I am sure you will crack all their little impenetrable secrets!☺

Thank you **Anto**, for always being ready to share your experience and knowledge, especially with the hippocampal cultures! Thank you, **Anaïs**, for sharing with me your bioinformatic dark magic skills, for being so available and patient even with data arrived in a rush at the very last weeks of my PhD. Thank you for making your explanations easy to follow even by a newbie like me.

My PhD journey wouldn't have been the same without all my colleagues and friends that accompanied and supported me throughout these years!

Dear **Julie**, thank you for being the most present colleague and the most caring friend, the first one to cheer at my successes and to support me when things were not going in the right direction. Always ready to help, no matter what it would take: postponing your own things or staying longer at the end of the day, trying to give me ideas and helping me through the trouble shooting processes. Thank you for remaining patient even when my stress level would tend to stress yourself, too. Biking with you every morning has also been such an adventure! Under the sweating sun or the cold rain nothing has ever stopped us! Thank you for sharing every commuting with me.

Dear **Fanny**, thank you for your kindness, patience, and help. You always found time for explanations, even when we were working in shifts and every minute was precious, or just for a few words to help me stop and breathe when days were getting too heavy. You were always there to help me in any way you could, even when your schedule was much more overwhelming than mine. Thank you, **Ron** and **Sebastian**, for accompanying me throughout this journey with your humor and laughs, both at the lab or gathered around a good dinner. Thank you, **Laura,** for your always present support and kindness, you always found the right words to encourage me. Thank you also for making sure we would make the best out of our free time! For organizing great chilling or dancing events that would gather us all – they have

always been great opportunities to recharge our batteries! **Lucas**, you have been such a reference point throughout! You gave me the warmest welcome once arrived in Liege, introduced me to your adventurous lifestyle and to the bike commuting. Thank you for just being you, for your contagious enthusiasm, your thoughtful insights and ability to listen. Your company has made my PhD journey a better adventure. Together with **Margaux, Bilal, Cyrine, Alexandra**, you all made my arrival in Liege a great experience and immediately made me feel at home. Thank you for your friendship and for all the time spent together, that I will always cherish.

A special thanks goes to all the members of the Nguyen's group. Thanks to all of you, working in this group has been an unforgettable journey. Your team spirit, solidarity and kindness made every step of the way filtered by advices, support, kind words but also a lot of fun. Thank you, **Jolien**, for your cheerfulness and friendship, for all the stories about Flemish culture and for your enthusiasm and determination that have always been so contagious! Thank you, **Miriam**, for creating such a great working place with your (Mediterranean – the best one☺) sunny and outgoing personality, for always making time for a little catching-up chat and for bringing us together for the greatest costume party and after work drinks. Thank you, **Carla**, for all the feedback, advices and motivational conversations we had throughout the years! You always showed me your support and believed I could reach my objectives. Your intuitions and explorative approaches have been such a great inspiration for me all along the way! Thank you, **Sophie** and **Ira**, for all the advices, discussions and feedback received all these years! **Maïlis** and **Max**, you were my first office fellows and I wish to thank you for the great atmosphere and discussions we had together. I will always remember how you two organized the best GIGA neuro's Christmas party of all time! **Nico!** We started the PhD journey together and, let me tell you, you have been such a hero and an example! Your determination and resilience are unbeatable, and I wish you the best of luck for the last kilometers of the marathon! I truly believe that the end of your thesis will be brilliant and full of satisfaction. **Mathilde, Gerald, Katya, Roman, Claire, Florence, Martin** – thank you for all the conversations along the hallways or at side-by-side benches! Thanks to all of you the lab retreats and events wouldn't have been the same, full of laughs, unity and collaboration.

What would it be the Nguyen's team without the greatest working environment at GIGA neuro! Thank you, **Vini** and **Sonia**, for the early morning talks and laughs, and for always being ready to listen and to share your thoughts, experiences and advices. I want to also thank **Tine, Mona, Mary, Nathalie S. and Nathalie M.** for always being ready for a PhD-to-PhD chat, for the reciprocal support and for all the shared daily moments. Thank you, **Julie B**., for supporting the bike community and for all the shopping and mechanical bike advices given to Romain that were indirectly for me! I would also like to thank **Charlotte C.** and **Vincent**, who always took the time to have a few words with me, at any moment we would meet along the hallways.

I would like to dedicate a special thanks to **Nathalie K.** and **Bernard C.,** for their daily help on the bench and for providing ideas and support at any test I wished to experiment on. Thank

you also for your infinite dedication at organizing the lab events, in such a way that nothing would be missing, that everything would be perfect and exciting. Lastly, without all of you, **Pierre-Bernard, Alex, Laurent M., Larisia and Jessica**, working at our unit wouldn't be possible! Thank you very much for all your daily work and attention, and for being always ready to share your technical experience or helping with organization and paper work.

I need to thank also many people from the GIGA Flow Cytometry and Cell Imaging platforms, without whose technical help and advices I wouldn't have been able to set up many experiments. Thank you **Raafat, Céline and Sandra** for all the help and lessons at the FACS, and thank you **Alexandre** and **Gaëtan** for all the training, advices and help at the microscope, and for always being ready to try new set-ups and camera demos.

Un grazie special va alla mia **famiglia**, che mi ha sempre supportata durante tutti questi anni e senza la quale non avrei potuto realizzare tutti i traguardi che ho raggiunto, ad ultimo questo dottorato. Grazie per avermi sempre incoraggiata ad esplorare nuovi paesi e mettermi alla prova, nonostante questo volesse dire lasciare casa e vedersi solo raramente. Grazie per i consigli ogni qual volta dovessi prendere una grande decisione, per la comprensione e l'incoraggiamento dato ad ogni momento difficoltoso. E da ultimo, grazie per il sostegno che ancora una volta mi avete mostrato per il nuovo capitolo che presto si aprirà.

Romain. This achievement is as much mine as it is yours. Without you everything would have been different, my days and my journey as a PhD. You were my strength behind every tough moment, the encouragement at every crossroad and my biggest supporter throughout. You could find the good when I could see only shadows and motivate me to go forward every time. You made this 5-year journey not only about the lab, making sure I would take the deserved rest and good care of myself. You made me discover the beauty of nature and the spirit of adventure, opening my mind to a new way of looking at things. You have been by pillar and my source of happiness every day and I am looking forward to discovering all the adventures the future holds for us.

List of abbreviations

AD	Alzheimer's Disease
AIS	Axon initial segment
Alkbh8	Alkylation repair homolog 8
ALS	Amyotrophic lateral sclerosis
AP2	Adaptor protein 2
APC	Adenomatous poluposis coli
APP	Amyloid precursor protein
ATAT1	α-tubulin N-acetylatransferase 1
BDNF	Brain-derived neurotrophic factor
BORC	BLOC-one-related complex
BRP	Bruchpilot
Btz	Barentsz
cAMPK2a	Calcium/calmodulin-dependednt protein kinase 2 alpha
CBP80	Cap binding protein 80
CCP	Clathrin-coated pit
CDK1	Cyclin-dependent kinase 1
cKO	Conditional knock-out
CMT2A	Charcot-Marie-Tooth disease type 2A
CMT2F	Charcot-Marie-Tooth disease type 2F
CSRP1	Cysteine and glycine rich protein 1
Ctu1/2	Cytosolic thiouridylase homolog 1/2
DCV	Dense-core vesicle
dHMN2B	Distal hereditary motor neuropathy 2B
DHX30	DExH-box helicase 30
DRG	Dorsal root ganglion
DYRK	Dual-specificity tyrosine-regulated kinase
EB	End-binding proteins
EE	Early endosome
EEA1	Early endosome antigen 1
EPSP	Excitatory-post synaptic potential
ES	Embryonic stem
FEJC	Exon junction complex
FUS	Fused in sarcoma
HIP1B	FTS-HOOK-intercating protein 1B
FAOS	Fluorescent-activated organelle sorting
FERRY	Five-subunit endosomal Rab5 and RNA/ribosome intermediary
FMRP	Fragile X mental retardation protein
FTLD	Frontotemporal lobar dementia
FTS	Fused toes protein
FXS	Fragile X Syndrome
HAT	Histone acetyltransferase
HD	Huntington's disease
HDAC	Histone deacetylase
HDAC6	Histone deacetylase 6
HSP	Hereditary spastic paraplegia
HSPB1	Heat shock protein family B member 1
HSP70	Heat shock protein 70
Htt	Huntingtin
KHC	Kinesin heavy chain

KLC	Kinesin light chain
LAMP1	Lysosome-associated membrane protein
LE	Late endosome
Lmnb2	LaminB2
MAP	Microtubule-associated protein
Mcm5s2	5-methoxycarbonylmethyl-2-thiouridine
Mfn2	Mitofusin-2
MNB	Minibrain
MCAK	Mitotic centromere-associated kinesin
MLL	mademoiseLLE
MT	Microtubules
NGF	Nerve growth factor
NMJ	Neuro-muscular junction
NT3	eurotrophin-3
OE	Overexpression
OMM	Mitochondria outer membrane
PB	Processing body
PD	Parkinson's disease
Pink	PTEN-induced kinase 1
PSEN1	Presenilin1
PTM	Post-translational modifications
RAB	Ribosome-associated vesicle
RBP	RNA-binding protein
RILP	Rab7-interacting lysosomal protein
RNP	Ribonucleoprotein
RRM	RNA recognition motif
SAM	S-adenosyl-l-methionine
SETD2	SET-domain containing 2
SG	Stress granule
SMA	Spinal muscular atrophy
SMN	Survival of motor neuron
SNAP25	Synaptosomal-associated protein 25
SRP	Signal recognition particle
SKIP	SifA-kinesin-interacting protein
Stau2	Staufen2
SVP	Synaptic vesicle precursor
TCP	Tubulin carboxypeptidase
TIGER	TIS granule-ER
TSA	Trichostatin A
TTL	Tubulin tyrosine ligase
TTLL	Tubulin tyrosine ligase-like
TTX	Tetradotoxin
UTR	Untranslated region
ZBP1	Zipcode binding protein 1
+TIPS	Plus-end tracking proteins

Table of contents

INTRODUCTION

Neurons are unique cells that set apart from all the other cell types present in our body for a plethora of features, ranging from their morphology, properties, and functions. Neurons are highly polarized cells with a complex branched morphology, constituted, in most cases, by a single axon which can cover extremely long distances (hundreds of centimeters) and a set of shorter dendritic ramifications. Both axons and dendrites extend from the cell soma and, ought to their length and ramifications, constitute 99% of the entire neuron cytoplasm. During brain development, neurons extend their axons over very long distances following extracellular cues until reaching their final localization, where they settle to form contact sites with other neighboring neurons. Through these contact sites called synapses, neurons can receive, process, and send information to other cells, forming a structurally and functionally coordinated cellular network with a high computational power. Accordingly, besides being polarized cells, neurons also display a remarkable degree of subcellular compartmentalization to sustain their functions. Synapses form between the axonal terminal of a neuron (pre-synapse) and specialized dendritic domain called spines (post-synapse) and can distribute through the length of neurites. For this reason, a single neuron can form pre- and post-synapses with up to 10,000 and 100,000 neurons, respectively (reviewed in: Holt, Martin, & Schuman, 2019).

To sustain this complex morphology and the cell-to-cell connectivity, neurons distribute, pools of neurotransmitters, proteins, mRNAs and organelles throughout their peripheral compartments to constantly sustain their energetic needs and support their localized activities. All these constituents are trafficked along the neurites through the activity of the molecular motors, which run along the MT network following a bidirectional motion. Motors can either move from the cell soma to the periphery to supply these sites, or retrogradely from the synaptic terminals to the cell soma for the recycling or degradation of molecules, or for the transport of signaling neurotransmitters (reviewed in: Cason & Holzbaur, 2022).

Given the broad variety of cargos and their associated function, their subtype-specific distribution throughout the cytoplasm is achieved through a regulatory system composed of: 1) cargo-specific motors and adaptor proteins (reviewed in: Cason & Holzbaur, 2022); 2) MTs diversity in their constitutive units and in the PTMs that decorate either their external or luminal surface (reviewed in: Janke & Magiera, 2020). Through these elements, a given cargo

is distributed in a temporal and spatially restricted manner to exert its functions where and when needed.

1. Microtubules

Compared to all other cell types, neurons are unique cells ought to their polarity and branched morphology which is characterized by a complex dendritic arbor and an extremely long axon which can span from few micrometers to over a meter-long. Neurons require a constant supply of proteins, RNAs, lipids and organelles throughout all their sub-compartments, to sustain their complex morphology and physiological functions. The peripheral distribution of these molecules is achieved through an efficient and dynamic transport system which requires microtubules (MTs), motor proteins, adaptors, and cargos for its proper functioning. MTs form a structural network within every peripheral compartment that serves as tracks for the trafficking of motor proteins. Motor proteins modulate the bidirectional transport of their associated cargos through interactions with adaptor proteins. Anterograde transport dynamics are key for synapses integrity and function, both at dendrites and axons. Equally important is the retrograde transport of cargos towards the cell soma which ensures neurotrophic signaling (retrograde flow of information triggered by internalized neurotrophins as growth factors that evokes and modulates cellular responses), degradation pathways (removal of damaged organelles or proteins from the cytoplasm to recycle their constituents for new biosynthetic purposes), and injury-induced responses (axon-to-soma communication triggered by peripheral nerve injury to modulate transcriptional and translational programs for neuronal regeneration).

Apart from regulating transport dynamics, MTs play an essential role in sustaining the structural and functional integrity of neurons throughout their development, growth, and maintenance. Accordingly, MTs can regulate many intracellular processes, from the mitosis and meiosis of neuronal progenitors to the migration of newly born and differentiating neurons towards their final localization.

Mutations in genes encoding for MT-associated proteins or in the component of the transport machinery which leads to axonal transport impairments have been reported in a broad range of neurological disorders, including Amyotrophic lateral sclerosis (ALS) which presents with a progressive degeneration of motor neurons, leading to muscle atrophy and paralysis (Baron

et al. 2022), frontotemporal lobar dementia (FTLD) which is characterized by a loss of cortical neurons in the frontal and temporal lobes resulting in apathy and executive dysfunctions (Combs et al. 2021), Parkinson's Diseases (PD) (Prots et al. 2018) and Alzheimer's Disease (AD) (Kopeikina et al. 2011; Wang et al. 2019). As many of these genes are ubiquitously expressed in all cells, but their genetic alternations cause pathological phenotypes only in a subset of neuronal subtypes, it is hypothesized that the downstream transport defects are regarded as causative factors in the disease.

1.1 Microtubule structure and dynamics

MT are filaments of the cytoskeleton that are highly conserved across all eukaryotic cells. They appear as hollow cylinders constituted of parallel protofilaments assembled with side-to-side contacts and formed by the heterodimerization of α-tubulin and β-tubulin monomers. The number of constituting protofilaments regulates the diameter and conformation of a given MT. *In vivo*, MTs are composed of 13 protofilaments displaying a diameter of around 25 nm, but in different neuronal subtypes their number can vary between 11 and 16 (reviewed in: Janke and Magiera 2020). In C. elegans, while the majority of MTs have 11 protofilaments, touch receptor neurons display MTs composed of 15 protofilaments (Chalfie and Thomson 1982). Tubulin monomers are formed of a globular body responsible for the tubulin-tubulin interactions and MT assembly, and a negatively charged C-terminal tail that projects to the outer surface of the MTs and that is key for MT properties and functions.

Assembled MTs have an intrinsic polarity due to the head-to-tail assembly of their constitutive dimers. Along the axons, MT are organized in parallel bundles with their plus-end directed outwards, towards the distal axon tip. On the contrary, they arrange with a mixed orientation within dendrites (Yau et al. 2016).

Although mechanically rigid, MTs are extremely dynamic in their structure, as phases of polymerization alternate to depolymerizations in a process called *dynamic instability*. This behavior is explained through the "GTP-cap" model. Tubulin, a GTPase, binds GTP and forms GTP-associated αβ-tubulin heterodimers that are incorporated into the growing end of MTs. Shortly after incorporation, GTP is hydrolyzed leading to conformational changes and instability in the MT lattice made of GDP-tubulin dimers. As GTP hydrolysis occurs with a delay, the progressive incorporation of new dimers forms a "cap" of GTP-tubulin at the

growing end, which confers stability to the MT lattice and prevents its polymerization (Alushin et al. 2014) **(Figure 1)**. However, patches of remnant GTP-tubulin dimers have been identified along the axonal shaft, suggesting the GTP hydrolysis is not always complete during MT polymerization (Dimitrov et al. 2008).

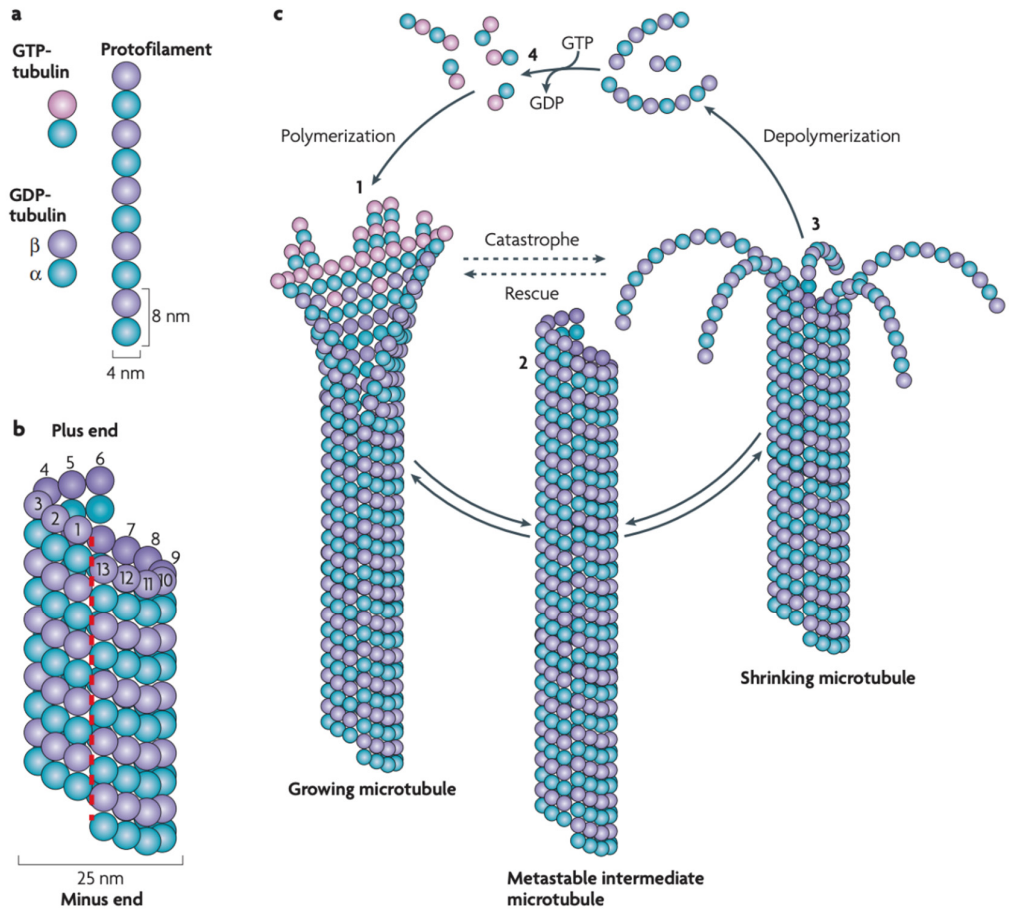

Figure 1. MT structure and dynamic instability. (A) Heterodimers of α/β-tubulin subunits assemble in a head-to-tail fashion into protofilaments. **(B)** In mammals, 13 parallel protofilaments assemble forming the cylindrical and hollow architecture of MTs. **(C)** MTs are dynamic structures undergoing alternating cycles of polymerization and depolymerization. Figure adopted from (Akhmanova and Steinmetz 2008).

1.2 Microtubule-associated proteins

As their name suggests, MT-associated proteins (MAPs) bind to MTs and regulate their dynamics, organization, and functions. Among these are: 1) structural MAPS; 2) plus-end tracking proteins; 3) MT severing enzymes; 4) motor proteins.

Structural MAPS regulate MT polymerization as well as transport dynamics. While the microtubule-associated protein 6 (MAP6) acts as MT stabilizer and it is enriched at stable domains of MTs, tau, on the contrary, accumulates on labile domains of MTs to promote their growth (Qiang et al. 2018). Additionally, tau plays an important role in regulating transport dynamics in a spatially-restricted manner. It is preferentially enriched on highly-bent curved regions of MTs as at synapses (Balabanian, Berger, and Hendricks 2017), where it favors the directionality of dyneins while completely inhibiting the motor activity of kinesins (Dixit et al. 2008). Similarly, doublecortin also decorated curved MTs although its local contribution has not yet been elucidated (Bechstedt, Lu, and Brouhard 2014) **(Figure 2 A)**.

Plus-end tracking proteins (+TIPS) accumulate at the growing end of MTs where they contribute to the regulation of its dynamics and to the initiation of the dynein-mediated retrograde trafficking of organelles (Moughamian et al. 2013). Their binding selectivity might be ought to the recognition of tubulin or protofilament sides that are otherwise masked within the MT hollow structure. Among these proteins are the end-binding (EB) proteins, CLIPs, and motor proteins that play a role in regulating MT dynamics (reviewed in: Akhmanova & Steinmetz, 2008) **(Figure 2 B)**.

MT severing enzymes, such as spastin, katanin and fidgetin, cut MTs into smaller fragments. Spastin, however, apart from its severing activity, can also regulate MT dynamics by decelerating its shrinkage. Overall, this enzyme increases the number of MT fragments and promotes their growth, therefore increasing the overall MT mass (Kuo et al. 2019) **(Figure 2 C)**.

Motor proteins traffic along the MT network to transport their associated cargos. The plus-end directed kinesin families of motors transport their cargos from the cell soma to the presynaptic sites along dendrites and axons to sustain signaling events and the functional integrity of these peripheral regions. The cytoplasmic dynein 1 is instead directed towards the minus end of MTs, promoting the retrograde transport of proteins and organelles back to cell soma for recycling **(Figure 2 D)**. While these two classes of motors can modulate the fast transport of organelles (400 mm/day or 1 μm/s), they can also promote at a much slower pace the distribution of cytoplasmic components, such as tubulin dimers, neurofilaments (<8 mm/day or <0.1 μm/s).

Kinesins are subdivided into 14 classes based on their structural and functional properties, with the most characterized being the kinesin-1, kinesin-2 and kinesin-3 families.

Members of the Kinesin-1 family are heterotetramers of two kinesin light chains (KLCs) and two kinesin heavy chains (KHCs). Of note, the KHCs present multiple domains: 1) a MT-binding head corresponding to the motor domain that hydrolyzes ATP for the motor activity; 2) a stalk domain which promotes the dimerization of the two heavy chains; 3) a cargo-binding domain. Some kinesins localize preferentially to the axons as KIF5B/C, others to dendrites as KIF17, and others in both as KIF5A. Interestingly, the binding of kinesin-1 to MTs stabilize the unstable GDP-lattice of dynamic MTs by changing the conformation of its GDP-tubulin subunits and aligning to that of GTP-tubulin (Peet, Burroughs, and Cross 2018).

The Kinesin-3 family members are homodimers formed of two heavy chains, containing a motor domain, a stalk domain, and a cargo binding domain. They can be axon-selective (KIF13B), dendritic-selective (KIF1C) or ubiquitous (KIF1A). Differently from the other families, kinesin-3 family members undergo dimerization only upon binding to organelles, to become motors with high motility and ability to transport efficiently their cargos (Soppina et al. 2014).

While there are multiple genes encoding for the motor domain of each single family of kinesins, the motor domain of the cytoplasmic dynein, the motor driving the retrograde transport, is encoded by a single gene. The motor domain is generated by the homodimerization of two heavy chains and consists in a ring-like structure made of 6 AAA+ (ATPase Associated with diverse cellular Activities) domains, which modulate cycles of ATP hydrolysis that promotes cycles of MT binding (reviewed in: Cianfrocco, Desantis, Leschziner, & Reck-Peterson, 2015). On the contrary, the light chains are encoded by different genes. For their processivity, dyneins form a complex with their activator dynactin, among whose subunits are p25 and dynamitin/p50 that regulate the binding to the cargos, or p150glued that mediates the binding to the dynein and to MTs (reviewed in: Cason & Holzbaur, 2022).

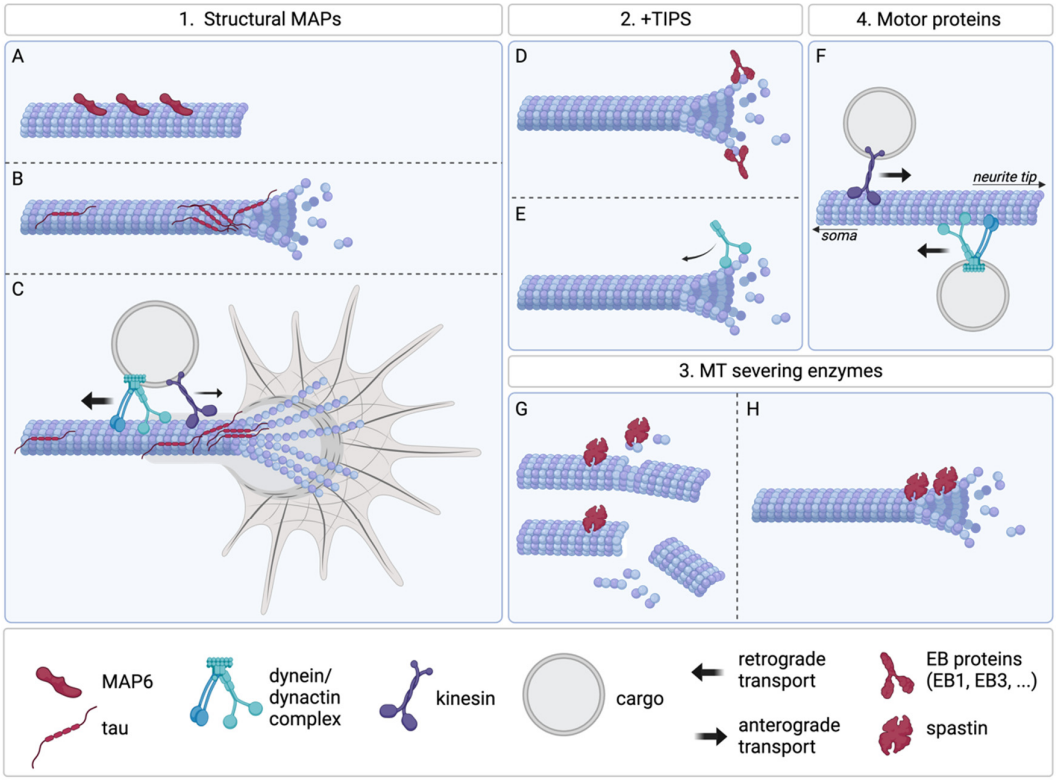

Figure 2. Schematic representation of how MAPs can modulate the structure, dynamics, and functions of MTs. (A-C) Structural MAPS regulate MT dynamics. MAP6 stabilizes MTs **(A)**, while tau promotes their growth **(B)** and the MT-based transport dynamics **(C). (D, E)** + TIPS can regulate the plus-ends dynamics of MTs **(D)** and the transport of motors **(E). (G, H)** MT severing enzymes can regulate MTs structure **(G)** or growth **(H). (F)** Motor proteins benefit from MTs for their processivity and transport of cargos.

1.3 Cargos

1.3.1 Spatial selectivity of cargos

Cargos are not always equally distributed throughout all neurites but can display a spatial preference for either the axonal or dendritic compartment. This specificity does not only rely on their associated motor proteins but also on the organization and characteristics of the MT network. Although plus-end out MTs can be found both in dendrites and axons, a recent study elucidated how plus-end kinesins can have a selectivity for axons. Interestingly, the Kinesin-1 family member KIF5B run preferentially on acetylated MTs (Guardia et al. 2016). As acetylated MTs are oriented minus-end out along dendrites, Kinesin-1 is trafficked from the dendritic periphery to the cell soma, to then distribute within axons where all MTs are plus-end out,

preventing further entries into dendrites (Tas et al., 2017). Contrarily, kinesin-3 members KIF1B and KIF1A have a binding preference for tyrosinated MTs (Guardia et al. 2016) **(Figure 3 A)**. As tyrosinated MTs are directed plus-end out along dendrites, these motors can enter both axons and dendrites. Thanks to these findings, the mechanism that drives the axon-selective preference of specific motors started to be elucidated. Thanks to these findings, the mechanism that drives the axon-selective preference of specific motors started to be elucidated. It has also been proposed that some kinesins recognize and have a high affinity for the segments of remnant GTP-tubulin dimers present along axons (Dimitrov et al. 2008). These binding sites enable the axonal distribution of a given motor (Nakata et al. 2011) **(Figure 3 B)**.

The exclusion from axons for dendritic vesicles has instead been attributed to the structural organization of the axon initial segment (AIS), which acts as a filtering system. The AIS is characterize by a network of actin filaments and its specific motor protein myosin Va interacts with dendritic vesicles to reroute them to the cell soma away from the axonal entry (Al-Bassam et al. 2012) **(Figure 3 C)**.

Multiple motors have also been associated to both axonal and dendritic trafficking (reviewed in: Cason & Holzbaur, 2022).

Lastly, the switch between anterograde to retrograde transport at the end of neurites is triggered by a broad range of plus-end interacting proteins (+TIPs), including EB1, EB3 (Moughamian et al. 2013) and Lis1 (Huang et al. 2012), which interact with the dynein-dynactin complex modulating its recruitment onto the MTs and processivity **(Figure 3 D)**.

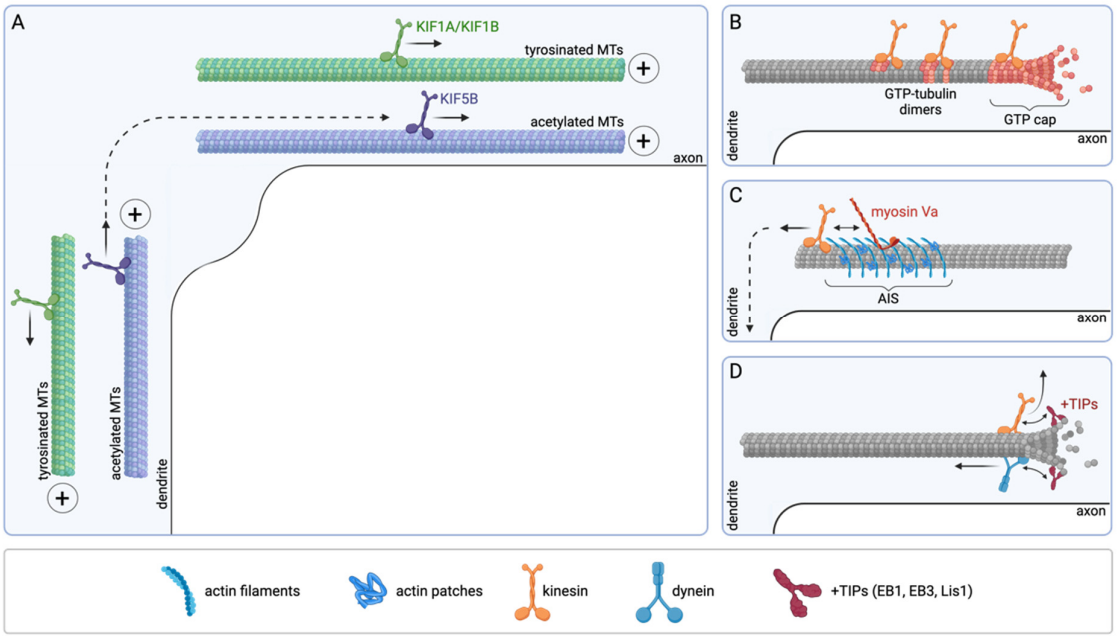

Figure 3. Mechanisms driving the spatially-restricted trafficking of motor proteins. (A) Within dendrites, differentially modified and polarized MTs guide kinesins towards axons (KIF5B) or also within dendrites (KIF1A/KIF1B). **(B)** GTP-caps at MT plus-ends and remnant GTP-tubulin patches along the MT lattice drive the localization and accumulation of kinesin (KIF5) motor proteins**. (C)** The network of actin filaments at the AIS prevents the axonal entrance of dendritic motors (KIF5). **(D)** + TIPS regulate motor's recruitment onto MTs and their processivity.

1.3.2 Cargos cooperation

It is suggested that every cargo is concurrently associated with both kinesins and dyneins. This applies to both cargos that display a bidirectional motion and to those that follow a unique directionality. Roughly, 1-4 kinesins and 1-5 dyneins might cooperate for the motility of a single cargo (Hendricks et al. 2010).

Two distinct theories support how cooperative but functionally antagonistic motors can define the motility of a cargo. On the one hand, the "tug of war" model suggests that the overall direction and velocity of a cargo is dictated by the number of motors of a given family and by their relative strength. On the other hand, the "opposite model" foresees a single motor family at a time being active and defining the cargo motility (reviewed in: Cason & Holzbaur, 2022). Globally, the preferential activity of a motor over another can be defined by its own tertiary structure and by its associated scaffolding proteins. Kinesins can mask and auto-inhibit their own motor domain with one of their subunits, and this inhibition can be

reversed by scaffolding proteins. These scaffolding proteins can equally regulate the anterograde and retrograde transport of a given cargo.

1.3.3 Cargos subtypes

The efficient delivery of cargos to and from the peripheral compartments of neurons is essential to sustain the homeostasis of neurons. The function of every organelle subtype complies with a specific neuronal need and their impaired function or transport have been widely correlated to neurological disorders. The transport pattern of each organelle is dictated by multiple factors ranging from their motor proteins and their specificity for different MTs features to their expressing membrane proteins that drive the interaction to a selective panel of interacting partners.

Synaptic vesicle precursors (SVPs) contain proteins and neurotransmitters destined to pre-synapses to sustain synaptic activity and move preferentially in an anterograde direction. Their transport is mediated by members of the kinesin-3 family and their adaptors proteins. Accordingly, the transport of SVPs was impaired in Drosophila liprin-α mutants (Miller et al. 2005) and in mouse hippocampal neurons expressing a DENN/MADD variant that lacks the KIF1A- and KIF1Bβ-binding domain (Niwa, Tanaka, and Hirokawa 2008) **(Figure 4 A)**. Differently from SVPs, dense-core vesicles (DCVs) store neuropeptides, hormones, and growth factors as BDNF. Their transport is bidirectional as they traffic anterogradely to pre-synapses to exert their synaptic functions, to then return retrogradely to the axon initial segment. Their bidirectional transport is dictated by the phosphorylation state of the scaffolding protein huntingtin (htt). When phosphorylated, htt recruits kinesin-1 to vesicles promoting their anterograde motion but when dephosphorylated this bond is released to favor the dynein-dynactin-mediated retrograde transport (Colin et al. 2008) **(Figure 4 B)**.

Signaling endosomes are membrane-bound organelles generated by endocytosis upon neurotrophins binding to their cognate receptors, responsible for the degradation of no-longer functional proteins or organelles. When immature they express EEAS1 and Rab5 (defined as early endosomes, EE), when mature they are positive for Rab7 (late endosomes, LE), which will further translate into degradative lysosomes expressing the lysosomal-associated membrane protein (LAMP1).

As they mature and are transported along the axons, their directionality changes according to the motor effectors they interact with.

The anterograde transport of EEs is modulated by KIF16B motor and its interaction with Rab5 and its effector protein hVPS34 (Hoepfner et al. 2005), while their retrograde transport is modulated by HOOK1 which links Rab5 to the dynein-dynactin complex, as shown by its KD which impairs the EE trafficking to the soma (Olenick, Dominguez, and Holzbaur 2018). In human cells, Hook1 was found to exert its function in concert with the fused toes protein (FTS) and the FTS–HOOK-interacting protein 1B (FHIP1B) (Christensen et al. 2021) **(Figure 4 C)**. Rab7-interacting lysosomal protein (RILP) is the adaptor protein modulating the retrograde transport of Rab7+ LEs (Johansson 2007) **(Figure 4 D)**. A subgroup of Rab7 LEs can however acquire Arl8b, which promotes the recruitment of multiple partners forming the Arl8b/SKIP/HOPS/TBC1D15 complex. Through this complex, Rab7 is removed from LE which can now engage in the kinesin-driven plus-end directed transport (Jongsma et al. 2020) **(Figure 4 E)**.

Lysosomes are autophagic organelles that degrade and recycle misfolded proteins, damaged organelles or other cellular debris and are therefore essential in maintaining neuronal homeostasis. They can undergo bidirectional transport. Their anterograde motion is mediated by the adaptor SifA-kinesin-interacting protein (SKIP) that mediate the binding of the lysosomal membrane protein Arl8 to the light chain of kinesin-1 (Rosa-Ferreira & Munro, 2011). The lysosomal membrane protein BLOC-one-related complex (BORC) with its associated partners Arl8 and SKIP are also essential to modulate the anterograde transport of lysosomes via its binding to both members of the kinesin-1 (KIF5B) and kinesin-3 (KIF1Bβ and KIF1A) families (Farías et al. 2017; Guardia et al. 2016). Their retrograde transport has instead been associated to the binding of a broad variety of adaptors, including RUFY 3/4 and its partner JIP4 which interact with the lysosomal transmembrane protein TMEM55B (Kumar et al. 2022; Willett et al. 2017) **(Figure 4 F)**.

Mitochondria are uncommonly polyfunctional organelles with biological roles that span from energy supply to regulation of metabolic homeostasis and are therefore necessary to maintain neuronal development and function. Because of their multiple roles, mitochondria are distributed throughout all neuronal compartments via long-distance transport. Their bidirectional transport is modulated by a number of adaptor proteins that interact with the

mitochondrial Rho-like GTPase miro and induce the mitochondria recruitment onto both kinesins and dynein motors. Among these adaptors are TRAK1 and TRAK2 (Milton in *Drosophila*) which form a complex with both kinesin-1 and the dynein-dynactin complex, regulating mitochondria anterograde and lis1-dependent retrograde processivity, respectively (Fenton, Jongens, and Holzbaur 2021; Glater et al. 2006; Henrichs et al. 2020). Recent findings elucidate the bilateral interaction of the TRAK proteins with both motor families. On the one hand, these adaptors can simultaneously recruit both motors but activate only kinesin-1 to modulate the anterograde MT-based transport. On the other hand, they regulate the minus-end directed transport by interacting only with the dynein-dynactin complex, precluding their binding to the kinesin motors. Through this mechanism, TRAK1/2 succeed to coordinate the activity of both motor families and prevent any competitive processivity (Canty et al. 2023). While other adaptors as syntabulin (Cai, Gerwin, and Sheng 2005) and FEZ1 (Fujita et al. 2007) have been additionally shown to contribute to their trafficking, synthaphilin is responsible for mitochondria arrest (Chen 2013) **(Figure 4 G)**.

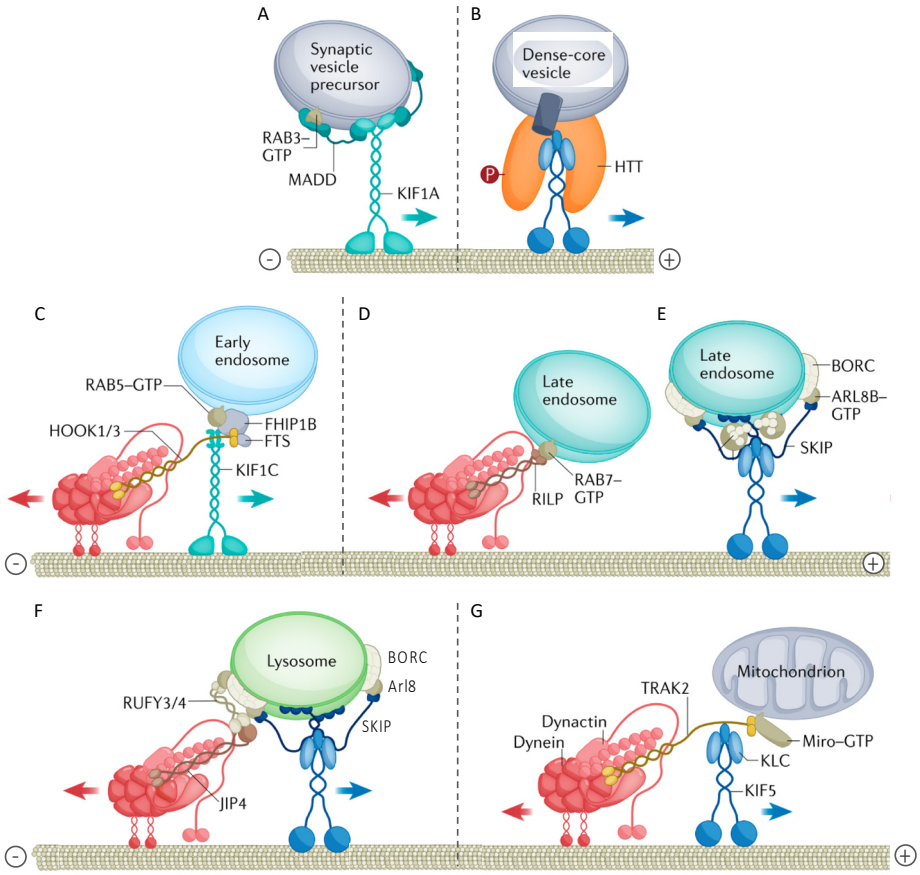

Figure 4. Schematic of the cargo-specific adaptor proteins regulating their motor-driven bidirectional transport. While synaptic vesicle precursors **(A)** and dense-core vesicles (B) predominantly undergo anterograde transport, early **(C)** and late **(D, E)** endosomes, lysosomes **(F)** and mitochondria **(G)** display a bidirectional motion. Adapted from: (Cason & Holzbaur, 2022)

2. The Tubulin Code

The ability of MTs to display different behaviors and modulate several functions is attributed to multiple factors, including the existence of different tubulin variants and tubulin post-translational modifications (PTM) which, together, define the commonly named *tubulin code*. The *tubulin code*, together with the MT affinity for a broad range of MT associated proteins (MAPs), define MTs behaviors.

2.1 Tubulin isotypes

Multiple variants of the α and β-tubulin monomers have been identified, and their number differ across species: while humans have 9 isotypes for both α-tubulin and β-tubulin, in the mouse α-tubulin and β-tubulin are encoded by 3 and 7 genes, respectively. Furthermore, tubulin isotypes expression can be cell-types specific (β3-tubulin is for this reason considered as a neuronal marker) (reviewed in: Gasic, 2022). The broad variety of tubulin isotypes and their ability to heterodimerize into highly organized structures define MTs as tubular structures with heterogenous composition. Most interestingly, the variations across isotypes are predominantly found within their C-terminal tails and can involve only a few amino acids. This heterogeneity confers MT different structural features, a selective affinity for specific MAPs and susceptibility towards preferred PTMs. Purified human α1B/β2B and α1B/β3 MTs revealed different architecture and dynamics. Accordingly, compared to α1B/β3 MTs which are formed of 13 protofilaments, α1B/β2B MTs have 14 protofilaments which confer them increased flexibility, resistance to passive disassembly as well as to depolarization induced by the MT-associated protein (MAP) mitotic centromere-associated kinesin (MCAK) (Ti, Alushin, and Kapoor 2018). Interestingly, the increased stability of β2B MTs compared to β3 MTs is ascribed to the core of the tubulin subunits, as chimeric β2B and β3 tubulins generated by swapping their C terminal tails displayed the same dynamic proprieties of the native isotypes (Pamula, Ti, and Kapoor 2016). The role of subtype-specific tubulins has also been investigated at a cellular level. As missense mutations in TUBB3 have been linked to brain

development defects including cortical gyration malformations (Poirier et al. 2010), the TUBB3 neuron-specific isoform has been studied in the context of cortical development. Loss of TUBB3 disrupts the migration of cortical neurons, which could by rescued by the overexpression (OE) of TUBB3 but not of other three beta-tubulin subunits (TUBB1, TUBB2B, TUBB4A). However, Tubb1a, Tubb2a and Tubb2b also display segregated functions during cortical development. Accordingly, the loss of Tubb1a lead to severe cortical malformations compared to the mild cortical defects observed upon the loss of the other two variants (Bittermann et al. 2019). Additionally, partial loss of Tubb1a has been associated to a lower number of assembled MTs and axonal transport defects in new born mice, which further developed into adult-onset ataxia correlated with smaller synapses at the neuromuscular junction (NMJ) (Buscaglia et al. 2020). Different tubulin isoforms therefore retain unique proprieties that preclude their interchangeability. The structural heterogeneity of MT is therefore a key determinant for their broad range of properties and functions.

It is now well established that tubulin isotypes can influence the dynamic properties of MTs. Brain-derived MTs devoid of the beta-III tubulin isotype show an increased polymerization rate, suggesting that tubulin-isotypes can play a role in regulating MT assembly and catastrophe. This isotype-driven propriety was hypothesized to be driven by a unique phosphorylation site in proximity of the C-terminal tail, suggesting that isotype-specific PTMs modulate MT dynamics (Banerjee et al. 1990). Interestingly, a wealth of *in vitro* studies has additionally shown that tubulin isotypes are key determinant for the number of protofilaments constituting the MT cylindric architecture. The existence of a different number of isotypes across species can therefore justify the species-specific MT structure.

2.2 Post-translational modifications

Post-translational modification (PTMs) consists in the covalent addition or removal of chemical groups to/from amino acid residues of a protein mediated by catalyzing enzymes. PTMs have been mostly observed on the C-terminal residues of tubulin monomers that project outside of the MT tubular structure. Given the disposition of the tubulin C-terminal tails with respect to the MT lattice, PTMs have major roles in modulating MT dynamics and function, as well as interaction with MAPs and interacting partners. The most studied MT PTMs are detyrosination/tyrosination (Peris et al. 2022), polyglutamylation (Genova et al. n.d.), polyglycylation (Wloga et al. 2009) and phosphorylation (Ori-McKenney et al. 2016). In

addition, two PTMs take place inside the lumen of MTs on the same Lysin40 residues of α-tubulin, namely tubulin acetylation (L'Hernaul and Rosenbaum 1985) and methylation (Park et al. 2016). Overall, the catalyzing enzymes for these PTMs can have either a preference for the polymerized form of MT (polyglutamylation and acetylation), or decorate equally MT and their constituting soluble dimers (phosphorylation), or selectively target unassembled dimers (tyrosination) (reviewed in: Janke & Magiera, 2020).

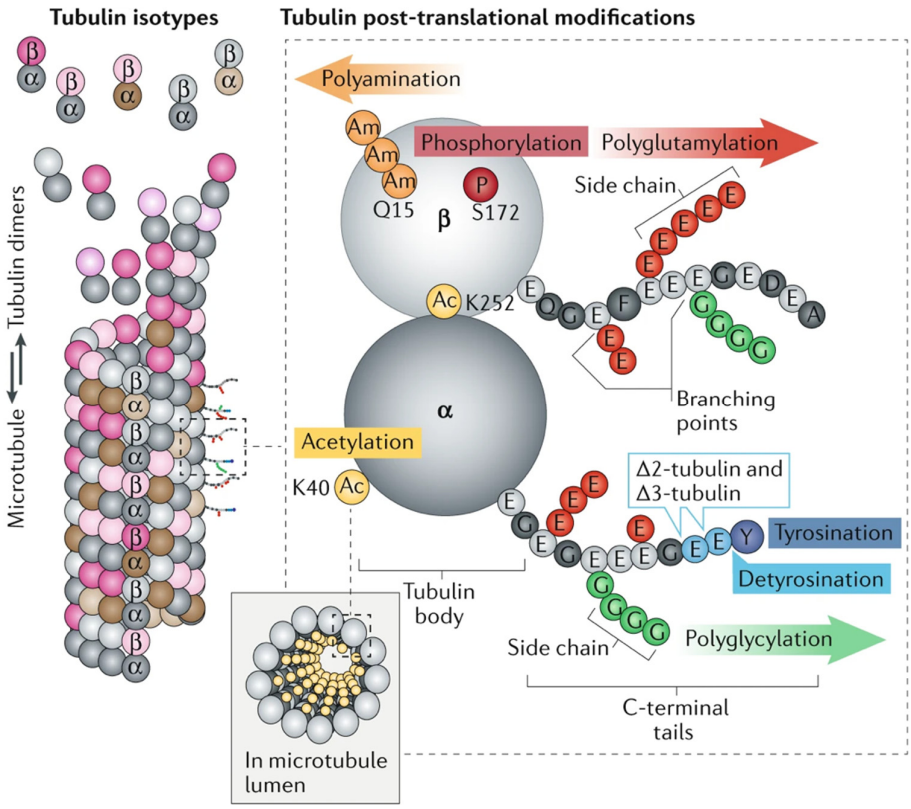

Figure 5. The *tubulin code*. The diversity of MTs is ascribed to: **1)** the existence of different tubulin genes encoding for different tubulin isotypes that can assemble heterogeneously during MT formation; **2)** broad variety of enzymatically-catalyzed PTMs localized at globular body of tubulins (as phosphorylation), at their C-terminal tails (as glutamylation, glycylation, tyrosination, and detyrosination), or inside the MT lumen (acetylation). Adapted from (Janke and Magiera 2020).

2.3 Post-translational modifications decorating the MT lattice

Tubulin detyrosination/tyrosination consists in the enzymatic removal and re-addition of a tyrosine residues at the C terminal tail of most tubulins, catalyzed, respectively, by tubulin

tyrosine ligase (TTL) and tubulin carboxypeptidase (TCP). Detyrosinated residues can be further truncated to generate truncated tubulin isotypes (Peris et al. 2022).

Tubulin polyglutamylation and polyglycylation refer to the addition of multiple glutamate residues at sites of glutamate or glycine residues of tubulin C-terminal tails, respectively. The polyglutamylases, also called tubulin tyrosine ligase-like (TTLL) enzymes, can generate glutamate chains of different length, linear or branched, and prefer either α- or β-tubulin isotypes (Janke et al. 2005).

Phosphorylation at any β-tubulin isotype at serine 172 (S172) is catalyzed either by cyclin-dependent kinase 1 (CDK1) or by Minibrain (MNB), a dual-specificity tyrosine-regulated kinase (DYRK) (Fourest-Lieuvin et al. 2006; Ori-McKenney et al. 2016).

All these PTMs that decorate the MT lattice can modulate MT dynamics, either directly or indirectly by the action of MAPs. Among the PTMs displaying such a function is tubulin phosphorylation. *In vitro* polymerization assays show a dramatic decreased tubulin polymerization in the presence of MNB, which is prevented by the expression of a kinase-dead MNB variant or a mutant form lacking its MT-binding domain (Ori-McKenney et al. 2016). Another PTM-driven mechanism controlling MT dynamics involves the activity of molecular motors. Accordingly, a growing body of evidences show that tubulin tyrosination can regulate MT dynamics by modulating MTs interactome. The mitotic centromere-associated kinesin (MCAK), a plus-end directed kinesin-13 family motor, triggers the depolymerization of taxol-stabilized tyrosinated MTs, while its activity was significantly diminished on detyrosinated taxol-stabilized MTs (Peris et al. 2009). Conversely, the dynactin subunit p150-Glued, which promotes the retrograde transport of the associated dynein motor, binds preferably to tyrosinated tubulin patches distributed at the plus-end of dynamic MTs where it exerts an anti-catastrophe activity (Lazarus et al. 2013; Wang et al. 2014).

Another function attributed to PTMs as α-tubulin tyrosination and α/β-polyglutamylation is the regulation of the processivity of a selective range of motors. Accordingly, *in vitro* assays show that the depletion of tyrosine at the tubulin C-terminal tail can decrease and increase, respectively, the processivity of kinesin-1 and kinesin-2. These evidences indicate that while kinesin-1 is sensitive to tyrosination, kinesin-2 activity relies on detyrosinated tubulin sites. The processivity of both kinesins was also improved upon addition of glutamate chains at the C-terminal tails. However, tubulins with different degrees of hyper-glutamylation can exhibit

different affinity for a given motor. Specifically, while both short (3 residues, as found in the brain) and long (10 residues) glutamate chains influence kinesin-2 motility, kinesin-1 is sensitive only to long chains. However, the kinesin-13 family motor MCAK, which is sensitive to tyrosinated MTs, does not rely on glutamate chains to exert its functions, further underlying the broad variety of MAPs that can interact with MT and their associated broad spectrum of functions (Sirajuddin, Rice, and Vale 2014).

Polyglutamylation also plays an essential role in controlling MT severing. The severing activity of spastin linearly increases with the number of glutamate residues per tubulin until a threshold value after which its activity is inhibited (Valenstein and Roll-Mecak 2016).

2.4 Post-translational modifications within the microtubule lumen

2.4.1 Tubulin acetylation

Acetylation is a well characterized PTM that occurs at the lysin 40 residues located within MT lumen. Although occurring on the same Lys40 residues, tubulin methylation, which is catalyzed by the histone methyltransferase SET-domain containing 2 (SETD2), has only been identified recently (Young Park et al. 2016).

In mice, α-tubulin N-acetyltransferase 1 (ATAT1) is the only enzyme that catalyze tubulin acetylation (Akella et al. 2010). Its activity is reversibly antagonized by the histone deacetylases (HDAC6 is the most abundant in mammalian cells), which remove acetyl groups from the lys40 residues of α-tubulin (Hubbert et al. 2002).

Acetylation of α-tubulin does not occur on cytosolic tubulin heterodimers but on already assembled and stable MTs, as the neurons develop (reviewed in: Janke & Montagnac, 2017). Accordingly, cortical neurons plated in culture for 4 hours develop growth cones whose MT network appear as tyrosinated but not acetylated. It is after 90 minutes in culture that the extended neurites anticipating the growth cones display stable and acetylated MTs (Mansfield and Gordon-Weeks 1991; Tanaka, Ho, and Kirschner 1995). The acetylation of MTs is not only developmentally regulated, but also spatially organized within neuronal dendrites and axons. Within neurites, MTs are organized in equally modified bundles that retain precise proprieties and regulate distinct biological processes. While bundles of acetylated MTs are preferentially oriented minus-end out, bundles of tyrosinated MTs have the opposite orientation, and each of these differently-modified bundles guide the trafficking of a subset

of molecular motors (Balabanian et al. 2017; Tas et al. 2017). Lastly, within a single MT, acetylation is not uniformly distributed as acetylated domains alternate to not-acetylated domains (Webster and Borisy 1989; Xu et al. 2017).

2.4.2 Enzymes contributing to tubulin acetylation

Acetylation is regulated by a stochiometric balance between the enzymatic activity of histone acetylases (HATs) and histone deacetylases (HDACs), that catalyze the acetylation and deacetylation, respectively, of the lys40 α-tubulin residues. In mammals, ATAT1 is the only MT HAT (Akella et al. 2010) and its stability is partly regulated via its interaction with the Cip/Kip family member p27Kip1 (Morelli et al. 2018). Contrarily, multiple HDACs exist and are highly conserved across species, including HDAC6, the most abundant in mammalian cells. The activity of the HAT and HDAC enzymes is reversible and tuned to an equilibrium that ensure cellular homeostasis (reviewed in: Parbin et al., 2014).

Because acetylation occurs on already assembled MTs at their inner surface, it has been widely debated how ATAT1 could enter the MT lumen to exert its activity. Despite the numerous efforts in answering this question, the debate remains open. *In vitro* experiments suggest that ATAT1 can access the MT lumen either by its extremities or through breaks and bends along its structure, depending on the stability and structural integrity of the lattice **(Figure 6 A-B).** Accordingly, ATAT1 activity was assessed either on stabilized MTs which revealed acetylation sites preferentially localized at MT entry sites, or on damaged MTs whose sparse cracks along the lattice appeared as dense sites of tubulin acetylation (Coombes et al. 2016). However, this observation is in contrast with other *in vitro* reports showing how stabilized MTs exposed to ATAT1 display a stochastic distribution of acetylation patches along the MT lattice, both at its ends and along the lattice (Ly et al. 2016; Szyk et al. 2014). It is pivotal to keep in mind that these discrepancies might be attributed to different sample preparation methods, which could affect the structural integrity of MTs and have a major impact on their biophysical proprieties, including the accessibility to its lumen. Despite the controversies, it is also possible that the two suggested models are not mutually exclusive.

In vitro experiments revealed that kinesins and dyneins exert ATP-dependent mechanical forces on the MT lattice to sustain their trafficking. These forces induce the removal of tubulin dimers from the lattice causing MT cracks that, if not efficiently repaired with a new incorporation of free tubulin dimers, it can lead to MT destruction (Andreu-Carbó et al. 2022;

Triclin et al. 2021) **(Figure 6 B)**. Motor-induced damage of the MT lattice has also been recently confirmed in a cellular system. The kinesin1-induced cracks along MTs are used by HDAC6, but not ATAT1, to enter the MT lumen and generate deacetylation domains that expand progressively from the breaking point (Andreu-Carbó et al. 2022). The motor-induced MT damage has recently been reported also in cellular systems, where the expression of a mutant kinesin form with increased motility leads to MT breakage and fragmentations (Budaitis et al. 2022). However, whether motor-induced impairment of MT integrity can occur also in physiological conditions, and whether cells retain the ability to activate the downstream self-repairing mechanisms that have been described in *in vitro* reconstituted systems, have yet to be confirmed.

Despite the debate around the MT entry points of ATAT1, a growing body of studies starts to unveil the molecular mechanism guiding ATAT1 to MTs. A first mechanism suggests that ATAT1 doesn't have an affinity only for the lysin40 residues within the MT lumen, but also for the external surface of the lattice. The recruitment on the external MT surface would thus facilitate its entry to the MT lattice (Howes et al. 2014) **(Figure 6 C)**. An alternative emerging model suggests that ATAT1 could approach MTs by hitchhiking on intra-cellular structures. ATAT1 was found to localize on clathrin-coated pits (CCPs) by interacting with its adaptor protein 2 (AP2), thus promoting tubulin acetylation (Montagnac et al. 2013) **(Figure 6 D)**. In line with these observations, a more recent study published as preprint suggests that ATAT1 localizes at mitochondria by forming a stable complex with the mitochondria outer membrane proteins mitofusin-2 (mfn2) and miro, and with the kinesin-1 motor. Once released from this complex, atat1 would catalyze MT acetylation from putative entry sites (Kumar et al. 2023) **(Figure 6 E)**. Whether other organelle subtypes can modulate the transport and localization at MT entry sites of ATAT1 is still an open question.

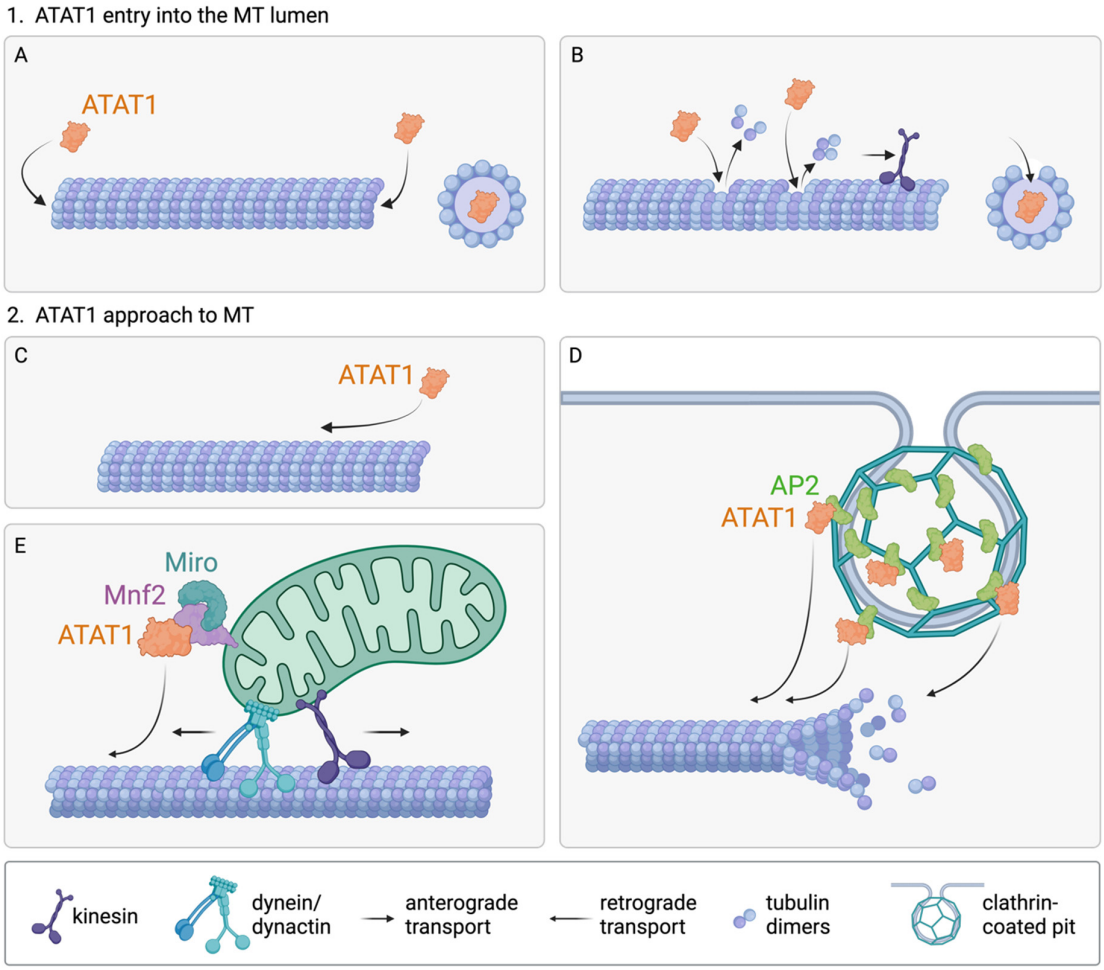

Figure 6. Mechanistic insights into the ATAT1 acetylating activity. ATAT1 might enter the MT lumen via its extremities **(A)** or through cracks along the MT lattice induced my trafficking motors **(B)**. ATAT1 might approach MTs ought to its affinity for its surface **(C)**, or as shuttled by CCPs **(D)** or trafficking mitochondria **(E)**.

Another key player that emerged to have a role in tubulin acetylation is the Elongator complex, a highly conserved macro-molecular assembly of around 850 KDa in size. It is composed of 6 subunits organized in two sub-complexes, each one present in duplicates. The core sub-complex includes the subunits 1-2-3 (Elp1–Elp3), where Elp3 represents the enzymatic core, as it harbors two highly conserved domains including the N-terminal S-adenosyl-l-methionine (SAM) domain and the C-terminal histone acetyltransferases (HAT) domain. The subunits 4-5-6 (Elp4-5-6) form the accessory subcomplex (reviewed in: Dalwadi & Yip, 2018). Elongator has been described in the nervous system. Its subunits are expressed in the mouse developing cerebral cortex (Creppe et al. 2009; Tielens et al. 2016), at synapses of the ventral nerve cord neurons in *third-insta larvae* (Miśkiewicz et al. 2011), on motile

vesicles isolated from adult mice brain (Hinckelmann et al. 2016) and on signaling endosomes isolated from ES-derived motoneurons (Debaisieux et al. 2016)

Across all eukaryotes, Elongator is primarily known as a tRNA modifier as it modifies uridines at the wobble position of tRNAs. This role is modulated by its SAM domain (Huang, Johansson, and Byström 2005). Together with the methyltransferase Alkylation repair homolog 8 (Alkbh8) and the thiouridylases cytosolic thiouridylase homolog 1/2 (Ctu1/Ctu2), Elongator is the first enzyme that contributes to the reaction cascade that catalyze the generation and addition of the 5-methoxycarbonylmethyl-2-thiouridine (mcm5s2) modification to the wobble uridine (U_{34}) of tRNAs (reviewed in: Rapino, Delaunay, Zhou, Chariot, & Close, 2017). The mcm5s2U34 modification is essential for a subset of tRNAs to decode efficiently their cognate codons and to regulate the translation of codon-biased genes (Goffena et al. 2018; Huang et al. 2005). Accordingly, loss of this modification correlates with a codon-biased ribosome pausing and triggered aggregation of translated proteins, leading to impaired protein homeostasis and cellular fitness (Laguesse et al. 2015; Nedialkova and Leidel 2015). Further insights into this mechanism reveal that the U_{34}-mediated control of protein output is not only determined by the codon content of an mRNA but also by the presence of hydrophilic motifs within the translated protein (Rapino et al. 2021).

A study performed in *Saccharomyces cerevisiae* showed that the deletion of each single subunit of the complex leads to similar gene expression patterns, suggesting that all the constitutive subunits are essential for the activity of the complex (Krogan and Greenblatt 2001). In agreement, although the catalytic activity of the complex resides in the elp3 subunits, brain tissue and fibroblasts from FD patients, which bear a mutation in the Elp1/IKAP gene that results into aberrant splicing, show reduced levels of mcm5s2U modifications (Karlsborn et al. 2014).

Ought to its HAT domain, Elongator is also known for its acetylating activity and for the broad range of substrates it targets. As it was found to interact with the RNA polymerase II (Kim, Lane, and Reinberg 2002), Elongator was soon identified a transcriptional regulator of multiple proteins, many of which are also important for the development and maintenance of the nervous system. Among these are the anti-apoptotic heat shock protein 70 (HSP70) (Han et al. 2007), and regulators of cell migration and actin cytoskeleton (Close et al. 2006; Creppe et al. 2009; Tielens et al. 2016).

In *Drosophila*, Elongator catalyzes the acetylation of Bruchpilot (BRP), an integral protein at presynaptic active zones, to regulate the recruitment of synaptic vesicles at pre-synapses and ensure a proper neurotransmitter release (Miśkiewicz et al. 2011).

Lastly, Elongator was suggested to contribute to the acetylation of α-tubulin. Its subunits were found to co-precipitate with α-tubulin and the overexpression (OE) of elp3 but not of a HAC-defective variant was found to increase tubulin acetylation levels (Creppe et al. 2009). As a reduction in tubulin acetylation via the expression of tubulin K40A (dominant negative tubulin form that cannot be acetylated) induces the same migratory defects observed in the absence of Elongator, Elongator was suggested to modulate the migration and branching of cortical projection neurons partly via MT acetylation (Creppe et al. 2009).

2.4.3 Functions of tubulin acetylation

Given the peculiarity of tubulin acetylation, multiple studies tried to elucidate its biological function at a molecular level. Today, it is widely accepted that tubulin acetylation confers MTs stability, resistance to bending and a longer lifespan. Firstly, by weakening protofilament interactions, tubulin acetylation increases MTs flexibility (Portran et al. 2017) and resistance to mechanical forces induced by actomyosin contractions, thus preventing downstream breakage (Xu et al. 2017). Secondly, by constraining MT architecture and dynamics, tubulin acetylation can regulate the stability of MTs (Wei et al. 2018). ATAT1-depleted hippocampal neurons lacking tubulin acetylation do not only display increased MT debundling at nascent branching points along axons and increased MT invasion at growth cones, but also increased dynamics. Accordingly, an increased MT growth and increased catastrophe frequency decrease the growth lifetime of MT plus-ends (Wei et al. 2018). Additionally, MEC-17 (ATAT1 paralog in *C. elegans*) mutants displayed high degree of MT instability due to enhanced MT dynamics which lead to axonal degeneration, phenotype that could be rescued by administration of a MT-stabilizing drug (Neumann and Hilliard 2014). These evidences favor a model in which acetylation would confer stability to MTs.

While it was originally believed that the trafficking of motors is solely determined by MT polarity, a groundbreaking study showed for the first time that PTMs including acetylation and polyglutamylation play an essential complementary role in controlling motor transport. *Reed at colleagues* performed a battery of *in vitro* studies using MTs devoid of specific PTM

sites and showed that loss of α-tubulin lysin40 sites significantly deplete the MT binding capacity to kinesin-1 motors (Reed et al. 2006).

A growing number of *in vivo* studies correlated tubulin acetylation to transport dynamics by rescuing the transport defects associated to a broad spectrum of neurodegenerative diseases with a pharmacological or genetic manipulation of the deacetylating or/and acetylating enzymes (d'Ydewalle et al. 2011; Dompierre et al. 2007; Godena et al. 2014; Guo, Stoklund Dittlau, and Van Den Bosch 2020; Kim et al. 2016). Pharmacological inhibition via trichostatin A (TSA) of histone deacetylases including HDAC6 was shown to increase tubulin acetylation, the recruitment of motors on the MT, and the transport dynamics of BDNF-expressing vesicles (Dompierre et al. 2007). TSA treatment proved out to rescue the transport defects of BDNF-vesicles displayed in mouse striatal cells expressing the Huntington's Disease (HD)-associated htt mutations (Dompierre et al. 2007). *Drosophila* motor neurons expressing LRRK2 variants linked to Parkinson's Disease (PD) show defects in mitochondria axonal transport which can be rescued by promoting tubulin acetylation, either via broad or selective inhibition of the histone deacetylases or via the overexpression of ATAT1 (Godena et al. 2014). Charcot-Marie-Tooth disease 2F (CMT2F) and distal hereditary motor neuropathy 2B (dHMN2B) are examples of disorders of the peripheral nervous system that equally arise from mutations in the heat-shock protein (HSPB1) gene and present with impaired axonal transport dynamics. Dorsal root ganglion (DRG) neurons isolated from adult mice expressing a disease-associated HSPB1 mutation (d'Ydewalle et al. 2011), as well as motor neurons derived from iPSCs of CMT2F and dHMN2B patients (Kim et al. 2016), display impaired mitochondria axonal transport dynamics and reduced tubulin acetylation, phenotypes that could be reversed upon HDAC6 inhibition. Similarly, tubulin acetylation and mitochondria axonal transport defects associated to mitofusin-2 (mfn2) mutations linked to Charcot-Marie-Tooth type 2A (CMT2A) could be rescued by HDAC6 inhibitors (Kumar et al. 2023). Lastly, pharmacological inhibition of HDAC6 was show to restore the transport defects of mitochondria and ER-derived vesicles in iPS-derived motor neurons isolated from Amyotrophic lateral sclerosis (ALS) patients bearing mutations in the FUS gene (Guo et al. 2017).

Interestingly, the contribution of tubulin acetylation in the regulation of axonal transport dynamics also emerged from the study of $p27^{Kip1}$ as regulator of ATAT1 stability. Loss of $p27^{Kip1}$ in mice or of its ortholog Dacapo in *Drosophila* impairs axonal transport dynamics,

which can be restored either via HDAC6 inhibition or ATAT1 overexpression (Morelli et al. 2018).

To investigate the importance of tubulin acetylation at a tissue level, mice with germline deletion of ATAT1 were generated and characterized. Atat1 expression was lost in a broad variety of tissues but most abundantly in the brain, testis, renal pelvis and gastrointestinal tract. Surprisingly, loss of ATAT1, and therefore of tubulin acetylation, doesn't affect the embryo viability but correlates only with a slightly deformed dentate gyrus (Kim et al. 2013), with enlarged lateral ventricles due to hypoplasia of the septum and striatum and impaired neuronal migrations to these areas (Li et al. 2019). Loss of ATAT1, and therefore tubulin acetylation, has also been correlated with cortical development alterations. Downregulation of ATAT1 expression in cortical progenitors impairs the morphology and migration of cortical projection neurons, defects that could be reduced upon HDAC6 knockdown or OE of tubulin K40Q, variant that mimics tubulin acetylation (Li et al. 2012). Furthermore, ATAT1-depleted mice showed callosal projections neurons, the upper layer cortical neurons whose axons project through the corpus callosum to the contralateral somatosensory cortex, with increased overbranching (Wei et al. 2018). A conditional gene deletion approach was instead adopted to selectively investigate the role of tubulin acetylation in sensory neurons. Conditional Atat1 KO (cKO) mice displayed decreased touch sensation. This observation was associated to an increased stiffness of the deacetylated sensory neurons, a decreased sensitivity of their expressed mechanoreceptors and downstream evoked current (Morley et al. 2016). Despite the various defects identified, after performing a broad battery of behavioral tests, loss of ATAT1 was only found to induce an anxiety-like behavior (Kalebic, Sorrentino, et al. 2013; Wei et al. 2018).

2.4.4 Transport-associated diseases

Given the importance of axonal transport in sustaining the morphology and activity of neurons, defects in this intracellular process have been widely correlated to multiple neurological disorders. Mutations in all the components of the transport machinery, including MTs, molecular motors, adaptors and cargos can lead to MT instability, loss of motor binding to MTs, and impaired motor recruitment of their associated cargos. These phenotypes have been widely correlated to a broad range of neurodegenerative diseases.

The amyloid precursor protein (APP) and presenilin1 (PSEN1) are adaptor proteins that modulate kinesin recruitment of APP synaptic vesicles (Szpankowski, Encalada, and Goldstein 2012), and their mutations, which have been widely linked to familial AD, correlate with axonal transport defects (Calkins et al. 2011; Pigino et al. 2003). Equally, pathological post-translational modifications in the kinesin heavy chain (KHC) subunit or mutations in its adaptor KIF5A have been correlated to a plethora of other neurodegenerative diseases, including hereditary spastic paraplegia (HSP) (Liu et al. 2014; Schule et al. 2008), amyotrophic lateral sclerosis (ALS) (Nicolas et al. 2018), and Charcot- Marie Tooth disease (Liu et al. 2014). CMT has additionally been linked to mutations in the DYNC1H1 dynein subunit and downstream retrograde transport abnormalities (Zhao et al. 2016). Impaired organization of MTs or misfunctioning of their MAPs can lead to an impaired binding of motor proteins and cargos, and these defects have additionally been described in multiple disorders. For example, most of the HSP cases are linked to mutations in the MT-severing enzyme spastin which inhibit fast axonal transport dynamics and impair the intracellular distribution of organelles (Leo et al. 2017). Mutations in tau, another MAP with a key role in MT dynamics and motor recruitment onto MTs, correlates with axonal transport deficits. The tau mutation associated to FTD results in tau hypophosphorylation, decreased tau binding to MTs and impaired mitochondria axonal transport (Rodríguez-Martín et al. 2016).

Altered levels of tubulin acetylation and downstream axonal transport defects have also been widely correlated to a broad spectrum of neurodegenerative diseases, including HD (Dompierre et al. 2007), PD (Godena et al. 2014), CMT2F and dHMN2B (d'Ydewalle et al. 2011; Kim et al. 2016), CMT2A (Kumar et al. 2023) and ALS (Guo et al. 2017). In all these cases, HDAC6 inhibitors restore tubulin acetylation level and improve transport defects, further strengthening the link between this PTM and the diseases pathophysiology.

3. Local translation

3.1 Introducing local translation: what and why

Neurons are highly polarized cells, with long processes namely dendrites and axons that extend from the cell soma, defining subcellular compartments with distinct molecular identity and functions. Within every and each one of the neuronal sub-compartments (soma/dendrites/axon) we can identify domains (AIS, synapses, boutons) as well as

macromolecular complexes and structures (ER, Golgi, mitochondria, organelles and ribosomes) that are heterogeneously distributed according to their functions. In particular, the identification within axons and synapses of one of these structures has challenged one of the cores believes of molecular biology. The identification of ribosomes, the machinery that sustain protein synthesis, within these peripheral regions lead to the discovery that proteins are not only synthesized within the cell soma but can also be translated far away from this site through a mechanism defined as *local translation*. Since then, a plethora of studies started to investigate the advantages associated to a localized translation of proteins and to identify its regulatory mechanisms.

Accordingly, local translation is a highly efficient system adopted by neurons to enable a quick and spatially restricted supply of proteins when most needed. Through this system, neurons can efficiently remodel the proteome of a given sub-compartment to respond efficiently to environmental stimuli or to comply with one of their biological needs.

The translation of peripherally localized mRNAs has been so far described in multiple neuronal subtypes, including hippocampal (Glock et al. 2021; Hafner et al. 2019; Perez et al. 2021; Tushev et al. 2018; Younts et al. 2016) and dopaminergic (Hobson et al. 2022) neurons, as well as retinal ganglion (RGC) cells (Cagnetta et al. 2018; Cioni, Koppers, and Holt 2018; Shigeoka et al. 2016; Wong et al. 2017). In these polarized cells, proteins were found to be synthesized throughout their branched ramifications, not only along neurites but also within the most peripheral sub-compartments including synapses (Hafner et al. 2019; Oostrum et al. 2023) and growth cones (Leung et al. 2018; Rangaraju, Tom Dieck, and Schuman 2017; Zivraj et al. 2010). The subcellular localization of mRNAs however appears as a highly conserved process throughout evolution, as it was identified not only in other non-neuronal cells within and outside the central nervous system but also in fungi and budding yeasts. Among the glial cells, local translation events were identified along the astrocyte processes (Sakers et al. 2017) and their terminal endfeet contacting blood vessels (Boulay et al. 2017) or neuronal synapses (Sakers et al. 2017). In addition such events have also been reported within the myelinating sheets oligodendrocytes form around axons (Torvund-Jensen et al. 2014), the microglia processes (Vasek et al. 2021) and endfeet of radial glia cells (Pilaz et al. 2016). Outside of the central nervous system, mRNA transport and its peripheral translation were identified as key process for the embryonic patterning of *Drosophila* oocytes (Lasko 2020), in

migrating fibroblasts (Jung et al. 2014) and tumorigenic human cell lines (Popovic D, Nijenhuis W, Kapitein C L 2020; Yan et al. 2016).To reach a given peripheral site where they will be ultimately translated, transcripts need to be transported from their site of transcription, the nucleus. There are multiple advantages from transporting mRNAs for their local translation than transporting proteins from point to point within the cell: 1) temporal and spatial controlled expression of proteins; 2) quantitative advantage under the protein output perspective; 3) qualitative control of the newly translated proteins.

First, the transport and localization of mRNAs along neurites and at synapses ensure that proteins can be translated only where needed. In this way, neurons can spare energy by preventing an overproduction of proteins for a heterogeneous distribution everywhere in the cell. Furthermore, this transcript relocation system favors a temporal control of translation events, as localized mRNAs start to be translated only when mostly needed, in response to environmental stimuli or cellular activity. Thanks to this ability, cells can adjust their proteome quickly and in an energetically advantageous manner.

Secondly, the local translation of an mRNA also retains a quantitative advantage. In fact, as a single mRNA can translate multiple copies of the correspondent protein (Biever et al. 2020), a single mRNA can contribute significantly to a local protein pull of that given transcript. The protein output obtained from the long-distance transport of a single mRNA is more abundant than the transport of a single protein to a given localization. Lastly, local translation ensures the structural and functional integrity of newly translated proteins where and when it's mostly needed. Accordingly, with this mechanism a newly synthetized protein doesn't burn part of her lifetime elsewhere, for example while being transported.

As developing and maturing neurons need to constantly remodel their proteome to respond as efficiently as possible to environmental stimuli and to comply with their energetic needs, local translation becomes a process of extreme importance thorough the life of a neuron. A broad range of proteins were found to be translated during axonal growth, branching, synaptic formations, and activity. In RGC axons, hotspots of β-actin mRNAs reside at sites of branch emergence and their localized translation is important for their axonal harboring (Wong et al. 2017). In mouse hippocampal neurons, the recruitment at pre-synapses of the synaptosomal-associated protein 25 (SNAP25) transcript and its localized translation contribute to the assembly of pre-synaptic sites (Batista, Martínez, and Hengst 2017).

Additionally, presynaptic translation is essential for an induced long-term plasticity of GABA release in mature hippocampal interneurons (Younts et al. 2016). Local translation has been recognized a role also at post-synapses, as the dendritic-localized translation of synaptic related receptors such as the calcium/calmodulin-dependent protein kinase 2 alpha (CaMK2a) and mGluR has been linked to the modulation of synaptic plasticity and learning (Huber, Kayser, and Bear n.d.; Miller et al. 2002).

3.1.2 Mechanisms regulating mRNA transport

To be spatially distributed, mRNAs need to be directed through two main mechanisms that started to be elucidated only recently, namely co-translational targeting and motor-mediated transport.

Co-translational targeting describes the process by which newly-translated secreted proteins (so defined as destined to be either secreted extracellularly or incorporated within ER, Golgi, organelles or plasma membrane) are directed to the ER. In detail, translating peptides retain a specific amino acid targeting sequence that is recognized by the signal recognition particle (SRP) and guided to its cognate receptor expressed on the ER for ER internalization (Jan, Williams, and Weissman 2014) **(Figure 7 D)**.

Other transcripts can be transported to peripheral compartments through an ATP-dependent and motor-driven mechanism in the form of ribonucleoprotein (RNP) granules. RNP granules are membraneless structures incorporating mRNAs, RNA-binding proteins (RBPs) and ribosomes that form by phase-separation from the cytoplasm into condensates with liquid-like properties (reviewed in: Formicola, Vijayakumar, & Besse, 2019). Accordingly, electron microscopy analysis on RNA granules isolated either from mouse cortical cultures or P5 rat whole brain reveal that granules are RNAse-sensitive and display a compact morula-like structure, where ribosomes constitute their functional unit (El Fatimy et al. 2016; Kipper, Mansour, and Pulk 2022). These granules are translationally repressed, as unable to incorporate radioactive amino acids and therefore initiate translation (Krichevsky and Kosik 2001). Very low amount of the leucine tRNA, the translation initiation factors eIF4E and 4G and the elongation factor eEF2, as well as of the poly A binding protein PABP1 were identified. On the contrary, RBPs with translation inhibitory proprieties as FMRP were abundant (Anadolu et al. 2022; Krichevsky and Kosik 2001). However, upon KCl-induced depolarization, RNP granules reorganize into less compact structures, enabling polysomes to extend out of

the granule for translation initiation (Krichevsky and Kosik 2001). Although the general model describes RNA granules as incorporating paused/stalled polysomes, ribosome footprint studies of RNP granules identified not only transcripts that are preferentially translated by polysomes, but also by monosomes (Anadolu et al. 2022). Among the most abundant mRNAs are the somatodendritic CaMKII, trkB and NMDAR1 (Krichevsky and Kosik 2001) and the cytoskeleton proteins beta-actin, Tubb2b and map1b, expressed both within dendrites and axons (Anadolu et al. 2022).

How these granules undergo long-distance transport along neurites for their peripheral distribution and localized translation has been the focus of multiple groups. Immunoprecipitation studies started to show that RNAse-sensitive granules enclosing a subset of mRNAs and RBPs associate to motors of the kinesin superfamily (Dictenberg et al. 2008; Kanai, Dohmae, and Hirokawa 2004). Through their binding to motors, RNP granules can undergo a MT-dependent bidirectional motion for their axonal distribution and functional roles at peripheral sites (Medioni et al. 2014). This transport mechanism was reported for the RBP fragile X mental retardation protein (FMRP), which interacts with kinesins through its C-terminal domain (Dictenberg et al. 2008) and with the dynein-dynactin complex through the adaptor protein BicD (Bianco et al. 2010). Loss of FMRP was found to reduce the stimuli-induced bidirectional transport and dendritic distribution of its target CaMKIIa mRNA, impairing dendritic spine morphology (Dictenberg et al. 2008). Similarly, the bidirectional transport of the RBP Imp enables the axonal distribution of the associated chickadee mRNAs, to ultimately modulate axonal growth and branching (Medioni et al. 2014).

Together with transported RNP granules, other examples of membrane-less assemblies are stress granules (SGs) and processing bodies (PBs), which generate under stress conditions. The assembly of these granules is part of the integrated stress response mechanism set up by the cell to restore cell homeostasis. Their assembly is triggered by the phosphorylation and therefore silencing of the translation initiator eIF2alpha, followed by the recruitment and agglomeration of mRNAs, RBPs, ribosomes as well as pro-apoptotic molecules. Within these granules, its constituents are protected from stress-induced damage and maintained silenced, to prevent their translation initiation or initiation of apoptosis (Thomas et al. 2011). However, the advent of single molecule imaging techniques has started to challenge the idea that only silenced transcripts can be found within SGs. By using the SunTag technology which

enables the live imaging tracking of a transcript undergoing active translation (Yan et al. 2016), translating mRNAs have been visualized on SGs, seldomly transitioning from these granules to the cytosol, confirming the dynamic state of these structures (Mateju et al. 2020).

3.1.2 RNA binding proteins regulating mRNAs transport and localized translation

In the last 20 years, a major focus has been directed to the study of the β-actin mRNA, shedding light on the mechanisms regulating its subcellular distribution and aggregation into RNP granules. By providing a broader understanding of how, when, and why this transcript is associated to molecular motors and regulatory proteins, many groups established the foundations of these intracellular mechanisms. This field is now extending its focus to hundreds of other mRNAs, thanks to the technological advances based on both sequencing and imaging screening approaches.

The fate of mRNAs is defined by the concurring or subsequent binding of multiple RBPs to cis-acting regulatory motifs within the untranslated regions (UTRs) of mRNAs. Through this binding, RBPs regulate their translation state, as well as modulate the recruitment of motor proteins to promote the MT-directed transport of mRNAs. A given RBP can, however, target multiple transcripts. This propriety confers RBPs a moderate adaptability, and, consequently, allows neurons to reply quickly and efficiently to stimuli. One of the first identified adaptors of β-actin mRNA is zipcode binding protein 1 (ZBP1), which recognize and bind to the 54 nucleotide-long regulatory zipcode region within the transcript's 3'UTR (Ross et al. 1997). Through co-localization and co-fractionation studies, ZBP1 was found to work in joint with other interactors, namely Htt and HAP1, to bind to the zip-code region of β-actin mRNA. Their association to KIF5A and the cytoplasmic dynein regulates the transcript's bidirectional MT-dependent motion (Ma et al. 2011). Furthermore, a regulatory mechanism described for both β-actin and β-2B tubulin mRNAs assigns the adenomatous polyposis coli (APC) protein the propriety to tether the APC-binding motif found within their 3'UTRs to the KAP3-loaded KIF2 (also called KIF3A/B) motor and regulate their long-distance transport. Thanks to its preferential affinity for β-tubulin mRNA whose expression level is 10 times lower than β-actin mRNA, APS efficiently regulates the trafficking of both transcripts (Baumann et al. 2020). Another transcript found to interact with a set of RBPs for its dendritic distribution is Rac1. While TDP43 and FMRP are essential to modulate its anterograde transport and distribution into dendritic spines, its interaction with Staufen regulates its retrograde trafficking. TDP43 is

also a translator repressor, that maintains Rac1 granules translationally silenced during their transport for their ultimate release at spines, sites of local translation (Chu et al. 2019).

A growing body of evidences is now supporting a model describing a heterogeneous population of RNP granules with the shared role of maintaining the enclosed transcripts at a translationally repressed state. The isolation of two different granule subtypes expressing either Staufen2 (Stau2) or Barentsz (Btz) revealed that only one third of their protein interactome was shared. This list includes FMRP, Pur-α and DDX6 which all contribute to RNA localization, and many translational repressors including ZBP1 and FMRP. Their heterogeneity was also found at the mRNA level, as some transcripts were common in both granules (Lypla1) or enriched in one of the two (Arc and Linkk1 mRNAs in Btz granules while CaMKII-alpha mRNA in Stau2 granules) (Fritzsche et al. 2013). Accordingly, endogenous CaMKII-alpha, MAP2 and Sept7 mRNAs distribute along dendrites with a not-overlapping pattern, suggesting that they are sorted in different granule types for their long distance transport (Tübing et al. 2010).

Despite their heterogeneity, RNP granules are all believed to enclose translationally silent mRNAs. Dendritic RNP granules were found to express the cap binding protein 80 (CBP80), component of the cap binding complex, and Y14/RBM8A, component of the exon junction complex (EJC), which together associate to a target mRNA for its nuclear export and agglomeration into RNP granules. As their disassociation from the transcripts occurs upon translation initiation, their identification within granules indicates that the sequestrated transcript are translationally silent (Wang et al. 2017). While most granules are translationally repressed, it is clear that RNP granules also retain the machinery required for translation initiation. Half of the proteins identified within RNP granules isolated from mouse brain corresponded to ribosomal subunits (El Fatimy et al. 2016). These proteins were found together with the ATP-dependent helicase of the DEAD box family (DHX30), which contribute to the mRNAs unwinding, and the translation initiation factors eIF3b and eIF3c (El Fatimy et al. 2016). Furthermore, the advent of new imaging technologies that enable the live imaging tracking of a given transcript and its translation dynamics revealed that β-actin mRNA granules can undergo active translation along dendrites (Wu et al. 2016). These data suggest that the heterogeneity in protein and transcript content found across different RNP granules can also be extended to their translational proprieties. It can therefore be speculated that

their unique identity could underline different transport dynamics and functions, to ultimately regulate the fate of different transcripts.

3.1.3 External cues driving mRNAs transport and local translation

The fact the RNP granules are highly dynamic structures that can quickly rearrange their architecture, the fact that they accommodate RBPs whose activity can be quickly adjusted by PTMs, and the fact that they are associated to motor complexes, make these condensates prone to respond rapidly and efficiently to environmental fluctuations. Extrinsic cues or intrinsic events can trigger their subcellular relocation and structural remodeling, to provide peripheral compartment with a newly synthesized pull of proteins, needed to sustain a given cellular response.

Given the importance of β-actin for the formation and stabilization of spines (reviewed in: Lei, Omotade, Myers, & Zheng, 2016), multiple studies converged their attention to its transcript, with the aim on unravelling the factors triggering its peripheral localization and local translation. β-actin mRNA, along with peripherin and vimentin transcripts, owe their axonal localization to the neuronal exposure to neurotrophic factors (NGF, BDNF). This mechanism is transcript-specific, as Uch-L1 (neurodegenerative-associated protein), grp78/BiP and HSP70 (ER proteins) were not sensitive to these factor's gradients (Willis et al. 2005). A given transcript, however, can respond to a broad range of stimuli that can act in coordination or individually to elicit a given cellular response. Accordingly, neurotrophin-3 (NT-3) can also elicit a ZBP1-dependent distribution of β-actin mRNA within growth cones of cultured neurons, effect that was inhibited upon expression of antisense oligonucleotide to the beta-actin zipcode region (Zhang et al. 2001). Furthermore, the transport within growth cones of β-actin mRNA and its co-transported regulatory protein Vg1RBP (homolog of the zipcode binding protein 1, ZBP1, in mouse neurons) can also be modulated by Netrin-1 for its distribution and localized translation (Leung et al. 2006). Glutamatergic signal and activity patterns that define neuronal maturation have also been identified as priming events for mRNAs trafficking and for their translation at peripheral sites. A photochemical activation of glutamate receptors at dendritic spines to elicit a localized excitatory post-synaptic potential (EPSP) triggers the trafficking to and local recruitment at spines of beta-actin mRNAs, where they undergo localized translation (Yoon et al. 2016). However, KCl-induced depolarization has been shown to correlate not only with an increased dendritic localization of ZBP1 granules

containing β-actin mRNAs, but also of Rac1 and map1b mRNAs associated to TDP43 (Chu et al. 2019; Tiruchinapalli et al. 2003). More recently, neuronal activity elicited either via KCl-induced depolarization or tetradotoxin (TTX)-withdrawal paradigm was correlated to cycles of Arc1 mRNA transport to selective dendritic domain enriched in spines, forming local hubs of locally translated Arc1 proteins induced by eIF4E (Das et al. 2023). These data suggest that the cue-driven distribution of mRNAs is regulated in space and time and that this regulatory mechanism is essential to remodel their local proteome and to sustain their localized functions.

3.1.4 Ribosome transport

Ribosomes have been widely identified along neurites (Hafner et al. 2019; Shigeoka et al. 2016) and described as translationally active both in form of monosomes and polysomes (Biever et al. 2020). Their transport can be modulated via multiple mechanisms: 1) via motor-based transport; 2) as part of RNP granules; 2) via association to membrane-bound organelles. In *C. elegans*, the axonal distribution of ribosomes is regulated by UNC-16, adaptor protein for the kinesin-1-mediated cargos transport, and rely on microtubule proteins, as their mutated forms impair the ribosomal axonal distribution (Noma et al. 2017). Ribosomes also constitute the structural units of RNP granules (El Fatimy et al. 2016) which undergo a MT-based and motor-driven bidirectional transport (Dictenberg et al. 2008; Kanai et al. 2004; Medioni et al. 2014). However, while ribosome-containing RNP granules can be transported by trafficking lysosomes (Kipper et al. 2022; Liao et al. 2019), polysomal chains have been identified on ER-derived ribosome-associated vesicles (RABs) where they arrange into spiral-like structures (Carter et al. 2020). The presence of ribosomes along neurites and their association to transcript-enriched granules allows neurons to modulate their proteome with a spatially restricted and temporally controlled manner.

3.2 mRNAs translation coupled to membrane-bound organelles

While on the one hand RNP granules can undergo bidirectional transport along the MT network through their direct interaction with the transport machinery, on the other hand they can also tether on membrane bound organelles, such as the ER, mitochondria, lysosomes, and endosomes.

3.2.1 Endoplasmic Reticulum

The ER is a membrane-bound organelle with a unique architecture that distributes throughout the entire cytoplasm of a cell, including the peripheral compartments of neuronal cells. The "rough" domain has a high density of ribosomes at its surface and is primarily localized around the nucleus where it organizes in a network of folded sheets. The "smooth" ER, ribosome-pour, extends to the peripheral compartments of a cell forming a network of interconnected tubules, seldom forming cisternae **(Figure 7 A)**. Their axonal localization is due to their bidirectional movement along MT modulated by two independent mechanisms: 1) via the formation of the TAC complex, generated from the interaction between the ER protein STIM1 and the MT-associated protein EB1; in this way, the ER is anchored to MTs and moves according to their growth or retraction **(Figure 7 B)**; 2) via the interaction with motor proteins which modulate the bidirectional sliding of the associated ER along the MT network (reviewed in: Öztürk, O'Kane, & Pérez-Moreno, 2020) **(Figure 7 C)**.

Among its broad range of functions, the ER is also a key player in the secretory pathway. This pathway refers to the cellular process that involves the transport on newly synthesized proteins and lipids thought the endoplasmic reticulum (ER) and Golgi apparatus to their ultimate intra- or extracellular localization (reviewed in: Sicari, Igbaria, & Chevet, 2019). It was in the contest of the secretory pathway that the organelle-associated translation was first described in non-neuronal cells.

One of the most characterized mechanisms of ER-associated translation involves the signal recognition peptide (SRP) which recognizes signal peptides at the N'-terminal sequence of translating proteins and direct it to its cognate receptor expressed on the ER. Upon binding, the associated mRNA/ribosomes complex is translocated to the Sec translocon, a protein conducting channel located on the ER membrane, for its entry into the ER (Zhang and Shan 2014) **(Figure 7 D)**.

ER-couple translation can also be modulated by the synergistic activity of cytoplasmic RBPs and adaptor proteins associating to newly translated polypeptide chains. This mechanism was described in a range of non-neuronal human cell lines for the CD47 mRNA, which encodes for a plasma membrane protein belonging to the immunoglobulin superfamily. The binding at uridine-rich domains within its 3'UTR by the RBP TIS11B induce the formation of reticular peri-nuclear assemblies that intertwine with the ER to form the TIGER (TIS granule-ER) domain (Ma and Mayr 2018). Within these granules, mRNAs can undergo active translation. Thanks

to the further binding of the RBP Hur (ELAVL1) onto the 3'UTR of the CD47 mRNA, recruitment of SET which targets the newly translated CD47 C-terminus, and mobilization of RAC1 which triggers the peptide mobilization to the ER membrane, the CD47 protein is thereafter trafficked to the ER via the Sec translocon. TIS granules are enriched with several transcripts including BCL2, CD274, as well as other proteins as HSPA8, a chaperone with important role for the folding of newly synthesized proteins (Berkovits and Mayr 2015; Ma and Mayr 2018) **(Figure 7 E)**.

Whether ER-associated translation occurs along neurites is still an open question. Recent findings show that mRNA-associated ribosomes interact with the ER to promote local translation, as shown by the decreased ribosomal distribution and translation events along axons upon disruption of the ER architecture (Koppers et al. 2022). This interaction is modulated by the binding of ribosomes to their cognate receptor p180 and is mRNA dependent. Accordingly, while pulldown assays for p180 identified ribosomal proteins as major interactors, their detection decreased significantly when RNA digestion was performed before the assay (Koppers et al. 2022) **(Figure 7 F)**. This study paves the way to the idea that translation is also coupled to axonal ER but given the dynamicity of this organelle there's still a lot to be elucidated on the mechanisms regulating this process and its functional outcomes at a subcellular level. Interestingly, ER-derived vesicles identified along dendrites display on their outer membrane clusters of ribosomes arranged in a spiral-like fashion that resemble polysomal assemblies (Carter et al. 2020). Together with the ribosome-associated ERs trafficking along axons, these ribosome-associated vesicles (RAVs) can therefore serve as mobile platform for the translation machinery contributing to a spatial regulation of local translation **(Figure 7 F)**.

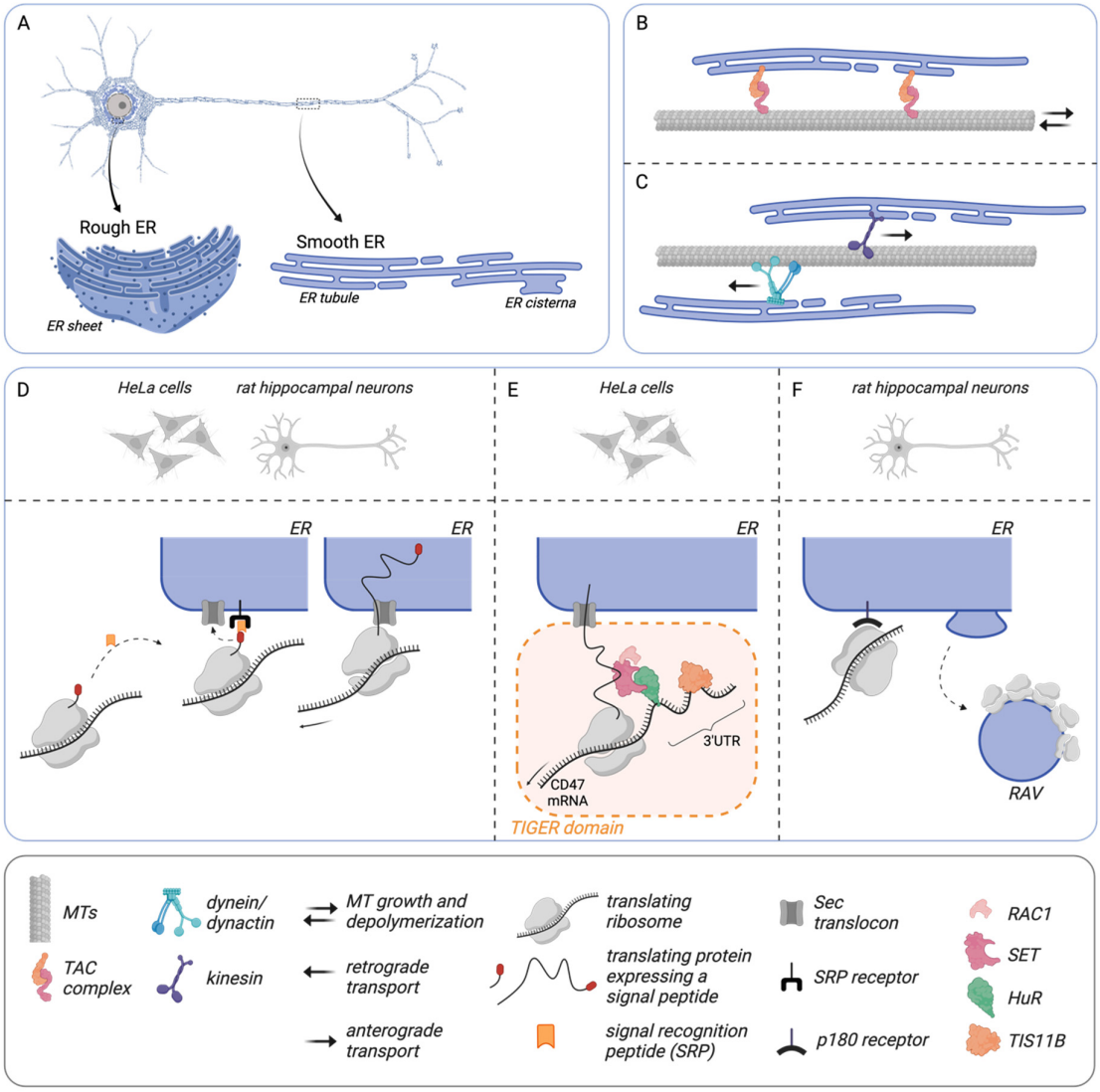

Figure 7. The ER, its transport dynamics and associated translation. (A) The ER distributes within the entire volume of a neuron and differentiates into the ribosome-rich rough ER in the cell soma, and the smooth ER composed of tubules and cisternae within neurites. Panel **(A)** was adapted from (Öztürk et al. 2020). **(B, C)** Mechanisms regulating the ER motility. The ER can either bind onto MTs and follow its dynamics **(B)**, or associate to molecular motors which regulate their bidirectional motion. **(D-F)** The ER and its associated translation events. Translating peptides can be recognized by the SRP and directed to the ER for their internalization **(D).** TIGER domain-associated transcripts can undergo active translation to be then trafficked to the associated ER for their internalization **(E).** Ribosomes localize on ER-derived vesicles, as well as on the ER outer membrane while undergoing active translation **(F)**.

3.2.2 Mitochondria

Mitochondria are exceptional organelles that play a broad range of biological functions and are therefore essential to sustain neuronal development and activity. They cover crucial roles in metabolism and calcium homeostasis, as they regulate ATP production, lipid biogenesis, ROS production and calcium clearance. These organelles distribute throughout every neuronal subcompartment, ought to their dynamic and remodeling architectures able to undergo fusion and fission, and to their association to the transport machinery (reviewed in: Rangaraju, Lewis, et al., 2019). Mitochondria also localize at synapses where they provide the energy supply needed to sustain local translation events during synaptic plasticity (Rangaraju, Lauterbach, and Schuman 2019) **(Figure 8 A)**. Whether mitochondria contribute to local translation only by providing the required energy supply (Rangaraju, Lauterbach, et al. 2019) or also by other means has not been elucidated yet. Recent insights come from studies that started to elucidate the role of mitochondria as shuttling platform for translating mRNAs (Harbauer et al. 2022).

Mitochondria proteins are generally nuclear-encoded and have a very short half-life. For this reason, it becomes very challenging for these proteins to reach peripheral compartments without being previously degraded. To overcome these limitations and guarantee an efficient supply and turnover of their constitutive proteins, mitochondria can shuttle mitochondrial transcripts on their outer membrane, thus providing a platform for their active translation. Accordingly, a compelling number of combined transcriptome and translatome datasets detected nuclear-encoded mitochondria mRNAs engaged in translation along neurites and at synapses (Glock et al. 2021; Hobson et al. 2022; Shigeoka et al. 2016). A pioneering study that supports this model used a *proximity-specific ribosomal profiling technique* to characterize translation events at a subcellular compartment resolution, e.g. at mitochondria. This technique consists in the biotinylation of ribosomes expressing a biotin acceptor peptide, their interaction with a biotin-ligase fused to the mitochondria outer membrane (OMM), and their isolation for sequencing of their associated transcripts **(Figure 8 B)**. Over 85% of the identified targets were annotated as mitochondrial. This study, combined with the dentification of ribosomes at the surface of mitochondria (Gold et al. 2017), strongly advocate for the mitochondria-coupled translation (Williams, Jan, and Weissman 2014).

These observations pave the way for mechanistical studies to understand how a given transcript could be shuttled on mitochondria. In mouse neurons, the transcript encoding for the mitochondrial PTEN-induced kinase 1 (pink), protein with a key role in axonal mitophagy, anchors to mitochondria via two conjoint mechanisms: 1) the AMPK-mediated interaction with the RNA-associated protein SYNJ2a and its mitochondria-associated binding partner SYNJ2BP; 2) its own translating polypeptide chain. This latest requirement defines a mechanism described as *co-translational targeting*, where the newly synthesized chain retains a targeting sequence for sub-compartments or organelles as mitochondria. Accordingly, treatment with the translation inhibitor puromycin prevents the interaction *in situ* between SYNJ2BP and SYNJ2a, along with the distribution of the target mRNA via mitochondria hitchhiking. In such manner, mitochondria can distribute Pink1a mRNA to peripheral compartments and at the same time provide a constant supply of newly synthesized PINK1 proteins to drive the mitophagy reaction cascade (Harbauer and Schwarz 2022; Hees and Harbauer 2023) **(Figure 8 C)**. However, compelling evidences show that mitochondria can sustain the dynamic turnover of their protein content not only via translation events occurring on their outer membrane, but also occurring in their proximity. LaminB2 mRNA (lmnb2), essential for mitochondria integrity, is translated on Rab7 late endosomes that creates persistent contact points with nearby mitochondria. The integrity and activity of late endosomes is essential to regulate their localized translation events as disruption of their functions decreases significantly LaminB2 translation (Cioni et al. 2019) **(Figure 8 D)**. As for the case of late endosomes, transcripts encoding for nuclear derived mitochondrial proteins have been identified on early endosomes (Schuhmacher et al. 2023). These studies propose a functional coordination between organelle subtypes, where the translation potential of one supports the structural integrity of the other.

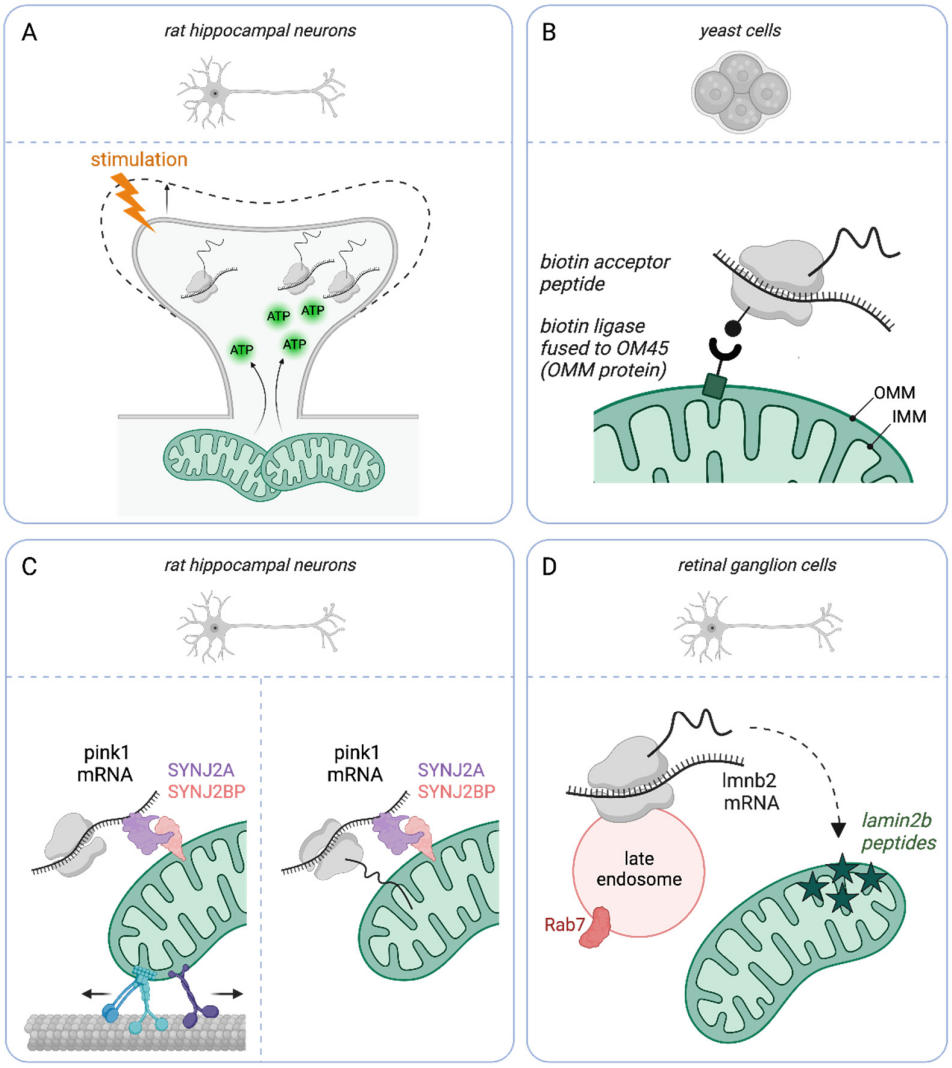

Figure 8. Mitochondria coupled-translation. (A) At synapses, mitochondria provide the energy for local translation and induced-morphological plasticity. **(B)** Schematic of the *proximity-specific ribosomal profiling* technique used in yeast cells to characterize the mitochondria-associated translation events. **(C)** Mitochondrial mRNAs are transported and translated on mitochondria to sustain mitophagy. **(D)** Mitochondrial mRNAs are translated on nearby endosomes to support the integrity of nearby mitochondria.

3.3.3 Endosomes

Endosomes are dynamic organelles that form by the invagination of the plasma membrane. They play a major role in maintaining cellular homeostasis and synaptic plasticity, as they are involved in the internalization, transport and sorting of molecules such as proteins, receptors and neurotransmitters for their degradation, storage or recycling to the plasma membrane (reviewed in: Roney, Cheng, & Sheng, 2022). Emerging evidences are however pinpointing a

new correlation between endosomes and translation regulation. Constituents of RNP granules as ribosomes, RBPs and mRNAs were identified on both early (rab5-expressing) and late (rab7-expressing) endosomes (Cioni et al. 2019).

Recently, early endosomes have been investigated for their biased anterograde transport and for their promising role in distributing mRNAs along neurites. In HEK cells, early endosomes (EEs) carry the five-subunit endosomal Rab5 and RNA/Ribosome intermediary (FERRY) complex which interacts with monosomes and polysomes and modulates the recruitment of a selective range of mRNAs, the majority of which are nuclear encoded mitochondria proteins. Loss of the FERRY complex subunit Fy-2 decreases the complex colocalization with early endosomes, suggesting that this subunit mediates the binding of the complex to EEs, and loss of the FERRY complex decreases the colocalization between EES and the identified mRNAs (Schuhmacher et al. 2023). Interestingly, subcellular resolution analysis confirmed the colocalization of these transcripts with FERRY-loaded EEs along axonal projections (Schuhmacher et al. 2023) **(Figure 9 A).**

While both early and late endosomal populations can traffic RNP granules along axons (Cioni et al. 2019; Schuhmacher et al. 2023), only Rab7 endosomes are essential to regulate the translation dynamics of the associated mRNAs. Global translation along axons as well as candidate-specific translation on late endosomes (as shown for LaminB2 mRNA) were both significantly reduced upon chemical-induced perturbation of late endosomes function (Cioni et al. 2019) **(Figure 9 C).** While the function of endosomes as platforms for the translation machinery starts to be elucidated, whether this mechanism is restricted for a given population of transcripts remains an open question. To characterize the endosome-associated transcriptome, *Popovich and colleagues* used Hela cells to combine an affinity isolation approach with spatial transcriptomics and identified a population of transcripts with an endosomal and translation-dependent subcellular distribution. Among these transcripts, Early Endosomal Antigen 1 (EEA1) mRNA was found to tether onto these organelles via its coding region and interacts with the translation-inhibitor Cysteine And Glycine Rich Protein 1 (CSRP1), which controls its protein output (Popovic D, Nijenhuis W, Kapitein C L 2020) **(Figure 9 B).**

Given the limited knowledge on endosome-couple translation in mammalian cells, other less complex systems, where this mechanism has been more widely studied, are being used as a

model and source of information. In the past decade, the corn fungus pathogen *ustilago maidis* has attracted the attention of neurobiologists as it presents anatomical features that can be compared to those of neurons. Accordingly, this fungus has a highly polarized morphology and presents with MT-dependent transport along their hyphae protrusions. Growing hyphae enable the infection of the host and are therefore essential for the fungus virulence (Vollmeister et al. 2012). It was in this system that the mechanism of hitchhiking, the co-transport of mRNA and endosomes, was first described. Through this mechanism, the mRNA encoding for the septin Cdc3 anchors onto Rab5+ endosomes to be transported along the hyphae and sustain their growth (Baumann et al. 2014). Rrm4 is the most characterized RBP mediating the mRNA-endosome cotransport via its three N-terminal RNA recognition motifs (RRMs) and two C-terminal MademoiseLLE (MLL) domains. Through its RRMs, Rrm4 recognize multiple binding motifs not only in the 3'UTR but also along ORFs, at the start and stop codons (Olgeiser et al. 2019). On the other hand, the two MML domains recognize the adaptor protein Upa1 which, in turn, interacts with the endosomal PIP3 lipids via its FYVE zinc finger domain. Accordingly, loss of Upa1 impaired the transport and distal localization of Rrm4-bound Cdc3 mRNAs and correspondent proteins. These observations led the authors propose a model where Rrm4 mediates the endosomal transport and local translation of the Cdc3 mRNA for the peripheral distribution of functional proteins (Pohlmann et al. 2015). Rrm4 has been shown to form RNP-endosome complexes also in partnership with Pab1 (Pohlmann et al. 2015) and by interacting with a broad subsets of transcripts encoding for mitochondrial, vesicular transport and cytoskeleton proteins (Olgeiser et al. 2019). All four septins mRNAs (cdc3, cdc10, cdc11, cdc12) and the correspondent proteins assembled into heteromers are co-transported on endosomes **(Figure 9 D).** The heteromer formation is a prerequisite for the septins trafficking, as indicated by their impaired peripheral localization upon loss of their α-helix, essential region for septin-septin interactions. Interestingly, the transport of the septin proteins is also dependent on the mRNA-binding protein Rrm4, as its absence significantly decreased their long-distance transport. Thus, this study proposes a model where septin mRNAs are translated on endosomes where they further assemble into heterodimers for their delivery to the hyphae growth pole (Zander et al. 2016). This model is further supported by the identification of ribosomes on Upa/Rrm4-associated endosomes (Pohlmann et al. 2015).

Because of the similarities in the structural organization of the MTs and the transport machinery, the process describing mRNAs being shuttled by moving endosomes while undergoing active translation might not be restricted to *u. maidis* but might occur also in more complex systems as mammalian neurons.

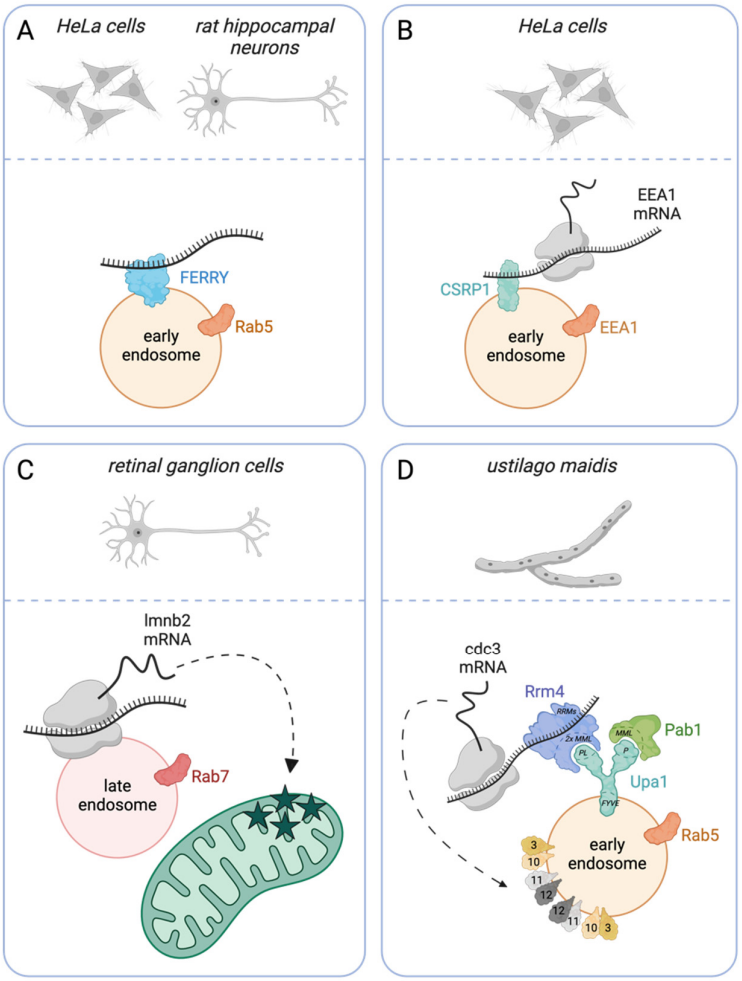

Figure 9. Endosome-coupled translation. (A) In neurons, the FERRY complex couples a subset of transcripts to Rab5+ early endosomes. **(B)** The adaptor protein CSRP1 tethers the endosomal EEA1 mRNAs to early endosomes and controls its translation. **(C)** In neurons, Rab7+ late endosomes shuttle the mitochondrial lmnb2 mRNA to supply the nearby mitochondria with newly translated peptides and support their structural integrity. **(D)** In fungi, the septin Cdc3 mRNAs are transported and translated on Rab5+ early endosomes via the Upa1/Rrm4/Pab1 complex, supplying the vesicles with newly translated proteins.

3.3.4 Lysosomes

Lysosomes contribute to the maintenance of cellular homeostasis by controlling the degradation and recycling of intracellular proteins, organelles and lipids (reviewed in: Roney,

Cheng, & Sheng, 2022). Recent findings suggest that, similarly to other membrane-bound organelles as mitochondria and endosomes, lysosomes could also serve as transporting units for other macromolecular structures such as RNP granules. EM analysis of neuronal RNA granules isolated from newborn rat brains show morula-like structures abundantly associated with cytoskeleton-like structures and seldom in proximity with lysosomes. Cytoskeletal components and multiple Rabs were also identified as constituents of the isolated granules through a complementary proteomic approach (Kipper et al. 2022). This study strongly indicates that RNP granules traffic through a MT-based transport, which can occur through a lysosome-mediated hitchhiking mechanism. This mechanism is modulated by annexin A11 (ANXA) which serves as molecular tether between the two organelles (Liao et al., 2019). Whether local translation can occur on lysosomes hasn't been investigated yet.

3.3 Toolbox to investigate local translation

3.3.1 Transcriptome/translatome analysis of peripheral compartments

Our current knowledge about sub-compartments localization of mRNAs comes from the over-time development of techniques with increased resolution and sensitivity. Approaches as microdissections and fractionations that allow the separation of subcellular compartments are used to prepare a more and more resolved starting material (such as neuropils, isolated dendrites and/or axons, cell somas or subcellular organelles). Their combination with sequencing strategies, which are more and more recurrently combined with high throughput *in situ* hybridization analysis, generate subcellular transcriptomic pictures with an extremely high level of detailed information. By looking at the populations of transcripts found within these peripheral compartments, we can therefore have a first overview of the potential candidates undergoing localized translation. A pioneered approach from the Schuman's lab takes advantage of the laminar organization of the hippocampus to microdissect soma-free neuropils from its CA1 region. This approach was used to perform RNA-seq analysis and identify transcripts with dendritic and/or axonal origins (Cajigas et al. 2012). This dataset was later combined with a translatome readout and bioinformatic filtering to identify the neuropil-up translatome of glutamatergic neurons, devoid of GABAergic and glia contaminants. This descriptive study shows that transcripts preferentially translated at neuropils have longer 3'UTRs than soma-up transcripts but unchanged translation efficiency, which is influenced by the length of their UTRs and coding sequence (Glock et al. 2021).

To further deepen the current knowledge on compartment-specific transcriptome and bring it to a single cell resolution, scRNA-seq was performed on laser-dissected soma and dendritic processes of individual cultured hippocampal neurons. Somatic transcriptome analysis enabled the identification of glutamatergic and GABAergic neuronal subtypes, which revealed both common and unique dendritic transcripts. This method can therefore identify inter-cellular heterogeneity within the same or different neuronal subtypes (Perez et al. 2021). This study also aims at understanding if different neuronal subtypes undergo the same local translation dynamics along neurites. To this aim, it combines the use of cre-driven conditional mouse lines with click chemistry and illustrate how local translation is a common property of neuronal dendrites, despite their origin (Perez et al. 2021).

Laser microdissection was also employed to isolate much smaller subcompartments as growth cones. Here, translation is developmentally regulated, as the number and species of localized transcripts increased with the maturation of the neurons (Zivraj et al. 2010).

A step forward in increasing subcellular resolution was achieved when the synaptosomes preparation procedure was combined with the fluorescence-activated synaptosomes sorting (FASS) for downstream mass spectrometry analysis. This workflow was applied to cre-inducible SypTOM mice to sort and characterize the synaptic proteome of different cell-type-specific synapses isolated from different microdissected brain areas. The dataset generated from this experimental set-up draws a comprehensive picture of the common and subtype-specific proteomic traits underlining synapses diversity (Oostrum et al. 2023).

Ribosome profiling is a revolutionary technique that characterizes the ribosome-protected mRNA fragments via high-throughput sequencing, providing a snapshot of mRNA translation. It enabled the translatome profiling of neuropils microdissected from rat hippocampal slices and the identification of ribosomal mRNAs as locally translated for their downstream incorporation into pre-existing ribosomes (Fusco et al. 2021). Only recently, however, this technology has been adopted for single cell analysis. When applied to mouse unfertilized oocytes or fertilized embryos from 1-cell to 8-cell stages, it was possible to characterize the translation changes at a single cell level during embryonic development (Cenik and Can 2021). Lastly, the advent of the spatial transcriptomic revolution, that interrogates a full tissue transcriptome by preserving its spatial context and cellular resolution, opened the way to a new frontier of datasets with multiple dimensions. This pioneering technology led to the

development of a single-cell spatial translatome approach that unravel the protein synthesis dynamics of tissue-specific isolated cells at a subcellular resolution (Zeng et al. 2023).

3.3.2 Isolation of membrane-bound organelles

While on the one hand a broad set of methodologies were developed to interrogate the transcriptome and translatome of subcellular compartments such as soma, neurites, and synapses, on the other hand parallel strategies evolved to further refine and bring the analysis resolution to the level of macromolecular complexes as ribosomes and membrane-bound organelles (ER, golgi, vesicles). Membrane-bound organelles play a broad variety of essential functions in the maintenance of cell homeostasis and their dysregulation has been widely associated to a spectrum of neurological and non-neurological diseases. It is therefore imperative to isolate these organelles not only to characterize their composition and therefore unveil their biological roles but also to identify pathological proteomic and transcriptomic changes that could lead to the identification of disease-related biomarkers and the development of therapeutic strategies.

Gradient centrifugation represented the golden standard method for the isolation of membrane bound organelles, including vesicles (Even et al. 2019), lysosomes (Gao et al. 2017), endosomes (Pensalfini et al. 2021), and mitochondria (Hubbard et al. 2019; Jeandard et al. 2023). However, this strategy was rapidly outshined by affinity purification methods, that use beads-conjugated antibodies targeting an organelle's surface protein. This strategy is less time consuming and yields to a purer isolated fraction, has been widely employed to purify organelles expressing tagged membrane proteins from a broad range of neuronal and non-neuronal cell types. Beads coupled to antibodies targeting the endogenous EEA1 or CKAP4 proteins enabled the affinity purification from homogenized Hela cells of early endosomes or ER, respectively, for subsequent transcriptome analysis (Popovic D, Nijenhuis W, Kapitein C L 2020). Sorting endosomes were also isolated from embryonic stem (ES)-cell derived motoneurons by exploiting the reaction developed by a cell to the exposure to tetanus neurotoxin and its binding fragment H_CT. Cells internalize this toxin by endocytosis into signaling endosomes that undergo retrograde transport towards the soma. Firstly, ES cells are exposed to isotopically-tagged amino acids to label translating proteins. Then, they are differentiated into motoneurons and exposed to H_CT for its internalization. Lastly, H_CT labelled endosomes are sorted via magnetic purification for downstream proteomic analysis

of their SILAC-labelled proteome (Debaisieux et al. 2016). Affinity purification was also applied to characterize the lysosomal proteome of *C. elegans* transgenic lines generated with tissue-specific promoters to express lysosomal membrane proteins tagged with 3 tandem HA epitopes in different cellular types, including neurons (Yu et al. 2022).

More recently, flow cytometry has been adopted to sort fluorescently-labelled organelles by fluorescent-activate organelle sorting (FAOS). Although this strategy requires a more laborious set-up optimization, it has been successfully used to isolate not only membrane bound organelles as secretory granules (Gauthier et al. 2008), extracellular vesicles (Cao et al. 2008) and ER (Horste et al. 2022) but also liquid phase-separated granules as TIS11B granules (Horste et al. 2022; Ma and Mayr 2018) with a common strategy that includes a careful cell lysis, brief centrifugation for sample clearing and ultimately FAOS.

3.4 Translation-associated diseases

Local translation in neuronal peripheral compartments requires the long-distance transport of mRNAs which is achieved through the assembly and proper functioning of a mRNA transport system. This system encompasses RNP granules with their mRNAs and associated RBPs, motor proteins and their adaptors, and its disruption has been correlated to neurological disorders.

Disease-causing mutations in genes encoding for RBPs and adaptor proteins have been associated to mRNA transport and translation defects, all together recalling the importance of the integrity of the RNP granule transport machinery. The RBP fused in sarcoma (FUS) participates in a broad range of mechanisms, such as RNA splicing, distribution and degradation, and associated mutations have been correlated to both ALS and FTD. Spinal cord transcriptomic analysis from humanized FUS mice encoding the ALS-linked FUS mutations unfold synaptic disfunction, activated integrated stress response and protein translation inhibition. These molecular alterations translate into motor and cognitive deficits (López-Erauskin et al. 2018). TDP-43 is another RBP that regulates RNA metabolism and modulates the formation of RNP granules. Its mutations impair mRNA transport and are likewise linked to ALS (Alami et al. 2014). FMRP protein deficiency caused by mutations in the FMR1 gene has been correlated to the Fragile X Syndrome (FXS), a neurodevelopmental disorder characterized by altered dendritic morphology. Given the importance of FMRP for mRNA

trafficking and translation regulation, its downregulation alters the subcellular distribution of its target mRNAs Map1b and Calm1, as well as axonal growth (Wang et al. 2015). Survival of motor neuron (SMN) is an adaptor protein that serves as molecular tether between the RBP IMP1 and beta-actin mRNA, promoting the condensation of RNPs (Donlin-Asp et al. 2017). Mutations in the SMN1 gene lead to a decrease in SMN expression level which is recognized as leading cause for spinal muscular atrophy (SMA). SMN deficiency leads to impaired RNP assembly and decreased association with the MT network (Donlin-Asp et al. 2017).

Disease-associated mutations have also been identified in the molecular players that regulate the hitchhiking mechanisms used by RNP granules to traffic along neurites. Rab7 is membrane protein of late endosomes (LE) that scaffold motors for the endosomal recruitment onto MTs, and its mutated variants associated with CMT2B compromise LE trafficking and local translation of the mitochondrial protein laminB2 (Cioni et al. 2019). ANXA11 serves as molecular tether between RNP granules and moving lysosomes. Its mutations have been linked to ALS and shown to interfere with the hitchhiking mechanism therefore reducing RNP granule transport (Liao et al. 2019). The FERRY complex modulates the recruitment of transcripts and ribosomes on early endosomes and its loss leads to a decreased distribution of their associated mRNAs (Schuhmacher et al. 2023). It has been reported that the FERRY complex plays a role in regulating neuronal development and activity and its loss-of-function mutations correlate to neurological conditions such as intellectual disability (Bhoj et al. 2016).

In the past decade significant advancements in the field of local translation have been achieved, unraveling its regulatory molecular mechanisms and molecular players. However, much more need to be elucidated and implemented with the current knowledge frame to better understand the pathophysiology of translation-associated diseases.

Disease	**Gene product**	**Subcellular function**	**Defects**	**References**
ALS, FTD	FUS	RBP	- Synaptic disfunction - Activated stress responce - Translation inhibition - Motor and cognitive deficits	(López-Erauskin et al. 2018)
ALS	TDP43	RBP	- Impaired mRNA transport	(Alami et al. 2014)
FXS	FMRP	RBP	- Impaired mRNA transport and distribution - Axonal growth defects	(Wang et al. 2015)
SMA	SMN	Adaptor protein between β-actin mRNA and RBP IMP1	- Impaired assembly and association to MTs of RNP granules	(Donlin-Asp et al. 2017)

CMT2B	Rab7	Membrane protein of LE	- Impaired trafficking of LEs - Impaired translation of laminB2	(Cioni et al. 2019)
ALS	ANXA11	adaptor protein between RNP granules and lysosomes	- Impaired transport of RNP granules	(Liao et al. 2019)
ID	FERRY complex	adaptor protein between ribosome-associated mRNAs and EE	- Impaired mRNA transport and distribution	(Schuhmacher et al. 2023)

Table 1: Translation-associated diseases.

AIMS OF THE STUDIES

My work is divided into the following two chapters:

Chapter 1: Unraveling the role of membrane-bound organelles in the regulation of MT acetylation and axonal transport dynamics.

The link between MT acetylation and transport dynamics has been reported through multiple *in vitro* evidences, describing the importance of this PTM for the recruitment and binding of molecular motors to MTs (Dompierre et al. 2007; Reed et al. 2006). Multiple studies strengthened this finding by showing how low tubulin acetylation levels that characterize multiple neurological disorders correlate with impaired transport dynamics (d'Ydewalle et al. 2011; Dompierre et al. 2007; Godena et al. 2014; Guo et al. 2017; Kim et al. 2016). These defects could be rescued by pharmacological inhibition of the deacetylating enzyme HDAC6 and subsequent restoration of tubulin acetylation levels, suggesting a link between tubulin acetylation and transport dynamics. However, given the aspecificity of some HDAC6 inhibitors used in these studies, it's still not clear whether the rescued phenotype can solely be ascribed to the recovered tubulin acetylation levels or also to other secondary targets that could have been modulated, directly or indirectly, the transport dynamics. Whether there is a causal relationship between tubulin acetylation and axonal transport has yet to be clarified.

This chapter presents the content of two studies that aim at:

1) Clarifying the link between tubulin acetylation and axonal transport by assessing the contribution of ATAT1, the enzyme that catalyzes tubulin acetylation, to the axonal transport dynamics of membrane-bound organelles across different species;
2) Identifying the mechanism through which ATAT1 modulates its acetylating activity;
3) Understanding if there's a functional correlation between ATAT1 and the Elongator complex, which has also been shown to engage in MT acetylation.

Chapter 2: Establishing the toolkit to uncover the transcriptome and translatome of motile cargos.

Since the discovery that proteins can be translated locally within peripheral compartments (Hafner et al. 2019; Shigeoka et al. 2016), multiple studies set out to elucidate both the transcriptome and the translatome of subcellular domains, progressively refining the resolution to the scale of a synapse. Recently, membrane-bound organelles started to attract

the attention of many, as foci of translating peptides were identified on mitochondria and endosomes (Cioni et al. 2019; Harbauer et al. 2022; Schuhmacher et al. 2023). These studies, however, focus on investigating the organelle-associated localization and translation of a given target of interest. First, it remains unresolved whether local translation could occur on cargos undergoing bidirectional motion. Secondly, a comprehensive characterization of the transcripts shuttled and translated on motile cargos hasn't been performed yet.

This chapter details the methodologies developed to:

1) Isolate motile cargos from a transgenic mouse line to characterize its proteome and associated transcriptome;
2) Generate a stable cell line of neuron-like cells expressing the SunTag system to determine the translation dynamics of candidate transcripts.

CHAPTER I

SUMMARY of the results

1. ATAT1-enriched vesicles promote microtubule acetylation via axonal transport

A growing body of evidence supports the link between tubulin acetylation and axonal transport, showing that the axonal transport defects found in multiple neurodegenerative diseases can be rescued by pharmacological inhibition of the deacetylase HDAC6 (d'Ydewalle et al. 2011; Dompierre et al. 2007; Godena et al. 2014; Guo et al. 2017; Kim et al. 2016). As HDAC6 can deacetylate other substrates than α-tubulin (Zilberman et al. 2009), the effects observed upon the use of HDAC6 inhibitors might not be uniquely ascribed to a restoration of the acetylation level of MTs. To dissect the link between tubulin acetylation and transport dynamics, we sought to investigate how ATAT1, the only known tubulin acetyltransferase (Kalebic, Sorrentino, et al. 2013) with no other targets than K40 residues of α-tubulin (Shida et al. 2010), could impact axonal transport. To this aim, we set out to study how loss of ATAT1 activity would modulate the axonal transport of membrane-bound organelles in mouse cortical neurons and motoneurons of *Drosophila* third instar larvae.

Ex vivo, ATAT1 downregulation led to impaired lysosomes transport along the projections of callosal neurons in organotypic slices. *In vitro*, plated cortical neurons with KD-depleted or sh-reduced ATAT1 levels displayed transport defects of organelles that could be rescued upon OE of ATAT1 or of the acetylation-mimicking tubulin variant K40Q. *In vivo*, we tracked dynamics of SVPs movement along fly larvae motoneurons upon Atat1/2 KD and found transport defects that could be restored upon HDAC6 KD or pharmacological inhibition with TBA. These results suggest that ATAT1-mediated tubulin acetylation is a key regulator of axonal transport dynamics across species. To unambiguously assess how transport dynamics are modulated by the loss of tubulin acetylation, we set up an *in vitro* assay where purified and labelled vesicles are loaded on polymerized and labelled MTs isolated from ATAT1 KO mice (not acetylated) or WT littermates (acetylated). Vesicular transport was impaired when MT were not acetylated, confirming our previous results, and further supporting the link between tubulin acetylation and transport dynamics.

To assess how ATAT1 reaches MTs and promotes their acetylation, we assessed its subcellular distribution along axons of mouse and human neurons, where it was partially codistributed

with vesicular markers. Firstly, we could confirm its vesicular enriched distribution by mass spectrometry. Secondly, axonal transport recordings of lysosomes and ATAT1-GFP foci in mouse cortical neurons revealed their cotransport. Lastly, vesicular treatment with proteinase-K showed that ATAT1 is localized at the external vesicular membrane. Given its vesicular localization, we identified the sequence downstream of the ATAT1 catalytic domain responsible for the its binding to vesicles. We generated a truncated ATAT1 variant lacking the vesicular binding domain and observed decreased tubulin acetylation levels upon its expression in Hela cells, when compared to the expression of the full length ATAT1. Taken together, these data suggest that the vesicular pool of ATAT1 is essential to efficiently acetylate MTs.

To test whether the transport of vesicles was required for the ATAT1-mediated MTs acetylation, we disrupted either the bidirectional axonal transport via high concentration of ciliobrevin D, or more specifically the retrograde movement via expression of shRNA-mediated KD of Lis1. In both cases, we detected decreased levels of tubulin acetylation, suggesting that the vesicular pool of ATAT1 exerts its acetylating activity when vesicles are motile. To confirm this hypothesis, we performed an *in vitro* assay to evaluate the ability of vesicles to acetylate unmodified MTs in the presence/absence of acetyl-CoA, the substrate of ATAT1. While motile WT vesicles acetylate MTs in the presence of acetyl-CoA, vesicles isolated from ATAT1 KO mice or WT vesicles in the absence of acetyl-CoA were unsuccessful. Taken together, our data show that a vesicular pool of ATAT1 modulates MT acetylation thus regulating axonal transport dynamics.

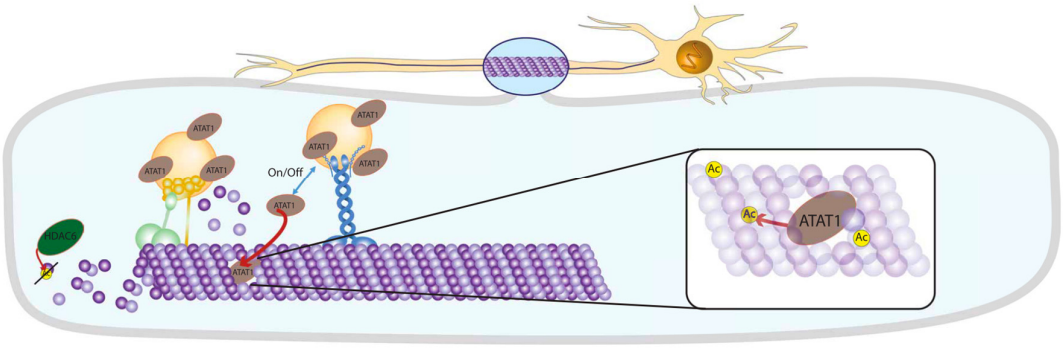

Figure 10: Proposed model illustrating how the vesicular pool of ATAT1 can modulate MT acetylation and therefore sustain axonal transport. We show that a vesicular pool of ATAT1 regulates MTs acetylation and therefore the MT-dependent axonal transport. As the motors are known to create damage points along the MT lattice from their passage (Andreu-Carbó

et al. 2022; Triclin et al. 2021), we hypothesize that these cracks could be used by ATAT1 to access the MT and modulate the acetylation of α-tubulin lysin40 residues.

1.1 Contributions

I contributed to this study by performing mouse experiments. I prepared, seeded and cultured primary cortical neurons in microfluidics devices and performed live imaging recordings of the axonal transport dynamics of lysosomes under the supervision of Loic Broix **(Fig. 1 M-Q)**. I performed immunofluorescent staining for ATAT1 and vesicular markers on hIPSC-derived projection neurons that were generated by Romain Le Bail, and performed super resolution imaging under the supervision of Loic Broix **(Fig. 4 B).** I validated tamoxifen-inducible or constitutive sh-expressing plasmids upon their transfection in N2a cells and western-blotting analysis of their protein extracts **(Fig. S1A, S; 6A)**. Lastly, I prepared, seeded and cultured primary cortical neurons for immunofluorescent staining of GFP, Lis1, total and acetylated tubulin, followed by image acquisition and analysis **(Fig. S6B-G, I-K).**

2. ATP-citrate lyase promotes axonal transport across species

Elongator is a dodecameric complex composed of 6 subunits with elp3 being the catalytic core. Elongator is highly expressed in the nervous system (Creppe et al. 2009; Hinckelmann et al. 2016; Miśkiewicz et al. 2011) and despite its canonical function as a tRNAs modifier (reviewed in: Rapino et al. 2017), its activity has also been associated to tubulin acetylation. Accordingly, loss of elongator correlated with decreased expression levels of this PTM (Creppe et al. 2009; Solinger et al. 2010). As tubulin acetylation relies on the vesicular pool of ATAT1, which catalyze the addition of acetyl groups to α-tubulin lysin40 residues (Even et al. 2019), we wondered how Elongator could contribute to tubulin acetylation and whether it is functionally correlated to ATAT1.

To answer these questions, we first reported that tubulin acetylation levels are decreased and transport dynamics impaired in cortical neurons isolated from Elp3 cKO mice. Secondly, we probed the same parameters in cortical neurons isolated from Atat1 KO mice, with/without co-downregulation of Elp3. We show that the loss of elp3 doesn't have additive effects on the decreased acetylation levels and transport dynamics defects reported upon ATAT1 loss. These results suggest that Elongator and ATAT1 can modulate these phenotypes by acting on the same molecular pathway. These results were confirmed *in vivo* by using *D.*

Melanogaster third insta larvae in which elp3 subunits were KD in combination or not with ATAT1 KD. Accordingly, the decreased tubulin acetylation levels and transport dynamics detected upon loss of Elongator, which could be rescued by ELP3 OE or HDAC6 KD, were not further modulated by the loss of ATAT1.

We then set out to assess how Elongator and ATAT1 cooperate in regulating tubulin acetylation and transport dynamics. We first excluded the hypothesis that Elongator could modulate these parameters by regulating the expression or activity of the enzyme responsible for the regulation of MT acetylation, ATAT1 itself or of the deacetylating enzyme HDAC6. Then, we tested if Elongator modulates the production of acetyl-CoA, the substrate of ATAT1 required for its acetylation activity. In mouse cortical extracts, we found that expression of Acly and ACSS2, enzymes catalyzing the production of acetyl-CoA from the cleavage of citrate and acetate, respectively, were significantly reduced in the absence of Elp3. Subcellular fractionation analysis of WT cortical lysate showed that, while Acly was highly enriched in the vesicular fraction together with ATAT1 and Elongator subunits, ASCC2 was mostly cytosolic. Accordingly, immunofluorescence analysis showed Acly foci partially codistributed with vesicular markers in mouse cortical neurons. Furthermore, the expression and activity (ability to produce acetyl-CoA) of vesicular pool of Acly decreased upon Elp3 loss. These data suggest that Elongator could modulate the levels of the vesicular pool of Acly.

We first tested whether Elongator modulates tubulin acetylation by regulation the vesicular pool of Acly. For this we showed that a pharmacological inhibition of Acly in mouse cortical neurons phenocopied the tubulin acetylation and transport defects observed upon loss of Elongator. Additionally, fly larvae motoneurons not only displayed the same defects upon Acly KD, but also showed that the acetylation and transport defects due to Elongator loss could be rescued by Acly OE. We therefore show that Elongator regulates tubulin acetylation and axonal transport by regulating Acly expression.

To assess the clinical relevance of our findings, we analyzed fibroblasts from FD patients which bear a loss-of-function mutation in the Elp1 subunit of Elongator which leads to decreased levels of both elp1 and elp3. Compared to matched controls, FD fibroblasts displayed decreased tubulin acetylation and transport defects, which could be rescued by HDCA6 inhibition. FD cells also displayed decreased Acly levels, and inhibition of the residual Acly led to a further dose-dependent loss of tubulin acetylation. Lastly, Acly OE could rescue both

tubulin acetylation expression and MT-based transport in FD cells. These data suggest that the Elp3-dependent mechanisms investigated in mouse and fly are conserved in human cells, and that the Elp3-dependent defects in tubulin acetylation and axonal transport might contribute to the etiology of the disease.

To understand how Elongator modulates Acly expression, we first assessed its activity as a tRNA modifier. To this end, we performed polysomal fractionation of cortical extracts from WT and Elp3 cKO mice but did not detect any difference in Acly mRNA expression. Secondly, we hypothesized that Elongator could regulate Acly translation. We used the puromycylation assay combined with the puro-PLA assay to visualize newly translating Acly peptides along mouse cortical neurites but identified the same number of Acly peptides in the presence or absence of Elongator. Lastly, to test if Elongator could modulate Acly expression by regulating its stability, we performed the cycloheximide assay in FD fibroblasts which displayed a decrease Acly half-life when compared to their matched control. In agreement with IP analysis showing an interaction between Acly and the Elongator complex, these results suggest that Elongator modulates tubulin acetylation and transport dynamics by stabilizing Acly peptides. We therefore identified the enzymatic cascade that regulates tubulin acetylation and MT-dependent axonal transport and that is likely to occur on motile vesicles.

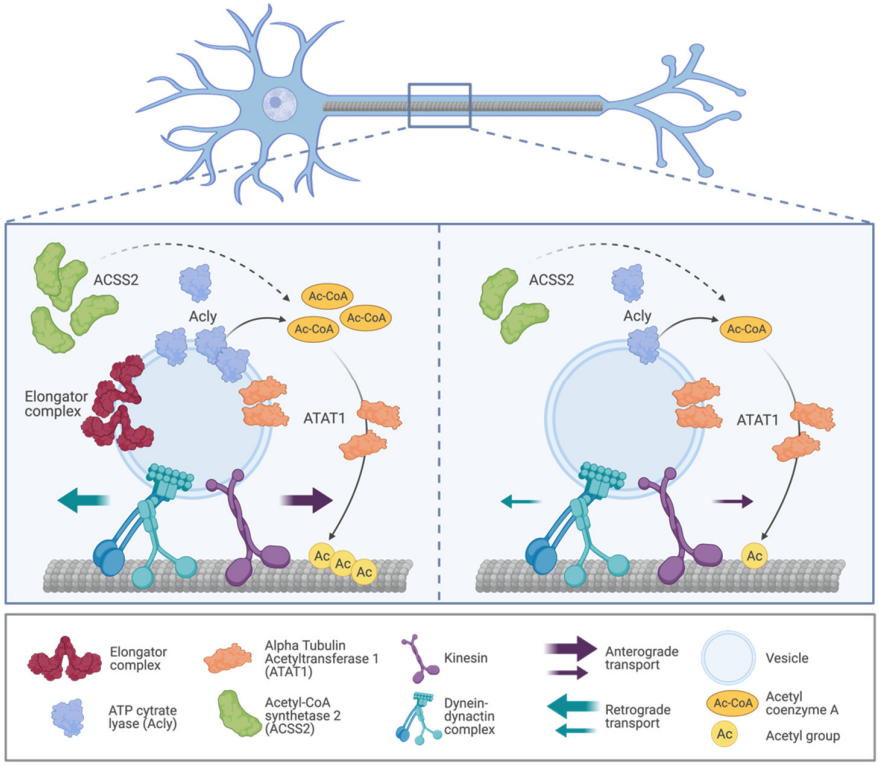

Figure 11: proposed model for the molecular cascade regulating tubulin acetylation and axonal transport dynamics. Acly and ACSS2 are the two enzymes that catalyze the production of Acetyl-CoA, providing to ATAT1 the substrate to catalyze MT acetylation (Even et al. 2019). While ACSS2 has a cytosolic localization, Acly is predominantly vesicular. Together with ATAT1 and Acly, we also identified on vesicles the Elongator complex. We describe a molecular cascade that is likely occurring on vesicles, where Elongator regulates the stability and expression level of Acly. In the absence of Elongator, Acly expression decreases and with it the availability of Acetyl-CoA, which in turn leads to a decreased MT acetylation mediated by the vesicular pool of ATAT1. Adapted from (Even et al. 2021).

2.1 Contributions

I contributed to this study by performing mouse experiments. I managed the breeding of transgenic mouse lines to collect P0 cortices and obtain their protein lysate for western blotting analysis of Acly, ACSS2 **(Fig. 2F-H)**, as well as of acetylated and total tubulin **(Fig. S1A)**. I prepared, seeded and cultured primary cortical neurons for: 1) for immunofluorescent staining of Acly and vesicular markers followed by super-resolution image acquisition **(Fig. 2M, N)** and of total and acetylated tubulin upon pharmacological treatment with the Acly inhibitor hydroxycitric acid (HCA) **(Fig. 3A)**; 2) puromycilation assay combined with proximity ligation assay (PLA) and downstream image acquisition and analysis **(Fig. 5C-F)**. I prepared, seeded and cultured primary cortical neurons in microfluidics devices and recorded axonal transport dynamics of lysosomes upon pharmacological treatment with HCA **(Fig. 3B-D; S3A)**. I seeded and performed the cycloheximide assay on human fibroblasts lines (from FD patients and controls) and performed western-blotting analysis on their protein extracts **(Fig. 5G, H)**. Lastly, I performed western-blotting analysis on fly head lysates for acetylated and total tubulin **(Fig. S3H)**.

ATAT1-enriched vesicles promote microtubule acetylation via axonal transport

CELL BIOLOGY

ATAT1-enriched vesicles promote microtubule acetylation via axonal transport

Aviel Even[1]*, Giovanni Morelli[2,3]*, Loïc Broix[2]*, Chiara Scaramuzzino[4,5], Silvia Turchetto[2], Ivan Gladwyn-Ng[2], Romain Le Bail[2], Michal Shilian[1], Stephen Freeman[2], Maria M. Magiera[6,7], A. S. Jijumon[6,7], Nathalie Krusy[2], Brigitte Malgrange[2], Bert Brone[3], Paula Dietrich[8], Ioannis Dragatsis[8], Carsten Janke[6,7], Frédéric Saudou[4,5,9], Miguel Weil[1]*†, Laurent Nguyen[2]*†

Microtubules are polymerized dimers of α- and β-tubulin that underlie a broad range of cellular activities. Acetylation of α-tubulin by the acetyltransferase ATAT1 modulates microtubule dynamics and functions in neurons. However, it remains unclear how this enzyme acetylates microtubules over long distances in axons. Here, we show that loss of ATAT1 impairs axonal transport in neurons in vivo, and cell-free motility assays confirm a requirement of α-tubulin acetylation for proper bidirectional vesicular transport. Moreover, we demonstrate that the main cellular pool of ATAT1 is transported at the cytosolic side of neuronal vesicles that are moving along axons. Together, our data suggest that axonal transport of ATAT1-enriched vesicles is the predominant driver of α-tubulin acetylation in axons.

INTRODUCTION

Neurons are polarized cells, structurally and functionally divided into somatodendritic and axonal compartments. Axons are often long and characterized by intense bidirectional microtubule (MT)–dependent transport of cargos to control critical functions, including cell survival and neurotransmission. Cargos such as vesicles and membrane organelles (e.g., mitochondria, endosomes, and lysosomes) as well as proteins and messenger ribonucleoprotein complexes are loaded on molecular motors to undergo axonal transport along MTs. The anterograde transport is powered by the kinesin superfamily, while retrograde transport involves cytoplasmic dynein (*1*). Posttranslational modifications (PTMs) of MTs have been suggested to modulate axonal transport (*2*, *3*). Specifically, the acetylation of MTs may contribute to this process by enhancing the recruitment of kinesin and dynein and their mobility (*4*, *5*). Moreover, increasing MT acetylation improves the transport deficits resulting from mutations in *Huntingtin* and *LRRK2* genes (*4*, *6*). The acetylation of α-tubulin in MTs is driven by the α-tubulin *N*-acetyltransferase 1 (ATAT1)/MEC17 (*7*, *8*). Recent in vitro experiments performed with recombinant ATAT1 have suggested that it can enter the lumen of MTs from their extremities and/or lateral imperfection (*9*, *10*) and passively diffuses to promote acetylation of α-tubulin K40 residues (*11*, *12*). However, it remains unclear how ATAT1 reaches and acetylates MTs in living cells. This question is particularly important in neurons where axons and dendrites cover long distances with rather homogenously acetylated MTs. To decipher how ATAT1 promotes MT acetylation in neurons, we combined cell-free assays with cellular and molecular analyses of ex vivo (organotypic slices) or cultured mouse cortical projection neurons (in microfluidic chambers) and motoneurons of *Drosophila* larvae in vivo. Our work unveils the existence of a predominant pool of ATAT1 at the cytosolic side of motile vesicles, whose active transport promotes acetylation of α-tubulin in MTs. Therefore, we propose that the transport of ATAT1-enriched vesicles is a predominant driver of axonal MT acetylation.

RESULTS

Loss of Atat1 interferes with axonal transport in neurons across species

ATAT1 promotes the acetylation of α-tubulin in MTs, a PTM that favors the recruitment of kinesin and dynein and their mobility along axons (*4*, *5*, *13*). To test whether loss of Atat1 impairs axonal transport in cortical projection neurons in situ, we performed time-lapse recordings of organotypic brain slices from postnatal (P) day 2 wild-type (WT) mice. For this purpose, embryonic day 14.5 (E14.5) mouse embryos were in utero electroporated (IUE) with a combination of 4OH-tamoxifen (4OHT)–inducible Cre, Cre-inducible short hairpin RNA against Atat1 (shAtat1) (fig. S1A), Cre-inducible red fluorescent protein, and Lamp1-Emerald plasmids. Successive injections of 4OHT allowed us to identify the callosal projection of IUE neurons and record the transport of Lamp1-Emerald–positive lysosomes (Fig. 1, A and B, and movie S1). We showed that the 4OHT-induced knockdown (KD) of *Atat1* in callosal projection neurons 3 days after IUE at E14.5 (to maintain the expression of *Atat1* during the migration of projection neurons) impaired both anterograde and retrograde axonal transports recorded at P2 (Fig. 1, A to F, and fig. S1B). The KD of *Atat1* led to the reduction of the average and instantaneous velocities (Fig. 1, C and D) and the run length and to the increase of the pausing time of lysosomes (Fig. 1, E and F). These data were confirmed in cortical projection neurons from E14.5 *Atat1* knockout mice (*Atat1 KO*) or their corresponding WT controls (*14*) cultured for 5 days in vitro (DIV) in microfluidic devices and incubated with fluorescent probes to follow the transport of lysosomes and mitochondria along axonal MTs (Fig. 1, G and H, and movies S2 and S3). The average velocities

[1]Laboratory for Neurodegenerative Diseases and Personalized Medicine, Department of Cell Research and Immunology, The George S. Wise Faculty for Life Sciences, Sagol School of Neurosciences, Tel Aviv University, Ramat Aviv 69978, Israel. [2]GIGA-Stem Cells and GIGA-Neurosciences, Interdisciplinary Cluster for Applied Genoproteomics (GIGA-R), University of Liège, CHU Sart Tilman, Liège 4000, Belgium. [3]BIOMED Research Institute, University of Hasselt, Hasselt 3500, Belgium. [4]Grenoble Institut des Neurosciences, GIN, Univ. Grenoble Alpes, F-38000 Grenoble, France. [5]Inserm, U1216, F-38000 Grenoble, France. [6]Institut Curie, PSL Research University, CNRS UMR 3348, F-91405 Orsay, France. [7]Université Paris-Sud, Université Paris-Saclay, CNRS UMR3348, F-91405 Orsay, France. [8]Department of Physiology, University of Tennessee Health Science Center, Memphis, TN 38163, USA. [9]CHU Grenoble Alpes, F-38000 Grenoble, France.
*These authors contributed equally to this work.
†Corresponding author. Email: lnguyen@uliege.be (L.N.); miguelw@tauex.tau.ac.il (M.W.)

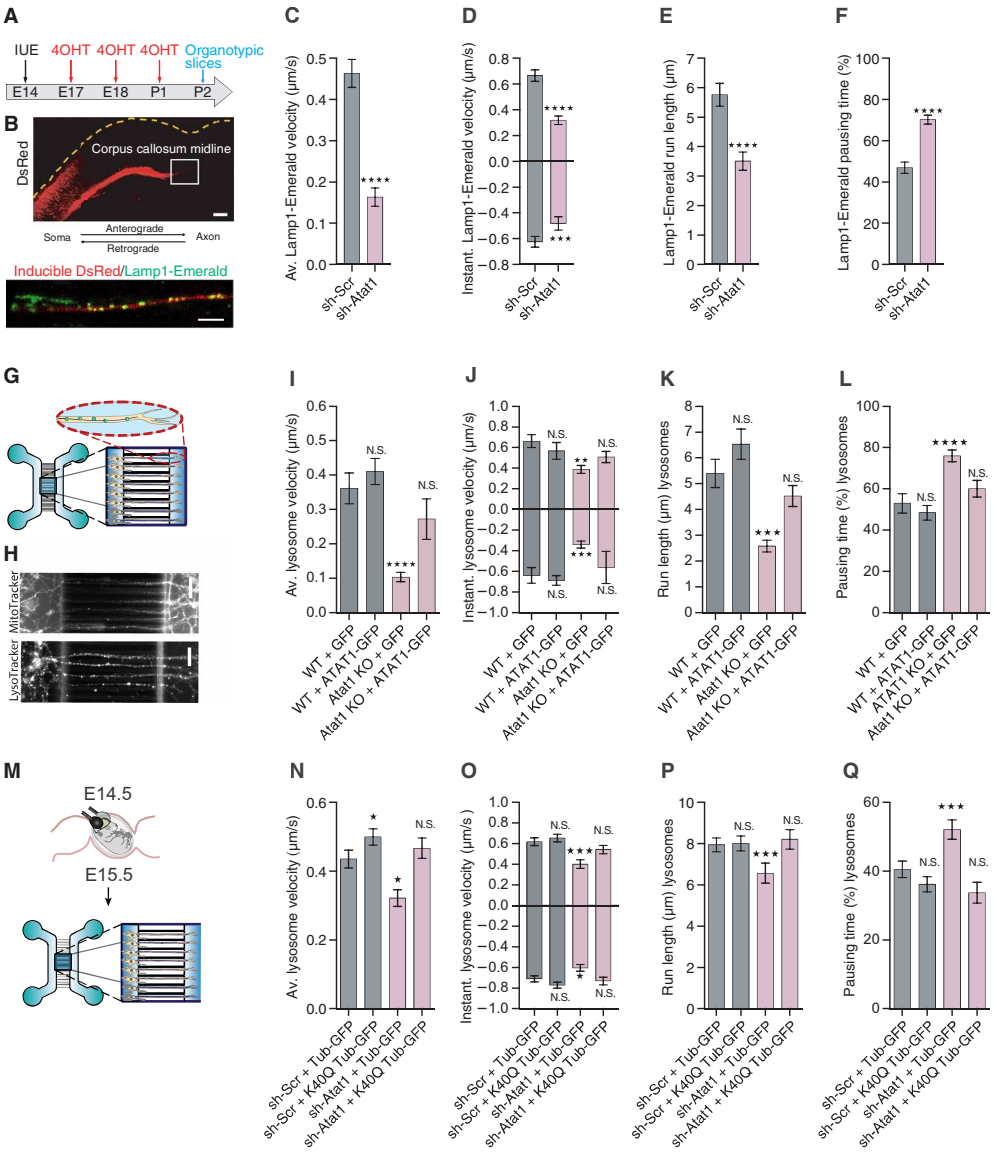

Fig. 1. Depletion of Atat1 prevents acetylation of α-tubulin and interferes with fast axonal transport of organelles ex vivo and in vitro. (**A**) Experimental setup used to perform axonal transport recordings in organotypic brain slice. (**B**) Labeling of lysosome Lamp1-Emerald^{+} (green) and inducible dsRed (red) in axons crossing the corpus callosum of a P2 mouse cortical section. Scale bars, 200 μm (top) and 10 μm (bottom). (**C** to **F**) Histograms showing axonal transport parameters of Lamp1-Emerald (lysosomes) to analyze average velocity (C), instantaneous velocity (D), run length (E), and pausing time (F). (**G**) Microfluidic device setup used for recording axonal transport in cortical neurons. (**H**) Labeling of lysosomes and mitochondria with fluorescent probes (LysoTracker and MitoTracker) in cortical neurons cultured 5 DIV and isolated from E14.5 WT or *Atat1* KO mouse embryos. Scale bars, 50 μm. (**I** to **L**). Histograms showing parameters of axonal transport of lysosomes to analyze average velocity (I), instantaneous velocity (J), run length (K), and pausing time (L) of mouse cortical neurons transfected with GFP or ATAT1-GFP, cultured 5 DIV, and isolated from E14.5 from WT or *Atat1* embryos. (**M**) Experimental setup for time-lapse recording of axonal transport in E15.5 cortical neurons isolated from E14.5 IUE mouse embryos and cultured 5 days in microfluidic device. N.S., not significant. (**N** to **Q**) Histograms showing parameters of axonal transport of lysosomes (LysoTracker) to analyze average velocity (N), instantaneous velocity (O), run length (P), and pausing time (Q) in mouse cortical neurons cultured 5 DIV from E15.5 embryos transfected with WT α-tubulin GFP (Tub-GFP) or acetylation mimic K40Q α-tubulin GFP (K40Q Tub-GFP) together with sh-Scramble (sh-Scr) or sh-Atat1. Description of graphical summaries here within are histograms of means ± SEM, while statistical analyses of (C to F) are two-tailed Mann-Whitney and (I, J, K, L, N, O, P, and Q) are Kruskal-Wallis test. Specifically [(C) $P < 0.0001$ and U = 17,455; (D) $P < 0.0001$ and U = 3044 and $P = 0.0002$ and U = 6372 for anterograde and retrograde, respectively; (E) $P < 0.0001$ and U = 20,972; (F) $P < 0.0001$ and U = 26,168; (I) $P < 0.0001$ and K = 54.03; (J) $P = 0.0033$ and K = 13.74 and $P < 0.0001$ and K = 36.45 for anterograde and retrograde, respectively; (K) $P < 0.0001$ and K = 38.29; (L) $P < 0.0001$ and K = 34.05; (N) $P < 0.0001$ and K = 31.88; (O) $P = 0.0006$ and K = 17.43 and $P = 0.0002$ and K = 20.19 for anterograde and retrograde, respectively; (P) $P < 0.0001$ and K = 22.29; and (Q) $P < 0.0001$ and K = 28.7).

(Fig. 1I and fig. S1, G, M, N, and R), anterograde and retrograde instantaneous velocities (Fig. 1J and fig. S1, H, M, N, and R), and run lengths (Fig. 1K and fig. S1, I, M, N, and R) of moving vesicles and mitochondria were reduced, while their pausing time were increased (Fig. 1L and fig. S1, J, M, N, and R). These modified vesicular parameters were associated with an impairment in the overall flux of organelles in *Atat1* KO mice (fig. S1, K, L, M, and N), likely arising from the reduced recruitment of motors onto MTs. Western blotting analyses revealed that lack of ATAT1 expression in newborn cortical neurons resulted in the absence of MT acetylation (fig. S1, O and P) without affecting the expression level of histone deacetylase 6 (HDAC6), the main α-tubulin deacetylase (fig. S1, O and Q). Expression of catalytically active ATAT1–green fluorescent protein (GFP) (*15*, *16*) in cortical neurons from E14.5 WT and *Atat1* KO embryos rescued the average velocity (Fig. 1I and fig. S1R), anterograde and retrograde instantaneous velocities (Fig. 1J and fig. S1R), run length (Fig. 1K and fig. S1R), and pausing time (Fig. 1L and fig. S1R) of lysosomes. To confirm that the defects in axonal transport upon down-regulation of *Atat1* arise from reduced α-tubulin acetylation, we coexpressed the acetyl mimic α-tubulin K40Q with shAtat1 (fig. S1S) in projection neurons of WT E14.5 embryos. We isolated the electroporated neurons 1 day after electroporation and cultured them 5 days in microfluidic devices (Fig. 1M). Our recordings showed that expression of α-tubulin K40Q rescued the average and instantaneous transport velocities of lysosomes (Fig. 1, N and O, and fig. S1X) and mitochondria (fig. S1, T, U, and Y), as well as their run lengths (Fig. 1P and fig. S1, V, X, and Y) and pausing time (Fig. 1Q and fig. S1, W, X, and Y) resulting from *Atat1* KD at E14.5.

We further examined whether the role of ATAT1 in axonal transport is conserved in vivo in *Drosophila melanogaster*. We assessed the transport of synaptotagmin-GFP vesicles in axons of third-instar larva motoneurons (Fig. 2, A and B, and movie S4) upon RNA interference (RNAi)–mediated KD of *Atat1/2* (the orthologs of mouse *Atat1* in *D. melanogaster*). Individual KDs of *Atat1* and *Atat2* were not compensated by expression of other α-tubulin acetylation regulators (fig. S2, A and B) and led to the reduction of average velocity (Fig. 2C and fig. S2C), anterograde and retrograde instantaneous velocities (Fig. 2D and fig. S2C), as well as run length (Fig. 2E and fig. S2C) of synaptotagmin-GFP vesicles, with associated increase of their pausing time (Fig. 2F and fig. S2C). The transport defects were not resulting from global protein aggregation along axons (fig. S2D) but were more likely associated with the decreased acetylation of MTs (Fig. 2, G and H). This was further supported by a genetic rescue of axonal transport upon concomitant depletion of the main α-tubulin deacetylase *Hdac6* (*17*) (fig. S2E) in motoneurons from individual KD of *Atat1* or *Atat2* larva (Fig. 2, C to F, and fig. S2C), where residual Atat activity can promote MT acetylation (Fig. 2, G and H). These data were also supported in the third-instar larvae fed for 30 min before recordings with 10% sucrose solution containing tubastatin (TBA), a specific inhibitor of HDAC6 (*18*), which rescued all measured axonal transport parameters (Fig. 2, I to L, and fig. S2F).

Impaired axonal transport in larvae or adult fly motoneurons leads to locomotor behavior deficits (*18*). We thus monitored the climbing index of adult flies as well as the crawling speed and peristaltic body-wave frequency of their larvae as functional readouts of single or combined KD of *Atat1/2* (*6*, *19*). These motoneuron-dependent activities were affected upon conditional KD of *Atat1/2* expression (Fig. 2, M to O) and were rescued by either a concomitant genetic depletion of *Hdac6* (Fig. 2, M to O) or inhibition of HDAC6 activity using TBA (Fig. 2, P and Q). The disruption of motor behaviors was most likely a consequence of fast axonal transport defects, since we did not observe morphological changes at the neuromuscular junctions' synapses (fig. S2, G and H) and the RNAi-mediated KD was restricted to motoneurons (see Materials and Methods). Together, these data support that ATAT1 promotes the acetylation of axonal MTs across vertebrate and invertebrate species and that acetylation of the MTs tracks is an important regulator of fast axonal transport.

We next assessed in a cell-free in vitro molecular transport assay how the reduction of K40 acetylation on MTs affects bidirectional axonal transport. For this purpose, purified vesicles were added to in vitro polymerized and polarity-marked MTs (to determine transport directionality), where 10% of rhodamine-labeled (acetylated) tubulin were mixed with either unacetylated tubulin from *Atat1* KO mouse brains or with endogenously acetylated tubulin from WT littermates (control) (Fig. 3, A and B, and movie S5). While MTs from *Atat1* KO mouse brains were lacking acetylation (*20*), they were not showing defects of polyglutamylation, glutamylation, tyrosination, or the abundance of Δ2 tubulin PTMs (Fig. 3C). In vitro transport analyses showed that vesicles' anterograde and retrograde instantaneous velocities (Fig. 3D and fig. S3A), together with their run lengths (Fig. 3E and fig. S3A), were reduced when vesicles were transported along *Atat1* KO brain-derived MTs as compared with acetylated MTs isolated from WT brains. These data were comparable to the one obtained in neurons in vitro and in vivo (Figs. 1, D and E, and 2, D and E) and further demonstrate that loss of α-tubulin K40 acetylation impairs MT-dependent transport.

Atat1 is transported along MTs at the external surface of motile vesicles

Axons and dendrites are highly enriched in long-lived MTs, whose acetylation depends on ATAT1 distribution and activity. In vitro experiments have previously reported that recombinant ATAT1 undergoes slow and passive diffusion inside MT lumen (*12*). However, it remains unclear how ATAT1 reaches the MTs in living neurons; thus, we studied its axonal distribution in cultured cortical neurons isolated from E14.5 mice. Mouse cortical neurons were transfected with a combination of plasmids coding for brain-derived neurotrophic factor (BDNF)–mCherry and ATAT1-GFP and cultured 5 DIV. Analysis by superresolution microscopy revealed a punctate distribution of ATAT1 along axons, partially overlapping with the dense core vesicle marker BDNF, suggesting a possible vesicular enrichment of ATAT1 (Fig. 4A). The vesicular enrichment of ATAT1 was further confirmed in cultured human projection neurons derived from pluripotent stem cells, showing that expression of endogenous ATAT1 broadly codistributes with lysosomes (LAMP1 positive) and precursors of synaptic vesicles (SV2C and synaptophysin positives) along their axon (Fig. 4B).

To confirm the vesicular expression of ATAT1, we performed liquid chromatography–tandem mass spectrometry (LC-MS/MS) on vesicular extracts isolated from the cortex of newborn mice. The analysis of the vesicular enriched fraction detected 3648 proteins whose overlap with published vesicular proteomes was, in average, 75% (*21*–*23*) (Fig. 4C). These analyses showed that ATAT1, but not HDAC6, is detected together with kinesins and dyneins in a mid-range fraction of the vesicular proteomic content (Fig. 4D and table S1). Western blot analysis of the subcellular fractions obtained from

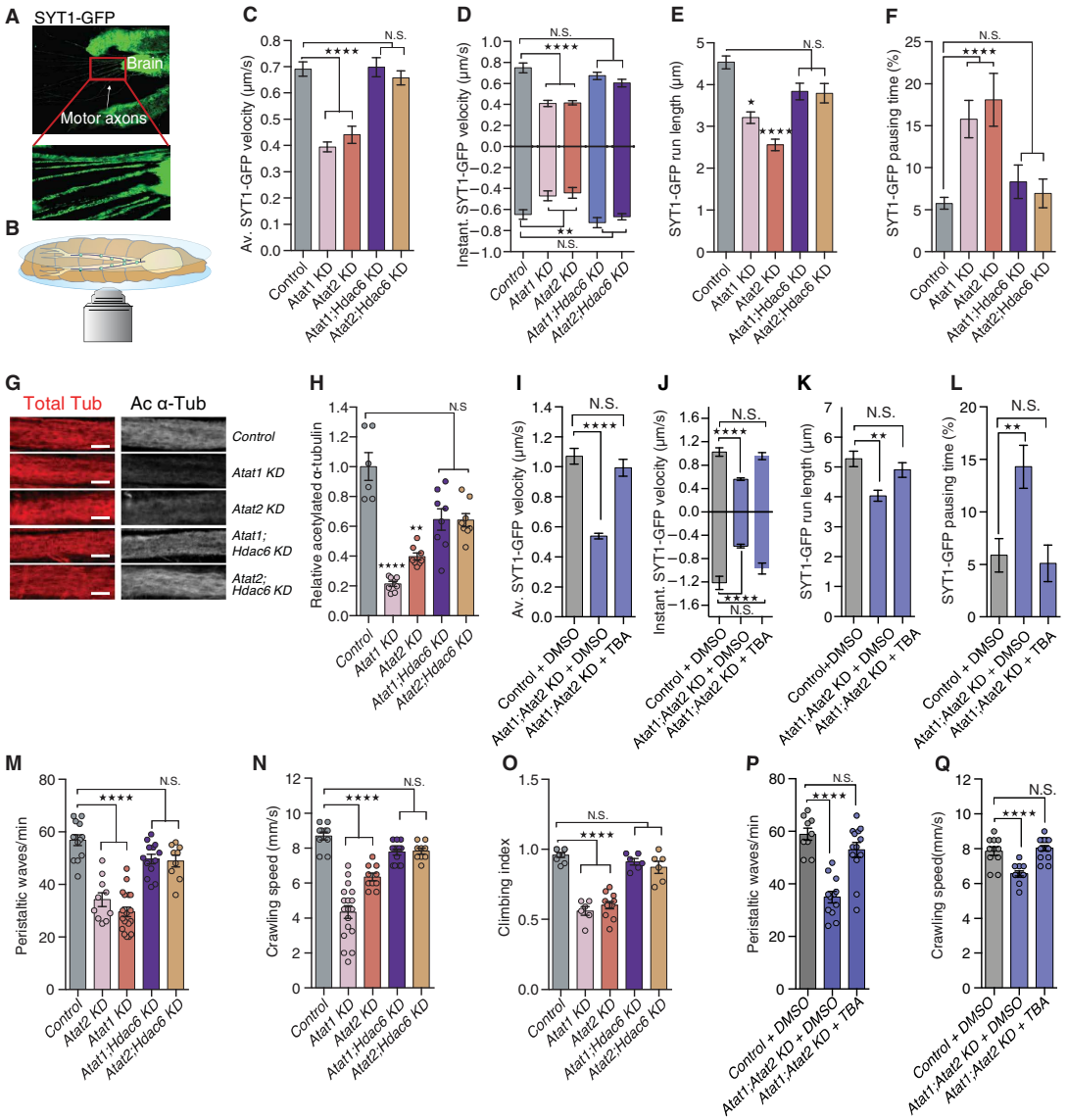

Fig. 2. Depletion of Atat1 prevents acetylation of α-tubulin and interferes with fast axonal transport of organelles in vivo. (**A** and **B**) In vivo live-imaging setup used to record axonal transport of synaptotagmin-GFP (SYT1-GFP in green) in *D. melanogaster* third-instar larvae expressing UAS:RNAi under a motoneuron-specific driver (D42:GAL4) to analyze average velocity (**C**), instantaneous velocity (**D**), run length (**E**), and pausing time (**F**). (**G** and **H**). Analyses of immunolabeled motoneurons from third-instar larvae to detect total α-tubulin (Tot α-tub) and acetylated α-tubulin (Ac α-tub). Scale bars, 10 µm. (**I** to **L**) Axonal transport recording in *Atat1;Atat2* KD third-instar larvae fed for 30 min before recording with 10% sucrose with 1 mM TBA or dimethyl sulfoxide (DMSO) to measure SYT1-GFP average velocity (I), instantaneous velocity (J), run length (K), and pausing time (L). (**M** and **N**) Larva peristaltic movements and crawling speed in third-instar larvae expressing RNAi under a motoneuron-specific driver (D42:GAL4). (**O**) Climbing index in adult flies expressing RNAi under a motor neuron-specific driver. (**P** and **Q**) Larva peristaltic movements and crawling speed in third-instar larvae expressing RNAi under a motoneuron-specific driver (D42:GAL4) or in control and *Atat1;Atat2* KD larva prefed for 30 min with 10% sucrose with 1 mM TBA or DMSO. Description of graphical summaries here within are histograms of means ± SEM, while statistical analyses of (C, D, E, F, H, I, J, K, and L) are Kruskal-Wallis and (M to Q) is one-way analysis of variance (ANOVA). Specifically [(C) $P < 0.0001$ and K = 60.10; (D) $P < 0.0001$ and K = 65.80 and $P < 0.0001$ and K = 76.02 for anterograde and retrograde respectively; (E) $P < 0.0001$ and K = 25.39; (F) $P < 0.0001$ and K = 9.6; H, $P < 0.0001$ and K = 30.09; (I) $P < 0.0001$ and K = 121.1; (J) $P < 0.0001$ and K = 62.57 and $P < 0.0001$ and K = 50.34 for anterograde and retrograde, respectively; (K) $P < 0.0001$ and K = 24.3; (L) $P < 0.0001$ and K = 12.96, M, $P < 0.0001$ and $F(4, 58) = 34.55$; (N) $P < 0.0001$ and $F(4, 55) = 40.83$; (O) $P < 0.0001$ and $F(4, 33) = 45.61$; (P) $P < 0.0001$ and $F(7, 71) = 27.29$; and (Q) $P < 0.0001$ and $F(7, 83) = 47.65$]. In addition, post hoc multiple comparisons for (C, D, E, F, I, J, K, L, and H) Dunn's tests, for (M to Q) is Dunnett's test and are *$P < 0.05$, **$P < 0.01$, ***$P < 0.001$, and ****$P < 0.0001$. The total number of samples analyzed were as follows: (C to F) 110 to 276 vesicle tracks from 7 to 12 larvae per group; (H) 6 to 8 larvae per group; (I to L) 112 to 161 vesicle tracks from at 6 to 8 larvae per group; (M and N) 9 to 18 larvae per group; (O) 6 to 11 assays per group; and (P and Q) 8 to 9 larvae per group.

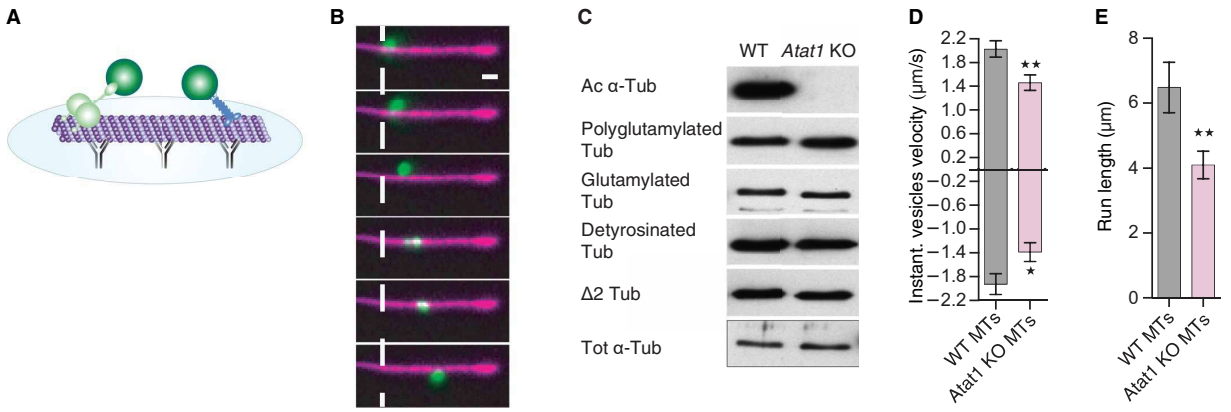

Fig. 3. Vesicle transport is reduced on nonacetylated MTs in vitro. (**A**) Scheme representing the experimental setup to study in vitro transport and acetylation assays. (**B**) Total internal reflection fluorescence (TIRF) image series of rhodamine-labeled MTs (10%, purple) with a transported DIO (green)–labeled vesicle from mouse brains. Scale bar, 2 μm; presented frames are in a 400-ms interval. (**C**) Western blott (WB) analyses to detect acetylated, glutamylated, polyglutamylated detyrosinated, Δ2, or total α-tubulin (Tub) in cortical brain extracts of WT or *Atat1* KO adult mice. (**D** and **E**) In vitro transport assay of vesicles purified from WT mice with nonacetylated α-tubulin from *Atat1* KO mouse brain or endogenously acetylated α-tubulin from WT mice. Histogram of anterograde and retrograde instantaneous velocities (D) and run length (E) of moving vesicles. Description of graphical summaries here within are histograms of means ± SEM, statistical analyses of (D) and (E) are two-tailed *t* test. Specifically [(D) $P = 0.0299$ and t, df(2,273,32) and $P = 0.0054$ and t, df(2,971,34) for retrograde and anterograde, respectively; and (E) $P = 0.0086$ and U = 50]. The total number of samples analyzed were as follows: (D and E) 16 to 20 vesicles from three WT or *Atat1* KO mice.

protein extract of newborn mouse brains confirmed the selective enrichment of ATAT1 in the vesicular fraction (P3), contrasting with the predominant cytosolic distribution of HDAC6 (S3) (Fig. 4E). Moreover, time-lapse recordings showed that ATAT1-GFP clusters move bidirectionally together with lysosomes (LysoTracker, Fig. 4F) and dense core vesicles (BDNF-mCherry, Fig. 4F) at velocities that are consistent with axonal transport in transfected cortical projection neurons (Fig. 4, G and H, and movie S6) (*24*). These data demonstrate that ATAT1 is enriched in the vesicular fraction and that it is transported along axons by motile vesicles.

ATAT1 binds to clathrin-coated vesicles via an AP2 binding domain (amino acids 307 to 387) (*25*), which is only conserved by its isoforms 1 and 2 (Fig. 4I). Our LC-MS/MS analysis did not detect peptides corresponding to the AP2 binding domain of ATAT1 in purified vesicles extracts (fig. S4A), and Western blott (WB) performed on mice cortical brain extracts only detected the presence of ATAT1 isoforms 3 and 4 (Fig. 4E), suggesting that the AP2 binding domain is not required for the recruitment of ATAT1 to motile vesicles.

To identify ATAT1's vesicle binding domain, we engineered distinct truncated ATAT1 forms by deleting amino acid sequences between the minimal catalytic domain of ATAT1 (amino acids 1 to 196) and the C-terminal part of isoform 4 (amino acids 1 to 333) (Fig. 4I). These constructs were next used to transfect human embryonic kidney (HEK) 293 cells and analyzed for their subcellular localization by WB (Fig. 4, J and K). ATAT1 isoform 4 and its amino acid 1 to 286 truncation were enriched in vesicles [vesicles (P3)/cytosol fraction ratio (S3) > 1], while the other truncated forms (1 to 242 and 1 to 196) preferentially localized in the cytosol (P3/S3 < 1) (Fig. 4K). Moreover, expression of the vesicular-enriched ATAT1 isoforms was more efficiently raising the level of α-tubulin acetylation when expressed in HeLa S3 cells as compared to the others (Fig. 4, L and M). Together, these data suggest that the amino acid sequence of ATAT1 comprised between amino acids 242 to 333 is required for both its vesicular enrichment and efficient α-tubulin acetylation.

To decipher whether ATAT1 is encapsulated within the intravesicular lumen and/or associated with the extravesicular membrane, we performed a mild proteinase K digestion to remove protein anchored at the external surface of vesicles (*26*). The treatment led to a dose-dependent reduction of ATAT1 and dynein intermediate chain (DIC) without altering levels of the intravesicular protein α-synuclein (Fig. 4N) (*26*). Together, these data suggest that ATAT1 is enriched at the cytosolic side of moving vesicles, from where it may be released in vicinity of MTs to promote α-tubulin acetylation and modulate axonal transport.

The vesicular pool of Atat1 controls axonal transport by promoting acetylation of MTs

We first performed LC-MS/MS on vesicular extracts isolated from the cortex of newborn WT or *Atat1* KO mice to check whether loss of Atat1 interferes with axonal transport by altering the vesicular proteome. The analysis revealed that, from 44 differentially detected proteins (fig. S5A and table S2), none of the 29 molecular motor proteins (fig. S5B and table S3) nor the 16 glycolytic enzymes (fig. S5C and table S4) were significantly affected by lack of Atat1 expression. Moreover, gene ontology (GO) data analysis of the differentially detected proteins did not reveal significantly enriched processes, function, or cellular component upon Atat1 loss in vesicular extracts. Since we did not detect any differences of the *Atat1* KO vesicular proteome that can explain the reduction of MT acetylation, we hypothesized that Atat1-enriched vesicle displacement on MTs might be required for their acetylation. To test this hypothesis, we cultured mouse cortical neurons with the cytoplasmic dynein inhibitor ciliobrevin D (20 μM) (*27*) to disrupt axonal transport of vesicles. This led to a mild reduction (33%) of MT acetylation in the soma of the neurons (Fig. 5, A and B) and a severe reduction (67%)

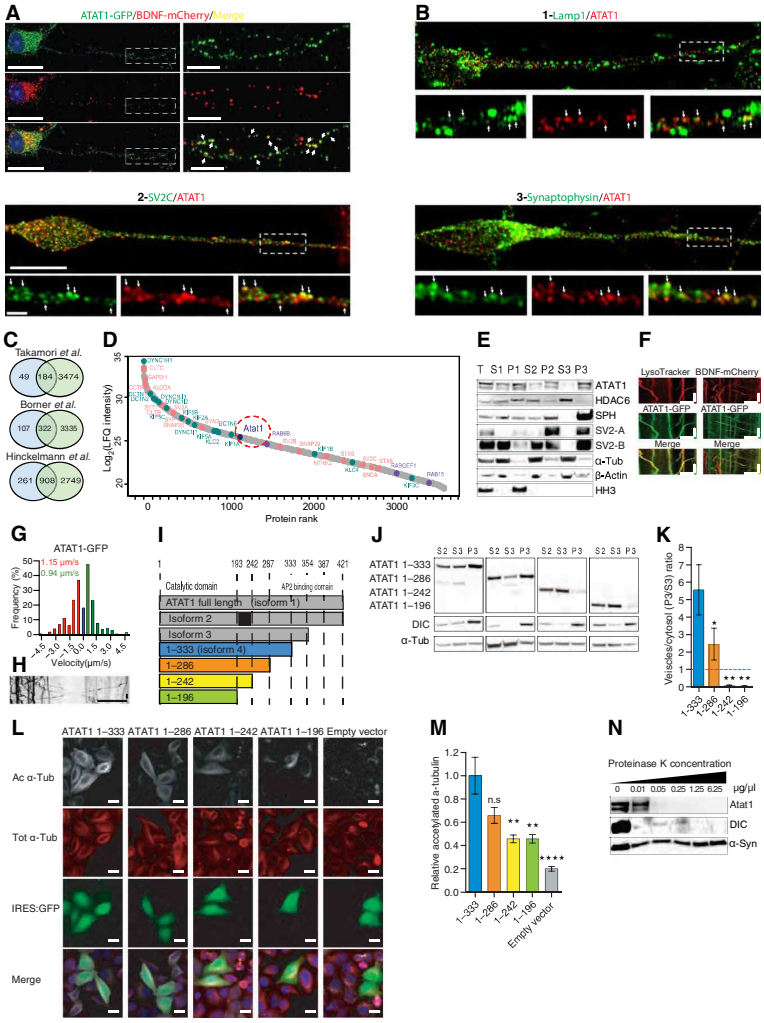

Fig. 4. ATAT1 is a vesicular-enriched protein that localizes on the cytosolic side of the vesicular membrane. (**A**) Superresolution image of a transfected E14.5 cortical neuron-cultured 5 DIV and labeled for 4′ 6-diamidino-2-phenylindole (DAPI) (blue), ATAT1-GFP (green), and BDNF-mCherry (red). Scale bar is 20 μm for the original image and 5 μm for the magnified area. (**B**) Superresolution imagine of day 36 human projecting neurons derived from hIPSCs and immunostained for ATAT1 along with 1, Lamp1; 2, SV2C; and 3, synaptophysin. Arrowheads indicate codistribution of markers. Scale bar is 10 and 1 μm for the original image and magnified area, respectively. (**C**) Venn diagrams of vesicular content identified by LC-MS/MS in this work and previous publications. (**D**) LC-MS/MS of vesicle fraction isolated from newborn mouse brain cortices, proteins were ranked by intensity and plotted according to their relative abundance (gray spots). Atat1 (pink) detection among proteins previously identified as vesicular components (purple) and molecular motors (green) ($n = 3$, graph represent the mean intensity value). (**E**) Subcellular fractionation (T, total; S1, postnuclear; P1, nuclear; S2, cytosol and vesicles; P2, larges membranes; S3, cytosol; and P3, vesicles) of mouse brain cortex showing predominant vesicular enrichment of Atat1, immunostained with antibodies (Table 1) against ATAT1 (isoform 3 and 4 corresponding to 37 and 30 kDa), histone deacetylase 6 (HDAC6), synaptophysin (SPH), synaptic vesicle glycoprotein 2A/B (SV2A/B), β-actin, α-tubulin (α-tub), and histone H3 (HH3) antibodies. (**F**) Kymographs of ATAT1-GFP and LysoTracker or BDNF-mCherry in E14.5 cortical neurons axons cultured 5 DIV, showing partial cotransport of Atat1 and lysosomes or BDNF-mCherry. Scale bars, 10 μm (*x*) and 20 s (*y*). (**G** and **H**) Bin distribution and kymograph of ATAT1-GFP transport velocities in transfected E14.5 cortical neurons cultured 5 DIV ($n = 5$; *n* for anterograde =143, retrograde = 179). Scale bars, 10 μm (*x*) and 20 s (*y*). (**I**) Schematic representation of truncated ATAT1 isoform four constructs. (**J** and **K**) Subcellular fractions of cultured HEK293 cells were analyzed using WB to detect ATAT1 truncated forms (J), vesicles/cytosol (P3/S3) ratios were quantified to identify vesicular enrichment (ratio > 1) of the various truncated ATAT1 forms (K). (**L** and **M**) Transfected HeLa cells with ATAT1:IRES-GFP truncated constructs were immunolabeled for acetylated α-tubulin (Ac α-tub, gray), total α-tubulin (Tot α-tub, red), and DAPI (blue) and analyzed for their relative acetylated α-tubulin levels [Ac α-tub/Tot α-tub ratio, controls are set to 1, (M)]. Scale bar, 10 μm. (**N**) WB analysis of cerebral cortex vesicles subjected to proteinase-K digestion. Intravesicular α-synuclein is digestion resistant, while the outer vesicular membrane motor protein DIC as well as Atat1 were digested in an enzymatic concentration–dependent manner. Description of graphical summaries here within are histograms of means ± SEM; statistical analyses of (K) is one-way ANOVA and (M) is Kruskal-Wallis. Specifically [(K) $P = 0.0018$ and $F_{(3,12)} = 17.29$; (M) $P < 0.0001$ and K = 83.16]. In addition, post hoc multiple comparisons are Holm-Sidak's tests (K), and Dunn's test (M); $^{*}P < 0.05$, $^{**}P < 0.01$, and $^{****}P < 0.0001$. The total number of samples analyzed were four independent HEK293 cultures (K) and four independent HeLa cultures (M) per ATAT1 truncation construct.

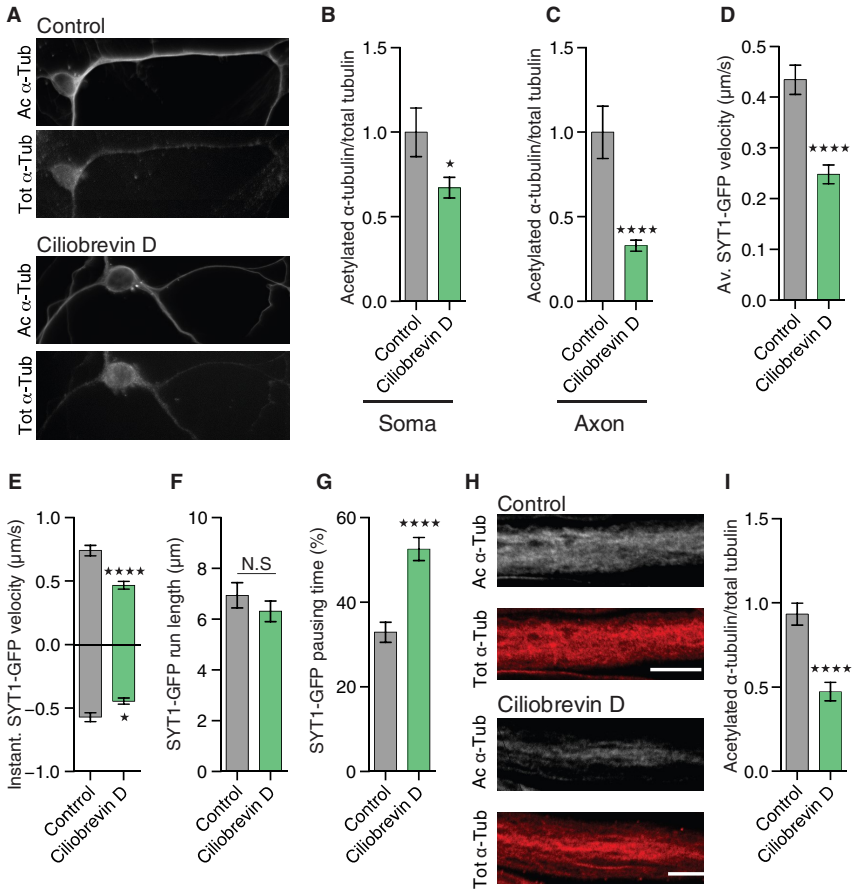

Fig. 5. Ciliobrevin disrupts α-tubulin acetylation and axonal transport in vitro and in vivo. (**A** to **C**) Immunolabeled cortical neurons from E14.5 mice embryos treated with 20 μM of ciliobrevin D of control buffer 1 hour before fixation, showing total α-tubulin (Tot α-tub) and acetylated α-tubulin (Ac α-tub) in the soma (B) or distal axons (C) of the neurons. Scale bar, 10 μm. (**D** to **G**) Axonal transport in motoneurons from synaptotagmin-GFP *D. melanogaster* third-instar larvae fed during 2 hours with 800 μM of DMSO (control) or ciliobrevin D before the analysis of average SYT1-GFP vesicle velocity (D), instantaneous velocity (E), run length (F), and pausing time (G). (**H** and **I**) Immunolabeled motoneurons from third-instar larvae fed with 800 μM of ciliobrevin D 2 hours before sacrifice, showing total α-tubulin (Tot α-tub) and acetylated α-tubulin (Ac α-tub). Scale bar,10 μm. Description of graphical summaries here within are histograms of means ± SEM; statistical analyses of (B) and (C) are two-tailed *t* test, while those of (D) to (G) are two-tailed Mann-Whitney. Specifically, [(B) $P = 0.0419$ and t, $df_{(2.051, 58)}$); (C) $P < 0.0001$ and U = 699; (D) $P < 0.0001$ and U = 23,096; (E) $P = 0.0005$ and U = 3857 and $P = 0.0209$ and U = 3,293 for anterograde and retrograde, respectively; (F) $P = 0.7385$ and U = 37,999; (G) $P < 0.0001$ U = 28,877; and (I) $P < 0.0001$ and U = 336). The total number of samples analyzed was (B and C) 29 to 50 neurons from four embryos; (D to G) = 116 to 279 SYT1-GFP tracks from 6 to 8 larvae per group; and (I) 37 to 49 neurons from 8 to 10 larvae. *$P < 0.05$ and ****$P < 0.0001$.

of acetylation of distal axonal MTs (Fig. 5, A and C) as a result of a reduction of axonal transport (Fig. 5D and fig. S6L). At this concentration, ciliobrevin D blocks both retrograde and anterograde transports (*27*); we thus specifically reduced retrograde transport by knocking down Lis1 in mouse cortical neurons (fig. S6, A to H). This led to a reduction of MT acetylation in the axon but not in the soma of these neurons (fig. S6, I to K). Moreover, feeding *Drosophila* third-instar larvae with ciliobrevin D (800 μM) disrupted anterograde and retrograde axonal transport (Fig. 5, E to G, and fig. S6A) and decreased MT acetylation (Fig. 5, H and I) in motoneurons in vivo to a level comparable with the one observed upon expression of *Atat1/2* RNAi (Fig. 2, G and H). These results show that disrupting axonal transport impairs MT acetylation, a defect that correlates with a lack of mobility of Atat1-enriched vesicles along the axonal MTs.

To test whether the vesicular pool of Atat1 promotes the acetylation of α-tubulin in MTs, we isolated subcellular fractions from newborn mouse cortices and then assessed their ability to promote the acetylation of nonacetylated MTs isolated from HeLa cells (*8*), compared with endogenously acetylated bovine brain MTs (control) (Fig. 6A). We observed that most of the MT acetyltransferase activity was detected in the vesicular fraction (Fig. 6B), an activity that was lost in either vesicles isolated from *Atat1* KO mice or vesicles incubated without acetyl–coenzyme A (CoA), the acetyl group donor for Atat1-dependent MT acetylation (Fig. 6, C to E) (*15*). Moreover, the vesicular fraction was able to promote the acetylation of MTs over several hours in vitro, as suggested by the strong reduction of CoA release upon incubation with vesicles from *Atat1* KO mice, as compared to WT control (Fig. 6F). These findings suggest that the

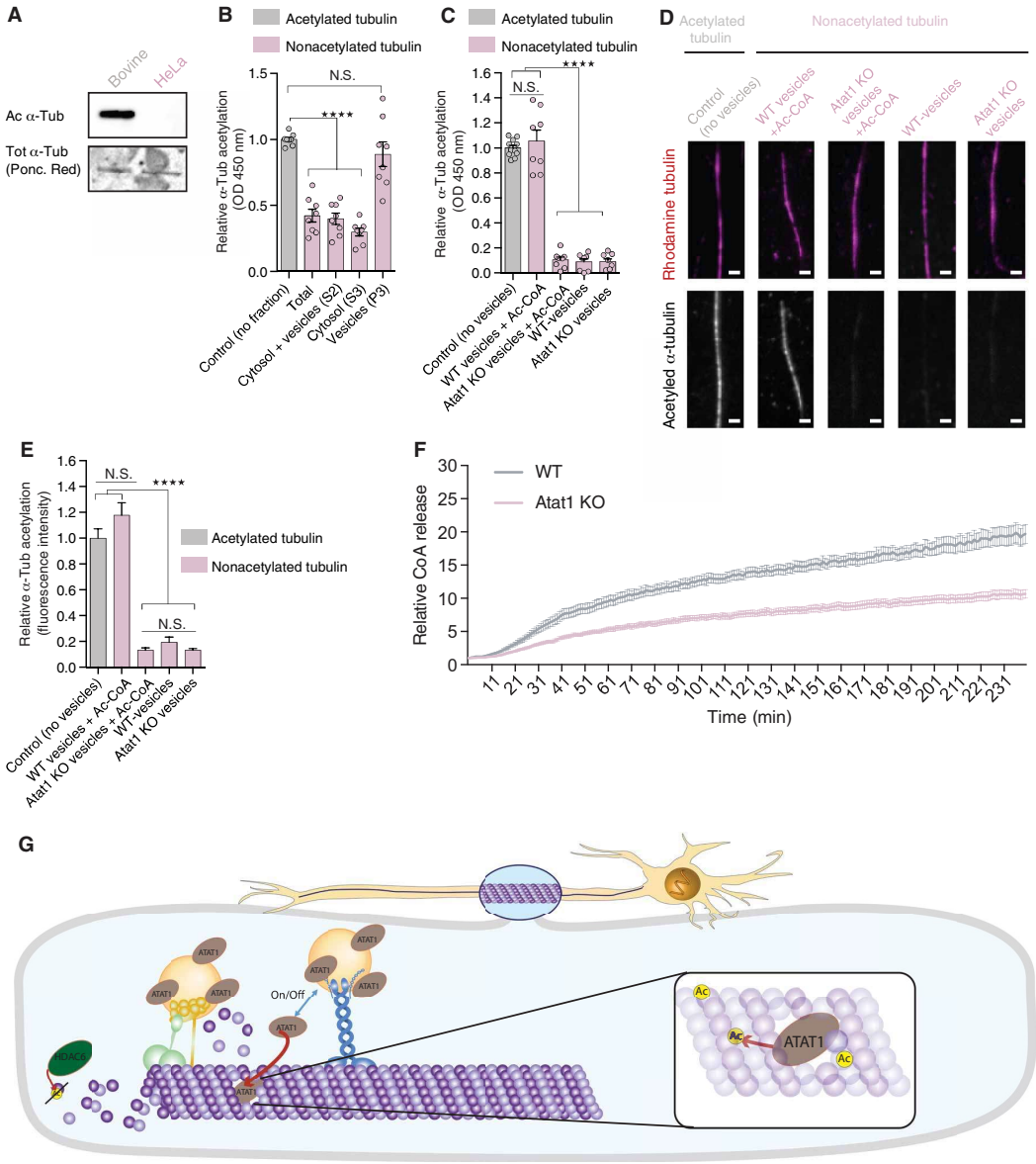

Fig. 6. Vesicles predominantly promote α-tubulin acetylation via ATAT1. (**A**) WB analysis of purified tubulin from bovine brain and HeLa cells, showing acetylated α-tubulin (Ac α-tub). Ponceau red identified total α-tubulin (Tot α-tub) on corresponding extracts. (**B** and **C**) In vitro enzyme-linked immunosorbent assay (ELISA)–based α-tubulin acetylation assay of polymerized nonacetylated MTs from HeLa cells; incubated with subcellular fraction (B); or with vesicular fractions isolated from WT or *Atat1 KO* mouse brain cortices with acetyl-CoA or vehicle (C). Purified bovine endogenously acetylated MTs served as control. (**D** and **E**) α-Tubulin acetylation assay of in vitro polymerized nonacetylated MTs from HeLa cells incubated with vesicular fractions (P3) isolated from WT or *Atat1* KO mouse brain cortices and acetyl-CoA or vehicle. Purified bovine endogenously acetylated MTs served as control. Fluorescent signal was measured for total α-tubulin by using rhodamine dye and for acetylated α-tubulin by immunolabeling. Scale bar, 2 μm. (**F**) In vitro α-tubulin acetylation assay based on CoA release from acetyl-CoA by incubating vesicles from WT or *Atat1* KO mice with polymerized nonacetylated MTs from HeLa cells. (**G**) Scheme depicting the axonal transport (anterograde and retrograde) of vesicles enriched in ATAT1 at their external surface. The proper acetylation of MTs is linked to the axonal transport of these vesicles and we propose that axonal transport transiently disrupt the MT lattice by creating transient openings through which ATAT1 relocates intralumenally to promote K40 α-tubulin acetylation. Description of graphical summaries here within are histograms of means ± SEM, while statistical analyses of (B and C) are one-way ANOVA; (D) is Kruskal-Wallis and (F) is two-way ANOVA. Specifically [(B) $P < 0.0001$ and $F_{(4,35)}=35.56$; (C) $P < 0.0001$ and $F_{(4,38)}=158.3$; (E) $P < 0.0001$ and K = 120.8; (F) $P < 0.0001$ and $F_{(1,3360)} = 8113$) In addition, post hoc multiple comparisons are Sidak's tests (B and C): Dunn's test (D); ****$P < 0.0001$. The total number of samples analyzed were as follows: (B and C) eight subcellular brain cortical fractions from eight newborn mice; (E) = 29 to 46 MTs, (F) 240 sample points (1/min) of purified vesicles from three WT and three *Atat1* KO mouse brain cortices.

Table 1. List of antibodies and their dilution used for ELISA assays, immunostainings, and/or Western blottings.

Protein	Company	Cat no.	WB	IF	ELISA
α-Tubulin	Sigma-Aldrich	T9026	1:5000		1:2,000
α-Tubulin*	DSHB	12G10	1:500		
α/β-Tubulin	Cytoskeleton	ATN02-A		1:150	
Acetylated α-tubulin	Sigma-Aldrich	T7451	1:15,000	1:15,000	
Polyglutamylated tubulin	AdipoGen	AG-25B-0030	1:10,000		
Glutamylated tubulin	AdipoGen	AG-20B-0020	1:10,000		
Detyrosinated tubulin	Millipore	AB3201	1:1,000		
Δ2-Tubulin	Millipore	AB3203	1:2,000		
Lis1	Santa Cruz	Sc-393320	1:100	1:100	
ATAT1	Sigma-Aldrich	HPA046816	1:2000	1:120	
GAPDH	Millipore	MAB374	1:300		
LAMP1	Abcam	Ab25630		1:20	
Synaptophysin	Synaptic Systems	101 004		1:1000	
SV2C	Synaptic Systems	119 204		1:500	
GFP	Origene	TP401	1:5000		
GFP	Abcam	Ab6673		1:1000	
β-Actin	Sigma-Aldrich	A3853	1:20,000		
HDAC6	Santa Cruz Biotechnology	sc-5258	1:200		
GFP	Molecular Probes	A11122	1:1000		
ATAT1	Maxence Nachury		1:1000		
CSP** (cystein-string protein)	DSHB	DCSP-2 (D6D)		1:10	
HRP	Sigma-Aldrich	P97899		1:1,000	
FLAG	Sigma-Aldrich	F3165	1:1,000		
Synaptophysin	Sigma-Aldrich	s5768	1:1,000		
Histone H3	cell signaling	9715	1:5,000		
Synuclein	Abcam	ab51252	1:5,000		
DIC	Millipore	MAB1618	1:500		
SV2***	DSHB	AB 2315387	1:100		
β-Tubulin	cell signaling	2146		1:100	
Goat anti mouse	Jackson ImmunoResearch Labs	115–035-003	1:10,000	1:200	1:5,000
Goat anti rabbit	Jackson ImmunoResearch Labs	111-035-003	1:10,000	1:200	
Donkey anti goat	Jackson ImmunoResearch Labs	705-035-003	1:10,000		

*12G10 anti–α-tubulin was deposited to the DSHB by J. Frankel/E.M. Nelsen (DSHB hybridoma product 12G10 anti–α-tubulin). **DCSP-2 (6D6) was deposited to the DSHB by S. Benzer [DSHB hybridoma product DCSP-2 (6D6)]. ***SV2 was deposited to the DSHB by K.M. Buckley (DSHB hybridoma product SV2).

pool of vesicular Atat1 provides an enzymatic activity that promotes MT acetylation and thereby fast axonal transport (Fig. 6G).

DISCUSSION

Here, we show that loss of *Atat1*(/2), thereby MT acetylation, impairs bidirectional axonal transport in mouse cortical neurons in culture or in organotypic slice as well as in fly larva motoneurons in vivo, ultimately resulting in locomotor defects in adult flies. Our work revealed the existence of a large pool of functional Atat1 at the external surface of different types of motile vesicles, including lysosomes and precursors of synaptic vesicles. Moreover, blocking MT-dependent transport impaired α-tubulin acetylation, further suggesting that Atat1-enriched vesicles have to be transported along MT to promote α-tubulin acetylation. Treatment with high concentration of ciliobrevin D (that blocks both retrograde and anterograde transport;

Fig. 5E) or expression of shLis1 (that blocks retrograde transport; fig. S6E) significantly reduced MT acetylation in the axon, while only ciliobrevin D treatment did so in the soma. This suggests a possible predominant role for the anterograde transport of Atat1-enriched vesicles to promote α-tubulin acetylation in the soma, a hypothesis whose validation would require additional experiments.

Increasing MT acetylation has been shown to compensate for axonal transport defects in fly, mouse, and human models (*6*, *16*). However, the role of Atat1 in axonal transport has been debated, since loss of Atat1/MEC17 expression impairs axonal transport in *Caenorhabditis elegans* neurons (*28*) but not in hippocampal and dorsal root ganglia neurons from adult mice (*29*). This apparent discrepancy may reflect different contributions of Atat1, thereby MT acetylation to axonal transport in distinct neuronal populations. It is also unexpected that, while acute deletion of *Atat1* impairs MT acetylation, neuronal migration, and axon branching in the developing rodent cortex (*30*), *Atat1* KO mice only show mild neurological abnormalities such as increased anxiety and impairments in mechanosensation (*14*, *29*). Such discrepancy may reflect a stronger requirement for Atat1 during development and early life, as suggested by its decreasing expression after birth in the cerebral cortex of both mice (*30*) and humans (*31*) (figure S7, 2018 Allen Institute for Cell Science. BrainSpan Atlas of the Developing Human Brain. Available from: brainspan.org/rnaseq/search/index.html).

Recent work performed in vitro has suggested that ATAT1 diffuses in the lumen of MTs where it induces acetylation of α-tubulin K40 (*12*). While the mode of intraluminal relocation of ATAT1 remains controversial (*11*, *12*), we now suggest that motile vesicles bring ATAT1 in close vicinity to MTs, which is in accord with the detection of ATAT1 at the surface of MTs by electronic scanning microscopy (*9*). Supposing that molecular transport triggers transient MT lattice deformations (*32*, *33*) and disruption (*34*), one can postulate that locally released vesicular ATAT1 could reach the MT lumen to acetylates α-tubulin K40 in vivo via these dynamic lateral openings (*35*).

The results of our work, together with the observation that vesicular glyceraldehyde-3-phosphate dehydrogenase (GAPDH) activity contributes to local generation of adenosine triphosphate (ATP) for fast-moving vesicles (*24*), show that vesicles have on-board enzymatic machinery that can act locally and modulate their own transport by changing their molecular environment. Our work suggests, in particular, that in neurons, vesicle-associated enzymes can locally modify MT tracks, thus optimizing axonal transport. Reduced acetylation of MTs also affect their flexibility and thus resistance to physical breakage after repeated mechanical stress (*10*, *36*), and loss of Atat1/MEC17 in *C. elegans* leads to MT instability and axonal degeneration (*28*). Therefore, it would be interesting to test whether a reduced vesicular axonal transport, as observed in neurodegenerative diseases (*37*), might contribute to the neurodegeneration process via curtailing the acetylation of α-tubulin, hence leading to a global weakening and breakage of axonal MTs.

MATERIALS AND METHODS

Mice

Mice were euthanized and brain cortices were harvested either at P0 to P2 for biochemical analysis or E14.5 for preparation of cortical neuronal cultures. *Atat1*$^{+/-}$ mice were used to obtain WT and KO mice (*14*). Mice were maintained with access to food and water ad libitum and kept at a constant temperature (19° to 22°C) and humidity (40 to 50%) on a 12:12-hour light/dark cycle according to the guidelines of the Belgian Ministry of Agriculture and in agreement with the European Community Laboratory Animal Care and Use Regulations (86/609/CEE, Journal Officiel des Communautés Européennes L358, 18 December 1986). All experimental procedures were performed in strict accordance with the recommendations of the European Community (86/609/EEC) for care and use of laboratory animals under the supervision of authorized investigators.

D. melanogaster maintenance and lines

Flies were kept at a 25°C incubator with a 12-hour light and dark cycle. Crosses were performed at 25°C, first-instar larvae were transferred to a 29°C incubator until use. For axonal transport, behavioral experiments and immunolabeling D42-Gal4-UAS: Syt1-GFP or D42-Gal4 virgin females were crossed with upstream activation sequence (UAS)–RNAi carrying lines. For quantitative polymerase chain reaction (qPCR) analysis, elav-Gal4 females were crossed with UAS-RNAi males. All RNAi inserts sequences were validated by Sanger sequencing.

Drosophila lines were acquired from the Vienna Drosophila Resource Center (VDRC) and the Bloomington Drosophila Stock Center (BDSC). UAS-*Syt1:GFP* (BDSC 6925), UAS-RNAi *Atat1* (VDRC CG3967), UAS-RNAi *Atat2* (VDRC CG17003), UAS-RNAi *Hdac6* (BDSC 51181), and UAS-RNAi *Zpg* (VDRC CG10125) were used as control. Elav-Gal4 (BDSC 458) or D42-Gal4 (BDSC 8816) flies were used for specific activation of a UAS sequence in postmitotic neurons or motor neurons, respectively. All RNAi insert sequences were validated by Sanger sequencing.

Constructs

BDNF-mCherry was previously used in (*24*) and ATAT1-GFP (27099), pCALNL-DsRed (13769), and pEGFP α-tubulin K40Q (105302) were purchased from Addgene (www.addgene.org/). pEGFP-Tub was obtained from Clontech (www.takarabio.com/). pCAG mEmerald-LAMP1 and pCAG mito-DsRED were provided by F. Polleux (Columbia University, New York, USA), and pCAG-iCreERT2 was provided by A. Tye (NIMR, UK). pCX-Cre plasmid was designed and provided by X. Morin (Institut de Biologie de l'Ecole Normale Superieure IBENS, France). ATAT1 truncation constructs, FLAG-ATAT1(amino acids 1 to 333), FLAG-ATAT1(amino acids 1 to 286), FLAG-ATAT1(amino acids 1 to 242), and FLAG-ATAT1(amino acids 1 to 196) were synthesized as gBlocks and inserted to a pCIG2 vector. The *Atat1* short hairpin RNA (shRNA) sequence was 5′-GCAGCAAATCATGACTATTGT-3′ (*30*). *Atat1* sequence was inserted in pBS/U6-ploxPneo plasmid (provided by X. Coumoul). Lis1 shRNA sequence was 5′-GAGATGAACTA-AATCGAGCTA-3′ (*38*) and was subcloned in pCA-b-EGFPm5 silencer 3, a gift from M. Vermeren (King's College London, UK). All construct sequences were verified by Sanger sequencing.

Cell lines culture, transfections, and drug treatment

Mouse neuroblastoma N2A cells were cultured in Dulbecco's modified Eagle's medium (DMEM) (Gibco) supplemented with 10% fetal calf serum at 37°C with 5% CO_2. To test shAtat1 efficiency, we treated N2A cells with 4OHT (1 μM) 24 and 48 hours after lipofection with Lipofectamine 2000 (Invitrogen), and cell lysis or fixation was performed 48 hours after the first treatment with 4OHT.

Neuronal cell culture

E14.5 mouse brain cortices were dissected and mechanically dissociated in Hanks' balanced salt solution (HBSS) (Sigma-Aldrich, H6648)

supplemented with 1.5% glucose. Cells were cultured at a confluence of ~70% with Neurobasal Medium (Gibco, Invitrogen, 21103049) supplemented with 2% B27 (Gibco, Invitrogen, 17504044), 1% penicillin/streptomycin (Gibco, Invitrogen, 15140122), and 1% GlutaMAX (Gibco, Invitrogen, 35050061) at 37°C. Nucleofections of E14.5 cortical neurons were performed using Mouse Neuron Nucleofector Kit (VPG-1001, Lonza) according to the manufacturer's protocol.

Human-induced pluripotent stem cell culture and generation of cortical projection neurons

Human embryonic stem cell research and protocols were approved by the Ethics Committee of the University of Liège (no. B70720096466); all experiments were conducted according to its guidelines. Human-induced pluripotent stem cell (hIPSC) line GM23446 (Coriell Institute) was maintained on Geltrex-coated dishes (Gibco) in DMEM/F12 supplemented with 20% KO serum replacement (Gibco), 100 μM nonessential amino acids (NEAA) (Gibco), 100 μM 2-mercaptoethanol, and basic fibroblast growth factor (100 ng/ml; PeproTech, London, UK), conditioned on γ-irradiated mouse embryonic fibroblasts. Cells were passaged routinely with collagenase A (1 mg/ml; Roche).

Generation of human cortical neurons was performed as described in (*39*). Briefly, hiPSCs were dissociated with TrypLE (Gibco) for 4 min at 37°C and cultured on Geltrex-coated dished in Pluripro medium (Cell Guidance Systems) until they reached confluency. Neural induction was triggered with media making use of dual SMAD inhibition and tankyrase inhibitor to enhance forebrain fate: DMEM/F12 containing N2 (Gibco), B27 (Gibco), penicillin/streptomycin (1:100; Gibco), glucose (0.8 mg/ml; Carl Roth HN06.2), NEAA, GlutaMAX (Gibco), cyclic adenosine 3′,5′-monophosphate (0.15 ng/ml; Sigma-Aldrich, A9501-1G), 500 nM A83-01 (Miltenyi Biotec, 130-106-274), 200 nM LDN-193189 (Miltenyi Biotec, 130-103-925), and 2 μM XAV939 (Enzo Life Sciences, BML-WN100-0005). Medium was changed daily, and cells were passaged at day 8 with 0.5 M EDTA. Cells were maintained until day 18 and replated at a density of 12,000 cells/cm^2 in neural differentiation media containing 1:1 DMEM/F12/Neurobasal, N2, B27, penicillin/streptomycin, glucose (0.8 mg/ml), NEAA, and GlutaMAX. Neural differentiation media were changed every other day, and Geltrex (1:100) was added 4 days before fixation with 4% paraformaldehyde (PFA) at day 32 to prevent detachment of the neurons.

Immunofluorescence

Mouse cerebral cortical neurons, N2A cells, HeLa S3 cells, and human projection neurons derived from hiPSCs were fixed using 4% PFA for 20 min at room temperature (RT) and washed with phosphate-buffered saline (PBS) + 0.3% Triton X-100. Antigen retrieval was performed for nucleofected cerebral cortical neurons using 10 mM sodium citrate (pH 9) for 1 hour at 60°C. After washing, neurons were incubated in blocking solution (PBS + 0.3% Triton X-100 + 10% normal donkey serum) for 1 hour at RT. Following overnight incubation with primary antibodies (Table 1) in blocking solution at 4°C, washing, incubation with secondary antibodies (PBS + 0.3% Triton X-100 + 1% normal donkey serum) at RT for 1 hour, and washing, coverslips were mounted on a microscope slide using Mowiol.

D. melanogaster larvae were dissected in PBS to expose brain and motor neurons, after dissection larvae were fixed with 4% PFA for 20 min at RT, washed with PBS + 0.2% (CSP staining) or 0.3% (α-tubulin acetylation staining) Triton X-100, and incubated in blocking solution PBS and 0.2% (CSP staining) or 0.3% (α-tubulin acetylation staining) Triton X-100 + 1% bovine serum albumin (BSA) for 30 min at RT. Following overnight incubation with primary antibodies at 4°C, washing, and incubation with secondary antibodies at RT for 2 hours, the larvae were mounted on a microscope slide using Mowiol. After washing in PBS + 0.3% Triton X-100, samples were incubated in blocking solution (PBS + 5% normal donkey serum + 0.3% Triton X-100) for 1 hour at RT. Following overnight incubation with antibodies at 4°C, washing, and incubation with secondary antibodies at RT for 2 hours, the larvae were mounted on a microscope slide using Mowiol. Images were acquired with a Nikon A1Ti confocal microscope (60× lens) for all analyses, except ATAT1-GFP and BDNF-mCherry staining that was acquired with the Airyscan superresolution module of a Zeiss LSM 880 confocal microscope. HeLa cells were plated at densities of 10,000 for 96-well black-bottom plates. The following day, cells were transfected using calcium phosphate with 0.01 μg/96-well plates of ATAT1:IRES-GFP truncated-form plasmids. Twenty-four hours after transfection, cells were fixed using 4% PFA and blocked and permeabilized using PBS + 3% fetal bovine saline (FBS) + 0.1% Triton X-100 for 1 hour. Following overnight incubation with primary [total α/β-tubulin (ATN02-A) and acetylated α-tubulin (T9026)] antibodies at 4°C, washing, and incubation with secondary antibodies at RT for 2 hours, cells were imaged using an IN Cell 2200 microscope (GE Healthcare).

Western blotting

Mouse brain cortices from *Atat1* KO mice (*20*) or HEK293 or N2A cells were homogenized on ice in radioimmunoprecipitation assay buffer or 320 mM sucrose, 4 mM Hepes buffer for subcellular fractions, with protease inhibitor cocktail (Roche, P8340 or Sigma-Aldrich, S8820) and 5 μM trichostatin A (Sigma-Aldrich, T8552). Subsequently, samples were boiled and reduced by 5 min of incubation at 70°C with loading buffer and were loaded on SDS–polyacrylamide gel electrophoresis gel to be finally transferred to a nitrocellulose membrane. For α-tubulin acetylation analysis, 2 μg of protein lysate was loaded on a gel; for analysis of all other proteins, 30 μg of lysate was used. Membranes were imaged using Amersham Imager 600 (General Electric, 29083461), and band densitometry was measured using ImageJ.

Subcellular fractionation

Subcellular fractionation of a frozen mouse brain cortex or cultured HEK293 cells was performed as previously described (*24*).

MS analysis

All chemicals were purchased from Sigma-Aldrich unless stated otherwise. Pellets from three independent samples of vesicles isolated from the brain cortex of WT or *Atat1* KO mice were solubilized using 5% SDS. Samples were then loaded onto the commercial S-Trap columns (ProtiFi, USA); for washing the detergents, reduction with 5 mM dithiothreitol (DTT), 10 mM iodoacetamide, and overnight digestion with trypsin (Promega) at 50:1 protein:trypsin ratio. Eluted peptides were dried using a vacuum centrifuge and stored in −80°C. Ultra LC/MS grade solvents were used for all chromatographic steps. Each sample was loaded using splitless nano ultraperformance LC (UPLC) (10 kpsi nanoACQUITY; Waters Corporation, Milford, MA, USA). The mobile phase was as follows: (A) H_2O + 0.1% formic acid and (B) acetonitrile + 0.1% formic acid. Desalting of the samples was performed online using a Reversed-Phase Symmetry C18 trapping column (internal diameter of 180 μm, 20 mm in length,

and 5 μm particle size; Waters Corporation). The peptides were then separated using a T3 High Strength Silica nanocolumn (internal diameter of 75 μm, 250 mm in length, and 1.8-μm particle size; Waters Corporation) at 0.35 μl/min. Peptides were eluted from the column into the mass spectrometer using the following gradient: 4 to 30% B in 155 minutes, 30 to 90% B in 5 min, maintained at 90% for 5 min, and then back to initial conditions. The nanoUPLC was coupled online through a nanoelectrospray ionization emitter (10-μm tip; New Objective, Woburn, MA, USA) to a quadrupole orbitrap mass spectrometer (Q Exactive Plus, Thermo Fisher Scientific), using a FlexIon nanospray apparatus (Proxeon). Data were acquired in a data-dependent acquisition mode, using a top 10 method. MS1 resolution was set to 70,000 [at 200 mass/charge ratio (m/z)], mass range of 300 to 1650 m/z, and AGC of 3e6, and maximum injection time was set to 60 ms. MS2 resolution was set to 17,500, quadrupole isolation 1.7 m/z, AGC of 1e5, dynamic exclusion of 60 s, and maximum injection time of 60 ms. Raw data were processed with MaxQuant v1.6.0.16. The data were searched with the Andromeda search engine against the SwisssProt human proteome database appended with common lab protein contaminants and the following modifications: carbamidomethyl on C and oxidation of M. Quantification was based on the Label-free quantitation method, based on unique peptides. *t* test with the Holm-Sidak method for multiple comparison was used for determination of statistical significance after logarithmic transformation. GO data analysis of the differentially detected proteins was done using GOrilla tool (*40*) (http://cbl-gorilla.cs.technion.ac.il), using two ranked lists and a P value of 10×10^{-3} as threshold.

Proteinase K sensitivity assay

Proteinase K sensitivity assay was performed as previously described (*26*). Fifty micrograms of vesicles (P3) were incubated with increasing concentration of proteinase K to reach a final concentration of 0, 0.05, 0.25, 1.25, and 6.25 μg/μl in digestion buffer (10 mM Hepes, 10 mM KCL, 2 mM EGTA, and 300 mM sucrose) in a total volume of 50 μl, for 30 min at 37°C. To end the reactions, 5 mM phenylmethylsulfonyl fluoride (PMSF) with Laemmli buffer, followed by immediate boiling and reduction of the samples in 95°C for 5 min.

Microfluidics device fabrication and axonal transport recordings in mice cortical neurons and *Drosophila* third-instar larvae

Microfluidics devices were prepared as described in (*41*). Axonal transport recording was performed after 5 DIV, as previously described (*16*), using an inverted confocal microscope (Nikon, A1Ti), at a 600-ms interval for 60 s using 60× lens. For cell culture, the recording microscope chamber was heated at 37°C and supplied with 5% CO_2.

Locomotor activity and climbing assay

Larval locomotion assays were performed by placing third-instar *D. melanogaster* larvae in the center of 15-cm petri dishes coated with 3% agar (*42*). Millimeter paper was glued below each 15-cm petri dish to quantify distance traveled. Crawling speed was extrapolated from distance traveled in 1 min; peristaltic activity was defined as complete posteroanterior contraction of the larvae in 1 min. Climbing assay for adult flies was performed as previously described in (*43*). Ten flies per group were allowed to climb an empty polystyrene tube for 1 min in three sequential assays. Climbing index was defined as average ratio successful climbs over 15 cm of the total number of flies in a group.

Lysosome transport analysis in organotypic slice

Mice purchased from Janvier were anesthetized with isoflurane (Abbott Laboratories) in an oxygen carrier before the administration of temgesic (Schering-Plough). Endotoxin-free plasmids were injected into lateral ventricles of E14.5 mouse embryo forebrains using a FemtoJet microinjector (Eppendorf) with 0.1% fast green for visualization. Injection was followed by electroporation (5 pulses of 24 mV at 50-ms intervals for 950 ms) using platinum electrodes (Sonidel, catalog no. CUY650P3) connected to an electroporator (ECM 830, BTX). Embryos were coelectroporated with tamoxifen-inducible CreERT2 expressing plasmid along with two Cre-dependent constructs expressing DsRed and shAtat1/sh-scrambled and with LAMP1-Emerald–expressing plasmid. After electroporation, embryos were placed back in the abdominal cavity. For injection, 4OHT and progesterone were dissolved in ethanol 100% at concentrations of 20 and 10 mg/ml, respectively, and then diluted with nine volumes of corn oil (Sigma-Aldrich). Diluted tamoxifen solution (2 mg/ml, 100 μl per mouse) was intraperitoneally injected three times at E17, E18, and P1, and pups brains were dissected at P2. Brains were embedded in agarose 4% HBSS solution and cut into coronal sections (300 μm) using a vibratome (Leica VT1000S, Leica Microsystems). The slices were placed on Matrigel-coated (Corning) MatTek glass-bottom dishes and covered with half-diluted Matrigel with supplemented Neurobasal culture medium. Sections were incubated for 30 min at 37°C before imaging. Time-lapse imaging was performed on a Zeiss Super Resolution LSM 880 Airyscan Elyra S1 (×63 magnification) at a 500-ms interval for 60 s at the corpus callosum midline. The recoding microscope chamber was heated at 37°C and supplied with 5% CO_2.

qPCR analysis

Ten adult fly heads were collected in TRIzol Reagent (Ambion, Life Technologies), followed by RNA extraction performed using the manufacturer's instructions. After deoxyribonuclease treatment (Roche), 1 μg of RNA was reverse-transcribed with RevertAid Reverse Transcriptase (Fermentas). qPCR was performed using a LightCycler 480 (Roche), with SYBR Green mix according to the manufacturer's instructions (Roche). Analysis was done using $2^{-\Delta\Delta}$CT method after defining primer efficiencies, *Rpl13* and *Pgk* served for normalization (*44*). The following primers were used: *Rpl13*, AGGAGGCGCAAGAAATC (forward) and CTTGCTGCGGTACTCCTTGAG (reverse); *Pgk*, TCCTGAAGGTCCTCAACAACATG (forward) and TCCACCAGTTTCTCGACGATCT (reverse); *Atat1*, CAGTCCCGCACGCTGACGAG (forward) and ACGCGCATGGTGGAGCAGAC (reverse); *Atat2*, TCCCAAGTCAAGGGAGACAC (forward) and TGCGGAAAGAGGTGCTTAAT (reverse); and *Hdac6*, CAAGCCCAAAGTCAAGCACT (forward) and ACCCAGTTCTCCCCCGTC (reverse).

Ciliobrevin treatment

Drug treatments of cortical neuronal cultures were performed using 20 μM (Sigma-Aldrich 250401) diluted in dimethyl sulfoxide (DMSO) for 2 hours. For third-instar larva, drugs were fed in 10% sucrose solution supplemented with either 1 mM TBA (Sigma-Aldrich, SML0044) or 800 μM Ciliobrevin D and DMSO for 30 min and 2 hours, respectively.

Purification of tubulin from mouse brains or HeLa cells

Nonacetylated α-tubulin was obtained from HeLa S3 cells (American Type Culture Collection, CCL-2.2TM) for in vitro acetylation assays

or from WT and *Atat1* KO mouse brains for in vitro transport assay according to the protocol adapted from (*45*). Cells were lysed in BRB80 [80 mM K^- Pipes (pH 6.8), 1 mM $MgCl_2$, and 1 mM EGTA] supplemented with 1 mM β-mercaptoethanol, 1 mM PMSF, and protease inhibitors at 4°C. The soluble fraction was obtained by ultracentrifugation, followed by tubulin polymerization at 30°C min by adding 1 mM guanosine triphosphate (GTP) and 30% glycerol. MTs were pelleted by ultracentrifugation at 30°C for 30 min and depolymerized in BRB80 at 4°C; soluble tubulin was clarified by ultracentrifugation at 4°C. The second polymerization round was performed for 30 min at 30°C in the presence of high-molarity Pipes to remove mitogen-activated proteins; the MT pellet was sedimented by ultracentrifugation. MTs were then depolymerized in BRB80 at 4°C, and soluble tubulin was clarified and snap-frozen.

In vitro α-tubulin acetylation assays

Half-area 96-well plates (Greiner, 674061) were coated with 5-μg tubulin from HeLa cells or bovine brain (Cytoskeleton, catalog no. HTS02-A) in 25 μl of ultrapure water for 2.5 hours at 37°C, followed by blocking (PBS + 3% BSA + 3% skim milk + 3% FBS) for 1 hour at 37°C, and washing with PBS + 0.05% Tween 20. Twenty-five micrograms of the total, S2, S3, or P3 fractions isolated from the P0 mouse brain cortex were diluted in 2× histone acetyltransferase (HAT) buffer (Sigma-Aldrich, EPI001A) supplemented with protease inhibitor cocktail, 5 μM trichostatin, and 50 μM acetyl-CoA (Sigma-Aldrich, A2056) or vehicle (H_20) were added per well for incubation of 2 hours at 37°C with shaking at 100 revolutions per minute. The wells were washed and incubated overnight with acetylated α-tubulin antibody (1:2000) in blocking buffer (PBS + 0.05% Tween 20 + 3% BSA) at 4°C, and wells were washed and incubated for 2 hours at 37°C with peroxidase-conjugated goat anti-mouse antibody (1:5000) in antibody blocking buffer; following another wash, the samples were incubated with trimethylboron/E (Merck Millipore, ES001), and the reaction was stopped with H_2SO_4.

CoA release was measured using HAT activity colorimetric assay kit (Sigma-Aldrich, EPI001), as indicated by the manufacturer's instructions. Twenty-five micrograms of P3 fraction were incubated with 5 μg of tubulin in black-bottom μClear plate (Greiner, 655090) for 4 hours, and signal was measured every minute.

In vitro MT-dependent transport assay

WT or *Atat1* KO mouse brain was fractionated in vesicle buffer [10 mM Hepes-KOH, 175 mM L-aspartic acid, 65 mM taurine, 85 mM betaine, 25 mM glycine, 6.5 mM $MgCl_2$, 5 mM EGTA, 0.5 mM D-glucose, 1.5 mM $CaCl_2$, and 20 mM DTT (pH 7.2), with protease inhibitors], using increasing centrifugation speed with a final sucrose gradient step to isolate motility vesicles as described in (*23*). Rhodamine-labeled seeds were prepared by incubating a mix of rhodamine labeled with unlabeled purified tubulin from bovine brain (Cytoskeleton, catalog no. HTS02-A) or HeLa cells (isolated as described above) at a ratio of 1:10 for 1 hour at 37°C. The elongation was carried in GTP-BRB80 buffer (80 mM Pipes, 1 mM $MgCl_2$, 1 mM EGTA, and 1 mM GTP) for 30 min at 37°C, followed by incubation for 20 min with 50 μM Taxol to stabilize MTs.

The in vitro polymerized rhodamine-labeled MTs from WT or *Atat1* KO mouse brains were seeded in a flow chamber and purified vesicles diluted in motility buffer [BRB80, 0.5% Pluronic F127, 1 mM Taxol, BSA in BRB80 (10 mg/ml), 1 M DTT, glucose oxidase (0.5 mg/ml), 20 mM Mg-ATP, glucose (15 mg/ml), and catalase (470 U/ml)] were labeled with the green fluorescent lipophilic carbocyanine [DiOC18(3), Thermo Fisher Scientific] tracer, loaded in the chambers with 50 μM acetyl-CoA or vehicle, to acquire using a total internal reflection fluorescence (TIRF) microscope. For immunofluorescence analysis, MTs were fixed after the assay with 100% methanol for 10 min at −20°C, then incubated in blocking solution (PBS + 1% BSA) with acetylated α-tubulin antibody (1:10,000) and goat anti-mouse Alexa 647 antibody (1:1000) for 2 hours at RT. Recordings were performed by using a TIRF microscope (Nikon, Eclipse Ti), at 200-ms intervals, using 60× lens.

Quantification of MT acetylation levels using immunofluorescence

Fluorescence intensity levels were measured by Fiji (https://imagej.net/Fiji/Downloads). Regions of interest of 30 μm long for *D. melanogaster*, or the complete length for in vitro polymerized MTs, accounting for the full width of the motoneurons/MTs were used. The levels of acetylated α-tubulin and total α-tubulin levels were extracted from mean intensity levels. Background levels were subtracted, and the ratio of acetylated α-tubulin/tubulin was calculated.

Analysis of MT-dependent transport

Kymographs were generated for single blind analysis using ImageJ plugin-KymoToolBox (fabrice.cordelieres@curie.u-psud.fr). For *D. melanogaster* analysis, StackReg plugin was used to align frames. Vesicles were considered stationary if speed was lower than 0.1 μm/s.

Statistics

All experiments (except WB and quantitative reverse transcription PCR analyses) were performed under single-blinded condition, and statistical analyses were generated with GraphPad Prism Software 6.0 or GraphPad Prism Software 7.0 for proteomic analysis.

SUPPLEMENTARY MATERIALS

Supplementary material for this article is available at http://advances.sciencemag.org/cgi/content/full/5/12/eaax2705/DC1

Fig. S1. Analysis of axonal transport parameters in WT and Atat1 KO mice.
Fig. S2. Validation of RNAi efficiency, mRNA expression of MTs modifying enzymes, representative kymographs of axonal transport, and protein aggregation in *D. melanogaster*.
Fig. S3. Kymographs of in vitro transport assay.
Fig. S4. Identified peptides of ATAT1 by LC-MS/MS.
Fig. S5. LC-MS/MS proteomics on vesicular extracts from WT and ATAT1 KO mice.
Fig. S6. Acute KD of Lis1 leads to defect in retrograde transport and dampens the acetylation of MTs.
Fig. S7. Expression of Atat1 in the cerebral cortex of human in the course of development and life.
Table S1. Intensity-ranked proteins in vesicle fractions from WT or Atat1 KO mice detected by LC-MS/MS.
Table S2. Differentially detected proteins in vesicle fractions from WT or Atat1 KO mice detected by LC-MS/MS.
Table S3. Identified molecular motors in vesicle fractions from WT or Atat1 KO mice detected by LC-MS/MS.
Table S4. Identified glycolytic enzymes in vesicle fractions from WT or Atat1 KO mice detected by LC-MS/MS.
Movie S1. Representative movie of Lamp1-Emerald trafficking in axons of cortical brain slice.
Movie S2. Representative movie of lysosome trafficking in axons located in the distal part of PDMS chambers.
Movie S3. Representative movie of mitochondria trafficking in axons located in the distal part of PDMS chambers.
Movie S4. Representative movie of synaptotagmin-GFP trafficking in motoneurons of third-instar larvae.
Movie S5. Representative movies of vesicles trafficking in vitro over polymerized rhodamine-labeled MTs.
Movie S6. Representative movie of ATAT1-GFP trafficking in axons located in the distal part of PDMS chambers.

View/request a protocol for this paper from *Bio-protocol*.

REFERENCES AND NOTES

1. N. Hirokawa, S. Niwa, Y. Tanaka, Molecular motors in neurons: Transport mechanisms and roles in brain function, development, and disease. *Neuron* **68**, 610–638 (2010).
2. C. Janke, J. C. Bulinski, Post-translational regulation of the microtubule cytoskeleton: Mechanisms and functions. *Nat. Rev. Mol. Cell Biol.* **12**, 773–786 (2011).
3. Y. Song, S. T. Brady, Post-translational modifications of tubulin: Pathways to functional diversity of microtubules. *Trends Cell Biol.* **25**, 125–136 (2015).
4. J. P. Dompierre, J. D. Godin, B. C. Charrin, F. P. Cordelières, S. J. King, S. Humbert, F. Saudou, Histone deacetylase 6 inhibition compensates for the transport deficit in Huntington's disease by increasing tubulin acetylation. *J. Neurosci.* **27**, 3571–3583 (2007).
5. N. A. Reed, D. Cai, T. L. Blasius, G. T. Jih, E. Meyhofer, J. Gaertig, K. J. Verhey, Microtubule acetylation promotes kinesin-1 binding and transport. *Curr. Biol.* **16**, 2166–2172 (2006).
6. V. K. Godena, N. Brookes-Hocking, A. Moller, G. Shaw, M. Oswald, R. M. Sancho, C. C. J. Miller, A. J. Whitworth, K. J. De Vos, Increasing microtubule acetylation rescues axonal transport and locomotor deficits caused by LRRK2 Roc-COR domain mutations. *Nat. Commun.* **5**, 5245 (2014).
7. J. S. Akella, D. Wloga, J. Kim, N. G. Starostina, S. Lyons-Abbott, N. S. Morrissette, S. T. Dougan, E. T. Kipreos, J. Gaertig, MEC-17 is an α-Tubulin acetyltransferase. *Nature* **467**, 218–222 (2010).
8. T. Shida, J. G. Cueva, Z. Xu, M. B. Goodman, M. V. Nachury, The major α-Tubulin K40 acetyltransferase α-TAT1 promotes rapid ciliogenesis and efficient mechanosensation. *Proc. Natl. Acad. Sci. U.S.A.* **107**, 21517–21522 (2010).
9. S. C. Howes, G. M. Alushin, T. Shida, M. V. Nachury, E. Nogales, Effects of tubulin acetylation and tubulin acetyltransferase binding on microtubule structure. *Mol. Biol. Cell* **25**, 257–266 (2014).
10. Z. Xu, L. Schaedel, D. Portran, A. Aguilar, J. Gaillard, M. P. Marinkovich, M. Théry, M. V. Nachury, Microtubules acquire resistance from mechanical breakage through intralumenal acetylation. *Science* **356**, 328–332 (2017).
11. C. Coombes, A. Yamamoto, M. M. Clellan, T. A. Reid, M. Plooster, G. W. G. Luxton, J. Alper, J. Howard, M. K. Gardner, Mechanism of microtubule lumen entry for the α-Tubulin acetyltransferase enzyme αTAT1. *Proc. Natl. Acad. Sci. U.S.A.* **113**, E7176–E7184 (2016).
12. N. Ly, N. Elkhatib, E. Bresteau, O. Piétrement, M. Khaled, M. M. Magiera, C. Janke, E. L. Cam, A. D. Rutenberg, G. Montagnac, αTAT1 controls longitudinal spreading of acetylation marks from open microtubules extremities. *Sci. Rep.* **6**, 35624 (2016).
13. L. Balabanian, C. L. Berger, A. G. Hendricks, Acetylated microtubules are preferentially bundled leading to enhanced kinesin-1 motility. *Biophys. J.* **113**, 1551–1560 (2017).
14. G. W. Kim, L. Li, M. Gorbani, L. You, X. J. Yang, Mice lacking α-Tubulin acetyltransferase 1 are viable but display α-Tubulin acetylation deficiency and dentate gyrus distortion. *J. Biol. Chem.* **288**, 20334–20350 (2013).
15. T. Shida, J. G. Cueva, Z. Xu, M. B. Goodman, M. V. Nachury, The major α-Tubulin K40 acetyltransferase αTAT1 promotes rapid ciliogenesis and efficient mechanosensation. *Proc. Natl. Acad. Sci. U.S.A.* **107**, 21517–21522 (2010).
16. G. Morelli, A. Even, I. Gladwyn-Ng, R. L. Bail, M. Shilian, J. D. Godin, E. Peyre, B. A. Hassan, A. Besson, J.-M. Rigo, M. Weil, B. Brône, L. Nguyen, $p27^{Kip1}$ Modulates Axonal Transport by Regulating α-Tubulin Acetyltransferase 1 Stability. *Cell Rep.* **23**, 2429–2442 (2018).
17. C. Hubbert, A. Guardiola, R. Shao, Y. Kawaguchi, A. Ito, A. Nixon, M. Yoshida, X.-F. Wang, T.-P. Yao, HDAC6 is a microtubule-associated deacetylase. *Nature* **417**, 455–458 (2002).
18. K. V. Butler, J. Kalin, C. Brochier, G. Vistoli, B. Langley, A. P. Kozikowski, Rational design and simple chemistry yield a superior, neuroprotective HDAC6 inhibitor, tubastatin A. *J. Am. Chem. Soc.* **132**, 10842–10846 (2010).
19. C. D. Nichols, J. Becnel, U. B. Pandey, Methods to assay Drosophila behavior. *J. Vis. Exp.* **7**, 3795 (2012).
20. N. Kalebic, S. Sorrentino, E. Perlas, G. Bolasco, C. Martinez, P. A. Heppenstall, αTAT1 is the major α-Tubulin acetyltransferase in mice. *Nat. Commun.* **4**, 1962 (2013).
21. S. Takamori, M. Holt, K. Stenius, E. A. Lemke, M. Grønborg, D. Riedel, H. Urlaub, S. Schenck, B. Brügger, P. Ringler, S. A. Müller, B. Rammner, F. Gräter, J. S. Hub, B. L. De Groot, G. Mieskes, Y. Moriyama, J. Klingauf, H. Grubmüller, J. Heuser, F. Wieland, R. Jahn, Molecular Anatomy of a Trafficking Organelle. *Cell* **127**, 831–846 (2006).
22. G. H. H. Borner, M. Harbour, S. Hester, K. S. Lilley, M. S. Robinson, Comparative proteomics of clathrin-coated vesicles. *J. Cell Biol.* **175**, 571–578 (2006).
23. M.-V. Hinckelmann, A. Virlogeux, C. Niehage, C. Poujol, D. Choquet, B. Hoflack, D. Zala, F. Saudou, Self-propelling vesicles define glycolysis as the minimal energy machinery for neuronal transport. *Nat. Commun.* **7**, 13233 (2016).
24. D. Zala, M.-V. Hinckelmann, H. Yu, M. M. L. da Cunha, G. Liot, F. P. Cordelières, S. Marco, F. Saudou, Vesicular glycolysis provides on-board energy for fast axonal transport. *Cell* **152**, 479–491 (2013).
25. G. Montagnac, V. Meas-Yedid, M. Irondelle, A. Castro-Castro, M. Franco, T. Shida, M. V. Nachury, A. Benmerah, J.-C. Olivo-Marin, P. Chavrier, αTAT1 catalyses microtubule acetylation at clathrin-coated pits. *Nature* **502**, 567–570 (2013).
26. H.-J. Lee, S. Patel, S.-J. Lee, Intravesicular localization and exocytosis of α-synuclein and its aggregates. *J. Neurosci.* **25**, 6016–6024 (2005).
27. R. Sainath, G. Gallo, The dynein inhibitor Ciliobrevin D inhibits the bidirectional transport of organelles along sensory axons and impairs NGF-mediated regulation of growth cones and axon branches. *Dev. Neurobiol.* **75**, 757–777 (2015).
28. B. Neumann, M. A. Hilliard, Loss of MEC-17 leads to microtubule instability and axonal degeneration. *Cell Rep.* **6**, 93–103 (2014).
29. S. J. Morley, Y. Qi, L. Iovino, L. Andolfi, D. Guo, N. Kalebic, L. Castaldi, C. Tischer, C. Portulano, G. Bolasco, K. Shirlekar, C. M. Fusco, A. Asaro, F. Fermani, M. Sundukova, U. Matti, L. Reymond, A. De Ninno, L. Businaro, K. Johnsson, M. Lazzarino, J. Ries, Y. Schwab, J. Hu, P. A. Heppenstall, Acetylated tubulin is essential for touch sensation in mice. *eLife* **5**, e20813 (2016).
30. L. Li, D. Wei, Q. Wang, J. Pan, R. Liu, X. Zhang, L. Bao, MEC-17 deficiency leads to reduced α-Tubulin acetylation and impaired migration of cortical neurons. *J. Neurosci.* **32**, 12673–12683 (2012).
31. J. A. Miller, S.-L. Ding, S. M. Sunkin, K. A. Smith, L. Ng, A. Szafer, A. Ebbert, Z. L. Riley, J. J. Royall, K. Aiona, J. M. Arnold, C. Bennet, D. Bertagnolli, K. Brouner, S. Butler, S. Caldejon, A. Carey, C. Cuhaciyan, R. A. Dalley, N. Dee, T. A. Dolbeare, B. A. C. Facer, D. Feng, T. P. Fliss, G. Gee, J. Goldy, L. Gourley, B. W. Gregor, G. Gu, R. E. Howard, J. M. Jochim, C. L. Kuan, C. Lau, C.-K. Lee, F. Lee, T. A. Lemon, P. Lesnar, B. M. Murray, N. Mastan, N. Mosqueda, T. Naluai-Cecchini, N.-K. Ngo, J. Nyhus, A. Oldre, E. Olson, J. Parente, P. D. Parker, S. E. Parry, A. Stevens, M. Pletikos, M. Reding, K. Roll, D. Sandman, M. Sarreal, S. Shapouri, N. V. Shapovalova, E. H. Shen, N. Sjoquist, C. R. Slaughterbeck, M. Smith, A. J. Sodt, D. Williams, L. Zöllei, B. Fischl, M. B. Gerstein, D. H. Geschwind, I. A. Glass, M. J. Hawrylycz, R. F. Hevner, H. Huang, A. R. Jones, J. A. Knowles, P. Levitt, J. W. Phillips, N. Šestan, P. Wohnoutka, C. Dang, A. Bernard, J. G. Hohmann, E. S. Lein, Transcriptional landscape of the prenatal human brain. *Nature* **508**, 199–206 (2014).
32. I. A. Kent, P. S. Rane, R. B. Dickinson, A. J. Ladd, T. P. Lele, Transient pinning and pulling: A mechanism for bending microtubules. *PLOS ONE* **11**, e0151322 (2016).
33. A. D. Bicek, E. Tüzel, A. Demtchouk, M. Uppalapati, W. O. Hancock, D. M. Kroll, D. J. Odde, Anterograde microtubule transport drives microtubule bending in LLC-PK1 epithelial cells. *Mol. Biol. Cell* **20**, 2943–2953 (2009).
34. S. Triclin, D. Inoue, J. Gaillard, Z. M. Htet, M. De Santis, D. Portran, E. Derivery, C. Aumeier, L. Schaedel, K. John, C. Leterrier, S. Reck-Peterson, L. Blanchoin, M. Thery, Self-repair protects microtubules from their destruction by molecular motors. *bioRxiv* , 499020 (2018).
35. J. F. Díaz, I. Barasoain, J. M. Andreu, Fast kinetics of Taxol binding to microtubules. Effects of solution variables and microtubule-associated proteins. *J. Biol. Chem.* **278**, 8407–8419 (2003).
36. D. Portran, L. Schaedel, Z. Xu, M. Théry, M. V. Nachury, Tubulin acetylation protects long-lived microtubules against mechanical ageing. *Nat. Cell Biol.* **19**, 391–398 (2017).
37. M.-V. Hinckelmann, D. Zala, F. Saudou, Releasing the brake: Restoring fast axonal transport in neurodegenerative disorders. *Trends Cell Biol.* **23**, 634–643 (2013).
38. J. W. Tsai, Y. Chen, A. R. Kriegstein, R. B. Vallee, LIS1 RNA interference blocks neural stem cell division, morphogenesis, and motility at multiple stages. *J. Cell Biol.* **170**, 935–945 (2005).
39. V. Iefremova, G. Manikakis, O. Krefft, A. Jabali, K. Weynans, R. Wilkens, F. Marsoner, B. Brändl, F.-J. Müller, P. Koch, J. Ladewig, An organoid-based model of cortical development identifies non-cell-autonomous defects in Wnt signaling contributing to miller-dieker syndrome. *Cell Rep.* **19**, 50–59 (2017).
40. E. Eden, R. Navon, I. Steinfeld, D. Lipson, Z. Yakhini, *GOrilla*: A tool for discovery and visualization of enriched GO terms in ranked gene lists. *BMC Bioinformatics* **10**, 48 (2009).
41. S. Gluska, M. Chein, N. Rotem, A. Ionescu, E. Perlson, Tracking Quantum-Dot labeled neurotropic factors transport along primary neuronal axons in compartmental microfluidic chambers. *Methods Cell Biol.* **131**, 365–387 (2016).
42. S. A. Shaver, C. A. Riedl, T. L. Parkes, M. B. Sokolowski, A. J. Hilliker, Isolation of larval behavioral mutants in Drosophila melanogaster. *J. Neurogenet.* **14**, 193–205 (2000).
43. R. P. Chambers, G. B. Call, D. Meyer, J. Smith, J. A. Techau, K. Pearman, L. M. Buhlman, Nicotine increases lifespan and rescues olfactory and motor deficits in a Drosophila model of Parkinson's disease. *Behav. Brain Res.* **253**, 95–102 (2013).
44. G. Morelli, A. Avila, S. Ravanidis, N. Aourz, R. L. Neve, I. Smolders, R. J. Harvey, J.-M. Rigo, L. Nguyen, B. Brône, Cerebral cortical circuitry formation requires functional glycine receptors. *Cereb. Cortex* **27**, 1863–1877 (2016).
45. M. Barisic, R. S. e Sousa, S. K. Tripathy, M. M. Magiera, A. V. Zaytsev, A. L. Pereira, C. Janke, E. L. Grishchuk, H. Maiato, Mitosis. Microtubule detyrosination guides chromosomes during mitosis. *Science* **348**, 799–803 (2015).

Acknowledgments: We thank B. Franco (ULiège) and S. Bodakuntla (Institut Curie) for technical assistance; M. Nachury for sharing ATAT1 antibody and K. Sadoul for providing the *Atat1* KO mice; Y. Levin from The de Botton Protein Profiling Institute of the Nancy and Stephen Grand Israel National Center for Personalized Medicine, Weizmann Institute of Science for the proteomic analysis; F. Polleux, from Columbia University, New York, USA, for providing pCAG mEmerald-LAMP1, and pCAG mito-DsRED plasmids; and E. Even for graphical

design. **Funding:** A.E.'s stay at GIGA Research Institute of the University of Liège was funded by EMBO Short-Term Fellowships (ASTF 174-2016); his stay at F.S.'s lab was supported by TAU Global Research and Training Fellowship, Ela Kodesz Institute, and the Scientific and Academic Cooperation Office of the French embassy in Tel Aviv. A.E., M.S., and M.W.'s research was supported by the Israel Science Foundation (grant no. 1688/16). C.S. was supported by a Postdoctoral fellowship from FRM and by EMBO LTF (ALTF 693-2015). S.T., L.B., L.N., and B.M. are PhD fellow, Postdoctoral fellow, Senior Research Associates and Director from FRS-FNRS, respectively. This work was supported by the FRS-FNRS, the Fonds Léon Fredericq (L.N. and B.M.), the Fondation Médicale Reine Elisabeth (L.N. and B.M.), the Fondation Simone et Pierre Clerdent (L.N.), the Belgian Science Policy [IAP-VII network P7/20 (L.N.) and IAP-VII network P7/10 (B.B.)], and the ERANET Neuron STEM-MCD and NeuroTalk (L.N.); grants from Agence Nationale de la Recherche [ANR-14-CE35-0027-01 PASSAGE (F.S.), ANR-15-JPWG-0003-05 JPND CIRCPROT (F.S.), ANR-15-IDEX-02 NeuroCoG (F.S.), ANR-10-IDEX-0001-02, and ANR-11-LBX-003 (C.J.) in the framework of the "Investissements d'avenir" program]; the LABEX celtisphybio 8 (C.J.); and the Fondation pour la Recherche Médicale (FRM, équipe labellisée, to F.S.). C.J. is supported by the Institut Curie, the French National Research Agency (ANR) award ANR-17-CE13-0021 and the Fondation pour la Recherche Medicale (FRM) grant DEQ20170336756. J.A.S. was supported by the European Union's Horizon 2020 research and innovation program under the Marie Sklodowska-Curie grant agreement no. 675737 and the FRM grant FDT201904008210. M.M.M. was supported by the Fondation Vaincre Alzheimer (grant no. FR-16055p). **Author contributions:** A.E., G.M., F.S., M.W., and L.N. designed the study. A.E. and G.M. performed and interpreted most experiments. L.B. and S.T. designed and performed ex vivo experiments, contributed to in vitro transport experiments and superresolution imaging, and reviewed the manuscript with the help of coauthors. C.S. performed in vitro motility assays under the supervision of F.S. I.G.-N. contributed to cell cultures, transport experiment in mice, and cloning. R.L.B. contributed to *Drosophila* work. M.S. contributed to cell cultures and biochemical work. M.M.M. and A.S.J. produced and purified nonacetylated MTs. M.M.M. performed analysis of tubulin PTMs. S.F. maintained *Atat1 KO* animal colonies and contributed to cortical tissue dissections. N.K. provided technical assistance for molecular biology and mouse husbandry. M.W. and L.N. contributed to data interpretation; and A.E., G.M., M.W., and L.N. wrote the manuscript with input from all coauthors. **Competing interests:** The authors declare that they have no competing interests. **Data and materials availability:** An earlier version of the work can be found at bioRxiv 542464; doi: https://doi.org/10.1101/542464. All data needed to evaluate the conclusions in the paper are present in the paper and/or the Supplementary Materials. Additional data related to this paper may be requested from the authors.

Submitted 8 March 2019
Accepted 28 October 2019
Published 18 December 2019
10.1126/sciadv.aax2705

Citation: A. Even, G. Morelli, L. Broix, C. Scaramuzzino, S. Turchetto, I. Gladwyn-Ng, R. Le Bail, M. Shilian, S. Freeman, M. M. Magiera, A. S. Jijumon, N. Krusy, B. Malgrange, B. Brone, P. Dietrich, I. Dragatsis, C. Janke, F. Saudou, M. Weil, L. Nguyen, ATAT1-enriched vesicles promote microtubule acetylation via axonal transport. *Sci. Adv.* **5**, eaax2705 (2019).

ATP-citrate lyase promotes axonal transport across species

nature COMMUNICATIONS

ARTICLE

https://doi.org/10.1038/s41467-021-25786-y OPEN

ATP-citrate lyase promotes axonal transport across species

Aviel Even[1,10], Giovanni Morelli[2,3,10], Silvia Turchetto[2,10], Michal Shilian[1], Romain Le Bail[2], Sophie Laguesse[2], Nathalie Krusy[2], Ariel Brisker[1], Alexander Brandis[4], Shani Inbar[1], Alain Chariot[5], Frédéric Saudou[6,7,8], Paula Dietrich[9], Ioannis Dragatsis[9], Bert Brone[3], Loïc Broix[2], Jean-Michel Rigo[3], Miguel Weil[1,11]✉ & Laurent Nguyen[2,11]✉

Microtubule (MT)-based transport is an evolutionary conserved process finely tuned by posttranslational modifications. Among them, α-tubulin acetylation, primarily catalyzed by a vesicular pool of α-tubulin N-acetyltransferase 1 (Atat1), promotes the recruitment and processivity of molecular motors along MT tracks. However, the mechanism that controls Atat1 activity remains poorly understood. Here, we show that ATP-citrate lyase (Acly) is enriched in vesicles and provide Acetyl-Coenzyme-A (Acetyl-CoA) to Atat1. In addition, we showed that Acly expression is reduced upon loss of Elongator activity, further connecting Elongator to Atat1 in a pathway regulating α-tubulin acetylation and MT-dependent transport in projection neurons, across species. Remarkably, comparable defects occur in fibroblasts from Familial Dysautonomia (FD) patients bearing an autosomal recessive mutation in the gene coding for the Elongator subunit ELP1. Our data may thus shine light on the patho-physiological mechanisms underlying FD.

[1] Laboratory for Neurodegenerative Diseases and Personalized Medicine, The Shmunis School of Biomedicine and Cancer Research, The George S. Wise Faculty for Life Sciences, Sagol School of Neurosciences, Tel Aviv University, Ramat Aviv 69978, Israel. [2] Laboratory of Molecular Regulation of Neurogenesis, GIGA-Stem Cells, Interdisciplinary Cluster for Applied Genoproteomics (GIGA-R), University of Liège, C.H.U. Sart Tilman, Liège 4000, Belgium. [3] BIOMED Research Institute, Hasselt 3500, Belgium. [4] Life Sciences Core Facilities, Weizmann Institute of Science, Rehovot, Israel. [5] Laboratory of Medical Chemistry, GIGA-Stem Cells, Interdisciplinary Cluster for Applied Genoproteomics (GIGA-R), University of Liège, C.H.U. Sart Tilman, Liège 4000, Belgium. [6] Univ. Grenoble Alpes, Inserm, U1216, CHU Grenoble Alpes, Grenoble Institut Neurosciences, 38000 Grenoble, France. [7] Inserm, U1216, F-38000 Grenoble, France. [8] CHU Grenoble Alpes, F-38000 Grenoble, France. [9] Department of Physiology, University of Tennessee Health Science Center, Memphis, TN 38163, USA. [10] These authors contributed equally: Aviel Even, Giovanni Morelli, Silvia Turchetto. [11] These authors jointly supervised this work: Miguel Weil, Laurent Nguyen. ✉email: miguelw@tauex.tau.ac.il; lnguyen@uliege.be

Axonal transport is an evolutionary conserved process that delivers cargoes to distant subcellular compartments. It is supported by molecular motors (kinesins and dyneins) running along microtubule (MT) tracks and is particularly important for projection neurons that send axons to distant targets. MT-dependent transport contributes to neuronal development in growing dendrites and axons via slow axonal transport of cytoskeletal elements and, later, it sustains survival and homeostasis of neurons via fast axonal transport of organelles including mitochondria, lysosomes, and vesicles carrying various types of proteins (growth factors, synaptic proteins…). Axonal transport defect is a hallmark of several neurodegenerative disorders, whose disruption affects neuronal function and survival[1–4]. This is exemplified by the loss of activity of the Elongator complex, which is associated with both neurodegeneration and axonal transport defects[5,6]. This molecular complex, conserved from yeast to human, is composed of two copies of six distinct protein subunits (Elp1 to Elp6)[7]. Elp3 is the enzymatic core of the Elongator and harbors two highly conserved subdomains, a tRNA acetyltransferase[8] and a S-adenosyl methionine binding domains[9]. Elp1 is the scaffolding subunit of the complex, but disruption of any of the Elongator subunits leads to comparable phenotype in eukaryotes, suggesting that all subunits are essential for the integrity and activity of the complex[10,11]. Elongator serves molecular functions in distinct subcellular compartments[12] but predominantly accumulates in the cytoplasm where it promotes the formation of 5-methoxycarbonylmethyl (mcm^5) and 5-carbamoylmethyl (ncm^5) on side-chains of wobble uridines (U_{34}) of selected tRNAs, thereby regulating protein translation[8,13]. Convergent observations support a role for Elongator in intracellular transport in the nervous system as Elp3 is enriched at the presynaptic side of neuromuscular junction buttons in flies, where its expression is required for synapse integrity and activity[14,15]. Elongator subunits are also detected in protein extracts from purified motile vesicles isolated from the mouse cerebral cortex[16], and they colocalize with the vesicular markers SV2 and RAB3A in human embryonic stem cells derived neurons[17]. In humans, mutation of the gene coding for ELP1, underlies Familial dysautonomia (FD), a devastating disease that mostly affects the development and survival of neurons from the autonomic nervous systems[18,19]. Moreover, other neurological disorders are also associated with mutations affecting the expression or the activity of Elongator[5,20–23]. Experimental data on animal models show that interfering with Elongator activity promotes early developmental and progressive neurodegenerative defects, including poor axonal transport and maintenance[24–27]. At the molecular level, loss of Elongator correlates with poor acetylation of α-tubulin lysine 40 (K40) in neuronal microtubules (MT)[6,25,28]. This post-translational modification (PTM) modulates axonal transport by facilitating the recruitment of molecular motors to MTs[29] and the loading of motile vesicles on motors[6]. The acetylation of MTs relies mostly on a vesicular pool of tubulin acetyltransferase 1 (Atat1)[30] that catalyzes the transfer of acetyl groups from Acetyl-Coenzyme-A (Acetyl-CoA) onto lysine 40 (K40) of α-tubulin[31,32]. How loss of Elongator affects MT acetylation, and whether a functional correlation between Elongator and Atat1 exists, remains to be explored.

Here, by combining cellular and molecular analyses in mouse cortical neurons in vitro and fly larva motoneurons (MNs) in vivo, we show that Elongator is expressed in vesicles and modulates axonal transport and acetylation of α-tubulin across species by regulating the stability of ATP-citrate lyase (Acly). This enzyme is enriched in vesicles and produces acetyl-coA, thereby providing acetyl groups for Atat1 activity towards MTs. Importantly, analysis of primary fibroblasts from FD patients show molecular defects comparable to those observed in mice and fly projection neurons depleted in Elongator. Therefore, our data may shine a light on the pathophysiological mechanisms underlying FD and other neurological disorders resulting from impaired Elongator activity.

Results

Elongator and Atat1 cooperate in a common pathway to regulate the acetylation of α-tubulin and axonal transport. In order to understand how Elongator controls tubulin acetylation and MT-based transport, we performed complementary experiments in distinct animal models that lack Elongator activity. We compared the level of α-tubulin acetylation in cultured cortical projection neurons (PN) that were isolated from embryonic (E) day 14.5 WT or Elp3cKO mouse embryos (conditional loss of *Elp3* in cortical progenitors upon breeding *Elp3*lox/lox[33] and FoxG1:Cre[34] transgenic mice). Axon of *Elp3* cKO PNs, as well as cortical extracts from E14.5 Elp3 cKO embryos displayed significant reduction of α-tubulin acetylation (Fig. 1a, Supplementary Fig. 1a). We next assessed axonal transport in PNs that were cultured in microfluidic devices for 5 days and incubated with specific dyes to track lysosomes (LysoTracker®) and mitochondria (MitoTracker®) movements by time-lapse videomicroscopy (Fig. 1b). PNs showed a significant reduction of average and moving velocities (in anterograde and retrograde directions) of lysosomes and mitochondria along axons, which correlated with an increase of their pausing time, as compared to WT PNs (Supplementary Fig. 1b–h). These results confirmed that loss of Elongator activity leads to defects of α-tubulin acetylation and molecular transport in cortical neurons. Since a vesicular pool of Atat1 promotes acetylation of α-tubulin, thereby controls axonal transport in cortical PNs[30], we postulated that Atat1 and Elongator might contribute to axonal transport via a shared molecular pathway. To test this hypothesis, we infected cortical PNs from E14.5 WT and *Atat1* KO mice with lentiviruses expressing either sh-Elp3 or sh-Control (Supplementary Fig. 1i–j), and we cultured them in microfluidics devices for five days (Fig. 1b). Targeting Elp3 in WT neurons impaired lysosomes and mitochondria transport across PN axons. However, we did not observe an additive effect on MT acetylation or axonal transport kinetics upon reduction of Elp3 expression in *Atat1* KO PNs (which show reduced acetylation of α-tubulin) (Fig. 1c–e, Supplementary Fig. 1k–o). Comparable observations were made in vivo in MNs of *Drosophila melanogaster* 3rd instar larvae obtained by crossing UAS:*Elp1* or UAS:*Elp3 RNAi* fly lines with D42:Gal4 (further called *Elp1* KD and *Elp3* KD). The knockdown efficiency of the UAS:*Elp1 and* UAS:*Elp3* in postmitotic neurons was validated in adult fly heads (Elav:Gal4 driver; Supplementary Fig. 1p–r). We first confirmed that the level of α-tubulin acetylation was reduced in *Elp1* and *Elp3* KD 3rd instar larvae MNs, a defect genetically rescued by expressing human (h) ELP3 or by co-targeting the main α-tubulin deacetylase Hdac6 with RNAi (*Elp1;Hdac6* KD, *Elp3;Hdac6* KD) (Fig. 1f, Supplementary Fig. 1r). Moreover, knocking down both *Elp3* and *Atat1* (*Elp3;Atat1* KD) did not further reduce the α-tubulin acetylation level, as compared to *Elp3* KD alone (Fig. 1f; $p = 0.259$ and $p = 0.775$, respectively). In vivo time-lapse recording of the synaptotagmin-GFP axonal transport (SYT1-GFP) in MNs of anesthetized fly 3rd instar larvae (Fig. 1g) correlated with levels of α-tubulin acetylation (Fig. 1f). We observed a reduction of both the average and moving velocities of SYT1-GFP vesicles together with an extension of their pausing time both in *Elp1* KD or *Elp3* KD larvae when compared to controls, and with no cumulative defects in *Elp3;Atat1* KD flies (Fig. 1h–j, Supplementary Fig. 1s). Moreover, knocking down *Hdac6* fully rescued the observed axonal transport defects observed in Elp1/3 KD in 3rd instar larvae MNs

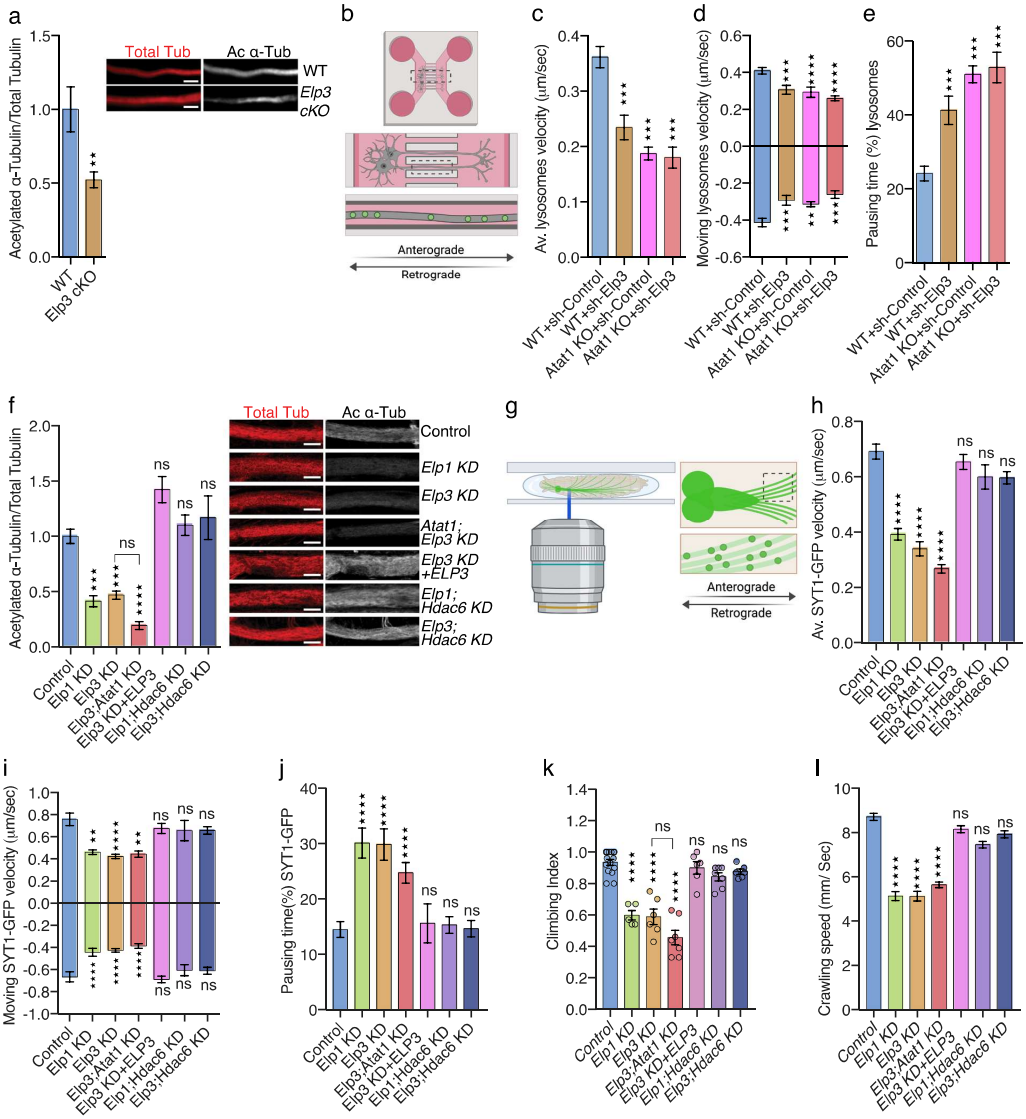

(*Elp1;Hdac6* KD, *Elp3;Hdac6* KD) (Fig. 1h–j, Supplementary Fig. 1s).

Interfering with Elongator activity affects codon-biased translation that can ultimately lead to protein aggregation[35], thereby blocking axonal transport[36]. However, we did not detect significant protein aggregation in the axon of either cultured cortical neurons from *Elp3* cKO mice (Supplementary Fig. 1t) or motoneurons from *Elp1* or *Elp3* KD 3rd instar larvae in vivo (Supplementary Fig. 1u), while axonal aggregates formed upon blocking proteasome activity with MG132 incubation. Altogether, these results suggest that the axonal transport defects observed in Elongator deficient neurons unlikely result from a local accumulation of protein aggregates.

Since impaired axonal transport in fly MNs leads to locomotion defects[1,37], we measured larvae crawling speed and adult flies climbing index as functional readouts of axonal transport activity in MNs[30,37]. These parameters were affected upon depletion of either *Elp1* or *Elp3* (Fig. 1k–l), and were likely resulting from MT acetylation and axonal transport defects, as they were rescued by the knockdown of *Hdac6* (Fig. 1k–l) and no morphological changes of neuromuscular junction synapses were observed (Supplementary Fig. 1v).

Elongator shares high amino acid similarity across species (Supplementary Fig. 1w). Expression of human *ELP3* in MNs of 3rd instar larvae of *Elp3* KD flies (*Elp3* KD + *ELP3*) rescued α-tubulin acetylation (Fig. 1f), axonal transport parameters (Fig. 1h–j, Supplementary Fig. 1s) and locomotion behavior defects (Fig. 1k–l), indicating that ELP3, and by extension Elongator, has a conserved evolutionary role from human to fly in axonal transport. Moreover, we show that loss of Elongator activity does not worsen the axonal phenotype of *Atat1* KO neurons, further suggesting that these molecules act in a common

Fig. 1 Reduction of Elongator activity leads to axonal transport defects in mouse and fly. a Immunolabelings and quantification of acetylated α-tubulin (Ac α-Tub) and total tubulin (Tot Tub) levels in axon of E14.5 WT and *Elp3 cKO* mice cortical neurons cultured for 5 DIV in microfluidic devices. Scale bar is 10 µm. **b** Experimental set up to record axonal transport by time-lapse microscopy in E14.5 mice cortical neurons cultured for 5 DIV in microfluidic devices. **c–e** Histograms showing axonal transport of lysosomes (LysoTracker®) in WT or *Atat1 KO* cultured neurons infected with sh-Control or sh-*Elp3* to analyze average (av.) velocity **c**, moving velocity **d,** and percentage of pausing time **e**. **f–l** Study of *Drosophila melanogaster* expressing RNAi under a motoneuron (MN)-specific driver (D42:GAL4); *Elp1* KD, *Elp3* KD, *Atat1; Elp3* KD, *Elp3* KD + human *ELP3, Elp1; Hdac6* KD and *Elp3;Hdac6* KD. **f** Immunolabelings and quantification of acetylated α-tubulin (Ac α-Tub) and total tubulin (Tot Tub) levels in MN axons of 3rd instar larvae, genotype as indicated. Scale bar is 10 µm. **g** Experimental set up for in vivo time-lapse recording of Synaptotagmin-GFP (Syt1-GFP) axonal transport in 3rd instar larvae motoneurons, to analyze average (av.) velocity **h**, moving velocity **i**, and percentage of pausing time **j**. **k–l** Locomotion assays: histograms of the climbing index of adult flies **k** and the crawling speed of 3rd instar larvae **l**. Description of graphical summaries here within are histograms of means ± SEM. Significance was determined by: **a** two-sided *t* test, **c**, **d**, **e**, **f**, **h**, **i**, **j**, **l** two-sided Kruskal–Wallis test, and **k** two-sided one-way analysis of variance (ANOVA). Specifically, [(**a**) $p = 0.0070$, $t = 2.812$, df = 5; (**c**) $p < 0.0001$ and $K = 80.47$; (**d**) $p < 0.0001$, $K = 34.30$ and $p < 0.0001$, $K = 23.46$ for anterograde and retrograde, respectively, (**e**) $p < 0.0001$ and $K = 73.34$, (**f**) $p < 0.0001$, and $K = 88.16$, (**h**) $p < 0.0001$ and $K = 223.6$, (**i**) $p < 0.0001$, $K = 110.3$, and $p < 0.0001$, $K = 45.69$ for anterograde and retrograde, respectively, (**j**)$p < 0.0001$, $K = 46.06$, (**k**) $p < 0.0001$, $F = 28.74$; (**l**) $p < 0.0001$, $K = 86.04$. In addition, the post hoc multiple comparisons, to analyze statistical difference of each condition compared to control for (**c**, **d**, **e**, **f**, **h**, **i**, **j**, **l**) Dunn's test, for (**k**) Dunnet's test and are $^{**}p < 0.01$, $^{***}p < 0.001$, and $^{****}p < 0.0001$. **a** Number of axons: WT $n = 28$; Elp3 cKO $n = 28$. 3 mice per group. **c** Number of vesicles: WT + sh-Control $n = 334$; WT + sh-Elp3 $n = 101$; Atat1 KO + sh-Control $n = 278$; Atat1 KO + sh-Elp3 $n = 79$. 3 mice per group. **d** Number of vesicles: WT + sh-Control $n = 180$ (anterograde), $n = 135$ (retrograde); WT + sh-Elp3 $n = 66$ (anterograde), $n = 56$; Atat1 KO + sh-Control $n = 129$ (anterograde), $n = 163$ (retrograde); Atat1 KO + sh-Elp3 $n = 58$ (anterograde), $n = 41$ (retrograde). 3 mice per group. **e** Number of vesicles: WT + sh-Control $n = 333$; WT + sh-Elp3 $n = 104$; Atat1 KO + sh-Control $n = 278$; Atat1 KO + sh-Elp3 $n = 79$. 3 mice per group. **f** Number of motoneurons: Control $n = 32$; Elp3 KD $n = 20$; Elp1 KD $n = 18$; Elp3;Atat1 KD $n = 19$; Elp3 KD + hELP3 $n = 14$; Elp1;Hdac6 KD $n = 36$; Elp3;Hdac6 KD $n = 15$. 5 larvae per group. **h** Number of vesicles: Control $n = 487$; Elp1 KD $n = 130$; Elp3 KD $n = 217$; Elp3;Atat1 KD $n = 143$; Elp3 KD + ELP3 $n = 397$; Elp1;Hdac6 KD $n = 80$; Elp3;Hdac6 KD $n = 421$. Number of larvae per group: Control: $n = 7$; Elp1 KD, Elp3 KD, Elp3;Atat1 KD, Elp3 KD + ELP3, Elp1;Hdac6 KD, Elp3;Hdac6 KD $n = 12$. **i** Number of vesicles: Control $n = 127$ (anterograde), $n = 159$ (retrograde); Elp1 KD $n = 118$ (anterograde), $n = 105$ (retrograde); Elp3 KD $n = 194$ (anterograde), $n = 203$ (retrograde); Elp3;Atat1 KD $n = 68$ (anterograde), $n = 81$ (retrograde); Elp3 KD + ELP3 $n = 173$ (anterograde), $n = 247$ (retrograde); Elp1;Hdac6 KD $n = 50$ (anterograde), $n = 39$ (retrograde); Elp3;Hdac6 KD $n = 283$ (anterograde), $n = 264$ (retrograde). Number of larvae per group: Control: $n = 7$; Elp1 KD, Elp3 KD, Elp3;Atat1 KD, Elp3 KD + ELP3, Elp1;Hdac6 KD, Elp3;Hdac6 KD $n = 12$. **j** Number of vesicles: Control $n = 488$; Elp1 KD $n = 217$; Elp3 KD $n = 130$; Elp3;Atat1 KD $n = 429$; Elp3 KD + ELP3 $n = 90$; Elp1;Hdac6 KD $n = 427$; Elp3;Hdac6 KD $n = 397$. Number of larvae per group: Control: $n = 7$; Elp1 KD, Elp3 KD, Elp3;Atat1 KD, Elp3 KD + ELP3, Elp1;Hdac6 KD, Elp3;Hdac6 KD $n = 12$. **k** Number of vials: Control $n = 15$; Elp1 KD $n = 5$; Elp3 KD $n = 6$; Elp3;Atat1 KD $n = 7$; Elp3 KD + ELP3 $n = 6$; Elp1;Hdac6 KD $n = 7$; Elp3;Hdac6 KD $n = 6$. Each vial contains 10 adult flies. **l** Larvae per group: Control $n = 21$; Elp1 KD $n = 15$; Elp3 KD $n = 12$; Elp3;Atat1 KD $n = 18$; Elp3 KD + ELP3 $n = 17$; Elp1;Hdac6 KD $n = 12$; Elp3;Hdac6 KD $n = 12$. Source data are provided with this paper.

molecular pathway to modulate MT acetylation and axonal transport[31,32].

Loss of Elongator impairs the production of acetyl-CoA, thereby interfering with Atat1- mediated MT acetylation. Since *Hdac6* knockdown rescued the axonal transport deficits observed in neurons lacking Elongator activity (Fig. 1h–j), we tested whether these defects may arise from a change of expression or activity of Hdac6 and/or Atat1, the enzymes that control α-tubulin de/acetylation, respectively[38,39]. Since no change in Hdac6 and Atat1 (isoform #3 and #4)[30] expression in cortical extracts from *Elp3* cKO and WT littermate newborn mice (Fig. 2a–c) were observed, we measured the activity of these enzymes. The deacetylation activity of Hdac6 toward MTs, assessed in vitro by incubating free acetylated α-tubulin from bovine brains with cortical extracts from newborn *Elp3* cKO or WT littermate controls[38], was comparable between conditions (Fig. 2d). Atat1 activity was measured by using an in vitro α-tubulin acetylation assay[30]. For this assay, pre-polymerized unacetylated MTs from HeLa cells were incubated with acetyl-CoA and P0 mouse brain extracts from *Elp3* cKO or WT littermate controls (Fig. 2e) to assess the level of acetylation of α-tubulin. In striking contrast to brain extracts from *Atat1* KO mouse pups, we did not observe any differences in MT acetylation levels between the cortical extracts from *Elp3* cKO and WT mice upon addition of acetyl-CoA (Fig. 2e). Altogether, these results suggest that loss of Elongator activity: i) does not impair α-tubulin acetylation by changing the expression or activity of Hdac6 or Atat1; ii) may interfere with the metabolic production of acetyl-CoA. Accordingly, western blotting of E14.5 Elp3cKO cortical extracts showed that expression of Acyl-coenzyme A synthetase short-chain family member (Acss2) and Acly, the enzymes that generate acetyl-CoA[40], were significantly reduced, as compared to control extracts (Fig. 2f–h). Since α-tubulin acetylation is mainly driven by a vesicular pool of Atat1 in axons[30], we performed sub-fractionation of cortical lysates (Fig. 2i; T: total, P1: nuclei, S2: cytosolic + vesicular, P2: membranes, S3: cytosolic, P3: vesicular) from adult WT mice to analyze the subcellular distribution of Acss2 and Acly. While Acss2 showed a strict cytosolic distribution (S3), we found that Acly was strongly enriched together with Elp1 and Elp3 in vesicles (P3) (Fig. 2j–l). These results were supported by immunolabeling of cortical neurons that show expression of Acly in some synapthophysin + vesicles and Lamp1 + late endosomes in PN axons (Fig. 2m–n). Moreover, proteomic analysis of cortical extracts from newborn mice confirmed the vesicular enrichment of several Elongator subunits, Atat1, Acly, but not Acss2 (Supplementary Fig. 2a). Altogether, these data suggest that α-tubulin acetylation could be regulated by homeostatic changes in Acly-dependent acetyl-CoA concentration, as previously observed for histone acetylation[41]. Specifically, we postulated that loss of Elongator could interfere with MT acetylation and axonal transport via reduction of Acly expression. To test this hypothesis, we performed an in vitro acetyl-CoA production assay (malate dehydrogenase coupled assay)[41], where subcellular fractions of cortical brain extracts from *Elp3* cKO and WT littermate newborns were mixed with Acly substrates (ATP, CoA, and citrate) (Fig. 2o). The vesicular fraction (P3), which is strongly enriched into Elongator subunits (Elp1 and Elp3), Atat1 and Acly (Fig. 2j, Supplementary Fig. 2a), more efficiently produced acetyl-coA (Fig. 2o–p). While cortical extracts from *Elp3* cKO E14.5 mouse embryos showed no change of *Acly* transcription (Fig. 2q), we observed a reduction of Acly expression (Fig. 2f–g) together with a correlative decrease of MTs acetylation (Supplementary

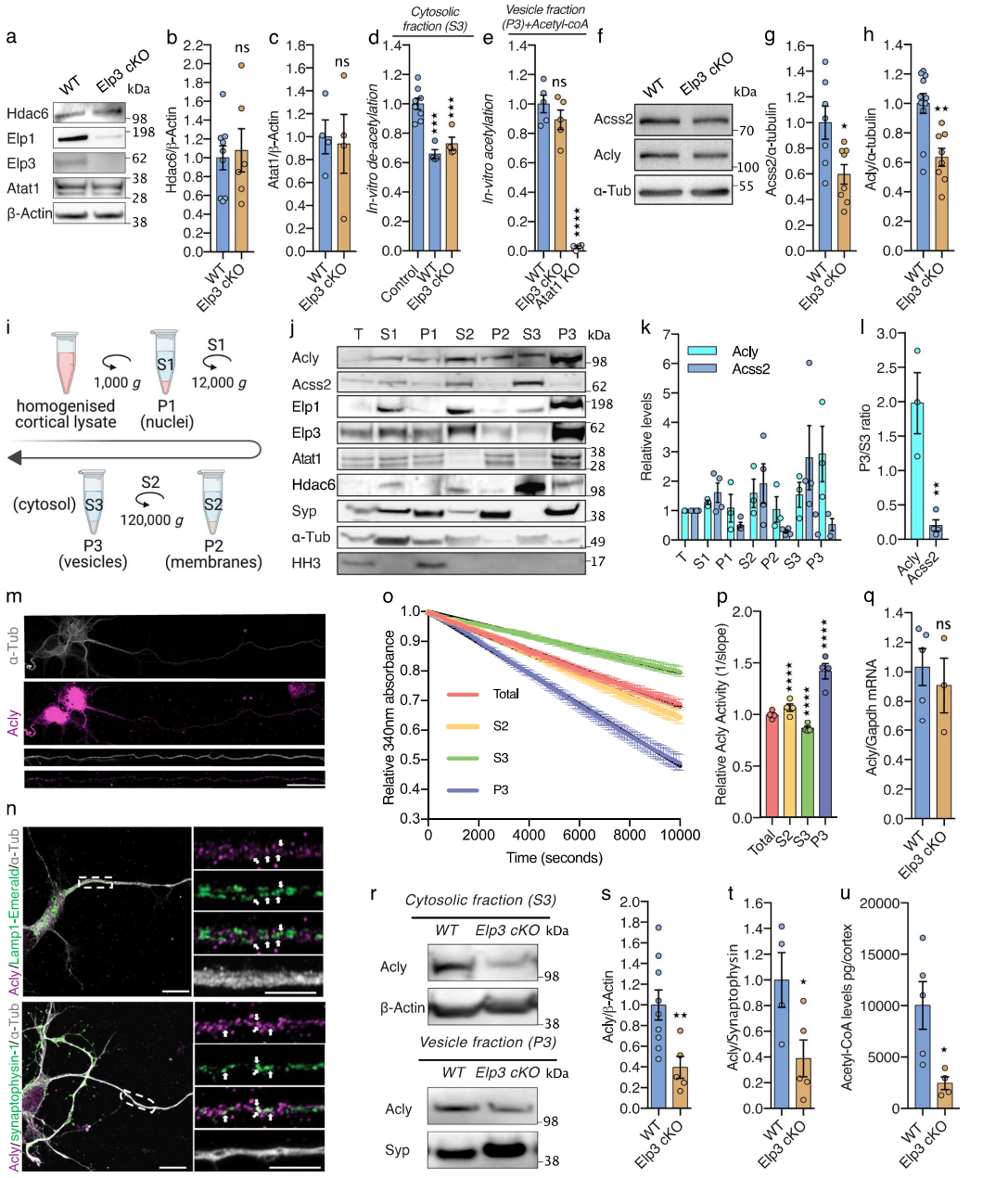

Fig. 1a). Indeed, the analysis of *Elp3* cKO and WT newborn cortices show a robust decrease of Acly protein level in both the cytosolic and the vesicular fractions (*P3*, Fig. 2r–t). Comparable reduction of Acly (but not Atat1) was detected by mass spectrometry in the vesiculome of P0 Elp1 KO brains (Supplementary Fig. 2b–d). Moreover, we detected a reduction of acetyl-CoA level in cortical extracts from *Elp3* cKO mice, as compared to WT newborn littermates by using LC-MS metabolic analysis (Fig. 2u). Altogether, these results support a molecular cooperation occurring at vesicles between the Elongator and Atat1 to drive MT acetylation via the regulated expression of the enzyme Acly, which provides acetyl-group donors to Atat1 for catalyzing α-tubulin acetylation in neurons.

Expression of Acly rescues both acetylation of α-tubulin and axonal transport defects in flies and mice that lack Elongator activity. In order to test whether Acly is required for proper axonal transport, we incubated WT mouse PNs with the Acly inhibitor hydroxycitric acid (HCA)[42]. This treatment reduced the level of α-tubulin acetylation in PNs axons (Fig. 3a). Moreover, incubation of

Fig. 2 Elongator deletion impairs tubulin acetylation and axonal transport via reduction of Acly-dependent acetyl-coA production. a–c Western blotting to detect and quantify Hdac6, Elp1, Elp3, Atat1 (isoform #3 and #4)[30], and ß-Actin in cortical extracts from newborn WT and *Elp3 cKO* mice. Histograms of proportion of Hdac6 **b** and Atat1 **c** expression to ß-Actin. **d** In vitro deacetylation assay of endogenously acetylated bovine brain tubulin incubated for 4 h with extracts (S3) of cortices isolated from WT, *Elp3 cKO*, or without tissue extract (control). **e** In vitro acetylation assay of nonacetylated MTs from HeLa cells incubated for 2 h with Acetyl-CoA and extracts (P3) of brain cortices isolated from WT, *Elp3 cKO* or *Atat1 KO* mice. **f–h** Immunoblotting to detect Acss2, Acly, and α-Tub cortical extracts from E14.5 WT and *Elp3 cKO* embryos and histograms of proportion of Acss2 (**g**) and Acly (**h**) expression to α-Tub. **i** Experimental pipeline for subcellular fractionation of P0 mouse cortical extracts: T, total; S1, post-nuclear; P1, nuclear; S2, cytosol and vesicles; P2, large membranes; S3, cytosol; and P3, vesicles. **j–l** Subcellular fractionation (T, S1, P1, S2, P2, S3, P3) of mouse brain cortex immunoblotted with specific antibodies to detect Acss2, Acly, Elp1, Elp3, Atat1 (isoform #3 and #4)[30], Hdac6, synaptophysin (Syp), α-tubulin (α-Tub), and Histone H3 (HH3). **k–l** Histograms of proportion of Acss2 and Acly across subcellular fractions **k** or expressed as P3/S3 ratio **l**. Immunolabelings of E14.5 mice cortical neurons cultured for 5 DIV to detect Acly (purple) and α-tubulin (α-Tub, grey) **m**; Acly, Synaptophysin-1 (green) and α-Tub (**n**, top); Acly, Lamp-1-Emerald (green) and α-Tub (**n**, bottom). Scale bars are 20 µm (m), 10 µm (**n**). **o–p** Analysis of Acly activity by malate dehydrogenase coupled method performed in WT and *Elp3 cKO* brain cortex lysates. Histogram of relative Acly activity over assay (**o**) and of slopes (**p**) from the linear phase of the reaction. **q** qRT-PCR analysis of *Acly* mRNA in cortical brain extracts of *Elp3 cKO* or WT littermate mice.**r–t** Immunoblots and quantification of cytosolic (S3, **s**) and vesicular (P3, **t**) fractions of Acly protein from newborn WT and *Elp3 cKO* mice brain cortices. **u** LC-MS quantification of Acetyl-CoA levels in WT and *Elp3 cKO* P0 mice brain cortex lysates. Description of graphical summaries here within are histograms of means ± SEM. Significance was determined by: **b**, **c**, **g**, **h**, **l**, **s**, **t** two-sided *t* test, **q**, **u** two-sided Mann–Whitney test, **d**, **e**, **p** two-sided one-way analysis of variance (ANOVA), and **o** two-sided two-way ANOVA. Specifically, [(**b**) $p = 0.8411$, $t = 0.2093$, df = 6; (**c**) $p = 0.7505$, $t = 0.3248$, df = 13; (**d**) $p < 0.0001$, $F = 21.30$; (**e**) $p < 0.0001$, $F = 85.29$; (**g**) $p = 0.0157$, $t = 0.2.776$, df = 13; (**h**) $p = 0.0013$, $t = 3.861$, df = 17; (**l**) $p = 0.0056$, $t = 4.638$, df = 5; (**o**) $p < 0.0001$, $F_{Interaction}$ (294, 882) = 68.07; (**p**) $p < 0.0001$, F = 1352; (**q**) $p = 0.5714$, $U = 5$; (**s**) $p = 0.0145$, $t = 2.855$, df = 12; (**t**) $p = 0.0428$, $t = 2.470$, df = 7; (**u**) $p = 0.0159$, $U = 0$. In addition, the post hoc multiple comparisons, to analyze statistical difference` of each condition compared to control for (**d**, **e**, **p**) are Holm-Sidak test, and are $^{*}p < 0.05$, $^{**}p < 0.01$, $^{***}p < 0.001$, and $^{****}p < 0.0001$. Number of mice: (**b**) WT $n = 9$; Elp3 cKO $n = 6$; (**c**) WT $n = 4$; Elp3 cKO $n = 4$; (**d**) Control $n = 8$; WT $n = 4$; cKO $n = 4$; (**e**) WT $n = 5$; Elp3 cKO $n = 5$; Atat1 KO $n = 4$; (**g**) WT $n = 7$; Elp3 cKO $n = 8$; (**h**) WT $n = 11$; Elp3 cKO $n = 8$; (**l**) WT $n = 3$ (Acly); WT $n = 4$ (ACSS2); (**o–p**) WT $n = 4$ for 99 time points; (**q**) WT $n = 5$; Elp3 cKO $n = 3$; (**s**) WT $n = 9$; Elp3 cKO $n = 5$; (**t**) WT $n = 4$; Elp3 cKO $n = 5$; (**u**) WT $n = 5$; Elp3 cKO $n = 4$. **e** $p = 0.031$, $t = 2.407$, df = 13. Source data are provided with this paper.

HCA reduced average and retrograde moving velocities of lysosomes along axons, which correlated with an increase of their pausing times, as compared to vehicle treatment (Fig. 3b–d, Supplementary Fig. 3a). We next analyzed 3rd instar larvae from *Acly* KD flies[43] whose MNs displayed reduced α-tubulin acetylation (Fig. 3e) together with impairment of SYT1-GFP vesicles transport (Fig. 3f–h, Supplementary Fig. 3b). Knocking down *Hdac6* fully rescued the level of α-tubulin acetylation (Fig. 3e) and the axonal transport defects observed in *Acly* KD MNs (*Acly* KD;*Hdac6* KD, *Acly*;*Hdac6* KD) (Fig. 3f–h, Supplementary Fig. 3b). We next postulated that the impairment of α-tubulin acetylation and axonal transport observed upon loss of Elongator (Supplementary Fig. 1a–h) may arise from the reduced expression of Acly in PNs. To test this hypothesis, we expressed human ACLY (which shares high amino acid homology with its murine and fly homologues; Supplementary Fig. 3c) in E14.5 control and Elp3cKO PNs that were cultured in microfluidic devices for 5DIV. We showed that the level of MT acetylation (Fig. 3i) and the lysosomes and mitochondria transport defects were rescued upon expression of ACLY (Fig. 3j–l, Supplementary Fig. 3d–g). Comparable data were obtained with *Elp3* KD flies (that also show reduction of Acly level in the brain, Supplementary Fig. 3h) that express Acly (UAS:Elp3 RNAi and UAS:Acly, *Elp3* KD + Acly) in MNs during development (3rd instar larvae), where both acetylation of α-tubulin and axonal transport of SYT1-GFP vesicles were rescued to control levels (Fig. 3m–p, Supplementary Fig. 3i). These data were also correlated with improvement of locomotion activities of *Elp3* KD 3rd instar larvae and adult flies upon Acly expression (Supplementary Fig. 3j–k).

Altogether, these results suggest that reduction of Acly expression leads to MTs acetylation and axonal transport defects in Elongator deficient neurons.

Fibroblasts from Familial Dysautonomia patients show defects of α-tubulin acetylation and MT-dependent transport. In order to place our findings in a human pathological context, we analyzed primary skin fibroblasts from FD patients carrying the splice site IVS20 + 6T_C variant in *ELP1*[44] that expressed barely detectable amount of ELP1 proteins and low level of ELP3, resulting from its instability upon nonassembly of the Elongator complex (Supplementary Fig. 4a)[25]. We observed a reduction of acetylation of α-tubulin and MT-dependent transport defects in FD fibroblasts (Supplementary Fig. 4b–g), which were comparable to those observed in neurons from Elongator loss of function fly and mouse models. This modification was not resulting from an increased deacetylation activity of HDAC6 toward MTs in extracts fibroblasts nor an intracellular protein aggregation that would affect MT-dependent transport in FD fibroblasts (Supplementary Fig. 4h–i). Both the reduction of α-tubulin acetylation and the defects of MT-dependent transport in cultured FD fibroblasts were rescued by blocking tubulin deacetylation with the HDAC6 specific inhibitor, Tubastatin (TBA; 10uM during 30 min) (Supplementary Fig. 4c–g). Similarly to the animal models, FD fibroblasts express reduced amount of ACLY proteins (Fig. 4a) and incubation with HCA for 8 h interfered in a dose-dependent manner with MT acetylation (Fig. 4b), in both control and FD fibroblasts, in line with the residual expression of ACLY observed in FD fibroblasts (Fig. 4a). We next showed that overexpression of ACLY in FD fibroblasts rescued the level of acetylation of α-tubulin (Fig. 4c), as well as the defects of MT-dependent transport of lysosomes (Fig. 4d–f, Supplementary Fig. 4j). Altogether, these results demonstrate that reduction of ACLY in FD fibroblasts leads to MT acetylation and MT-dependent transport impairments; these molecular defects likely contribute to the pathological mechanisms underlying FD.

Loss of elongator activity interferes with Acly stability. Elongator is a tRNA modifier and its loss of activity may directly impair the translation of *Acly* mRNAs. To address this question, we performed a polysomal fractionation of cortical extracts of P0 Elp3 cKO and WT littermates to analyze the association of *Acly* mRNAs with ribosomes[45] and found no differences between genotypes (Fig. 5a–b). These data were confirmed by labeling cultured Elp3 cKO an WT PNs with puromycin for 4 min, a tRNA analogue that incorporates into nascent peptides, causing their premature chain termination (reviewed in[46]). We visualized the de novo synthesis of Acly by combining anti-puromycin with

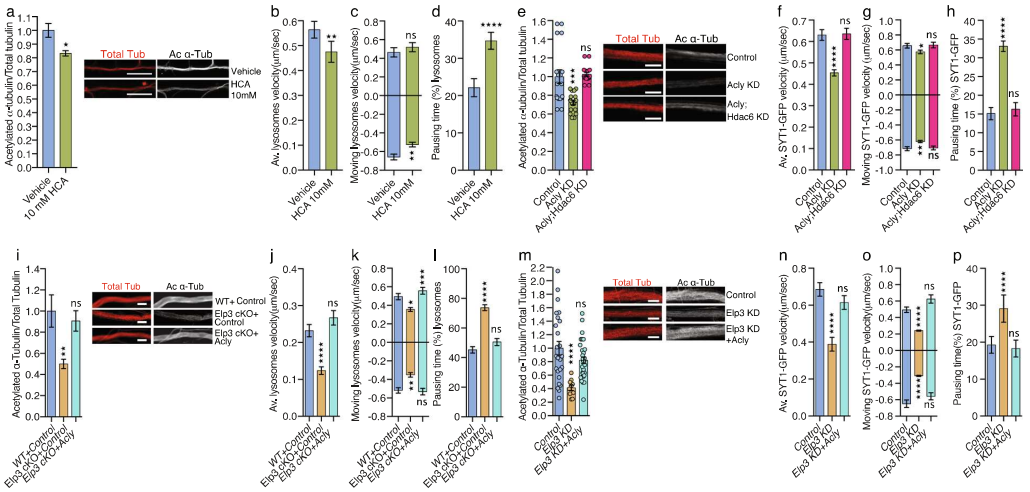

Fig. 3 Acly/ACLY expression rescues α-tubulin acetylation and molecular transport defects upon loss of Elongator activity in mouse and fly neurons. **a** Immunolabeling and quantification of acetylated α-tubulin (Ac α-Tub) and total tubulin (Tot α-Tub) levels in axons of DIV5 cultured cortical PNs isolated from E14.5 embryos and incubated with 10 mM hydroxy-citrate (HCA) during 8 h prior to fixation. Scale bar is 10 µm. **b**–**d** Time-lapse recording of axonal transport in corresponding PNs cultured for 5 DIV in microfluidic devices and treated with vehicle- or HCA-supplemented medium for 8 h showing (av.) velocity **b**, moving velocity **c,** and percentage of pausing time **d** of lysosomes (LysoTracker®). **e** Immunolabeling and quantification of acetylated α-tubulin (Ac α-Tub) and total tubulin (Tot α-Tub) levels in MN axons from 3rd instar larvae of *Drosophila melanogaster* control or expressing Acly RNAi (Acly KD) under a MN-specific driver (D42:GAL4). Scale bar is 10 µm. **f**–**h** Time-lapse recording of Synaptotagmin-GFP (Syt1-GFP) axonal transport in 3rd instar larvae MNs of control or *Acly* KD to analyze average (av.) velocity **f**, moving velocity **g**, and percentage of pausing time **h**. **i** Immunolabeling and quantification of acetylated α-tubulin (Ac α-Tub) and total tubulin (Tot α-Tub) levels in axons of cultured cortical PNs isolated from E14.5 WT and *Elp3cKO* embryos transfected with Acly or control. Scale bar is 10 µm. **j**–**l** Cortical neurons isolated from E14.5 WT and Elp3cKO embryos were transfected with control or ACLY expressing constructs and cultured for 5 DIV in microfluidic devices to perform time-lapse recording of axonal transport and measure average (av.) velocity **j**, moving velocity **k**, and percentage of pausing time **l** of lysosomes (LysoTracker®). **m** Immunolabeling and quantification of acetylated α-tubulin (Ac α-Tub) and total tubulin (Tot α-Tub) levels in MN axons of 3rd instar larvae: control, *Elp3* KD, and *Elp3* KD + human *ACLY*. Scale bar is 10 µm. **n**–**p** In vivo live imaging and behavior measurements in 3rd instar larva: control, *Elp3* KD, and *Elp3* KD + human *ACLY*. **n**–**p** Time-lapse recording of axonal transport of Synaptotagmin-GFP (Syt1-GFP) in MNs to analyze average (av.) velocity **n**, moving velocity **o**, and percentage of pausing time **p**. Description of graphical summaries here within are histograms of means ± SEM. Significance was determined by: **a** two-sided *t* test, **b–d** two-sided Mann–Whitney test, **i** two-sided one-way analysis of variance (ANOVA), and **e**, **f**, **g**, **h**, **j**, **k**, **l** two-sided Kruskal–Wallis one-way ANOVA. Specifically, [(**a**) $p = 0.0166$, $t = 2.445$, df = 81; (**b**) $p = 0.0039$, $U = 6807$; (**c**) $p = 0.2524$, $U = 2152$ and $p = 0.0032$, $U = 4559$ for anterograde and retrograde, respectively; (**d**) $p < 0.0001$, $U = 6201$; (**e**) $p < 0.0001$, $K = 26.17$; (**f**) $p < 0.0001$, $K = 55.55$; (**g**) $p = 0.0130$, $K = 8.69$ and $p = 0.0004$, $K = 15.55$ for anterograde and retrograde, respectively; (**h**) $p < 0.0001$, $K = 93.1$; (**i**) $p = 0.0042$, $F = 4.969$; (**j**) $p < 0.0001$, $K = 28.69$; (**k**) $p = 0.001$, $K = 13.85$ and $p < 0.0001$, $K = 251.5$; (**l**) $p < 0.0001$, $K = 24.74$; (**m**) $p = 0.0003$, $F = 9.158$; (**n**) $p < 0.0001$, $K = 21.66$; (**o**) $p < 0.0001$, $F = 25.90$, and $p < 0.0001$, $F = 20.96$ for anterograde and retrograde, respectively; (**p**) $p < 0.0001$, K = 22.35. In addition, the post hoc multiple comparisons, to analyze statistical difference of each condition compared to control for (**e**) Kruskal–Wallis test, for (**i**, **m**) is Dunnet's test, for (**f**, **g**, **h**, **j**, **k**, **l**, **n**, **o**, **p**) are Sidak's test and are $^{*}p < 0.05$, $^{**}p < 0.01$, $^{***}p < 0.001$, and $^{****}p < 0.0001$. **a** Number of axons: Vehicle $n = 88$; 10 mM HCA $n = 151$; 2 mice per group. **b**) Number of axons: Vehicle $n = 133$; 10 mM HCA $n = 129$. 2 mice per group. **c** Number of vesicles: Vehicle $n = 63$ (anterograde), $n = 113$ (retrograde); 10 mM HCA $n = 77$ (anterograde), $n = 105$ (retrograde). d Number of vesicles: Vehicle $n = 133$; 10 mM HCA $n = 129$. **e** Number of axons: Control $n = 9$; Acly KD n = 9; Acly;Hdac6 KD $n = 9$. 6 larvae per group. **f** Number of vesicles: Control $n = 234$; Acly KD $n = 422$; Acly;Hdac6 KD $n = 182$. 3 animals per group. **g** Number of vesicles: Control $n = 131$ (anterograde), $n = 134$ (retrograde); Acly KD $n = 195$ (anterograde), $n = 337$ (retrograde); Acly;Hdac6 KD $n = 89$ (anterograde), $n = 119$ (retrograde). **h** Number of vesicles: Control $n = 234$; Acly KD $n = 422$; Acly;Hdac6 KD $n = 182$. **i** Number of axons: WT + Control $n = 28$; Elp3 cKO + Control $n = 25$; Elp3 cKO + Acly $n = 23$. Number of mice per group: WT + Control $n = 5$; Elp3 cKO + Control $n = 3$; Elp3 cKO + Acly $n = 5$. **j** Number of vesicles: WT + Control $n = 441$; Elp3 cKO + Control n = 429; Elp3 cKO + Acly $n = 385$. Number of mice per group: WT + Control $n = 5$; Elp3 cKO + Control $n = 3$; Elp3 cKO + Acly $n = 5$. **k** Number of vesicles: WT + Control $n = 108$ (anterograde), $n = 143$ (retrograde); Elp3 cKO + Control $n = 111$ (anterograde), $n = 79$ (retrograde); Elp3 cKO + Acly $n = 103$ (anterograde), $n = 107$ (retrograde). Number of mice per group: WT + Control $n = 5$; Elp3 cKO + Control $n = 3$; Elp3 cKO + Acly $n = 5$. **l** Number of vesicles: WT + Control $n = 441$; Elp3 cKO + Control $n = 429$; Elp3 cKO + Acly $n = 385$. Number of mice per group: WT + Control $n = 5$; Elp3 cKO + Control $n = 3$; Elp3 cKO + Acly $n = 5$. **m** Number of axons: Control $n = 25$; Elp3 KD $n = 10$; Elp3 KD + Acly $n = 37$. 3 mice per group. **n** Number of vesicles: Control $n = 304$; Elp3 KD $n = 78$; Elp3 KD + Acly $n = 181$. Number of larvae per group: Control $n = 5$; Elp3 KD $n = 10$; Elp3 KD + Acly $n = 10$. **o** Number of vesicles: Control $n = 87$ (anterograde), $n = 141$; Elp3 KD $n = 99$ (anterograde), $n = 141$ (retrograde); Elp3 KD + Acly $n = 80$ (anterograde); $n = 81$ (retrograde). Number of larvae per group: Control $n = 5$; Elp3 KD $n = 10$; Elp3 KD + Acly $n = 10$. **p** Number of vesicles: Control $n = 252$; Elp3 KD $n = 84$; Elp3 KD + Acly $n = 234$. Source data are provided with this paper.

anti-Acly antibodies and performing proximity ligation assay (PLA) to reveal Acly puro-PLA puncta in PNs (Fig. 5c–d). We showed comparable somatic and axonal Acly puro-PLA puncta in PNs from both genotypes (Fig. 5e–f). Together, these data suggest that loss of Elongator activity does not interfere with the translation of *Acly* mRNAs in cortical PNs.

We next tested whether the stability of ACLY might be impaired upon loss of Elongator activity. For this purpose, we cultured

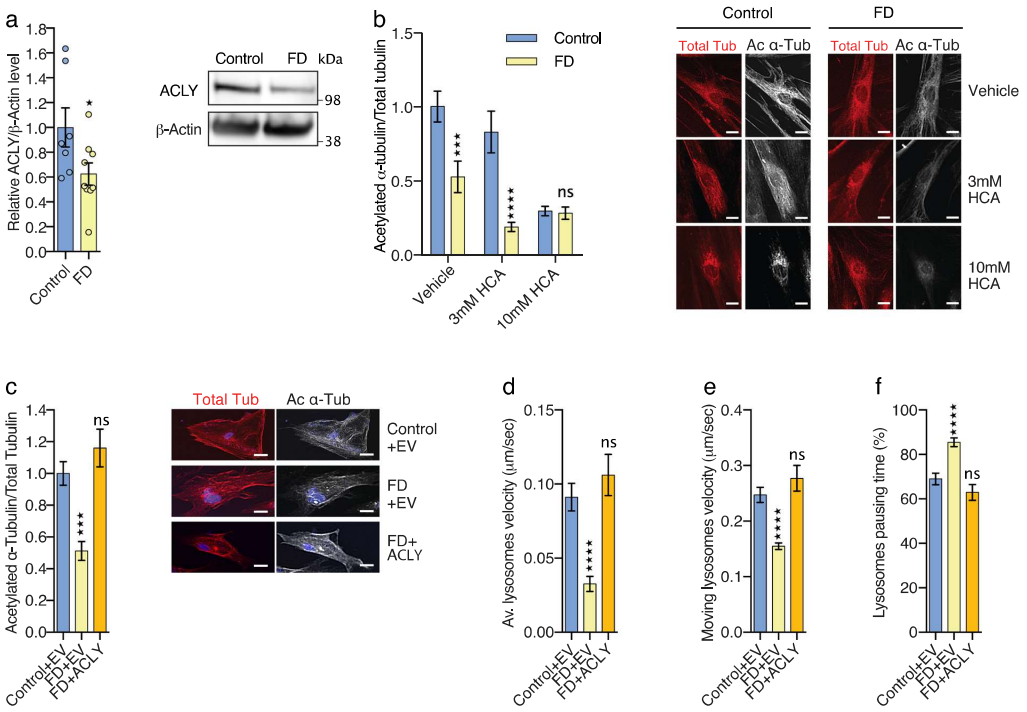

Fig. 4 ACLY expression rescues defects of α-tubulin acetylation and microtubule-dependent transport in human FD fibroblasts. a Immunoblotting of ACLY and ß-ACTIN in cultured human primary fibroblast extracts from Control and FD patients. **b** Immunolabeling and quantification of acetylated α-tubulin and total tubulin levels in primary fibroblasts from healthy controls and FD patients incubated with the ACLY inhibitor hydroxy-citrate acid (HCA). Scale bar is 50 μm. **c** Immunolabeling and quantification of acetylated α-tubulin and total α-tubulin levels in extracts from primary fibroblasts from healthy controls and FD patients transfected with control or ACLY expressing plasmids. Scale bar is 50 μm. **d**–**f** Time-lapse recording of MT-dependent transport of lysosome (LysoTracker®) in fibroblasts from Control or FD patients, transfected with Control or ACLY plasmids, to analyze average (av.) velocity (**d**), moving velocity (**e**) and percentage of pausing time (**f**). Description of graphical summaries here within are histograms of means ± SEM. Significance was determined by: (**a**) two-sided *t* test, (**b**) two-sided two-way analysis of variance (ANOVA), (**c**) two-sided ANOVA, and (**d**, **e**, **f**) two-sided Kruskal–Wallis one-way ANOVA. Specifically, [(**a**) $p = 0.0467$, $t = 2.181$, df = 14; (**b**) $p = 0.0038$, $F_{interaction}$ (2, 109) = 5.876; (**c**) $p < 0.0001$, $F = 13.17$; (**d**) $p < 0.0001$, $K = 48.95$; (**e**) $p < 0.0001$, $K = 35.10$; (**f**) $p < 0.0001$, $K = 40.98$. In addition, the post hoc multiple comparisons to analyze statistical difference of each condition compared to control for (**b**) is Sidak's test, for (**c**) is Dunnet's test, for (**d**, **e**, **f**) are Dunn's test, and are $^{*}p < 0.05$, $^{***}p < 0.001$, and $^{****}p < 0.0001$. **a** 5 human primary fibroblast lines per group. **b** Number of cells: Control $n = 26$ (Vehicle), $n = 18$ (3 mM HCA), $n = 20$ (10 mM HCA); FD $n = 18$ (Vehicle), $n = 15$ (3 mM HCA), $n = 18$ (10 mM HCA). Number of fibroblast lines per group: Control $n = 5$; FD $n = 4$. **c** Number of cells: Control + EV $n = 15$; FD + EV $n = 15$; FD + Acly $n = 15$. **d** Number of vesicles: Control + EV $n = 262$; FD + EV $n = 217$; FD + Acly $n = 143$. 5 human primary fibroblast lines per group. **e** Number of vesicles: Control + EV $n = 133$; FD + EV $n = 68$; FD + Acly $n = 89$. 5 human primary fibroblast lines per group. **f** Number of vesicles: Control + EV $n = 251$; FD + EV $n = 217$; FD + Acly $n = 143$. 5 human primary fibroblast lines per group. Source data are provided with this paper.

patient fibroblasts and performed cycloheximide chase assay to measure ACLY half-life in several lines of control and FD fibroblasts. We showed a reduction of ACLY stability in FD fibroblasts as compared to control lines (Fig. 5g–h), a phenotype that may result from the disruption of an interaction between the Elongator and Acly, as suggested by co-immunoprecipitation experiments performed in HEK293 cells (Supplementary Fig. 5a). Altogether, these data suggest that loss of Elongator activity reduces Acly/ACLY stability, thereby affecting the local production of acetyl-CoA required by ATAT1 to promote MT acetylation. Such regulation is likely to take place in motile vesicles (Fig. 5i).

Discussion

Here, we show that loss of Elongator activity impairs both the MT acetylation and bidirectional axonal transport in mouse cortical neurons in culture, as well as in fly motoneurons in vivo, ultimately resulting in locomotion deficits in flies. These defects are similar to those observed upon loss of Atat1 expression, the enzyme that catalyzes the acetylation of α-tubulin K40 residues in MTs. This shared phenotype prompted us to investigate a possible coordination between the Elongator and Atat1 in the control of MT-dependent axonal transport via α-tubulin acetylation. By combining conditional loss of function models with genetic experiments, we observed a molecular cooperation between Elongator and Atat1 and identified Acly as the common denominator, which provides acetyl groups from Acetyl-CoA to vesicular Atat1 and whose expression depends on Elongator activity. We showed that acute knockdown or pharmacological blockade of Acly impairs MT acetylation and axonal transport in fly and mouse, respectively. Here, the lower effect of HCA treatment on lysosome axonal transport may reflect a sub-efficient reduction of Acetyl CoA availability in mouse PNs, as

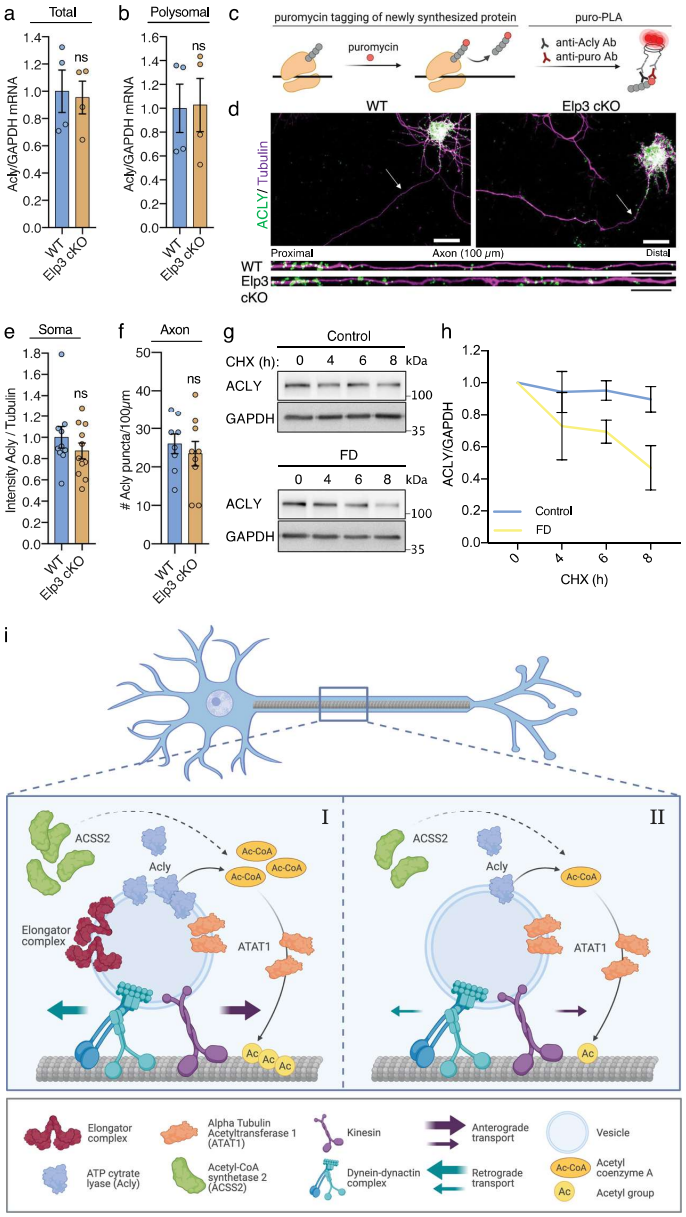

compared to the one obtained in the genetic fly model. On the other hand, raising Acly level not only rescued axonal transport defects in both mouse and fly Elongator models but also improved locomotion activity of *Elp3* KD larvae and flies. We found that loss of Elongator activity does not affect the transcription and translation of *Acly* but rather impairs Acly/ACLY stability. Our in vitro data suggest that Elongator may regulate Acly/ACLY protein stability via molecular interaction, as previously reported for other cytoplasmic proteins[37] (Supplementary Fig. 5). Another non-mutually exclusive mechanism that may act downstream Elongator would involve the regulation of the acetyltransferase[47] P300/CBP-associated factor (PCAF), which is known to increase Acly stability by promoting its acetylation[47].

We previously showed that motile vesicles are the main driver of MT acetylation in axons[30] and Elongator subunits and Atat1 have been detected in protein extracts from purified motile vesicles[16,30]. Here, we found that the vesicular fraction isolated from mouse cerebral cortical extracts does not only express Elongator subunits and Atat1, but it is also enriched with a functional pool of Acly (Fig. 2j–l). Therefore, we postulate that an Elongator/Acly/Atat1 (EAA) signaling pathway may directly act at vesicles to promote MT acetylation, further supporting their non-canonical role as a platform for local signaling and for

Fig. 5 Elongator depletion reduces the stability but not translation of Acly. a–b Transcriptional and translational analysis of Acly mRNA in cortex lysate from newborn WT and Elp3 cKO mice. qPCR quantification of Acly mRNA normalized to GAPDH obtained from lysed cortex (total) (**a**) or from polysomal fraction (polysomal) enriched by sucrose gradient ultracentrifugation of cytoplasmic cortical lysate (**b**) (values are means ± SEM; unpaired *t* test). **c–f** Analysis of local translation events of Acly in cultured cortical PNs from E14.5 WT and Elp3cKO embryos. Schematic of the puro-PLA principle to visualize newly synthesized peptides (**c**). Representative images of newly synthesized Acly in cortical PNs cultured five days in vitro and treated 4 min with puromycin before fixation and processing for puro-PLA; puro-Acly PLA puncta (green), α-tubulin (purple) (**d**). Quantification of somal puro-PLA fluorescence intensity normalized to α-tubulin (**e**) and axonal number of puro-PLA puncta over 100 μm segments (**f**) (values are means ± SEM; unpaired *t* test). Scale bar is 20 μm (top panels) and 10 μm (bottom panels). **g–h** Immunoblotting and quantification of ACLY and GAPDH in human primary fibroblast extracts from Control and FD patients incubated with cycloheximide (CHX, 50 µg/mL) for 0, 4, 6, and 8 h. **i** Summary scheme showing a central role played by Acly in the control of both α-tubulin acetylation and microtubule-dependent transport, which are impaired upon loss of Elongator activity. Description of graphical summaries here within are histograms of means ± SEM. Significance was determined by: (**a**, **b**, **e**, **f**) two-sided *t* test, (**e**) two-sided two-way ANOVA. Specifically, [(**a**) $p = 0.8244$, $t = 0.2318$, df = 6; (**b**) $p = 0.9303$, $t = 0.9114$, df = 6; (**e**) $p = 0.3160$, $t = 1.03$, df = 19; (**f**) $p = 0.5484$, $t = 0.6141$, df = 15; (**h**) $p < 0.0034$, $F_{\text{Interaction}}$ (1, 22) = 10.78). (**a**, **b**) 4 animals per group. **e** Number of axons: WT $n = 10$; Elp3 cKO $n = 11$. 2 animals per group. **f** Number of axons: WT $n = 8$; Elp3 cKO $n = 9$. 2 animals per group. **h** 4 human primary fibroblast lines per group. Source data are provided with this paper.

regulating axonal transport in particular (Fig. 5i). Since these molecules are also detected in the cytosolic fraction together with Acss2 (S3, Fig. 2j–l), whose expression is reduced upon loss of Elongator (Fig. 2f, h), we cannot rule out the contribution of some cytosolic Acetyl-CoA generated by Acss2 in the vicinity of MTs, which would explain the remaining basal level of MT acetylation seen upon axonal transport blockade[30]. We observed comparable defects of α-tubulin acetylation and MT-dependent transport in fly, mouse, and human cells lacking Elongator activity, which, together with similar observations made in C. elegans[6], suggest a strong functional conservation of the EAA pathway across species.

A tight control of axonal transport is indeed very important to ensure the homeostatic activity of neurons by delivering cargos to distant regions, thereby controlling cytoskeleton maintenance as well as spreading long-range intracellular signaling that ensures cellular maintenance and function. Impairment of axonal transport is considered as an early pathological feature shared by several neurodegenerative disorders[2,48,49]. Along this line, our results obtained with FD fibroblasts support those previously described in neurons[28] and suggest that loss of Elongator activity contribute to neurodegeneration by interfering at least with MT-dependent transport in FD patients via impairment of ACLY expression. We did not observe differences in MT deacetylation activity in FD and WT fibroblasts (Supplementary Fig. 4h), suggesting that reduction of MT acetylation in FD fibroblasts does not arise from changes of HDAC6 expression, in contrast to what others have reported[28].

More generally, α-tubulin acetylation not only modulates axonal transport but also provides resistance to mechanical bending to MTs[50]. Therefore, by controlling the cytoskeleton integrity and function, the EAA pathway likely acts as a key regulator of neuronal fitness whose progressive dysfunction may contribute to neuronal aging and even underlie neurodegeneration. Thus, targeting this molecular pathway may open therapeutic perspectives to prevent the onset or the progression of neurodegenerative disorders like FD characterized by poor axonal transport and degeneration.

Methods

Mice. All experiments performed in this study adhere to all relevant ethical regulations for animal testing and research. The animal work was approved by the ethical committee of the University of Liege under the license #18-2056.

Brains were harvested from mice at P0-P2 or E14.5. *FoxG1*:Cre $^{-/+}$/*Elp3* $^{lox/+}$ and *Elp3* $^{lox/lox}$ mice were time-mated to induce a conditional deletion of *Elp3* in the forebrain progenitors[33]. Brains were harvested from 10–16 months-old Elp1cKO and WT mice[27]. *Atat1* $^{+/-}$ mice were crossed together to obtain WT and KO mice[51]. Mice were housed under standard conditions (animals were bred in-house and maintained with ad libitum access to food and constant temperature (19–22 °C) and humidity (40–50%) under a 7am–7 pm light/dark cycle) and they were treated according to the guidelines of the Belgian Ministry of Agriculture in agreement with the European Community Laboratory Animal Care and Use Regulations (86/609/CEE, Journal Official des Communautés Européennes L358, 18 December 1986). Neuronal cultures were prepared from dissected E14.5 mice brain cortices, followed by mechanical dissociation in HBBS (Sigma–Aldrich, H6648) supplemented with 1.5% glucose. Cells were cultured at confluence of ~70% (for 5 days) with Neurobasal Medium (Gibco, Invitrogen, 21103049) supplemented with 2% B27 (Gibco, Invitrogen, 17504044), 1% Pen/Strep (Gibco, Invitrogen, 15140122), and 1% Glutamax (Gibco, Invitrogen, 35050061) at 37 °C.

Drosophila melanogaster. Flies were kept at 25 °C in incubator with regular 12-h light and dark cycle. All crosses were performed at 25 °C, after two days hatched first instar larvae were transferred in a 29 °C incubator until use.

UAS-RNAi carrying lines were crossed with D42-Gal4-UAS:Syt1-GFP virgin females for axonal transport recording and immunohistochemistry, with D42-Gal4 for behavioral experiments, or with Elav-Gal4 for qPCR and WB analysis (See Table 1). All RNAi inserts sequences were validated by DNA sequencing.

Human primary fibroblasts. Fibroblasts were cultured on polystyrene culture flasks (Corning) at 37 °C with 5% CO_2 in DMEM (Gibco, Invitrogen, 11965092) medium supplemented with 10% Fetal Calf Serum (Gibco, Invitrogen, 10500056), 1 mM Sodium pyruvate (Gibco, Invitrogen, 11360070), 1 mM non-essential amino acids (Gibco, Invitrogen, 11140050). Primary fibroblasts from five FD patients and age-matched controls were purchased from Coriell biobank (www.coriell.org) (Table 2).

Immunofluorescence. E14.5 cortical neurons were plated on coverslips in 24 well plate at a density of 30,000 cells and cultured for 5DIV. Neurons were fixed by incubation in 4% PFA-sucrose in PBS for 20 min at RT and washed with PBS + 0.3% Triton-X. After washing, neurons were incubated in blocking solution (PBS + 0.3% Triton-X + 10% normal donkey serum) for 1 h at RT. Following overnight incubation with primary antibodies in blocking solution at 4 °C, washing, and incubation with secondary antibodies (PBS + 0.3% Triton-X + 1% normal donkey serum) at RT for 1 h and washing, coverslips were then mounted on microscope slide using Mowiol. Images were acquired using a Nikon A1Ti confocal microscope (60x oil lens) or Airyscan super-resolution module on a Zeiss LSM-880 confocal (63x oil lens).

Larvae were dissected in PBS to expose the brain and MNs. After dissection larvae were fixed with 4% PFA for 20 min at RT, washed with PBS + 0.2% (CSP staining) or 0.3% (α-Tubulin acetylation staining) Triton-X and incubated in blocking solution PBS, 0.2% (CSP staining), or 0.3% (α-Tubulin acetylation staining) Triton-X + 1% BSA for 30 min at RT. Following overnight incubation with primary antibodies at 4 °C, washing and incubation with secondary antibodies at RT for 2 h, the larvae were mounted on microscope slide in Mowiol. Images were acquired using a Nikon A1Ti confocal microscope (60x oil lens).

Primary fibroblasts from FD patients or controls were plated at the concentration of 5000 cells in a 96-well plate (uClear, Grinere). Cells were fixed with 4% PFA for 10 min, washed, permeabilized, and blocked for 1 h at RT with 5% fetal bovine serum in PBS + 0.1% Triton-X. Following overnight incubation with acetylated α-tubulin (Sigma-Aldrich) and β-tubulin (cell signaling) antibodies, cells were washed with PBS + 0.05% Triton-X times and incubated with secondary antibodies for 1 h at RT. Finally, the cells were washed, and remained in PBS for image acquisition. Images were acquired using a IN Cell Analyzer 2200 fluorescent microscope (General Electric) using a 60x air lens.

Fluorescence intensity levels were measured by Fiji (https://imagej.net/Fiji/Downloads). To analyze α-tubulin and acetylated α-tubulin levels of mice cortical neuron axons and fly MNs, ROIs of 30 µm long axonal segments accounting for their full width were used. For human primary fibroblasts, ROI of the entire cell were outlined. α-tubulin and acetylated α-tubulin levels were extracted from mean intensity levels. Background levels were subtracted and the ratio of acetylated α-tubulin/α-tubulin was calculated.

Table 1 *Drosophila melanogaster* lines.

Line	Catalog number	Given name	Purchased from
Elav-Gal4	BDSC 458		Bloomington Drosophila Stock Center
huD42-Gal4	BDSC 8816		Bloomington Drosophila Stock Center
UAS:Syt-GFP	BDSC 6925		Bloomington Drosophila Stock Center
UAS:RNAi Zpg	VDRC CG10125	Control	Vienna Drosophila Resource Center
UAS:RNAi Elp1	VDRC CG10535	Elp1 KD	Vienna Drosophila Resource Center
UAS:RNAi Elp3	VDRC CG15433	Elp3 KD	Vienna Drosophila Resource Center
UAS:RNAi Atat1	VDRC CG3967	Atat1 KD	Vienna Drosophila Resource Center
UAS:RNAi Hdac6	BDSC 51181	Hdac6 KD	Bloomington Drosophila Stock Center
UAS:Human Elp3		hElp3	Kindly provided by Patrick Verstreken
UAS:Human ACLY	VDRC CG8322	hACLY	Vienna Drosophila Resource Center

Table 2 Human fibroblast lines.

Catalog number	Sex	Age	Sample description
GM02036	Female	11	Apparently Healthy
GM07492	Male	17	Apparently Healthy
GM07522	Female	19	Apparently Healthy
GM038	Female	3	Apparently Healthy
GM05659	Male	14	Apparently Healthy
GM02343	Female	24	Familial Dysautonomia
GM04589	Male	16	Familial Dysautonomia
GM04663	Female	2	Familial Dysautonomia
GM04959	Female	10	Familial Dysautonomia
GM04899	Female	12	Familial Dysautonomia

Vesicular and mitochondrial transport recording in vitro and in vivo. Axonal transport in mice cultured cortical neurons was recorded in microfluidics devices, prepared as described in[52]. Briefly, air bubbles were removed from mixed sylgard 184 elastomer (VossChemie Benelux, 1:15 ratio with curing agent) by centrifuging at 1000 × *g* for 5 min. The liquid was poured into the microfluidic device mold and was cured by 3 h incubation at 70 °C incubator. Molds were cut and washed twice with 70% ethanol, air dried in biological hood and placed on 35 mm glass-bottom dishes (MatTek, P35G-0-20-C) previously coated with 0.1 mg/mL poly-D-lysine (overnight incubation at 4 °C prior to washes and air drying). To increase the adhesiveness, the microfluidic chambers and dishes were heated to 70 °C before assembling. E14.5 mouse cortical neurons were isolated and resuspended at 40000 × 10^3 cells/μL for seeding at a 70% confluency into the microfluidic somal channel. After plating, the axonal and somal compartments of the microfluidic devices were filled with culture medium supplemented with 50 ng/ml or 20 ng/ml BDNF (PeproTech, 450-02), respectively. Labeling were done on after 5DIV by adding 1 µM LysoTracker® Red DND-99 (ThermoFisher Scientifics, L7528), MitoTracker® Green FM (ThermoFisher Scientifics, M7514) or MitoTracker® Deep Red FM (ThermoFisher Scientifics, M22426) 30 min prior to time-lapse recordings. Axonal transport recording in *Drosophila Melanogaster* MNs were done on 3rd instar larvae expressing UAS:RNAi and Syt1-GFP. Larvae were anaesthetized with ether vapors (8 min) and mounted dorsally on microscope slide using 80% glycerol. Recordings of mice cortical neurons and *Drosophila melanogaster* MNs were performed on an inverted confocal microscope Nikon A1Ti (60x oil lens) or Zeiss LSM-880 confocal (63x oil lens) at 600 ms frame interval.

Intracellular transport in human primary fibroblasts was recorded 3 days after plating, by adding 1 µM LysoTracker® Red DND-99 (ThermoFisher Scientifics, L7528) 30 min prior to time-lapse recordings. Recordings of human primary fibroblasts were performed using in-cell 2200 (General Electric) using 60X air lens, at 2 s frame intervals, using temperature (37 °C) and CO_2 control.

Video analysis was performed by generation of kymographs for single-blind analysis using ImageJ plugin-KymoToolBox (fabrice.cordelieres@curie.u-psud.fr). Average velocity is defined as the cumulative distance traveled by an organelle divided by the total amount of time, therefore it includes the pausing time. Moving velocity is defined by the cumulative distance traveled anterograde or retrograde divided by the time traveled anterograde or retrograde, therefore it excludes the pausing time. Moving velocity for anterograde is represented by positive values and retrograde by negative values. Pausing time is defined as the percentage of time that an organelle spends at a velocity lowered than 0.1 µm/sec out of the total traveling time. All kymographs show anterograde (left to right direction) and retrograde (right to left) moving vesicles. For analysis of axonal transport in *Drosophila melanogaster*, the StackReg plugin was used to align frames.

Plasmids and drug treatments. For silencing of *Elp3* in mouse cortical neurons we inserted sh-*Elp3* 5'GCACAAGGCUGGAGAUCGGUU3' or a control sequence sh-Control 5′-TACGCGCATAAGATTAGGG-3′ previously described in[25,53]. The viral packaging vector is PSPAX2 and the envelope is VSV-G. The lentiviral vector is pCDH-cmv-EF1-copGFP (CD511B1), and the promotor was replaced by a U6 promoter. For expression of human ACLY in E14.5 mice cortical neurons, cells in suspension were transfected with pEF6-Acly (Addgene plasmid # 70765, a gift from Kathryn Wellen)[54] or pEF6 (control) and GFP (from VPG-1001, Lonza) using Mouse Neuron Nucleofector® Kit (VPG-1001, Lonza) according to the manufacturer's protocol. GFP-positive neurons were used for analysis. To assay the subcellular localization of Acly in respect to lamp1-positive late endosomes/lysosomes in mouse cortical neurons, pCAG mEmerald-LAMP1 provided by F. Polleux (Columbia University, New York, USA) was transfected using Mouse Neuron Nucleofector® Kit (VPG-1001, Lonza) according to manufacturer's protocol. For expression of human ACLY in cultured human primary fibroblasts, cells were transfected with pEF6-Acly (Addgene plasmid # 70765, a gift from Kathryn Wellen)[54] or pEF6 (control) and GFP (from VPG-1001, Lonza) using Lipofectamine® 2000 according to manufacturer's protocol. GFP-positive cells were used for analysis. Tubastatin A (TBA, 20 µM) or Hydroxy-citrate (HCA, 3 mM or 10 mM) were dissolved in Ultra-Pure Water (UPW) and added to cell cultures 2 h or 8 h, respectively, prior to recording.

Real-time quantitative PCR analysis (qRT-PCR). One mouse cortex or ten adult fly heads were collected in TRIzol Reagent (Ambion, Life Technologies) followed by RNA extraction performed following the manufacturer's instructions. After DNAse treatment (Roche), 1 µg of RNA was reverse transcribed with RevertAid Reverse Transcriptase (Fermentas). RT-qPCR was performed using Quant Studio (Thermo) and TaqMan primers for mice, or a Light Cycler 480 (Roche) with Syber Green mix for *Drosophila melanogaster*. Analyses were done using the 2-$^{\Delta\Delta}$CT method[55] with the primers listed in Table 3.

Protein aggregation assay. Cultured mice cortical neurons or human primary fibroblasts at 60% confluency were incubated with PROTEOSTAT® (Enzo Life-Sciences) to detect protein aggregates.

Locomotion activity and climbing assays. Larval crawling speed assays were performed by placing 3rd instar larvae in the center of 15-cm petri dishes coated with 3% agar, as previously published[56]. Velocities were extrapolated by measuring the distance traveled in 1 min. The climbing assay was performed as previously described in[57], by measuring the average ratio of successful climbs over 15 cm for 10 adult flies.

Western blot. Mouse brain cortices, adult fly heads, or human primary fibroblasts were quickly homogenized on ice in RIPA buffer, or 320 mM sucrose, 4 mM HEPES buffer for subcellular fractions. Protease inhibitor cocktail (Roche, P8340 or Sigma-Aldrich, S8820) and 5 µM Trichostatin-A (Sigma-Aldrich, T8552) were added to inhibit protein degradation and α-tubulin deacetylation.

Immunoblotting was performed with the primary and secondary antibodies listed in Supplementary Table 1. We used 2 µg of protein lysate for α-tubulin acetylation analysis and 20–30 µg for all other proteins. Nitrocellulose membranes were imaged using Amersham Imager 600 (General Electric, 29083461) and band densitometry was measured using FIJI.

Subcellular fractionation. Subcellular fractionation of frozen mice brain cortex was performed as previously described[30]. Tissues or cells were homogenized in 320 mM sucrose, 4 mM HEPES, pH 7.4 (fractionation buffer). The homogenate was centrifuged for 10 min at 1000 × *g* to obtain a pellet (P1) (nuclear fraction) and a post-nuclear fraction (S1). The supernatant (S1) was centrifuged for 40 min at 12,000 × *g* to obtain large membranes (P2) and vesicle-enriched cytosolic fraction (S2). Finally, S2 was centrifuged again for 90 min at 120,000 × *g* using a TLA 120.1 fixed angle rotor in Optima TLX Benchtop Ultracentrifuge to obtain vesicle

Table 3 List of PCR primers.

Gene	Forward	Reverse	Organism
Acly	Hs00982738_m1 (Thermo)		mice
Gapdh	Mm99999915_g1 (Thermo)		mice
TBP	CCACGGTGAATCTGTGCT	GGAGTCGTCCTCGCTCTT	fly
Elp1	TCGGCGGTTCCTTTCCAAAC	GGTCCGATGCAACTTCAGATT	fly
Elp3	AAGAAGTTGGGCGTGGGATT	ATCCTTTTTGGCTTCGTGCG	fly

fraction (P3) and a cytosolic fraction (S3). The vesicle fraction was gently washed once with fractionation buffer, and resuspended by vigorous pipetting with the same buffer.

Mass spectrometry analysis. Pellets from three independent samples of pooled vesicles isolated from the brain cortex of WT or *Elp1 KD* mice were solubilized using 5% SDS. The samples were dissolved in 10 mM DTT 100 mM Tris and 5% SDS, sonicated, and boiled at 95 °C for 5 min. The samples were precipitated in 80% acetone. The protein pellets were dissolved in 9 M Urea and 100 mM ammonium bicarbonate than reduced with 3 mM DTT (60 °C for 30 min), modified with 10 mM iodoacetamide in 100 mM ammonium bicarbonate (room temperature for 30 min in the dark), and digested in 2 M Urea, 25 mM ammonium bicarbonate with modified trypsin (Promega), overnight at 37 °C in a 1:50 (M/M) enzyme-to-substrate ratio. The resulting tryptic peptides were desalted using C18 tips (Harvard) dried and resuspended in 0.1% Formic acid. Samples were analyzed by LC-MS/MS using Q Exactive plus mass spectrometer (Thermo) fitted with a capillary HPLC (easy nLC 1000, Thermo). The peptides were loaded onto a homemade capillary column (20 cm, 75 micron ID) packed with Reprosil C18-Aqua (Dr Maisch GmbH, Germany) in solvent A (0.1% formic acid in water). The peptides mixture was resolved with a (5 to 28%) linear gradient of solvent B (95% acetonitrile with 0.1% formic acid) for 60 min followed by a gradient of 28–95% for 15 min, and 15 min at 95% acetonitrile with 0.1% formic acid in water at flow rates of 0.15 µl/min. Mass spectrometry was performed in a positive mode using repetitively full MS scan followed by high collision-induced dissociation (HCD, at 35 normalized collision energy) of the 10 most dominant ions (>1 charges) selected from the first MS scan. The mass spectrometry data were analyzed using the MaxQuant software 1.5.1.2. (//www.maxquant.org) using the Andromeda search engine, searching against the mouse uniprot database with a mass tolerance of 20 ppm for the precursor masses and 20 ppm for the fragment ions. Peptide- and protein-level false discovery rates (FDRs) were filtered to 1% using the target-decoy strategy. Protein table were filtered to eliminate the identifications from the reverse database, and common contaminants and single peptide identifications. The data were quantified by label-free analysis using the same software, based on extracted ion currents (XICs) of peptides enabling quantitation from each LC/MS run for each peptide identified in any of the experiments. The mass spectrometry proteomics data have been deposited to the ProteomeXchange Consortium via the PRIDE partner repository with the dataset identifier PXD021186.

In vitro α-tubulin assay. In vitro α-tubulin acetylation assay was performed as previously described[30]. Briefly, 96-well half-area plates (Greiner, 674061) were coated with 5 µg tubulin from HeLa cells or bovine brain (Cytoskeleton, catalog no. HTS02-A) in 25 µL of ultrapure water for 2.5 h at 37 °C, blocked (PBS + 3% BSA + 3% skim milk + 3% FBS) for 1 h at 37 °C, and washed with PBS + 0.05% Tween 20. Wells were incubated for 2 h at 37 °C with shaking at 140x *g* with 25 µg of the total, S2, S3, or P3 fractions isolated from P0 mouse brain cortex previously diluted in 2× histone acetyltransferase (HAT) buffer (Sigma–Aldrich, EPI001A) supplemented with protease inhibitor cocktail, 5 µM trichostatin, and 50 µM acetyl-CoA (Sigma-Aldrich, A2056) or vehicle (H20) for control. After washes and overnight incubation at 4 °C with acetylated a-tubulin antibody (1:2000) in blocking buffer (PBS + 0.05% Tween 20 + 3% BSA), wells were washed and incubated for 2 h at 37 °C with peroxidase-conjugated goat antimouse antibody (1:5000) in antibody blocking buffer. Wells were then washed and incubated with trimethylboron/E (Merck Millipore, ES001) whose reaction was thereafter stopped with H2SO4. Following the manufacturer's instructions, the HAT activity colorimetric assay kit (Sigma–Aldrich, EPI001) was used to measure CoA release.

α-Tubulin deacetylation assay. α-Tubulin deacetylation assay was performed as previously described in[38]. Briefly, 96-well half-area plates (Greiner, 674061) were coated with 1 µg tubulin in 50 µl of ultra-pure water for 2.5 h at 37 °C, followed by blocking (PBS, 3% BSA, 3% skim milk, 3% fetal bovine serum) for 1 h at 37 °C, and washing with PBS + 0.05% Tween-20. 10 µg of cytosolic fraction isolated from newborn mice brain cortex in deacetylation buffer (50 mM Tris-HCl at pH 7.6, 120 mM NaCl, 0.5 mM EDTA) supplemented with protease inhibitor cocktail and phosphatase inhibitor (to avoid dephosphorylation of HDAC6) were added per well for incubation of 4 h at 37 °C with shaking at 120x *g*. The wells were washed and incubated overnight at 4 °C with acetylated α-tubulin antibody (1:2000) in blocking buffer (PBS + 0.05% Tween-20 + 3%BSA). Wells were subsequently washed and incubated for 2 h at 37 °C with Peroxidase-conjugated Goat antimouse antibody (1: 5000) in antibody blocking buffer. After the final washes, the peroxidase activity was probed with TMB/E (ES001, Merck Millipore), and the reaction stopped with H_2SO_4.

Acly activity assay. Acly activity assay was measured as previously described in[41]. Briefly, cells or brain extracts were disrupted by passing them 15 times in 25-gauge needle in 100 mM Tris-HCL buffer, supplemented with protease and phosphatase inhibitors. 5ug of cells/brain lysate were added to the reaction mix (200 mM Tris-HCL pH 8.4, 20 mM $MgCl_2$, 20 mM sodium citrate, 1 mM DTT, 0.1 mM NADH (Sigma-Aldrich, N8129), 6 U/mL Malate dehydrogenase (Sigma-Aldrich, M1567), 0.5 mM CoA (Sigma-Aldrich, C3019) with or without ATP (Sigma-Aldrich, A1852). Acly activity was measured every 100 s for 4 h, in the volume of 50ul in a 384 well plate using 340 nm OD read. Acly specific activity was calculated as the change in absorbance in the presence or absence of ATP. For statistical comparison Acly activity was defined as the slope from the linear range of the reaction.

Acetyl-CoA sample preparation and LC-MS/MS analysis. Acetyl-CoA was extracted as previously described[58]. Briefly, cold methanol (500 µl; −20 °C) was added to the cell pellets, and the mixture was shaken for 30 s (10 °C, 2000 r.p.m., Thermomixer C, Eppendorf). Cold chloroform (500 µl; −20 °C) was added, the mixture was shaken for 30 s, and 200 µl of water (4 °C) added afterwards. After 30 s shaking and 10 min on ice, the mixture was centrifuged (21,000 × *g*, 4 °C, 10 min). The upper layer was collected and evaporated. The dry residue was re-dissolved in eluent buffer (500 µl) and centrifuged (21,000 × *g*, 4 °C, 10 min) before placing in LC-MS vials. Acetyl CoA was analyzed as previously described[59]. Briefly, the LC-MS/MS instrument consisted of an Acquity I-class UPLC system and Xevo TQ-S triple quadrupole mass spectrometer (both Waters) equipped with an electrospray ion source. LC was performed using a 100 × 2.1-mm i.d., 1.7-µm UPLC Kinetex XB-C18 column (Phenomenex) with mobile phases A (10 mM ammonium acetate and 5 mM ammonium hydrocarbonate buffer, pH 7.0, adjusted with 10% acetic acid) and B (acetonitrile) at a flow rate of 0.3 mL min-1 and column temperature of 25 °C. The gradient was set as follows: 0–5.5 min, linear increase 0–25% B, then 5.5–6.0 min, linear increase till 100% B, 6.0–7.0 min, hold at 100% B, 7.0–7.5 min, back to 0% B, and equilibration at 0% B for 2.5 min. Samples kept at 4 °C were automatically injected in a volume of 5 µl. Mass spectrometry was performed in positive ion mode, monitoring the MS/MS transitions m/z 810.02 → 428.04 and 810.02 → 303.13 for acetyl-CoA. Spikes of defined amounts of AcCoA were added to the samples to confirm the absence of signal inhibition (matrix effect) in the analyzed extracts. Quantification of AcCoA was done against an external calibration curve with 1–1000 ng mL−1 range of AcCoA concentrations using TargetLynx software (Waters).

Polysomal fractionation. Polysome-bound RNA was purified from the cortical extract of P0 pups according to Laguesse et al.[45]. Briefly, fresh mouse cortex was snap-frozen in 1.5 mL Eppendorf tube, pulverized in liquid nitrogen with a pestle, and kept on dry ice for 5 min. The powder was resuspended in 1 mL lysis buffer (10 mM Trish pH 8.0, 150 mM NaCl, 5 mM $MgCl_2$, 1% NP-40, 0.5% sodium deoxycholate, 40 mM dithiothreitol, 10 mM Ribonucleoside Vanadyl Complex, 200 µg/mL cycloheximide and 400 U/mL RNAsin). 200 µL of the homogenate was used to isolate total RNA using TRIzol reagent. The remaining 800 µL were centrifuged for 10 s at 12.000 × *g* to discard nuclei, and the supernatant was collected. Ribosomes were further released by adding 800 µL of 2X extraction buffer (200 mM Tris pH 7.5, 300 mM NaCl, and 200 µg/mL cycloheximide) and samples were centrifuged at 12,000 × *g* for 5 min at 4 °C to remove mitochondria and membranous debris. The resulting supernatant was loaded onto a 8 mL 15–45% sucrose gradient and centrifuged at 100,000 × *g* (at r_{min}), 4 °C for 2 h without brake, by using a SW4Ti rotor (Beckman Coulter). The four first 500 µL bottom fractions were collected and digested with proteinase K buffer (400 µg/mL Proteinase K, 10 mM EDTA, 1% SDS) at 37 °C for 30 min, to be thereafter extracted with phenol-chloroform. Polysomal fractions were assayed for purity by assessing the presence of 28 S and 18 S ribosomal RNA bands on an agarose gel, and by measuring absorbance at 254 nm, as previously described[60].

Puro-PLA and immunostaining. Puro-PLA was performed as previously described[61] to label newly synthesized proteins of interest. In brief, neurons cultured 5 days in vitro were incubated with 10 µg/mL puromycin for 4 min, quickly

washed with warm PBS, and fixed for 10 min in 4% PFA-sucrose. After fixation and permeabilization, the Duolink assay (DUO92007; DUO92004; DUO92002 Sigma) was performed as recommended by the manufacturer using the following primary antibodies: puromycin 1:75 (PMY-2A4 DSHB); Acly 1:100 (OAGA04026 Aviva Systems Biology). Following puro-PLA, cells were post-fixed for 10 min in PFA-sucrose, washed with PBS, blocked with 5% donkey serum in PBS, and labelled with antitubulin antibody 1:1000 (ab6160) in Duolink Antibody Diluent (Sigma) for 1 h. After incubation with fluorophore-labelled secondary antibody for 1 h and further washes, cells were mounted with Fluorescence Mounting medium (S3023 Agilent Dako). Images were acquired with a Zeiss LSM-880 microscope using × 40 oil objective. Images were processed with ImageJ (NIH).

Cycloheximide pulse-chase assay. Primary fibroblasts from FD patients or healthy controls were cultured in 6-well plates at 80% confluency before treatment with 50 µg/mL cycloheximide (CHX) (C7698 Sigma) for 0 h, 4 h, 6 h, 8 h. All samples were harvested simultaneously by washing the cells in each well with ice-cold PBS, adding in each well 150 µL cell lysis buffer (50 mM Tris-HCl, pH 8, containing 150 mM NaCl, 1% NP-40 supplemented with complete proteinase inhibitor cocktail (Roche)) and subsequent mechanical scraping. Following incubation on ice for 30 min, samples were centrifuged for 20 min at 13,000 x g to collect the supernatant. Protein concentration of each sample was measured by using the Protein Assay Kit (Pierce Biotechnology, Rockford) according to the manufacturer's instructions. All samples were resuspended in SDS buffer before WB analysis.

Co-immunoprecipitation analysis. Co-immunoprecipitation experiments were performed in HEK293 cells (Merck Chemicals, Brussels). Pierce Crosslink immunoprecipitation kit (#26147) was used following the manufacturer's instructions. For Elp3-FLAG and Myc-Acly analysis 4 µg of Myc (Cell signaling), Flag (Sigma-Aldrich), or general mouse IgG (Millipore) were crosslinked using DSS to protein A/G. For detection by WB of Elp3-Flag or Myc-Acly Elp3 (Jesper Svejstrup) antibody and Acly (cell signaling) were used.

Statistics and Reproducibility. Every experiment was repeated independently at least two times under single-blinded condition and statistical analyses were generated with GraphPad Prism Software 7.0. For statistical analysis, data normality was assessed via D'Agostino-Pearson omnibus normality test or Shapiro–Wilk normality test. Comparison between two groups with normally distributed samples was performed with two-sided unpaired *t* test, while comparisons among more than two groups with one-way or two-way analysis of variance (ANOVA) followed by Sidak's, Dunn's or Dunnet's post hoc test. If normality was not reached, Mann-Whitney or Kruskal–Wallis test were performed, to compare between two groups or among more than two groups, respectively.

Reporting summary. Further information on research design is available in the Nature Research Reporting Summary linked to this article.

Data availability

The proteomic data generated in this study have been deposited in the ProteomeXChange database and can be accessed via the CX accession number: PXD021186. Proteomic data supporting the findings of this study are available within the paper and its supplementary information files. Source data are provided with this paper.

Received: 3 August 2020; Accepted: 24 August 2021;
Published online: 07 October 2021

References

1. Godena, V. K. et al. Increasing microtubule acetylation rescues axonal transport and locomotor deficits caused by LRRK2 Roc-COR domain mutations. *Nat. Commun.* **5**, 5245 (2014).
2. Gauthier, L. R. et al. Huntingtin controls neurotrophic support and survival of neurons by enhancing BDNF vesicular transport along microtubules. *Cell* **118**, 127–138 (2004).
3. Mo, Z. et al. Aberrant GlyRS-HDAC6 interaction linked to axonal transport deficits in Charcot-Marie-Tooth neuropathy. *Nat. Commun.* **9**, 1007 (2018).
4. Wang, Q., Tian, J., Chen, H., Du, H. & Guo, L. Amyloid beta-mediated KIF5A deficiency disrupts anterograde axonal mitochondrial movement. *Neurobiol. Dis.* **127**, 410–418 (2019).
5. Bento-Abreu, A. et al. Elongator subunit 3 (ELP3) modifies ALS through tRNA modification. *Hum. Mol. Genet* **27**, 1276–1289 (2018).
6. Solinger, J. A. et al. The Caenorhabditis elegans Elongator complex regulates neuronal alpha-tubulin acetylation. *PLoS Genet* **6**, e1000820 (2010).
7. Glatt, S. et al. The Elongator subcomplex Elp456 is a hexameric RecA-like ATPase. *Nat. Struct. Mol. Biol.* **19**, 314–320 (2012).
8. Lin, T. Y. et al. The Elongator subunit Elp3 is a non-canonical tRNA acetyltransferase. *Nat. Commun.* **10**, 625 (2019).
9. Paraskevopoulou, C., Fairhurst, S. A., Lowe, D. J., Brick, P. & Onesti, S. The Elongator subunit Elp3 contains a Fe4S4 cluster and binds S-adenosylmethionine. *Mol. Microbiol.* **59**, 795–806 (2006).
10. Close, P. et al. Transcription impairment and cell migration defects in elongator-depleted cells: implication for familial dysautonomia. *Mol. Cell* **22**, 521–531 (2006).
11. Petrakis, T. G., Wittschieben, B. O. & Svejstrup, J. Q. Molecular architecture, structure-function relationship, and importance of the Elp3 subunit for the RNA binding of holo-elongator. *J. Biol. Chem.* **279**, 32087–32092 (2004).
12. Nguyen, L., Humbert, S., Saudou, F. & Chariot, A. Elongator - an emerging role in neurological disorders. *Trends Mol. Med.* **16**, 1–6 (2010).
13. Dauden, M. I. et al. Molecular basis of tRNA recognition by the Elongator complex. *Sci. Adv.* **5**, eaaw2326 (2019).
14. Miskiewicz, K. et al. ELP3 controls active zone morphology by acetylating the ELKS family member Bruchpilot. *Neuron* **72**, 776–788 (2011).
15. Singh, N., Lorbeck, M. T., Zervos, A., Zimmerman, J. & Elefant, F. The histone acetyltransferase Elp3 plays in active role in the control of synaptic bouton expansion and sleep in Drosophila. *J. Neurochem.* **115**, 493–504 (2010).
16. Hinckelmann, M. V. et al. Self-propelling vesicles define glycolysis as the minimal energy machinery for neuronal transport. *Nat. Commun.* **7**, 13233 (2016).
17. Lefler, S. et al. Familial dysautonomia (FD) human embryonic stem cell derived PNS neurons reveal that synaptic vesicular and neuronal transport genes are directly or indirectly affected by IKBKAP downregulation. *PLoS One* **10**, e0138807 (2015).
18. Anderson, S. L. et al. Familial dysautonomia is caused by mutations of the IKAP gene. *Am. J. Hum. Genet.* **68**, 753–758 (2001).
19. Slaugenhaupt, S. A. et al. Tissue-specific expression of a splicing mutation in the IKBKAP gene causes familial dysautonomia. *Am. J. Hum. Genet.* **68**, 598–605 (2001).
20. Cohen, J. S. et al. ELP2 is a novel gene implicated in neurodevelopmental disabilities. *Am. J. Med Genet. A.* **167**, 1391–1395 (2015).
21. Addis, L. et al. Microdeletions of ELP4 are associated with language impairment, autism spectrum disorder, and mental etardation. *Hum. Mutat.* **36**, 842–850 (2015).
22. Kojic, M. et al. Elongator mutation in mice induces neurodegeneration and ataxia-like behavior. *Nat. Commun.* **9**, 3195 (2018).
23. Simpson, C. L. et al. Variants of the elongator protein 3 (ELP3) gene are associated with motor neuron degeneration. *Hum. Mol. Genet.* **18**, 472–481 (2009).
24. Abashidze, A., Gold, V., Anavi, Y., Greenspan, H. & Weil, M. Involvement of IKAP in peripheral target innervation and in specific JNK and NGF signaling in developing PNS neurons. *PLoS One.* **9**, e113428 (2014).
25. Creppe, C. et al. Elongator controls the migration and differentiation of cortical neurons through acetylation of alpha-tubulin. *Cell* **136**, 551–564 (2009).
26. George, L. et al. Familial dysautonomia model reveals Ikbkap deletion causes apoptosis of Pax3+ progenitors and peripheral neurons. *Proc. Natl Acad. Sci. USA.* **110**, 18698–18703 (2013).
27. Dietrich, P., Alli, S., Shanmugasundaram, R. & Dragatsis, I. IKAP expression levels modulate disease severity in a mouse model of familial dysautonomia. *Hum. Mol. Genet.* **21**, 5078–5090 (2012).
28. Naftelberg, S. et al. Phosphatidylserine Ameliorates Neurodegenerative Symptoms and Enhances Axonal Transport in a Mouse Model of Familial Dysautonomia. *PLoS Genet.* **12**, e1006486 (2016).
29. Reed, N. A. et al. Microtubule acetylation promotes kinesin-1 binding and transport. *Curr. Biol.* **16**, 2166–2172 (2006).
30. Even, A. et al. ATAT1-enriched vesicles promote microtubule acetylation via axonal transport. *Sci. Adv.* **5**, eaax2705 (2019).
31. Akella, J. S. et al. MEC-17 is an alpha-tubulin acetyltransferase. *Nature* **467**, 218–222 (2010).
32. Shida, T., Cueva, J. G., Xu, Z., Goodman, M. B. & Nachury, M. V. The major alpha-tubulin K40 acetyltransferase alphaTAT1 promotes rapid ciliogenesis and efficient mechanosensation. *Proc. Natl Acad. Sci. USA* **107**, 21517–21522 (2010).
33. Laguesse, S. et al. A dynamic unfolded protein response contributes to the control of cortical neurogenesis. *Dev. Cell* **35**, 553–567 (2015).
34. Hebert, J. M. & McConnell, S. K. Targeting of cre to the Foxg1 (BF-1) locus mediates loxP recombination in the telencephalon and other developing head structures. *Dev. Biol.* **222**, 296–306 (2000).
35. Nedialkova, D. D. & Leidel, S. A. Optimization of codon translation rates via tRNA modifications maintains proteome integrity. *Cell* **161**, 1606–1618 (2015).
36. Lee, W. C., Yoshihara, M. & Littleton, J. T. Cytoplasmic aggregates trap polyglutamine-containing proteins and block axonal transport in a Drosophila

model of Huntington's disease. *Proc. Natl Acad. Sci. USA* **101**, 3224–3229 (2004).
37. Morelli, G. et al. p27(Kip1) Modulates Axonal Transport by Regulating alpha-Tubulin Acetyltransferase 1 Stability. *Cell Rep.* **23**, 2429–2442 (2018).
38. Hubbert, C. et al. HDAC6 is a microtubule-associated deacetylase. *Nature* **417**, 455–458 (2002).
39. Kalebic, N. et al. alphaTAT1 is the major alpha-tubulin acetyltransferase in mice. *Nat. Commun.* **4**, 1962 (2013).
40. Zhao, S. et al. ATP-citrate lyase controls a glucose-to-cetate Metabolic Switch. *Cell Rep.* **17**, 1037–1052 (2016).
41. Wellen, K. E. et al. ATP-citrate lyase links cellular metabolism to histone acetylation. *Science* **324**, 1076–1080 (2009).
42. Ismail, A., Doghish, A. S., Elsadek, B. E. M., Salama, S. A. & Mariee, A. D. Hydroxycitric acid potentiates the cytotoxic effect of tamoxifen in MCF-7 breast cancer cells through inhibition of ATP citrate lyase. *Steroids* **160**, 108656 (2020).
43. Dietzl, G. et al. A genome-wide transgenic RNAi library for conditional gene inactivation in Drosophila. *Nature* **448**, 151–156 (2007).
44. Dong, J., Edelmann, L., Bajwa, A. M., Kornreich, R. & Desnick, R. J. Familial dysautonomia: detection of the IKBKAP IVS20(+6T -> C) and R696P mutations and frequencies among Ashkenazi Jews. *Am. J. Med Genet* **110**, 253–257 (2002).
45. Laguesse, S. et al. Prosapip1-dependent synaptic adaptations in the nucleus accumbens drive alcohol intake, seeking, and reward. *Neuron* **96**, 145–159 e8 (2017).
46. Broix L., Turchetto S., & Nguyen L. Coordination between transport and local translation in neurons. *Trends Cell Biol.* **31**, 372–386 (2021).
47. Lin, R. et al. Acetylation stabilizes ATP-citrate lyase to promote lipid biosynthesis and tumor growth. *Mol. Cell* **51**, 506–518 (2013).
48. Baldwin, K. R., Godena, V. K., Hewitt, V. L. & Whitworth, A. J. Axonal transport defects are a common phenotype in Drosophila models of ALS. *Hum. Mol. Genet* **25**, 2378–2392 (2016).
49. Millecamps, S. & Julien, J. P. Axonal transport deficits and neurodegenerative diseases. *Nat. Rev. Neurosci.* **14**, 161–176 (2013).
50. Xu, Z. et al. Microtubules acquire resistance from mechanical breakage through intralumenal acetylation. *Science* **356**, 328–332 (2017).
51. Kim, G. W., Li, L., Gorbani, M., You, L. & Yang, X. J. Mice lacking alpha-tubulin acetyltransferase 1 are viable but display alpha-tubulin acetylation deficiency and dentate gyrus distortion. *J. Biol. Chem.* **288**, 20334–20350 (2013).
52. Gluska, S., Chein, M., Rotem, N., Ionescu, A. & Perlson, E. Tracking Quantum-Dot labeled neurotropic factors transport along primary neuronal axons in compartmental microfluidic chambers. *Methods cell Biol.* **131**, 365–387 (2016).
53. Kawauchi, T., Chihama, K., Nabeshima, Y. & Hoshino, M. Cdk5 phosphorylates and stabilizes p27kip1 contributing to actin organization and cortical neuronal migration. *Nat. Cell Biol.* **8**, 17–26 (2006).
54. Lee, J. V. et al. Akt-dependent metabolic reprogramming regulates tumor cell histone acetylation. *Cell Metab.* **20**, 306–319 (2014).
55. Morelli, G. et al. Cerebral cortical circuitry formation requires functional glycine eceptors. *Cereb. Cortex* **27**, 1863–1877 (2017).
56. Shaver, S. A., Riedl, C. A., Parkes, T. L., Sokolowski, M. B. & Hilliker, A. J. Isolation of larval behavioral mutants in Drosophila melanogaster. *J. Neurogenet.* **14**, 193–205 (2000).
57. Chambers, R. P. et al. Nicotine increases lifespan and rescues olfactory and motor deficits in a Drosophila model of Parkinson's disease. *Behavioural Brain Res.* **253**, 95–102 (2013).
58. Wang, S., Wang, Z., Zhou, L., Shi, X. & Xu, G. Comprehensive analysis of short-, medium-, and long-chain acyl-coenzyme A by online two-dimensional liquid chromatography/mass spectrometry. *Anal. Chem.* **89**, 12902–12908 (2017).
59. Avidan, O., Brandis, A., Rogachev, I. & Pick, U. Enhanced acetyl-CoA production is associated with increased triglyceride accumulation in the green alga Chlorella desiccata. *J. Exp. Bot.* **66**, 3725–3735 (2015).
60. Liu, F. et al. mTORC1-dependent translation of collapsin response mediator protein-2 drives neuroadaptations underlying excessive alcohol-drinking behaviors. *Mol. Psychiatry* **22**, 89–101 (2017).
61. Dieck, T. et al. Direct visualization of newly synthesized target proteins in situ. *Nat. Methods* **12**, 411–414 (2015).

Acknowledgements

We thank Maria M. Magiera and Carsten Janke for providing non acetylated Hela Tubulin. We thank Patrik Verstreken for sharing Elp3KD flies, M. Nachury for sharing ATAT1 antibody and X.J. Yang for providing the Atat1 KO mice, T. Lahusen from American Gene Technologies for creating viral sh-RNA particles, the Smoler Proteomics Center at the Technion for proteomic analysis and E. Even for graphical design. All graphical figures were created with BioRender.com. We are grateful to Francesca Bartolini and Marina Mikhaylova for their constructive feedback on the manuscript as well as to all members of the Nguyen and Weil laboratories for their critical reading. L.N. is Director from F.R.S- F.N.R.S. This work was supported by the F.R.S.-F.N.R.S. (Synet; EOS 0019118F-RG36), the Fonds Leon Fredericq (L.N.), the Fondation Médicale Reine Elisabeth (L.N.), the Fondation Simone et Pierre Clerdent (L.N), the Belgian Science Policy (IAP-VII network P7/20 (L.N.)), and the ERANET Neuron STEM-MCD and NeuroTalk (L.N.); grants from Agence Nationale de la Recherche (ANR-18-CE16-0009-01 AXYON (F.S.); ANR-15-IDEX-02 NeuroCoG (F.S.) in the framework of the "Investissements d'avenir" program); Fondation pour la Recherche Médicale (FRM, DEI20151234418, F.S.). A.E.'s stay at GIGA Research Institute of the University of Liège was funded by EMBO Short-Term Fellowships (ASTF 174-2016), A.E., M.S., and M.W.'s research was supported by the Israel Science Foundation (grant no. 1688/16). The authors declare no competing financial interests.

Author contributions

A.E., G.M., M.W., S.T. and L.N. designed the study. A.E., G.M. and S.T. performed and interpreted most experiments. M.S. and R.L.B. are to be considered as equal contributors. R.L.B. contributed to the *Drosophila* work with help of N.K.. M.S. contributed to cell culture and molecular work with L.B., Ar.B., S.I. and S.L. Al.B. performed the LC-MS/MS analysis. P.D. and I.D. maintained *Elp1 KD* mice colonies and provided brain material. F.S., A.C., B.B and J.M.R provided guidance and help for experiments. M.W. and L.N. contributed to data interpretation; and A.E., G.M., S.T., M.W. and L.N. wrote the manuscript with input from all coauthors.

Competing interests

The authors declare no competing interests.

Additional information

Supplementary information The online version contains supplementary material available at https://doi.org/10.1038/s41467-021-25786-y.

Correspondence and requests for materials should be addressed to Miguel Weil or Laurent Nguyen.

Peer review information *Nature Communications* thanks Alexandre Baffet, and the other, anonymous, reviewer(s) for their contribution to the peer review of this work. Peer reviewer reports are available.

Reprints and permission information is available at http://www.nature.com/reprints

Publisher's note Springer Nature remains neutral with regard to jurisdictional claims in published maps and institutional affiliations.

CHAPTER II

Context of the study

Neurons are highly polarized cells characterized by a complex branched morphology presenting with multiple dendrites and a single axon than can extend for very long distances, up to hundreds of centimeters. Their architecture is essential to establish connections with thousands of other cells through the formation of contact sites, the synapses, thus forming a network of functionally interconnected cells. Through synapses, neurons receive, process and pass information to the neighboring cells, and this process enables us to generate and store memories, to think and act. The number, size and strength of synapses change with time and experience, in a process called synaptic plasticity (Sutton and Schuman 2006). To support these dynamic structural changes and allow a prompt response at these peripheral sites, mRNAs need to be displaced for very long distances to reach these peripheral sites, where are ultimately translated via a process defined as local translation (Hafner et al. 2019; Rangaraju, Lauterbach, et al. 2019; Shigeoka et al. 2016). By producing proteins locally when and where mostly needed, neurons developed an efficient system to regulate the proteome in restricted subcellular compartments, such as along neurites and at synapses.

Since the identification of this mechanism, a plethora of studies leveraged the recent advances in the high throughput screenings techniques coupled to isolation and/or fractionation methods to characterize the populations of mRNAs (transcriptome) (Cajigas et al. 2012; Perez et al. 2021; Zivraj et al. 2010) and to identify those undergoing active translation (translatome) (Glock et al. 2021; Hobson et al. 2022; Oostrum et al. 2023; Shigeoka et al. 2016) within restricted subcellular domains, as neurites and synapses. More recently, however, the resolution in the study of local translation further restricted to single membrane-bound organelles, which started to emerge as multi-functional units able to exert other roles than their well described canonical ones. Organelles such as endosomes, mitochondria and the ER were found to be associated with the translation machinery (ribosomes) and translating peptides. Most interestingly, these translating proteins are key to sustain the structural integrity of the associated organelles, as the mitochondria membrane protein laminb2 (Cioni et al. 2019), the mitophagy-associated PINK1 kinase (Harbauer et al. 2022) and endosome membrane protein EEA1 (Popovic D, Nijenhuis W, Kapitein C L 2020).

Recent findings describe organelles as self-sustaining machineries, able to support their own MT-based transport by producing the required energy and modulating the acetylation of MTs, a key modulator of transport dynamics (Even et al. 2019, 2021; Hinckelmann et al. 2016).

Proteins undergo a constant turnover that requires the replacement of damaged peptides with a newly translated pool. We therefore hypothesize that trafficking organelles, together with supporting their own motion, might also sustain their structural integrity by translating in loco their constitutive proteins. This mechanism would allow organelles to safeguard their own architecture while exerting their motion-dependent range of functions.

To the best of our knowledge, it remains to be determined whether local sites of translation could occur on cargos while undergoing bidirectional motion, and whether the newly translated proteins, while renewing the organelles architecture, would also ensure their optimal activities. Furthermore, a comprehensive characterization of the population of transcripts shuttled and translated on motile cargos is still missing.

This project aims to:

1) Isolate motile cargos from a transgenic mouse line to characterize its proteome and associated transcriptome;
2) Generate a stable cell line of neuron-like cells expressing the SunTag system to determine the translation dynamics of candidate transcripts.

RESULTS

1. *Motile cargos* purification for proteomics and transcriptomics analysis.

To characterize the population of transcripts undergoing MT-based bidirectional transport, we used the Thy1:p50-GFP mouse line, which express the dynactin subunit dynamitin (also called p50) fused to GFP under the control of the Thy1 neuronal promoter at levels that do not disrupt its integrity and function (Ross et al. 2006). As p50 promotes the dynein-mediated recruitment of vesicles for their MT-directed transport (reviewed in: Cason and Holzbaur 2022), we reasoned that its isolation would enable the purification of motor-associated cargos, including vesicles and their associated transcriptome, as well as RNP granules **(Figure 12 A)**. Furthermore, the existence of single dynactin variant, its required binding to dynein for its processivity, and the association of the dynein/dynactin complex to every *motile cargo* make dynactin an ideal candidate to target for the isolation of all motor-associated cargos. From here on, we will define the dynein/p50-associated cargos as *motile cargos.*

We first performed immunofluorescent analysis of postnatal day 13 (P13) coronal brain slices to characterize the GFP expression pattern, thereby the distribution of p50. GFP expression was extended to multiple brain regions, including the hippocampus **(Figure 12 B, C1)**, layer V of the cortex **(Figure 12 B, C2, D)**, amygdala **(Figure 12 B, C3)** and thalamus **(Figure 12 B, C4)**.

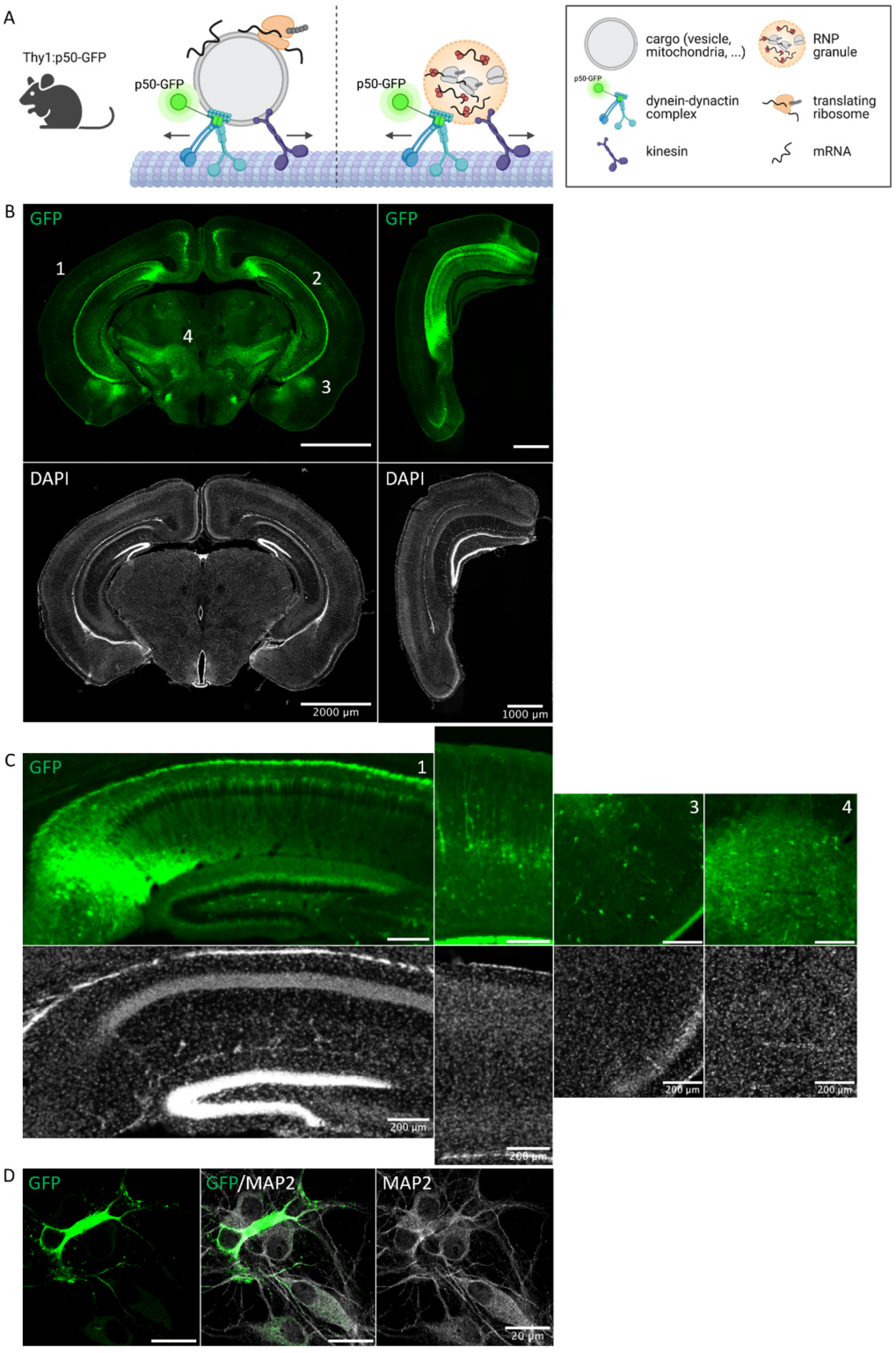

Figure 12. GFP expression pattern characterization of Thy1:p50-GFP mice. (A) Schematic representation of p50-GFP associated *motile cargos*. **(B)** GFP and DAPI Immunofluorescent analysis in P13 coronal brain sections of Thy1:p50-GFP mice. **(C)** GFP and DAPI expression pattern in closed-up selected brain regions expressing GFP-positive nuclei: hippocampus (1),

cortex (2), amygdala (3) and thalamus (4). **(D)** Immunofluorescent analysis for GFP and MAP2 (dendritic marker) of DIV12 hippocampal neurons obtained from E15.5 p50-GFP+/- embryos.

The Thy1:p50-GFP mouse was originally generated to isolate the dynein-p50-GFP complex by MT affinity and ATP release (Ross et al. 2006). This strategy enabled the purification of the complex while preserving its integrity and motility properties. This molecular preparation, however, was devoid of kinesin-1 and kinesin-2, suggesting that this methodology does not fully preserve the protein-protein interactions between motors and associated vesicles, which would have otherwise allowed co-isolation of the vesicle-associated kinesin motors. p50-GFP mice were also employed to purify the full brain vesicular fraction by high-speed centrifugation followed by sucrose gradient fractionation (Caviston et al. 2007). Yet, this strategy allowed the isolation of both motile (motor-bound) and not motile (not associated with motors) vesicles, as in vitro transport analysis reported that only 60% of the isolated vesicles were motile.

We set out to overcome these limitations and purify *motile cargos* to analyze both their proteome and associated transcriptome. While the former analysis would enable the molecular characterization of the sorted population, the latter would define the population of mRNAs that are trafficked by motors either through their direct association or via the hitchhiking mechanism **(Figure 13 A).** To this aim, we used mechanical lysis to process the full brain deprived of the cerebellum of 2-month old Thy1:p50-GFP mice, compared to their WT littermates. We thereafter performed a centrifugal step to discard nuclei and unlized cells (pellet 1, P1), and applied fluorescent particle sorting (Hubstenberger et al. 2017) to the obtained pre-sorted fraction (supernatant 1, S1) to isolate GFP+ events (p50-GFP associated cargos) from GFP- events (cytosolic components not bound to p50-GFP) **(Figure 13 A).** Unlized cells were identified by size and granularity in the P1 fraction and excluded from the analysis **(Figure 13 B)**, as well as auto-fluorescent events identified from the remaining fraction labelled as *lysate* **(Figure 13 C, D)**. Lastly, size and fluorescence allowed us to discriminate GFP+ and GFP- events which display only a partial overlap in their size and granularity profile **(Figure 13 C, D)**. Re-analysis of the sorted fractions by flow cytometry (FACS) lead to a purity of ∼40% for the GFP+ fraction and ∼80% for the GFP- fraction **(Figure 13 E).** For both proteomics and RNA-seq analysis, every S1 fraction was sorted for 3 hours, which lead to the collection of 250,000-500,000 events per fraction, depending on the abundance of GFP+ events.

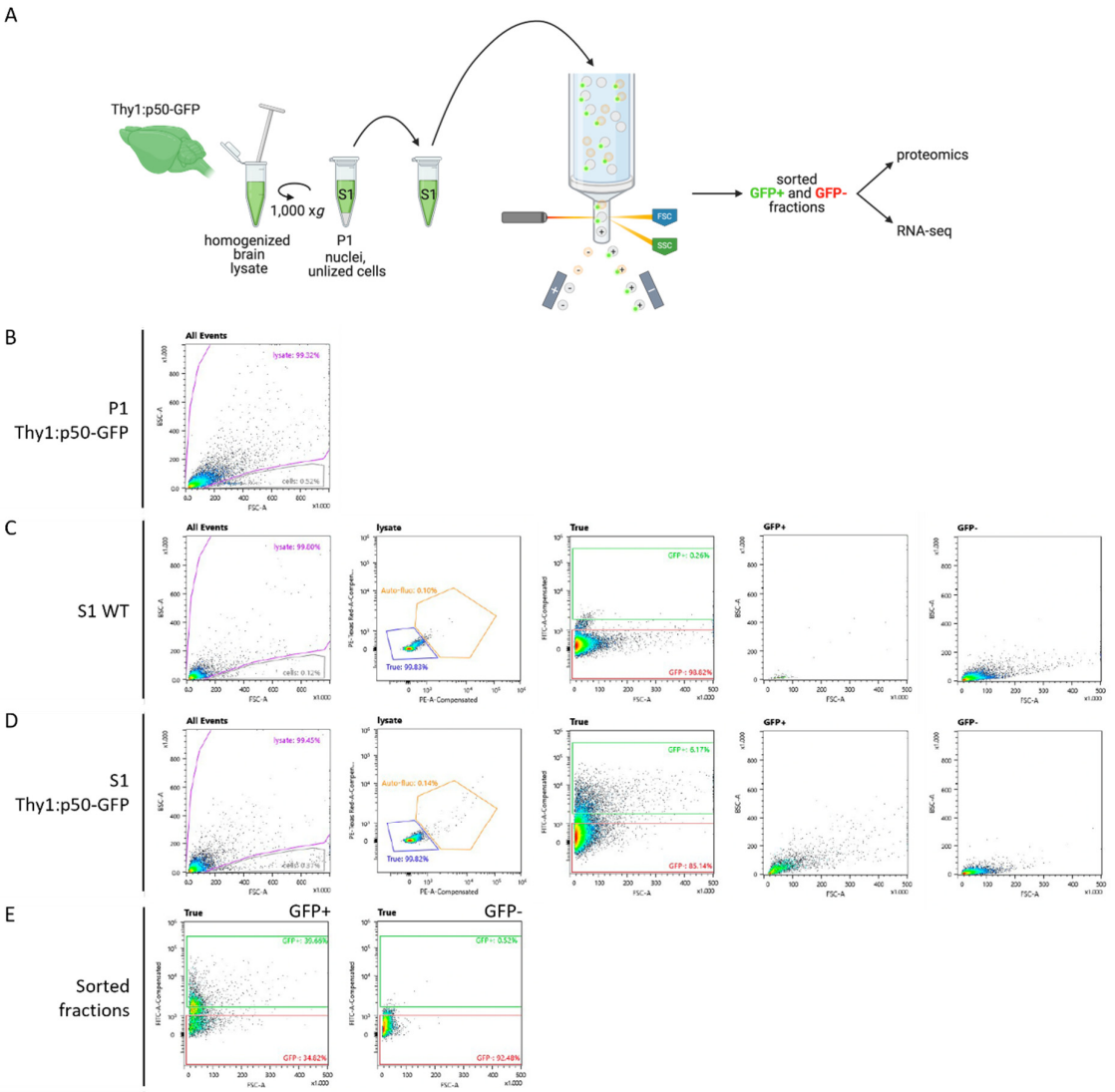

Figure 13. Fluorescent particle sorting of p50-GFP and its associated cargos. (A) Experimental procedure to isolate *motile cargos* from 2 month-old Thy1:p50-GFP mouse brains by fluorescent particle sorting. S1, supernatant; P1, pellet. **(B-D)** Gating strategy to isolate p50-GFP associated cargos. **(B)** P1 fraction analysis by forward scatter channel (FSC) and back-scatter channel (BSC) performed to discriminate the population of unlysed cells ("cells") from the particles representing the lysed sample ("lysate"). **(C-D)** Gating strategy used to identify p50-GFP+ particles from the S1 fraction isolated from full brain lysate of Thy1:p50-GFP mice and correspondent WT littermates. Populations of unlyzed and lysed cells were differentiated as done for the P1 fraction. The "lysate" population was then displayed in a new intensity plot analyzing the fluorescence of phycoerythrin (PE)-texas red and phycoerythrin-alexa fluor (PE-A) to exclude the autofluorescent events ("auto-fluo") for the downstream analysis. The remaining events defined as "true" were then plotted to assess their FSC and FITC fluorescence. The distribution of events observed from the S1 WT sample was used to identify the FITC signal threshold and define the GFP+ and GFP- gates. GFP+ and GFP- gates were then analyzed separately for their FSC and BSC parameters. **(E)** re-analysis of

sorted fractions plotted by FSC and FITC fluorescence intensity. On average, the GFP+ sorted fractions present a 40% purity compared to the GFP- sorted fraction.

To verify the specificity of the sorting, we performed an ultracentrifugation of the sorted fractions and analyzed the concentrated pellets by western-blotting. When analyzing the GFP content of the sorted fractions, we detected a strong GFP enrichment in the GFP+ fraction, compared to its GFP- counterpart **(Figure 14 A).** Electron microscopy analysis identified vesicles within both sorted fractions **(Figure 14 B)**, showing that the sorting strategy did not affect the morphological integrity of vesicles. Combined immunogold staining confirmed the presence of GFP particles only in the GFP+ fraction, either surrounding globular objects in the nanometer scale which could correspond to *motile cargos*, or as isolated subunits which could underline RNP granules bound to dynein-dynactin complex **(Figure 14 C)**. To assess whether the sorting strategy wouldn't compromise the quality of the fraction-associated transcripts, we extracted RNA from the sorted fractions and analyzed its quality, which revealed an ideal integrity index for RNA-seq analysis **(Figure 14 D)**.

We are currently performing mass spectrometry and RNA-seq analysis, each one on three biological replicates. The first dataset that will be generated will provide a comprehensive overview of the *motile cargos* subtypes that can be sorted through our experimental workflow. The second one, unique in its kind, will instead unravel the population of mRNA transcripts constituting or associated with the dynein-dynactin complex and therefore undergoing active transport. These transcripts could be transported either in the form of RNP granules or associated to membrane-bound organelles, either as translationally silent or undergoing active translation (Anadolu et al. 2022; Cioni et al. 2019; Schuhmacher et al. 2023). We will perform an enrichment analysis by comparing the sorted fractions to the pre-sorted sample, to identify candidate mRNAs that are preferentially transported or that are not associated with the transport machinery. We will thereafter perform Gene Ontology (GO) enrichment analysis and select transcripts on interest whose transport could underlie specific functions in distal subcellular locations and would require their localized translation.

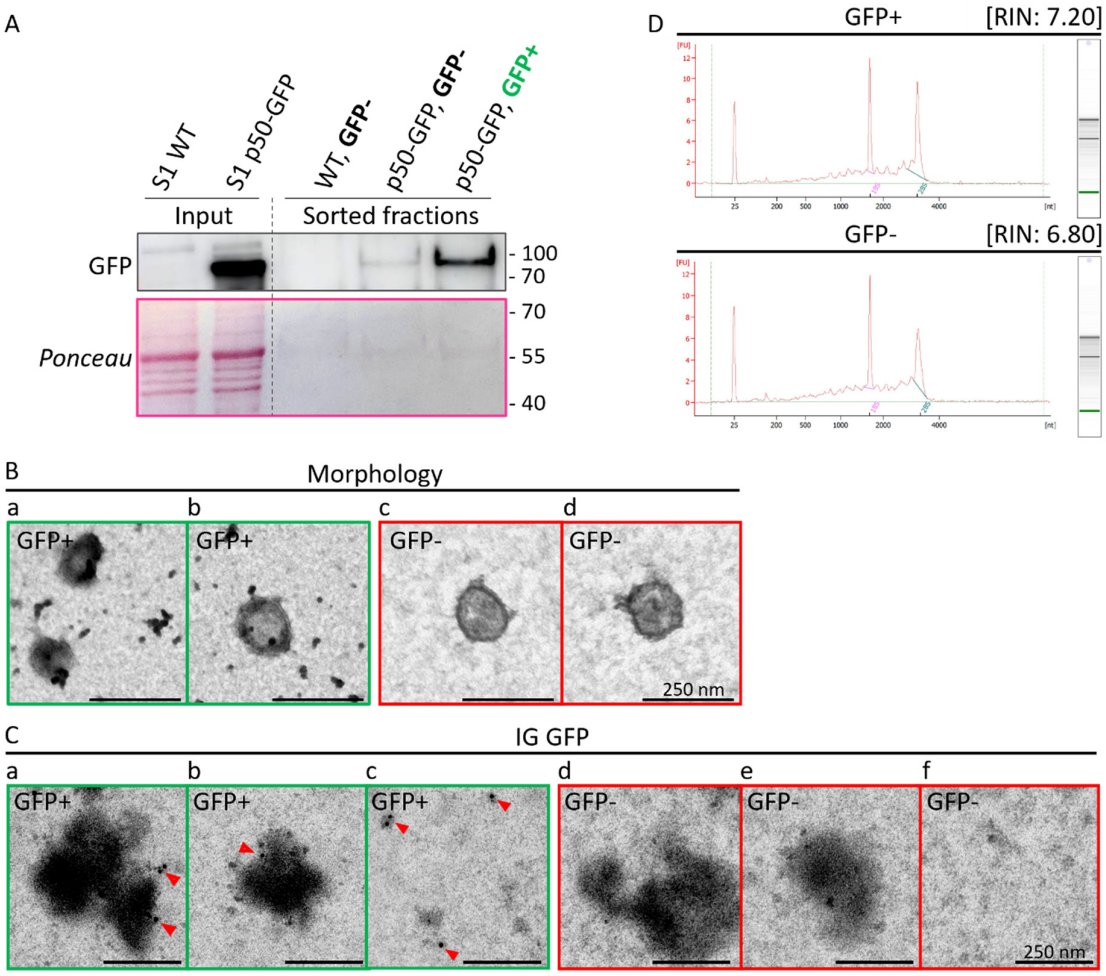

Figure 14. Biochemical and morphological characterization of the GFP+ and GFP- sorted fractions. (A) Western blotting analysis of GFP+ and GFP- sorted fractions upon ultracentrifugation showing GFP enrichment in the GFP+ fraction. **(B)** Examples of intact vesicles with lipid bilayer membranes identified in both GFP+ (a, b) and GFP- (c, d) sorted fractions by electron microscopy analysis. **(C)** immunogold labelling of sorted fractions showing GFP gold signal only in the GFP+ fraction, either in surrounding of globular objects (a, b) or as single units (c), suggesting the association of p50-GFP to either organelles or to RNP granules, respectively. No immunogold signal was detected in the GFP- fraction (d-f). **(D)** Bioanalyzer results of RNA samples extracted from GFP+ and GFP- sorted fractions. In every fraction, the two peaks below 2000 and 4000 correspond to the ribosomal RNAs and the underling areas are used to infer the RNA integrity index (RIN) of the relative sample.

To refine the transcriptomic dataset and uniquely identify the ribosome-associated transcripts (therefore engaged in translation) among the population of trafficking mRNAs, we crossed Thy1:p50-GFP mice with RiboTag mice (Shigeoka et al. 2016) that express the HA-tagged ribosomal protein 22 (rpl22-HA) only in VGlut1+ neurons **(Figure 15 A)**. The RiboTag mouse enables the isolation of ribosomes from a selected cellular subtype and the elution of their associated mRNAs to probe the cellular translational landscape. As ribosomes are known to be transported on *motile cargos* (Carter et al. 2020; El Fatimy et al. 2016; Kipper et al. 2022; Liao et al. 2019), the co-expression of p50-GFP and rpl22-HA within a given cell type would enable the immunoprecipitation of HA-tagged ribosomes from previously sorted *motile cargos* (p50-GFP-associated *motile cargos*; GFP+ events) **(Figure 13 A)**. The downstream sequencing of the ribosome-associated transcripts would enable the characterization of the translating mRNAs associated to *motile cargos* – the *motile cargos*' translatome. Given the GFP expression pattern of Thy1:p50-GFP mice being preferentially localized in the deep layer cortical neurons and pyramidal layer neurons of the hippocampus**(Figure 12 A),** and the exclusive distribution of VGlut1-expressing neurons in the cortex and hippocampus **(Figure 15 B)**, we generated p50-GFP$^{+/-}$;Rpl22-HA$^{L/+}$;Vglut1-cre/+ mice displaying cortical and hippocampal neurons coexpressing GFP and HA **(Figure 15 B-D)**. Interestingly, however, while only a small fraction of the fluorescently-labelled cortical neurons were GFP+/HA+ positive (5.89%), a broader double positive neuronal population was present in the pyramidal layer of the hippocampus (23.08%) **(Figure 15 C-E)**.

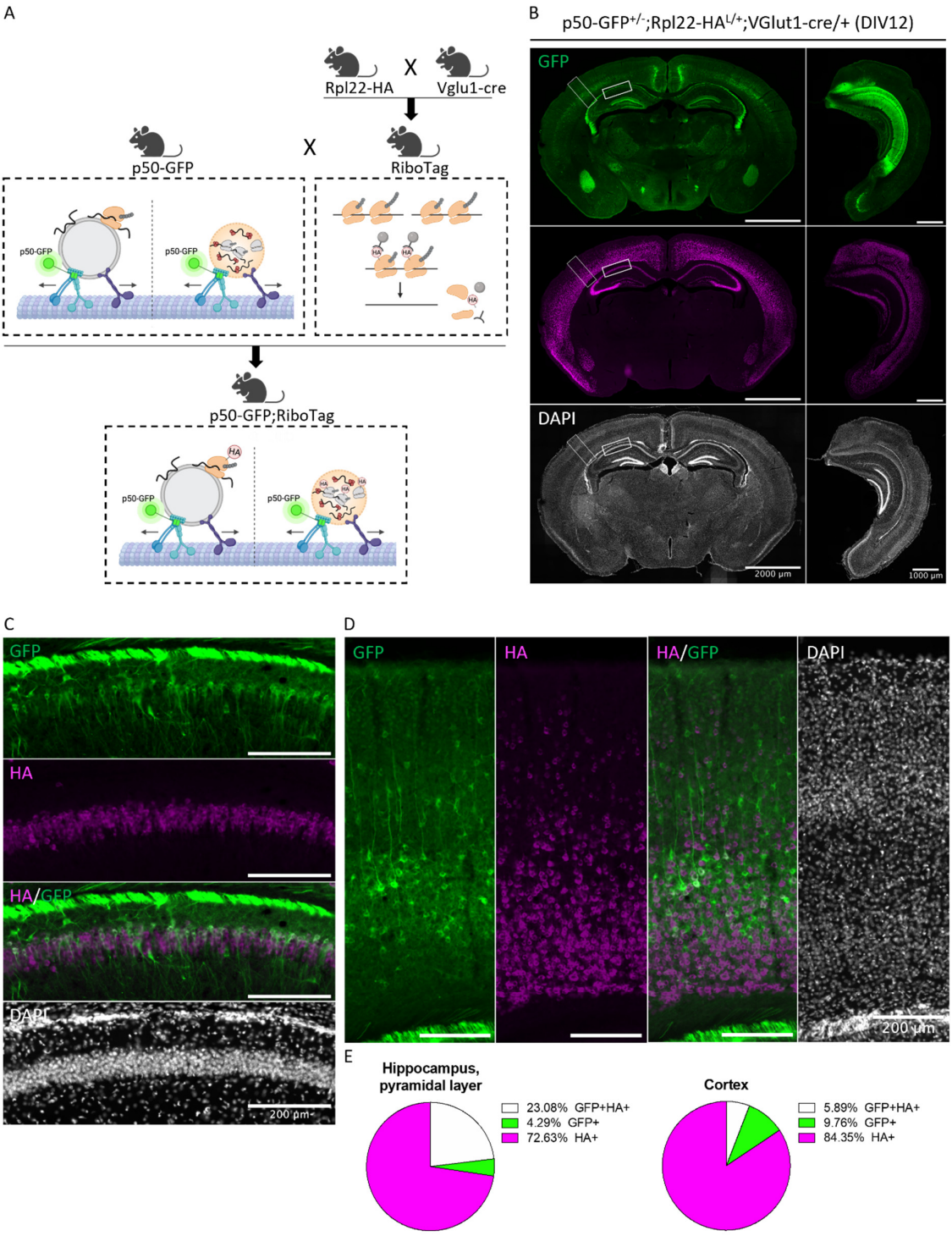

Figure 15. GFP and HA expression pattern characterization in P13 p50-GFP$^{+/-}$;Rpl22-HA$^{L/+}$;Vglut1-cre/+ brain slices. (A) Schematic representation of the breeding strategy to generate p50-GFP$^{+/-}$;Rpl22-HA$^{L/+}$;Vglut1-cre/+ mice. **(B)** Representative coronal brain slices of P13 p50-GFP$^{+/-}$;Rpl22-HA$^{L/+}$;Vglut1-cre/+ mice immunostained for GFP (green), HA (purple) and DAPI (white). Panels on the left represent a medial level, panels on the right a caudal level. **(C, D)** Magnifications of the inserts traced in (B) representing the pyramidal layer of the hippocampus **(C)** and the cortex **(D). (E)** Pie chart showing the proportion of cells expressing

GFP, HA, or both in the pyramidal layer of the hippocampus (top panel) or cortex (bottom panel).

To evaluate the subcellular distribution of p50-GFP and rpl22-HA, and to maximize the analysis of neurons coexpressing GFP and HA, we prepared hippocampal cultures from E15.5 p50-GFP$^{+/-}$;Rpl22-HA$^{L/+}$;Vglut1-cre/+ mouse embryos **(Figure 16 A, B)**. Previously, ribosomes have been identified on membrane-bound organelles as lysosome, early and late endosomes along RGC axons (Cioni et al. 2019) and on ER-derived vesicles along dendrites of mouse hippocampal neurons (Carter et al. 2020). To study the spatial relationship between ribosomes and *motile cargos* we employed super-resolution airyscan microscopy and observed isolated although rare GFP foci codistributed with HA-tagged ribosomes **(Figure 16 C-F)**. Given the heterogeneity in subunit composition of ribosomes (Genuth et al. 2022), we additionally assessed the distribution pattern of the ribosomal protein 24 (rpl24) and found examples of p50-GFP motors positive for the assessed ribosomal subunit. These results suggest that p50-GFP motors can also associate with the translation machinery.

We are currently setting up the experimental strategy to immunoprecipitate rpl22-HA ribosomes by using dynabeads associated with anti-HA antibodies (Shigeoka et al. 2016) from sorted p50-GFP-associated *motile cargos* (GFP+ events). This strategy would allow the isolation of ribosome-associated mRNAs to ultimately define the translatome of *motile cargos*. We would therefore identify among the transcriptome dataset, obtained from fluorescent particle sorting of p50-GFP molecules and downstream RNA-seq analysis, those mRNA candidates that are engaged in translation while being transported as *motile cargos*.

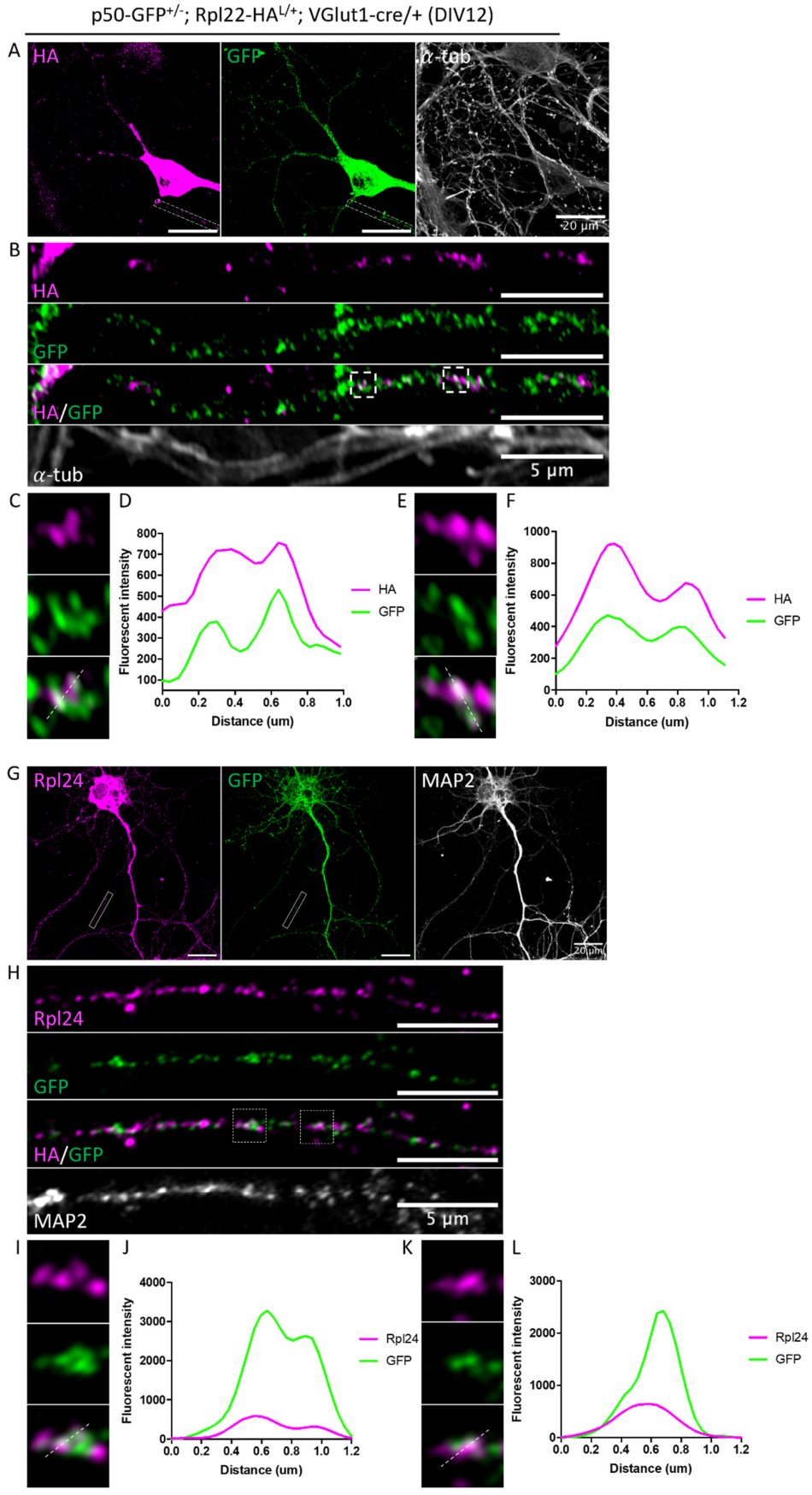
p50-GFP+/-; Rpl22-HAL/+; VGlut1-cre/+ (DIV12)
A
HA
GFP
α-tub
20 μm
B
HA
GFP
HA/GFP
α-tub
5 μm
C
D
Fluorescent intensity
Distance (um)
HA
GFP
E
F
Fluorescent intensity
Distance (um)
HA
GFP
G
Rpl24
GFP
MAP2
20 μm
H
Rpl24
GFP
HA/GFP
MAP2
5 μm
I
J
Fluorescent intensity
Distance (um)
Rpl24
GFP
K
L
Fluorescent intensity
Distance (um)
Rpl24
GFP

Figure 16. subcellular characterization of p50-GFP$^{+/-}$;Rpl22-HA$^{L/+}$;VGlut1-cre/+ hippocampal neurons. (A-F) Hippocampal neurons harvested from E15.5 p50-GFP$^{+/-}$;Rpl22-HA$^{L/+}$;VGlut1-cre/+ embryos were probed for GFP, HA and α-tubulin. Example of a neuron expressing GFP and HA **(A)**, a closed-up of a selected neurite segment **(B)**, and a closed-up of representative instances of codistributed GFP and HA foci **(C, E)**, with the correspondent intensity profile lines from GFP/HA merged images **(D, F)**. **(G-L)** Hippocampal neurons probed for GFP, Rpl24 and the dendritic marker MAP2. Example of a neuron expressing GFP and rpl24 **(G)**, a closed-up of a selected neurite segment **(H)**, and a closed-up of representative examples of codistributed GFP and rpl24 foci **(I, K)**, with the correspondent intensity profile lines **(J, L)**.

2. *In vitro* system to study axonal transport and local translation dynamics

To assess whether the candidate mRNAs are actively translating while being associated to the transport machinery, we set to exploit the SunTag fluorescent tagging system. This live imaging technology interrogates the translation dynamics of a given transcript while following its own displacement over time (Yan et al. 2016). It consists of three different expressing plasmids that need to be co-expressed in a given target cell **(Figure 23 A)**.

To overcome the limitations of primary neuronal cultures, we decided to express the SunTag system in a stable cell line as easier to transfect and to preserve over a very long time through freezing/thawing cycles. As cell line of choice, we employed the neuro-2a (N2a) cells, neural-crest deriving neuroblastoma cells that undergo neuronal differentiation upon serum deprivation and exposure to environmental stimuli such as retinoic acid (RA) (Kumar and Katyal 2018; Namsi et al. 2018). Differentiated N2a cells have been widely used to investigate the molecular mechanism driving neuronal differentiation (Evangelopoulos, Weis, and Krüttgen 2005; Kumar and Katyal 2018), as well as the subcellular distribution of mRNAs within their peripheral neurites (Taliaferro et al. 2016). While multiple concentrations of RA have been tested, we chose the dose that confers the lowest toxicity while inducing the highest percentage of differentiated cells (6μM), as compared to other concentrations and biomolecules tested (Namsi et al. 2018). As previously reported, upon serum deprivation and treatment with RA, cells display outgrowing neurites indicative of their differentiation into neuron-like cells **(Figure 17 A, B)**. To determine whether differentiated N2a cells represent a good in vitro model to investigate the translation dynamics of candidate mRNAs in relation to their microtubule (MT)-associated transport machinery, we decided to assess the dynamics of lysosome trafficking along their neurites. We labelled endogenous lysosomes by using the fluorescent dye Lysotracker and found that, although localized along the neurites of

differentiated N2a cells, lysosomes were not undergoing bidirectional motion but were rather immobile **(Figure 17 C)**.

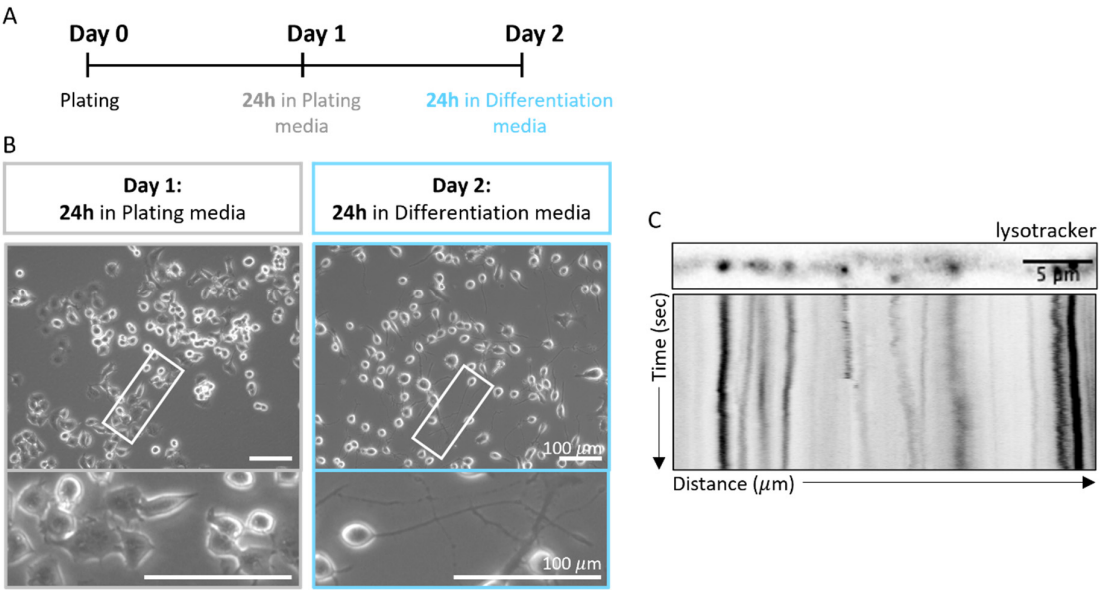

Figure 17. Analysis of lysosome transport kinetics in N2a cells differentiated following *Namsi et colleague's* experimental procedure. (A) Scheme representing the experimental paradigm described by *Namsi et colleagues* to differentiate N2a cells into neuron-like cells. **(B)** Morphological characterization of N2a upon differentiation protocol. **(C)** Representative kymograph tracking lysosomes position over time along a neurite of differentiated N2a cells. The kymograph shows the presence of multiple lysosomes along the neurite length which remained immobile for the entire recording time (2 minutes).

We hypothesized that the absence of MT-associated transport could be ascribed to the metabolic changes associated to the differentiation process cells are undergoing. Accordingly, serum withdrawal alone can induce N2a differentiation through activation of the MAPK/ERK pathway which engage EGFR (Epidermal Growth Factor Receptor), Akt (protein kinase B) and ERK1/2 (extracellular signal-regulated kinase 1/2) (Evangelopoulos et al. 2005). To reestablish the transport dynamics of organelles, we ought to expose the differentiated N2a cells to the growing medium conditions commonly used for neuronal primary cultures **(Figure 18 A)**. We reasoned that this media (therefore called as *recovery media*) would stabilize the metabolic state of the cells and recover the physiological intracellular processes described in primary neurons such as axonal transport (Even et al. 2019). 48 hours after media change, the differentiated N2a cells (hereafter referred to as d-N2a) display unaltered neurite length but increased branching, when compared to their morphology previously acquired upon serum

deprivation and RA treatment **(Figure 18 B-D)**. These newly differentiated cells comprise an heterogenous population of neuron-like cells with different degree of maturation, as indicated by the increased levels of β-III tubulin and neurofilament protein, markers for immature and mature neurons, respectively **(Figure 18 E-J)**.

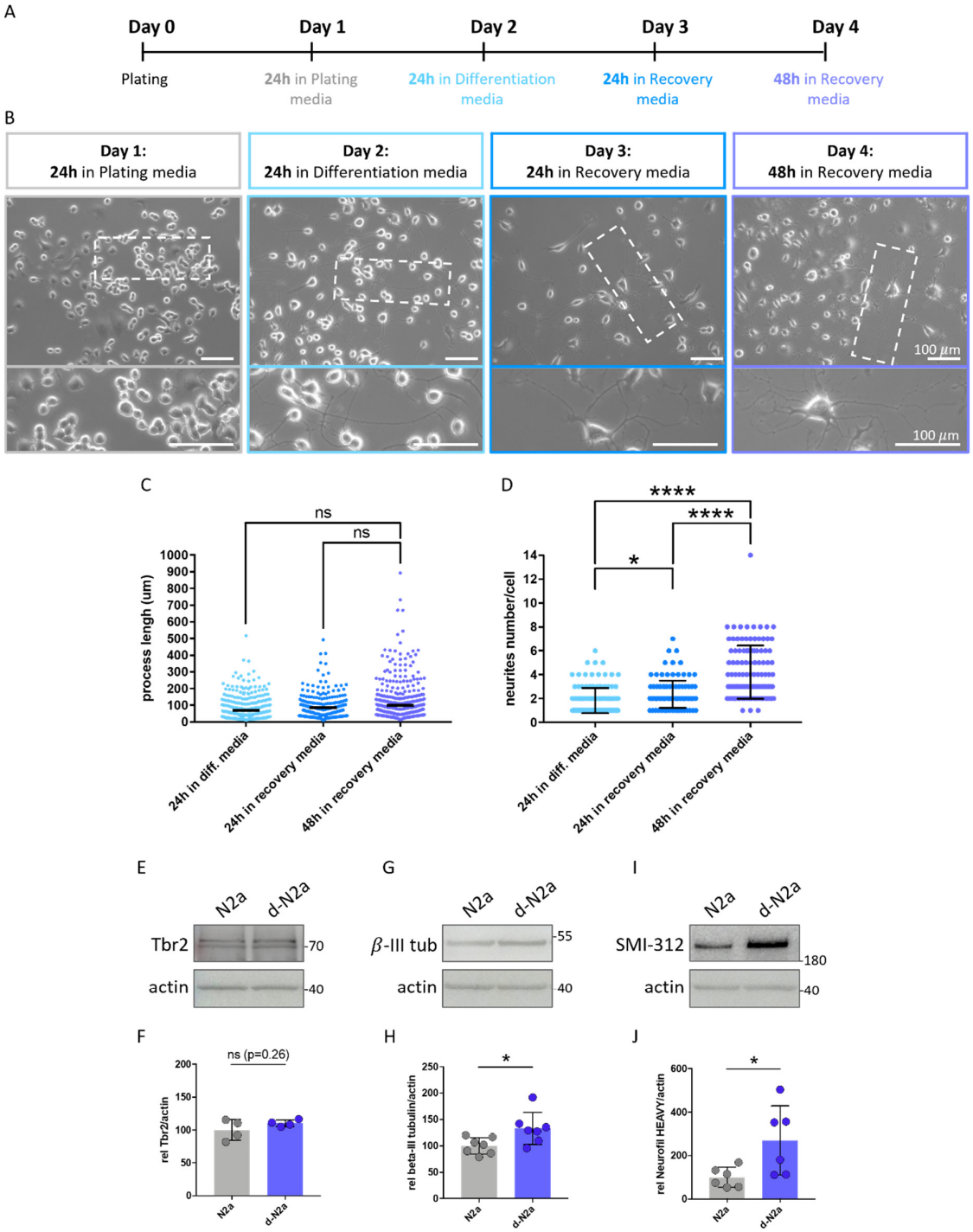

Figure 18. Morphological and biochemical analysis of N2a cells upon differentiation with the newly adopted protocol. (A) Scheme describing the adopted protocol established to differentiate N2a into neuron-like cells. **(B)** Morphological characterization of the N2a cells undergoing the three day-step differentiation protocol, consisting in 24h exposure to the differentiation media (serum deprivation and treatment with 6μM retinoic acid) followed by 48h treatment with the recovery media (neurobasal media supplemented with glutamine and B27). **(C, D)** Analysis of neurite length and number of N2a cells at every step of the differentiating protocol. **(E-J)** Western blotting analysis of the d-N2a generated following the adopted differentiation protocol, compared to untreated N2a cells. Protein lysates were probed for markers of intermediate progenitors (Tbr2, P<0.2629), immature neurons (β-III tubulin, P<0.0256), and mature neurons (neurofilament proteins, P<0.0312).

After replacing the differentiation media with the recovery media for 48 hours, we attempted to record the lysosomes transport dynamics along neurites of the d-N2a. Lysosomes displayed a bidirectional motion with an average velocity of 0.308 μm/sec, which is comparable to that of mouse cortical neurons **(Figure 19 A-E)** (Even et al. 2019, 2021). To assess whether the transport dynamics were restricted to lysosomes or extended to other organelle subtypes, we expressed a synaptophysin-expressing plasmid fused to the mCherry protein (synaptophysin-mCherry) in the differentiating cells 24 hours after the exposure to the recovery media. We recorded highly motile synaptophysin+ vesicles undergoing anterograde and retrograde transport displaying an average velocity of 0.764 μm/sec **(Figure 19 F-J)**. This analysis confirms the suitability of the d-N2a generated through our adopted differentiation protocol for studying the transport kinetics of membrane-bound organelles.

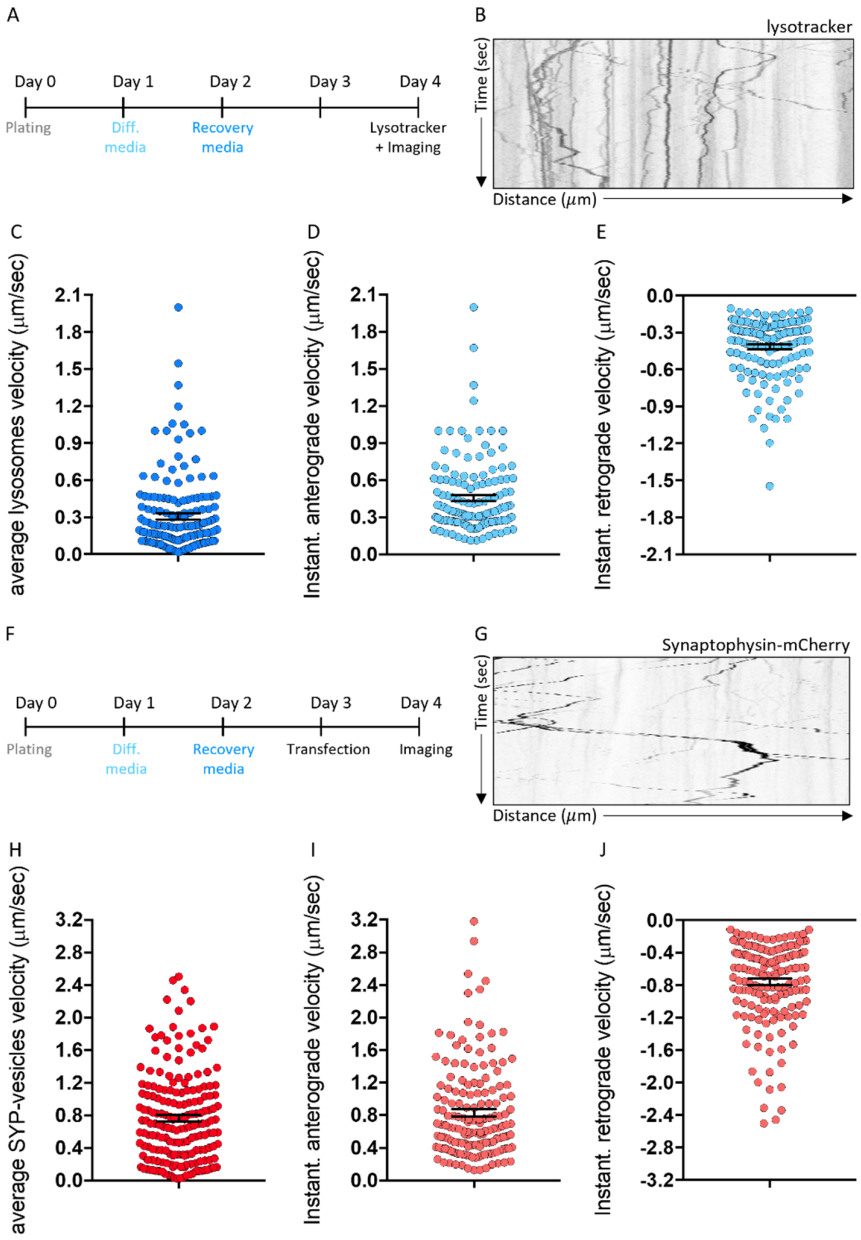

Figure 19. Transport dynamics analysis of membrane-bound organelles along neurites of d-N2a cells. (A) Experimental paradigm describing the adopted differentiation protocol. To label lysosomes, the lysotracker dye is added to the cultures at the moment of the recordings. **(B)** Representative kymographs showing lysosomes trafficking along a d-N2a cell's neurite. **(C)** Analysis of lysosome average velocity (which comprises motile and immotile lysosomes), anterograde and retrograde velocities of motile lysosomes. Number of vesicles analyzed: 155 for mean speed; 139 for retrograde velocity; 105 for anterograde velocity. **(F)** Experimental paradigm describing the adopted differentiation protocol. To label synaptophysin-expressing vesicles, cells were transfected with a synaptophysin-mCherry at day 3 of the differentiation protocol, 24 h before imaging. **(G)** Representative kymographs showing the transport dynamics of synaptophysin+ vesicles along a neurite of a d-N2a cell. **(H-J)** Quantification of average, anterograde and retrograde velocity of synaptophysin+ vesicles. Number of vesicles analyzed: 186 for mean speed; 165 for retrograde velocity; 157 for anterograde velocity.

To verify if, likewise in neurons, local translation occurs along the processes of these newly d-N2a cells, we first analyzed the expression pattern of the ribosomal protein 24 (rpl24). Immunofluorescent staining showed an heterogenous distribution of ribosomes along the neurites of d-N2a **(Figure 20 A, B)** indicating a peripheral distribution of the translation machinery. To assess whether peripheral ribosomes are engaged in active translation, we performed the puromycylation assay which uses the tRNA analogue puromycin that incorporates into translating peptides inducing their release from ribosomes, and an anti-puromycin antibody to visualize all tagged peptides therefore providing a readout of the global protein synthesis in the cell **(Figure 20 E)** (David et al. 2012). We treated N2a and d-N2a cultures with a short 3-minute burst of puromycin, to avoid overestimation of the local translation events along neurites that would have occurred with a long puromycin exposure due to long-range diffusion of the ribosome-released peptides. We detected puromycin signal throughout the length of neurites, which was depleted when cells were pretreated with the translation inhibitor anisomycin **(Figure 20 C-F)**. These data reveal that d-N2a cells share the ability of primary neurons to localize protein translation in peripheral compartments. The d-N2a obtained through our adopted protocol represent a valid in vitro model to study transport and local translation dynamics.

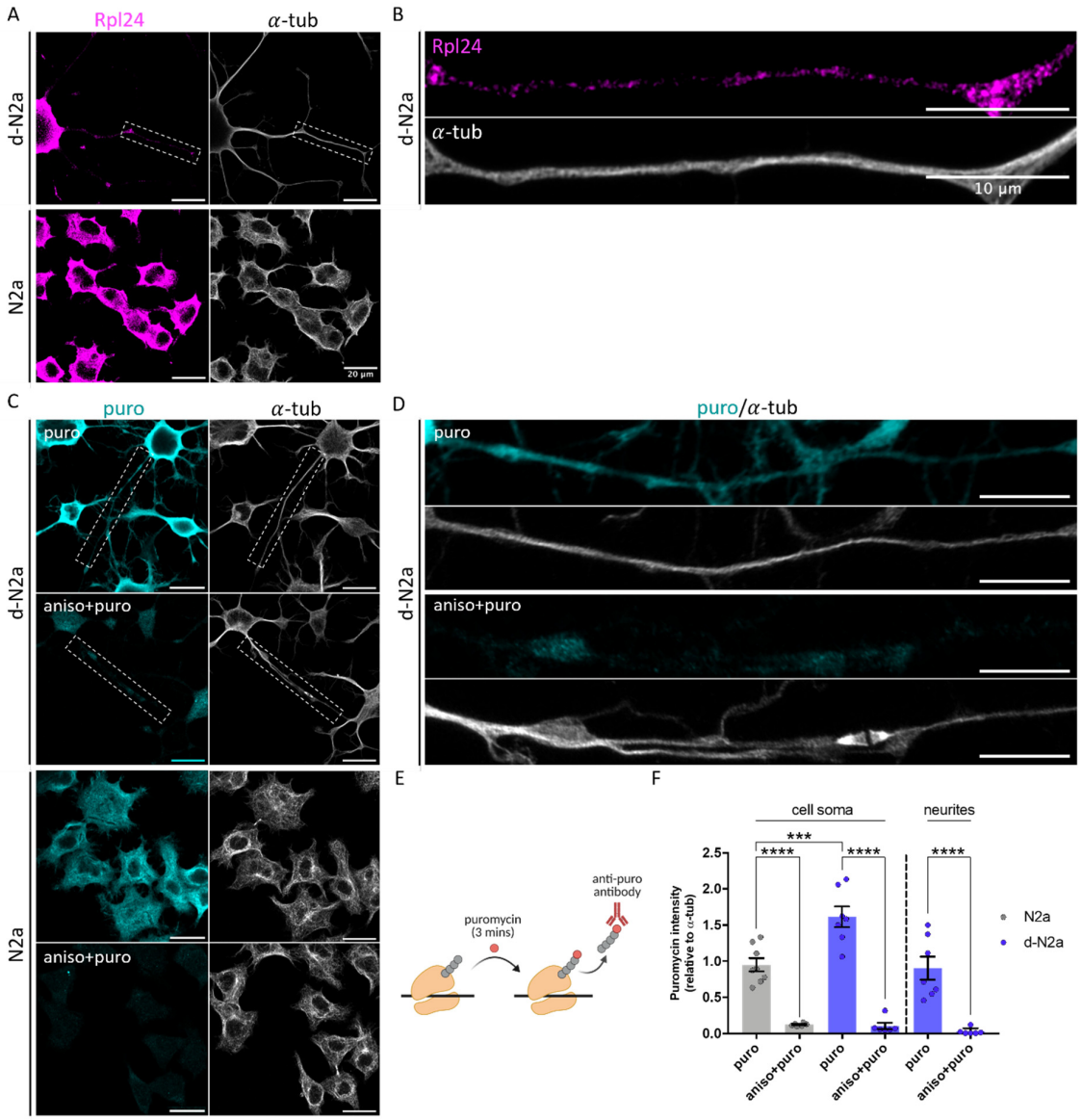

Figure 20. Ribosomes and translating peptides are distributed along neurites of d-N2a cells. **(A, B)** Expression pattern analysis of rpl24 in N2a and d-N2a cells. Cells were co-stained for α-tubulin. **(B)** Rpl24 foci were abundantly identified throughout the neurites of d-N2a cells. **(C-F)** Puromycylation assay performed in N2a and d-N2a cells. **(C, D)** Immunofluorescence analysis of puromycin labelling in N2a and d-N2a treated with puromycin, with/without 40 minutes pretreatment with the translation inhibitor anisomycin. **(D)** Puromycin labelling along neurites of d-N2a cells, with/without pretreatment with anisomycin**. (E)** Schematic of the puromycylation assay: cultures are treated for 3 minutes with the tRNA analogue puromycin, fixed and immunolabelled with an anti-puromycin antibody. **(F)** Bar graph analyzing puromycin fluorescent intensity in cell soma (N2a and d-N2a) and neurites (d-N2a). Data shown as mean $\pm$ SD. Number of cells analyzed: n=8 (N2a, puro), n=6 (N2a, aniso+puro), n=7 (d-N2a, puro), n=6 (d-N2a, aniso+puro). ***P=0.0002, ****P<0.0001; 2-way ANOVA with Sidak's multiple comparison test.

Given the role of local translation for synapses proteome (Hafner et al. 2019; Oostrum et al. 2023), we wondered if the differentiation protocol induced the establishment of other neuron-like features as synapses formation. We performed immunofluorescent staining for the presynaptic marker VGlut1 and the postsynaptic marker PSD95 and assessed the formation of excitatory synapses by probing their signal colocalization. We detected VGlut1/PSD95 synapses along the neurites of d-N2a **(Figure 21 A-C)**, suggesting that d-N2a are functionally integrated into neuronal network.

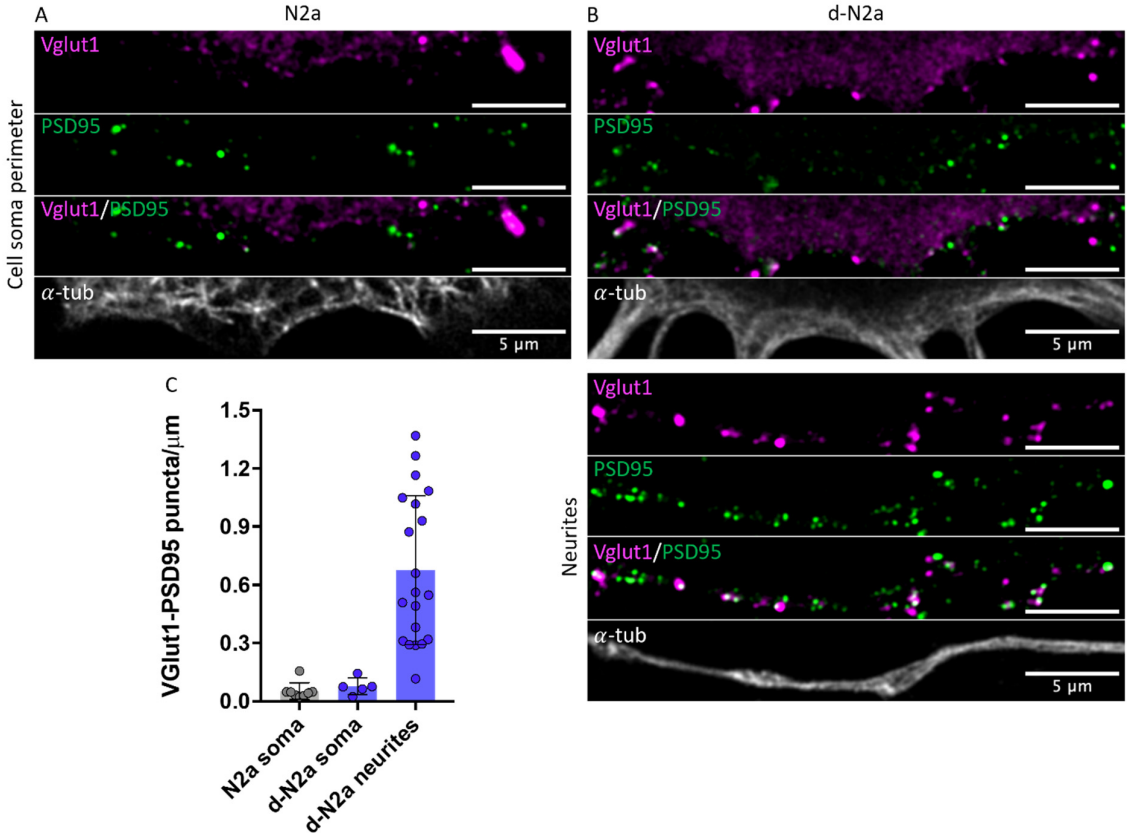

Figure 21. Identification of excitatory synapses along neurites of d-N2a cells. (A, B) N2a and d-N2a cells were probed for the pre-synapses (VGlut1) and post-synapses (PSD-95) markers to identify excitatory synapses by assessing their colocalization. VGlut1 and PSD-95 signal was assessed along the cell soma perimeter of both N2a and d-N2a cells, and along the neurites of d-N2a cells. **(C)** Correspondent bar graph analysis. Data shown as mean ± SD. Number of cells analyzed: n=8 (N2a), n=5 (d-N2a, soma), n=20 (d-N2a, neurites). T-test, parametric.

To test the electrophysiological properties of the d-N2a cells, we performed patch-clamp in whole cell configuration recordings on both N2a and d-N2a cells **(Figure 22 A).** We found that neither N2a nor d-N2a cells were able to elicit an evoked action potential when studied in

current-clamp mode **(Figure 22 B)**. In accordance, voltage-clamp recordings showed that both d-N2a and N2a cells exhibited inward Na+ current upon depolarizing voltage steps of 10 mV increment, which however was not followed by repolarizing outward K+ current **(Figure 22 C, D)**. However, d-N2a were more hyperpolarized than their undifferentiated counterparts **(Figure 22 E)**. We next measured the excitatory postsynaptic current (EPSC) in voltage clamp mode by holding the membrane potential of N2a and d-N2a cells at -70 mV. We recorded an increased frequency of EPSC in d-N2a compared to N2a cells, which was abolished by treatment with the glutamatergic receptor antagonists APV (D(-)-2-amino-5-phosphonovaleric acid) and CNQX (6-cyano-7- nitroquinoxaline-2,3-dione). This reduction, however, was not altered by a sequential blocking of the $GABA_A$ receptor with the antagonist Picrotoxin (PiTX) **(Figure 22 F-I).** On the other hand, we did not detect any difference in the EPSC amplitude between N2a and d-N2a cells **(Figure 22 F, J-L)**. These data suggest that d-N2a cells, although not retaining the excitability proprieties of mature neurons, present synaptic activity modulated by glutamatergic current.

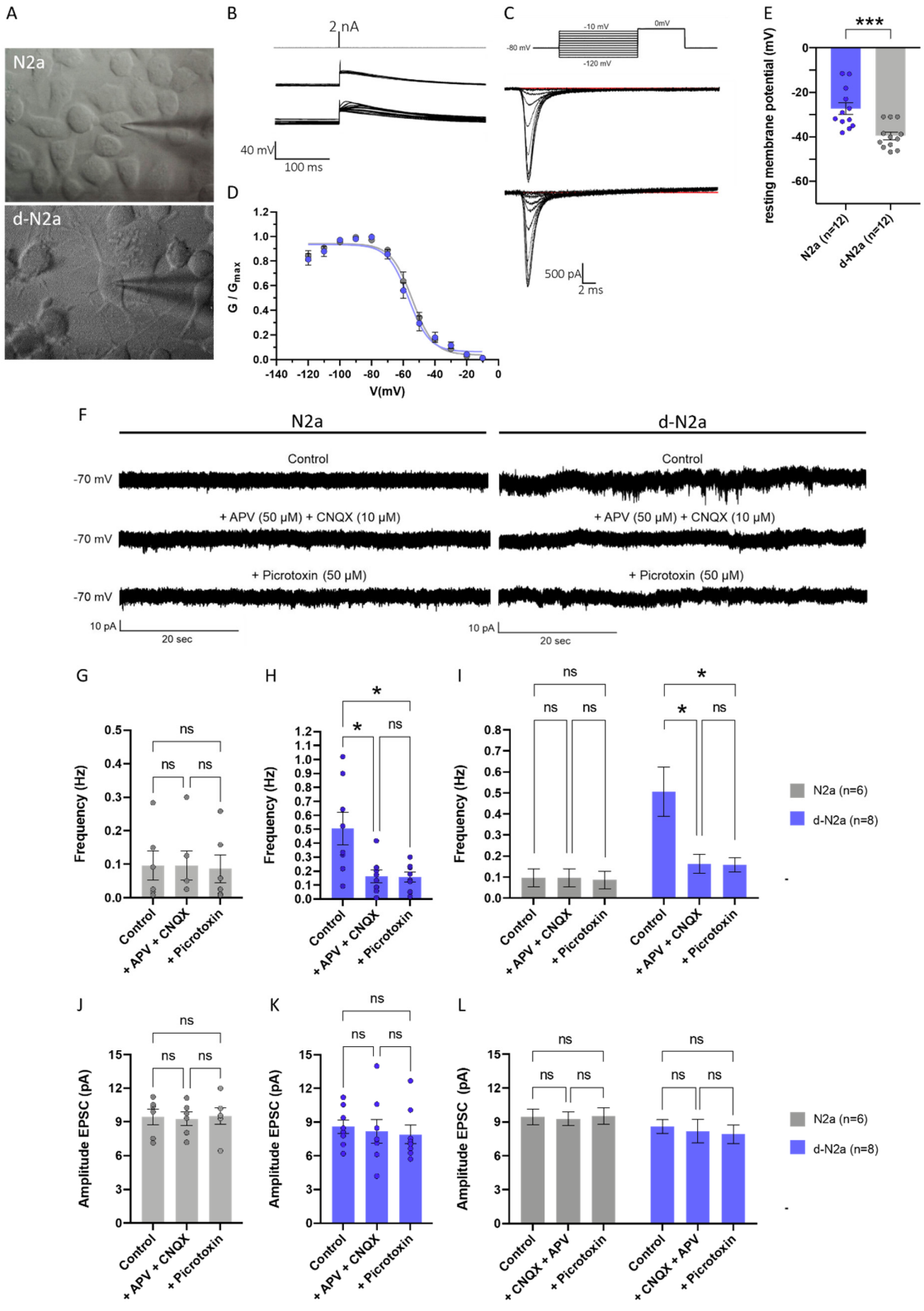

Figure 22. Electrophysiological characterization of d-N2a cells. (A) Image of a patch-clamped N2a and d-N2a cell. **(B)** Representative trace of a current clumped d-N2a cell upon injection of high current. No action potential was evoked. Number of cells analyzed: n=12 (N2a), n=12

(d-N2a). **(C)** Bar graph analyzing membrane resting potential of N2a and d-N2a cells. **(D)** Representative trace of a voltage clumped d-N2a cell showing evoked N2+ current in response to depolarizing step current injections. **(E)** Representative current traces of excitatory postsynaptic currents (EPSC) of individual N2a and d-N2a cells recorded in voltage clump at -70mV. Upon recording of the cell's synaptic response, glutamatergic synaptic currents were blocked with 50 μM APV and 10 μM CNQX. Sequentially, GABA currents were additionally blocked with 50 μM picrotoxin. Number of cells analyzed: n=6 (N2a), n=8 (d-N2a)**.**
(F-H) Column graph analysis of EPSC frequency of single N2a cells **(F)**, d-N2a cells **(G)** and combined N2a and d-N2a cells **(H)**, before and after sequential treatment with APV+CNQX and picrotoxin. **(I-K)** Column graph analysis of EPSC amplitude of single N2a cells **(F)**, d-N2a cells **(G)** and combined N2a and d-N2a cells **(H)**, before and after sequential treatment with APV+CNQX and picrotoxin. Data shown are mean $\pm$ SE. **(F)** Nonparametric Friedman test with Dunn's multiple comparison test. (G, I, J) One-way ANOVA with Tukey's multiple comparison test; *P=0.0332. (H, K) Two-way ANOVA with Tukey's multiple comparison test; *P=0.0332.

3. Establishing the SunTag system in N2a cells

To study the translation dynamics of the candidate mRNAs, we expressed the SunTag system in N2a cells, which will be then differentiated at the moment of the experiment. This system enables the live tracking of a given transcript and the concomitant visualization of its correspondent protein being translated over time (Yan et al. 2016). Among the three plasmids constituting this system, the reporter plasmid encodes for the protein of interest fused at its N-terminus to a repeating peptide array called SunTag. As the gene of interest is translated, the SunTag peptides will be recognized by GFP-tagged single-chain antibody fragments (scFv-GFP), that are encoded by the second plasmid. Newly synthesized proteins will thus appear as bright green fluorescent foci at the site of translation. To track the mRNA of interest, the reporter plasmid presents 24 copies of a hairpin sequence within its 3'UTR (PP7 binding sites), which are recognized by the mCherry-fused PP7 bacteriophage coat proteins that are encoded by the third plasmid. Individual mRNA molecules will therefore appear as bright red dots **(Figure 23 A)**. The expression of the reporter plasmid is regulated by a Tet-ON system which is based on the co-expression of the Tet repressor protein (TetR). TetR silences the transcription of the reporter gene, and its activity is released upon doxycycline administration. Thus, the Tet-ON system allows the control of the timing of expression of a given gene. To generate a SunTag-expressing N2a cell line, we transduced N2a cells with scFv-GFP, PP7-mCherry and TetR. Antibiotic-selected cells expressing TetR were then FACS-sorted to select the cells co-expressing both scFv-GFP and low levels of PP7-mCherry (mCherry low) **(Figure 23 B)**. To test the functionality of the SunTag system in the newly selected cells, we

transfected the previously characterized reporter plasmid SunTag$_{24x}$-kif18b (Yan et al. 2016) and upon doxycycline addition assessed its translation dynamics. Immunofluorescence analysis revealed the appearance of scFv-GFP foci **(Figure 23 C)**, and live imaging recordings confirmed that the observed signal corresponded to newly translated proteins as it disappeared upon puromycin treatment **(Figure 23 D, E)**. We therefore established the SunTag system in N2a cells that upon differentiation acquire neuron-like features as axonal transport and local translation, making this cell line ideal to investigate the dynamics of candidate mRNAs, and assess whether they can be translated while trafficking along neurites.

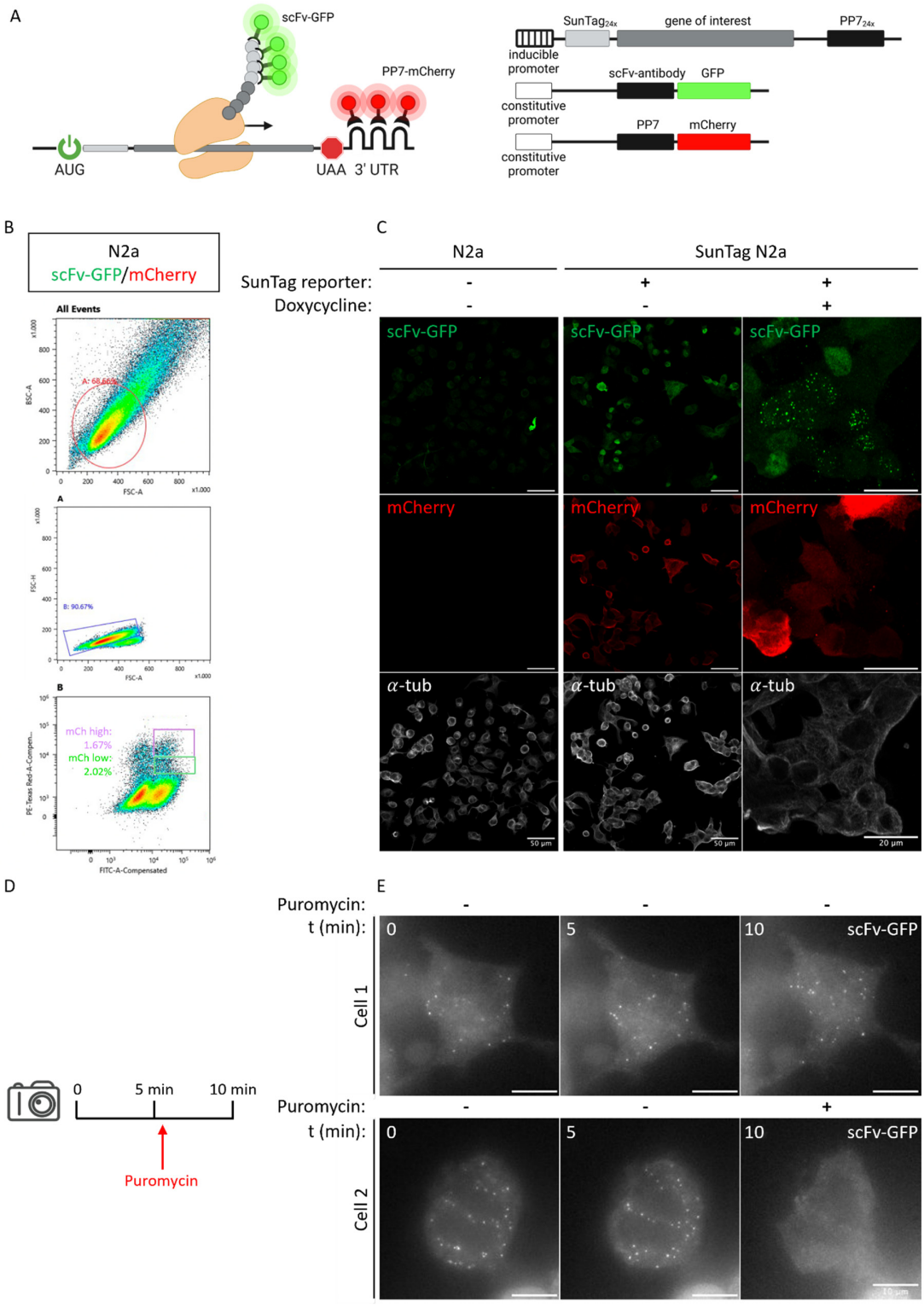

Figure 23. Generation of a N2a SunTag cell line. (A) Schematic of the SunTag imaging system. A reporter mRNA encoding the protein of interest is fused at its N-terminus to a repeating peptide array called SunTag, which is recognized by GFP-fused antibodies as the reporter is translated. Translating peptides are visualized as bright green fluorescent spots at the site of translation. In addition, the mRNA molecule is fluorescently labeled through the binding of

mCherry-PP7 coat proteins to the hairpin loops downstream the stop codon UAA. **(B)** Gating strategy to FACS-sort N2a cells expressing mCherry-PP7 and scFv-GFP. All cells were visualized by FSC and BSC (gate A). Gate B was defined to exclude doublets by using FSC-area (A) versus FSC-height (H). The selected population of single cells was analyzed by FITC and PE-texas red, to identify the cells population co-expressing either GFP and low mCherry fluorescence (mCh low), or GFP and high mCherry fluorescence (mCh high). The former population was used for downstream analysis. **(C)** Immunofluorescent analysis of N2a or N2a cells expressing the SunTag system probed for GFP, mCherry and α-tubulin. Differently from the N2a cells, a heterogeneous cytoplasmic GFP and mCherry signal was detected in the SunTag N2a cells. Upon transduction of the SunTag reporter $SunTag_{24x}$-Kif18b-$PP7_{24x}$ (addgene #74928) and its doxycycline-induced activation, GFP foci appeared corresponding to newly translated Kif18b proteins. **(D, E)** Two representative SunTag N2a cells analyzed via live imaging for their GFP fluorescence. **(D)** Three pictures were taken at 5 minutes interval, with/without puromycin treatment between the second and third. **(E)** Cell 1 shows a stable scFv-GFP expression over time. Cell 2 displays no more scFv-GFP signal upon puromycin treatment, suggesting that the GFP foci previously visualized corresponded to newly translated proteins.

Material and methods

Animals

All experiments performed were approved by the ethical committee of the University of Liege under the license #19-2173.

Thy1:p50-GFP mice were a kind gift from Dr. Frederic Saudou and Dr. Erika Holzbaur. Thy1:p50-GFP mice were maintained at their hemizygous state in the B6SJL hybrid background. To generate $Rpl22^{L/L}$;$VGlut1^{cre/+}$;$p50\text{-}GFP^{+/-}$ mice: 1) $Rpl22^{L/L}$ and $VGlut1^{cre/cre}$ were crossed to generate $Rpl22^{L/+}$;$VGlut1^{cre/+}$ mice; 2) $Rpl22^{L/+}$;$VGlut1^{cre/+}$ mice were intercrossed to generate $Rpl22^{L/L}$;$VGlut1^{cre/cre}$ mice; 3) $Rpl22^{L/L}$;$VGlut1^{cre/cre}$ mice were crossed with Thy1:$p50\text{-}GFP^{+/-}$ to generate $Rpl22^{L/L}$;$VGlut1^{cre/+}$;$p50\text{-}GFP^{+/-}$ mice.

Mice were housed under standard conditions at constant temperature (19–22 °C) and humidity (40–50%) under a 7am–7 pm light/dark cycle. Mice were maintained with access to food ad libitum and treated according to the guidelines of the Belgian Ministry of Agriculture in agreement with the European Community Laboratory Animal Care and Use Regulations (86/609/CEE, Journal Official des Communautés Européennes L358, 18 December 1986).

List of PCR primers

Gene	Forward	Reverse
p50-GFP	GGATCTCAAGCCCTCAAG	CTTGGACCTCATGCAGTAGG
RiboTag	GGG AGG CTT GCT GGA TAT G	TTT CCA GAC ACA GGC TAA GTA CAC
VGlut1-cre	ATGAGCGAGGAGAAGTGTGG	(VGlut1 WT) GTGGAAGTCCTGGAAACTGC (VGlut1 cre) CCCTAGGAATGCTCGTCAAG

Table 2. List of PCR primers used.

Sample preparation

Forebrains of 2-month old Thy1:p50-GFP mice or their WT littermates were homogenized on ice in 1mL lysis buffer (4mM HEPES, 320mM sucrose, Milli-Q water, pH 7.4) supplemented with 100U/mL *SUPERase In* (ThermoFisher, #AM2696), 100μg/mL cycloheximide (Sigma, #C7698-1G), and Complete EDTA-free Protease Inhibitor Cocktail (Sigma, #11836170001) by using a Dounce homogenizer (15 strokes for both the loose and tight plunger), followed by 10 passages through a syringe with a 26G gauge needle (BD, #305501). The homogenate was clarified by centrifugation at 800 x g, 4°C, for 10 min. After collecting the supernatant (S1), the pellet was resuspended in 500 μL lysis buffer by using a syringe with 26G gauge needle

(10 passages), and centrifuged at 800 x g, 4°C, for 10 min. The supernatant was collected and pulled with the previous S1 fraction (organelle-rich fraction). As an imput for MS and RNA-seq analysis, 100 uL of S1 were stored at -80°C with/without 300 uL trizol (ThermoFisher, #15596018), respectively. The pellet (P1) contains nuclei and unlised cells and was kept for fluorescent particle sorting analysis.

Fluorescent particle sorting

p50-GFP *motile cargos* were sorted on a SONY MA900 Multi-Application Cell Sorted equipped with a 100 μm nozzle. The forward-scatter (FSC) threshold was decreased from 6% to 1.5% to visualize subcellular particles. Particles were detected by using the Forward-scattered light (FSC) and the Back-scatter channel (BSC). After excluding the population of unlised cells identified through the analysis of the P1 fraction (labelled as "cells"), the remaining population which accounts for more than 99% of all the events ("lysate") is cleared from the autofluorescent events ("autofluo"). The remaining events ("true") are detected according to their FSC and green fluorescence. By comparing the events distribution of a Ty1:p50-GFP or WT sample, the GFP+ events were identified. Sorting gates were drawn for GFP+ and GFP- particles. Due to biological variations and lysis efficiency, GFP+ events represented between 1-9% of all detected events. Note that sample pressure was adjusted to detect between 1,000-2,000 events per second; if sample pressure adjustments were not sufficient to meet this requirement, the S1 fraction was further diluted with lysis buffer. This requirement is important for the purity of the sorting. Sorting was performed in normal mode which allowed a 98-99% and 86-91% sorting efficiency for, respectively, the GFP- and GFP+ fractions. S1 samples were sorted for 3 hours, to collect between 250,000-500,000 events per fraction. For RNA-seq analysis, samples were sorted in 15 mL tubes containing 3mL trizol (ThermoFisher, #15596018) and stored at -80°C. For MS analysis, fractions were sorted in 4mL polyclear centrifuge tubes (Seton Scientific, #7010). At the end of the 3 hours sorting, tubes were top off with PBS and 3 uL GlycoBlue coprecipitant (ThermoFisher, #AM9515). Ultracentrifugation was performed at 100,000 x g, 4°C, for 2 hours by using an Optima XPN-80 (Beckman Counter) with compatible rotor SW60-Ti (Beckman Counter). Supernatant was removed and the tube containing the glycoblue-labelled pellet snap frozen and stored at -80°C. For WB analysis, upon ultracentrifugation, pellets were resuspended in 40 μL 5X SDS sample loading buffer and stored at -20°C.

N2a maintenance and differentiation

Neuro2A cells (ATCC, #CCL-131) were maintained in Dulbecco's modified Eagle's medium (DMEM) (Biowest, #L0103) supplemented with 10% FBS (Sigma, #F7524) and 1% penicillin/streptomycin, at 37 °C, 5% CO_2 conditions. Seeding density was adjusted according to the seeding area: for IF and electrophysiological studies, cells were plated on plastic coverslips (Kisker, #330164) at the density of 40,000 cells/well; for transport analysis, 15,0000 cells were plated per MatTek glass bottom dishes (MatTek Corporation, #P35G-0-20-C); for WB studies, 100,000 cells/well were seeded onto plastic 6-well plates (uncoated). To induce differentiation into neuron-like cells, 24 hours after plating, the culturing media was replaced by the differentiation media (serum-free DMEM, 1% penicillin/streptomycin (Biowest, #L0022), 6 μM retinoic acid (Sigma, #R2625) according to (Namsi et al. 2018). 24 hours after, differentiated cells were switched to the recovery media [neurobasal media (Gibco, #21103049) supplemented with Glutamax (ThermoFisher, #35050038), 1X B27 (ThermoFisher, #17504044), 1% penicillin/streptomycin (Biowest, #L0022)] for 48 hours, reaching the analysis time point. N2a cells kept untreated for the entire duration of the differentiation protocol and maintained in the culturing media were used as experimental control. For IF, cells were either left untreated or treated for 3 minutes with 10 μg/mL puromycin (Sigma, #A1113803), with or without pretreatment with 40 μM anisomycin (Sigma, #A5862) for 40 min. Cells were then washed three times with PBS, and fixed with 4% PFA (Electron Microscopy Sciences, #15710) for 10 min at room temperature before three washes of 10 min PBS. For WB studies, cells were transferred on ice, washed three times with ice-cold PBS, and detached by scraping in 100 μL NP40 lysis buffer (150 mM NaCl, 50 mM Tris-Cl pH 8, 1% NP40) supplemented with Complete EDTA-free Protease Inhibitor Cocktail (Sigma, #11836170001). To promote lysis, cells were placed under constant agitation for 30 min at 4°C and centrifuged at 13,000 x g for 10 min at 4°C to collect the supernatant.

Primary cortical culture preparation

Primary cultures of cortical neurons were generated at the embryonic day 14 (E14) from embryos of Thy1:p50-GFP+/- mice. From each dissected embryo, tails biopsies were collected for genotyping. Cortices were dissected in PBS supplemented with 1.5% glucose. Tissue was digested in trypsin-EDTA (0.05%) (Gibco, #25300096) for 15 min at 37 °C followed by trypsin inactivation in fetal bovine serum (FBS) (Sigma, #F7524) for 10 min at room temperature.

After 2 washes with culture media [neurobasal media (Gibco, #21103049) supplemented with Glutamax (ThermoFisher, #35050038), 1X B27 (ThermoFisher, #17504044), 1% penicillin/streptomycin (Biowest, #L0022)], cortices were mechanically dissociated in 500 μL culture media by pipetting very gently up and down with a 1 mL pipette. Cells suspension was filtered through a 40 μm mesh (Roth, #CLY9.1) and cells counted before plating at a density of 35,000 cells/well on 12 mm glass coverslips which were coated overnight with 0,1 mg/mL Poly-D-Lysine (Sigma, #P0899) at 4°C followed by three washes with PBS. Cultures were maintained in culture media, and every three days half of the media was replaced with fresh pre-warmed culture media. Cells were fixed at DIV12 with 4% PFA (Electron Microscopy Sciences, #15710) for 10 min at room temperature before three washes of 10 min PBS.

Primary hippocampal culture preparation

Primary mouse hippocampal cultures were prepared with E15.5 embryos from $Rpl22^{L/+;}VGlut1^{cre/+;}p50\text{-}GFP^{+/-}$ mice. Hippocampi were dissected in HBSS (Biowest, #L0612) and digested with 9:10 papain (Worthington, #LK003150) and 1:10 DNase I (Sigma, D5025) for 30 minutes at 37 °C. Tissues were washes with plating media [DMEM, 10% FBS (Sigma, #F7524), 1% penicillin/streptomycin (Biowest, #L0022)] and mechanically dissociated in 500 μL plating media by pipetting up and down (max 20 times) with a 1 mL pipette. Cells suspension was filtered through a 40 μm mesh (Roth, #CLY9.1) and cells counted. 12 mm coverslips were coated with 0.1 mg/mL poly-L-ornithine (Merck, #P4638) at 37°C for 40 min, followed by ON incubation at 4 °C with 5 μg/mL laminin (Merck, # L2020-1MG). Cells were plated at the density of 35,000 cells per coverslips in plating media. Upon cells attachment (1 hour), plating media was replaced by culture media [neurobasal media (Gibco, #21103049) supplemented with Glutamax (ThermoFisher, #35050038), 1X B27 (ThermoFisher, #17504044), 1% penicillin/streptomycin (Biowest, #L0022)]. Every three days half of the media was replaced with fresh pre-warmed culture media. Cells were fixed at DIV12 with 4% PFA (Electron Microscopy Sciences, #15710) for 10 min at room temperature before three washes of 10 min PBS.

Western blot

Protein lysate from N2a/d-N2a cells or S1 fractions from mouse brain lysate were quantified via Pierce™ BCA Protein Assay Kit (ThermoFisher, # 23225) and normalized to 1 μg/μL in 5X

SDS sample loading buffer with 5 min boiling at 95°C. 15 μg proteins or 35 μL of sorted sample (previously pelleted and resuspended in 40 μL of 5X SDS sample loading buffer) were then fractionated on 5%-10% PAGE gels and transferred to nitrocellulose membranes (Fisher Scientific, #15269794). Upon assessing the quality of the transfer by staining with Ponceau S staining solution (ThermoFisher, #A40000279), membranes were blocked in 5% nonfat dry milk in Tris-buffered saline supplemented with 0.1% Tween 20 (TBST) for 1 hour at room temperature. Incubation with primary antibodies in 5% TBST were performed ON. After 3 washings of 10 min each with TBST, membranes were probed with the following horseradish peroxidase (HRP)-conjugated secondary antibodies for 1h at room temperature: goat anti-mouse (1:5,000) (ThermoFisher, #G-21040); goat anti-rabbit (1:5,000) (ThermoFisher, #G-21234); goat anti-chicken (1:5,000). Membranes were then washed 3 times in TBST, developed with Pierce™ ECL Western Blotting Substrate (ThermoFisher, # 32106).

Electron microscopy imaging

Ultrastructural characterization

Pellets of isolated vesicles were fixed in 2.5% glutaraldehyde (diluted in Sorensen's buffer: 0.1 M Na_2HPO_4/NaH_2PO_4 buffer, pH 7.4) for 1 hour at 4°C and post-fixed for 30 min in 2% OsO_4 (diluted in 0.1 M Sorensen's Buffer). After dehydration in graded ethanol, samples were embedded in Epon resin (Sigma-Aldrich, #45359). Ultrathin sections obtained with a Reichert Ultracut S ultramicrotome (Reichert Technologies) were contrasted with 2% uranyl acetate (Fluka, cat. no. 94260) and 4% lead citrate (Merck, cat. no. 7398). Samples were examined under a Jeol TEM JEM-1400 Transmission Electron Microscope (Jeol, Peabody, MA, USA) at 80 kV, and photographed using an 11-megapixel camera system (Quemesa, Olympus).

GFP Immunogold labelling

For immunolabeling, isolated vesicles adsorbed on formvar-carbon coated grids were fixed in 2% paraformaldehyde (diluted in 0.1 M Sorensen's buffer) for 10 min, rinsed in buffer and blocked for 30 min in PBS (0.14 M NaCl, 6 mM Na_2HPO_4, 4 mM KH_2PO_4, pH 7.2) containing 1% BSA (1%,) supplemented with normal goat serum (1/30 dilution). Sections were washed in PBS containing 0.2% BSA and incubated with anti-GFP antibody, 1/500 dilution in PBS containing 0.2% BSA and normal goat serum 1/50 for 3 h. After three washes in PBS (pH 7.2) containg 1% BSA and an additional wash in PBS (pH 8.2) containing 0.2% BSA, sections were

incubated with secondary antibody (goat anti rabbit IgG coupled with 10 nm gold particles (electron microscopy sicences, cat 25109) diluted 1/40 in PBS, pH 8.2, containing 0.2% BSA) for 1 h. Finally, sections were washed four times in PBS (pH 8.2) containing 0.2% BSA, fixed in 2.5% glutaraldehyde (diluted in 0.1 M Sorensen's buffer, pH 7.4) for 10 min, washed four times in deionized water, stained with uranyl acetate and lead citrate and allowed to dry. For negative controls, the sample was incubated with secondary antibody only (omitting the primary antibody step). Pictures were made with a Jeol JEM-1400 transmission electron microscope.

RNA extraction from sorted fractions

Sorted fractions collected in trizol (ThermoFisher, #15596018) within 15 mL tubes were flash frozen with dry ice and stored at -80°C. RNA isolation was performed following the manufacturer's recommendation, with minor variations. Briefly, after thawing the sample at room temperature, the sample was split into 1,5 mL Eppendorf tubes so that every tube would contain $\leq$ 1 mL. Upon adding 200 μL chloroform (Roth, #6340.4) per every 1 mL trizol present in every Eppendorf tube, tubes were vortexed for 15 seconds and incubated at room temperature for 2-3 min. Tubes were centrifuged at 12,000 x g for 15 min at 4°C, to allow the solution to separate into a lower protein-rich phase, a DNA-rich interphase, and an upper aqueous phase containing RNAs. Aqueous phases were carefully transferred into new Eppendorf tubes. For every 500 μL of acqueous phase collected 10 μL GlycoBlue Coprecipitant (ThermoFisher, #AM9515) were added. An equal volume of ice-cold isopropanol was then added, maintaining a 1:1 ratio with the aqueous phase, regardless of the initial volume of trizol used. To promote and maximize RNA precipitation, tubes were incubated overnight at -20 °C. The following day, to collect the precipitated RNA, one tube at a time was centrifuged at 12,000 x g for 30 min at 4 °C. Upon discarding the supernatant, the content of the second Eppendorf tube was transferred into the first tube, to pull together the RNA from the first two tubes. Upon centrifugation (12,000 x g for 30 min at 4 °C) and removal of the supernatant, the content of the third Eppendorf tubes was transferred into the first one, to pull the RNA from the third tube to that of the first and second tubes. This procedure was performed until the RNA content of all Eppendorf tubes were pulled together. The pulled RNA pellet was then dislodged from the tube walls by adding 1 mL of 75% ethanol, and centrifuged at 12,000 x g for 5 min at 4 °C. Upon removal of the supernatant, the RNA pellet was left to air dry for 10

minutes, resuspended in 12 uL of RNAase-free water and kept on ice for 30 minutes before reading RNA quality and concentration on a nanodrop.

Immunofluorescence

Fixed hippocampal cultures were washed 3 times in PBS, simultaneously permeabilized and blocked for 1 hour in 0.1% TritonX-100 (Sigma, #T8787) + 0.5% normal donkey serum (Bioconnect, #017-000-121) in PBS, and incubated overnight at 4 °C with primary antibodies prepared in blocking solution. After 3 washes of 10 min in 0.1% TritonX-100 in PBS, cultures were incubated in the dark with Alexa Fluor-conjugated secondary antibodies for 1 hour at room temperature. Cultures were then washed three times for 10 min in 0.1% TritonX-100 in PBS followed by one quick wash in MilliQ water before mounting the coverslips in Fluorescence Mounting Medium (Agilent, #S3023) and let them air dry overnight in the dark.

Immunofluorescence of the SunTag system

Staining was performed as described in (Boersma et al. 2020), with slight modifications. Briefly, N2a cells expressing the SunTag system that were treated for 1 hour with 1 μg/mL doxycycline (Sigma, #D3072-1ML) were fixed with 4% PFA for 10 min at room temperature. Cells were then permeabilized with 0.1% TritonX-100 in PBS for 5 minutes, blocked with 5% normal donkey serum (Bioconnect, #017-000-121) + 50 mM NH_4Cl in PBS for 45 minutes. Primary antibodies in blocking solution were incubated overnight at 4 °C. After three washes of 10 min with 50 mM NH_4Cl in PBS, cells were incubated with Alexa Fluor-conjugated secondary antibodies in blocking solution for 1 hour at room temperature. After 2 washes of 10 min with PBS, coverslips were mounted in Fluorescence Mounting Medium (Agilent, #S3023) and let them air dry overnight in the dark.

Protein	Company	Cat no.	Species	WB	IF
tubulin YL1/2	Abcam	ab6160	rat	-	1:1,000
α-tubulin	Sigma	T9026	mouse	-	1:1,000
Tuj1	Covance	MMS-435P	mouse	-	1:1,000
MAP2	Abcam	ab5392	chicken	1:4,000	1:5,000
GFP	Gentaur	04404-26	rat	1:1,000	1:1,000
HA	Abcam	Ab9110	rabbit	-	1:500
Rpl24	Proteintech	17082-1-AP	rabbit	-	1:500
puromycin	DSHB	PMY-2A4	mouse	-	1:60
VGlut1	Synaptic systems	135307	goat	-	1:500
PSD-95	Synaptic systems	124 011	mouse	-	1:500

RFP	Rockland antibodies & assays	600-401-379	rabbit	-	1:1,000
Tbr2	Abcam	ab23345	rabbit	1:1,000	-
β-III tubulin	Synaptic systems	302304	Guinea pig	1:1,000	-
SMI-312	Biolegend	837904	mouse	1:500	-
Actin-HRP	Sigma	A3854		1:15,000	-
Donkey anti mouse	ThermoFisher	A-21202		-	1:500
Donkey anti rabbit	ThermoFisher	A-21206		-	1:500
Goat anti guinea pig	Jackson Immunoresearch	706-545-148		-	1:500
Goat anti rat	Jackson Immunoresearch	712-545-150		-	1:500
Donkey anti-chicken	Jackson Immunoresearch	703-605-155		-	1:500
Goat anti-Mouse IgG (H+L) HRP	ThermoFisher	G-21040		1:5,000	-
Goat anti-Rabbit IgG HRP	ThermoFisher	G-21234		1:5,000	-
Goat anti-guinea pig IgG (H+L) HRP	ThermoFisher	A18769		1:5,000	-

Table 3: primary and secondary antibodies used.

Electrophysiological recordings

Whole-cell recordings

Experiments were realized on cultured N2a and d-N2a. Cells were placed in a recording chamber and were perfused with oxygenated artificial cerebrospinal fluid (aCSF) with the following composition (in mM): 125 NaCl, 25 $NaHCO_3$, 2.5 KCl, 2 $CaCl_2$, 1.25 NaH_2PO_4, 1 $MgCl_2$ et 25 D-glucose (pH: 7.3-7.4; osmolarity: ~320 mOsml/l). Cells were visualized using infrared-Doth gradient contrast optics on a Zeiss Axio Examiner A1 microscope equipped with a CCD camera (C7500-51; Hammamatsu, Japan). Whole-cell patch-clamp recordings were realized at room temperature (21-24°C°). Patch pipettes were pulled from thick-walled borosilicate glass tubing (outer diameter: 2 mm, inner diameter: 1 mm, Hilgenberg, Masfeld, Germany) with a horizontal puller (P-97; Sutter Instruments, Novato, CA, USA). Pipettes were filled with an intracellular potassium gluconate solution composed of (mM): 120 K-gluconate, 20 KCl, 2 MgCl2, 4 Na2ATP, 0.5 NaGTP, 7 Na2-phosphocreatine, 0.1 EGTA, 10 HEPES (pH= 7,3; osmolarity: ~302 mOsm/l). When filled with the intracellular solution, tip resistances were between 2 and 5 MΩ. Recordings in which the series resistance was ≥ 10 MΩ were discarded. This micropipette was, then, placed into a pipette holder in order to go down carefully into

the recording chamber filled with aCSF. A positive pressure (~30 mbar) was applied inside the micropipette to prevent the obstruction of the tip by debris. Thanks to a monitoring by a camera, the micropipette was positioned on the cell of interest creating an electrical seal in the order of 50 MΩ of resistance. A negative pressure was applied in order to create an invagination of the cell membrane inside the micropipette. This will lead to the sealing of the micropipette and the increase of the resistance up to 1-20 GΩ (*Giga Ohm Seal*). This configuration is called "cell attached" and is used in order to study the current from ion channels inside the part of the membrane sealed to the micropipette. However, the "whole-cell" configuration is required in order to study the total current of a cell. To achieve it, a brief suction was applied in order to disrupt the cell membrane under the pipette tip. A continuity will be formed between the glass of the micropipette and the lipid bilayer. An inconvenient of whole-cell configuration is that the inside of the cell is dialyzed with the solution inside the micropipette. On the opposite, an advantage of such configuration is the control over extracellular and intracellular solution compositions.

Once the "whole-cell configuration is obtained, the cell will be under the Ohm law:

$$\mathrm{Vm} = \mathrm{Rm} \times \mathrm{I}$$

Where Vm represents the membrane potential (mV), Rm is the membrane resistance (MΩ) and I is the injected current (pA). The patch-clamp technique allows to control either the potential (voltage-clamp mode) in order to record currents, or the current (current-clamp mode) to monitor fluctuation in potential such as action potentials. The Rm is an intrinsic parameter of the cell, which depends on the number of leak channels expressed at the membrane surface. It cannot be controlled.

Data acquisition and analysis

Recordings were performed using a mutliclamp 700B amplifier (Molecular Devices, San Jose, CA, USA) connected to a computer via a Digidata 1550 interface (Molecular Devices). Data were acquired with pClamp 10.5 (Molecular Devices). The voltage-clamp signal was Bessel filtered at 4 KHz and sampled at 10 KHz. The Current-clamp signal was Bessel filtered at 10 KHz and sampled at 10 KHz. Bridge balance was adjusted for current recordings. Data analysis were realized using pClamp 10.5 (clampfit), MiniAnalysis (v6.0.7; Synaptosof Inc.) and Prism 9 (GraphPad software, La Jolla, CA, USA).

Synaptic transmission

Synaptic transmission was investigated by doing voltage-clamp recordings at -70 mV. First, synaptic transmission was recorded in aCSF as a control condition. Then, excitatory synaptic transmission was blocked by the application of NMDA (D-2-amino-5-phosphonopentanoic acid (D-APV), 50 µM) and AMPA/Kainate (6-cyano-7-nitroquinoxaline-2,3-dione (CNQX), 10 µM) receptors specific blockers. Finally, picrotoxin (50 µM), a blocker of inhibitory synaptic transmission was added. To detect synaptic transmission, MiniAnalysis was used and every single event was inspected and selected visually over a 2 minutes recording. To obtain an averaged synaptic transmission, events were superimposed to the initial phase of the current rise. The averaged event was filtered at 2 KHz.

Sodium and potassium currents

Cells were held at -80 mV for the characterization of sodium and potassium currents with rectangular pulses. A 50 ms potential pulse to +120 mV was systematically applied before each test pulse to obtain complete recovery from fast inactivation. Then, steps of 10 mV from -120 mV to -10 mV were realized to record sodium currents. A last pulse at 0 mV for 30 ms was induce to record potassium currents.

Action potential generation

The ability of N2a and dN2a cells to generate action potentials was investigated by realizing current-clamp recordings. Short (100 ms) pulses of current (2 nA) were injected to elicit actions potentials.

Pharmacological agents

Chemicals were purchased as follows: D-APV (Tocris, Bioscience). The remaining chemicals and all salts were purchased from Sigma-Aldrich.

Statistical analysis

Statistical analysis was performed using Prism 9, using the adequate statistical test. The distribution of the data points following the normality or not has been tested using Shapiro-Wilk test. Membrane potential data were tested by paired T-test. The frequency and amplitudes of the synaptic transmission were tested by one-way ANOVA with a post hoc Tukey's test. Experimental values are expressed in terms of mean ± standard error of the mean (SEM). Error bars in the figures also represent SEM.

Transport imaging and analysis

For lysosome imaging, d-N2a grown in MatTek glass bottom dishes (MatTek Corporation, #P35G-0-20-C) were incubated at the moment of the imaging session with 100 nM LysotrackerTM Red (ThermoFisher, #L7528) in imaging medium [NeuroBasal medium minus phenol-red (ThermoFisher, #12348017), supplemented with Glutamax (ThermoFisher, #35050038), 1X B27 (ThermoFisher, #17504044), 1% penicillin/streptomycin (Biowest, #L0022)]. Lysosome transport was recorded along neurites. To imagine synaptophysin+ vesicles, cells were transfected 24 hours after the addition of the recovery media with lipofectamine 2000 (ThermoFisher, #11668019), according to the manufacturer's recommendations. Cells were imaged in a temperature (37 °C) and CO2-controlled chamber, on a Zeiss 880 by using the Fast Airyscan mode with an Apochromat 63 × oil-immersion objective. Movies were acquired with a frame rate of 600-ms for 2 minutes. Transport was analyzed using the KymoToolBox plugin, as described in (Turchetto et al. 2022).

Histological analysis

P13 mice were rapidly anaesthetized with pentobarbital (Euthasol, 150 mg/kg) administered intraperitoneally and transcardially perfused with 4 % (weight/vol.) paraformaldehyde in PBS. Brains were post-fixed overnight at 4 °C. After three washes of 15 min with PBS, brains were cryoprotected in 20% sucrose in PBS overnight at 4°C. Brains were embedded in OCT (Richard-Allan Scientific Neg50), and stored at -80 °C. 40 μm thick free-floating sections were cut with a LEICA cryostat (LEICA, #CM30505) and stored at +4 °C in PBS until they were processed for IHC. Sections were washed twice with PBS for 10 min, blocked in 0.3% TritonX-100 + 10% donkey serum in PBS for 1 hour at room temperature, and incubated overnight at +4°C with primary antibodies in 0.3% TritonX-100 + 1% donkey serum in PBS. After three washes with 0.3% TritonX-100 in PBS, sections were incubated with DAPI (2 μg/mL, Sigma, #D9542) and Alexa Fluor-conjugated secondary antibodies in 0.3% TritonX-100 + 5% donkey serum in PBS for 2 hours at room temperature. Following three washes of 10 min with 0.3% TritonX-100 in PBS, sections were stored in PBS until mounting on superfrost slides (Fisher Scientific Epredia, #J1800AMNZ) and cover-slipped. Images were taken with an epifluorescent slide scanner

DISCUSSION

Chapter I

With the two studies presented in **chapter I** we provide new evidence supporting a causal link between tubulin acetylation and transport dynamics. Moreover, we provide new insights into the molecular cascade regulating the vesicles-driven ATAT1-mediated MTs acetylation. Through *in vivo*, *ex vivo* and *in vitro* assays, we show that ATAT1 promotes the acetylation of axonal MTs, essential regulator of axonal transport dynamics. We identify a vesicular pool of ATAT1 and unravel its displacement over MTs as an essential prerequisite to modulate its acetylation activity. Lastly, we provide new insight into the molecular cascade upstream ATAT1 activity, which sees the Elongator complex regulating the stability of Acly, enzyme that catalyze the conversion of citrate into Acetyl-CoA providing ATAT1 with the substrate required for its acetylating activity.

1. α-tubulin acetylation is required for axonal transport dynamics

The role of tubulin acetylation in relation to transport dynamics emerged with two pioneering studies that provided a role of this PTM for MT binding and processivity of molecular motors (Dompierre et al. 2007; Reed et al. 2006). *In vitro* MT binding assays performed with isolated axonemes loaded on MTs with modified PTM sites, or *in vitro* gliding assays performed with axonemes with not acetylated MTs loaded on kinesins, show that loss of α-tubulin acetylating sites decreased for over 90% the kinesins binding capacity to MTs (Reed et al. 2006). Accordingly, an increased tubulin acetylation induced upon pharmacological inhibition of HDAC6 can promote MT recruitment of motors and transport dynamics (Dompierre et al. 2007).

Additionally, other studies dissected the acetylation-dependent association of motors to MTs showing that acetylation as well as other PTMs regulate the directionality and spatial selectivity of a subgroup of cargos. Acetylated MTs can be run only by specific kinesins subtypes (Guardia et al. 2016), and used as selective tracks for a preferential reorientation from dendrites towards axons (Tas et al. 2017).

In light of these studies, it started to become clear that a PTM that occurs within the MT lumen can nevertheless modulate the affinity for and binding to MTs of molecular motors. A plethora of studies investigated the correlation between low tubulin acetylation levels and the transport defects reported in multiple disease models, including HD (Dompierre et al.

2007), CMTD (d'Ydewalle et al. 2011; Kim et al. 2016), PD (Godena et al. 2014) and ALS (Guo et al. 2017). All these studies show how the pharmacological inhibition of HDAC6 via Tubastatin or Tubacin (d'Ydewalle et al. 2011; Godena et al. 2014; Guo et al. 2017; Kim et al. 2016), or via HDAC6 inhibitors which also retain broader aspecific effects as Trichostatin (d'Ydewalle et al. 2011; Dompierre et al. 2007; Godena et al. 2014), recover tubulin acetylation levels and transport kinetics of a broad range of membrane-bound organelles, as BDNF vesicles, mitochondria and ER-derived vesicles.

The interpretation of these findings can, however, be challenged not only by some of the inhibitors used which target multiple subtypes of HDACs, but also by the specific HDAC6 inhibitors. As HDCA6 can recognize other substrates that α-tubulin, the restoration of axonal transport parameters upon pharmacological increase of tubulin acetylation could be associated to secondary effects ascribed to the activity of these alternative targets. Immunoprecipitation studies show that HDAC6 can interact with the plus-end tracking protein EB1 and the dynactin protein Arp1, suggesting that these interacting proteins could be responsible for the HDAC6-associated effects on MT dynamics that were found to be independent from its deacetylating activity (Zilberman et al. 2009). OE of a catalytically-dead HDAC6 variant (that has no effect on tubulin acetylation) can instead modulate MT dynamics by affecting their growth rate (Zilberman et al. 2009). It is therefore challenging to judge whether the effects on transport dynamics triggered by the pharmacological inhibition of HDAC6 are unambiguously ascribed to an increased tubulin acetylation or whether variations in MT dynamics might also contribute to the phenotype.

To explicitly decipher the role of tubulin acetylation on transport dynamics, it becomes crucial to use alternative strategies for modulating tubulin acetylation than the pharmacological inhibition of HDAC6. As ATAT1 was found to be the predominant enzyme catalyzing tubulin acetylation across species (Akella et al. 2010), and that its OE increases tubulin acetylation (Godena et al. 2014; Kalebic, Martinez, et al. 2013), multiple studies started to assess the importance of tubulin acetylation for transport dynamics by modulating ATAT1 expression levels. Of note, while its preferred target is α-tubulin, ATAT1 can also self-acetylate, as shown by mass-spectrometry analysis that identified acetylated lysin residues on ATAT1. A series of in vitro studies revealed that ATAT1 autoacetylation promotes tubulin acetylation, but it is not essential to modulate its interaction with MT (Kalebic, Martinez, et al. 2013). Nonetheless,

we cannot rule out that ATAT1 autoacetylation might have not-yet characterized downstream effects that could modulate transport dynamics via secondary interacting partners.

In the contest of axonal transport, the role of ATAT1 emerged as largely debated. In *C. elegans*, loss of MEC-17 (ATAT1 homolog) impairs the transport dynamics of mitochondria and kinesin-3-associated synaptic vesicles along the axons of mechanosensory neurons (Neumann and Hilliard 2014). On the contrary, in mouse DRG neurons and hippocampal neurons, loss of ATAT1 didn't correlate to defects in the transport of NGF+ vesicles and mitochondria, respectively (Morley et al. 2016). It is therefore possible that the contribution of ATAT1 in maintaining and regulating transport dynamics might be either species- or neuronal type-specific.

In our study, we demonstrate a predominant role for ATAT1 in regulating organelles transport along axons of mouse callosal projection neurons, primary cortical neurons, and D. melanogaster motoneurons. We show that the transport defects associated to the absence or KD of ATAT1 can be restored by, respectively, the OE of ATAT1 or the K40Q α-tubulin variant in mouse cortical neurons. Similarly, in drosophila motoneurons the HDAC6 KD can rescue tubulin acetylation levels and transport defects caused by KD of atat1 or atat2. These results were confirmed by *in vitro* data showing that unacetylated MTs prevent the trafficking of loaded motile vesicles, compared to acetylated MTs. Thus, in accordance with previous reports, acetylation might regulate transport dynamics in mouse cortical neurons as well as in Drosophila motoneurons, but not in other systems where this correlation was not identified.

2. Vesicles as self-sustaining organelles modulating their own transport

We show that the displacement of vesicles along MTs is required to promote tubulin acetylation, suggesting that the vesicular pool of ATAT1 plays a crucial role in modulating this MTs PTM. The pharmacological inhibition of both anterograde and retrograde motors via ciliobrevin, or the KD of the dynein-associated adaptor protein Lis 1 (adaptor protein required for dynein processivity) which selectively impairs retrograde transport, significantly decrease vesicular transport and tubulin acetylation levels.

These findings were complemented by in vitro assays that evaluated the ability of vesicles isolated from either WT or ATAT1 KO mice to acetylate MTs. While ATAT1-positive WT vesicles promoted MT acetylation in the presence of Ac-CoA, Ac-CoA was not sufficient when

associated to ATAT1 KO vesicles. These data suggest that the vesicular pool of atat1 promotes the acetylation of MTs by catalyzing the addition of acetyl groups to MTs.

With this study we firstly show that ATAT1, apart from having a cytoplasmic distribution and being associated to MTs (Kalebic, Martinez, et al. 2013), is also partially distributed on vesicles. Secondly, we provide evidence for a functional role of the ATAT1 vesicular pool in the regulation of the vesicular transport itself. We propose a model where vesicles appear as self-sustaining organelles capable of contributing to the mechanisms that fuel their own trafficking along MTs. The vesicular pool of ATAT1 serves as enzymatic pool that can locally covert acetyl-CoA into acetyl groups, available for their addition to lysin 40 residues within the MT lumen.

In agreement with our findings, a previous study described motile vesicles as energetically-autonomous, able to modulate their own transport by generating a local source of ATP, essential to sustain the bidirectional activity of molecular motors, through the glycolytic enzymes expressed at their membranes (Hinckelmann et al. 2016). In this way, vesicles do not rely on the cytosolic source of ATP but on the local pool produced thanks to their own associated glycolytic machinery. As an example, the motor protein and ATPase MCAK associates to and catalytically depolymerizes MTs upon ATP hydrolysis (Hunter et al. 2003). A local source of ATP could therefore support not only the activity of motors but also MT dynamics which in turn sustain neuronal structure and functions. Taken ours and this study together, vesicles are emerging as organelles with multiple functions, that do not only serve their canonical intracellular function but that can also present as motile platforms carrying the molecular machinery required to modulate their own motility. Given their functional autonomy, we speculate that they could additionally retain the ability of sustaining their own structural integrity, but this question has not been addressed yet.

3. Insights into the molecular cascade modulating MT acetylation

Here, we show that the loss of elongator in mouse cortical neurons as well as in motoneurons of *Drosophila* third insta larvae correspond to decreased tubulin acetylation and axonal transport defects.

We first investigated the role of the Elongator complex in the regulation of this PTM and axonal transport dynamics as our laboratory showed its importance for the migration and maturation of projection neurons in the cerebral cortex. Its loss of expression leads to

reduced MT acetylation in cortical projection neurons (Creppe et al. 2009; Tielens et al. 2016). Moreover, some subunits of the elongator complex were identified along with ATAT1 on motile vesicles isolated from adult mouse brain (Hinckelmann et al. 2016).

In cultured cortical neurons, depletion of its subunits Elp1 or elp3 led to a decrease of tubulin acetylation levels (Creppe et al. 2009). In agreement, forebrain extracts from elp1-depleted mice, as well as from fibroblasts derived from FD patients lacking the elp1 subunit, displayed decreased tubulin acetylation levels (Naftelberg et al. 2016). Although insights into the molecular mechanisms regulating the elongator-mediated tubulin acetylation came from non-neuronal cell lines, it was shown that OE of elp3 but not of an HAT-defective elp3 variant increases tubulin acetylation levels, suggesting that elongator may modulate tubulin acetylation through its HAT domain (Creppe et al. 2009).

The link between the elongator complex and PTMs on MT subunits is however not only restricted to tubulin acetylation. Two recent studies have recently shed new lights into a new non-canonical function of Elongator, which was found to regulate MT stability through tubulin poly-glutamylation. Accordingly, during the process of asymmetric cell division, Elongator associates with MTs and stabilizes their dynamics by increasing their polymerization speed and decreasing their catastrophe dynamics (Planelles-Herrero et al. 2022). Elongator regulates MT dynamics by binding to MTs growing ends through its subunits 1-2-3, and to tubulin heterodimers via the subunits 4-5-6. As a complex, it can therefore concentrate tubulin heterodimers at MT ends, promoting MT polymerization. Interestingly, elongator shows a selectivity for poly-glutamylated tubulin, driving the survival and enrichment of MTs with this specific PTM (Planelles-Herrero et al. 2023).

Our results strongly support the well-known correlation between tubulin acetylation and axonal transport and given the functional analogy between Elongator and ATAT1 in modulating tubulin acetylation, we unravel the correlation between these two players in the molecular cascade that catalyze the acetylation of lysin40 residues along MTs. Their correlation was not direct, as loss of Elongator affects neither the expression nor the activity of ATAT1. However, we identified Acly and ACSS2, the enzymes that catalyze the cleavage of citrate and acetate, respectively, into acetyl-CoA, to be down-regulated in the absence of Elongator. Differently from the cytosolic enrichment of ACSS2, we observed a vesicular enrichment for Acly where he was co-detected with ATAT1 and the Elongator subunits elp1 and elp3. These same players have been identified on sorted endosomes isolated from

embryonic stem (ES)-cell derived motoneurons via magnetic purification upon SILAC protein labelling (Debaisieux et al. 2016).

We further showed that the vesicular fraction is able to generate acetyl-CoA, suggesting that the vesicular pool of Acly is functionally active. Secondly, we identified a functional correlation between ATAT1 and Acly as: 1) the pharmacological inhibition of Acly in mouse cortical neurons, its KD in flies, or its downregulation in FD fibroblasts phenocopied the effects on tubulin acetylation and axonal transport observed upon loss of Elongator; 2) these defects could be rescued upon Acly OE; 3) elp1 loss in FD fibroblasts displayed decreased Acly stability, possibly via direct interaction as shown by immunoprecipitation assays. We therefore propose a model which is likely occurring on vesicles and that involves the functional cooperation between Elongator, Acly and ATAT1, where Elongator regulates the stability of Acly, which in turn regulates the acetyl-CoA availability providing to ATAT1 the substrate required for acetylating MTs.

Our study strengthens the view of motile vesicles as self-sustaining organelles that, in addition to their intracellular canonical functions, are capable of sustaining their energetic needs and transport kinetics by regulating enzymatic signaling cascades. By expressing the players of the preparatory and pay-off phase of the glycolysis, along with those of the α-tubulin acetylation molecular cascade, vesicles propel their own activity and motion, respectively. Given the recent evidence that describes Elongator as a regulator of MTs stability and long-life, we can therefore speculate that its presence on vesicles might serve multiple purposes. While on the one hand, he interacts with Acly to initiate the signaling cascade that leads to tubulin acetylation, on the other hand it might modulate MT stability, therefore preventing MT breakage and degeneration. These two functions together might represent another self-sustaining mechanism adopted by vesicles to favor their own motility.

4. Role of tubulin acetylation in neurological diseases.

We show that loss of Elongator corresponds to decreased tubulin acetylation and axonal transport defects in mouse cortical neurons and motoneurons of Drosophila. At a cellular level, loss of ATAT1, and therefore decreased tubulin acetylation, has been correlated to increased axon growth and branching by increasing MT debundling at nascent axonal points, MT invasion at growth cones and plus-end dynamics of MTs (Wei et al. 2018). Tubulin

acetylation emerges as a critical PTM that controls axonal growth and branching by dampening MT dynamics.

To better understand the impact of this PTM during development and aging, the ATAT1 KO mouse was largely interrogated at a systemic level. While, similarly to the brain, ATAT1 expression was lost in multiple other tissues, mice appeared viable (Kalebic, Sorrentino, et al. 2013; Kim et al. 2013) and with minor morphological abnormalities, including a slightly deformed dentate gyrus (Kim et al. 2013), enlarged lateral ventricles accompanied by impaired neuronal migration to the septum and striatum (Li et al. 2019), as well as axon overbranching in the somatosensory cortex (Wei et al. 2018).

Given the importance of MT dynamics in regulating neuronal morphology, and the importance of axonal branching and neuronal connectivity, it was highly unexpected when ATAT1 depleted mice were found to display only an anxiety-like behavior (Kalebic, Sorrentino, et al. 2013; Wei et al. 2018). All together, these findings suggest that alterations in tubulin acetylation may be attenuated or overcome at postnatal stages by compensatory mechanisms that would prevent an impact on neuronal connectivity and behavior establishment. Together with FD, this phenotype has been also described in a wide range of neurological diseases, such as HD (Dompierre et al. 2007), PD (Godena et al. 2014), CMT2F and dHMN2B (d'Ydewalle et al. 2011; Kim et al. 2016), CMT2A (Kumar et al. 2023) and ALS (Guo et al. 2017).

However, an extended set of evidence describe decreased levels of tubulin acetylation and impaired axonal transport kinetics in *in vitro* models for neurodegenerative diseases. We show decreased tubulin acetylation and axonal transport defects in skin-derived fibroblasts from FD patients bearing a loss-of-function mutation in the Elp1 subunit of the Elongator complex which leads to its disassembly. In these models, it is likely that disruption of cellular homeostasis results from a combination of cellular alterations that synergize leading to neurodegeneration. In these models, rescuing tubulin acetylation levels ameliorates only partially the disease phenotype, which might only be fully reversed when considering all the other secondary factors. Accordingly, flies expressing PD-associated mutations that correlate with deacetylated MTs and impaired transport display climbing and flight defects. While these defects could be rescued only partially upon HDAC6 KD, suggesting that the targeted molecular pathway is not the only contributor to the behavioral phenotype, the rescue was

complete upon pharmacological treatment with TSA, aspecific HDAC6 inhibitor whose effects might be ascribed also to secondary targets (Godena et al. 2014).

Given the potential of HDAC6 inhibitors to recover the tubulin acetylation levels and transport abnormalities found in multiple neurodegenerative diseases, the possibility of using such a compound in the clinic has been an option widely evaluated. The development of a compound that could restore even only partially one of the molecular phenotypes associated with these diseases might lead to the identification of an effective therapeutic strategy.

5. Perspectives

We show that the enzymatic machinery contributing to the acetylation of lysin40 residues of α-tubulin localize on vesicles and propose a model where vesicles exist as self-sustaining organelles capable of modulating MT acetylation to support their own trafficking. Through vesicles, ATAT1 can be distributed throughout the length of neurites and approach MTs at every potential site of luminal entry.

While we describe a mechanism through which the acetylation machinery composed of Elongator/Acly/ATAT1 is heterogeneously distributed along axons, it remains an open question how ATAT1 can enter the MT lumen to exert its acetylating activity. One hypothesis suggests that ATAT1 can access the MT lumen either by its extremities or through breaking points along its lattice, depending on the integrity and stability of the MTs assessed (Coombes et al. 2016). On the other hand, *in vivo* studies identified a stochastic distribution of acetylation segments along MTs, both at MT ends and along their length (Ly et al. 2016; Szyk et al. 2014). The answer to this debate might not to be restrictively identified in only one of these two hypotheses, but rather in a scenario where both possibilities are contemplated. As the entry of ATAT1 into the MT lumen represents the final step of the acetylating cascade, unravelling how MTs can be internalized into the MT lumen, would not only be informative on the catalyzing activity of ATAT1, but would also provide new information of the other not-yet well-characterized intraluminal PTM that also occurs on lyin40 residues (tubulin methylation) (Park et al. 2016).

One of the latest identified PTMs is the methylation of lysin40 residues of α-tubulin facing the inner side of the MT lumen, the same sites that are targeted by ATAT1 to promote tubulin acetylation. As two distinct PTMs can occur on the same residues, and as tubulin acetylation

is known to contribute significantly to MT properties, the idea that this second PTM could also contribute to MTs regulation started to be investigated.

In accordance with the fact that SEDT2 can methylate both soluble and polymerized tubulins (Park et al. 2016), *in vitro* studies showed that tubulin methylation promotes MT nucleation and polymerization (Xie et al. 2021). Compared to the contribution of acetylation which ensures MT stability (Portran et al. 2017; Xu et al. 2017), methylation regulates MT polymerization. These two PTM might therefore have a complementary role in regulating MT homeostasis, where one promotes MT formation and the other ensures their long-lasting stability. By promoting MT formation, tubulin methylation regulates the MT number and the polarized morphology of neurons, ensuring their morphological transition and cortical migration during brain development (Koenning et al. 2021; Xie et al. 2021).

However, whether tubulin methylation might also play a role in regulating transport dynamics has not yet been addressed. At the tip of neurites or growth cones, the expression pattern of tubulin methylation is discordant with that of tubulin acetylation but overlapping with that of tubulin tyrosination (Koenning et al. 2021). It has been reported that the expression patterns of acetylated and tyrosinated tubulin segregate along neurites forming differentially modified MT bundles with different polarity and affinity for motor proteins (Balabanian et al. 2017; Tas et al. 2017). It would be therefore interesting to assess the functional correlation between tubulin methylation and tyrosination, whether they have similar impact on transport dynamics.

Interestingly, cell migratory defects observed upon loss of ATAT1 (Li et al. 2012; Xie et al. 2021) could be rescued by OE of an enzymatically-active SETD2 variant or tubulin^{K40F}, tubulin variant that mimics tri-methylation. Contrarily, however, similar migration defects induced by loss of SETD2 could not be rescued by overexpressing the tubulin K40Q variant that mimics K40 tubulin acetylation (Xie et al. 2021). While these results suggest that tubulin methylation and acetylation are two functionally correlated PTMs, more investigations are needed to understand why this cooperation might be unidirectional. Together with the analogous role for these two PTMs in regulating neuronal development and migration, their decreased expression has additionally been correlated to comparable behavioral outcomes. Accordingly, both the ATAT1 KO mice (Wei et al. 2018) and heterozygous SEDT2 KI mice display an anxiety-like behavior (Koenning et al. 2021). Therefore, on the one hand these two PTMs occurring at the same K40 residues might play different roles at a sub cellular level, as in the regulation of

MTs homeostasis. On the other hand, as shown by the cell migratory defects and behavior-like phenotypes observed upon the loss of either one of the two catalyzing enzymes, these two PTMs might be functionally correlated in their downstream effects at a cellular and behavioral level. Overall, more studies are needed to dissect the contribution of tubulin methylation at both molecular and cellular level, and to clarify the correlation between this PTM and the tubulin acetylation.

Chapter II

The study presented in **chapter II** aims at providing a comprehensive characterization of the transcripts associated to *motile cargos*, and uncovering whether some of these transcripts could undergo direct translation while being transported. In this chapter, we provide a detailed overview of the toolbox set-up to address these objectives. First, we developed a methodology to isolate the global population of *motile cargos* by leveraging the Thy1:p50-GFP mouse model and purifying via fluorescent activated particle sorting the p50-GFP-associated events – the *motile cargos*. We are currently analyzing: 1) the proteomic composition of the *motile cargos*, to delineate the cargo subtypes isolated through this methodology; 2) the transcriptome of the *motile cargos*, to identify their associated transcripts. Secondly, to track in live imaging the spatial trajectories of a given mRNA as well as its translation dynamics, we expressed the SunTag system in N2a cells and developed a protocol to induce their differentiation in neuron-like cells recapitulating axonal transport and local translation.

1. How to investigate the transcriptome of *motile cargos*

Here, we describe a newly set-up methodology to characterize the transcriptome and proteome of *motile cargos*. To this aim, we used the Thy1:p50-GFP mouse (Caviston et al. 2007; Ross et al. 2006) which expresses the dynamitin subunit p50 fused to GFP under the neuronal promoter Thy1. As p50 modulates the recruitment of cargos to the dynein/dynactin subcomplex, this mouse model enables us to track and/or isolate motor-associated cargos, thereafter defined as *motile cargos*. Using fluorescent activated particle sorting (FAPS), we isolated *motile cargos* from adult mouse brain lysate and validated their morphological integrity as well as retention and quality of their associated RNAs. We are currently generating proteomic and transcriptomic datasets of brain-isolated *motile cargos*. While the first one will characterize the cargo subtypes associated to the dynein/dynactin complex and verify the presence of their associated translation and transport machinery, the second will identify the associated mRNA populations. Taken together, these two datasets will provide a comprehensive picture of: 1) all the mRNAs, silent or ribosome-associated, in RNP granules or organelle-associated, that can undergo retrograde or bidirectional transport; 2) the

organelle subtypes isolated through our method that could, all or in part, cotransport the identified transcripts.

Since the identification of the translation machinery along neurites and synapses, which corresponded to active translation sites (Hafner et al. 2019; Shigeoka et al. 2016), multiple studies broadly provided spatially and temporally resolved snapshots of the transcriptome of subcellular compartments (as neurites or synapses, as opposed to cell soma). Their physical isolation was achieved via a broad range of strategies, both *in vivo* (microdissection of mouse hippocampal neuropils of the C1 region, fluorescent-activated synaptosomes sorting from mouse brain sub regions) (Cajigas et al. 2012; Fusco et al. 2021; Oostrum et al. 2023) and *in vitro* (laser dissection of dendrites or growth cones of cultures cultures) (Perez et al. 2021; Zivraj et al. 2010). However, this information has never been refined to reach a nanometer resolution and define the transcriptome associated to motors.

The proteomic composition of organelles has long been investigated upon their isolation either via sedimentation or via sucrose gradient centrifugation. However, with new technological advancements, only recently researchers started to shine lights onto organelles-associated transcriptome. By combining RNA-seq of affinity purified-early endosomes with spatial transcriptomics on cells that were treated or not with the translation inhibitor puromycin, *Popovic and colleagues* not only succeeded in characterizing the organelle-associated transcriptome, but also identified those transcripts whose association to endosome is translation-dependent (Popovic D, Nijenhuis W, Kapitein C L 2020). More recently, a transcriptomic approach was developed to enable the identification and differentiation between surface and luminal resident mitochondria transcriptome (Jeandard et al. 2023). This method consists in exposing mitochondria to an RNase gradient and inferring, based on the transcript's resistance to this gradient, the transcript's localization (surface-localized or luminal resident) in relation to mitochondria membranes. The specificity and sensitivity of this method was validated by identifying as resident transcripts almost all mitochondria (mt)-tRNAs, as well as (mt)-long coding and non-coding RNAs, and as surface-associated transcripts multiple mRNAs and cytosolic tRNAs (Jeandard et al. 2023). While these datasets have been generated from non-neuronal cells as human Hela (Popovic D, Nijenhuis W, Kapitein C L 2020) and HEK293 cells (Jeandard et al. 2023), organelles- and motors-associated transcriptome have not yet been investigated in mouse neurons. Our datasets will

therefore provide a new understanding of how transcripts are translocated via long-distance transport to peripheral localizations.

Peripheral localization of mRNAs relies on their association to RBPs to form RNP granules and on the direct or indirect association to motor proteins.

Upon their binding, RBPs instruct the associated mRNA regarding its final localization as well as its translation state, whether it has to stay silent or upon ribosome binding undergo translation. As an example, TDP43 is a polyvalent RBP modulating the transport of different RNP granules. It was identified in granules enclosing Neurofilament-L (Nefl) transcripts, for which it regulates their bidirectional transport by selectively promoting their anterograde motion (Alami et al. 2014). Further insights into the functions of TDP43 came from investigating the dynamics of granules enclosing Rac1 mRNAs. While the RBP Staufen recruits to the granules the dynein/dynactin complex for their retrograde transport, TDP43 in association with FMRP recruits kinesin1 to modulate their anterograde transport and dendritic distribution within spines, where it triggers their translation (Chu et al. 2019).

Thus, through the synergistic activity of RBPs and motors, RNP granules are highly motile. Along RGC axons, 20% of Cy3-labelled granules undergo bidirectional transport displaying both slow (<0.1 μm/sec) and fast (>1 μm /sec) dynamics (Cioni et al. 2019). When looking at single transcripts, the extensively characterized actin mRNA also displays a high degree of motility. Along dendrites of hippocampal neurons, actin mRNAs traffic with bidirectional motion and fast dynamics (1-1.3 μm/sec). Surprisingly, the number of detectable moving transcripts increased by extending the duration of the acquisition, and almost all actin mRNAs displaced over recordings of 1h30min (only ~6% stationary particles) (Yoon et al. 2016). These data revealed that actin is a highly dynamic transcript, and that it undergoes alternating cycles of immobility and motion. Transcripts that displayed equally high dynamics are cyclinD2 and Kif26a, whose transport was recorded *in vivo* along radial glia processes (2.4 μm/s) (Pilaz et al. 2016). While many RNP granules might be transported directly by motors, many can hitch a ride on membrane-bound organelles (Cioni et al. 2019; Liao et al. 2019). This was true when looking at both the whole RNP granules population or at target transcripts known to undergo bidirectional trafficking along neurites. Accordingly, along RGC axons more than half of all Cy3-labelled RNP granules were cotransported with endosomes (24% with EE; 40% with LE) (Cioni et al. 2019), and the axons of cortical neurons 20% of actin mRNA were found to

colocalize with Lamp1+ lysosomes (Liao et al. 2019). These studies suggest that hitchhiking might be a predominant mechanism through which transcripts are transported along neurites. Whether this mechanism applies only to endosomes and lysosomes or extends to other motile organelles as mitochondria, SVPs and DCVs has still to be seen. Our experimental set-up aims at providing an unbiased characterization of all trafficking mRNAs, independently of their interaction to motors (direct or indirect) and on the type or cargo they might be associated to (RNP granules or membrane bound organelles).

2. Can vesicles self-sustain their own proteome?

Although membrane-bound organelles have long been characterized for their canonical functions, emerging evidence suggests they can also retain secondary properties that allow them to self-sustain their own transport via two mechanisms.

This model firstly emerged from a study that reports motile vesicles as energetically autonomous, able to produce a local source of ATP needed to modulate the processivity of their associated molecular motors and therefore for their MT-based bidirectional transport (Hinckelmann et al. 2016). Proteomic analysis of vesicles isolated from mouse brain showed that they retain all enzymes involved in the two phases of the glycolytic cascade that convert glucose into pyruvate by generating ATP. In addition, complementary functional assays identify ATP as the fuel used by the vesicles to modulate their own transport. Accordingly: 1) vesicular transport could be initiated with the only addition of glucose and low amount of ATP; 2) when the first enzyme of the preparatory phase or any of the pay-off phase were pharmaceutically inhibited or KD, respectively, the vesicular transport was abruptly decreased (Hinckelmann et al. 2016). All together, these evidences describe vesicles as capable of producing the energy required for their motility via their associated glycolytic machinery. A local source of ATP available when most needed would thus retain a spatial and temporal advantage over the cytosolic source of ATP to sustain efficiently the vesicles' needs. This model was complemented by our studies which show how vesicles retain the components of the enzymatic cascade modulating MTs acetylation, which in turn regulates vesicular trafficking (Even et al. 2019, 2021). In agreement, we show that: 1) contrarily from vesicles isolated from ATAT1 KO mice, ATAT1-positive vesicles can acetylate unmodified MTs suggesting that the vesicular pool of ATAT1 can modulate this PTM; 2) the motor-dependent

vesicular displacement along MTs is necessary to ensure MT acetylation, as inhibition of motor activity leads to decreased levels of this PTM (Even et al. 2019, 2021).

However, whether vesicles can either sustain their own MT-based transport via other not-yet identified mechanism, or their own functions, or their own structural integrity has not been yet addressed.

Although not yet known for vesicles, it has been reported that also ribosomes can control their structural integrity by remodeling their proteomic composition (Fusco et al. 2021; Shigeoka et al. 2019). By labelling newly translated proteins via SILAC and subsequently isolating compartment-specific ribosomes for their proteomic studies, newly synthesized ribosomal proteins were identified in pre-existing ribosomes. The newly incorporating ribosomal proteins are all surface proteins within the ribosomal architecture and have very short half-lives compared to other ribosomal proteins (Fusco et al. 2021). Thus, ribosome can replace existing subunits with newly translated ones to ensure their structural integrity. This strategy may represent an advantageous way to regulate the pool of ribosomes within peripheral compartments, as opposed to the degradation of pre-existing and the synthesis of new ribosomes that might be more time and energy demanding. Furthermore, the incorporation of newly translated subunits into mature ribosomes appears as a highly dynamic process, as different subunits are incorporated in different environmental conditions as under oxidative stress (Fusco et al. 2021). Ribosomes could therefore specialize their proteomic composition to respond efficiently to external stimuli.

It is now clear that ribosomes are localized on the surface of membrane bound organelles, as lysosomes and endosomes (Cioni et al. 2019), ER tubules (Koppers et al. 2022) and ER-derived vesicles (Carter et al. 2020). While organelle-associated ribosomes might undergo dynamic subunits replenishment to ensure their integrity (Fusco et al. 2021; Shigeoka et al. 2019), we hypothesize that organelles themselves might leverage the activity of their associated translation machinery to sustain their morphology and therefore functionality. Organelle-associated vesicles could translate structural proteins important for their morphological integrity, for their MT-based transport (i.e. molecular motors and adaptor proteins), or for their canonical and non-canonical functions (i.e. membrane proteins modulating their anchoring/fusion properties or surfaces-expressed enzymes that contribute to their activities). We hypothesize that some of the transcripts that will be identified through our

motile cargos' transcriptome dataset are associated to ribosomes and undergoing active translation. If the transport of these transcripts occurs via hitchhiking, the correspondent newly-translated proteins could have a localized function in sustaining either the integrity of activity of the associated vesicles. If the transport of these transcripts occurs via direct interaction with the motors, the newly translated proteins might sustain the integrity and activity of the motor proteins.

Given the importance of the vesicular pool of Acly and ATAT1 in regulating MT acetylation and transport dynamics, we speculate that Acly and ATAT1 transcripts could be associated to vesicles and undergo active translation to supply their vesicular pool. As proteins, we identified Acly and ATAT1 in the vesicular fraction isolated from mouse cortex (Even et al. 2019, 2021). Through IF and IP studies performed on non-neuronal cells, ATAT1 was additionally found on clathrin-coated pits via interaction with the clathrin adaptor AP2 (Montagnac et al. 2013), and on mitochondria by interacting with MFN2 (Kumar et al. 2023). Proteomic studies revealed the presence of ATAT1 also on signaling endosomes from ES-derived motoneurons (Debaisieux et al. 2016). Similarly, mass spectrometry analysis identified Acly on p50-associated motile vesicles purified from mouse brain (Hinckelmann et al. 2016), lysosomes isolated from mouse fibroblasts (Mosen et al. 2021) and neuronal signaling endosomes (Debaisieux et al. 2016). While much starts be characterized on the vesicular localization of Acly and ATAT1 proteins, little is known on their correspondent transcripts. Although, to our knowledge, transcriptomic profiles are available only for endosomes (Popovic D, Nijenhuis W, Kapitein C L 2020 - dataset not included in the preprint) and mitochondria (Jeandard et al. 2023) isolated from non-neuronal cells, Acly mRNA might be a transcript worth studying. Acly mRNA has not only been identified as a surface-attached mitochondrial transcripts (Jeandard et al. 2023), but also as an interactor of SYNJ2A, adaptor protein that binds to mRNAs for their recruitment onto mitochondria modulated by its binding partner SYNJ2BP (Harbauer et al. 2022). Whether Acly mRNA is localized on mitochondria only for its long-distance transport, for its import into mitochondria or to be locally translated has yet to be investigated. Our transcriptome dataset on *motile cargos* will thus report if Acly and ATAT1 mRNAs are located on these motile units for long distance transport.

We also speculate that among the transcripts that could be identified on *motile cargos* are those encoding for motor proteins. Their local translation might serve the structural integrity and functionality of the associated motor proteins. Interestingly, KIF1A mRNA is the only motor-encoding transcript identified on the mitochondria outer membrane (Jeandard et al. 2023). Interestingly, this transcript falls within the top 45 proteins with the shortest half-life measured *in vivo* from mouse brain cortex homogenate (Fornasiero et al. 2018). KIF1A is essential to modulate the DENN/MADD-dependent transport of DCVs (Lo et al. 2011; Niwa et al. 2008) and the BORC/Arl8-dependedant one of lysosomes (Guardia et al. 2016). Given its essential role for these organelles' subtypes and its rapid turnover, we hypothesize that the number of KIF1A motors associated to a given cargo (i.e., membrane-bound organelle or RNP granule) is maintained constant by a steady supply of newly synthesized proteins, achieved by a local translation of trafficked KIF1A mRNAs. Whether our transcriptome dataset will highlight other motor-encoding transcripts than KIF1A will have to be seen.

The motor-based trafficking of mRNAs encoding for motor proteins might also be supported by the concomitant transport of the Elongator complex. Subunits of the Elongator complex were identified on vesicles isolated from mouse brain (Even et al. 2021), and on signaling endosomes from ES-derived motoneurons (Debaisieux et al. 2016). We showed that Elongator regulates the stability and expression levels of Acly, the enzyme that catalyze the production of Acetyl-CoA required for the ATAT1-mediated acetylation of MTs (Even et al. 2021). While we propose this mechanism to occur on vesicles, one might also speculate that the vesicular pool of Elongator could not only contribute to MT acetylation but also exert its canonical role as a tRNA modifier. By modifying tRNAs at the wobble position (U_{34}), modification known to correlate with the decoding of preferential codons (AAA, GAA, and CAA) during translation elongation, Elongator regulates the codon-biased translation of a subgroup of genes (Goffena et al. 2018; Rapino et al. 2021). Among the genes with a high content of U_{34}-codons and whose translation was decreased upon loss of Elongator are several motor proteins, including KIF4A, KIF14, KIF15, KIF13B, KIF5A, KIF5C, and KIF1B. Whether the correspondent transcripts undergo bidirectional transport and whether their Elongator-dependent translation occurs on vesicles is an open question that hasn't been addressed yet.

Lastly, we hypothesize that transcripts encoding for constitutive proteins could additionally be found as associated to *motile cargos*. Pulling down assays from non-neuronal cells revealed that among the transcripts associated to the EE-bound FERRY complex are mRNAs encoding for endosomal proteins, including RAB5C, RAB7A and RAB1B (Schuhmacher et al. 2023). It seems plausible to think that endosomes could sustain the turnover of their constitutive proteins by translating locally the required subunits. Most interestingly, the FERRY complex also modulates the EE-mediated transport of a broad range of nuclear-derived mitochondria mRNAs encoding for mitochondrial matrix proteins (TIMM17B, TOMM40), mitochondrial ribosomes (MRPL37, MRPL40) and components of the mitochondrial cellular respirations (ATP5B) (Schuhmacher et al. 2023). In agreement, along RGC axons both Rab5- and Rab7-expressing endosomes were found to shuttle RNP granules. However, as only a perturbation of Rab7 activity and LE maturation reduced translation events along axons, only LE play a role in regulating local translation (Cioni et al. 2019). Live imaging studies identified on LE foci of translating Lamin B2 (LB2) peptides, important to sustain the morphology and membrane proprieties of mitochondria found in close proximity (Cioni et al. 2019). This study advocates for a functional cooperation between organelles, where the associated translation of one could benefit the integrity of the other. It still remains to be determined which are all the transcripts encoding for organelles proteins undergoing active transport and whether some of these might undergo active translation while associated to the transport machinery.

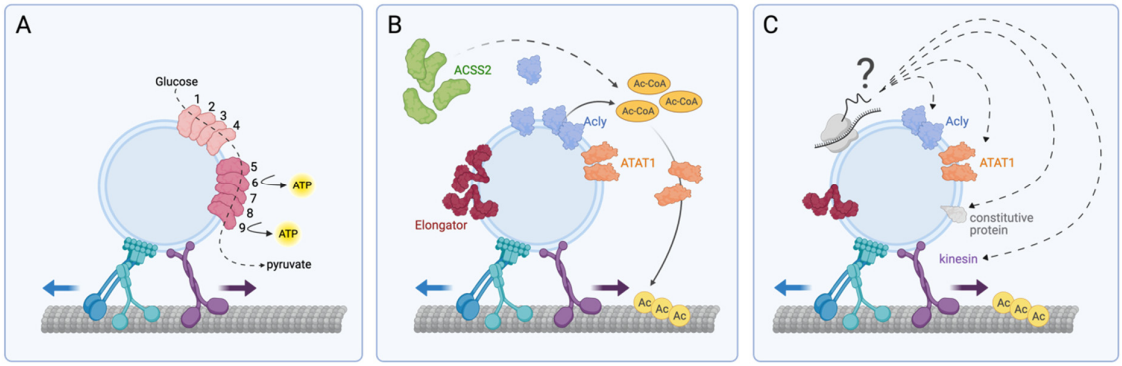

Figure 24. Membrane-bound organelles as self-sustaining machineries. (A) Motile vesicles retain all the enzymes of the glycolytic cascade that convert glucose into pyruvate by generating ATP from ADP. Enzymes of the preparatory phase are: HK (1), PGI (2), PFK (2), ALDO (4); enzymes of the pay-off phase are: GAPDH (5), PGK (6), PGM (7), ENO (8), PK (9). The ATP produced via glycolysis sustains the processivity of the molecular proteins associated to the vesicles. (B) Vesicles shuttle the enzymatic machinery regulating MTs acetylation and therefore transport dynamics. (C) Hypothesized model of *motile cargo*-associated translation.

Possible transcripts undergoing active translation on *motile cargos* encodes for: Acly and ATAT1, key enzymes in the molecular cascade regulating MT acetylation; constitutive proteins essential for the *motile cargo*'s integrity; kinesin motor proteins, essential for the trafficking of the *motile cargos*.

3. Setting-up the toolbox to unravel the correlation between the transport and translation machinery

From defining the transcriptome of peripheral compartments, a step-forward towards the understanding of the translation regulation of peripheral transcripts while maintaining a spatial resolution was achieved with the advent of the RiboTag technology (Shigeoka et al. 2016). The cre-driven expression of the HA-tagged ribosomal protein 22 (rpl22) in a spatially-restricted brain area enabled the characterization by HA immunoprecipitation of the ribosome-associated mRNAs, therefore generating for the first time translatome datasets. This technology has been extended to multiple neuronal subtypes as RGC axons (Shigeoka et al. 2016), glutamatergic neurons (Glock et al. 2021), and midbrain dopaminergic neurons (Hobson et al. 2022).

In order to provide a deeper level of understanding into the long-distance trafficking of mRNAs, we decided to complement the *motile cargo*'s transcriptome with two other analyses: 1) *motile cargo*'s translatome, to pinpoint the ribosome-associated transcripts out of the global mRNAs population; 2) live imaging of the translation dynamics of candidate mRNAs, to assess whether a given mRNA trafficking at axonal transport velocities can undergo active translation. By combining these two methods, we aim at bridging the gap between the available transcriptome and translatome datasets and the limited knowledge on vesicle-associated translation based on candidate-based approach studies.

To meet the first aim, we crossed the Thy1:p50-GFP mouse (Caviston et al. 2007; Ross et al. 2006) with the RiboTag mouse (Shigeoka et al. 2016) to generate a triple transgenic mouse expressing tagged ribosomes (rpl22-HA) and tagged *motile cargos* (p50-GFP) in VGlut1-expressing glutamatergic neurons. With this mouse, we aim to set up the IP of HA-tagged ribosomes from p50-GFP+ and p50-GFP- sorted fraction and elute the associated transcripts. This method would undoubtedly identify mRNAs engaged in translation.

For the second goal, we decided to employ the SunTag technology, which enables the live imaging tracking of a candidate mRNA as well as that of its correspondent translating peptide

(Yan et al. 2016). This strategy requires expression of three plasmids which, briefly, code for: 1) a candidate mRNAs, with a sequence of epitopes ("SunTag epitopes") upstream its CDS and hairpin loop-like secondary structures downstream the stop codon; 2) a mCherry-tagged cap proteins, that recognize the mRNA hairpin loops therefore labelling mRNAs; 2) a GFP-tagged nanobody, that recognize the SunTag epitopes thus labelling the peptide as it translates. A few reports successfully managed to express the SunTag system in mouse hippocampal neurons (Wang et al. 2016; Wu et al. 2016), as well as *in vivo* in Drosophila embryo (Dufourt et al. 2021). However, this strategy presents multiple technical challenges: 1) the expression level of each plasmid needs to be finely regulated, to ensure that the fluorescent background due to the unbound GFP-antibodies and mCherry-cap proteins is not too strong to mask the mRNA and protein signal, but not too weak to prevent a sharp visualization of the mRNA and peptide foci (Ruijtenberg et al. 2018); 2) the imaging set-up required for single molecule imaging as the SunTag technology requires a sensitive camera as EMCCD or sCMOS applied to a wide-field, confocal, spinning disk confocal or total Internal Reflection Fluorescence (TIRF) microscope (Ruijtenberg et al. 2018; Wu et al. 2016; Yan et al. 2016). To overcome some of the challenges associated with primary neuronal cultures (neurons are not mitotic cells, they cannot survive cycles of freezing and thawing, and are more challenging to transfect compared to other cell lines), we opted to use a stable neuronal cell line that would closely resemble and recapitulate the features of primary neurons.

We chose N2a cells, as the practice of using a serum-free media supplemented with retinoic acid has been widely used to induce their differentiation in neuron-like cells. Some studies modulated the N2a differentiation into neuron-like cells without addition of retinoic acid to the serum-free medium, showing that their neurites transcriptome was widely overlapping with that of mouse cortical neurons (Taliaferro et al. 2016). However, by complementing the differentiation media with retinoic acid, the differentiated cells displayed longer neurites and higher branching complexity (Kumar and Katyal 2018; Namsi et al. 2018). We therefore decided to reproduce this differentiation paradigm to generate neuron-like cells and assess whether they could recapitulate the dynamics of axonal transport and the local translation events that characterize primary neurons. We showed that the differentiated N2a cells generated through this protocol (Namsi et al. 2018) displayed immotile lysosomes along the neurites of d-N2a cells. On the contrary, our adopted protocol that implements a 2-day

recovery step in the culture medium commonly used for neuronal culture enabled the reestablishment of the bidirectional transport dynamics of lysosomes and synaptophysin+ vesicles. Additionally, their neurites are decorated with actively-translating ribosomes throughout their length, suggesting that proteins can be locally translated. The newly-generated d-N2a cells represent a heterogenous population of immature (β-III tubulin+) and mature (neurofilament+) neurons that express excitatory synapses which count for an increased frequency of EPSC, compared to control N2a cells. Here, we provide an *in vitro* system that recapitulates a broad set of intracellular processes found in primary neurons and that is well-suited to study the translation and transport dynamics' functional correlation via the SunTag technology. We believe that the d-N2a cells generated with our implemented differentiation protocol could be broadly used as a first line system to investigate the subcellular mechanisms of non-mitotic cells. This model could bridge the gap between immortalized non-neuronal cell lines and primary neuronal cultures, as it exhibits multiple neuronal proprieties that underline the ability to form a functional network of interconnected cells. As d-N2a cells display different degrees of maturation, we cannot however exclude that by further extending the exposure to the recovery media, supplementing it with growth factors knows to trigger morphological complexity and structural plasticity (Kellner et al. 2014), or with pharmaceutical compounds known for their synergistic effects in suppressing cell proliferation and promoting neuronal differentiation as Palbociclib (Ferguson et al. 2023), they could reach a higher level of maturation.

We stably expressed two of the three SunTag system's constructs in N2a cells (GFP-antibody and mCherry-cap protein), which will be implemented with the reporter plasmid expressing the transcript of interest at the moment of the experiment before inducing their differentiation. The *motile cargo*'s transcriptome will be filtered to identify candidates for the downstream imaging analysis, chosen according to their biological functions. Based on the proposed model that describes vesicles as self-sustaining organelles (Even et al. 2021; Hinckelmann et al. 2016), we will select transcripts whose localized translation could support the integrity, activity or proprieties of their associated cargos. Via the SunTag technology we will ultimately assess whether the selected transcript can be translated while trafficking at the dynamics of axonal transport. Our study will therefore provide a new level of understanding of how the transport and translation machinery cooperate, and whether one

(translating ribosomes) can support the integrity and functionality of the other (motor/organelle system).

4. Local translation defects correlate with neurological diseases

Understanding the mechanisms regulating the peripheral localization of mRNAs and their localized translation are crucial not only for deepening our understanding of the molecular processes sustaining neuronal homeostasis, but also to shed new lights into the pathomechanisms behind several neurological diseases. Multiple diseases have been widely associated with mutations in proteins that regulate mRNAs subcellular dynamics, e.g. constituents of RNP granules, adaptor proteins tethering mRNAs to membrane-bound organelles. However, pathological alterations in mRNAs homeostasis can be achieved also by axonal transport defects correlated to mutations in genes encoding for molecular motors, adaptor proteins and components of the cytoskeleton.

Fragile X syndrome (FXS) is the most common form of inherited intellectual disability and the predominant cause of autism. It is associated with the inherited loss of the fragile X mental retardation protein (FMRP), a major constituent of RBP granules where it regulated the fate of associated mRNAs. It is known to target multiple mRNAs and therefore its loss can lead to multiple subcellular defects associated with altered localization or translation of the associated transcripts. As FMRP is a translator repressor, its loss has been associated with increased protein synthesis, phenotype described in FXS.

Among the neurodegenerative diseases which present with defects associated to the formation, transport, and translational regulation of RNP granules are SMA and ALS. The survival motor neuron (SMN) protein is key for the RBPs association to mRNAs and for the MT-based transport of the assembled granules. Its mutations impairs the RNP assembly and have been linked to SMA (Donlin-Asp et al. 2017). ALS, the most common neurodegenerative disease affecting motoneurons, is linked to different alterations including in genes encoding for the RBPs FUS and TDP-43. These two RBPs are interacting partners (Ling et al. 2010) and serve as regulators of both trafficking and translation of RNP granules (Colombrita et al. 2012; Yasuda et al. 2013). FUS can also interact with SMN (Groen et al. 2013), suggesting that SMA and ALS might share common pathomechanisms. The evidences supporting a role for mRNA homeostasis, its distribution and translation regulation in the etiology of several neurological diseases raise the question of studying the molecular

mechanisms regulating these processes. It is therefore clear that more work needs to be done to better identify which altered process could be linked to diseases. In this scenario, our study might help deepening the knowledge of the field on which mRNAs are transported, if and how they are translated. This information might further pave the way for functional studies to elucidate the effects of their dysregulations in disease.

5. Perspectives

The candidates chosen from the motile cargos' transcriptome dataset will be investigated by using the SunTag system. We will express their coding sequence (CDS) and respective 3' and 5'-UTR regions, known to be key regulators for the trafficking of mRNAs, within SunTag reporter plasmids and investigate their translation dynamics along the neurites of d-N2a cells. This live imaging analysis could unfold one of the following scenarios: 1) the transcript is not translated along the neurites; 2) the transcript undergos active translation along neurites but without trafficking at the velocities of axonal transport dynamics; 3) the transcript displays axonal transport dynamics ($\geq$1 μm/s) while being translated. However, we cannot exclude that under different experimental conditions translationally-silenced or actively-translating but immotile transcripts could display different trafficking behaviors and/or become actively translating. Multiple studies reported the key roles that extracellular cues or fluctuating intracellular events have in the peripheral distribution of mRNAs and in modulating their localized translation. Above all, eliciting glutamatergic signaling (Yoon et al. 2016) or inducing membrane potential depolarization upon KCl exposure (Chu et al. 2019; Das et al. 2023; Tiruchinapalli et al. 2003) or a tetradotoxin (TTX)-withdrawal paradigm (Das et al. 2023) lead to a temporal and special control of the transcript localization and translation. Inducing neuronal activity through one of the above suggested options could therefore allow the identification of transcripts' phenotypes that couldn't have been otherwise revealed. The first and second scenario illustrated above could be therefore explained by limitations associated to the *in vitro* set-up and the lack of represented physiological events. We established a new protocol to differentiate N2a cells into neuron-like cells that recapitulate the axonal transport dynamics and local translation events that characterize neuronal cells. Translation dynamics have been widely studied using the SunTag system in a broad range of non-neuronal mitotic cells (Mateju et al. 2020; Wang et al. 2016; Wilbertz et al. 2019; Yan et al. 2016) and only a few reports succeeded in expressing such technology in neurons (Harbauer et al. 2022; Wang

et al. 2016; Wu et al. 2016). Whether the d-Na cells generated through our protocol retain the molecular signature (e.g. RBPs, adaptor proteins regulating hitchhiking mechanisms and motile cargo-associated translation) that would ensure the successful functioning of the SunTag system and its application to visualize trafficking mRNAs undergoing translation still remains an open question. To address this debate, the SunTag technology could be engineered to express actin (Chu et al. 2019; Tiruchinapalli et al. 2003; Yoon et al. 2016), the most characterized transcript undergoing active translation along neurites, and verify if its translation phenotypes could be reproduced along the neurites of d-N2a cells. If our hypothesis proves to be correct and our study will identify transcripts engaged in translation while being trafficked by the transport machinery, studies aimed at confirming the SunTag readout could be performed. We, however, acknowledge that this system consists in the overexpression of constructs which could alter the physiological stoichiometry of a given transcript and its correspondent protein, as well as physiological processes including transport dynamics and the hitchhiking mechanisms (e.g. of RNP granules). To validate these findings in more physiological conditions, neuronal and d-N2a cultures could be probed for the puromycilation assay combined with the puro-PLA assay (Even et al. 2021; Tom Dieck et al. 2015). By labelling all translating peptides with a quick burst of puromycin followed by the selected visualization of the translating candidate via puro-PLA, it will be possible to visualize in fixed cells foci of the translating candidate along neurites. The combined immunofluorescent staining of these cultures using antibodies against organelles markers (in case the translating mRNA would be associated to cargos) or motor proteins (in case the translating mRNA would be directly transported by the motors) would further inform on its association to the transport machinery. This set-up would therefore highlight the proportion of transcripts that are associated or not to the transport machinery, and the proportion that is preferentially transported via hitchhiking mechanisms.

To assess if the association of a transcript to the transport machinery is a prerequisite for its translation, puromycilation assay combined with the puro-PLA for the candidate target could be performed after disrupting in culture the dynamics of axonal transport. This aim could be achieved either via pharmacological inhibition (by using MTs destabilizing compounds as colchicine or nocodazole) or via gene knockdown for motor proteins. A decreased local translation of the candidate transcripts upon transport impairment would strengthen the link between the transport and translation machinery suggesting the existence of a functional

cooperation between their associated dynamics. These evidences would therefore strengthen the proposed model of membrane-bound organelles as self-sustaining machineries, not only by being energetically autonomous (Hinckelmann et al. 2016) and able to modulate their own transport dynamics (Even et al. 2019, 2021), but also by regulating their structural integrity via a local translation of their own constituent proteins.

REFERENCES

Akella, Jyothi S., Dorota Wloga, Jihyun Kim, Natalia G. Starostina, Sally Lyons-Abbott, Naomi S. Morrissette, Scott T. Dougan, Edward T. Kipreos, and Jacek Gaertig. 2010. “MEC-17 Is an α-Tubulin Acetyltransferase.” *Nature* 467(7312):218–22. doi: 10.1038/nature09324.

Akhmanova, Anna, and Michel O. Steinmetz. 2008. “Tracking the Ends: A Dynamic Protein Network Controls the Fate of Microtubule Tips.” *Nature Reviews Molecular Cell Biology* 9(4):309–22. doi: 10.1038/nrm2369.

Al-Bassam, Sarmad, Min Xu, Thomas J. Wandless, and Don B. Arnold. 2012. “Differential Trafficking of Transport Vesicles Contributes to the Localization of Dendritic Proteins.” *Cell Reports* 2(1):89–100. doi: 10.1016/j.celrep.2012.05.018.

Alami, Nael H., Rebecca B. Smith, Monica A. Carrasco, Luis A. Williams, Christina S. Winborn, Steve S. W. Han, Evangelos Kiskinis, Brett Winborn, Brian D. Freibaum, Anderson Kanagaraj, Alison J. Clare, Nisha M. Badders, Bilada Bilican, Edward Chaum, Siddharthan Chandran, Christopher E. Shaw, Kevin C. Eggan, Tom Maniatis, and J. Paul Taylor. 2014. “Axonal Transport of TDP-43 MRNA Granules in Neurons Is Impaired by ALS-Causing Mutations.” *Neuron* 81(3):536–43. doi: 10.1016/j.neuron.2013.12.018.

Alushin, Gregory M., Gabriel C. Lander, Elizabeth H. Kellogg, Rui Zhang, David Baker, and Eva Nogales. 2014. “High Resolution Microtubule Structures Reveal the Structural Transitions in Aβ–Tubulin upon GTP Hydrolysis.” *Cell* 157(5):1117. doi: 10.1016/J.CELL.2014.03.053.

Anadolu, Mina N., Senthilkumar Kailasam, Konstanze Simbriger, Jingyu Sun, Teodora Markova, Seyed Mehdi Jafarnejad, Francois Lefebvre, Joaquin Ortega, Christos G. Gkogkas, and Wayne S. Sossin. 2022. “Ribosomes in RNA Granules Are Stalled on MRNA Sequences That Are Consensus Sites for FMRP Association.” *Bioarxiv*. doi: 10.1101/2021.02.22.432349.

Andreu-Carbó, Mireia, Cornelia Egoldt, Marie-Claire Velluz, and Charlotte Aumeier. 2022. “Running Kinesin-1 Shapes the Microtubule Acetylation Gradient.” *Bioarxiv*. doi: 10.1101/2022.12.01.518806.

Balabanian, Linda, Christopher L. Berger, and Adam G. Hendricks. 2017. “Acetylated Microtubules Are Preferentially Bundled Leading to Enhanced Kinesin-1 Motility.” *Biophysical Journal* 113(7):1551. doi: 10.1016/J.BPJ.2017.08.009.

Banerjee, A., M. C. Roach, P. Trcka, and R. F. Luduena. 1990. “Increased Microtubule Assembly in Bovine Brain Tubulin Lacking the Type III Isotype of β-Tubulin.” *Journal of Biological Chemistry* 265(3):1794–99. doi: 10.1016/s0021-9258(19)40087-2.

Baron, Desiree M., Adam R. Fenton, Sara Saez-Atienzar, Anthony Giampetruzzi, Aparna Sreeram, Shankaracharya, Pamela J. Keagle, Victoria R. Doocy, Nathan J. Smith, Eric W. Danielson, Megan Andresano, Mary C. McCormack, Jaqueline Garcia, Valérie Bercier, Ludo Van Den Bosch, Jonathan R. Brent, Claudia Fallini, Bryan J. Traynor, Erika L. F. Holzbaur, and John E. Landers. 2022. “ALS-Associated KIF5A Mutations Abolish Autoinhibition Resulting in a Toxic Gain of Function.” *Cell Reports* 39(1). doi: 10.1016/J.CELREP.2022.110598/ATTACHMENT/EA35FA8E-6E37-4571-802F-989DC61ADAB6/MMC4.XLSX.

Batista, Andreia F. R., José C. Martínez, and Ulrich Hengst. 2017. “Intra-Axonal Synthesis of SNAP25 Is Required for the Formation of Presynaptic Terminals.” *Cell Reports* 20(13):3085–98. doi: 10.1016/j.celrep.2017.08.097.

Baumann, Sebastian, Artem Komissarov, Maria Gili, Verena Ruprecht, Stefan Wieser, and Sebastian P. Maurer. 2020. “A Reconstituted Mammalian APC-Kinesin Complex Selectively Transports Defined Packages of Axonal MRNAs.” *Science Advances*

6(11):eaaz1588. doi: 10.1126/sciadv.aaz1588.
Baumann, Sebastian, Julian König, Janine Koepke, and Michael Feldbrügge. 2014. "Endosomal Transport of Septin MRNA and Protein Indicates Local Translation on Endosomes and Is Required for Correct Septin Filamentation." *EMBO Reports* 15(1):94–102. doi: 10.1002/embr.201338037.
Bechstedt, Susanne, Kevan Lu, and Gary J. Brouhard. 2014. "Doublecortin Recognizes the Longitudinal Curvature of the Microtubule End and Lattice." *Current Biology* 24(20):2366–75. doi: 10.1016/J.CUB.2014.08.039.
Berkovits, Binyamin D., and Christine Mayr. 2015. "Alternative 3'UTRs Act as Scaffolds to Regulate Membrane Protein Localization." *Nature* 522(7556):363. doi: 10.1038/NATURE14321.
Bhoj, Elizabeth J., Dong Li, Margaret Harr, Shimon Edvardson, Orly Elpeleg, Elizabeth Chisholm, Jane Juusola, Ganka Douglas, Maria J. Guillen Sacoto, Karine Siquier-Pernet, Abdelkrim Saadi, Christine Bole-Feysot, Patrick Nitschke, Alekhya Narravula, Maria Walke, Michele B. Horner, Debra Lynn Day-Salvatore, Parul Jayakar, Samantha A. Schrie. Vergano, Mark A. Tarnopolsky, Madhuri Hegde, Laurence Colleaux, Peter Crino, and Hakon Hakonarson. 2016. "Mutations in TBCK, Encoding TBC1-Domain-Containing Kinase, Lead to a Recognizable Syndrome of Intellectual Disability and Hypotonia." *American Journal of Human Genetics* 98(4):782–88. doi: 10.1016/j.ajhg.2016.03.016.
Bianco, Ambra, Martin Dienstbier, Hannah K. Salter, Graziana Gatto, and Simon L. Bullock. 2010. "Bicaudal-D Regulates Fragile X Mental Retardation Protein Levels, Motility, and Function during Neuronal Morphogenesis." *Current Biology* 20(16):1487–92. doi: 10.1016/j.cub.2010.07.016.
Biever, Anne, Caspar Glock, Georgi Tushev, Elena Ciirdaeva, Tamas Dalmay, Julian D. Langer, and Erin M. Schuman. 2020. "Monosomes Actively Translate Synaptic MRNAs in Neuronal Processes." *Science* 367(6477):eaay4991. doi: 10.1126/science.aay4991.
Bittermann, Elizabeth, Zakia Abdelhamed, Ryan P. Liegel, Chelsea Menke, Andrew Timms, David R. Beier, and Rolf W. Stottmann. 2019. "Differential Requirements of Tubulin Genes in Mammalian Forebrain Development." *PLOS Genetics* 15(8):e1008243. doi: 10.1371/JOURNAL.PGEN.1008243.
Boersma, Sanne, Huib H. Rabouw, Lucas J. M. Bruurs, Tonja Pavlovič, Arno L. W. van Vliet, Joep Beumer, Hans Clevers, Frank J. M. van Kuppeveld, and Marvin E. Tanenbaum. 2020. "Translation and Replication Dynamics of Single RNA Viruses." *Cell* 183(7):1930-1945.e23. doi: 10.1016/j.cell.2020.10.019.
Boulay, Anne Cécile, Bruno Saubameá, Nicolas Adam, Stéphanie Chasseigneaux, Noémie Mazaré, Alice Gilbert, Mathieu Bahin, Leïla Bastianelli, Corinne Blugeon, Sandrine Perrin, Juliette Pouch, Bertrand Ducos, Stéphane Le Crom, Auguste Genovesio, Fabrice Chrétien, Xavier Declèves, Jean Louis Laplanche, and Martine Cohen-Salmon. 2017. "Translation in Astrocyte Distal Processes Sets Molecular Heterogeneity at the Gliovascular Interface." *Cell Discovery* 3:17005. doi: 10.1038/CELLDISC.2017.5.
Budaitis, Breane G., Somayesadat Badieyan, Yang Yue, T. Lynne Blasius, Dana N. Reinemann, Matthew J. Lang, Michael A. Cianfrocco, and Kristen J. Verhey. 2022. "A Kinesin-1 Variant Reveals Motor-Induced Microtubule Damage in Cells." *Current Biology* 32(11):2416-2429.e6. doi: 10.1016/j.cub.2022.04.020.
Buscaglia, Georgia, Kyle R. Northington, Jeffrey K. Moore, and Emily Anne Bates. 2020. "Reduced TUBA1A Tubulin Causes Defects in Trafficking and Impaired Adult Motor Behavior." *ENeuro* 7(2). doi: 10.1523/ENEURO.0045-20.2020.

Cagnetta, Roberta, Christian K. Frese, Toshiaki Shigeoka, Jeroen Krijgsveld, Christine E. Holt, Roberta Cagnetta, Christian K. Frese, Toshiaki Shigeoka, Jeroen Krijgsveld, and Christine E. Holt. 2018. "Rapid Cue-Specific Remodeling of the Nascent Axonal Proteome." *Neuron* 29–46. doi: 10.1016/j.neuron.2018.06.004.

Cai, Qian, Claudia Gerwin, and Zu Hang Sheng. 2005. "Syntabulin-Mediated Anterograde Transport of Mitochondria along Neuronal Processes." *The Journal of Cell Biology* 170(6):959. doi: 10.1083/JCB.200506042.

Cajigas, Iván J., Georgi Tushev, Tristan J. Will, Susanne Tom Dieck, Nicole Fuerst, and Erin M. Schuman. 2012. "The Local Transcriptome in the Synaptic Neuropil Revealed by Deep Sequencing and High-Resolution Imaging." *Neuron* 74(3):453–66. doi: 10.1016/J.NEURON.2012.02.036.

Calkins, Marcus J., Maria Manczak, Peizhong Mao, Ulziibat Shirendeb, and P. Hemachandra Reddy. 2011. "Impaired Mitochondrial Biogenesis, Defective Axonal Transport of Mitochondria, Abnormal Mitochondrial Dynamics and Synaptic Degeneration in a Mouse Model of Alzheimer's Disease." *Human Molecular Genetics* 20(23):4515. doi: 10.1093/HMG/DDR381.

Canty, John T., Andrew Hensley, Merve Aslan, Amanda Jack, and Ahmet Yildiz. 2023. "TRAK Adaptors Regulate the Recruitment and Activation of Dynein and Kinesin in Mitochondrial Transport." *Nature Communications* 14(1):1376. doi: 10.1038/s41467-023-36945-8.

Cao, Zheng, Cunxi Li, James N. Higginbotham, Jeffrey L. Franklin, David L. Tabb, Ramona Graves-Deal, Salisha Hill, Kristin Cheek, W. Gray Jerome, Lynne A. Lapierre, James R. Goldenring, Amy-Joan L. Ham, and Robert J. Coffey. 2008. "Use of Fluorescence-Activated Vesicle Sorting for Isolation of Naked2-Associated, Basolaterally Targeted Exocytic Vesicles for Proteomics Analysis." *Molecular & Cellular Proteomics : MCP* 7(9):1651. doi: 10.1074/MCP.M700155-MCP200.

Carter, Stephen D., Cheri M. Hampton, Robert Langlois, Roberto Melero, Zachary J. Farino, Michael J. Calderon, Wen Li, Callen T. Wallace, Ngoc Han Tran, Robert A. Grassucci, Stephanie E. Siegmund, Joshua Pemberton, Travis J. Morgenstern, Leanna Eisenman, Jenny I. Aguilar, Nili L. Greenberg, Elana S. Levy, Edward Yi, William G. Mitchell, William J. Rice, Christoph Wigge, Jyotsna Pilli, Emily W. George, Despoina Aslanoglou, Maïté Courel, Robin J. Freyberg, Jonathan A. Javitch, Zachary P. Wills, Estela Area-Gomez, Sruti Shiva, Francesca Bartolini, Allen Volchuk, Sandra A. Murray, Meir Aridor, Kenneth N. Fish, Peter Walter, Tamas Balla, Deborah Fass, Sharon G. Wolf, Simon C. Watkins, José María Carazo, Grant J. Jensen, Joachim Frank, and Zachary Freyberg. 2020. "Ribosome-Associated Vesicles: A Dynamic Subcompartment of the Endoplasmic Reticulum in Secretory Cells." *Science Advances* 6(14). doi: 10.1126/sciadv.aay9572.

Cason, Sydney E., and Erika L. F. Holzbaur. 2022. "Selective Motor Activation in Organelle Transport along Axons." *Nature Reviews Molecular Cell Biology 2022* 1–16. doi: 10.1038/s41580-022-00491-w.

Caviston, Juliane P., Jennifer L. Ross, Sheila M. Antony, Mariko Tokito, and Erika L. F. Holzbaur. 2007. "Huntingtin Facilitates Dynein/Dynactin-Mediated Vesicle Transport." *Proceedings of the National Academy of Sciences of the United States of America* 104(24):10045–50. doi: 10.1073/PNAS.0610628104/SUPPL_FILE/10628FIG7.JPG.

Cenik, and Can. 2021. "Single Cell Quantification of Ribosome Occupancy in Early Mouse Development." *Bioarxiv*. doi: 10.1101/2021.12.07.471408.

Chalfie, Martin, and J. Nichol Thomson. 1982. "Structural and Functional Diversity in the

Neuronal Microtubules of Caenorhabditis Elegans." *J Cell BioCell Bio*.
Christensen, Jenna R., Agnieszka A. Kendrick, Joey B. Truong, Adriana Aguilar-Maldonado, Vinit Adani, Monika Dzieciatkowska, and Samara L. Reck-Peterson. 2021. "Cytoplasmic Dynein-1 Cargo Diversity Is Mediated by the Combinatorial Assembly of FTS–Hook–FHIP Complexes." *ELife* 10. doi: 10.7554/ELIFE.74538.
Chu, Jen Fei, Pritha Majumder, Biswanath Chatterjee, Shih Ling Huang, and Che Kun James Shen. 2019. "TDP-43 Regulates Coupled Dendritic MRNA Transport-Translation Processes in Co-Operation with FMRP and Staufen1." *Cell Reports* 29(10):3118-3133.e6. doi: 10.1016/j.celrep.2019.10.061.
Cianfrocco, Michael A., Morgan E. Desantis, Andres E. Leschziner, and Samara L. Reck-Peterson. 2015. "Mechanism and Regulation of Cytoplasmic Dynein." *Annual Review of Cell and Developmental Biology* 31:83. doi: 10.1146/ANNUREV-CELLBIO-100814-125438.
Cioni, Jean Michel, Max Koppers, and Christine E. Holt. 2018. "Molecular Control of Local Translation in Axon Development and Maintenance." *Current Opinion in Neurobiology* 51:86–94. doi: 10.1016/j.conb.2018.02.025.
Cioni, Jean Michel, Julie Qiaojin Lin, Anne V. Holtermann, Max Koppers, Maximilian A. H. Jakobs, Afnan Azizi, Benita Turner-Bridger, Toshiaki Shigeoka, Kristian Franze, William A. Harris, and Christine E. Holt. 2019. "Late Endosomes Act as MRNA Translation Platforms and Sustain Mitochondria in Axons." *Cell* 176(1–2):56. doi: 10.1016/J.CELL.2018.11.030.
Close, Pierre, Nicola Hawkes, Isabelle Cornez, Catherine Creppe, Charles A. Lambert, Bernard Rogister, Ulrich Siebenlist, Marie Paule Merville, Susan A. Slaugenhaupt, Vincent Bours, Jesper Q. Svejstrup, and Alain Chariot. 2006. "Transcription Impairment and Cell Migration Defects in Elongator-Depleted Cells: Implication for Familial Dysautonomia." *Molecular Cell* 22(4):521–31. doi: 10.1016/j.molcel.2006.04.017.
Colin, Emilie, Diana Zala, Géraldine Liot, Hélène Rangone, Maria Borrell-Pagès, Xiao Jiang Li, Frédéric Saudou, and Sandrine Humbert. 2008. "Huntingtin Phosphorylation Acts as a Molecular Switch for Anterograde/Retrograde Transport in Neurons." *EMBO Journal* 27(15):2124–34. doi: 10.1038/emboj.2008.133.
Colombrita, Claudia, Elisa Onesto, Francesca Megiorni, Antonio Pizzuti, Francisco E. Baralle, Emanuele Buratti, Vincenzo Silani, and Antonia Ratti. 2012. "TDP-43 and FUS RNA-Binding Proteins Bind Distinct Sets of Cytoplasmic Messenger RNAs and Differently Regulate Their Post-Transcriptional Fate in Motoneuron-like Cells." *The Journal of Biological Chemistry* 287(19):15635. doi: 10.1074/JBC.M111.333450.
Combs, Benjamin, Kyle R. Christensen, Collin Richards, Andrew Kneynsberg, Rebecca L. Mueller, Sarah L. Morris, Gerardo A. Morfini, Scott T. Brady, and Nicholas M. Kanaan. 2021. "Frontotemporal Lobar Dementia Mutant Tau Impairs Axonal Transport through a Protein Phosphatase 1γ-Dependent Mechanism." *The Journal of Neuroscience* 41(45):9431. doi: 10.1523/JNEUROSCI.1914-20.2021.
Coombes, Courtney, Ami Yamamoto, Mark McClellan, Taylor A. Reid, Melissa Plooster, G. W. Gan. Luxton, Joshua Alper, Jonathon Howard, and Melissa K. Gardner. 2016. "Mechanism of Microtubule Lumen Entry for the α-Tubulin Acetyltransferase Enzyme ATAT1." *Proceedings of the National Academy of Sciences of the United States of America* 113(46):E7176–84. doi: 10.1073/PNAS.1605397113/SUPPL_FILE/PNAS.1605397113.SM03.MOV.
Creppe, Catherine, Lina Malinouskaya, Marie Laure Volvert, Magali Gillard, Pierre Close,

Olivier Malaise, Sophie Laguesse, Isabelle Cornez, Souad Rahmouni, Sandra Ormenese, Shibeshih Belachew, Brigitte Malgrange, Jean Paul Chapelle, Ulrich Siebenlist, Gustave Moonen, Alain Chariot, and Laurent Nguyen. 2009. "Elongator Controls the Migration and Differentiation of Cortical Neurons through Acetylation of α-Tubulin." *Cell* 136(3):551–64. doi: 10.1016/j.cell.2008.11.043.

d'Ydewalle, Constantin, Jyothsna Krishnan, Driss M. Chiheb, Philip Van Damme, Joy Irobi, Alan P. Kozikowski, Pieter Vanden Berghe, Vincent Timmerman, Wim Robberecht, and Ludo Van Den Bosch. 2011. "HDAC6 Inhibitors Reverse Axonal Loss in a Mouse Model of Mutant HSPB1–Induced Charcot-Marie-Tooth Disease." *Nature Medicine* 17(8):968–74. doi: 10.1038/nm.2396.

Dalwadi, Udit, and Calvin K. Yip. 2018. "Structural Insights into the Function of Elongator." *Cellular and Molecular Life Sciences* 75:1613–22. doi: 10.1007/s00018-018-2747-6.

Das, Sulagna, Pablo J. Lituma, Pablo E. Castillo, Robert H. Singer, Sulagna Das, Pablo J. Lituma, Pablo E. Castillo, and Robert H. Singer. 2023. "Maintenance of a Short-Lived Protein Required for Long-Term Memory Involves Cycles of Transcription and Local Translation." *Neuron* 1–14. doi: 10.1016/j.neuron.2023.04.005.

David, Alexandre, Brian P. Dolan, Heather D. Hickman, Jonathan J. Knowlton, Giovanna Clavarino, Philippe Pierre, Jack R. Bennink, and Jonathan W. Yewdell. 2012. "Nuclear Translation Visualized by Ribosome-Bound Nascent Chain Puromycylation." *Journal of Cell Biology* 197(1):45–57. doi: 10.1083/jcb.201112145.

Debaisieux, Solène, Vesela Encheva, Probir Chakravarty, Ambrosius P. Snijders, and Giampietro Schiavo. 2016. "Analysis of Signaling Endosome Composition and Dynamics Using SILAC in Embryonic Stem Cell-Derived Neurons." *Molecular & Cellular Proteomics* 15(2):542–57. doi: 10.1074/mcp.M115.051649.

Dictenberg, Jason B., Sharon A. Swanger, Laura N. Antar, Robert H. Singer, and Gary J. Bassell. 2008. "A Direct Role for FMRP in Activity-Dependent Dendritic MRNA Transport Links Filopodial-Spine Morphogenesis to Fragile X Syndrome." *Developmental Cell* 14(6):926–39. doi: 10.1016/j.devcel.2008.04.003.

Dimitrov, Ariane, Mélanie Quesnoit, Sandrine Moutel, Isabelle Cantaloube, Christian Poüs, and † Franck Perez. 2008. "Detection of GTP-Tubulin Conformation in Vivo Reveals a Role for GTP Remnants in Microtubule Rescues." *Science*.

Dixit, Ram, Jennifer L. Ross, Yale E. Goldman, and Erika L. F. Holzbaur. 2008. "Differential Regulation of Dynein and Kinesin Motor Proteins by Tau." *Science (New York, N.Y.)* 319(5866):1086. doi: 10.1126/SCIENCE.1152993.

Dompierre, J. P., J. D. Godin, B. C. Charrin, F. P. Cordelieres, S. J. King, S. Humbert, and F. Saudou. 2007. "Histone Deacetylase 6 Inhibition Compensates for the Transport Deficit in Huntington's Disease by Increasing Tubulin Acetylation." *Journal of Neuroscience* 27(13):3571–83. doi: 10.1523/JNEUROSCI.0037-07.2007.

Donlin-Asp, Paul G., Claudia Fallini, Jazmin Campos, Ching Chieh Chou, Megan E. Merritt, Han C. Phan, Gary J. Bassell, and Wilfried Rossoll. 2017. "The Survival of Motor Neuron Protein Acts as a Molecular Chaperone for MRNP Assembly." *Cell Reports* 18(7):1660. doi: 10.1016/J.CELREP.2017.01.059.

Dufourt, Jeremy, Maelle Bellec, Antonio Trullo, Matthieu Dejean, Sylvain De Rossi, Cyril Favard, and Mounia Lagha. 2021. "Imaging Translation Dynamics in Live Embryos Reveals Spatial Heterogeneities." *Science* eabc3483. doi: 10.1126/science.abc3483.

Evangelopoulos, Maria Elephteria, Joachim Weis, and Alex Krüttgen. 2005. "Signalling Pathways Leading to Neuroblastoma Differentiation after Serum Withdrawal: HDL

Blocks Neuroblastoma Differentiation by Inhibition of EGFR." *Oncogene 2005 24:20* 24(20):3309–18. doi: 10.1038/sj.onc.1208494.

Even, Aviel, Giovanni Morelli, Loïc Broix, Chiara Scaramuzzino, Silvia Turchetto, Ivan Gladwyn-Ng, Romain Le Bail, Michal Shilian, Stephen Freeman, Maria M. Magiera, A. S. Jijumon, Nathalie Krusy, Brigitte Malgrange, Bert Brone, Paula Dietrich, Ioannis Dragatsis, Carsten Janke, Frédéric Saudou, Miguel Weil, and Laurent Nguyen. 2019. "ATAT1-Enriched Vesicles Promote Microtubule Acetylation via Axonal Transport." *Science Advances* 5(12):eaax2705. doi: 10.1126/sciadv.aax2705.

Even, Aviel, Giovanni Morelli, Silvia Turchetto, Michal Shilian, Romain Le Bail, Sophie Laguesse, Nathalie Krusy, Ariel Brisker, Alexander Brandis, Shani Inbar, Alain Chariot, Frédéric Saudou, Paula Dietrich, Ioannis Dragatsis, Bert Brone, Loïc Broix, Jean Michel Rigo, Miguel Weil, and Laurent Nguyen. 2021. "ATP-Citrate Lyase Promotes Axonal Transport across Species." *Nature Communications 2021 12:1* 12(1):1–14. doi: 10.1038/s41467-021-25786-y.

Farías, Ginny G., Carlos M. Guardia, Raffaella De Pace, Dylan J. Britt, and Juan S. Bonifacino. 2017. "BORC/Kinesin-1 Ensemble Drives Polarized Transport of Lysosomes into the Axon." *Proceedings of the National Academy of Sciences* 114(14):E2955–64. doi: 10.1073/pnas.1616363114.

El Fatimy, Rachid, Laetitia Davidovic, Sandra Tremblay, Xavier Jaglin, Alain Dury, Claude Robert, Paul De Koninck, and Edouard W. Khandjian. 2016. "Tracking the Fragile X Mental Retardation Protein in a Highly Ordered Neuronal RiboNucleoParticles Population: A Link between Stalled Polyribosomes and RNA Granules" edited by J. C. Darnell. *PLOS Genetics* 12(7):e1006192. doi: 10.1371/journal.pgen.1006192.

Fenton, Adam R., Thomas A. Jongens, and Erika L. F. Holzbaur. 2021. "Mitochondrial Adaptor TRAK2 Activates and Functionally Links Opposing Kinesin and Dynein Motors." *Nature Communications* 12(1). doi: 10.1038/S41467-021-24862-7.

Ferguson, Kirsty M., Sarah L. Gillen, Lewis Chaytor, Evon Poon, Daniel Marcos, Roshna Lawrence Gomez, Laura M. Woods, Lidiya Mykhaylechko, Louis Elfari, Barbara Martins da Costa, Yann Jamin, Jason S. Carroll, Louis Chesler, Fahad R. Ali, and Anna Philpott. 2023. "Palbociclib Releases the Latent Differentiation Capacity of Neuroblastoma Cells." *Developmental Cell* 0(0). doi: 10.1016/J.DEVCEL.2023.08.028.

Formicola, Nadia, Jeshlee Vijayakumar, and Florence Besse. 2019. "Neuronal Ribonucleoprotein Granules: Dynamic Sensors of Localized Signals." *Traffic* 20(9):639–49. doi: 10.1111/tra.12672.

Fornasiero, Eugenio F., Sunit Mandad, Hanna Wildhagen, Mihai Alevra, Burkhard Rammner, Sarva Keihani, Felipe Opazo, Inga Urban, Till Ischebeck, M. Sadman Sakib, Maryam K. Fard, Koray Kirli, Tonatiuh Pena Centeno, Ramon O. Vidal, Raza Ur Rahman, Eva Benito, André Fischer, Sven Dennerlein, Peter Rehling, Ivo Feussner, Stefan Bonn, Mikael Simons, Henning Urlaub, and Silvio O. Rizzoli. 2018. "Precisely Measured Protein Lifetimes in the Mouse Brain Reveal Differences across Tissues and Subcellular Fractions." *Nature Communications 2018 9:1* 9(1):1–17. doi: 10.1038/s41467-018-06519-0.

Fourest-Lieuvin, Anne, Leticia Peris, Vincent Gache, Isabel Garcia-Saez, Céline Juillan-Binard, Violaine Lantez, and Didier Job. 2006. "Microtubule Regulation in Mitosis: Tubulin Phosphorylation by the Cyclin-Dependent Kinase Cdk1." *Molecular Biology of the Cell* 17(3):1041. doi: 10.1091/MBC.E05-07-0621.

Fritzsche, Renate, Daniela Karra, Keiryn L. Bennett, Foongyee Ang, Jacki E. Heraud-Farlow,

Marco Tolino, Michael Doyle, Karl E. Bauer, Sabine Thomas, Melanie Planyavsky, Eric Arn, Anetta Bakosova, Kerstin Jungwirth, Alexandra Hörmann, Zsofia Palfi, Julia Sandholzer, Martina Schwarz, Paolo Macchi, Jacques Colinge, Giulio Superti-Furga, and Michael A. Kiebler. 2013. "Interactome of Two Diverse RNA Granules Links MRNA Localization to Translational Repression in Neurons." *Cell Reports* 5(6):1749–62. doi: 10.1016/j.celrep.2013.11.023.

Fujita, Toshitsugu, Andrés D. Maturana, Junko Ikuta, Juri Hamada, Sebastien Walchli, Tadaki Suzuki, Hirofumi Sawa, Marie W. Wooten, Toshihide Okajima, Kenji Tatematsu, Katsuyuki Tanizawa, and ichi Kuroda. 2007. "Axonal Guidance Protein FEZ1 Associates with Tubulin and Kinesin Motor Protein to Transport Mitochondria in Neurites of NGF-Stimulated PC12 Cells." doi: 10.1016/j.bbrc.2007.07.050.

Fusco, Claudia M., Kristina Desch, Aline R. Dörrbaum, Mantian Wang, Anja Staab, Ivy C. W. Chan, Eleanor Vail, Veronica Villeri, Julian D. Langer, and Erin M. Schuman. 2021. "Neuronal Ribosomes Exhibit Dynamic and Context-Dependent Exchange of Ribosomal Proteins." *Nature Communications 2021 12:1* 12(1):1–14. doi: 10.1038/s41467-021-26365-x.

Gao, Yanpan, Yanyu Chen, Shaohua Zhan, Wenhao Zhang, Feng Xiong, and Wei Ge. 2017. "Comprehensive Proteome Analysis of Lysosomes Reveals the Diverse Function of Macrophages in Immune Responses." *Oncotarget* 8(5):7420. doi: 10.18632/ONCOTARGET.14558.

Gasic, Ivana. 2022. "Regulation of Tubulin Gene Expression: From Isotype Identity to Functional Specialization." *Frontiers in Cell and Developmental Biology* 10. doi: 10.3389/FCELL.2022.898076.

Gauthier, Daniel J., Jacqueline A. Sobota, Francesco Ferraro, Richard E. Mains, and Claude Lazure. 2008. "FLOW CYTOMETRY-ASSISTED PURIFICATION AND PROTEOMIC ANALYSIS OF THE CORTICOTROPES DENSE-CORE SECRETORY GRANULES." *Proteomics* 8(18):3848. doi: 10.1002/PMIC.200700969.

Genova, Mariya, Lenka Grycova, Verena Puttrich, Maria M. Magiera, Zdenek Lansky, Carsten Janke, and Marcus Braun. n.d. "Tubulin Polyglutamylation Differentially Regulates Microtubule-Interacting Proteins." doi: 10.15252/embj.2022112101.

Genuth, Naomi R., Zhen Shi, Koshi Kunimoto, Victoria Hung, Adele F. Xu, Craig H. Kerr, Gerald C. Tiu, Juan A. Oses-Prieto, Rachel E. A. Salomon-Shulman, Jeffrey D. Axelrod, Alma L. Burlingame, Kyle M. Loh, and Maria Barna. 2022. "A Stem Cell Roadmap of Ribosome Heterogeneity Reveals a Function for RPL10A in Mesoderm Production." *Nature Communications 2022 13:1* 13(1):1–19. doi: 10.1038/s41467-022-33263-3.

Glater, Elizabeth E., Laura J. Megeath, R. Steven Stowers, and Thomas L. Schwarz. 2006. "Axonal Transport of Mitochondria Requires Milton to Recruit Kinesin Heavy Chain and Is Light Chain Independent." *The Journal of Cell Biology* 173(4):545. doi: 10.1083/JCB.200601067.

Glock, Caspar, Anne Biever, Georgi Tushev, Belquis Nassim-Assir, Allison Kao, Ina Bartnik, Susanne tom Dieck, and Erin M. Schuman. 2021. "The Translatome of Neuronal Cell Bodies, Dendrites, and Axons." *Proceedings of the National Academy of Sciences* 118(43):e2113929118. doi: 10.1073/PNAS.2113929118/-/DCSUPPLEMENTAL.

Godena, Vinay K., Nicholas Brookes-Hocking, Annekathrin Moller, Gary Shaw, Matthew Oswald, Rosa M. Sancho, Christopher C. J. Miller, Alexander J. Whitworth, and Kurt J. De Vos. 2014. "Increasing Microtubule Acetylation Rescues Axonal Transport and Locomotor Deficits Caused by LRRK2 Roc-COR Domain Mutations." *Nature*

Communications 5. doi: 10.1038/ncomms6245.
Goffena, Joy, Frances Lefcort, Yongqing Zhang, Elin Lehrmann, Marta Chaverra, Jehremy Felig, Joseph Walters, Richard Buksch, Kevin G. Becker, and Lynn George. 2018. "Elongator and Codon Bias Regulate Protein Levels in Mammalian Peripheral Neurons." *Nature Communications* 9(1). doi: 10.1038/s41467-018-03221-z.
Gold, Vicki AM, Piotr Chroscicki, Piotr Bragoszewski, and Agnieszka Chacinska. 2017. "Visualization of Cytosolic Ribosomes on the Surface of Mitochondria by Electron Cryo-tomography." *EMBO Reports* 18(10):1786–1800. doi: 10.15252/embr.201744261.
Groen, Ewout J. N., Katsumi Fumoto, Anna M. Blokhuis, Joo Yeon Engelen-Lee, Yeping Zhou, Dianne M. A. van den Heuvel, Max Koppers, Femke van Diggelen, Jessica van Heest, Jeroen A. A. Demmers, Janine Kirby, Pamela J. Shaw, Eleonora Aronica, Wim G. M. Spliet, Jan H. Veldink, Leonard H. van den Berg, and R. Jeroen Pasterkamp. 2013. "ALS-Associated Mutations in FUS Disrupt the Axonal Distribution and Function of SMN." *Human Molecular Genetics* 22(18):3690–3704. doi: 10.1093/hmg/ddt222.
Guardia, Carlos M., Ginny G. Farías, Rui Jia, Jing Pu, and Juan S. Bonifacino. 2016. "BORC Functions Upstream of Kinesins 1 and 3 to Coordinate Regional Movement of Lysosomes Along Different Microtubule Tracks." *Cell Reports* 17(8):1950. doi: 10.1016/J.CELREP.2016.10.062.
Guo, Wenting, Maximilian Naujock, Laura Fumagalli, Tijs Vandoorne, Pieter Baatsen, Ruben Boon, Laura Ordovás, Abdulsamie Patel, Marc Welters, Thomas Vanwelden, Natasja Geens, Tine Tricot, Veronick Benoy, Jolien Steyaert, Cynthia Lefebvre-Omar, Werend Boesmans, Matthew Jarpe, Jared Sterneckert, Florian Wegner, Susanne Petri, Delphine Bohl, Pieter Vanden Berghe, Wim Robberecht, Philip Van Damme, Catherine Verfaillie, and Ludo Van Den Bosch. 2017. "HDAC6 Inhibition Reverses Axonal Transport Defects in Motor Neurons Derived from FUS-ALS Patients." *Nature Communications* 8(1). doi: 10.1038/S41467-017-00911-Y.
Guo, Wenting, Katarina Stoklund Dittlau, and Ludo Van Den Bosch. 2020. "Axonal Transport Defects and Neurodegeneration: Molecular Mechanisms and Therapeutic Implications." *Seminars in Cell and Developmental Biology* 99:133–50. doi: 10.1016/j.semcdb.2019.07.010.
Hafner, Anne Sophie, Paul G. Donlin-Asp, Beulah Leitch, Etienne Herzog, and Erin M. Schuman. 2019. "Local Protein Synthesis Is a Ubiquitous Feature of Neuronal Pre- And Postsynaptic Compartments." *Science* 364(6441). doi: 10.1126/science.aau3644.
Han, Qiuju, Xiaozhe Hou, Dongmei Su, Lina Pan, Jizhou Duan, Liguo Cui, Baiqu Huang, and Jun Lu. 2007. "HELP3 Subunit of the Elongator Complex Regulates the Transcription of HSP70 Gene in Human Cells." *Acta Biochimica et Biophysica Sinica* 39(6):453–61. doi: 10.1111/j.1745-7270.2007.00293.x.
Harbauer, Angelika B., J. Tabitha Hees, Simone Wanderoy, Inmaculada Segura, Whitney Gibbs, Yiming Cheng, Martha Ordonez, Zerong Cai, Romain Cartoni, Ghazaleh Ashrafi, Chen Wang, Fabiana Perocchi, Zhigang He, and Thomas L. Schwarz. 2022. "Neuronal Mitochondria Transport Pink1 MRNA via Synaptojanin 2 to Support Local Mitophagy." *Neuron* 110(9):1516-1531.e9. doi: 10.1016/J.NEURON.2022.01.035.
Harbauer, Angelika B., and Thomas L. Schwarz. 2022. "Mitochondrial Hitch-Hiking of Pink1 MRNA Supports Axonal Mitophagy." *Autophagy*. doi: 10.1080/15548627.2022.2070332/FORMAT/EPUB.
Hees, J. Tabitha, and Angelika B. Harbauer. 2023. "Insulin Signaling Regulates Pink1 MRNA Localization via Modulation of AMPK Activity to Support PINK1 Function in Neurons."

BioRxiv. doi: 10.1101/2023.02.06.527276.
Hendricks, Adam G., Eran Perlson, Jennifer L. Ross, Harry W. Schroeder, Mariko Tokito, and Erika L. F. Holzbaur. 2010. “Motor Coordination via a Tug-of-War Mechanism Drives Bidirectional Vesicle Transport.” *Current Biology* 20(8):697. doi: 10.1016/J.CUB.2010.02.058.
Henrichs, Verena, Lenka Grycova, Cyril Barinka, Zuzana Nahacka, Jiri Neuzil, Stefan Diez, Jakub Rohlena, Marcus Braun, and Zdenek Lansky. 2020. “Mitochondria-Adaptor TRAK1 Promotes Kinesin-1 Driven Transport in Crowded Environments.” *Nature Communications* 11(1):3123. doi: 10.1038/s41467-020-16972-5.
Hinckelmann, María-Victoria, Amandine Virlogeux, Christian Niehage, Christel Poujol, Daniel Choquet, Bernard Hoflack, Diana Zala, and Frédéric Saudou. 2016. “Self-Propelling Vesicles Define Glycolysis as the Minimal Energy Machinery for Neuronal Transport.” *Nature Communications* 7(1):13233. doi: 10.1038/ncomms13233.
Hobson, Benjamin D., Linghao Kong, Maria Florencia Angelo, Ori J. Lieberman, Eugene V. Mosharov, Etienne Herzog, David Sulzer, and Peter A. Sims. 2022. “Subcellular and Regional Localization of MRNA Translation in Midbrain Dopamine Neurons.” *Cell Reports* 38(2):110208. doi: 10.1016/J.CELREP.2021.110208.
Hoepfner, Sebastian, Fedor Severin, Alicia Cabezas, Bianca Habermann, Anja Runge, David Gillooly, Harald Stenmark, and Marino Zerial. 2005. “Modulation of Receptor Recycling and Degradation by the Endosomal Kinesin KIF16B.” *Cell* 121(3):437–50. doi: 10.1016/j.cell.2005.02.017.
Holt, Christine E., Kelsey C. Martin, and Erin M. Schuman. 2019. “Local Translation in Neurons: Visualization and Function.” *Nature Structural and Molecular Biology* 26(7):557–66. doi: 10.1038/s41594-019-0263-5.
Horste, Ellen L., Gang Zhen, Mervin M. Fansler, Xiuzhen Chen, Flora C. Y. Lee, Jernej Ule, Christine Mayr, and Gerstner Sloan Kettering. 2022. “Subcytoplasmic Location of Translation Controls Protein Output.” *BioRxiv* 2022.11.04.515216. doi: 10.1101/2022.11.04.515216.
Howes, Stuart C., Gregory M. Alushin, Toshinobu Shida, Maxence V. Nachury, and Eva Nogales. 2014. “Effects of Tubulin Acetylation and Tubulin Acetyltransferase Binding on Microtubule Structure.” *Molecular Biology of the Cell* 25(2):257. doi: 10.1091/MBC.E13-07-0387.
Huang, Bo, M. J. O. Johansson, and Anders S. Byström. 2005. “An Early Step in Wobble Uridine TRNA Modification Requires the Elongator Complex.” *Rna* 11(4):424–36. doi: 10.1261/rna.7247705.
Huang, Julie, Anthony J. Roberts, Andres E. Leschziner, and Samara L. Reck-Peterson. 2012. “Lis1 Acts as a ‘Clutch’ between the ATPase and Microtubule-Binding Domains of the Dynein Motor.” *Cell* 150(5):975. doi: 10.1016/J.CELL.2012.07.022.
Hubbard, W. Brad, Christopher L. Harwood, Paresh Prajapati, Joe E. Springer, Kathryn E. Saatman, and Patrick G. Sullivan. 2019. “Fractionated Mitochondrial Magnetic Separation for Isolation of Synaptic Mitochondria from Brain Tissue.” *Scientific Reports 2019 9:1* 9(1):1–13. doi: 10.1038/s41598-019-45568-3.
Hubbert, Charlotte, Amaris Guardiola, Rong Shao, Yoshiharu Kawaguchi, Akihiro Ito, Andrew Nixon, Minoru Yoshida, Xiao Fan Wang, and Tso Pang Yao. 2002. “HDAC6 Is a Microtubule-Associated Deacetylase.” *Nature* 417(6887):455–58. doi: 10.1038/417455a.
Huber, Kimberly M., Matthew S. Kayser, and Mark F. Bear. n.d. *Role for Rapid Dendritic*

Protein Synthesis in Hippocampal MGluR-Dependent Long-Term Depression.
Hubstenberger, Arnaud, Maïté Courel, Marianne Bénard, Sylvie Souquere, Michèle Ernoult-Lange, Racha Chouaib, Zhou Yi, Jean Baptiste Morlot, Annie Munier, Magali Fradet, Maëlle Daunesse, Edouard Bertrand, Gérard Pierron, Julien Mozziconacci, Michel Kress, and Dominique Weil. 2017. "P-Body Purification Reveals the Condensation of Repressed MRNA Regulons." *Molecular Cell* 68(1):144-157.e5. doi: 10.1016/J.MOLCEL.2017.09.003.
Hunter, Andrew W., Michael Caplow, David L. Coy, William O. Hancock, Stefan Diez, Linda Wordeman, and Jonathon Howard. 2003. "The Kinesin-Related Protein MCAK Is a Microtubule Depolymerase That Forms an ATP-Hydrolyzing Complex at Microtubule Ends." *Molecular Cell* 11(2):445. doi: 10.1016/S1097-2765(03)00049-2.
Jan, Calvin H., Christopher C. Williams, and Jonathan S. Weissman. 2014. "Principles of ER Cotranslational Translocation Revealed by Proximity-Specific Ribosome Profiling." *Science* 346(6210). doi: 10.1126/SCIENCE.1257521/SUPPL_FILE/REVISION1_MS1257521TABLES6.TXT.
Janke, Carsten, and Maria M. Magiera. 2020. "The Tubulin Code and Its Role in Controlling Microtubule Properties and Functions." *Nature Reviews Molecular Cell Biology*. doi: 10.1038/s41580-020-0214-3.
Janke, Carsten, and Guillaume Montagnac. 2017. "Causes and Consequences of Microtubule Acetylation." *Current Biology* 27(23):R1287–92. doi: 10.1016/j.cub.2017.10.044.
Janke, Carsten, Krzysztof Rogowski, Dorota Wloga, Catherine Regnard, Andrey V. Kajava, Jean Marc Strub, Nevzat Temurak, Juliette Van Dijk, Dominique Boucher, Alain Van Dorsselaer, Swati Suryavanshi, Jacek Gaertig, and Bernard Eddé. 2005. "Biochemistry: Tubulin Polyglutamylase Enzymes Are Members of the TTL Domain Protein Family." *Science* 308(5729):1758–62. doi: 10.1126/science.1113010.
Jeandard, Damien, Anna Smirnova, Akinyemi Mandela Fasemore, Léna Coudray, Nina Entelis, Konrad U. Förstner, Ivan Tarassov, and Alexandre Smirnov. 2023. "CoLoC-Seq Probes the Global Topology of Organelle Transcriptomes." *Nucleic Acids Research* 51(3):e16–e16. doi: 10.1093/nar/gkac1183.
Jongsma, Marlieke LM, Jeroen Bakker, Birol Cabukusta, Nalan Liv, Daphne van Elsland, Job Fermie, Jimmy LL Akkermans, Coenraad Kuijl, Sabina Y. van der Zanden, Lennert Janssen, Denise Hoogzaad, Rik van der Kant, Ruud H. Wijdeven, Judith Klumperman, Ilana Berlin, and Jacques Neefjes. 2020. "SKIP-HOPS Recruits TBC1D15 for a Rab7-to-Arl8b Identity Switch to Control Late Endosome Transport." *The EMBO Journal* 39(6):e102301. doi: 10.15252/EMBJ.2019102301.
Jung, Hosung, Christos G. Gkogkas, Nahum Sonenberg, and Christine E. Holt. 2014. "Remote Control of Gene Function by Local Translation." *Cell* 157(1):26–40. doi: 10.1016/j.cell.2014.03.005.
Kalebic, Nereo, Concepcion Martinez, Emerald Perlas, Philip Hublitz, Daniel Bilbao-Cortes, Karol Fiedorczuk, Annapaola Andolfo, and Paul A. Heppenstall. 2013. "Tubulin Acetyltransferase ATAT1 Destabilizes Microtubules Independently of Its Acetylation Activity." *Molecular and Cellular Biology* 33(6):1114. doi: 10.1128/MCB.01044-12.
Kalebic, Nereo, Simona Sorrentino, Emerald Perlas, Giulia Bolasco, Concepcion Martinez, and Paul A. Heppenstall. 2013. "ATAT1 Is the Major α-Tubulin Acetyltransferase in Mice." *Nature Communications* 4. doi: 10.1038/ncomms2962.
Kanai, Yoshimitsu, Naoshi Dohmae, and Nobutaka Hirokawa. 2004. "Kinesin Transports RNA: Isolation and Characterization of an RNA-Transporting Granule." *Neuron* 43(4):513–25.

doi: 10.1016/j.neuron.2004.07.022.
Karlsborn, Tony, Hasan Tükenmez, Changchun Chen, and Anders S. Byström. 2014. “Familial Dysautonomia (FD) Patients Have Reduced Levels of the Modified Wobble Nucleoside Mcm5s2U in TRNA.” *Biochemical and Biophysical Research Communications* 454(3):441–45. doi: 10.1016/J.BBRC.2014.10.116.
Kellner, Yves, Nina Gödecke, Tobias Dierkes, Nils Thieme, Marta Zagrebelsky, and Martin Korte. 2014. “The BDNF Effects on Dendritic Spines of Mature Hippocampal Neurons Depend on Neuronal Activity.” *Frontiers in Synaptic Neuroscience* 6(MAR):78911. doi: 10.3389/FNSYN.2014.00005/ABSTRACT.
Kim, Go Woon, Lin Li, Mohammad Gorbani, Linya You, and Xiang Jiao Yang. 2013. “Mice Lacking α-Tubulin Acetyltransferase 1 Are Viable but Display α-Tubulin Acetylation Deficiency and Dentate Gyrus Distortion.” *Journal of Biological Chemistry* 288(28):20334–50. doi: 10.1074/jbc.M113.464792.
Kim, Jae Hyun, William S. Lane, and Danny Reinberg. 2002. “Human Elongator Facilitates RNA Polymerase II Transcription through Chromatin.” *Proceedings of the National Academy of Sciences of the United States of America* 99(3):1241. doi: 10.1073/PNAS.251672198.
Kim, Ji-Yon, So-Youn Woo, Young Bin Hong, Heesun Choi, Jisoo Kim, Hyunjung Choi, Inhee Mook-Jung, Nina Ha, Jangbeen Kyung, Soo Kyung Koo, Sung-Chul Jung, and Byung-Ok Choi. 2016. “HDAC6 Inhibitors Rescued the Defective Axonal Mitochondrial Movement in Motor Neurons Derived from the Induced Pluripotent Stem Cells of Peripheral Neuropathy Patients with HSPB1 Mutation.” *Stem Cells International* 2016:1–14. doi: 10.1155/2016/9475981.
Kipper, Kalle, Abbas Mansour, and Arto Pulk. 2022. “Neuronal RNA Granules Are Ribosome Complexes Stalled at the Pre-Translocation State.” *Journal of Molecular Biology* 434(20):167801. doi: 10.1016/j.jmb.2022.167801.
Koenning, Matthias, Xianlong Wang, Menuka Karki, Rahul Kumar Jangid, Sarah Kearns, Durga Nand Tripathi, Michael Cianfrocco, Kristen J. Verhey, Sung Yun Jung, Cristian Coarfa, Christopher Scott Ward, Brian Thomas Kalish, Sandra L. Grimm, W. Kimryn Rathmell, Ricardo Mostany, Ruhee Dere, Matthew Neil Rasband, Cheryl Lyn Walker, and In Young Park. 2021. “Neuronal SETD2 Activity Links Microtubule Methylation to an Anxiety-like Phenotype in Mice.” *Brain* 144(8):2527–40. doi: 10.1093/brain/awab200.
Kopeikina, Katherine J., George A. Carlson, Rose Pitstick, Adam E. Ludvigson, Alan Peters, Jennifer I. Luebke, Robert M. Koffie, Matthew P. Frosch, Bradley T. Hyman, and Tara L. Spires-Jones. 2011. “Tau Accumulation Causes Mitochondrial Distribution Deficits in Neurons in a Mouse Model of Tauopathy and in Human Alzheimer’s Disease Brain.” *The American Journal of Pathology* 179(4):2071. doi: 10.1016/J.AJPATH.2011.07.004.
Koppers, Max, Nazmiye Özkan, Ha H. Nguyen, Daphne Jurriens, Janine Mccaughey, Riccardo Stucchi, Maarten Altelaar, Lukas C. Kapitein, Casper C. Hoogenraad, and Ginny G. Farias. 2022. “Axonal ER Tubules Regulate Local Translation via P180/RRBP1-Mediated Ribosome Interactions.” *BioRxiv*. doi: 10.1101/2022.11.30.518484.
Krichevsky, Anna M., and Kenneth S. Kosik. 2001. *Neuronal RNA Granules: A Link between RNA Localization and Stimulation-Dependent Translation*. Vol. 32.
Krogan, Nevan J., and Jack F. Greenblatt. 2001. “Characterization of a Six-Subunit Holo-Elongator Complex Required for the Regulated Expression of a Group of Genes in Saccharomyces Cerevisiae.” *MOLECULAR AND CELLULAR BIOLOGY* 21(23):8203–12. doi: 10.1128/MCB.21.23.8203-8212.2001.

Kumar, A., D. Larrea, M. E. Pero, P. Infante, M. Conenna, G. J. Shin, W. B. Grueber, L. Di Marcotullio, E. Area-Gomez, and F. Bartolini. 2023. “MFN2-Dependent Recruitment of ATAT1 Coordinates Mitochondria Motility with α-Tubulin Acetylation and Is Disrupted in CMT2A.” *BioRxiv* 2023.03.15.532838. doi: 10.1101/2023.03.15.532838.

Kumar, Gaurav, Prateek Chawla, Neha Dhiman, Sanya Chadha, Sheetal Sharma, Kanupriya Sethi, Mahak Sharma, and Amit Tuli. 2022. “RUFY3 Links Arl8b and JIP4-Dynein Complex to Regulate Lysosome Size and Positioning.” *Nature Communications* 13(1). doi: 10.1038/S41467-022-29077-Y.

Kumar, Mukesh, and Anju Katyal. 2018. “Data on Retinoic Acid and Reduced Serum Concentration Induced Differentiation of Neuro-2a Neuroblastoma Cells.” *Data in Brief* 21:2435–40. doi: 10.1016/J.DIB.2018.11.097.

Kuo, Yin Wei, Olivier Trottier, Mohammed Mahamdeh, and Jonathon Howard. 2019. “Spastin Is a Dual-Function Enzyme That Severs Microtubules and Promotes Their Regrowth to Increase the Number and Mass of Microtubules.” *Proceedings of the National Academy of Sciences of the United States of America* 116(12):5533–41. doi: 10.1073/PNAS.1818824116/SUPPL_FILE/PNAS.1818824116.SM03.AVI.

L’Hernaul, Steven W., and Joel L. Rosenbaum. 1985. “Chlamydomonas α-Tubulin Is Posttranslationally Modified by Acetylation on the ε-Amino Group of a Lysine.” *Biochemistry* 24(2):473–78. doi: 10.1021/bi00323a034.

Laguesse, Sophie, Catherine Creppe, Danny D. Nedialkova, Sebastian A. Leidel, Juliette D. Godin, and Laurent Nguyen. 2015. “A Dynamic Unfolded Protein Response Contributes to the Control of Cortical Neurogenesis.” doi: 10.1016/j.devcel.2015.11.005.

Lasko, Paul. 2020. “Patterning the Drosophila Embryo: A Paradigm for RNA-based Developmental Genetic Regulation.” *Wiley Interdisciplinary Reviews. RNA* 11(6). doi: 10.1002/WRNA.1610.

Lazarus, Jacob E., Armen J. Moughamian, Mariko K. Tokito, and Erika L. F. Holzbaur. 2013. “Dynactin Subunit P150Glued Is a Neuron-Specific Anti-Catastrophe Factor.” *PLOS Biology* 11(7):e1001611. doi: 10.1371/JOURNAL.PBIO.1001611.

Lei, Wenliang, Omotola F. Omotade, Kenneth R. Myers, and James Q. Zheng. 2016. “Actin Cytoskeleton in Dendritic Spine Development and Plasticity.” *Current Opinion in Neurobiology* 39:86. doi: 10.1016/J.CONB.2016.04.010.

Leo, Lanfranco, Carina Weissmann, Matthew Burns, Minsu Kang, Yuyu Song, Liang Qiang, Scott T. Brady, Peter W. Baas, and Gerardo Morfini. 2017. “Mutant Spastin Proteins Promote Deficits in Axonal Transport through an Isoform-Specific Mechanism Involving Casein Kinase 2 Activation.” *Human Molecular Genetics* 26(12):2321–34. doi: 10.1093/HMG/DDX125.

Leung, Kin Mei, Francisca P. G. Van Horck, Andrew C. Lin, Rachel Allison, Nancy Standart, and Christine E. Holt. 2006. “Asymmetrical β-Actin MRNA Translation in Growth Cones Mediates Attractive Turning to Netrin-1.” *Nature Neuroscience* 9(10):1247. doi: 10.1038/NN1775.

Leung, Kin Mei, Bo Lu, Hovy Ho Wai Wong, Julie Qiaojin Lin, Benita Turner-Bridger, and Christine E. Holt. 2018. “Cue-Polarized Transport of β-Actin MRNA Depends on 3’UTR and Microtubules in Live Growth Cones.” *Frontiers in Cellular Neuroscience* 12:300. doi: 10.3389/FNCEL.2018.00300/FULL.

Li, Lei, Dan Wei, Qiong Wang, Jing Pan, Rong Liu, Xu Zhang, and Lan Bao. 2012. “MEC-17 Deficiency Leads to Reduced α-Tubulin Acetylation and Impaired Migration of Cortical Neurons.” *Journal of Neuroscience* 32(37):12673–83. doi: 10.1523/JNEUROSCI.0016-

12.2012.
Li, Lin, Sriram Jayabal, Mohammad Ghorbani, Lisa Marie Legault, Serge McGraw, Alanna J. Watt, and Xiang Jiao Yang. 2019. “ATAT1 Regulates Forebrain Development and Stress-Induced Tubulin Hyperacetylation.” *Cellular and Molecular Life Sciences* 76(18):3621–40. doi: 10.1007/S00018-019-03088-3/FIGURES/9.
Liao, Ya-Cheng, Michael Fernandopulle, Guozhen Wang, Heejun Choi, Ling Hao, Catherine M. Drerup, Seema Qamar, Jonathon Nixon-Abell, Yi Shen, William Meadows, Michele Vendruscolo, Tuomas Knowles, Matthew Nelson, Magda Czekalska, Greta Musteikyte, Rajan Patel, Christina Stephens, Amalia Pasolli, Lucy Forrest, Peter St George-Hyslop, Jennifer Lippincott-Schwartz, and Michael E. Ward. 2019. “RNA Granules Hitchhike on Lysosomes for Long-Distance Transport, Using Annexin A11 as a Molecular Tether.” *Cell* 179(1):147-164.e20. doi: 10.2139/ssrn.3312723.
Ling, Shuo-Chien, Claudio P. Albuquerque, Joo Seok Han, Clotilde Lagier-Tourenne, Seiya Tokunaga, Huilin Zhou, and Don W. Cleveland. 2010. “ALS-Associated Mutations in TDP-43 Increase Its Stability and Promote TDP-43 Complexes with FUS/TLS.” *Proceedings of the National Academy of Sciences* 107(30):13318–23. doi: 10.1073/pnas.1008227107.
Liu, Yo Tsen, Matilde Laurá, Joshua Hersheson, Alejandro Horga, Zane Jaunmuktane, Sebastian Brandner, Alan Pittman, Deborah Hughes, James M. Polke, Mary G. Sweeney, Christos Proukakis, John C. Janssen, Michaela Auer-Grumbach, Stephan Zuchner, Kevin G. Shields, Mary M. Reilly, and Henry Houlden. 2014. “Extended Phenotypic Spectrum of KIF5A Mutations: From Spastic Paraplegia to Axonal Neuropathy.” *Neurology* 83(7):612–19. doi: 10.1212/WNL.0000000000000691.
Lo, K. Y., A. Kuzmin, S. M. Unger, J. D. Petersen, and M. A. Silverman. 2011. “KIF1A Is the Primary Anterograde Motor Protein Required for the Axonal Transport of Dense-Core Vesicles in Cultured Hippocampal Neurons.” *Neuroscience Letters*. doi: 10.1016/j.neulet.2011.01.018.
López-Erauskin, Jone, Takahiro Tadokoro, Michael W. Baughn, Brian Myers, Melissa McAlonis-Downes, Carlos Chillon-Marinas, Joshua N. Asiaban, Jonathan Artates, Anh T. Bui, Anne P. Vetto, Sandra K. Lee, Ai Vy Le, Ying Sun, Mélanie Jambeau, Jihane Boubaker, Deborah Swing, Jinsong Qiu, Geoffrey G. Hicks, Zhengyu Ouyang, Xiang Dong Fu, Lino Tessarollo, Shuo Chien Ling, Philippe A. Parone, Christopher E. Shaw, Martin Marsala, Clotilde Lagier-Tourenne, Don W. Cleveland, and Sandrine Da Cruz. 2018. “ALS/FTD-Linked Mutation in FUS Suppresses Intra-Axonal Protein Synthesis and Drives Disease Without Nuclear Loss-of-Function of FUS.” *Neuron* 100(4):816-830.e7. doi: 10.1016/j.neuron.2018.09.044.
Ly, Nathalie, Nadia Elkhatib, Enzo Bresteau, Olivier Piétrement, Mehdi Khaled, Maria M. Magiera, Carsten Janke, Eric Le Cam, Andrew D. Rutenberg, and Guillaume Montagnac. 2016. “ATAT1 Controls Longitudinal Spreading of Acetylation Marks from Open Microtubules Extremities.” *Scientific Reports 2016 6:1* 6(1):1–10. doi: 10.1038/srep35624.
Ma, Bin, Jeffrey N. Savas, Man Shan Yu, Brady P. Culver, Moses V. Chao, and Naoko Tanese. 2011. “Huntingtin Mediates Dendritic Transport of β-Actin MRNA in Rat Neurons.” *Scientific Reports 2011 1:1* 1(1):1–11. doi: 10.1038/srep00140.
Ma, Weirui, and Christine Mayr. 2018. “A Membraneless Organelle Associated with the Endoplasmic Reticulum Enables 3’UTR-Mediated Protein-Protein Interactions.” *Cell* 175(6):1492-1506.e19. doi: 10.1016/j.cell.2018.10.007.

Mansfield, S. G., and P. R. Gordon-Weeks. 1991. “Dynamic Post-Translational Modification of Tubulin in Rat Cerebral Cortical Neurons Extending Neurites in Culture: Effects of Taxol.” *Journal of Neurocytology* 20(8):654–66. doi: 10.1007/BF01187067.

Mateju, Daniel, Bastian Eichenberger, Franka Voigt, Jan Eglinger, Gregory Roth, and Jeffrey A. Chao. 2020. “Single-Molecule Imaging Reveals Translation of MRNAs Localized to Stress Granules.” *Cell* 183(7):1801-1812.e13. doi: 10.1016/j.cell.2020.11.010.

Medioni, Caroline, Mirana Ramialison, Anne Ephrussi, and Florence Besse. 2014. “Imp Promotes Axonal Remodeling by Regulating Profilin MRNA during Brain Development.” *Current Biology* 24(7):793–800. doi: 10.1016/j.cub.2014.02.038.

Miller, Kyle E., Jamin DeProto, Nancy Kaufmann, Bharatkumar N. Patel, April Duckworth, and David Van Vactor. 2005. “Direct Observation Demonstrates That Liprin-α Is Required for Trafficking of Synaptic Vesicles.” *Current Biology* 15(7):684–89. doi: 10.1016/J.CUB.2005.02.061.

Miller, Stephan, Masahiro Yasuda, Jennifer K. Coats, Ying Jones, Maryann E. Martone, and Mark Mayford. 2002. “Disruption of Dendritic Translation of CaMKIIα Impairs Stabilization of Synaptic Plasticity and Memory Consolidation.” *Neuron* 36(3):507–19. doi: 10.1016/S0896-6273(02)00978-9.

Miśkiewicz, Katarzyna, Liya E. Jose, André Bento-Abreu, Marcus Fislage, Ines Taes, Jarosław Kasprowicz, Jef Swerts, Stephan Sigrist, Wim Versées, Wim Robberecht, and Patrik Verstreken. 2011. “ELP3 Controls Active Zone Morphology by Acetylating the ELKS Family Member Bruchpilot.” *Neuron* 72(5):776–88. doi: 10.1016/j.neuron.2011.10.010.

Montagnac, Guillaume, Vannary Meas-Yedid, Marie Irondelle, Antonio Castro-Castro, Michel Franco, Toshinobu Shida, Maxence V. Nachury, Alexandre Benmerah, Jean Christophe Olivo-Marin, and Philippe Chavrier. 2013. “ATAT1 Catalyzes Microtubule Acetylation at Clathrin-Coated Pits.” *Nature* 502(7472):567. doi: 10.1038/NATURE12571.

Morelli, Giovanni, Aviel Even, Ivan Gladwyn-Ng, Romain Le Bail, Michal Shilian, Juliette D. Godin, Elise Peyre, Bassem A. Hassan, Arnaud Besson, Jean-Michel Rigo, Miguel Weil, Bert Brône, and Laurent Nguyen. 2018. “P27Kip1 Modulates Axonal Transport by Regulating α-Tubulin Acetyltransferase 1 Stability.” *Cell Reports* 23(8):2429–42. doi: 10.1016/j.celrep.2018.04.083.

Morley, Shane J., Yanmei Qi, Loredana Iovino, Laura Andolfi, Da Guo, Nereo Kalebic, Laura Castaldi, Christian Tischer, Carla Portulano, Giulia Bolasco, Kalyanee Shirlekar, Claudia M. Fusco, Antonino Asaro, Federica Fermani, Mayya Sundukova, Ulf Matti, Luc Reymond, Adele De Ninno, Luca Businaro, Kai Johnsson, Marco Lazzarino, Jonas Ries, Yannick Schwab, Jing Hu, and Paul A. Heppenstall. 2016. “Acetylated Tubulin Is Essential for Touch Sensation in Mice.” *ELife* 5(DECEMBER2016):25. doi: 10.7554/eLife.20813.

Mosen, Peter, Anne Sanner, Jasjot Singh, and Dominic Winter. 2021. “Targeted Quantification of the Lysosomal Proteome in Complex Samples.” *Proteomes* 9(1):1–17. doi: 10.3390/PROTEOMES9010004.

Moughamian, Armen J., Gregory E. Osborn, Jacob E. Lazarus, Sandra Maday, and Erika L. F. Holzbaur. 2013. “Ordered Recruitment of Dynactin to the Microtubule Plus-End Is Required for Efficient Initiation of Retrograde Axonal Transport.” *Journal of Neuroscience* 33(32):13190–203. doi: 10.1523/JNEUROSCI.0935-13.2013.

Naftelberg, Shiran, Ziv Abramovitch, Shani Gluska, Sivan Yannai, Yuvraj Joshi, Maya Donyo, Keren Ben-Yaakov, Tal Gradus, Jonathan Zonszain, Chen Farhy, Ruth Ashery-Padan, Eran Perlson, and Gil Ast. 2016. “Phosphatidylserine Ameliorates Neurodegenerative

Symptoms and Enhances Axonal Transport in a Mouse Model of Familial Dysautonomia." *PLoS Genetics* 12(12):1006486. doi: 10.1371/JOURNAL.PGEN.1006486.
Nakata, Takao, Shinsuke Niwa, Yasushi Okada, Franck Perez, and Nobutaka Hirokawa. 2011. "Preferential Binding of a Kinesin-1 Motor to GTP-Tubulin–Rich Microtubules Underlies Polarized Vesicle Transport." *Journal of Cell Biology* 194(2):245–55. doi: 10.1083/jcb.201104034.
Namsi, Amira, Thomas Nury, Haithem Hamdouni, Aline Yammine, Anne Vejux, Dominique Vervandier-Fasseur, Norbert Latruffe, Olfa Masmoudi-Kouki, and Gérard Lizard. 2018. "Induction of Neuronal Differentiation of Murine N2a Cells by Two Polyphenols Present in the Mediterranean Diet Mimicking Neurotrophins Activities: Resveratrol and Apigenin." *Diseases* 6(3):67. doi: 10.3390/DISEASES6030067.
Nedialkova, Danny D., and Sebastian A. Leidel. 2015. "Optimization of Codon Translation Rates via TRNA Modifications Maintains Proteome Integrity." *Cell* 161(7):1606–18. doi: 10.1016/j.cell.2015.05.022.
Neumann, Brent, and Massimo A. Hilliard. 2014. "Loss of MEC-17 Leads to Microtubule Instability and Axonal Degeneration." *Cell Reports* 6(1):93. doi: 10.1016/J.CELREP.2013.12.004.
Nicolas, Aude, Kevin P. Kenna, Alan E. Renton, Christopher E. Shaw, Bryan J. Traynor, John E. Landers Correspondence, and Bryan Traynor@nih Gov. 2018. "Genome-Wide Analyses Identify KIF5A as a Novel ALS Gene." *Neuron* 97. doi: 10.1016/j.neuron.2018.02.027.
Niwa, Shinsuke, Yosuke Tanaka, and Nobutaka Hirokawa. 2008. "KIF1Bβ- and KIF1A-Mediated Axonal Transport of Presynaptic Regulator Rab3 Occurs in a GTP-Dependent Manner through DENN/MADD." *Nature Cell Biology* 10(11):1269–79. doi: 10.1038/ncb1785.
Noma, Kentaro, Alexandr Goncharov, Mark H. Ellisman, and Yishi Jin. 2017. "Microtubule-Dependent Ribosome Localization in C. Elegans Neurons." *ELife* 6(Dcc):1–23. doi: 10.7554/eLife.26376.
Olenick, Mara A., Roberto Dominguez, and Erika L. F. Holzbaur. 2018. "Dynein Activator Hook1 Is Required for Trafficking of BDNF-Signaling Endosomes in Neurons." *J. Cell Biol* 218(1):220–33. doi: 10.1083/jcb.201805016.
Olgeiser, Lilli, Carl Haag, Susan Boerner, Jernej Ule, Anke Busch, Janine Koepke, Julian König, Michael Feldbrügge, and Kathi Zarnack. 2019. "The Key Protein of Endosomal MRNP Transport Rrm4 Binds Translational Landmark Sites of Cargo MRNAs." *EMBO Reports* 20(1):1–17. doi: 10.15252/embr.201846588.
Oostrum, Marc van, Thomas Blok, Stefano L. Giandomenico, Susanne tom Dieck, Georgi Tushev, Nicole Fürst, Julian Langer, Erin M. Schuman*, and Max. 2023. "The Proteomic Landscape of Synaptic Diversity across Brain Regions and Cell Types." *Bioarchive*. doi: https://doi.org/10.1101/2023.01.27.525780.
Ori-McKenney, Kassandra M., Richard J. McKenney, Hector H. Huang, Tun Li, Shan Meltzer, Lily Yeh Jan, Ronald D. Vale, Arun P. Wiita, and Yuh Nung Jan. 2016. "Phosphorylation of β-Tubulin by the Down Syndrome Kinase, Minibrain/DYRK1a, Regulates Microtubule Dynamics and Dendrite Morphogenesis." *Neuron* 90(3):551. doi: 10.1016/J.NEURON.2016.03.027.
Öztürk, Zeynep, Cahir J. O'Kane, and Juan José Pérez-Moreno. 2020. "Axonal Endoplasmic Reticulum Dynamics and Its Roles in Neurodegeneration." *Frontiers in Neuroscience* 14:48. doi: 10.3389/FNINS.2020.00048/BIBTEX.
Pamula, Melissa C., Shih Chieh Ti, and Tarun M. Kapoor. 2016. "The Structured Core of

Human β Tubulin Confers Isotype-Specific Polymerization Properties." *The Journal of Cell Biology* 213(4):425. doi: 10.1083/JCB.201603050.

Parbin, Sabnam, Swayamsiddha Kar, Arunima Shilpi, Dipta Sengupta, Moonmoon Deb, Sandip Kumar Rath, and Samir Kumar Patra. 2014. "Histone Deacetylases: A Saga of Perturbed Acetylation Homeostasis in Cancer." *Journal of Histochemistry and Cytochemistry* 62(1):11. doi: 10.1369/0022155413506582.

Park, In Young, Reid T. Powell, Durga Nand Tripathi, Ruhee Dere, Thai H. Ho, T. Lynne Blasius, Yun Chen Chiang, Ian J. Davis, Catherine C. Fahey, Kathryn E. Hacker, Kristen J. Verhey, Mark T. Bedford, Eric Jonasch, W. Kimryn Rathmell, and Cheryl Lyn Walker. 2016. "Dual Chromatin and Cytoskeletal Remodeling by SETD2." *Cell* 166(4):950. doi: 10.1016/J.CELL.2016.07.005.

Peet, Daniel R., Nigel J. Burroughs, and Robert A. Cross. 2018. "Kinesin Expands and Stabilises the GDP-Microtubule Lattice." *Nature Nanotechnology* 13(5):386. doi: 10.1038/S41565-018-0084-4.

Pensalfini, Anna, Ying Jiang, Seonil Kim, and Ralph A. Nixon. 2021. "Assessing Rab5 Activation in Health and Disease." Pp. 273–94 in *Anna.Pensalfini@nki.rfmh.org. Methods Mol Biol*. Vol. 2293.

Perez, Julio D., Susanne Tom Dieck, Beatriz Alvarez-Castelao, Georgi Tushev, Ivy C. W. Chan, and Erin M. Schuman. 2021. "Subcellular Sequencing of Single Neurons Reveals the Dendritic Transcriptome of Gabaergic Interneurons." *ELife* 10:1–26. doi: 10.7554/ELIFE.63092.

Peris, Leticia, Julie Parato, Xiaoyi Qu, Jean Marc Soleilhac, Fabien Lanté, Atul Kumar, Maria Elena Pero, José Martínez-Hernández, Charlotte Corrao, Giulia Falivelli, Floriane Payet, Sylvie Gory-Fauré, Christophe Bosc, Marian Blanca Ramirez, Andrew Sproul, Jacques Brocard, Benjamin Di Cara, Philippe Delagrange, Alain Buisson, Yves Goldberg, Marie Jo Moutin, Francesca Bartolini, and Annie Andrieux. 2022. "Tubulin Tyrosination Regulates Synaptic Function and Is Disrupted in Alzheimer's Disease." *Brain* 145(7):2486–2506. doi: 10.1093/brain/awab436.

Peris, Leticia, Michael Wagenbach, Laurence Lafanechère, Jacques Brocard, Ayana T. Moore, Frank Kozielski, Didier Job, Linda Wordeman, and Annie Andrieux. 2009. "Motor-Dependent Microtubule Disassembly Driven by Tubulin Tyrosination." *The Journal of Cell Biology* 185(7):1159. doi: 10.1083/JCB.200902142.

Pigino, Gustavo, Gerardo Morfini, Alejandra Pelsman, Mark P. Mattson, Scott T. Brady, and Jorge Busciglio. 2003. "Alzheimer's Presenilin 1 Mutations Impair Kinesin-Based Axonal Transport." *Journal of Neuroscience* 23(11):4499–4508. doi: 10.1523/JNEUROSCI.23-11-04499.2003.

Pilaz, Louis Jan, Ashley L. Lennox, Jeremy P. Rouanet, and Debra L. Silver. 2016. "Dynamic MRNA Transport and Local Translation in Radial Glial Progenitors of the Developing Brain." *Current Biology* 26(24):3383–92. doi: 10.1016/J.CUB.2016.10.040/ATTACHMENT/CBCFCCB5-0BC5-4F7A-B33C-85071A602D8B/MMC5.MP4.

Planelles-Herrero, Vicente Jose, Alice Bittleston, Carole Seum, Marcos Gonzalez Gaitan, and Emmanuel Derivery. 2022. *Elongator Stabilizes Microtubules to Control Central Spindle Asymmetry and Polarized Trafficking of Cell Fate Determinants*. Vol. 24. Springer US.

Planelles-Herrero, Vicente José, Mariya Genova, Alice Bittleston, Kerrie E. McNally, Gianluca Degliesposti, Maria M. Magiera, Carsten Janke, and Emmanuel Derivery. 2023. "Elongator Is a Microtubule Polymerase Selective for Poly-Glutamylated Tubulin."

BioRxiv 2023.05.10.540202. doi: 10.1101/2023.05.10.540202.
Pohlmann, Thomas, Sebastian Baumann, Carl Haag, Mario Albrecht, and Michael Feldbrügge. 2015. "A FYVE Zinc Finger Domain Protein Specifically Links MRNA Transport to Endosome Trafficking." *ELife* 4(MAY). doi: 10.7554/eLife.06041.
Poirier, Karine, Yoann Saillour, Nadia Bahi-Buisson, Xavier H. Jaglin, Catherine Fallet-Bianco, Rima Nabbout, Laetitia Castelnau-Ptakhine, Agathe Roubertie, Tania Attie-Bitach, Isabelle Desguerre, David Genevieve, Christine Barnerias, Boris Keren, Nicolas Lebrun, Nathalie Boddaert, Féréchté Encha-Razavi, and Jamel Chelly. 2010. "Mutations in the Neuronal β-Tubulin Subunit TUBB3 Result in Malformation of Cortical Development and Neuronal Migration Defects." *Human Molecular Genetics* 19(22):4462. doi: 10.1093/HMG/DDQ377.
Popovic D, Nijenhuis W, Kapitein C L, Pelkmans L. 2020. "Co-Translational Targeting of Transcripts to Endosomes." *BioRxiv*. doi: https://doi.org/10.1101/2020.07.17.208652.
Portran, Didier, Laura Schaedel, Zhenjie Xu, Manuel Théry, and Maxence V. Nachury. 2017. "Tubulin Acetylation Protects Long-Lived Microtubules against Mechanical Ageing." *Nature Cell Biology* 19(4):391–98. doi: 10.1038/ncb3481.
Prots, Iryna, Janina Grosch, Razvan Marius Brazdis, Katrin Simmnacher, Vanesa Veber, Steven Havlicek, Christian Hannappel, Florian Krach, Mandy Krumbiegel, Oliver Schütz, André Reis, Wolfgang Wrasidlo, Douglas R. Galasko, Teja W. Groemer, Eliezer Masliah, Ursula Schlötzer-Schrehardt, Wei Xiang, Jürgen Winkler, and Beate Winner. 2018. "α-Synuclein Oligomers Induce Early Axonal Dysfunction in Human IPSC-Based Models of Synucleinopathies." *Proceedings of the National Academy of Sciences of the United States of America* 115(30):7813–18. doi: 10.1073/PNAS.1713129115/-/DCSUPPLEMENTAL.
Qiang, Liang, Xiaohuan Sun, Timothy O. Austin, Hemalatha Muralidharan, Daphney C. Jean, Mei Liu, Wenqian Yu, and Peter W. Baas. 2018. "Tau Does Not Stabilize Axonal Microtubules but Rather Enables Them to Have Long Labile Domains." *Current Biology* 28(13):2181-2189.e4. doi: 10.1016/j.cub.2018.05.045.
Rangaraju, Vidhya, Marcel Lauterbach, and Erin M. Schuman. 2019. "Spatially Stable Mitochondrial Compartments Fuel Local Translation during Plasticity." *Cell* 176(1–2):73-84.e15. doi: 10.1016/j.cell.2018.12.013.
Rangaraju, Vidhya, Tommy L. Lewis, Yusuke Hirabayashi, Matteo Bergami, Elisa Motori, Romain Cartoni, Seok Kyu Kwon, and Julien Courchet. 2019. "Pleiotropic Mitochondria: The Influence of Mitochondria on Neuronal Development and Disease." *Journal of Neuroscience* 39(42):8200–8208. doi: 10.1523/JNEUROSCI.1157-19.2019.
Rangaraju, Vidhya, Susanne Tom Dieck, and Erin M. Schuman. 2017. "Local Translation in Neuronal Compartments: How Local Is Local?" *EMBO Reports*. doi: 10.15252/embr.201744045.
Rapino, Francesca, Sylvain Delaunay, Zhaoli Zhou, Alain Chariot, and Pierre Close. 2017. "TRNA Modification: Is Cancer Having a Wobble?" *Trends in Cancer* 3(4):249–52. doi: 10.1016/j.trecan.2017.02.004.
Rapino, Francesca, Zhaoli Zhou, Ana Maria Roncero Sanchez, Marc Joiret, Christian Seca, Najla El Hachem, Gianluca Valenti, Sara Latini, Kateryna Shostak, Liesbet Geris, Ping Li, Gang Huang, Gabriel Mazzucchelli, Dominique Baiwir, Christophe J. Desmet, Alain Chariot, Michel Georges, and Pierre Close. 2021. "Wobble TRNA Modification and Hydrophilic Amino Acid Patterns Dictate Protein Fate." *Nature Communications 2021 12:1* 12(1):1–14. doi: 10.1038/s41467-021-22254-5.

Reed, Nathan A., Dawen Cai, T. Lynne Blasius, Gloria T. Jih, Edgar Meyhofer, Jacek Gaertig, and Kristen J. Verhey. 2006. “Microtubule Acetylation Promotes Kinesin-1 Binding and Transport.” *Current Biology* 16(21):2166–72. doi: 10.1016/j.cub.2006.09.014.

Rodríguez-Martín, Teresa, Amy M. Pooler, Dawn H. W. Lau, Gábor M. Mórotz, Kurt J. De Vos, Jonathan Gilley, Michael P. Coleman, and Diane P. Hanger. 2016. “Reduced Number of Axonal Mitochondria and Tau Hypophosphorylation in Mouse P301L Tau Knockin Neurons.” *Neurobiology of Disease* 85:1. doi: 10.1016/J.NBD.2015.10.007.

Roney, Joseph C., Xiu-Tang Cheng, and Zu-Hang Sheng. 2022. “Neuronal Endolysosomal Transport and Lysosomal Functionality in Maintaining Axonostasis.” *Journal of Cell Biology* 221(3). doi: 10.1083/jcb.202111077.

Rosa-Ferreira, Cláudia, and Sean Munro. 2011. “Arl8 and SKIP Act Together to Link Lysosomes to Kinesin-1.” *Developmental Cell* 21(6):1171–78. doi: 10.1016/j.devcel.2011.10.007.

Ross, Anthony F., Yuri Oleynikov, Edward H. Kislauskis, Krishan L. Taneja, and Robert H. Singer. 1997. “Characterization of A-Actin MRNA Zipcode-Binding Protein.” *MOLECULAR AND CELLULAR BIOLOGY* 17(4):2158–65.

Ross, Jennifer L. Processiv. bidirectional motion of dynein-dynactin complexes in vitro, Karen Wallace, Henry Shuman, Yale E. Goldman, and Erika L. F. Holzbaur. 2006. “Processive Bidirectional Motion of Dynein-Dynactin Complexes in Vitro.” *Nature Cell Biology* 8(6):562–70. doi: 10.1038/ncb1421.

Ruijtenberg, Suzan, Tim A. Hoek, Xiaowei Yan, and Marvin E. Tanenbaum. 2018. *Imaging Translation Dynamics of Single MRNA Molecules in Live Cells*. Vol. 1649. edited by I. Gaspar. New York, NY: Springer New York.

Sakers, Kristina, Allison M. Lake, Rohan Khazanchi, Rebecca Ouwenga, Michael J. Vasek, Adish Dani, and Joseph D. Dougherty. 2017. “Astrocytes Locally Translate Transcripts in Their Peripheral Processes.” *Proceedings of the National Academy of Sciences of the United States of America* 114(19):E3830–38. doi: 10.1073/PNAS.1617782114/-/DCSUPPLEMENTAL.

Schuhmacher, Jan S., Susanne Tom Dieck, Markus T. Bohnsack, Erin M. Schuman, and Marino Zerial. 2023. “The Rab5 Effector FERRY Links Early Endosomes with MRNA Localization.” *Molecular Cell* 83. doi: 10.1016/j.molcel.2023.05.012.

Schule, R., B. P. H. Kremer, J. Kassubek, M. Auer-Grumbach, V. Kostic, T. Klopstock, S. Klimpe, S. Otto, S. Boesch, B. P. van de Warrenburg, and L. Schols. 2008. “SPG10 Is a Rare Cause of Spastic Paraplegia in European Families.” *Journal of Neurology, Neurosurgery & Psychiatry* 79(5):584–87. doi: 10.1136/jnnp.2007.137596.

Shida, Toshinobu, Juan G. Cueva, Zhenjie Xu, Miriam B. Goodman, and Maxence V. Nachury. 2010. “The Major α-Tubulin K40 Acetyltransferase ATAT1 Promotes Rapid Ciliogenesis and Efficient Mechanosensation.” *Proceedings of the National Academy of Sciences of the United States of America* 107(50):21517–22. doi: 10.1073/PNAS.1013728107/-/DCSUPPLEMENTAL.

Shigeoka, Toshiaki, Hosung Jung, Jane Jung, Benita Turner-Bridger, Jiyeon Ohk, Julie Qiaojin Lin, Paul S. Amieux, and Christine E. Holt. 2016. “Dynamic Axonal Translation in Developing and Mature Visual Circuits.” *Cell* 166(1):181–92. doi: 10.1016/j.cell.2016.05.029.

Shigeoka, Toshiaki, Max Koppers, Ho-Wai Wong, Hosung Jung, William A. Harris, Christine E. Holt Correspondence, Hovy Ho-Wai Wong, Julie Qiaojin Lin, Roberta Cagnetta, Asha Dwivedy, Janaina De Freitas Nascimento, Francesca W. Van Tartwijk, Florian Strö, Jean-

Michel Cioni, Julia Schaeffer, Mark Carrington, Clemens F. Kaminski, and Christine E. Holt. 2019. “On-Site Ribosome Remodeling by Locally Synthesized Ribosomal Proteins in Axons.” *CellReports* 29:3605-3619.e10. doi: 10.1016/j.celrep.2019.11.025.

Sicari, Daria, Aeid Igbaria, and Eric Chevet. 2019. “Control of Protein Homeostasis in the Early Secretory Pathway: Current Status and Challenges.” *Cells 2019, Vol. 8, Page 1347* 8(11):1347. doi: 10.3390/CELLS8111347.

Sirajuddin, Minhajuddin, Luke M. Rice, and Ronald D. Vale. 2014. “Regulation of Microtubule Motors by Tubulin Isotypes and Posttranslational Modifications.” *Nature Cell Biology* 16(4):335. doi: 10.1038/NCB2920.

Solinger, Jachen A., Roberta Paolinelli, Holger Klöß, Francesco Berlanda Scorza, Stefano Marchesi, Ursula Sauder, Dai Mitsushima, Fabrizio Capuani, Stephen R. Stürzenbaum, and Giuseppe Cassata. 2010. “The Caenorhabditis Elegans Elongator Complex Regulates Neuronal α-Tubulin Acetylation.” *PLoS Genetics* 6(1). doi: 10.1371/journal.pgen.1000820.

Soppina, Virupakshi, Stephen R. Norris, Aslan S. Dizaji, Matt Kortus, Sarah Veatch, Michelle Peckham, and Kristen J. Verhey. 2014. “Dimerization of Mammalian Kinesin-3 Motors Results in Superprocessive Motion.” *Proceedings of the National Academy of Sciences of the United States of America* 111(15):5562–67. doi: 10.1073/PNAS.1400759111/SUPPL_FILE/PNAS.201400759SI.PDF.

Sutton, Michael A., and Erin M. Schuman. 2006. “Dendritic Protein Synthesis, Synaptic Plasticity, and Memory.” *Cell* 127(1):49–58. doi: 10.1016/j.cell.2006.09.014.

Szpankowski, Lukasz, Sandra E. Encalada, and Lawrence S. B. Goldstein. 2012. “Subpixel Colocalization Reveals Amyloid Precursor Protein-Dependent Kinesin-1 and Dynein Association with Axonal Vesicles.” *Proceedings of the National Academy of Sciences of the United States of America* 109(22):8582–87. doi: 10.1073/PNAS.1120510109/SUPPL_FILE/PNAS.201120510SI.PDF.

Szyk, Agnieszka, Alexandra M. Deaconescu, Jeffrey Spector, Benjamin Goodman, Max L. Valenstein, Natasza E. Ziolkowska, Vasilisa Kormendi, Nikolaus Grigorieff, and Antonina Roll-Mecak. 2014. “Molecular Basis for Age-Dependent Microtubule Acetylation by Tubulin Acetyltransferase.” *Cell* 157(6):1405. doi: 10.1016/J.CELL.2014.03.061.

Taliaferro, J. Matthew, Marina Vidaki, Ruan Oliveira, Sara Olson, Lijun Zhan, Tanvi Saxena, Eric T. Wang, Brenton R. Graveley, Frank B. Gertler, Maurice S. Swanson, and Christopher B. Burge. 2016. “Distal Alternative Last Exons Localize MRNAs to Neural Projections.” *Molecular Cell* 61(6):821. doi: 10.1016/J.MOLCEL.2016.01.020.

Tanaka, Elly, Tran Ho, and Marc W. Kirschner. 1995. “The Role of Microtubule Dynamics in Growth Cone Motility and Axonal Growth.” *Journal of Cell Biology* 128(1–2):139–55. doi: 10.1083/jcb.128.1.139.

Tas, Roderick P., Anaël Chazeau, Bas M. C. Cloin, Maaike L. A. Lambers, Casper C. Hoogenraad, and Lukas C. Kapitein. 2017. “Differentiation between Oppositely Oriented Microtubules Controls Polarized Neuronal Transport.” *Neuron* 96(6):1264-1271.e5. doi: 10.1016/j.neuron.2017.11.018.

Thomas, María Gabriela, Mariela Loschi, María Andrea Desbats, and Graciela Lidia Boccaccio. 2011. “RNA Granules: The Good, the Bad and the Ugly.” *Cellular Signalling* 23(2):324. doi: 10.1016/J.CELLSIG.2010.08.011.

Ti, Shih Chieh, Gregory M. Alushin, and Tarun M. Kapoor. 2018. “Human β-Tubulin Isotypes Can Regulate Microtubule Protofilament Number and Stability.” *Developmental Cell* 47(2):175-190.e5. doi: 10.1016/j.devcel.2018.08.014.

Tielens, Sylvia, Sandra Huysseune, Juliette D. Godin, Alain Chariot, Brigitte Malgrange, and Laurent Nguyen. 2016. “Elongator Controls Cortical Interneuron Migration by Regulating Actomyosin Dynamics.” *Nature Publishing Group* 26:1131–48. doi: 10.1038/cr.2016.112.

Tiruchinapalli, Dhanrajan M., Yuri Oleynikov, Sofija Kelič, Shailesh M. Shenoy, Adam Hartley, Patric K. Stanton, Robert H. Singer, and Gary J. Bassell. 2003. “Activity-Dependent Trafficking and Dynamic Localization of Zipcode Binding Protein 1 and β-Actin MRNA in Dendrites and Spines of Hippocampal Neurons.” *The Journal of Neuroscience* 23(8):3251. doi: 10.1523/JNEUROSCI.23-08-03251.2003.

Tom Dieck, Susanne, Lisa Kochen, Cyril Hanus, Maximilian Heumüller, Ina Bartnik, Belquis Nassim-Assir, Katrin Merk, Thorsten Mosler, Sakshi Garg, Stefanie Bunse, David A. Tirrell, and Erin M. Schuman. 2015. “Direct Visualization of Newly Synthesized Target Proteins in Situ.” *Nature Methods* 12(5):411–14. doi: 10.1038/nmeth.3319.

Torvund-Jensen, Julie, Jes Steengaard, Lasse Reimer, Linda B. Fihl, and Lisbeth S. Laursen. 2014. “Transport and Translation of MBP MRNA Is Regulated Differently by Distinct HnRNP Proteins.” *Journal of Cell Science* 127(7):1550–64. doi: 10.1242/JCS.140855/259783/AM/TRANSPORT-AND-TRANSLATION-OF-MBP-MRNA-IS.

Triclin, Sarah, Daisuke Inoue, Jérémie Gaillard, Zaw Min Htet, Morgan E. DeSantis, Didier Portran, Emmanuel Derivery, Charlotte Aumeier, Laura Schaedel, Karin John, Christophe Leterrier, Samara L. Reck-Peterson, Laurent Blanchoin, and Manuel Théry. 2021. “Self-Repair Protects Microtubules from Destruction by Molecular Motors.” *Nature Materials* 20(6):883–91. doi: 10.1038/s41563-020-00905-0.

Tübing, Fabian, Georgia Vendra, Martin Mikl, Paolo Macchi, Sabine Thomas, and Michael A. Kiebler. 2010. “Dendritically Localized Transcripts Are Sorted into Distinct Ribonucleoprotein Particles That Display Fast Directional Motility along Dendrites of Hippocampal Neurons.” *The Journal of Neuroscience* 30(11):4160. doi: 10.1523/JNEUROSCI.3537-09.2010.

Turchetto, Silvia, Romain Le Bail, Loic Broix, and Laurent Nguyen. 2022. “Molecular Analysis of Axonal Transport Dynamics upon Modulation of Microtubule Acetylation.” *Methods in Molecular Biology* 2431:207–24.

Tushev, Georgi, Caspar Glock, Maximilian Heumüller, Anne Biever, Marko Jovanovic, and Erin M. Schuman. 2018. “Alternative 3’ UTRs Modify the Localization, Regulatory Potential, Stability, and Plasticity of MRNAs in Neuronal Compartments.” *Neuron* 98(3):495-511.e6. doi: 10.1016/j.neuron.2018.03.030.

Valenstein, Max L., and Antonina Roll-Mecak. 2016. “Graded Control of Microtubule Severing by Tubulin Glutamylation.” *Cell* 164(5):911–21. doi: 10.1016/j.cell.2016.01.019.

Vasek, Michael J., Jelani D. Deajon-Jackson, Yating Liu, Haley W. Crosby, Jiwon Yi, Joseph D. Dougherty, and Joseph Dougherty. 2021. “Microglia Perform Local Protein Synthesis at Perisynaptic and Phagocytic Structures.” *BioRxiv* 2021.01.13.426577. doi: 10.1101/2021.01.13.426577.

Vollmeister, Evelyn, Kerstin Schipper, Sebastian Baumann, Carl Haag, Thomas Pohlmann, Janpeter Stock, and Michael Feldbrügge. 2012. “Fungal Development of the Plant Pathogen Ustilago Maydis.” *FEMS Microbiology Reviews* 36(1):59–77. doi: 10.1111/j.1574-6976.2011.00296.x.

Wang, Bin, Lin Pan, Manyi Wei, Qiong Wang, Wen Wen Liu, Nuoxin Wang, Xing Yu Jiang, Xu Zhang, and Lan Bao. 2015. “FMRP-Mediated Axonal Delivery of MiR-181d Regulates

Axon Elongation by Locally Targeting Map1b and Calm1." *Cell Reports* 13(12):2794–2807. doi: 10.1016/j.celrep.2015.11.057.

Wang, Chong, Boran Han, Ruobo Zhou, and Xiaowei Zhuang. 2016. "Real-Time Imaging of Translation on Single MRNA Transcripts in Live Cells." *Cell* 165(4):990–1001. doi: 10.1016/j.cell.2016.04.040.

Wang, Dan O., Kensuke Ninomiya, Chihiro Mori, Ayako Koyama, Martine Haan, Makoto Kitabatake, Masatoshi Hagiwara, Kazuhiro Chida, Shin Ichiro Takahashi, Mutsuhito Ohno, and Naoyuki Kataoka. 2017. "Transport Granules Bound with Nuclear Cap Binding Protein and Exon Junction Complex Are Associated with Microtubules and Spatially Separated from EIF4E Granules and P Bodies in Human Neuronal Processes." *Frontiers in Molecular Biosciences* 4(DEC):93. doi: 10.3389/FMOLB.2017.00093/FULL.

Wang, Qi, Jing Tian, Hao Chen, Heng Du, and Lan Guo. 2019. "Amyloid Beta-Mediated KIF5A Deficiency Disrupts Anterograde Axonal Mitochondrial Movement." *Neurobiology of Disease* 127:410–18. doi: 10.1016/J.NBD.2019.03.021.

Wang, Qianmin, Alvaro H. Crevenna, Ines Kunze, and Naoko Mizuno. 2014. "Structural Basis for the Extended CAP-Gly Domains of P150glued Binding to Microtubules and the Implication for Tubulin Dynamics." *Proceedings of the National Academy of Sciences of the United States of America* 111(31):11347–52. doi: 10.1073/PNAS.1403135111/-/DCSUPPLEMENTAL.

Webster, D. R., and G. G. Borisy. 1989. "Microtubules Are Acetylated in Domains That Turn over Slowly." *Journal of Cell Science* 92(1):57–65. doi: 10.1242/JCS.92.1.57.

Wei, Dan, Nannan Gao, Lei Li, Jing Xiang Zhu, Lei Diao, Jiansong Huang, Qing Jian Han, Shaogang Wang, Huaqing Xue, Qiong Wang, Qing Feng Wu, Xu Zhang, and Lan Bao. 2018. "α-Tubulin Acetylation Restricts Axon Overbranching by Dampening Microtubule plus-End Dynamics in Neurons." *Cerebral Cortex* 28(9):3332–46. doi: 10.1093/cercor/bhx225.

Wilbertz, Johannes H., Franka Voigt, Ivana Horvathova, Gregory Roth, Yinxiu Zhan, and Jeffrey A. Chao. 2019. "Single-Molecule Imaging of MRNA Localization and Regulation during the Integrated Stress Response." *Molecular Cell* 73(5):946-958.e7. doi: 10.1016/j.molcel.2018.12.006.

Willett, Rose, José A. Martina, James P. Zewe, Rachel Wills, Gerald R. V. Hammond, and Rosa Puertollano. 2017. "TFEB Regulates Lysosomal Positioning by Modulating TMEM55B Expression and JIP4 Recruitment to Lysosomes." *Nature Communications 2017 8:1* 8(1):1–17. doi: 10.1038/s41467-017-01871-z.

Williams, Christopher C., Calvin H. Jan, and Jonathan S. Weissman. 2014. "Targeting and Plasticity of Mitochondrial Proteins Revealed by Proximity-Specific Ribosome Profiling." *Science* 346(6210):748–51. doi: 10.1126/science.1257522.

Willis, Dianna, Wan Li Ka, Jun Qi Zheng, Jay H. Chang, August Smit, Theresa Kelly, Tanuja T. Merianda, James Sylvester, Jan Van Minnen, and Jeffery L. Twiss. 2005. "Differential Transport and Local Translation of Cytoskeletal, Injury-Response, and Neurodegeneration Protein MRNAs in Axons." *The Journal of Neuroscience* 25(4):778. doi: 10.1523/JNEUROSCI.4235-04.2005.

Wloga, Dorota, Danielle M. Webster, Krzysztof Rogowski, Marie Hélène Bré, Nicolette Levilliers, Maria Jerka-Dziadosz, Carsten Janke, Scott T. Dougan, and Jacek Gaertig. 2009. "TTLL3 Is a Tubulin Glycine Ligase That Regulates the Assembly of Cilia." *Developmental Cell* 16(6):867–76. doi: 10.1016/j.devcel.2009.04.008.

Wong, Hovy Ho Wai, Julie Qiaojin Lin, Florian Ströhl, Cláudio Gouveia Roque, Jean Michel

Cioni, Roberta Cagnetta, Benita Turner-Bridger, Romain F. Laine, William A. Harris, Clemens F. Kaminski, and Christine E. Holt. 2017. “RNA Docking and Local Translation Regulate Site-Specific Axon Remodeling In Vivo.” *Neuron* 95(4):852. doi: 10.1016/J.NEURON.2017.07.016.

Wu, Bin, Carolina Eliscovich, Young J. Yoon, and Robert H. Singer. 2016. “Translation Dynamics of Single MRNAs in Live Cells and Neurons.” *Science* 352(6292):1430–35. doi: 10.1126/science.aaf1084.

Xie, Xuan, Shaogang Wang, Mingyi Li, Lei Diao, Xingyu Pan, Jijun Chen, Weiguo Zou, Xu Zhang, Wenfeng Feng, and Lan Bao. 2021. “α-TubK40me3 Is Required for Neuronal Polarization and Migration by Promoting Microtubule Formation.” *Nature Communications 2021 12:1* 12(1):1–16. doi: 10.1038/s41467-021-24376-2.

Xu, Zhenjie, Laura Schaedel, Didier Portran, Andrea Aguilar, Jérémie Gaillard, M. Peter Marinkovich, Manuel Théry, and Maxence V. Nachury. 2017. “Microtubules Acquire Resistance from Mechanical Breakage through Intralumenal Acetylation.” *Science (New York, N.Y.)* 356(6335):328. doi: 10.1126/SCIENCE.AAI8764.

Yan, Xiaowei, Tim A. Hoek, Ronald D. Vale, and Marvin E. Tanenbaum. 2016. “Dynamics of Translation of Single MRNA Molecules In Vivo.” *Cell* 165(4):976–89. doi: 10.1016/j.cell.2016.04.034.

Yasuda, Kyota, Huaye Zhang, David Loiselle, Timothy Haystead, Ian G. Macara, and Stavroula Mili. 2013. “The RNA-Binding Protein Fus Directs Translation of Localized MRNAs in APC-RNP Granules.” *The Journal of Cell Biology* 203(5):737–46. doi: 10.1083/jcb.201306058.

Yau, Kah Wai, Philipp Schätzle, Elena Tortosa, Stéphane Pagès, Anthony Holtmaat, Lukas C. Kapitein, and Casper C. Hoogenraad. 2016. “Dendrites In Vitro and In Vivo Contain Microtubules of Opposite Polarity and Axon Formation Correlates with Uniform Plus-End-Out Microtubule Orientation.” *The Journal of Neuroscience* 36(4):1071. doi: 10.1523/JNEUROSCI.2430-15.2016.

Yoon, Young J., Bin Wu, Adina R. Buxbaum, Sulagna Das, Albert Tsai, Brian P. English, Jonathan B. Grimm, Luke D. Lavis, and Robert H. Singer. 2016. “Glutamate-Induced RNA Localization and Translation in Neurons.” *Proceedings of the National Academy of Sciences of the United States of America* 113(44):E6877–86. doi: 10.1073/pnas.1614267113.

Young Park, In, Pratim Chowdhury, Durga Nand Tripathi, Reid T. Powell, Ruhee Dere, Esteban A. Terzo, W. Kimryn Rathmell, and Cheryl Lyn Walker. 2016. “MAbs Methylated α-Tubulin Antibodies Recognize a New Microtubule Modification on Mitotic Microtubules.” doi: 10.1080/19420862.2016.1228505.

Younts, Thomas J., Hannah R. Monday, Barna Dudok, Matthew E. Klein, Bryen A. Jordan, István Katona, and Pablo E. Castillo. 2016. “Presynaptic Protein Synthesis Is Required for Long-Term Plasticity of GABA Release.” *Neuron* 92:479–92. doi: 10.1016/j.neuron.2016.09.040.

Yu, Yong, Shihong M. Gao, Youchen Guan, Peiwen Hu, Qinghao Zhang, Jiaming Liu, Bentian Jing, Qian Zhao, David M. Sabatini, Monther Abu-Remaileh, Sung Yun Jung, and Meng C. Wang. 2022. “Proteomic Profiling Reveals Lysosomal Heterogeneity in Association with Longevity.” *BioRxiv*. doi: 10.1101/2022.10.16.512400.

Zander, Sabrina, Sebastian Baumann, Stefanie Weidtkamp-Peters, and Michael Feldbrügge. 2016. “Endosomal Assembly and Transport of Heteromeric Septin Complexes Promote Septin Cytoskeleton Formation.” *Journal of Cell Science* 129(14):2778–92. doi:

10.1242/JCS.182824/VIDEO-10.
Zeng, Hu, Jiahao Huang, Jingyi Ren, Connie Kangni Wang, Zefang Tang, Haowen Zhou, Yiming Zhou, Hailing Shi, Abhishek Aditham, Xin Sui, Hongyu Chen, Jennifer A. Lo, and Xiao Wang. 2023. “Spatially Resolved Single-Cell Translatomics at Molecular Resolution.” *Science* 380(6652):2022.09.27.509605. doi: 10.1126/science.add3067.
Zhang, H. L., T. Eom, Y. Oleynikov, S. M. Shenoy, D. A. Liebelt, J. B. Dictenberg, R. H. Singer, and G. J. Bassell. 2001. “Neurotrophin-Induced Transport of a β-Actin MRNP Complex Increases β-Actin Levels and Stimulates Growth Cone Motility.” *Neuron* 31(2):261–75. doi: 10.1016/S0896-6273(01)00357-9.
Zhang, Xin, and Shu Ou Shan. 2014. “Fidelity of Co-Translational Protein Targeting by the Signal Recognition Particle.” *Annual Review of Biophysics* 43(1):381. doi: 10.1146/ANNUREV-BIOPHYS-051013-022653.
Zhao, Jing, Yi Wang, Huan Xu, Yuan Fu, Ting Qian, Deng Bo, Yan Xin Lu, Yi Xiong, Jun Wan, Xiang Zhang, Qiang Dong, and Xiang Jun Chen. 2016. “Dync1h1 Mutation Causes Proprioceptive Sensory Neuron Loss and Impaired Retrograde Axonal Transport of Dorsal Root Ganglion Neurons.” *CNS Neuroscience and Therapeutics* 22(7):593–601. doi: 10.1111/CNS.12552.
Zilberman, Yuliya, Christoph Ballestrem, Letizia Carramusa, Ralph Mazitschek, Saadi Khochbin, and Alexander Bershadsky. 2009. “Regulation of Microtubule Dynamics by Inhibition of the Tubulin Deacetylase HDAC6.” *Journal of Cell Science* 122(19):3531–41. doi: 10.1242/JCS.046813.
Zivraj, Krishna H., Yi Chun Loraine Tung, Michael Piper, Laura Gumy, James W. Fawcett, Giles S. H. Yeo, and Christine E. Holt. 2010. “Subcellular Profiling Reveals Distinct and Developmentally Regulated Repertoire of Growth Cone MRNAs.” *The Journal of Neuroscience* 30(46):15464–78. doi: 10.1523/JNEUROSCI.1800-10.2010.

ANNEX

SUPPLEMENTARY DATA: ATAT1-enriched vesicles promote microtubule acetylation via axonal transport

ScienceAdvances

ATAT1-enriched vesicles promote microtubule acetylation via axonal transport

Aviel Even, Giovanni Morelli, Loïc Broix, Chiara Scaramuzzino, Silvia Turchetto, Ivan Gladwyn-Ng, Romain Le Bail, Michal Shilian, Stephen Freeman, Maria M. Magiera, A. S. Jijumon, Nathalie Krusy, Brigitte Malgrange, Bert Brone, Paula Dietrich, Ioannis Dragatsis, Carsten Janke, Frédéric Saudou, Miguel Weil and Laurent Nguyen

Sci Adv **5** (12), eaax2705.
DOI: 10.1126/sciadv.aax2705

Science Advances
AAAS

advances.sciencemag.org/cgi/content/full/5/12/eaax2705/DC1

Supplementary Materials for

ATAT1-enriched vesicles promote microtubule acetylation via axonal transport

Aviel Even, Giovanni Morelli, Loïc Broix, Chiara Scaramuzzino, Silvia Turchetto, Ivan Gladwyn-Ng, Romain Le Bail, Michal Shilian, Stephen Freeman, Maria M. Magiera, A. S. Jijumon, Nathalie Krusy, Brigitte Malgrange, Bert Brone, Paula Dietrich, Ioannis Dragatsis, Carsten Janke, Frédéric Saudou, Miguel Weil*, Laurent Nguyen*

*Corresponding author. Email: lnguyen@uliege.be (L.N.); miguelw@tauex.tau.ac.il (M.W.)

Published 18 December 2019, *Sci. Adv.* **5**, eaax2705 (2019)
DOI: 10.1126/sciadv.aax2705

The PDF file includes:

Other Supplementary Material for this manuscript includes the following:

(available at advances.sciencemag.org/cgi/content/full/5/12/eaax2705/DC1)

Movie S2 (.avi format). Representative movie of lysosome trafficking in axons located in the distal part of PDMS chambers.
Movie S3 (.avi format). Representative movie of mitochondria trafficking in axons located in the distal part of PDMS chambers.
Movie S4 (.avi format). Representative movie of synaptotagmin-GFP trafficking in motoneurons of third-instar larvae.
Movie S5 (.avi format). Representative movies of vesicles trafficking in vitro over polymerized rhodamine-labeled MTs.
Movie S6 (.avi format). Representative movie of ATAT1-GFP trafficking in axons located in the distal part of PDMS chambers.

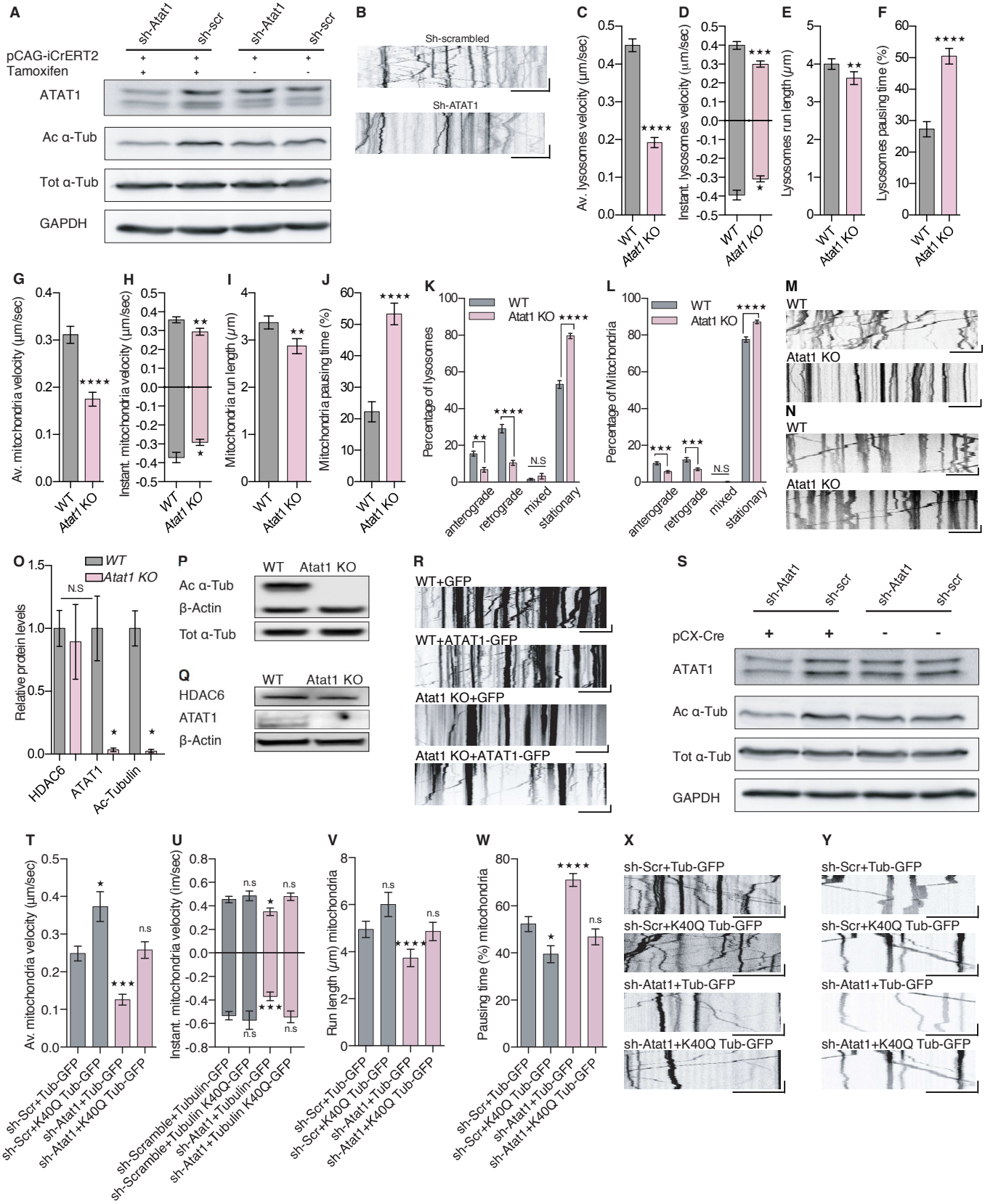
A
sh-Atat1
sh-scr
sh-Atat1
sh-scr
pCAG-iCrERT2
Tamoxifen
ATAT1
Ac α-Tub
Tot α-Tub
GAPDH
B
Sh-scrambled
Sh-ATAT1
C
Av. lysosomes velocity (μm/sec)
WT
Atat1 KO
D
Instant. lysosomes velocity (μm/sec)
E
Lysosomes run length (μm)
F
Lysosomes pausing time (%)
G
Av. mitochondria velocity (μm/sec)
H
Instant. mitochondria velocity (μm/sec)
I
Mitochondria run length (μm)
J
Mitochondria pausing time (%)
K
Percentage of lysosomes
WT
Atat1 KO
anterograde
retrograde
mixed
stationary
N.S
L
Percentage of Mitochondria
M
WT
Atat1 KO
N
WT
Atat1 KO
O
WT
Atat1 KO
Relative protein levels
N.S
HDAC6
ATAT1
Ac-Tubulin
P
WT
Atat1 KO
Ac α-Tub
β-Actin
Tot α-Tub
Q
WT
Atat1 KO
HDAC6
ATAT1
β-Actin
R
WT+GFP
WT+ATAT1-GFP
Atat1 KO+GFP
Atat1 KO+ATAT1-GFP
S
sh-Atat1
sh-scr
sh-Atat1
sh-scr
pCX-Cre
ATAT1
Ac α-Tub
Tot α-Tub
GAPDH
T
Av. mitochondria velocity (μm/sec)
sh-Scr+Tub-GFP
sh-Scr+K40Q Tub-GFP
sh-Atat1+Tub-GFP
sh-Atat1+K40Q Tub-GFP
U
Instant. mitochondria velocity (im/sec)
n.s
sh-Scramble+Tubulin-GFP
sh-Scramble+Tubulin K40Q-GFP
sh-Atat1+Tubulin-GFP
sh-Atat1+Tubulin K40Q-GFP
V
Run length (μm) mitochondria
W
Pausing time (%) mitochondria
X
sh-Scr+Tub-GFP
sh-Scr+K40Q Tub-GFP
sh-Atat1+Tub-GFP
sh-Atat1+K40Q Tub-GFP
Y
sh-Scr+Tub-GFP
sh-Scr+K40Q Tub-GFP
sh-Atat1+Tub-GFP
sh-Atat1+K40Q Tub-GFP

Fig. S1. Analysis of axonal transport parameters in WT and Atat1 KO mice. (**A**) WB analyses to detect ATAT1 (Isoform 3 and 4 corresponding to 37kd and 30kd), acetylated α-tubulin (Ac α-tub), total α-tubulin (Tot α-tub) and GAPDH levels in N2A cells extract transfected with inducible sh-RNA (sh-scr, sh-scrambled, or sh-Atat1) with or without CreERT2 Tamoxifen-driven expression plasmid. (**B**) Representative kymographs of transported LAMP1-Emerald (lysosomes) in axons running into the corpus callosum of brain section from P2 mouse *in utero* electroporated (IUE) with either sh-scrambled or sh-ATAT1. Scale bars are x: 10 µm, y: 20 seconds. (**C-J**) Histograms showing axonal transport of lysosomes and mitochondria to analyze average velocity (C, G), instantaneous velocity (D, H), run length (E, I) and pausing time (F, J) in E14.5 WT or *Atat1* KO cortical neurons cultured 5DIV. (**K-L)** Histograms representing the percentage of moving anterograde, retrograde, mixed and stationary lysosomes (K) and mitochondria (L) in E14.5 WT or *Atat1* KO cortical neurons cultured 5DIV. (**M-N**) Representative kymographs of transported lysosomes (M) and mitochondria (N) detected with fluorescent probes (LysoTracker and MitoTracker) in E14.5 WT or *Atat1* KO cortical neurons cultured 5DIV. Scale bars are x: 10 µm, y: 20 seconds. (**O-Q**) Histogram and WB analyses to detect total α-tubulin (Tot α-tub), acetylated α-tubulin (Ac α-tub) and β-Actin, Histone deacetylase 6 (HDAC6) and ATAT1 (Isoform 3 and 4 corresponding to 37kd and 30kd) levels in cortical brain extracts of newborn WT or *Atat1* KO mice. (**R**) Representative kymographs of transported lysosomes detected with fluorescent probes (LysoTracker) in cortical neurons cultured 5DIV from E14.5 WT or *Atat1* KO mouse embryos transfected with ATAT1-GFP or GFP. Scale bars are x: 10 µm, y: 20 seconds. (**S**) WB analyses to detect ATAT1 (Isoform 3 and 4 corresponding to 37kd and 30kd), acetylated α-tubulin (Ac α-tub), total α-tubulin (Tot α-tub) and GAPDH levels in N2A cells extract transfected with inducible sh-RNA with or without constitutive pCX-Cre expressing plasmid. (**T-W**) Histograms showing axonal transport of mitochondria (Mito-DsRed) to analyze average velocity (T), instantaneous velocity (U), run length (V) and pausing time (W) in mouse cortical neurons cultured 5DIV from E15.5 embryos IUE at E14.5 with Mito-DsRed, WT α-tubulin GFP (Tub-GFP) or acetylation mimic K40Q α-tubulin GFP (K40Q-Tub-GFP) together with either sh-Scrambled (sh-Scr) or sh-Atat1. (**X-Y**) Representative kymographs of transported lysosomes (X) and mitochondria (Y) detected with fluorescent probes (LysoTracker) and Mito-DsRed expressing plasmid in 5DIV mouse cortical neurons isolated from E15.5 embryos IUE electroporated at E14.5 with either WT α-tubulin GFP (Tub-GFP) or acetylation mimic K40Q α-tubulin GFP (K40Q-Tub-GFP), in

combination with either sh-Scrambled (sh-Scr) or sh-Atat1. Scale bars are x: 10 μm, y: 20 seconds.

Description of graphical summaries here within are histograms of means ± S.E.M, while statistical analyses of (C-J, O) are two-tailed Mann-Whitney; (K-L) are Two-Way ANOVA and (T-W) are Kruskal-Wallis test. Specifically (C, P<0.0001 & U=10,103; D, P=0.0005 & U=5447 while P=0.0205 & U=6372 for anterograde and retrograde respectively; E, P=0.0014 & U=23668; F, P<0.0001 U=19,160; G, P<0.0001 & U=5,815; H, P=0.0035 & U=1,909 while P=0.0241 & U=1,552 for anterograde and retrograde respectively; I, P=0.0017 & U=7652; J, P<0.0001 U=5,882; K, P< 0.0001 & F (3,78)= 23.86; L, P<0.0001 & F (3, 81) = 61.90; O, P=0.0286 & U=0 for acetylated α-tubulin, P=0.0286 & U=0 for ATAT1, and P=0.8286 & U=7 for HDAC6; T, P<0.0001 & K= 53.97; U, P=0.0033 & K= 13.73 while P=0.0011 & K=16.05 for anterograde and retrograde respectively; V, P<0.0001 & K= 31.3; W, P<0.0001 & K= 48.59). In addition, post-hoc multiple comparisons for (K-L) is Sidak's test, for (T-W) is Dunn's test and p values are *P<0.05, **P<0.01, ***P<0.001, ****P<0.0001. The total number of samples analyzed were: (C-J) 116-279 lysosomes tracks and 117-169 mitochondria tracks from 5 embryos of WT or *Atat1* KO; (K-L) 15 axons from 5 embryos of WT or *Atat1* KO; (O) 4 brain cortical extracts from newborn WT or *Atat1* KO mice, (T-W) 148-205 mitochondria& U=1,909 tracks from 3 E15.5 embryos transfected with sh-Scramble or Sh-Atat1.

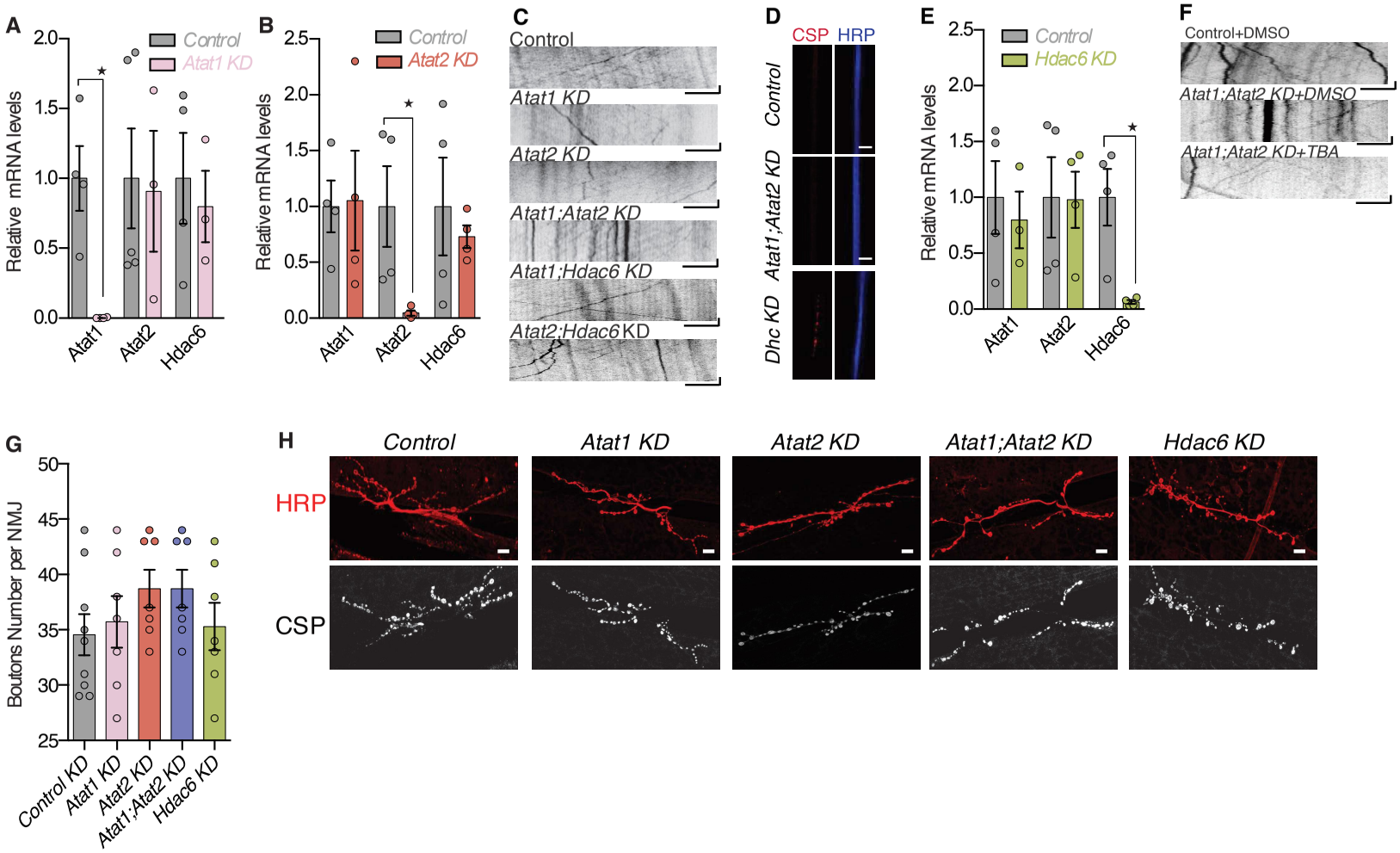
A
Relative mRNA levels
Control
Atat1 KD
Atat1
Atat2
Hdac6
B
Relative mRNA levels
Control
Atat2 KD
Atat1
Atat2
Hdac6
C
Control
Atat1 KD
Atat2 KD
Atat1;Atat2 KD
Atat1;Hdac6 KD
Atat2;Hdac6 KD
D
CSP HRP
Control
Atat1;Atat2 KD
Dhc KD
E
Relative mRNA levels
Control
Hdac6 KD
Atat1
Atat2
Hdac6
F
Control+DMSO
Atat1;Atat2 KD+DMSO
Atat1;Atat2 KD+TBA
G
Boutons Number per NMJ
Control KD
Atat1 KD
Atat2 KD
Atat1;Atat2 KD
Hdac6 KD
H
Control
Atat1 KD
Atat2 KD
Atat1;Atat2 KD
Hdac6 KD
HRP
CSP

Fig. S2. Validation of RNAi efficiency, mRNA expression of MTs modifying enzymes, representative kymographs of axonal transport, and protein aggregation in *D. melanogaster*. (**A-B**) mRNA levels of *Atat1*, *Atat2* and *Hdac6* in extracts from fly heads, expressing RNAi under pan-neuronal (elav:GAL4) specific driver from Control, *Atat1* KD and Atat2 KD. (**C**) Representative kymographs of Synaptotagmin-GFP in motoneuron axons of *Drosophila melanogaster* 3rd instar larvae expressing RNAi under a motoneuron specific driver (D42:GAL4). Scale bars are x: 5 µm, y: 10 seconds. (**D**) Nerves exiting the ventral ganglion of 3rd instar larvae expressing RNAi under motor neurons specific driver (D42:GAL4), immunolabeled to detect the neuronal marker horseradish peroxidase (HRP) and cysteine string protein (CSP) as marker for protein aggregation. Scale bar is 10 µm. (**E**) mRNA levels of *Atat1*, *Atat2* and *Hdac6* in fly heads, expressing RNAi under pan-neuronal (elav:GAL4) specific driver from Control and *Hdac6* KD. (**F**) Representative kymographs of Synaptotagmin-GFP in axons of *Drosophila melanogaster* 3rd instar larvae motoneurons expressing RNAi under a motoneuron specific driver (D42:GAL4). Scale bars are x: 5 µm, y: 10 seconds. (**G-H**) Histogram and representative images of M3/5 immunolabeled neuromuscular junction in 3rd instar larvae using anti-CSP (white) and anti-HRP (red) (n=5, $p<0.0001$, one-way ANOVA Tukey's multiple comparisons test). Scale bar is 30 µm. Description of graphical summaries here within are histograms of means ± S.E.M, statistical analyses of (A, B, E) are two-tailed Mann-Whitney and (G) is One-Way ANOVA. In addition, post-hoc multiple comparisons for (G) is Dunnett's test. Specifically (A, P=0.0286 & U=0 for *Atat1*, P=0.6786 & U=6 for *Atat2* and P=0.7492 & U=5 for *Hdac6*; B, P=0.999 & U=8 for *Atat1*, P=0.0286 & U=0 for *Atat2* and P=0.999 & U=8 for *Hdac6*; E, P=0.7429 & U=5 for *Atat1*, P=0.6571 & U=6 for *Atat2* and P=0.0286 & U=0 for *Hdac6*; G, P=0.4073 & $F_{(4,32)}=1.029$). The total number of samples analyzed was (A, B, E) 3-5 samples (of 10 fly's heads each) per group; (G) 7-9 larvae per group.

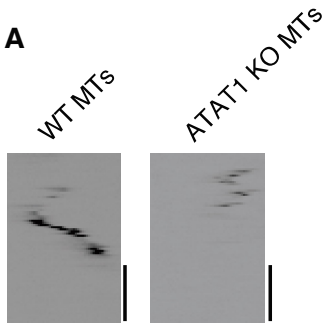

Fig. S3. Kymographs of in vitro transport assay. (**A**) Representative kymographs of i*n vitro* transport assay of vesicles purified from WT mice with non-acetylated tubulin from *Atat1* KO mice brain pre-incubated with either acetyl-CoA or endogenously acetylated tubulin from WT mice served as Control. Scale bars are x: 5 μm, y: 5 seconds.

A

Fig. S4. Identified peptides of ATAT1 by LC-MS/MS. (**A**) Amino-acid sequence of ATAT1 isoforms 1-5. The identified ATAT1 peptides (blue) in the vesicle fractions of WT newborn mouse brain cortices (n=3). Annotation of AP2 binding domain (red).

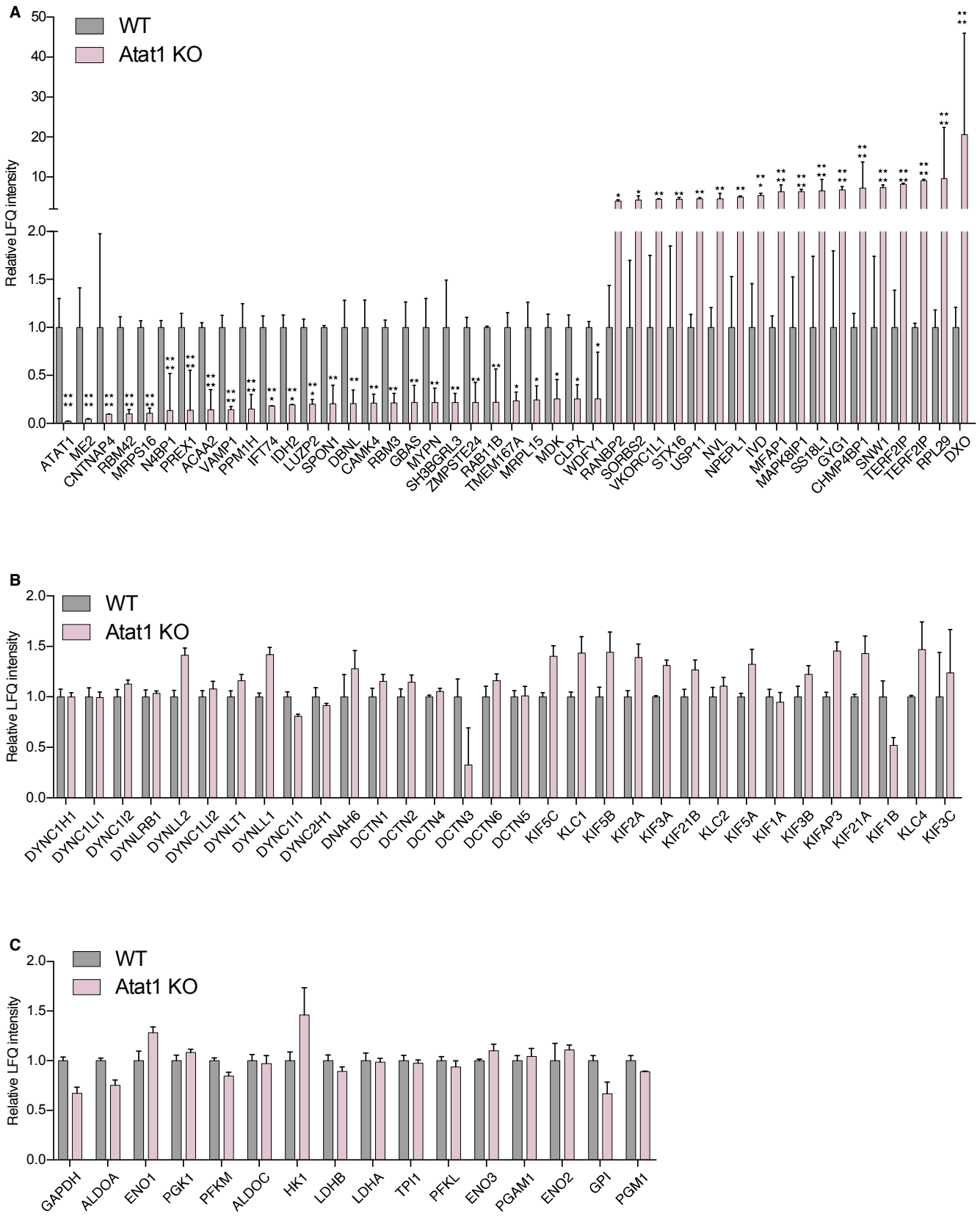
A
WT
Atat1 KO
Relative LFQ intensity
ATAT1
ME2
CNTNAP4
RBM42
MRPS16
N4BP1
PREX1
ACAA2
VAMP1
PPM1H
IFT74
IDH2
LUZP2
SPON1
DBNL
CAMK4
RBM3
GBAS
MYPN
SH3BGRL3
ZMPSTE24
RAB11B
TMEM167A
MRPL15
MDK
CLPX
WDFY1
RANBP2
SORBS2
VKORC1L1
STX16
USP11
NVL
NPEPL1
IVD
MFAP1
MAPK8IP1
SS18L1
GYG1
CHMP4BP1
SNW1
TERF2IP
TERF2IP
RPL29
DXO
B
WT
Atat1 KO
Relative LFQ intensity
DYNC1H1
DYNC1LI1
DYNC1I2
DYNLRB1
DYNLL2
DYNC1LI2
DYNLT1
DYNLL1
DYNC1I1
DYNC2H1
DNAH6
DCTN1
DCTN2
DCTN4
DCTN3
DCTN6
DCTN5
KIF5C
KLC1
KIF5B
KIF2A
KIF3A
KIF21B
KLC2
KIF5A
KIF1A
KIF3B
KIFAP3
KIF21A
KIF1B
KLC4
KIF3C
C
WT
Atat1 KO
Relative LFQ intensity
GAPDH
ALDOA
ENO1
PGK1
PFKM
ALDOC
HK1
LDHB
LDHA
TPI1
PFKL
ENO3
PGAM1
ENO2
GPI
PGM1

Fig. S5. LC-MS/MS proteomics on vesicular extracts from WT and ATAT1 KO mice. (**A-C**) Histograms of differentially detected proteins (A), molecular motors (B) and glycolytic enzymes (C) detected by LC–MS/MS in vesicles extracts isolated from newborn WT or *Atat1 KO* cortices. Description of graphical summaries here within are histograms of means ± S.E.M, specific values are indicated in Table 2 for A, Table 3 for B and Table C for C. Description of graphical summaries here within are histograms of means ± S.E.M, statistical analyses of (A, B, C) are T-Test with Holm-Sidak correction for multiple comparison and are **P*<0.05, ***P*<0.01, ****P*<0.001, *****P*<0.0001. The total number of samples analyzed was (A-C) 3 brain cortical vesicles extracts from newborn WT or *Atat1* KO mice; lack of * means non-significant differences.

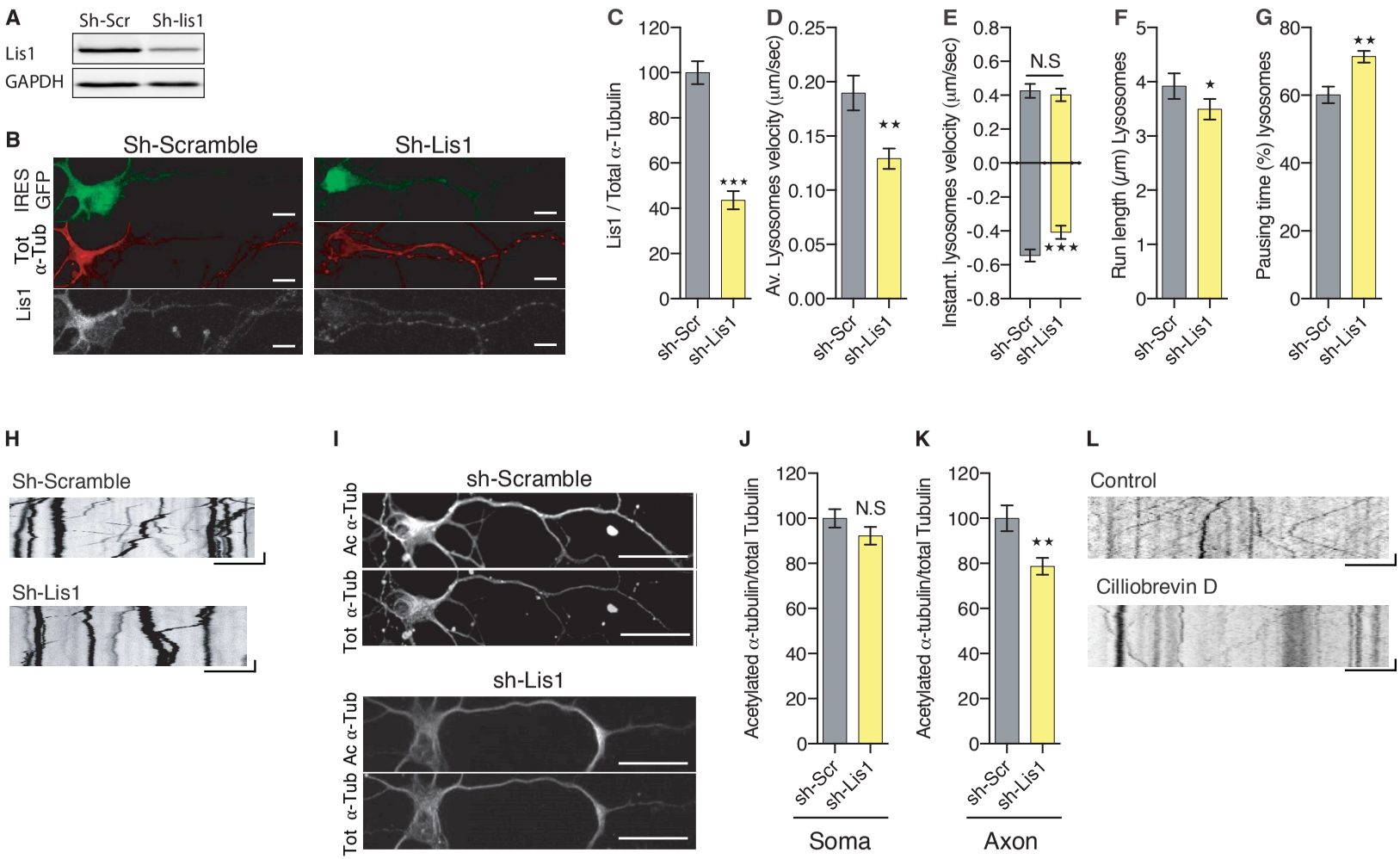
A
Sh-Scr
Sh-lis1
Lis1
GAPDH
B
Sh-Scramble
Sh-Lis1
IRES GFP
Tot α-Tub
Lis1
C
Lis1 / Total α-Tubulin
sh-Scr
sh-Lis1
D
Av. Lysosomes velocity (μm/sec)
E
Instant. lysosomes velocity (μm/sec)
N.S
F
Run length (μm) Lysosomes
G
Pausing time (%) lysosomes
H
Sh-Scramble
Sh-Lis1
I
sh-Scramble
sh-Lis1
Ac α-Tub
Tot α-Tub
J
Acetylated α-tubulin/total Tubulin
N.S
Soma
K
Axon
L
Control
Cilliobrevin D

Fig. S6. Acute KD of Lis1 leads to defect in retrograde transport and dampens the acetylation of MTs. (**A**) WB analyses to detect Lis1 and GAPDH levels in N2A cells extract transfected with sh-Scramble (sh-Scr) or sh-Lis1 expression plasmid. (**B-C**) Immunolabeling and fluorescence quantification to analyze the expression of Lis1 relative to α-Tub in E14.5 mouse cortical neurons transfected with either sh-Scrambled (sh-Scr) or sh-Lis1plasmids. Scale bars are 25 µm. (**D-G**) Histograms showing axonal transport of lysosomes to analyze average velocity (D), instantaneous velocity (E), run length (F) and pausing time (G) of lysosomes in E14.5 cortical neurons transfected with either sh-Scrambled (sh-Scr) or sh-Lis1 plasmid sand cultured 5DIV. (**H**) Representative kymographs of transported lysosomes detected with fluorescent probes (LysoTracker) in E14.5 cortical neurons transfected with sh-Scramble (she-Scr) or sh-Lis1 plasmids and cultured 5DIV. Scale bars are x: 10 µm, y: 20 seconds. (**I-K**) Immunolabeling and fluorescence quantification to analyze the expression of acetylated α-Tub and total α-Tub in neuron soma (J) or axon (K) of E14.5 mouse cortical neurons transfected with either sh-Scrambled (sh-Scr) or sh-Lis1 plasmids. Scale bars are 25 µm. (L) Representative kymographs of axonal transport in motoneurons from Synaptotagmin-GFP Drosophila melanogaster 3rd instar larvae fed during 2 hours with 800 µM of DMSO (Control) or Ciliobrevin D prior the analysis of average SYT1-GFP vesicle velocity. Description of graphical summaries here within are histograms of means ± S.E.M, while (C) is two-tailed student's t-test, (D-G and I-J) are two-tailed Mann-Whitney. Specifically (C, $P<0.0001$ & (t=8.71, df=22); D, $P=0.0023$ & U=66,770; E, $P=0.8137$ & U=2,567 and $P=0.0008$ & U=9,044 for anterograde and retrograde respectively; F, $P=0.0377$ & U=69,850 ; G, $P=0.0018$ U=67,117; J, $P=0.3723$ U=631; K, $P=0.0045$ U=183).

The total number of samples analyzed were: (C) 12 neurons from either sh-Scrambled or sh-Lis1 transfected cultures, (D-G) 320-478 lysosomes tracks from 3 embryos transfected either sh-Scrambled or sh-Lis1; (J-K) 35-41 somas and 24-28 axons from transfected with sh-Scramble or sh-Lis1.

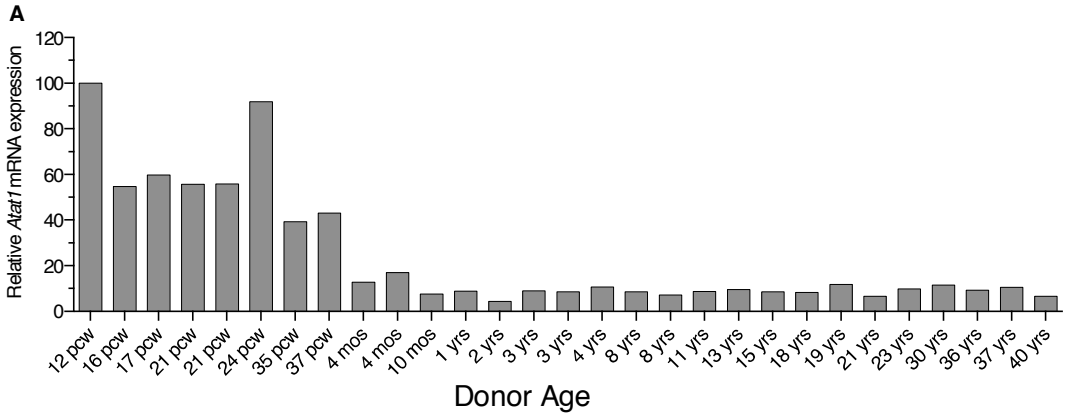

Fig. S7. Expression of Atat1 in the cerebral cortex of human in the course of development and life. (A) Histogram of relative expression of *Atat1* mRNAs in the cerebral cortex from human donors at different ages (post-conceptual weeks (pcw), mos (months), yrs (years)). The data was obtained from ©2018 Allen Institute for Cell Science. BrainSpan Atlas of the Developing Human Brain. Available from:www.brainspan.org/rnaseq/search/index.html).

Table S1. Intensity-ranked proteins in vesicle fractions from WT or Atat1 KO mice detected by LC-MS/MS.

Table S2. Differentially detected proteins in vesicle fractions from WT or Atat1 KO mice detected by LC-MS/MS.

Table S3. Identified molecular motors in vesicle fractions from WT or Atat1 KO mice detected by LC-MS/MS.

Table S4. Identified glycolytic enzymes in vesicle fractions from WT or Atat1 KO mice detected by LC-MS/MS.

Movie S1. Representative movie of Lamp1-Emerald trafficking in axons of cortical brain slice.

Movie S2. Representative movie of lysosome trafficking in axons located in the distal part of PDMS chambers.

Movie S3. Representative movie of mitochondria trafficking in axons located in the distal part of PDMS chambers.

Movie S4. Representative movie of synaptotagmin-GFP trafficking in motoneurons of third-instar larvae.

Movie S5. Representative movies of vesicles trafficking in vitro over polymerized rhodamine-labeled MTs.

Movie S6. Representative movie of ATAT1-GFP trafficking in axons located in the distal part of PDMS chambers.

SUPPLEMENTARY DATA: ATP-citrate lyase promotes axonal transport across species

Supplementary Figures for Even et al.

Supplementary Figure 1

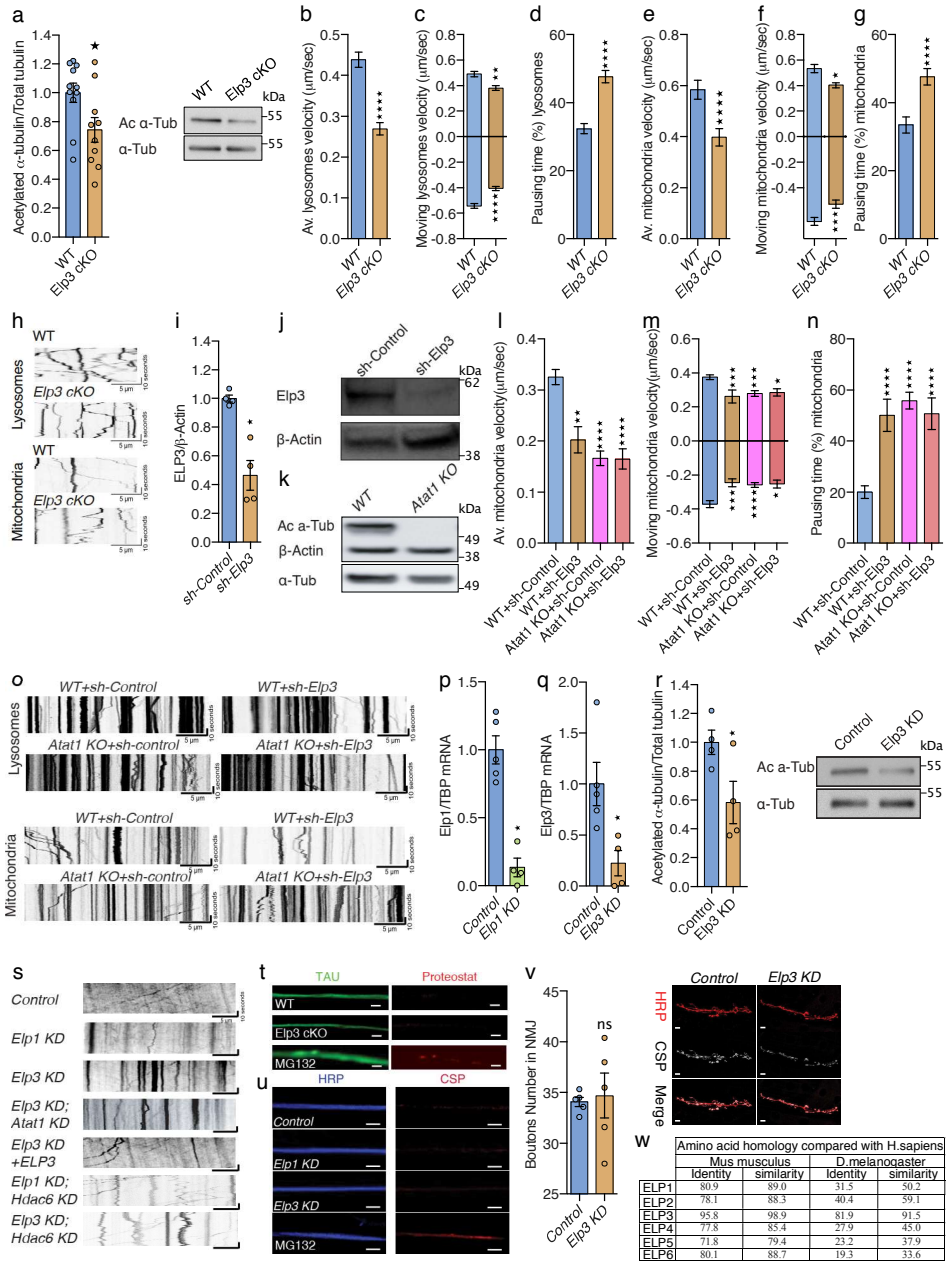

w

Amino acid homology compared with H.sapiens				
	Mus musculus		D.melanogaster	
	Identity	similarity	Identity	similarity
ELP1	80.9	89.0	31.5	50.2
ELP2	78.1	88.3	40.4	59.1
ELP3	95.8	98.9	81.9	91.5
ELP4	77.8	85.4	27.9	45.0
ELP5	71.8	79.4	23.2	37.9
ELP6	80.1	88.7	19.3	33.6

Supplementary Fig. 1: Kymographs of motile lysosomes, mitochondria and Synaptotagmin-GFP. RNAi targeting efficiency and neuromuscular junction assessment in fly model. (**a**) Immunoblotting and histogram of acetylated α-tubulin (Ac α-Tub), total α tubulin (Tot α-Tub)

in newborn *WT or Elp3cKO* mice cortical brain extracts. (**b-h**) Axonal transport recordings of PNs isolated from E14.5 WT or *Elp3 cKO* embryos and cultured for 5 DIV in microfluidic devices to analyze average (av.) velocity (**b, e**), moving velocity (**c, f**) and percentage of pausing time (**d, g**) of lysosomes (LysoTracker®) and mitochondria (MitoTracker®). (**h**) Representative kymographs of moving lysosomes (**top**) and mitochondria (**bottom**) in E14.5 in *WT or Elp3cKO* mice PNs axons cultured for 5 DIV in microfluidic devices. Scale bars are 10 seconds and 5 µm. (**i-j**) Immunoblotting and quantification of Elp3 and ß-Actin in cortical neurons transfected with sh-*Elp3* or sh-*Control*. (**k**) Immunoblotting of acetylated α-tubulin (Ac α-Tub), total α-tubulin (Tot α-Tub) and ß-Actin in extracts from P0 WT or *Atat1* KO brains. (**l-n**) Axonal transport analysis of mitochondria (MitoTracker®) in WT or *Atat1* KO neurons infected either with sh-Control or sh-*Elp3* to analyze average (av.) velocity (**l**), moving velocity (**m**) and percentage of pausing time (**n**). (**o**) Representative kymographs of lysosomes (**top**) and mitochondria (**bottom**) in E14 in WT or *Atat1 KO* neurons infected either with sh-Control or sh-*Elp3* mice cortical neurons axons cultured for 5 DIV in microfluidic devices. Scale bars are 10 seconds and 5 µm. (**p-q**) mRNA levels of *Elp1* and *Elp3* from fly head extracts, expressing RNAi under the pan-neuronal driver (Elav:GAL4) in control, *Elp1* KD (**p**) and *Elp3* KD (**q**). (**r**) Immunoblotting and histogram of acetylated α-tubulin (Ac α-Tub), total α-tubulin (Tot α-Tub) from fly head extracts, expressing RNAi under the pan-neuronal driver (Elav:GAL4) in control and *Elp3* KD. (**s**) Representative kymographs of Synaptotagmin-GFP (Syt1-GFP) in motoneurons from 3rd instar larvae of *Drosophila melanogaster* expressing RNAi under a motoneuron-specific driver (D42:GAL4); control, *Elp1* KD, *Elp3* KD, *Atat1; Elp3* KD, *Elp3* KD + human *ELP3 (ELP3), Elp1;Hdac6* KD and *Elp3;Hdac6* KD. Scale bars are 10 seconds and 5 µm. (**t**) Protein aggregation was estimated in axons (Tau+; in green) of cultured mice cortical neurons of WT, *Elp3cKO* and MG132 treated neurons (positive control) by the chemical dye Proteostat© as marker for protein aggregation (in red). Scale bar is 10 µm.

(**u**) Protein aggregation was estimated in motor neurons exiting the ventral ganglion of 3rd instar larvae expressing RNAi under motoneurons specific driver (D42:GAL4); control, *Elp1* KD, *Elp3* KD and *MG132 treatment* (positive control) by immunolabeling of cysteine string protein (CSP+; red) as marker for aggregation, and the neuronal marker horseradish peroxidase (HRP+; blue). Scale bar is 10 μm. (**v**) Representative images (**right**) of neuromuscular junctions in 3rd instar larvae immunolabeled for cysteine string protein (CSP) and horseradish peroxidase (HRP) and a histogram of its quantification (**left**). (**w**) Table comparing the amino acid homology of the mouse and fly Elongator complex subunits (ELP1-6) to the human sequence, by sequence identity and similarity. Description of graphical summaries here within are histograms of means ± SEM. Significance was determined by: (**a, r**) two-sided t-test, (**b, c, d, e, f, g, i, p, q, v**) two-sided Mann-Whitney test, and (**l, m, n**) two-sided Kruskal Wallis one-way ANOVA. Specifically, [(**a**) $p = 0.0270$, $t = 2.396$, $df = 19$; (**b**) $p < 0.0001$, $U = 111906$; (**c**) $p < 0.0001$, $U = 71910$ and $p = 0.0029$, $U = 45529$ for anterograde and retrograde, respectively; (**d**) $p < 0.0001$, $U = 68287$; (**e**) $p < 0.0001$, $U = 21672$; (**f**) $p = 0.0349$, $U = 20092$ and $p = 0.0002$, $U = 27975$ for anterograde and retrograde, respectively; (**g**) $p < 0.0001$, $U = 21907$; (**i**) $p = 0.0286$, $U = 0$; (**l**) $p < 0.0001$, $K = 67.88$; (**m**) $p < 0.0001$, $K = 25.42$ and $p < 0.0001$, $K = 25.89$ for anterograde and retrograde, respectively; (**n**) $p < 0.0001$, $K = 73.34$; (**p**) $p = 0.0159$, $U = 0$; (**q**) $p = 0.0159$, $U = 0$; (**r**) $p = 0.0487$, $t = 2.467$, $df = 6$**;** (**v**) $p = 0.6905$, $U = 10$]. In addition, the post hoc multiple comparisons, to analyze statistical difference of each condition compared to control for (**l, m, n**) are Dunn's test, and are *$p < 0.05$, **$p < 0.01$, ***$p < 0.001$, and ****$p < 0.0001$. (a) Number of mice: WT n = 11; Elp3 cKO n = 10. (**b**) Number of vesicles: WT n = 656; Elp3 cKO n = 423. 5 mice per group. (**c**) Number of vesicles: WT n = 417 (anterograde), n = 566 (retrograde); Elp3 cKO n = 254 (anterograde), n = 327 (retrograde). 5 mice per group. (**d**) Number of vesicles: WT n = 506; Elp3 cKO n = 366. 5 mice per group. (**e**) Number of vesicles: WT n = 239; Elp3 cKO n = 232. 5 mice per group. (**f**)

Number of vesicles: WT n = 209 (anterograde), n = 240 (retrograde); Elp3 cKO n = 218 (anterograde), n = 287 (retrograde). 5 mice per group. (**g**) Number of vesicles: WT n = 239; Elp3 cKO n = 232. 5 mice per group. (**i**) 4 animals per group. (**l**) Number of vesicles: WT+sh-Control n = 201; WT+sh-Elp3 n = 43; Atat1 KO+sh-Control n = 149; Atat1 KO+sh-Elp3 n = 42. 3 mice per group. (**m**) Number of vesicles: WT+sh-Control n = 112 (anterograde), n = 90 (retrograde); WT+sh-Elp3 n = 22 (anterograde), n = 34 (retrograde); Atat1 KO+sh-Control n = 64 (anterograde), n = 71 (retrograde); Atat1 KO+sh-Elp3 n = 30 (anterograde), n = 18 (retrograde). 3 mice per group. (**n**) Number of vesicles: WT+sh-Control n = 201; WT+sh-Elp3 n = 46; Atat1 KO+sh-Control n = 149; Atat1 KO+sh-Elp3 n = 42. 3 mice per group. (**p**) Number of fly brains: Control n = 5; Elp1 KD n = 4; (**q**) Number of fly brains: Control n = 5; Elp3 KD n = 4. **(r)** Number of fly brains: Control n = 4; Elp3 KD n = 4; (**v**) Number of 3rd instar larvae: Control n = 5; lp3 KD n = 5. Source data are provided with this paper.

Supplementary Figure 2

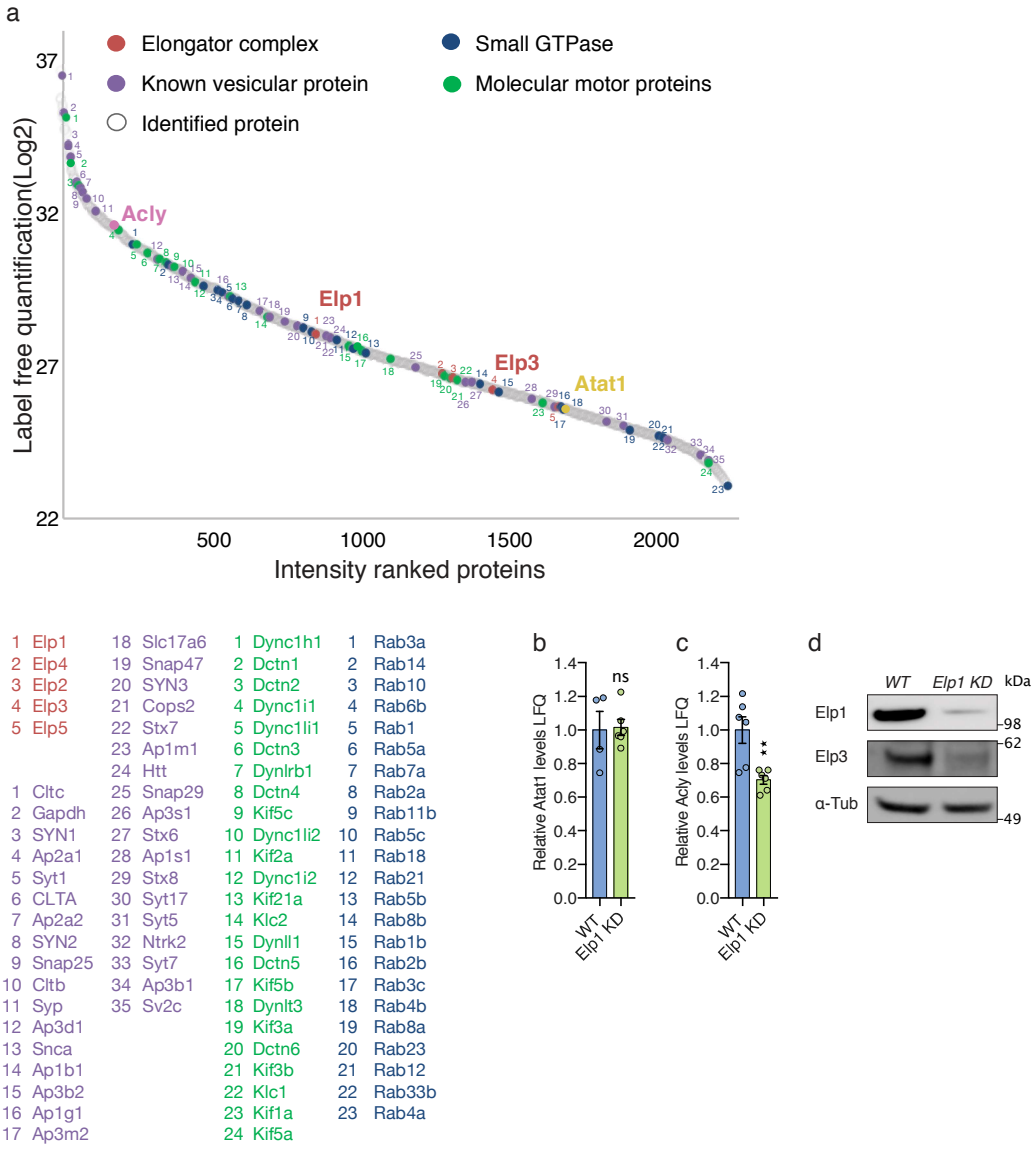

Supplementary Fig. 2: LC-MS/MS and Acly levels in E14.5 cortical brains. (a) LC-MS/MS proteomic analysis of vesicular fraction isolated from adult brain cortices of WT and *Elp1 KD* mice, proteins were ranked by intensity and plotted according to their relative abundance (gray spots). Acly (pink), Atat1 (yellow), and Elongator subunits (red) detection among proteins previously identified as vesicular components (purple), small GTpase (blue) and molecular

motors (green) (n = 3, graph represent the mean intensity value). (**b-c**) Histograms of relative Atat1 and Acly label-free quantification (LFQ) intensities analyzed by LC-MS/MS of P3 fraction from WT and *Elp1 KD* mice. (**d**) Immunoblotting to detect Elp1, Elp3 and α-tubulin (α-Tub) in cortical extracts from adult WT and *Elp1 KD* mice. Description of graphical summaries here within are histograms of means ± SEM. Significance was determined by two-sided Mann-Whitney test (**b,c)**. Specifically, [(**g**) p = 0.7619, U = 10; (**h**) p = 0.0087]. Number of mice: WT n = 4; Elp1 n = 6 (**b**); WT n = 6; Elp1 KD n = 6 (**c**). Source data are provided with this paper.

Supplementary Figure 3

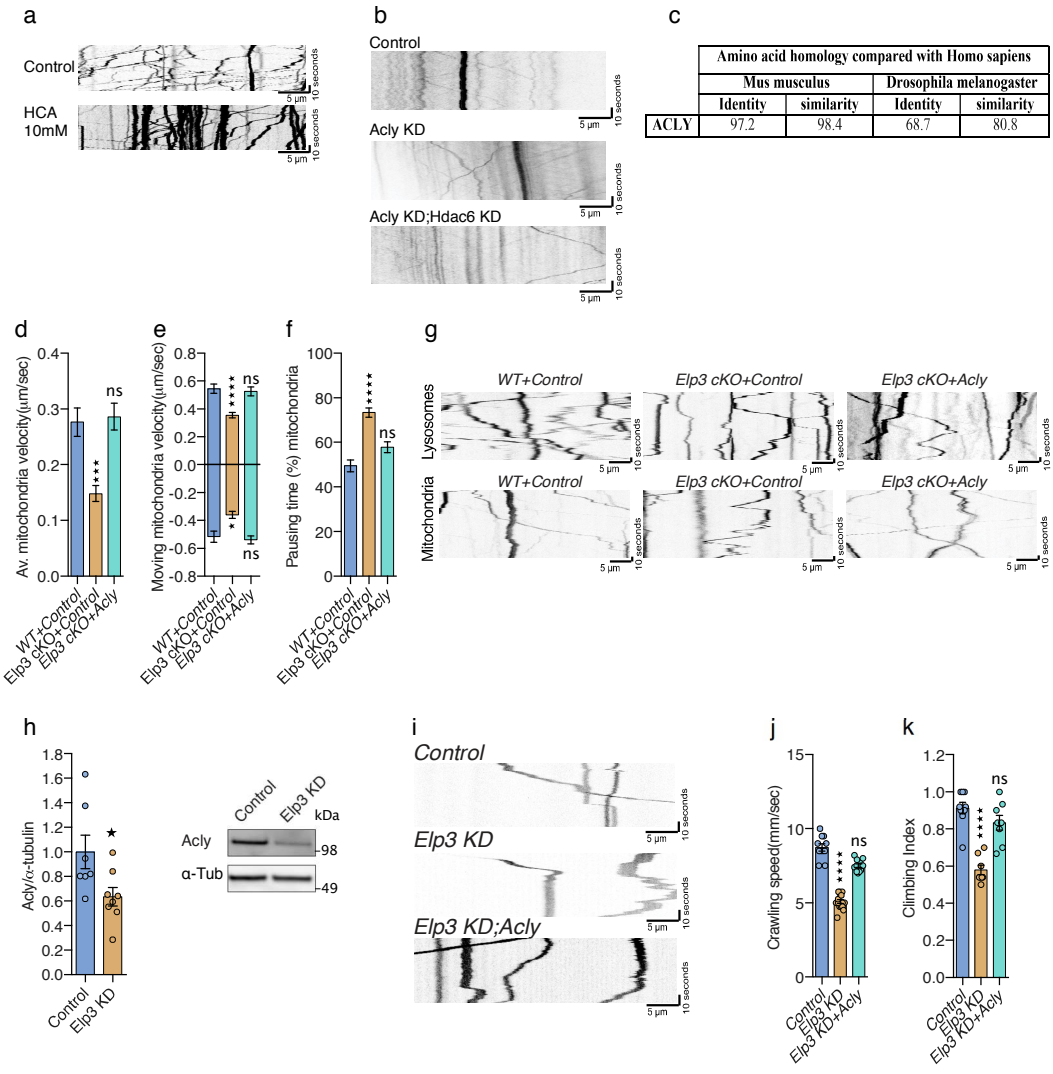

	Amino acid homology compared with Homo sapiens			
	Mus musculus		Drosophila melanogaster	
	Identity	similarity	Identity	similarity
ACLY	97.2	98.4	68.7	80.8

Supplementary Fig. 3: Expression of Acly/ACLY in mice cultured neurons and fly heads. Kymographs after time-lapse recording of motile lysosomes, mitochondria and Synaptotagmin-GFP+ vesicles (**a,b**). (**a**) Representative kymographs of lysosomes in E14.5 mice cortical neuron axons cultured for 5 DIV in microfluidic devices and incubated with 10mM hydroxycitrate acid (HCA) for 8 hours. Scale bars are 10 seconds and 5 µm. (**b**) Representative kymographs of Synaptotagmin-GFP (Syt1-GFP) in motoneurons from 3rd instar larvae of *Drosophila melanogaster* expressing RNAi under a motoneuron-specific driver

(D42:GAL4); control, *Acly KD* and *Acly;Hdac6 KD*. Scale bars are 10 seconds and 5 µm. (**c**) Table comparing the amino acid homology of the mouse and fly Acly to the human, by sequence identity and similarity. (**d-f**) Time-lapse recordings of axonal transport of mitochondria (MitoTracker®) from E14.5 cortical neurons of *WT or Elp3cKO* mice cultured 5 DIV in microfluidic devices transfected with control or *Acly* expressing constructs, to analyze average (av.) velocity (**d**), moving velocity (**e**) and percentage of pausing time (**f**). (**g**) Representative kymographs of lysosomes (**top**) and mitochondria (**bottom**) in E14.5 *WT or Elp3 cKO* mice cortical neuron axons transfected with Control or ACLY expressing construct and cultured 5 DIV in microfluidic devices. Scale bars are 10 seconds and 5 µm. (**h**) Immunoblotting and quantification of Acly and total tubulin expressions in *Drosophila melanogaster* head extracts from control or Elp3 RNAi (Elp3 KD) (under the pan-neuronal driver, Elav:GAL4) adult flies. (**i**) Representative kymographs of Synaptotagmin-GFP (Syt1-GFP) in 3rd instar larvae motor neurons expressing RNAi under a motoneuron-specific driver (D42:GAL4); control, *Elp3* KD and *Elp3* KD + *Acly*. Scale bars are 10 seconds and 5 µm. (**j-k**) Locomotion assays; histograms of climbing index of adult flies (**j**) and crawling speed of 3rd instar larvae (**k**), genotypes as indicated on graphs. Description of graphical summaries here within are histograms of means ± SEM. Significance was determined by: (**d, e, f**) two-sided Kruskal Wallis one-way ANOVA, (**h**) two-sided t-test, and (**j, k**) two-sided one-way analysis of variance (ANOVA). Specifically, [(**d**) $p < 0.0001$, $K = 27.47$; (**e**) $p < 0.0001$, $K = 26.16$ and $p = 0.0003$, $K = 16.04$ for anterograde and retrograde, respectively; (**f**) $p < 0.0001$, $K = 49.32$; (**h**) $p = 0.031$, $t = 2.407$, $df = 13$; (**j**) $p < 0.0001$, $F = 28.45$; (**k**) $p < 0.0001$, $F = 139.5$]. In addition, the post hoc multiple comparisons, to analyze statistical difference of each condition compared to control for (**d, e, f, j,k**) are Dunn's test, (**j,k**) Dunnet's, and are *$p < 0.05$, ***$p < 0.001$, and ****$p < 0.0001$. (**d**) Number of vesicles: WT+Control n = 318; Elp3 cKO+Control n = 383; Elp3 cKO+Acly n = 240. 5 mice per group. (**e**) Number of vesicles: WT+Control n =

87 (anterograde), n = 67 (retrograde); Elp3 cKO+Control n = 94 (anterograde), n = 54 (retrograde); Elp3 cKO+Acly n = 51 (anterograde), n = 63 (retrograde). 5 mice per group. (**f**) Number of vesicles: WT+Control n = 317; Elp3 cKO+Control n = 383; Elp3 cKO+Acly n = 379. 5 mice per group. (**h**) Number of larvae: Control n = 7; Elp3 KD n = 8. (**j**) Number of larvae: Control n = 11; Elp3 KD n = 15; Elp3 KD+Acly n = 12. (**k**) Number of larvae: Control n = 9; Elp3 KD n = 8; Elp3 KD+Acly n = 8. Source data are provided with this paper.

Supplementary Figure 4

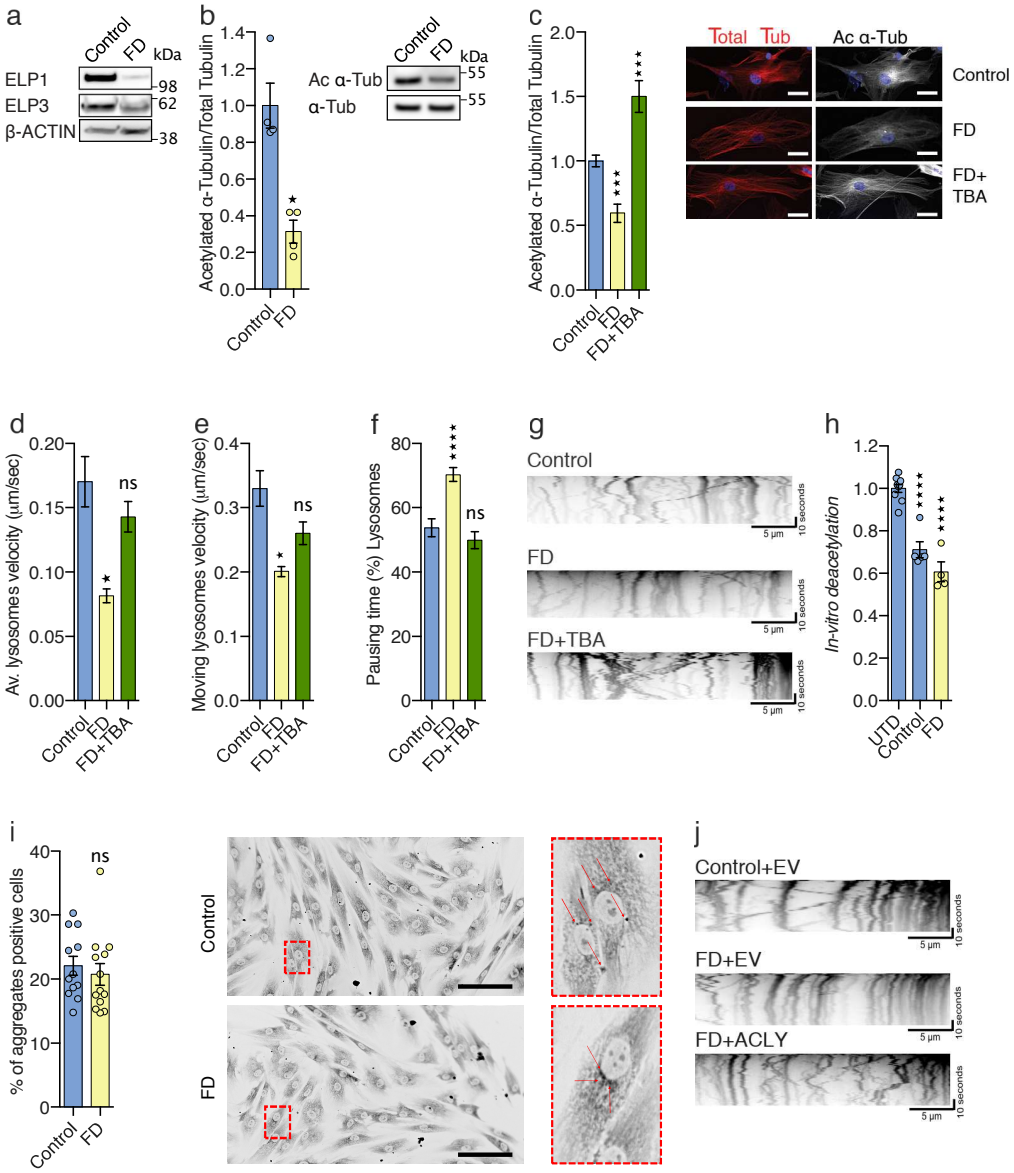

Supplementary Fig. 4: Pharmacological and genetic rescue of vesicular transport in FD fibroblasts. (a) Immunoblotting of ELP1, ELP3 and ß-ACTIN in human primary fibroblasts from healthy control and FD patients. (**b**) Immunoblotting and quantification of acetylated α-tubulin (Ac α-Tub), total α-tubulin (Tot α-Tub) in extracts from cultured controls or FD human primary fibroblasts. (**c**) Immunolabelings and quantification of acetylated α-tubulin (Ac α-Tub)

and total tubulin (Tot α-Tub) in human primary fibroblasts from controls and FD patients incubated with vehicle or Tubastatin (TBA). Scale bar is 50 µm. (**d-f**) Recording of moving lysosomes using live fluorescent probe (LysoTracker®) in primary control or FD cultured fibroblasts incubated with vehicle (DMEM media) or TBA to analyze average (av.) velocity (**d**), moving velocity (**e**) and percentage of pausing time (**f**). (**g**) Representative kymographs of transported lysosomes in human primary fibroblasts from healthy controls or FD patients incubated with vehicle (DMEM media) or Tubastatin (TBA). Scale bars are 10 seconds and 5µm. (**h**) In vitro deacetylation assay of endogenously acetylated bovine brain tubulin incubated for 4 hours with extracts of control and FD cultured fibroblasts or without tissue extract (control). (**i**) Protein aggregation was estimated in fibroblasts from healthy controls and FD patients after incubation with the chemical dye Proteostat©, a marker for protein aggregation (in black, see also red arrows). Scale bar is 50 µm. (**j**) Representative kymographs of transported lysosomes in human primary fibroblasts from healthy controls or FD patients transfected with ACLY or Control expressing constructs. Scale bars are 10 seconds and 5µm. Description of graphical summaries here within are histograms of means ± SEM. Significance was determined by: (**b, i**) two-sided Mann-Whitney test, (**c**) two-sided one-way analysis of variance (ANOVA), (**d, e, f**) two-sided Kruskal Wallis one-way ANOVA, and (**h**) two-sided one-way ANOVA. Specifically, [(**b**) $p = 0.0286$, $U = 0$ (**c**) $p < 0.0001$, $F = 30.36$; (**d**) $p < 0.0001$, $K = 24.26$; (**e**) $p < 0.0001$, $K = 23.82$; (**f**) $p < 0.0001$, $K = 44.79$; (**h**) $p < 0.0001$, $F = 48.27$ (**i**) $p = 0.3398$, $U = 60$]. In addition, the post hoc multiple comparisons, to analyze statistical difference of each condition compared to control for (**c**) is Dunnett's test, for (**d, e, f**) are Dunn's test, and are *$p < 0.05$, ***$p < 0.001$, and **** $p < 0.0001$. (**a**) Lysates from 5 human primary fibroblast lines from control and FD patients. (**b**) Lysates from 4 human primary fibroblast lines from control and FD patient. (**c**) Number of cells: Control n = 18; FD n = 30; FD+TBA n = 13. 5 human primary fibroblast lines from control and FD patients. (**d**)

Number of vesicles: Control n = 229; FD n = 273; FD+TBA n = 257. 5 human primary fibroblast lines from control and FD patients. (**e**) Number of vesicles: Control n = 174; FD n = 190; FD+TBA n = 202. (**f**) Number of vesicles: Control n = 237; FD n = 271; FD+TBA n = 267. (**h**) Lysates from human primary fibroblasts from control (n = 5) and FD (n = 4) patients. (**i**) Number of cells: Control n = 12; FD n = 13. Source data are provided with this paper.

Supplementary Figure 5

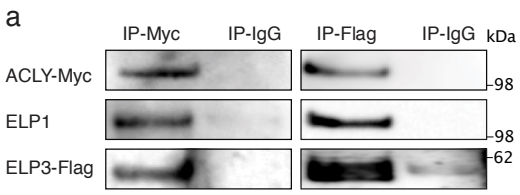

Supplementary Fig. 5: In vitro interaction between the Elongator subunits ELP1 and ELP3 with ACLY. (a) Western blotting with Flag or Myc antibodies showing co-immunoprecipitation between endogenous ELP1 or ELP3-Flag and ACLY-Myc in extracts from HEK293 cells co-transfected with ACLY-Myc and ELP3-Flag. IgG antibodies were used as Control. Source data are provided with this paper.

Supplementary Table 1
List of Antibodies used for western blotting

Protein	Company	Cat #	WB	IF	ELISA	IP
α-Tubulin	Sigma-Aldrich	T9026	1:5,000		1:2,000	
α/β-Tubulin (total tubulin)	Cytoskeleton	ATN02-A		1:150		
Tubulin YL1/2	Abcam	ab6160		1:1,000		
Acetylated α-Tubulin	Sigma-Aldrich	T7451	1:15,000	1:15,000		
β-Tubulin	Cell Signaling	2146		1:100		
β-actin	Sigma-Aldrich	A3853	1:20,000			
GAPDH	Millipore	MAB374	1:1,000			
HDAC6	Santa Cruz Biotechnology	sc-5258	1:200			
Atat1	Max Nachury		1:1000			
Tau-1	Millipore	MAB3420		1:500		
CSP	DSHB	DCSP-2 (D6D)		1:10		
Elp1/IKAP	Anaspec	AS-54494	1:500			
Elp3	Jesper Svejstrup		1:1,000			
HH3	Cell Signaling	9715	1:1,000			
Synaptophysin	Sigma-Aldrich	s5768	1:1,000			
Synaptophysin-1	Synaptic Systems	101004	1:1,000			

Acly	Aviva Systems Biology	OAGA04026		1:100		
Acly	Cell signaling	13390	1:1,000			
AceCS1	Cell Signaling	3658	1:1,000	1:100		
Myc	Cell Signaling	#2276				1:1,000
FLAG	Sigma-Aldrich	F3165				1:600
Goat anti mouse	Jackson ImmunoResearch Labs	115-035-003	1:10,000	1:200	1:5,000	
Goat anti rabbit	Jackson ImmunoResearch Labs	111-035-003	1:10,000	1:200		
Donkey anti goat	Jackson ImmunoResearch Labs	705-035-003	1:10,000			

Coordination between Transport and Local Translation in Neurons

CellPress

Trends in Cell Biology

Review

Coordination between Transport and Local Translation in Neurons

Loïc Broix,[1,2] Silvia Turchetto,[1,2] and Laurent Nguyen[1,*]

The axonal microtubules (MTs) support long-distance transport of cargoes that are dispatched to distinct cellular subcompartments. Among them, mRNAs are directly transported in membraneless ribonucleoprotein (RNP) granules that, together with ribosomes, can also hitchhike on fast-moving membrane-bound organelles for accurate transport along MTs. These organelles serve as platforms for mRNA translation, thus generating axonal foci of newly synthesized proteins. Local translation along axons not only supports MT network integrity but also modulates the processivity and function of molecular motors to allow proper trafficking of cargoes along MTs. Thus, identifying the mechanisms that coordinate axonal transport with local protein synthesis will shed new light on the processes underlying axon development and maintenance, whose deregulation often contribute to neurological disorders.

Highlights

The long-range transport of mRNA in RNP granules is intimately linked to the MT-transport machinery by recruitment of molecular motors through RNP granule RBPs.

RNP transport granules are mainly considered as translationally repressed structures but their high heterogeneity in RBP content or biophysical properties and the detection of translation in stress granules or moving polysomes may reflect various translational states.

RNP granules can also be indirectly transported in neurites by their tethering to membrane-bound organelles and mRNAs are translated at the surface of membrane-bound organelles demonstrating other levels of coordination between MT-based transport and translation.

The translation machinery is transported along MTs in neurites by molecular motors to sustain local protein synthesis away from the cell soma.

Local protein synthesis of MT-transport machinery is essential for the prompt regulation of transport in response to stimulation signals.

MT-Based Transport of mRNAs in Neurons

In the cytosol, mRNAs interact with RNA-binding proteins (RBPs) to assemble into macromolecular **RNP granules** (see Glossary) that are generated by the condensation of proteins and RNA into distinct liquid phase-separated structures [1]. These cytosolic membraneless organelles include **processing bodies**, **stress granules**, and RNA transport granules [2]. In neurons, RNA granules are actively transported along dendrites and axons to regulate the proteome of subcellular compartments and promote their growth, homeostasis, and survival. Their transport from the cell soma to distal parts of the axon and dendrites relies on MT-based transport, with the **kinesin family** of molecular motors promoting anterograde transport (plus-end directed transport) and **dynein** ensuring retrograde transport (minus-end directed transport) [3]. In contrast to the transport of **membrane-bound organelles** (e.g., mitochondria and lysosomes), which is mediated by the direct or indirect interaction between the molecular motors and membrane proteins and/or the lipid bilayer, the binding of molecular motors to membraneless RNP granules remains poorly understood.

Here, we discuss the current knowledge about MT-dependent transport in the context of **local translation** in neurons. We first describe the mechanisms responsible for the selection of RNP granules to be transported along axon or dendrites as well as the control of their translational activity during and after their transport. We then discuss the recent advances supporting an important role for membrane-bound organelles in the transport and local translation regulation of RNP granules and conclude by illustrating the interdependence between transport and local translation.

Regulation of Transport and Translation of mRNAs in RNP Granules

Proteomic analysis of purified RNP granules isolated from developmental or adult mouse brains has revealed that there are mostly composed of ribosomal proteins and translation factors (±50%), RBPs (±25%), as well as cytoskeleton-linked proteins (15%) [4–6]. The major RBPs present in RNP granules include heterogeneous nuclear ribonucleoproteins (hnRNPs), **DEAD-**

[1]GIGA Stem Cells, GIGA-Neurosciences, University of Liège, C.H.U. Sart Tilman, Liège 4000, Belgium
[2]These authors contributed equally

*Correspondence: Lnguyen@uliege.be (L. Nguyen).

box helicases, and various other RBPs involved in the transport or repression of mRNAs such as *fragile X mental retardation protein (FMRP)*, *Staufen1*, and *TAR-DNA binding protein (TDP)-43*. The selective enrichment in cytoskeleton-related proteins and motor proteins in particular dynein cytoplasmic 1 heavy chain (DYNC1H)1, KIF5 (kinesin superfamily), and myosin Va suggests that RNP granules are intimately linked to molecular transport along MTs and actin tracks in neurons. Of note, these proteomic studies were performed on mouse brain homogenates and thus do not discriminate between different populations of RNP granules that could localize specifically in axons or dendrites and cannot distinguish between neuronal from non-neuronal proteins.

Despite proteomic evidence suggesting that long-distance transport of RNP granules along MT involves kinesin and dynein molecular motors, it is still unclear how the transport machinery is recruited to membrane-less RNP granules and whether different molecular motor/adapter complexes loaded on RNP granules could ensure selective compartmentalization of mRNAs. Two recent studies addressed this issue by using either *in vitro* reconstitution [7] or living hippocampal neurons [8]. Both studies identified new motor adapters that link specific mRNAs directly to different molecular motors mediating mRNA localization (Figure 1A, Key Figure) [7,8]. In the first study, the authors described a direct link between kinesin-1 and *β-actin* mRNAs and its associated zipcode-binding protein 1 (ZBP1) through the molecular adaptor PAT1 (APP-tail 1), which facilitates the transport of *β-actin* mRNAs in dendrites upon brain-derived neurotrophic factor (BDNF) activation [8]. Of note, this complex shows specificity as it is not involved in the transport of other mRNAs enriched in RNA granules, such as *GABA-A receptor δ* and *Ca^{2+}/calmodulin-dependent protein kinase (CAMK)II* mRNAs. In the second work, the authors found that the RBP *adenomatous polyposis coli* (APC) favors the recruitment of axonal *β2B-tubulin* and *β-actin* mRNAs on kinesin-2 and that variations in guanine-rich sequences of their 3′ **untranslated region** (UTR) modulate the efficiency of transport and balance loading onto the molecular motor complexes [7]. Those studies underlie the complexity of the interaction existing between mRNAs and motors, as the same mRNA species (e.g., *β-actin*) can be transported by different kinesins and associated adaptors. Molecular transport processes are driven by several kinesins and dyneins loaded onto the same cargo, with some studies giving an approximation of 6–12 dyneins and 1–2 kinesins per single moving cargo along the MT tracks [9]. The coordination between the slow moving kinesin-1 and fast moving kinesin-3 at the **dense core vesicles** in dorsal root ganglion (DRG) neurons is necessary to finetune their speed to reach their proper distribution along axons [10]. The fact that kinesin-1 and kinesin-2 work in combination for the transport of RNP granules in *Xenopus* oocytes suggests a comparable regulation for the transport of RNP granules in neurons [11]. The presence of multiple motors at the surface of RNP granules could control their speed in order to distribute them evenly along the axon but could also be a way to allow navigation along oppositely orientated MTs, such as the ones present in dendrites. Another layer of complexity results from the existence of RBPs that can interact with distinct mRNAs. This is exemplified by FMRP that binds, to *MAP1B*, *CAMKII*, and *PSD-95*, among other mRNAs and that interact physically with molecular motors [12]. Although it is still unclear whether individual RNA granules assemble with one or distinct mRNA species, recent advances in quantitative single-molecule FISH techniques (Box 1) supports the notion that the majority of RNA granules contain one or two copies of the same mRNA in axons and dendrites [13,14].

Another superfamily of motors that is intimately linked to RNA granule motility are myosin motors and in particular the prominent brain unconventional myosin Va. In contrast to kinesin and dynein motors that move on MTs, class V myosins move along the actin cytoskeleton to ensure the short-range transport of their cargoes toward the barbed end of actin filaments [15]. An initial study based on the immunoprecipitation of the Puralpha RBP identified myosin Va together with FMRP and Staufen RBPs in the composition of the RNP granules [16]. This was recently

Glossary

DEAD-box helicases: superfamily of RNA helicases, RBPs characterized by a highly conserved Asp-Glu-Ala-Asp (DEAD) motif that hydrolyzes ATP to bind mRNAs and modulate all aspects of their metabolism, ranging from mRNA–protein stabilization and RNP disassembly to mRNA translation and decay.

Dense-core vesicle: membrane-bound organelle transporting neuropeptides and neurotrophins to be released into the presynaptic active zone following fusion with the presynaptic membrane.

Dynein: unique motor protein driving the retrograde transport whose motor domain is encoded by a single gene. Among the other subunits of the dynein complex are two light intermediate chains including DYNC1/1 which binds to the $p150^{Glued}$ subunit of the dynactin complex, the dynein activator.

Hyphae: multi- or uninucleate tubular protrusion of filamentous fungi as *Aspergillus nidulans* and *Ustilago maydis* containing polarized microtubules directing the motor-driven long-distance transport of cargoes.

Kinesin family: superfamily of motor proteins including the kinesin-1, kinesin-2, and kinesin-3 families contributing to the anterograde axonal transport dynamics. The motor domain of the kinesin-1 family members is composed of a heavy chains dimer encoded by the *KIF5A*, *KIF5B*, and *KIF5C* genes and a dimer of light chains (KLCs). Members of the kinesin-2 family retain a homodimeric motor domain encoded by the *KIF17* gene or heterodimeric complex (KIF3A–KIF3B or KIF3A–KIF3C) that interacts with an adaptor protein modulating the binding specificity to a given cargo. Members of the kinesin-3 family as KIF1A and KIF1B undergo dimerization to modulate their motility.

Local translation: protein synthesis occurring in subcellular compartments as opposed to the somatic space that enables the establishment and regulation of a localized and functionally specific proteome.

Membrane-bound organelles: functionally specialized and morphologically defined subcellular compartments enclosed by lipid bilayer, such as those forming the endosomal/lysosomal system and the secretory pathway.

confirmed by a series of studies showing the crucial role played by myosin Va in the delivery of FMRP, Puralpha, and Staufen 1, and translocated in liposarcoma/fused in sarcoma (TLS/Fus) RNP granules to the actin-rich dendritic spines of neurons [17–20]. As with myosin, kinesin and dynein motors are found in the same RNP granules, this suggest that the actin and MT cytoskeleton coordinates to regulate the transport of RNP granules. In accordance, it was described that myosin V negatively regulates the MT-dependent transport of mitochondria or ZBP-1 in the axon, suggesting that myosin V regulates the off-loading from MTs and the docking to actin-rich structures such as synapses [21,22]. The same mechanism was recently described in dendrites where F-actin patches localized at the base of synapses induce the stalling of lysosomes by slowing down MT-dependent transport [23]. Future studies will further elucidate how the coordination between the different actin- and MT-associated motors at RNP granules is orchestrated to achieve precise positioning of RNP granules in neurites in order to ensure proper neuronal functions.

Mechanisms That Select mRNAs for Axonal Transport

The molecular mechanisms allowing neurons to transport and sort distinct mRNAs to specific subcompartments, independently of their relative abundance, remains poorly understood. One insight comes from the existing diversity of 3′ UTRs for the same mRNAs in neurons that may serve as transport recognition sequence. Of note, mRNA isoforms with longer 3′ UTR preferentially localize to neurites and have greater half-lives than their somal isoforms [24]. Longer 3′ UTRs can bear additional motifs for the binding to RBPs, thus allowing mRNAs to engage with distinct transport dynamics that would ultimately direct them to different subcellular localizations [24]. Moreover, repeated binding sequences or variation in these sequences in 3′ UTR could regulate binding to RBPs [24]. Consistent with this idea, minor changes in RBP-binding regulatory motifs, such as guanine rich sequences, lead to different RNA-molecular motor loading efficacy, thereby giving an advantage for less abundant *β-tubulin* mRNAs over *β-actin* mRNAs [7]. While it is predominantly accepted that mRNA localization motifs are located in the 3′ UTR, some studies also uncovered transport recognition sequences in their 5′ UTR ends. For example, the 5′ UTR of neuritin mRNA drives their transport to the axon of DRG neurons while 5′ UTR sequences of mRNAs encoding for ribosomal proteins target them to the axons of cortical neurons [25,26]. Most research has focused on the identification of RBP-binding sequences that lead to the selective axonal localization of mRNAs but it is worth noting that recent evidence revealed the presence of RBP-binding sequences in the 3′ UTR that are used as a negative regulatory mechanism to exclude the mRNAs from the axon [27]. This mechanism is achieved through the presence of Pumilio-binding elements recognized by Pumilio-2, that retain some mRNAs such as *Gsk3b* in the cell soma, which is critical for proper axonal growth and branching in developing neurons [27].

Are Transported RNA Granules Translationally Silent?

One actively debated question in the field of translation is whether mRNAs are translationally active or repressed while trafficking in RNP granules along axonal MTs. According to the prevailing model, mRNAs are not translated while being transported to their final destination, where they start to be locally translated on demand [4,28]. This model mostly relies on proteomic studies made on RNP granules that identified several translational repressors [4–6,28]. However, it is still unclear whether granule mRNAs are translationally repressed at the **translation initiation** or **translation elongation** step. Despite the identification of initiation and elongation factors in RNP granules, the presence of exon junction complex (EJC), cap-binding complex (CBC), and poly(A)-binding protein (PABP), which need to be removed from mRNAs before initiation of translation, suggests that translation could be repressed at the initiation step [28]. Translational repression could indeed be achieved via different regulators or at different steps of the translation process, depending on the RNP granule content. Along this line, several studies have suggested that mRNAs are transported as stalled **polysomes** in RNP granules where they are paused at the

Polysomal profiling: sequencing approach that combines polysomal fractionation with RNA-sequencing to characterize the number of ribosomes loaded on a single mRNA, thus analyzing the translation rate of a given transcript.
Polysome: single mRNA occupied by multiple ribosomes.
Processing body: nonmembranous granule containing translationally repressed mRNAs and RBPs with a role in translation repression and decay pathways.
Ribonucleoprotein granule: membrane-less, dynamically and reversibly self-assembled liquid-like condensate of mRNAs and RBPs.
Ribosome footprint: sequencing of ribosome-occupied mRNA fragments; this technology informs on the number and position of translating ribosomes on a given transcript to define its translation efficiency and the codon-specific elongation speed.
Stress granule: non-membranous granule containing most cytoplasmic mRNAs but those encoding for heat shock proteins, whose formation is promptly induced in response to stress (e.g., oxidative stress, heat shock, UV irradiation, and hypoxia).
Translation elongation: mRNA decoding into the correspondent protein by progressive codon-anticodon pairing and loading of the tRNA-carried amino acid onto the newly synthesized polypeptide chain.
Translation initiation: the process of assembly of the initiator tRNA with the 40S and 60S ribosomal subunits into the 80S initiation complex at the starting codon of a given mRNA induced by initiation factors.
Untranslated region: noncoding sequence at the 5′ and 3′ mRNA ends containing regulatory sequences accessible to interactions with regulatory proteins that modulate their transport out of the nucleus and translation efficiency.

Key Figure

Coordination between Axonal Transport and Local Translation in Neurons.

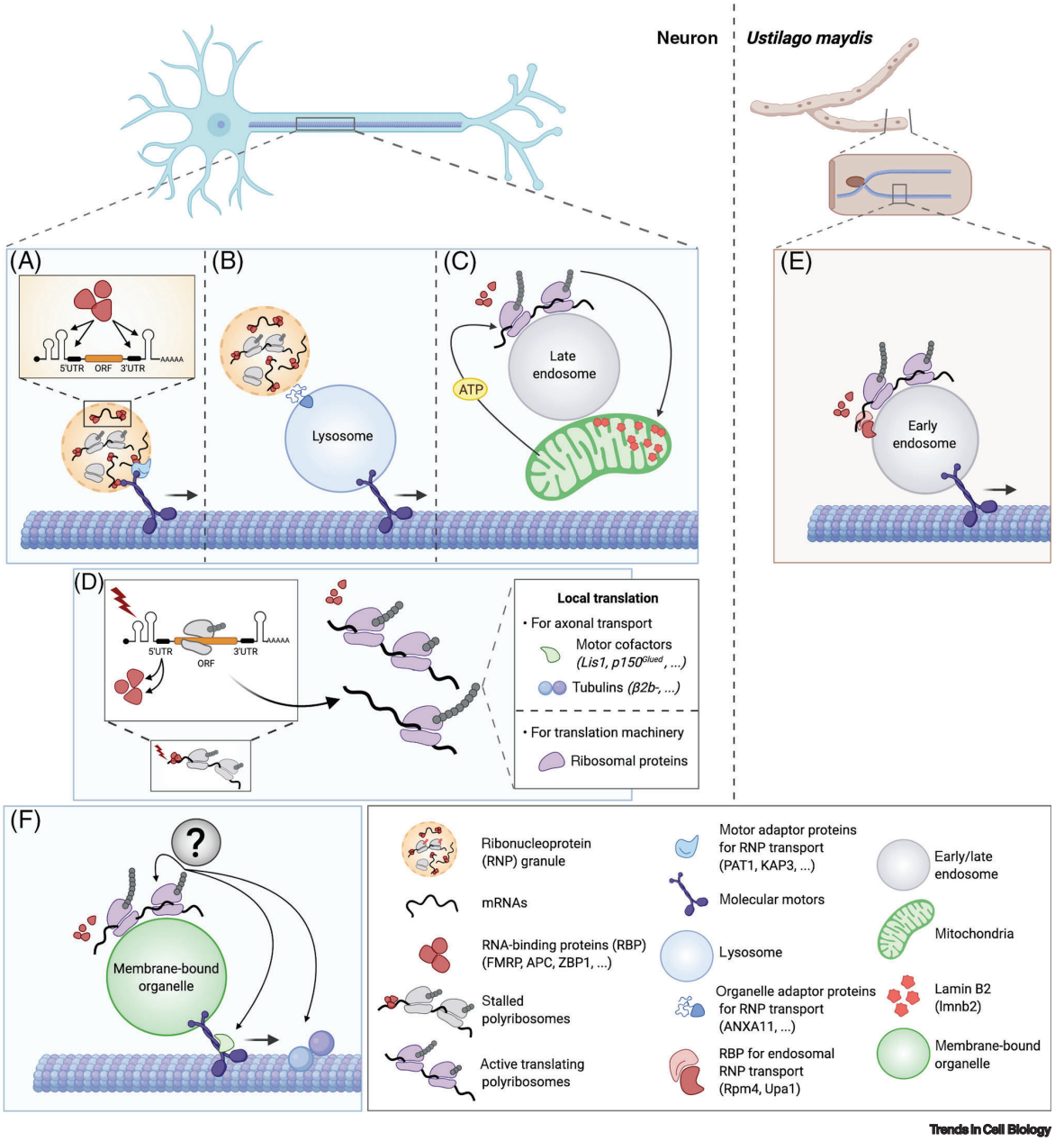

(See figure legend at the bottom of the next page.)

elongation phase, allowing for rapid completion of protein production upon local demands [29–33]. In addition to their content in translational repressors, specific biophysical properties of RNP granules are in favor of translation inhibition. RNP granules maintain a densely packed structure after treatment with EDTA or RNase, which is also characteristic of stalled polysomes [4]. Biophysical differences are observed between proximal and mid-axon RNP granules, with distal granules being less viscous, more dynamic, and formed with weaker hydrophobic interactions in comparison to the proximal ones [34]. Consistent with this notion, a recent study demonstrated that RNA granules can be formed of liquid-like smooth and solid-like rough scaffolds depending on the RBPs responsible for the granule condensation [35]. The authors show that liquid-like smooth substructure of granules increases the dynamics of RNP granules and the nascent polypeptides inside the granules in comparison to the solid-like rough substructure. RNP granules induced by expression of FMRP preferentially assembled into solid-like rough granules whereas Caprin-1 and TDP-43 induce the formation of liquid-like smooth RNP granules [35]. These observations are consistent with the existence of various types of transported granules and suggest that mRNA translation may occur in specific conditions that depend on RBP content and physical state of RNP granule. It is indeed tempting to envision a correlation between the translational status of RNP granules with their physical properties. The silent ones would have a viscous compact-close structure, while more dynamics and less viscous RNP granules including open polysomes structure would be compatible with mRNAs translation.

Learning about mRNA Translation from Stress Granules

The prevalent model posits that transported RNP granules are translationally silent. However, this model has recently been challenged by the visualization of active translation on a subset of stress-like RNA granules formed upon overexpression or mutations of the RBP Fus [36]. This result was confirmed by using single-molecule imaging of translation with the SunTag technology in stress granules [37]. The authors show that some actively translating mRNAs (that are not limited to stress-induced mRNAs) can be detected in stress granule where they undergo the three major steps of translation, initiation, elongation, and termination [37]. These data suggest that neuronal RNP granules, which share some protein content with stress granules, could serve as a platform for translation at rest and/or during transport. Consistent with this idea, new fluorescence live-imaging techniques to assess single-mRNA translation dynamics (Box 2) also identified translating polysomes that are moving in neurons with velocities consistent with fast axonal transport [38,39]. However, a recent study coupling ribopuromycylation (RPM) assay (Box 2) with SunTag imaging suggests that most polysomes moving in dendrites are indeed resistant to puromycin, thus likely stalled at post-initiation stage [31]. Such discrepancy may reflect the diversity of RNP granules that move in different neuronal compartments. Thus, it would be important to assess whether active translating polysomes move in the axon and further characterize their transport dynamics and physiological function. Moreover, similar studies in the mid/distal part of the axon would prevent bias in the detection of somal polysomes/RNP granules entering the axon and presenting with a different pattern of translation activity than long-distance transport RNP granules.

Figure 1. (A) mRNAs, ribosomes, stalled polysomes, and RBPs condensate as membrane-less RNP granules that are actively transported along microtubules by molecular motors associated to granule-specific adaptor proteins. RBPs regulate mRNAs localization through binding to sequence motifs in the 5′ UTR and 3′ UTR of mRNAs. (B) Indirect motor-mediated transport of RNP granules via tethering to lysosomes expressing adaptor proteins. (C) Static late endosomes serving as translation platform for proteins required for the survival of adjacent mitochondria which provide ATP for local translation. (D) Stimuli-induced local translation of proteins sustaining the integrity of the transport and translation machinery, including molecular motor cofactors, tubulin isotypes and ribosomal proteins. (E) In *Ustilago maydis*, active mRNAs translation occurs on trafficking early endosomes bearing transcript-specific RBP proteins. (F) Model proposed for mammal neurons showing mRNAs undergoing active translation while being hitchhiked on motile membrane-bound organelles. Subgroups of proteins essential for the transport and translation machinery could be actively translated to regulate the microtubule-based transport and organelles homeostasis. Abbreviations: ORF, open reading frame; RBP, RNA binding protein; RNP, ribonucleoprotein; UTR, untranslated region.

Coordination between Membrane-Bound Organelles Transport and Translation Machinery

In comparison to membrane-less RNP granules, long-range transport of membrane-bound organelles such as endosomes, lysosomes, and mitochondria along MT tracks is well documented. Unlike RNP granules, several adaptors and scaffolding proteins regulating the specific transport of the different membrane-bound organelles have been identified [40]. This is exemplified by the existence of BORC/Arl8/SKIP/kinesin-1 and TRAK/Milton/kinesin-1 ensembles that support axonal anterograde transport of lysosomal-associated membrane protein (LAMP)1-positive (late endosomes/lysosomes) vesicles and mitochondria, respectively [41–43].

Hitchhiking as an Alternative Mode of Axonal Transport for RNP Granules

A growing body of evidence arising from studies in filamentous fungi suggests the existence of another mechanism of long-range transport, termed 'hitchhiking' [44]. Instead of being directly transported by their own molecular motors, some vesicles attach to other motile membrane-bound organelles that act as vehicles to achieve indirect transport. mRNAs and polysomes have been identified as cargoes using hitch-hiking mechanism by docking onto moving early endosomes in filamentous fungi, which is required for their proper distribution along the **hyphae** (Figure 1E) [45–47]. A similar mechanism has been recently described in mammalian cells and particularly in neurons (Figure 1B) [48]. It was shown that RNP granules hitch a ride on motile lysosomes to ensure their long-distance transport in cultured primary neurons and zebrafish axons and use annexin A11 as a molecular adaptor linking both structures. While these studies support the existing coordination between long-distance transport of membrane-bound organelles and mRNA transport, multiple questions remain unanswered. First, are RNP granules also tethered to other membrane-bound vesicles (e.g., mitochondria or dense core vesicles) and how is their tethering regulated? In their study, the authors suggest that most RNP granules co-traffic with lysosomes carried by molecular motors. This claim is difficult to reconcile with other studies showing either that transported RNP granules directly interact with molecular motors or that most RNP granules move independently of endosomes in the axon of *Xenopus* retinal ganglion cells (RGCs) [49]. Moreover, it is still unknown whether hitch-hiking is only used for indirect transport or if this transport mode supports specific cellular functions. The proximity between mRNA granules and lysosomes could help for the rapid degradation of specific mRNAs and lysosomes/endosomes could serve as a signaling platform ultimately regulating

Box 1. Techniques to Image mRNAs in Neurons

In the past two decades, several approaches to image RNA species in fixed and live cells were developed to study their spatial and temporal distribution as well as transport dynamics.

The single-molecule fluorescent ISH (smFISH) technology was initially set up to target a given transcript with a combination of hybridizing oligonucleotides (ODNs) labeled with fluorophores [80,81] (Figure IA). Indirect labeling methods were developed to reduce background, increase fluorescent signal and detection sensitivity. These technologies adopt unlabeled primary probes that can be hybridized either by secondary fluorescent probes (single molecule inexpensive FISH; smiFISH) or by complex signal-amplifying probe systems (FISH-STICs; RNAscope) [82–84] (Figure IB,C). To map thousands of RNAs species at a single-cell resolution, the multiplexed error-robust FISH (MERFISH) image approach enables a progressively increased level of multiplexing, however at the expenses of increasing background signal and errors detection [85] (Figure ID). RNAs cellular dynamics within a living cell have been explored through labeling strategies using hybridizing probes or requiring genetic engineering of the target RNA. Untagged RNAs can be visualized through molecular beacons (MBs), single-stranded oligonucleotide probes whose hybridization with a target sequence induces the quencher separation from the probe-associated fluorophore and its emission of fluorescent light [86,87] (Figure IE). Another approach uses RNA fluorogenic RNA aptamers, oligonucleotide sequences whose secondary structure can be recognized by fluorogenic ligands, activated upon binding. Since the first RNA aptamer Spinach, many have been progressively developed with increasing physical stability, folding capacity and ability to bind to multiple fluorogens [88–91] (Figure IF). A key tool for the *in vivo* imaging of RNAs takes advantages of bacteriophage systems. Bacteriophage-derived RNA sequences enriched in hairpin loops are cloned within an RNA of interest to be recognized by bacteriophage-derived coat proteins (CPs) fused to fluorescent proteins. This strategy increases the fluorescence intensity of the tagged RNA over the background generated by freely diffusing CPs [92,93] (Figure IG). Comparatively, the PUM-HD probes are protein-based probes used in couple to target two neighboring RNA sequences. The probes are fused to each one of two fragments of a fluorescent protein, which is reconstituted emitting fluorescence light following probe hybridization to the RNA complementary regions [94] (Figure IH).

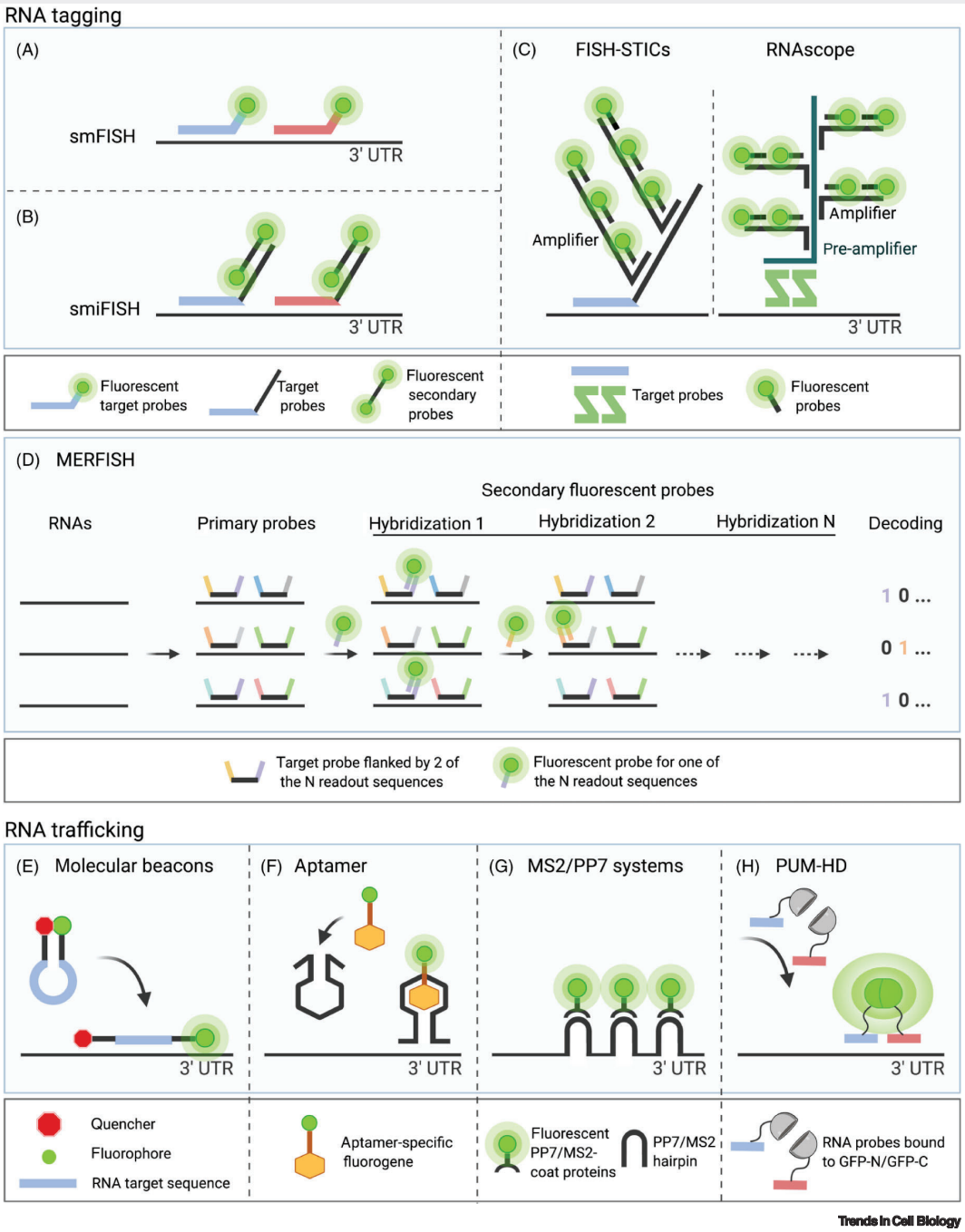

Figure I. Techniques to Visualize mRNAs in Fixed and Live Cells.

mRNA homeostasis and translation. Concerning this matter, it has been suggested that immature miRNAs hitch-hike on late endosome/lysosomes to be actively transported to distal compartments where they are ultimately processed to exert their translation regulatory functions [50].

Active mRNAs Translation at the Surface of Membrane-Bound Organelles

A recent study demonstrated that late endosomes (Rab7 positive) carry RNP granules at their membrane and provide sites for axonal local protein synthesis (Figure 1C) [49]. In particular, it was shown that local translation of lamin B2, a protein essential for mitochondrial integrity and axon maintenance [51], occurs at late endosomes that are in close proximity to mitochondria to sustain their function in axons. While it is not assessed whether local translation occurs during the transport of late endosomes in *Xenopus* RGCs or mammalian neurons, earlier evidence in filamentous fungi shows that mRNAs and polysomes undergo translation at the surface of moving early endosomes, supporting the existence of a mechanism that coordinates translation with transport in membrane-bound organelles (Figure 1E) [45,46,52]. The presence of active polysomes at the surface of membrane-bound vesicles in higher organisms might also occur. Recently, a new endoplasmic reticulum (ER)-derived type of vesicles named ribosome-associated vesicles (RAVs), due to the covering of this vesicles by 80S ribosomes at their surface, was identified in several secretory cells including neurons [53]. In neurons, RAVs were found to localize in dendrites, suggesting a possible function in local translation, not only through their role in the distribution of ribosomes into neurites, but also by providing a support for translation. Indeed, the fact that 80S ribosomes at the surface of RAVs are also found in polysomal assemblies together with putative elements of the translational machinery such as tRNAs and eukaryotic translation elongation factor 1a supports that RAVs are translationally active [53].

In comparison to polysomes included in densely packed and viscous RNP granules environment, the presence of polysomes at the surface of membrane-bound vesicles might provide a more dynamic and open structure to facilitate mRNA translation. Moreover, proteomic analysis of enriched fraction of p50–GFP-associated motile vesicles isolated from mouse brains revealed the presence of elements of the translational machinery such as small and large ribosomal subunits and initiation and elongation factors, even though their detection does not guarantee their activity [54]. Since late but not early endosomes are involved in local translation along the axon [49], it is tempting to speculate that the level of maturation of endosomes/lysosomes correlates with different translational machinery or translation profile.

Box 2. Toolbox to Visualize Protein Synthesis

The past 5 years have seen an expansion of the toolbox available to investigate RNA translation. Bacteriophage-derived systems are opening the way for imaging translation dynamics in living cells. These strategies are based on three transgenes that have to be co-integrated and stably coexpressed in the target cells: a reporter mRNA and two fluorescently-labeled antibodies/coat proteins able to recognize the mRNA and the correspondent translating polypeptide chain. While the *translating* RNA *imaging* by coat protein knock-off (TRICK) system allows one to visualize and discriminate untranslated mRNAs from those undergoing the first round of translation, the SunTag system studies the translation dynamics of a given transcript over time [95–97]. Recently, the SunTag system has been coexpressed with the orthologous MoonTag or HA frankenbody system for a dual-color imaging to visualize translation events on two different target RNAs [98–100] (Figure IA,B). To interrogate protein synthesis in an *in vitro* or *ex vivo* setting, puromycin-based methods are ideal. Puromycin is a tRNA analog that can be incorporated in nascent polypeptide chains inducing their elongation termination and release from the ribosomal translation site (puromycylation). Tagged polypeptide chains are detected via an anti-puromycin antibody (Figure IC) [101]. To specifically visualize the translation of a given protein, puromycylation is coupled to proximity ligation assay (PLA), an antibody-based method that was initially used to assess whether two targets are in close proximity [102] (Figure ID). Further progress was made with the ribopuromycylation (RPM) assay which combines puromycin administration with translation elongation inhibitors, such as cycloheximide or emetine, to prevent the nascent polypeptides to be released from active ribosomes [101,103] (Figure IE). Although this method was developed to visualize the site of active translation, recent studies questioned the efficacy of the strategy [104,105]. Ongoing translation can also be detected by metabolic labelling via the fluorescent noncanonical amino acid tagging (FUNCAT) technique. In relation to a peptide content in methionine, the analog azidohomoalanine (AHA) is incorporated in nascent peptide chains, to be thereafter visualized with a fluorophore conjugated via click chemistry [106] (Figure IF).

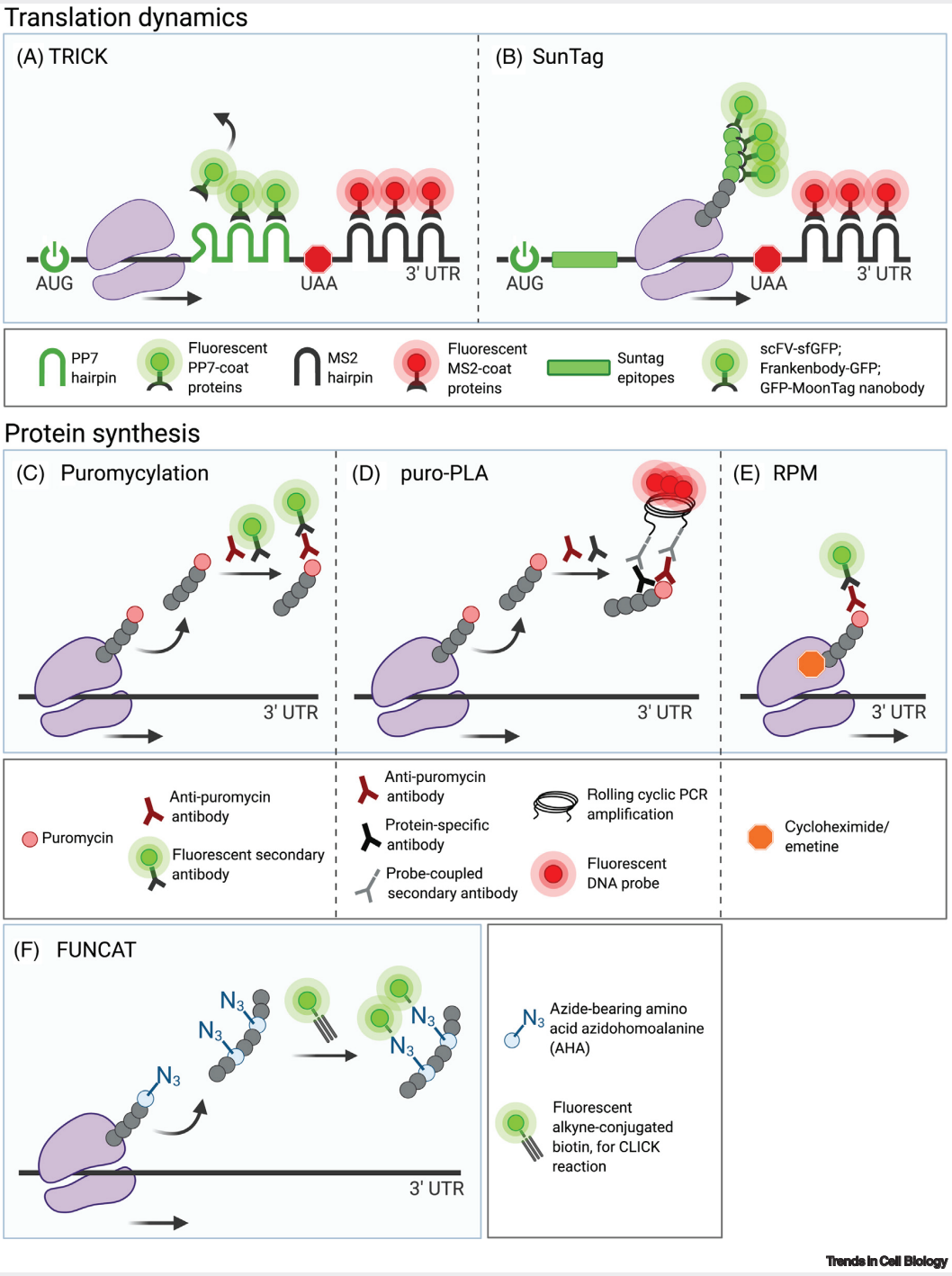

Figure I. Techniques to Label Translating Peptides.

In the future, it would be interesting to assess whether there is a functional correlation between mRNAs translation and their active transport and whether trafficked RNP granules provide membrane-bound vesicles with proteins important for their own shuttling activity. Emerging evidence shows that motile membrane-bound vesicles have an on-board enzymatic machinery that regulates their own transport along axons by either producing energy or modifying MT tracks [54–56]. Therefore, it is tempting to hypothesize that translation of proteins at the surface of motile vesicles could represent an additional mechanistic layer to control their own axonal transport.

Transport of the Translational Machinery

Little is known about the molecular mechanisms that dispatch ribosomes along neurites. Emerging evidence suggests that their transport could be mediated by direct interaction with molecular motors. Accordingly, ribosomal subunits can interact with the tail domain of the kinesin superfamily member KIF4 in dorsal root ganglia neurons [57]. Moreover, a loss-of-function of uncoordinated-16 (ortholog of JNK-interacting protein (JIP)-3), which serves as an adaptor between kinesins and cargoes, leads to the abnormal distribution of ribosomes along axons in *Caenorhabditis elegans* neurons [58]. Further indications come from fluorescent tracking of axonal polysomes that display a velocity concordant with fast axonal transport [38,39]. With the advent of **polysome profiling** and **ribosome footprinting** methods, a recent study showed that axonal mRNAs can be bound and translated by multiple or single ribosomes (monosomes) in neuronal processes [59]. Whether ribosomes in different organization states are moving at distinct velocities, and whether the velocity is imposed by the type of transport machinery, has not been investigated yet. Although ribosomes are known to be synthesized and assembled in the cell body before being transported along neurites, recent findings suggest that they could also undergo local assembly. Accordingly, a subset of ribosomal proteins is locally synthesized and incorporated into preexisting axonal ribosomes to locally maintain a specialized pool of functional translation machinery [60,61]. Nonetheless, the lack of pre-rRNAs and other factors involved in *de novo* ribosome biogenesis in neurites support a primary role for transport on local ribosome homeostasis [61]. The mRNAs encoding ribosomal proteins are also detected in RNP granules isolated from mouse full brain, suggesting that RNP granules could actively contribute to the axonal replenishment of ribosomes [4–6]. Along this line, a recent study demonstrated that the RBP TDP-43 binds to the 5′ UTR of ribosomal protein mRNAs and regulates their transport and translation and that locally translated ribosomal proteins are incorporated into native axonal ribosomes [25]. As impairment of TDP-43 function has been reported in neurodegenerative disorders such as amyotrophic lateral sclerosis and frontotemporal lobar degeneration, these data support the importance of the coordination between axonal transport and local protein synthesis for the maintenance of the axonal morphology (Box 3).

Transport Machinery Regulation by Local Protein Synthesis

Accumulating data support a key role for local translation in sustaining the homeostatic distribution of proteins involved in MT-dependent transport across distant compartments. Kinesin and dynein families of motors drive long-distance transport of cargoes and ultimately supply the machinery for local protein synthesis to distal cellular compartments [62]. Constituents of the transport machinery are also translated locally to respond to changes in transport demands along distal axons with spatial and temporal accuracy (Figure 1D). Kinesins and dyneins transcripts are found in excitatory presynapses and RNP granules isolated from mouse brain, as well as bound to ribosomes in retinal ganglion cell axons, suggesting their possible local translation [4,60,63]. Analysis of the axonal transcriptome of human motoneurons revealed enrichment for transcripts coding for proteins associated with MT-based transport such as bicaudal D homolog (BICD)2, KIF5C and KIF1C, supporting the local translation of key transport

Box 3. Transport Machinery and RNP Granules in Neurological Diseases

Defects in axonal transport have been described for a broad range of neurodegenerative diseases. Its impairment has been correlated to genetic alterations in its functional components, specifically the motor proteins and their adaptors, the MT building blocks and the trafficking cargos. Neurodegenerative diseases such as Alzheimer's disease, spinal and bulbar muscle atrophy (SMA, SBMA), Charcot-Marie-Tooth disease (CMT), and amyotrophic lateral sclerosis (ALS) have been associated with a large number of alterations in axonal-transport-related genes; all contributing to the onset of their early pathological features. This is exemplified by mutations affecting KIF5A leading to aberrant kinesin activity and anterograde transport dynamics, as well as in the dynein heavy chain DYNC1H1 or its adaptor dynactin complex which correlates with retrograde transport abnormalities [107]. MAPs play a key role in regulating MT organization and genetic variations perturbating their activity lead to MT destabilization and defects in motors binding, as described for Spastin, tau, and HSBP1 in hereditary spastic paraplegia, frontotemporal dementia, and CMT, respectively [107,108]. More recently, an increasing number of mutations in genes coding for RBPs or adaptors present in RNP granules have additionally been identified in some of the same neurodegenerative diseases [109]. Given the important role of RBPs in regulating and defining the ultimate axonal localization of mRNAs, mutations in different RBPs have been additionally described in different neurodegenerative diseases. Genetic variants of RBPs were found to disrupt the formation or trafficking of RNP granules leading to reduced axonal transport of numerous mRNAs, locally regulated translation and ultimately to axonal degeneration and neuronal cell death. Among these are the ALS-associated mutations in TDP-43, which lead to impaired anterograde transport of TDP-43-containing RNP granules, increased cytosolic accumulation of neurofilament mRNAs, its cognate target, and ultimately to neuronal cell death [110]. Linked to ALS are also mutations in the RNP-lysosome tethering adaptor annexin A11, which prevent RNPs from hitch-hiking on lysosomes and peripheral mRNAs localization [48]. Some identified causes of SBMA are genetic alterations in the survival of motor neurons, adaptor protein described in RNP granules implicated in the dysregulated axonal localization of a broad range of transcripts important for axonal growth and branching such as β-actin and Gap43 [111].

proteins in axon [64]. Furthermore, it has been shown that nerve growth factor (NGF) triggers the intra-axonal synthesis of dynein cofactors lissencephaly (Lis1) and p150Glued to promptly regulate retrograde transport of lysosomes in the axon upon demands [65]. Consistent with this idea, it was recently reported that vimentin, a scaffold protein previously described to play a role in the assembly of a dynein-dependent retrograde signaling complex, is locally translated in the axon upon neurodegenerative $A\beta_{1-42}$ signal exposure [66,67]. The same mechanism can be expected for kinesin cofactors as several of them are detected in the axonal translatome of *Xenopus* RGCs, such as huntingtin (regulates BDNF vesicles transport through kinesin-1), JIP3 (regulates kinesin-1 motility), *d*ifferentially *e*xpressed in *n*ormal versus *n*eoplastic/MAPK-activating death domain protein DENN/MADD (required for kinesin-3 dependent transport) and Fasciculation And Elongation Protein Zeta 1 Fez1 (activation of kinesin-1 motors) [68–70]. In particular, huntingtin protein was shown to be involved in the transport of dendritic RNP granules, suggesting that deregulation of local translation could contribute to the pathogenesis of Huntington's disease [71,72]. How molecular motors recruitment to cargoes is regulated during transport remains debated and different models have been suggested [73]. In the prevalent 'tug-of-war' model, anterograde and retrograde molecular motors are attached to the cargo and mechanically compete to determine the directionality of transport. Another model named coordination proposes that opposite motors are bound to the same cargo but the directionality is determined by motor adaptor proteins that coordinate the activation/inhibition of the motors in such a way that only one motor is active at a time. In the tug-of-war model, local translation of kinesins and/or dyneins might mediate changes of the stoichiometry of motors bound to cargo while, in the coordination model motor, adaptors would be locally synthesized to regulate motor activities, ultimately modulating the speed and directionality of transport. Molecular motors, and particularly dynein, are large complexes including multiple subunits. Therefore, the local synthesis of smaller molecular motor adaptors, such as Lis1 [65], would be a convenient way to tune rapid change in directionality or speed of axonal transport upon local demands. Whether local translation occurs within the axoplasm and/or at the surface of static/moving organelles remains to be determined.

Axonal MTs serve as tracks for molecular motors to transport a multitude of cargoes, including components of the MT cytoskeleton itself [62,74]. Given the slow transport rates of tubulin heterodimers and MT polymers, local translation of tubulins at distal axonal locations could allow the production of specific tubulin isoforms or to favor post-translational modification upon tubulin heterodimer assembly. Accordingly, ribosome-bound mRNAs encoding for tubulin subunits were identified in isolated axons of RGCs [60]. This mode of local translation of tubulin monomers would require the action of multiple chaperone proteins to promote their assembly into polymerization-competent heterodimers. Of note, prefoldin proteins such as chaperonin-containing tailless complex polypeptide CCT1) chaperonin, and tubulin cofactors TBCA-E are detected in the axonal proteome of cultured neurons and in the axonal growth cone of cortical projection neurons [75,76]. Furthermore, all CCT chaperonin proteins and the tubulin cofactors TBCA-D are detected in motile vesicles and APEX–Lamp1 (ascorbate peroxidase-catalyzed *proximity labeling)* proteomic analysis, respectively [48,54]. Consistent with this idea, local translation of *β2B-tubulin* was described as essential to control the dynamics of MTs in the growth cone of mouse DRG explant neurons [77]. Freely available tubulin has been suggested to contribute to the self-repair of MTs upon mechanical disruption caused by walking motors [78,79]. Therefore, local supply of tubulin originating from translating mRNAs at RNP granules or motile vesicles may sustain the structural dynamic changes of the MT network and MT-dependent transport (Figure 1F).

Concluding Remarks

Some neurons extend long axonal projections to connect to their distant target, which represents a major challenge to ensure their homeostasis and proper activity. Therefore, conserved mechanisms are at play to ensure rapid and local supply of key structural or signaling molecules to regions that are localized away from the soma. These processes include MT-based transport in both anterograde and retrograde direction (from the soma to the synapse and back) as well as local synthesis of protein. One long-standing and still unresolved question in the field is if and how both biological processes are coordinated (see Outstanding Questions). While it is now well accepted that some mRNAs and elements of the translational machinery are actively transported along axons, the mechanisms that control their sorting to specific cytosolic locations remain poorly understood. In addition, what controls the loading of such molecules on selective motors and whether some mRNAs are actively translated during their journey along the axon within RNP granules or at the surface of lysosome/late endosome, remain unclear. The advent of cutting edge technology to visualize mRNA translation coupled with ribosome profiling analysis should help clarifying this issue in the near future. It will also be important to decipher the function of *de novo* generated proteins in moving cargoes and understand whether this process is actively responding to intrinsic demand for homeostatic process (e.g., structural repair) as well as to synaptic activity, both of which are altered in neurodegenerative disorders.

Outstanding Questions

Is there specificity in the recruitment of mRNAs into different RNP granules? Could this specificity be generated by the loading onto different molecular motors?

Are all RNP granules translationally repressed during transport or is the high diversity of RNP granules has so far prevented us to identify translationally active RNP granules?

Some RNP granules hitchhike on motile lysosomes/late endosomes for long-distance transport. Could this proximity during transport allow cooperation between both structures? Lysosomes could help for the degradation of specific mRNAs or RNP granules could be a source of mRNAs for translation at the surface of lysosomes/late endosomes.

Is local translation occurring at the surface of motile membrane-bound vesicles in mammals? What are the cellular functions regulated by membrane-coupled translation? Could this local protein synthesis contribute to their own transport?

Acknowledgments

The work in the Nguyen laboratory is supported by the F.R.S.-F.N.R.S. (Synet; EOS 0019118F-RG36), the Fonds Leon Fredericq, the Fondation Médicale Reine Elisabeth, the Fondation Simone et Pierre Clerdent, the Belgian Science Policy (IAP-VII network P7/20), and the ERANET Neuron STEM-MCD and NeuroTalk. S.T., L.B., and L.N. are respectively PhD student, postdoctoral researcher, and senior research associates of the F.R.S- F.N.R.S. All figures were created with BioRender.com.

Declaration of Interests

The authors declare no competing interests.

References

1. Ries, R.J. *et al.* (2019) m6A enhances the phase separation potential of mRNA. *Nature* 571, 424–428
2. Anderson, P. and Kedersha, N. (2006) RNA granules. *J. Cell Biol.* 172, 803–808

3. Czaplinski, K. (2014) Understanding mRNA trafficking: are we there yet? *Semin. Cell Dev. Biol.* 32, 63–70
4. El Fatimy, R. *et al.* (2016) Tracking the fragile X mental retardation protein in a highly ordered neuronal ribonucleoparticles population: a link between stalled polyribosomes and RNA granules. *PLoS Genet.* 12, e1006192
5. Elvira, G. *et al.* (2006) Characterization of an RNA granule from developing brain. *Mol. Cell. Proteomics* 5, 635–651
6. Kanai, Y. *et al.* (2004) Kinesin transports RNA: isolation and characterization of an RNA-transporting granule. *Neuron* 43, 513–525
7. Baumann, S. *et al.* (2020) A reconstituted mammalian APC-kinesin complex selectively transports defined packages of axonal mRNAs. *Sci. Adv.* 6, eaaz1588
8. Wu, H. *et al.* (2020) A kinesin adapter directly mediates dendritic mRNA localization during neural development in mice. *J. Biol. Chem.* 295, 6605–6628
9. Hendricks, A.G. *et al.* (2010) Motor coordination via a tug-of-war mechanism drives bidirectional vesicle transport. *Curr. Biol.* 20, 697–702
10. Gumy, L.F. *et al.* (2017) MAP2 defines a pre-axonal filtering zone to regulate KIF1- versus KIF5-dependent cargo transport in sensory neurons. *Neuron* 94, 347–362.e7
11. Messitt, T.J. *et al.* (2008) Multiple kinesin motors coordinate cytoplasmic RNA transport on a subpopulation of microtubules in *Xenopus* oocytes. *Dev. Cell* 15, 426–436
12. Pasciuto, E. and Bagni, C. (2014) SnapShot: FMRP mRNA targets and diseases. *Cell* 158, 1446–1446.e1
13. Batish, M. *et al.* (2012) Neuronal mRNAs travel singly into dendrites. *Proc. Natl. Acad. Sci. U. S. A.* 109, 4645–4650
14. Turner-Bridger, B. *et al.* (2018) Single-molecule analysis of endogenous β-actin mRNA trafficking reveals a mechanism for compartmentalized mRNA localization in axons. *Proc. Natl. Acad. Sci. U. S. A.* 115, E9697–E9706
15. Hammer, J.A. and Sellers, J.R. (2012) Walking to work: roles for class v myosins as cargo transporters. *Nat. Rev. Mol. Cell Biol.* 13, 13–26
16. Ohashi, S. *et al.* (2002) Identification of mRNA/protein (mRNP) complexes containing Purα, mStaufen, fragile X protein, and myosin Va and their association with rough endoplasmic reticulum equipped with a kinesin motor. *J. Biol. Chem.* 277, 37804–37810
17. Yoshimura, A. *et al.* (2006) Myosin-Va facilitates the accumulation of mRNA/protein complex in dendritic spines. *Curr. Biol.* 16, 2345–2351
18. Mitsumori, K. *et al.* (2017) Components of RNA granules affect their localization and dynamics in neuronal dendrites. *Mol. Biol. Cell* 28, 1412–1417
19. Lindsay, A.J. *et al.* (2013) Identification and characterization of multiple novel Rab-myosin Va interactions. *Mol. Biol. Cell* 24, 3420–3434
20. Balasanyan, V. and Arnold, D.B. (2014) Actin and myosin-dependent localization of mRNA to dendrites. *PLoS One* 9, e92349
21. Pathak, D. *et al.* (2010) Evidence that myosin activity opposes microtubule-based axonal transport of mitochondria. *J. Neurosci.* 30, 8984–8992
22. Nalavadi, V.C. *et al.* (2012) Regulation of zipcode binding protein 1 transport dynamics in axons by myosin va. *J. Neurosci.* 32, 15133–15141
23. Bommel, B. *et al.* (2019) F-actin patches associated with glutamatergic synapses control positioning of dendritic lysosomes. *EMBO J.* 38, 1–17
24. Tushev, G. *et al.* (2018) Alternative 3′ UTRs modify the localization, regulatory potential, stability, and plasticity of mRNAs in neuronal compartments. *Neuron* 98, 495–511.e6
25. Nagano, S. *et al.* (2020) TDP-43 transports ribosomal protein mRNA to regulate axonal local translation in neuronal axons. *Acta Neuropathol.* 140, 695–713
26. Merianda, T.T. *et al.* (2013) Axonal localization of neuritin/CPG15 mRNA in neuronal populations through distinct 5′ and 3′ UTR elements. *J. Neurosci.* 33, 13735–13742
27. Martínez, J.C. *et al.* (2019) Pum2 shapes the transcriptome in developing axons through retention of target mRNAs in the cell body. *Neuron* 104, 931–946.e5
28. Fritzsche, R. *et al.* (2013) Interactome of two diverse RNA granules links mRNA localization to translational repression in neurons. *Cell Rep.* 5, 1749–1762
29. Graber, T.E. *et al.* (2017) UPF1 governs synaptic plasticity through association with a STAU2 RNA granule. *J. Neurosci.* 37, 9116–9131
30. Graber, T.E. *et al.* (2013) Reactivation of stalled polyribosomes in synaptic plasticity. *Proc. Natl. Acad. Sci. U. S. A.* 110, 16205–16210
31. Langille, J.J. *et al.* (2019) Polysomes identified by live imaging of nascent peptides are stalled in hippocampal and cortical neurites. *Learn. Mem.* 26, 351–362
32. Wells, D.G. (2006) RNA-binding proteins: a lesson in repression. *J. Neurosci.* 26, 7135–7138
33. Na, Y. *et al.* (2016) Real-time imaging reveals properties of glutamate-induced Arc/Arg 3.1 translation in neuronal dendrites. *Neuron* 91, 561–573
34. Gopal, P.P. *et al.* (2017) Amyotrophic lateral sclerosis-linked mutations increase the viscosity of liquid-like TDP-43 RNP granules in neurons. *Proc. Natl. Acad. Sci. U. S. A.* 114, E2466–E2475
35. Shiina, N. (2019) Liquid- and solid-like RNA granules form through specific scaffold proteins and combine into biphasic granules. *J. Biol. Chem.* 294, 3532–3548
36. Yasuda, K. *et al.* (2013) The RNA-binding protein Fus directs translation of localized mRNAs in APC-RNP granules. *J. Cell Biol.* 203, 737–746
37. Mateju, D. *et al.* (2020) Single-molecule imaging reveals translation of mRNAs localized to stress granules. *Cell* 183, 1801–1812
38. Wu, B. *et al.* (2016) Translation dynamics of single mRNAs in live cells and neurons. *Science* 352, 1430–1435
39. Wang, C. *et al.* (2016) Real-time imaging of translation on single mRNA transcripts in live cells. *Cell* 165, 990–1001
40. Guedes-Dias, P. and Holzbaur, E.L.F. (2019) Axonal transport: driving synaptic function. *Science* 366, eaaw9997
41. Farías, G.G. *et al.* (2017) BORC/kinesin-1 ensemble drives polarized transport of lysosomes into the axon. *Proc. Natl. Acad. Sci. U. S. A.* 114, E2955–E2964
42. van Spronsen, M. *et al.* (2013) TRAK/Milton motor-adaptor proteins steer mitochondrial trafficking to axons and dendrites. *Neuron* 77, 485–502
43. De Pace, R. *et al.* (2020) Synaptic vesicle precursors and lysosomes are transported by different mechanisms in the axon of mammalian neurons. *Cell Rep.* 31, 107775
44. Salogiannis, J. and Reck-Peterson, S.L. (2017) Hitchhiking: a non-canonical mode of microtubule-based transport. *Trends Cell Biol.* 27, 141–150
45. Higuchi, Y. *et al.* (2014) Early endosome motility spatially organizes polysome distribution. *J. Cell Biol.* 204, 343–357
46. Baumann, S. *et al.* (2014) Endosomal transport of septin mRNA and protein indicates local translation on endosomes and is required for correct septin filamentation. *EMBO Rep.* 15, 94–102
47. Olgeiser, L. *et al.* (2019) The key protein of endosomal mRNP transport Rrm4 binds translational landmark sites of cargo mRNAs. *EMBO Rep.* 20, 1–17
48. Liao, Y.-C. *et al.* (2019) RNA granules hitchhike on lysosomes for long-distance transport, using annexin A11 as a molecular tether. *Cell* 179, 147–164.e20
49. Cioni, J.-M. *et al.* (2019) Late endosomes act as mRNA translation platforms and sustain mitochondria in axons article late endosomes act as mRNA translation platforms and sustain mitochondria in axons. *Cell* 176, 56–72.e15
50. Corradi, E. *et al.* (2020) Axonal precursor mi RNA s hitchhike on endosomes and locally regulate the development of neural circuits. *EMBO J.* 39, 1–24
51. Yoon, B.C. *et al.* (2012) Local translation of extranuclear lamin B promotes axon maintenance. *Cell* 148, 752–764
52. Béthune, J. *et al.* (2019) Membrane-associated RNA-binding proteins orchestrate organelle-coupled translation. *Trends Cell Biol.* 29, 178–188
53. Carter, S.D. *et al.* (2020) Ribosome-associated vesicles: a dynamic subcompartment of the endoplasmic reticulum in secretory cells. *Sci. Adv.* 6, eaay9572

54. Hinckelmann *et al.* (2016) Self-propelling vesicles define glycolysis as the minimal energy machinery for neuronal transport. *Nat. Publ. Gr.* 7, 13233
55. Zala, D. *et al.* (2013) Vesicular glycolysis provides on-board energy for fast axonal transport. *Cell* 152, 479–491
56. Even, A. *et al.* (2019) ATAT1-enriched vesicles promote microtubule acetylation via axonal transport. *Sci. Adv.* 5, eaax2705
57. Bisbal, M. *et al.* (2009) KIF4 mediates anterograde translocation and positioning of ribosomal constituents to axons. *J. Biol. Chem.* 284, 9489–9497
58. Noma, K. *et al.* (2017) Microtubule-dependent ribosome localization in *C. elegans* neurons. *Elife* 6, 1–23
59. Biever, A. *et al.* (2020) Monosomes actively translate synaptic mRNAs in neuronal processes. *Science* 367, eaay4991
60. Shigeoka, T. *et al.* (2016) Dynamic axonal translation in developing and mature visual circuits. *Cell* 166, 181–192
61. Shigeoka, T. *et al.* (2019) On-site ribosome remodeling by locally synthesized ribosomal proteins in axons. *Cell Rep.* 29, 3605–3619.e10
62. Twelvetrees, A.E. (2020) The lifecycle of the neuronal microtubule transport machinery. *Semin. Cell Dev. Biol.* 107, 7481
63. Hafner, A.S. *et al.* (2019) Local protein synthesis is a ubiquitous feature of neuronal pre- And postsynaptic compartments. *Science* 364, eaau3644
64. Maciel, R. *et al.* (2018) The human motor neuron axonal transcriptome is enriched for transcripts related to mitochondrial function and microtubule-based axonal transport. *Exp. Neurol.* 307, 155–163
65. Villarin, J.M. *et al.* (2016) Local synthesis of dynein cofactors matches retrograde transport to acutely changing demands. *Nat. Commun.* 7, 13865
66. Walker, C.A. *et al.* (2018) Aβ 1–42 triggers the generation of a retrograde signaling complex from sentinel mRNA s in axons. *EMBO Rep.* 19, 1–13
67. Perlson, E. *et al.* (2005) Vimentin-dependent spatial translocation of an activated MAP kinase in injured nerve. *Neuron* 45, 715–726
68. Sun, F. *et al.* (2011) Sunday Driver/JIP3 binds kinesin heavy chain directly and enhances its motility. *EMBO J.* 30, 3416–3429
69. Blasius, T.L. *et al.* (2007) Two binding partners cooperate to activate the molecular motor Kinesin-1. *J. Cell Biol.* 176, 11–17
70. Niwa, S. *et al.* (2008) KIF1Bβ- and KIF1A-mediated axonal transport of presynaptic regulator Rab3 occurs in a GTP-dependent manner through DENN/MADD. *Nat. Cell Biol.* 10, 1269–1279
71. Ma, B. *et al.* (2011) Huntingtin mediates dendritic transport of β-actin mRNA in rat neurons. *Sci. Rep.* 1, 1–11
72. Savas, J.N. *et al.* (2010) A role for Huntington disease protein in dendritic RNA granules. *J. Biol. Chem.* 285, 13142–13153
73. Fu, M. meng and Holzbaur, E.L.F. (2014) Integrated regulation of motor-driven organelle transport by scaffolding proteins. *Trends Cell Biol.* 24, 564–574
74. Roy, S. (2014) Seeing the unseen: the hidden world of slow axonal transport. *Neuroscience* 20, 71–81
75. Chuang, C.F. *et al.* (2018) Unbiased proteomic study of the axons of cultured rat cortical neurons. *J. Proteome Res.* 17, 1953–1966
76. Poulopoulos, A. *et al.* (2019) Subcellular transcriptomes and proteomes of developing axon projections in the cerebral cortex. *Nature* 565, 365-360
77. Preitner, N. *et al.* (2014) APC is an RNA-binding protein, and its interactome provides a link to neural development and microtubule assembly. *Cell* 158, 368–382
78. Triclin, S. *et al.* (2018) Self-repair protects microtubules from their destruction by molecular motors. *bioRxiv* Published online December 17, 2018. https://doi.org/10.1101/499020
79. Dumont, E.L.P. *et al.* (2015) Molecular wear of microtubules propelled by surface-adhered kinesins. *Nat. Nanotechnol.* 10, 166–169
80. Femino, A.M. *et al.* (1998) Visualization of single RNA transcripts *in situ*. *Science* 280, 585–590
81. Raj, A. *et al.* (2008) Imaging individual mRNA molecules using multiple singly labeled probes. *Nat. Methods* 5, 877–879
82. Tsanov, N. *et al.* (2016) smiFISH and FISH-quant-a flexible single RNA detection approach with super-resolution capability. *Nucleic Acids Res.* 44, 165
83. Sinnamon, J.R. and Czaplinski, K. (2014) RNA detection *in situ* with FISH-STICs. *RNA* 20, 260–266
84. Wang, F. *et al.* (2012) RNAscope: A novel *in situ* RNA analysis platform for formalin-fixed, paraffin-embedded tissues. *J. Mol. Diagnostics* 14, 22–29
85. Chen, K.H. *et al.* (2015) Spatially resolved, highly multiplexed RNA profiling in single cells. *Science* 348, aaa6090-aaa6090
86. Tyagi, S. and Kramer, F.R. (1996) Molecular beacons: probes that fluoresce upon hybridization. *Nat. Biotechnol.* 14, 303–308
87. Tyagi, S. *et al.* (1998) Multicolor molecular beacons for allele discrimination. *Nat. Biotechnol.* 16, 49–53
88. Paige, J.S. *et al.* (2011) RNA mimics of green fluorescent protein. *Science* 333, 642–646
89. Filonov, G.S. *et al.* (2014) Broccoli: rapid selection of an RNA mimic of green fluorescent protein by fluorescence-based selection and directed evolution. *J. Am. Chem. Soc.* 136, 16299–16308
90. Dolgosheina, E.V. *et al.* (2014) RNA Mango aptamer-fluorophore: a bright, high-affinity complex for RNA labeling and tracking. *ACS Chem. Biol.* 9, 2412–2420
91. Chen, X. *et al.* (2019) Visualizing RNA dynamics in live cells with bright and stable fluorescent RNAs. *Nat. Biotechnol.* 37, 1287–1293
92. Buxbaum, A.R. *et al.* (2015) In the right place at the right time: visualizing and understanding mRNA localization. *Nat. Rev. Mol. Cell Biol.* 16, 95–109
93. Chao, J.A. *et al.* (2008) Structural basis for the coevolution of a viral RNA-protein complex. *Nat. Struct. Mol. Biol.* 15, 103–105
94. Yoshimura, H. (2018) Live cell imaging of endogenous RNAs using Pumilio homology domain mutants: principles and applications. *Biochemistry* 57, 200–208
95. Halstead, J.M. *et al.* (2016) *TRICK: A Single-Molecule Method for Imaging the First Round of Translation in Living Cells and Animals*, Elsevier
96. Ruijtenberg, S. *et al.* (2018) *RNA Detection*, Springer New York
97. Yan, X. *et al.* (2016) Dynamics of translation of single mRNA molecules *in vivo* resource dynamics of translation of single mRNA molecules *in vivo*. *Cell* 165, 976–989
98. Boersma, S. *et al.* (2019) Multi-color single-molecule imaging uncovers extensive heterogeneity in mRNA decoding. *Cell* 178, 458–472.e19
99. Morisaki, T. *et al.* (2016) Real-time quantification of single RNA translation dynamics in living cells. *Science* 352, 1425–1429
100. Zhao, N. *et al.* (2019) A genetically encoded probe for imaging nascent and mature HA-tagged proteins *in vivo*. *Nat. Commun.* 10, 2947
101. Buhr, F. *et al.* (2015) Design of photocaged puromycin for nascent polypeptide release and spatiotemporal monitoring of translation. *Angew. Chem. Int. Ed.* 54, 3717–3721
102. Tom Dieck, S. *et al.* (2015) Direct visualization of newly synthesized target proteins in situ. *Nat. Methods* 12, 411–414
103. Bastide, A. *et al.* (2018) The RiboPuromycylation Method (RPM): an immunofluorescence technique to map translation sites at the sub-cellular level. *Bio-Protocol* 8, 1–20
104. Hobson, B.D. *et al.* (2020) Elongation inhibitors do not prevent the release of puromycylated nascent polypeptide chains from ribosomes. *Elife* 9, 1–47
105. Enam, S.U. *et al.* (2020) Puromycin reactivity does not accurately localize translation at the subcellular level. *Elife* 9, 1–34
106. Dieterich, D.C. *et al.* (2010) *In situ* visualization and dynamics of newly synthesized proteins in rat hippocampal neurons. *Nat. Neurosci.* 13, 897–905
107. Guo, W. *et al.* (2020) Axonal transport defects and neurodegeneration: molecular mechanisms and therapeutic implications. *Semin. Cell Dev. Biol.* 99, 133–150

108. Millecamps, S. and Julien, J.-P. (2013) Axonal transport deficits and neurodegenerative diseases. *Nat. Rev. Neurosci.* 14, 161–176
109. Thelen, M.P. and Kye, M.J. (2020) The role of RNA binding proteins for local mRNA translation: implications in neurological disorders. *Front. Mol. Biosci.* 6, 1–13
110. Alami, N.H. *et al.* (2014) Axonal transport of TDP-43 mRNA granules in neurons is impaired by ALS-causing mutations. *Neuron* 81, 536–543
111. Donlin-Asp, P.G. *et al.* (2016) A role for the survival of motor neuron protein in mRNP assembly and transport. *Curr. Opin. Neurobiol.* 39, 53–61

Ex Vivo Recording of Axonal Transport Dynamics on Postnatal Organotypic Cortical Slices

STAR Protocols

CellPress
OPEN ACCESS

Protocol

Ex Vivo Recording of Axonal Transport Dynamics on Postnatal Organotypic Cortical Slices

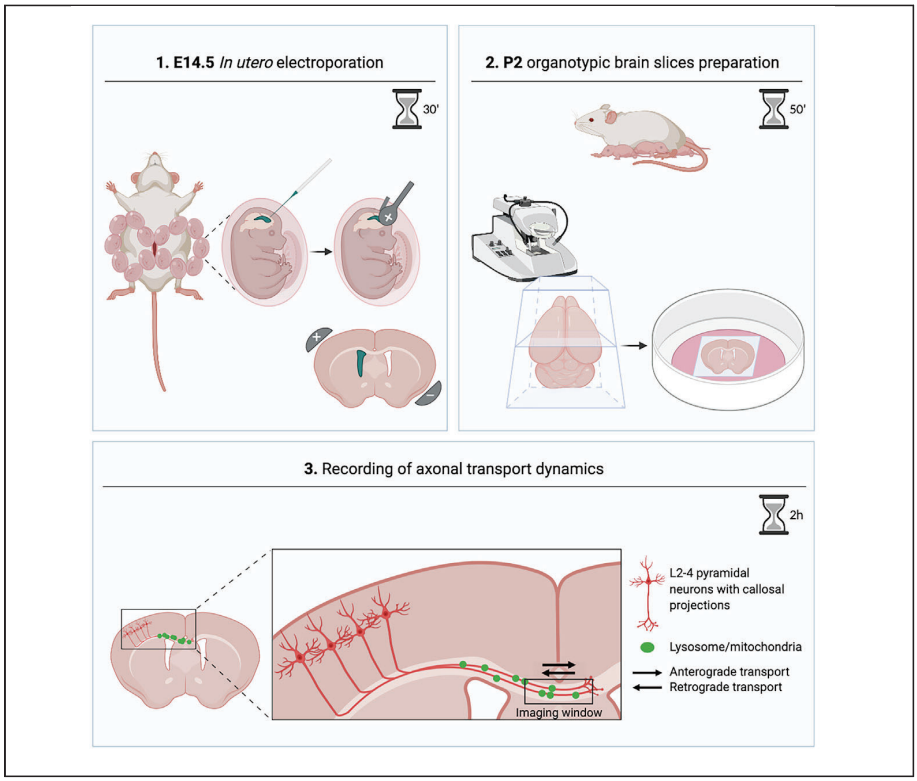

Axonal transport is a physiological process adopted by neurons to transport organelles, proteins, and other molecules along their axonal projections. Here, we describe a step-by-step protocol to record the dynamics of axonal transport along the projections of callosal neurons by combining the *in utero* electroporation technique with the preparation of postnatal organotypic cortical slices. This *ex vivo* protocol has been developed to investigate axonal transport in a physiological setting closely reproducing the *in vivo* environment.

Silvia Turchetto, Loic Broix, Laurent Nguyen

silvia.turchetto@student.uliege.be (S.T.)
lbroix@uliege.be, lbroix@uliege.be (L.B.)
lnguyen@uliege.be (L.N.)

HIGHLIGHTS

Descriptive method to electroporate DNA plasmids in the embryonic mouse cortex

Step-by-step procedure to generate and mount organotypic brain slices

Protocol to record and analyze axonal transport in callosal projection neurons

Guidelines for protocol troubleshooting and overview on its limitations

Turchetto et al., STAR Protocols *1*, 100131 December 18, 2020
https://doi.org/10.1016/j.xpro.2020.100131

STAR Protocols

CellPress
OPEN ACCESS

Protocol

Ex Vivo Recording of Axonal Transport Dynamics on Postnatal Organotypic Cortical Slices

Silvia Turchetto,[1,2,3,*] Loic Broix,[1,2,3,*] and Laurent Nguyen[1,4,*]

[1]GIGA-Stem Cells and GIGA-Neurosciences, Interdisciplinary Cluster for Applied Genoproteomics (GIGA-R), University of Liège, CHU Sart Tilman, Liège 4000, Belgium

[2]These authors contributed equally

[3]Technical Contact

[4]Lead Contact

*Correspondence: silvia.turchetto@student.uliege.be (S.T.), lbroix@uliege.be or lbroix@uliege.be (L.B.), lnguyen@uliege.be (L.N.)
https://doi.org/10.1016/j.xpro.2020.100131

SUMMARY

Axonal transport is a physiological process adopted by neurons to transport organelles, proteins, and other molecules along their axonal projections. Here, we describe a step-by-step protocol to record the dynamics of axonal transport along the projections of callosal neurons by combining the *in utero* electroporation technique with the preparation of postnatal organotypic cortical slices. This *ex vivo* protocol has been developed to investigate axonal transport in a physiological setting closely reproducing the *in vivo* environment.
For complete details on the use and execution of this protocol, please refer to Even et al. (2019).

BEFORE YOU BEGIN

Swiss mice are well suited for the described procedure, as noted for their large litters size and good maternal care. However, the strain of choice and/or the number of embryos to electroporate should be chosen in accordance with the duration of the *in utero* electroporation surgery. To enhance the viability rate, a maximum time of 30 min is therefore recommended.

Plasmid Preparation (for *In Utero* Electroporation; See Step 2 in the Step-By-Step Detailed Protocol)

Timing: 5 min

1. A mix of endotoxin-free plasmids is prepared in sterile nuclease-free water. One ug/µL of each plasmid is diluted in a total volume of 15 µL, with 0.1% (w/v) Fast green at 1/10 volume added to the plasmid solution to visualize the injection site.

   Note: to record axonal transport dynamics of membrane-bound organelles such as lysosomes and mitochondria, we combined a reporter gene-expressing plasmid to enable the visualization of the electroporated neurons with another construct coding for a fluorescent organelle-specific protein, such as Lamp1-emerald or DsRed-Mito as markers for lysosomes or mitochondria, respectively (Courchet et al. 2013).

2. Prepare microcapillaries for DNA injection by using a Needle Pipette Puller. To fabricate microcapillaries, we pull glass microcapillaries tubing with an inner diameter of 0.58 mm with a P-97 micropipette under the following conditions: heat, 634; pull, 92; velocity, 115; time, 210.

Note: the pulling parameters might need to be adapted when the heating filament is replaced.

⚠ CRITICAL: to ensure harmless perforation of the placenta and optimal injection of the plasmid solution, microcapillaries tip should be cut diagonally to generate an opening with slightly larger diameter; we recommend the use of spring scissors which enable the execution of sharp cuts (Figure 1).

Preparation for Surgery (for *In Utero* Electroporation; See Step 2 in the Step-By-Step Detailed Protocol)

Timing: 10 min

3. Transfer the pregnant dam into a clean cage filled with a paper towel for nest building.
4. Prepare surgical table as follows: make available autoclaved surgery toolbox and 50 mL syringe filled with warm sterile PBS; cut paper drape to create rhomboidal-shaped incision for the surgical field; turn on the heating pad to 37°C.
5. Fill capillaries with plasmids mix; for this, we recommend to use microloader tips and to cut the tip of the microcapillary filled with the solution just before starting the surgery, to prevent the solution from air drying. If using a microinjector, set the injection pressure that enables a 0.1–0.2 μL droplet of plasmid solution to be ejected from the microcapillary when the foot pedal is pressed.
6. Prepare the electroporation system: make available 3 mm ϕ platinum electrodes and set the electroporator for 5 pulses of 40 V at 50-ms intervals for 950 ms when electroporating E14.5 embryos.

Note: the electroporation parameters were set as previously described (Even et al. 2019), adjusted to the developmental stage of the embryos to electroporate. Settings should be arranged to a given experimental design.

Preparation of Tamoxifen Solution (if Temporal Control of Plasmid Expression Is Desired)

Timing: 10 min

7. Prepare a solution of 2 mg/mL 4-hydroxytamoxifen (4-OHT) containing 1 mg/mL progesterone by dissolving 20 mg of 4-OHT and 10 mg of progesterone in 100 μL ethanol 100% and diluting with 900 μL of corn oil, followed by water bath sonication for 5 min.

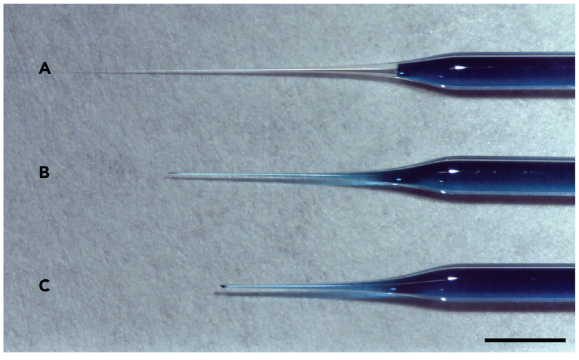

Figure 1. Microcapillary Cut for Plasmid Injection
(A) Uncut microcapillary filled with plasmid solution.
(B) Filled microcapillary cut at optimal length to enable ejection of 0.1–0.2 μL droplets of plasmid solution.
(C) Filled microcapillary deeply cut leading to suboptimal injection of plasmid solution. Scale: 0.2 μm.

Note: cover solution with foil as progesterone is sensitive to light.

Note: solution can be stored at +4° for up to one week.

Note: the solution is complemented with progesterone to counteract the mixed estrogen effect of tamoxifen which can cause fetal abortion.

Note: the injection paradigm has to be defined in accordance with the plasmid effects and experimental settings.

Preparation of Embedding Solution (for Brain Embedding; See Step 3 in the Step-By-Step Detailed Protocol)

Timing: 3–5 min

8. Prepare a 4% agarose solution for brain embedding by adding 1 g of low-melting agarose into a 50 mL conical tube containing 25 mL sterile HBSS; Keeping the cap loose, transfer the tube into a microwave and boil until all agarose particles are dissolved and the solution is clear.

   Note: monitor the solution to prevent excess boiling and overflow; stop the microwave when the solution starts to boil and mix by whirling the tube before repeating the step until complete melting. Wear heat-resistant gloves when manipulating the tubes to protect your hands from burns.

9. Transfer the solution into a 37°C incubator to allow cooling down.

Preparation of Slice Culture Medium (for Mounting of Cortical Slices; See Step 4 in the Step-By-Step Detailed Protocol)

Timing: 3–5 min

10. Let Matrigel thaw on ice; prepare culturing media for brain slices by mixing Matrigel with Neurobasal Medium supplemented with 2% B27, 1% penicillin/streptomycin and 1% GlutaMAX at 1:1 ratio; keep the solution on ice to prevent polymerization.

    Note: as recommended, Matrigel is stored at −20°C and left thawing in a 4°C refrigerator for 12–16 h to prepare one-time use aliquots. Frozen aliquots can be quickly thawed at 4°C the day of the experiment (~2 h for 1 mL aliquot).

KEY RESOURCES TABLE

REAGENT or RESOURCE	SOURCE	IDENTIFIER
Antibodies		
Anti-RFP antibody	Rockland antibodies & assays	600-401-379
Anti-GFP antibody	Abcam	Ab6673
DAPI	Sigma	D9542
Chemicals, Peptides, and Recombinant Proteins		
Isoflurane	Abbott Laboratories	N/A
Fast green	Sigma-Aldrich	F7252
Nuclease-free water	Schering-Plough	3098

(*Continued on next page*)

Continued

REAGENT or RESOURCE	SOURCE	IDENTIFIER
Buprecare 0.3 mg/mL injection	Animalcare	N/A
Fucithalmic Vet® 10 mg/g	Aventix	N/A
Tamoxifen	Sigma-Aldrich	T5648-1G
Corn oil	Sigma-Aldrich	C8267
Low melt agarose	Bio-rad	1613114
HBSS	Lonza	10-527F
Matrigel	Fisher Scientific	11573560
Progesterone	Sigma-Aldrich	P3972
Neurobasal Medium	Gibco, Invitrogen	21103049
B27	Gibco, Invitrogen	17504044
penicillin/streptomycin	Gibco, Invitrogen	15140122
GlutaMAX	Gibco, Invitrogen	35050061
Critical Commercial Assays		
Plasmid DNA, endotoxin-free Midi-prep kit from NucleoBond_Xtra Midi EF	Macherey-Nagel	740420
Experimental Models: Organisms/Strains		
E14.5 pregnant *RjOrl*:Swiss mice (outbred)	Janvier labs	
Recombinant DNA		
pCALNL-DsRed	(Matsuda and Cepko 2007)	Addgene: # 13769
pCAG mEmerald-LAMP1	(Lewis et al., 2016)	N/A
pCX memb-mCherry	(provided by Dr. Xavier Morin)	N/A
pCAG-iCreERT2	(Even et al. 2019)	N/A
Software and Algorithms		
Fiji-Image J	(Schindelin et al. 2012)	N/A
KymoToolBox - ImageJ	(Hinckelmann, Zala, and Saudou 2013)	N/A
Prism	GraphPad Software	N/A
Other		
Platinum electrodes	Sonidel	CUY650P3
Electroporator	BTX	ECM 830
Microinjector	Eppendorf	5252000013
Micropipette puller	Sutter Instrument	P-97
Isoflurane anesthesia station	Harvard Apparatus	34-1041
Heating pad	Beurer	HK 35 Heat pad
Surgical lamp with flexible arm	N/A	N/A
Borosilicate glass capillaries	Harvard Apparatus	30-0016
Sterile PBS	Lonza	17-512F
Syringe 5 mL	Becton Dickinson	SYR005J
Syringe 1 mL	Becton Dickinson	303172
Needle 26GA (0.45 × 10 mm)	Becton Dickinson	300300
Super GLUE-3	Loctite	N/A
Operating Manual Compact balance	KERN & Sohn GmbH	1.1
Vibratome Leica VT1000S	Leica Microsystems	VT1000S
Culture dish as embedding mold	Thermo Fisher Scientific	153066

(*Continued on next page*)

Continued

REAGENT or RESOURCE	SOURCE	IDENTIFIER
MatTek glass-bottom dishes	MatTek CORPORATION	P35G-0-20-C
FemtoJet microinjector	Eppendorf	5252000013
Forceps	Dumont 11295-20	11295-20
Hair removal cream	Veet	N/A
Ethanol	vwr	20816,298
Scissors	Fine Science Tool	14094-11
Perforated spoon	Moria	10370-18
Spring scissors	Aesculap	OC498-R
Ring forceps	Fine Science Tool	11103-09
Olsen-Hegar Needle Holder	Fine Science Tool	12002-14
Vycril suture 4-0	Ethicon	V310H
Microloader tips	Eppendorf	5242956003

STEP-BY-STEP METHOD DETAILS

Induction of Anesthesia

Timing: 3 min

Here we describe the method for induction and maintenance of anesthesia of the pregnant dam.

1. Weigh the mouse to define the amount of analgesic to administer pre- and post-surgery.
2. Prepare the analgesic buprenorphine (Buprecare®): 0.03 mg/mL dilution to administer 0.1 mg/kg.

   Note: once the action of the analgesic is over (buprenorphine is effective for 8–12 h), assess post-operative pain by scoring pain behaviors (i.e., by using Grimace Scale; Langford et al. 2010) and evaluate re-administration of analgesic, in accordance with local and national directives.

3. Sedate the pregnant dam in an induction chamber where a mixture of 96% air and 4% isoflurane circulates.

   Note: monitor the breathing rate to assess the state of sedation, which takes approximately 60 s.

4. Quickly, to prevent hypothermia, transfer the mouse on the heating pad with the abdomen facing down; apply ophthalmic lubricant (Fucithalmic Vet® 5 mg/g) to both eyes to prevent corneal drying, and inject the analgesic subcutaneously within the loose skin over the interscapular area.
5. With the abdomen facing up, place the nose of mouse inside the mask respirator and adjust the concentration of isoflurane vaporized to 2%.

   ⚠ CRITICAL: given the inter-individual variability in response to anesthesia, anesthesia depth should be closely monitored to prevent insufficient sedation or respiratory/cardiac depression. Parameters that can be clinically monitored are: 1) toe pinch response; 2) respiration rate (approximately 1 breath/s under optimal anesthesia); under too deep or too light anesthesia, flow rate of anesthetic should be adjusted to reach optimal anesthesia depth.

In Utero Cortical Electroporation and Post-op Care

Timing: ~20–25 min; should not exceed 30 min, to ensure optimal viability

The *in utero* electroporation technique consists of the injection of plasmid DNAs into the lateral ventricles of mouse brain embryos and their subsequent incorporation into the apical progenitors lining the ventricle surface by electroporation. By targeting the neuronal progenitors with reporter constructs, it is possible to trace the different steps of development of the derived cortical neurons.

6. Shave the abdomen wall with a depilatory cream and disinfect with 70% alcoholic solution (Figure 2A).
7. Make an incision of approximately 1.5 cm along the skin abdomen midline first, and peritoneum afterwards (Figure 2B).
8. Place a surgical field with a rhomboidal aperture over the abdomen and wet the drape and the open abdomen cavity with warm saline.

   Note: we suggest to hydrate the drape with warm sterile saline to favor the subsequent step of the procedure, as it would prevent the uterine horns pulled out of the abdomen cavity from attaching to the drape. Make sure to not soak the drape excessively, to avoid mouse hypothermia.

9. By using ring forceps, carefully pull the uterus out from the abdominal cavity by holding it at the gaps between embryos; expose one of the two uterine horns on the surgical drape and, when necessary, apply warm sterile phosphate-buffered saline (PBS) solution to prevent drying of the embryos during the whole surgical procedure (Figure 3A).
10. Gently, hold an embryo with ring forceps or your fingers while inserting the microcapillary through the uterus into the lateral ventricle and inject the DNA plasmid mix (approximately 0.5 μL) by using a mouth-controlled tube or a microinjector activated via the foot pedal. The green dye filling the ventricles indicates the success of the injection. To reduce the lethality rate, a given embryo should not be injected more than two times (Figures 3B–3E).

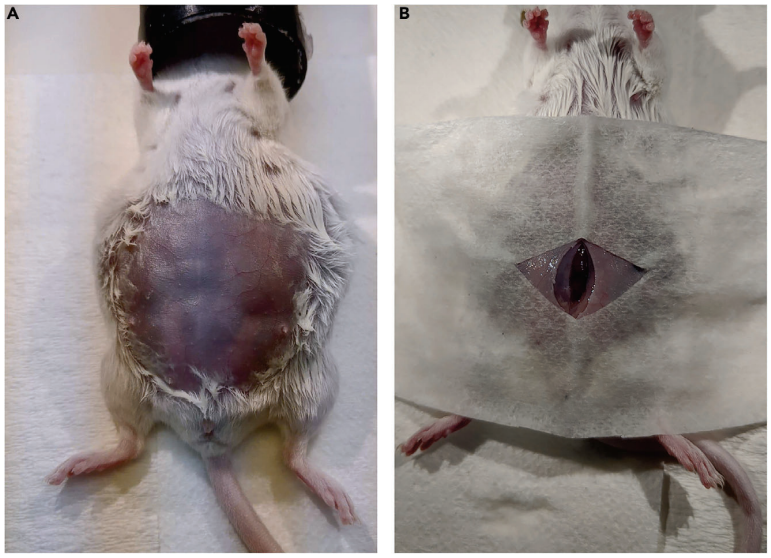

Figure 2. Preparation for Surgery
(A) Incision area. Shave the abdomen of the pregnant dam kept under anesthesia and disinfect the skin with an alcoholic solution.
(B) Skin incision. Cover the incision area with a surgical drape and incise the skin and peritoneum along the abdomen midline.

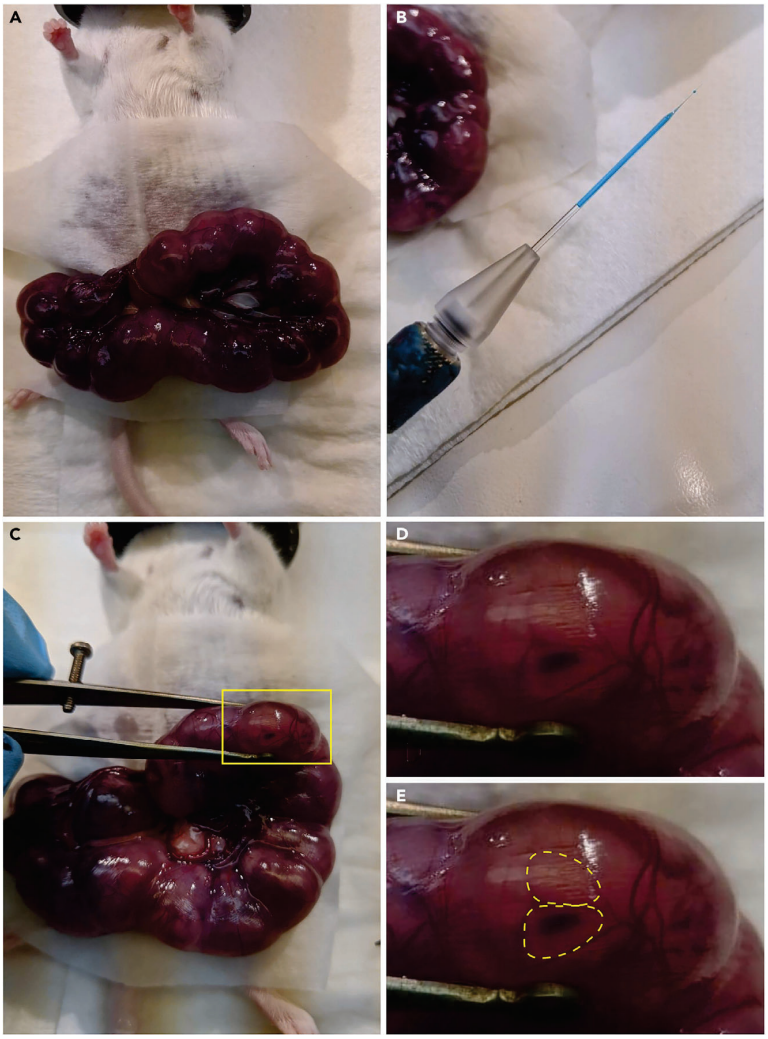

Figure 3. Microinjection of E14.5 Embryos

(A) Exposition of the uterine horns. Pull uterus horns out the abdomen cavity by holding it at the gaps between embryos and expose the uterine horns. Keep the uterus hydrated with warm sterile PBS during the entire procedure. (B–E) Embryos microinjection. (B) Cut diagonally the tip of a previously pulled microcapillary to enable an optimal ejection of the plasmid solution. (C–E) Inject the plasmid solution into one of the lateral ventricles of the embryo (yellow dotted line in E).

⚠ CRITICAL: make an oblique cut of the microcapillary with optimal width (see also the Trouble-shooting section). This is a critical factor for the success of the electroporation. Microcapillaries shortened sub-optimally could compromise the integrity of the perforated tissues as well as lead to undesired dispersion of the plasmid solution from the injected to the other interconnected ventricles. The tip of the capillary can be cut progressively, to identify the minimal cut which enables the ejection of 0.1–0.2 μL droplets of plasmid solution.

⚠ CRITICAL: If the fast green is observed in other regions than the ventricles or cannot be released from the microcapillary, change the position of the microcapillary by slowly pulling it back until the fast green can be injected and observed in the ventricle.

11. Place the anode on the injection site and the cathode on the opposite side of the brain, and deliver the electrical impulses by pressing the foot pedal of the electroporator; the correct delivery of the electric impulses is indicated by the formation of bubbles around the electrodes (Figure 4).

Note: electroporation at E14.5 was chosen for axonal transport recordings to target a sparse population of upper layer II-IV neurons, enabling the visualization of isolated fluorescent callosal projections.

Note: in order to target the callosal projection neurons, the electroporation is performed by placing the anode at 45° with respect to the intra-hemispherical plane.

⚠ CRITICAL: warm PBS should be made available during the entire procedure, to keep embryos and electrodes wet.

12. Once the plasmid injection and the electroporation have been performed on the remaining embryos, hydrate the uterine horn and, gently, slide it back into the abdomen cavity; repeat the same procedure on the second uterine horn.
13. Suture abdomen wall and skin; transfer the mouse from the operating table to a cage placed under a warming light and containing paper towel to monitor eventual bleeding. Monitor the mouse closely until recovery from anesthesia.

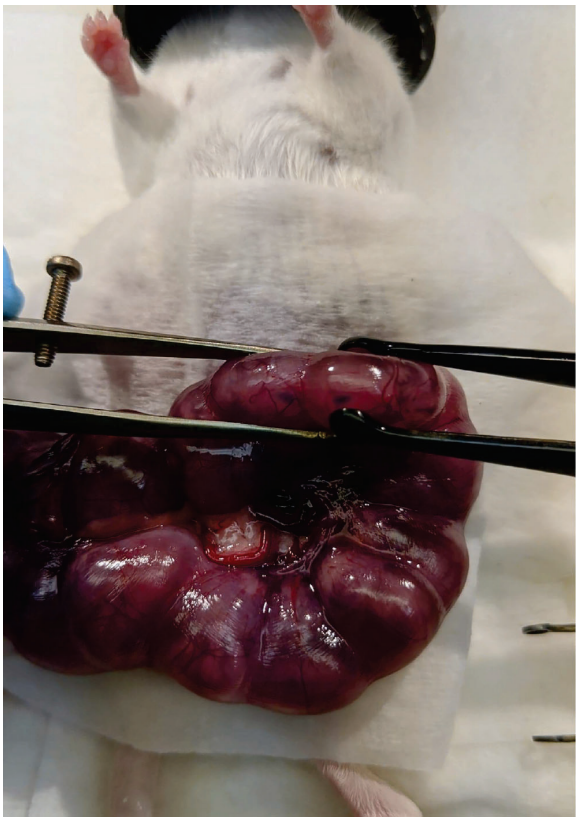

Figure 4. *In Utero* Electroporation of E14.5 Embryos
Hold the injected embryo with ring forceps to stabilize its position while placing the electrodes over the target site for electroporation.

⚠ CRITICAL: skin and muscle layer should be sutured separately: this measure would prevent damage of the underneath muscle suture and potentially lethal bleeding if the mouse would bite and remove the external skin suture.

14. After surgery, monitor and document the mouse well-being on a scoring sheet with daily observations by checking and evaluating the surgical wound, outer appearance, and spontaneous behavior. If properly performed, laparotomy for in utero electroporation is likely to not correlate with post-surgery symptoms of discomfort or pain.

Dissection and Embedding of P2 Brains

Timing: 30 min

Brain dissection of electroporated pups is performed at postnatal day two (P2), a stage at which the electroporated callosal projection neurons have crossed the interhemispheric midline. In order to provide mechanical support prior to slicing, dissected brains are embedded into an agarose matrix.

15. Decapitate the P2 pup with surgical scissors, carefully dissect out the full brain including olfactory bulbs, forebrain, and hindbrain as elsewhere described (Beaudoin et al. 2012), and collect into a petri dish containing ice-cold HBSS.

Note: we recommend to dissect and perform the protocol described below on one pup at a time, given the strict time window of some of the steps and the importance of their timing for a successful execution of the protocol.

Note: If a reporter plasmid was electroporated, dissected brains can be checked for fluorescence under a binocular microscope equipped with fluorescent illumination.

16. Place embedding molds on ice and pour the 4% agarose solution that was previously brought to 37°C

Note: we generally prefer petri-dishes over conventional embedding molds as their larger diameter facilitates the brain rotation within the polymerizing agarose solution and its orientation in the position of interest.

17. Quickly, remove the excess HBSS and transfer the brain into the agarose solution; with the forceps, rotate the brain gently and repeatedly while agarose polymerizes, until steady in the final position with the olfactory bulbs facing upwards and the coronal axis parallel to the mold bottom on an ice bucket.

⚠ CRITICAL: a gentle and repeated rotation of the brain within the agarose solution is important to remove the HBSS at the interface between the brain and the agarose solution; this precaution would prevent the detachment of the brain slice from the surrounding agarose layer while being sliced from the agarose block.

⚠ CRITICAL: orienting the brain within the agarose solution undergoing polymerization would simplify the downstream manipulation of the agarose block; By positioning the brain with the sectioning plane parallel to the mold bottom, the bottom side of the agarose block would not require further cutting adjustment and could be directly glued on the vibratome tray platform.

18. Let the agarose block solidify on ice for about 15 min.

Slicing and Mounting of Cortical Slices

Timing: 20 min

Organotypic brain slices are generated and mounted on coated glass-bottom dishes, to be used for recordings of axonal transport along the projections of callosal neurons.

19. Set the vibratome: fill the vibratome tray with cold HBSS and the vibratome bath with ice; adjust the sectioning parameters as follows (adjusted for a vibratome Leica VT100S): section thickness: 300 μm; cutting speed: 3; cutting frequency: 3.
20. Coat the glass-bottom dish with a thin layer of culture medium containing Matrigel, by adding with a pipette 1 mL solution and aspiring back most of the volume, leaving a thin pellicle; keep it at RT (below the polymerizing temperature of 37°C).
21. Once the agarose block is polymerized, shape it around the brain by making a cut at the rostral and ventral sides of the brain, parallel to each other and to the sectioning plane, at an approximate distance of 0.5 cm from the brain surface; apply the same procedure to remove the excess agarose also at the ventral and dorsal sides of the brain. We recommend cutting the block with a truncated pyramid shape making sure the olfactory bulbs of the brain face the minor base of the pyramid. This shape will provide a greater adhesion surface and will increase the stability of the agarose block glued onto the vibratome tray platform (Figures 5A–5C).
22. Glue the agarose block with the olfactory bulbs facing upwards onto the vibratome tray platform.
23. Fix the platform with the glued agarose block into the vibratome tray filled with cold HBSS.
24. Section the agarose block to generate coronal slices and collect with a spatula the brain sections containing the callosal projections crossing the midline in a dish filled with ice-cold HBSS; check

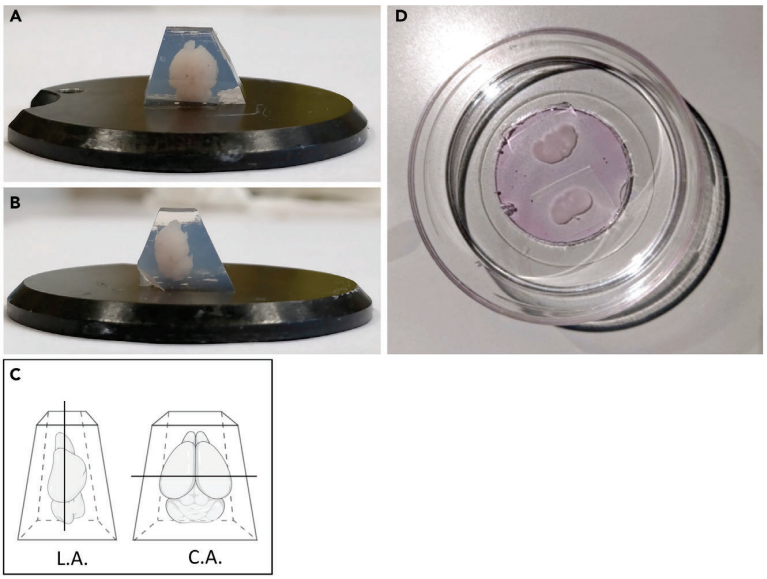

Figure 5. Cortical Slices Preparation

(A–C) Brain embedding. (A and B) Embed the brain in a 4% agarose solution ensuring the optimal positioning of the brain until agarose polymerization. Shape the agarose block to ensure a thickness of 0.5 cm from the brain surface, and glue the agarose block onto the vibratome tray platform. (C) Scheme for brain orientation within the agarose block. L.A., longitudinal axis; C.A., coronal axis.

(D) Mounting of cortical slices. Slice the embedded brain to generate coronal slices and transfer them onto coated glass-bottom dishes.

the collected slices for fluorescence and transfer onto coated MatTek dishes only the slices with the electroporated region of interest (Figure 5D).

Note: depending on the thickness of the agarose block, two or three sectioned slices can be placed per MatTek dish; it is very important to not overlap the edges of the agarose slices for an optimal live-imaging acquisition.

CAREFUL: gently manipulate the brain slices in order to avoid the separation of the brain slices from the surrounding agarose. Take care that the embedded brains stay at 4°C during the whole sectioning procedure by changing the HBSS regularly and refilling the vibratome bath with ice.

25. With a pipette, cover each section slice with a drop of culture medium containing Matrigel and place the glass-bottom dishes in the incubator at 37°C and 5% CO_2 for 20 min, to allow the Matrigel to polymerize and slices to recover.

CAREFUL: due to the short survival time of postnatal cultured organotypic brain slices (approximately 4 h), incubation times of all steps following brain dissection should be reduced to the minimum. Additionally, all steps should be performed at 4°C, by using ice-cold reagents and performing all the manipulations on ice. Altogether these measures would enable a longer recording time of axonal transport dynamics.

Transport Recordings

Timing: 2 h

After recovery in the incubator (at least 20 min), the transport dynamics of fluorescently labeled organelles/vesicles can be recorded along the projections of callosal neurons.

26. To record axonal transport dynamics, use a 63× oil lens with a working distance of 0.14 mm and position the bottom-glass dish within a recording chamber controlled at 37°C and 5% CO_2.
27. Acquire time-lapse images using a confocal microscope (here, Zeiss LSM 880) for a desired capturing time at the corpus callosum midline to discriminate the directionality of the transport. As the movement of mitochondria and lysosomes relies on fast axonal transport, it is recommended to image at least three frames per second for 60 s. The number of acquisitions per second can be adapted depending on the speed of the cargos.

Note: to locate the corpus callosum midline, we recommend to first use the 10× lens to identify the fluorescently labeled neurons in the electroporated hemisphere of the brain slice and follow the neuronal projections to the midline.

⚠ CRITICAL: set the microscope lasers at a power low enough to visualize the cargos for the entire acquisition time; as the neurons are sensitive to photodamage, this measure would limit the loss of fluorescent signal over time.

⚠ CRITICAL: given the critical survival time of the mounted brain slices, it is important to acquire the transport recording in the shortest time possible. For this, we recommend processing one brain at a time.

Optional Step of the Protocol: Tamoxifen Injection

Timing: 5 min

Tamoxifen is administered to activate a given Cre recombinase to temporally regulate the expression of a plasmid of interest. Tamoxifen is injected intra-peritoneally to the pregnant dam for a vertical diffusion via the blood system to the electroporated embryos, and after delivery to modulate the tamoxifen transmission to the pups via mother's milk.

28. To perform an IP injection, restrain the animal with the ventral abdomen facing up and the head slightly tilted downward. Insert the syringe at 4–5 mm depth into the lower right quadrant of the abdomen toward the mouse head, by keeping a 20°–30° angle to the abdominal surface; aspirate by pulling back syringe plunger to check if vital organs were punctured and, and if any fluid is aspirated inject slowly the tamoxifen solution. If aspirate is observed, withdraw and discard the needle, and gently perform the procedure again.

⚠ CRITICAL: injection volume should be the lowest possible (ideally less than 0.2 mL and needle size should be less than 21G). A new needle should be used for each animal, to reduce the risk of infection.

29. Observe the animal to check for signs of bleedings at injection site or sign of pain or distress due to complication of injection. If complications persist 24 h after the injection, the animal is sacrificed.

Note: misplaced intraperitoneal injections can lead to peritonitis, lacerations of abdominal organs, bleeding, or infections. All these complications are associated with pain or distress whose severity can be clinically evaluated (i.e., by using Grimace Scale; Langford et al. 2010).

Note: for optimal plasmids effect at postnatal stage P2, we routinely perform injections on pregnant dams E17.5 and E18.5, and one day after delivery. Frequency and number of doses administered justify the time needed for cre-driven recombination and expression of the plasmids of interest; adaptations might be necessary depending on the timing for tissue harvesting and biological effects of the plasmid/plasmids of interest.

EXPECTED OUTCOMES

This protocol has been developed to record the transport dynamics of motile vesicles and/or organelles along the axonal projection of layer II-V pyramidal neurons *ex vivo* on cortical slices. This procedure relies on the *in utero* electroporation of plasmids expressing fluorescently labeled membrane proteins targeting species-specific organelles. In opposition to transgenic animal models used for studies of axonal transport, the electroporation of fluorescent plasmids enables the selective visualization of a restricted population of neurons, to ultimately facilitate the tracking of vesicles trajectories (Mattedi and Vagnoni 2019).

Here, we report the use of the Lamp1:emerald or DsRed-mito expressing plasmids to selectively label and track lysosomes or mitochondria, respectively. A cortical slice prepared at postnatal day 2 (P2) following electroporation at E14.5 in the somatosensory cortex would typically manifest fluorescent callosal neurons projecting from the upper cortical layers to the contralateral hemisphere through the interhemispheric midline (Figure 6). At the interhemispheric midline, dotted fluorescent signals corresponding to Lamp1-expressing lysosomes or DsRed-expressing mitochondria is expected to move bidirectionally along the callosal projection of electroporated neurons (Figure 7C and Methods Video S1).

The *ex vivo* protocol described here was set up to study axonal transport dynamics in a new in vitro setting closer to the in vivo situation. In comparison to existing microfluidic devices, that are commonly used to physically separate axons from dendrites to facilitate the study of axonal transport, organotypic slices better recapitulate the cellular and chemical cortical environment of neurons

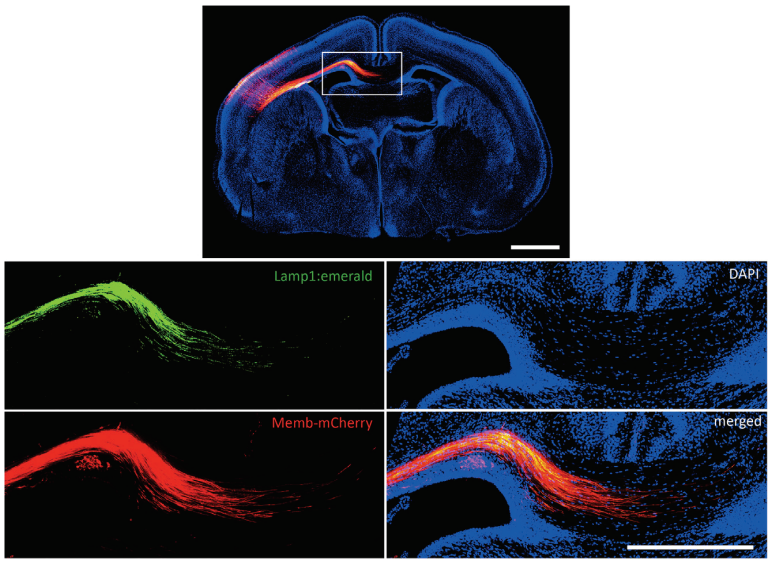

Figure 6. Representative Image of a Cortical Slice Collected at P2 following Electroporation at E14.5 of Lamp1:Emerald and Memb-mCherry

Electroporated L2–4 pyramidal neurons with callosal projections (red); Lamp1:emerald (green); nuclei (blue). Scale bar, 500 μm.

that plays an importante role in defining their metabolism and morphology (Polleux, Morrow, and Ghosh 2000; Villarin et al. 2016).

QUANTIFICATION AND STATISTICAL ANALYSIS

1. Download the FIJI/ImageJ plugin Kymotoolbox.
2. Open an image series in FIJI/ImageJ.
3. If necessary, separate stacked channels [Image | Color | Split channels] (Figure 7A).
4. Adjust the image proprieties [Image | Proprieties].
5. Select the Segmented Line Tool [right-click on the Line icon | Segmented Line] and set the width value that has to be used for the complete data analysis [double-click on the Segmented Line Icon].
6. Track the axon by drawing a segmented line along its length and add the defined line region of interest (ROI) to the ROI Manager [click t]. For subsequent calculations of vesicles run length, segmented lines of the same length should be traced. Export the obtained data set into excel (Figure 7B).
7. Generate a kymograph and corresponding video of the tracked axon [Plugin | KymoToolBox | Draw Kymo] by setting the width previously defined (see step 5) and ticking [Get Kymo] and [Get KymoStack] (Figures 7C and 7D and Methods Video S1).
8. Track the particles trajectories by drawing a segmented line along their length and add the defined ROIs to the ROI Manager, as previously described.
9. Analyze the particles displacement over time along the tracked axon [Plugin | KymoToolBox | Analyse Kymo] by defining the directionality of the motion [outward], setting the minimum speed for movement and selecting [Log all data]. Select [Show colored kymo] to generate a color-coded kymograph of the trajectories analyzed. We commonly consider vesicles as stationary when speed is lower than 0.1 μm/s (Figure 7E).
10. Export the Summary data set from the Result panel into Excel. We routinely analyze Average velocity (μm/s), Run length (μm), Pausing time (%).

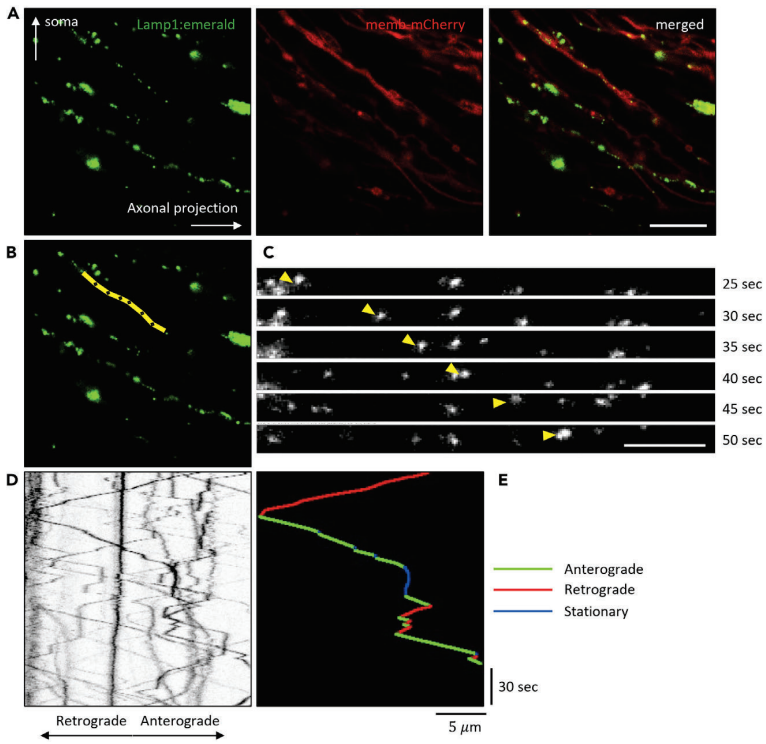

Figure 7. Axonal Transport Analysis of Lamp1-Positive Lysosomes in Cortical Projection Neurons of P2 Cortical Slices

(A) Representative image of memb-mCherry callosal projection neurons with Lamp1-expressing lysosomes (emerald) crossing the interhemispheric midline of P2 cortical slices. Scale bar, 10 μm.

(B and C) Kymograph generation and analysis. (B) Drawing of a segmented line along axon length. (C) 5-s interval snapshots of Lamp1:emerald lysosome displacement along tracked axon. Scale bar, 5 μm.

(D) Kymograph generated from tracked axon, used to characterize the trajectories of moving vesicles.

(E) Representative tracking of a vesicle moving with anterograde and retrograde motion; the vesicle is considered stationary when speed is lower than 0.1 μm/s. Scale bar, 5 μm.

LIMITATIONS

The *ex vivo* protocol described here was developed for recording intracellular trafficking within axonal projections of layer II-V pyramidal neurons. These neurons have an organized interhemispheric distribution that enables the visualization of all their subcellular compartments, from the cell soma to the axonal projections, within a coronal slice. For this reason, the transfection of this neuronal population via *in utero* electroporation is an ideal tool to visualize their spatial distribution and study their intracellular dynamics on a cortical slice. Accordingly, by recording axonal transport along the callosal projections at the interhemispheric midline, it is possible to precisely define the directionality of the organelles motility (i.e., whether it is moving with anterograde or retrograde motion) and standardize the location of the recording window with regard to the distance from the cell soma. If transport directionality and distance from the cell soma are parameters of interest in the analysis, recordings of axonal transport in other neuronal population with a more complex and not clearly organized spatial distribution might be associated with increasing technical challenges.

The ability to record transport dynamics in organotypic cortical slices is limited by the age of pups and the time of culture. In comparison to P2 slices that can be kept up to 4 h, cultures at later stages are expected to have a shorter survival rate and lower organelle-associated fluorescent signal.

The *in utero* electroporation technique enables the co-transfection of multiple plasmids, thus allowing multi-level genetic alterations. By co-electroporating plasmids that simultaneously enable the labeling of organelles and regulation of a given protein expression, it is possible to study the dynamics of axonal transport applied to a gene-dependent phenotype. If the expression level of a given protein has to be genetically regulated, i.e., via RNA interference technology, it is important to evaluate its physiological role during brain development and assess whether changes in its expression could affect key processes such as neuronal proliferation and migration. In these circumstances, it is recommended to control the timing of gene expression by using inducible plasmid systems that can be activated after a defined developmental stage.

If the *in utero* electroporation technique is used to regulate the expression level of a given protein, axonal transport dynamics cannot be investigated by using fluorescent dyes for organelles such as mitochondria (MitoTracker) and lysosomes (LysoTracker). These dyes would ubiquitously label every neuronal population of the cortical slices, preventing the unique visualization of motile organelles/vesicles along the electroporated neurons.

TROUBLESHOOTING

Problem 1

Suboptimal shortening of the microcapillary leading to a problem with injection.

Potential Solution

For a targeted injection of the plasmid solution, it is important to control the quality of the microcapillary tip. A microcapillary tip with an optimal internal diameter would enable a precise and harmless injection into cortical ventricles. A tip excessively shortened would present a too large internal diameter, which could potentially lead to difficulties in penetrating the uterine wall or damage of the amniotic sac with following leakage of amniotic fluid. On the other hand, a tip with a too narrow internal diameter due to insufficient shortening would prevent an efficient penetration of the uterine wall, as it could bend over the uterus surface and break. Lastly, if the injection is optimal but too much volume is released into a given ventricle leading to filling of the interconnected ventricles, the ejected volume can be reduced by controlling the pressure delivered by the injector. This measure would prevent the need for replacing the microcapillary. Overloading of the ventricles with plasmid solution could also cause hydrocephalus and ultimately lead to embryonic lethality. Therefore, to ensure optimal injection of the plasmid solution into the ventricle it is important to cut the capillary at the appropriate length ensuring the best compromise between penetrance and plasmid flow (Figure 1).

Problem 2

Low number of electroporated embryos or survival rate.

Potential Solution

If low electroporation rate is experienced, the surgeon should pay attention to: 1) concentration or quality of the plasmid solution (endotoxin-free plasmid solution is highly recommended); if the expression of the plasmid is unknown to the experimenter, *in vitro* transfection tests should be performed to assess the expression of fluorescence; 2) the site of injection; a crescent shape corresponding to the lateral ventricle should progressively fill and be visualized with fast green while injecting; 3) the correct positioning of the electrodes with respect to the neuronal population to electroporate; an imprecise orientation of the positively and negatively charged electrodes might lead to missed electroporation or electroporation of undesired neuronal population. 4) Electroporation settings should be determined according to the embryonic stage. Commonly, the electroporation voltage is increased at later embryonic stages in comparison to early stages while other parameters remain constant (E14.5: 40 V, E15.5: 45 V). Electrodes with a larger diameter (5 mm) can be used to target a larger area of the brain with the same pulse conditions than the 3 mm electrodes.

To improve the low survival rate of electroporated embryos: 1) keep the surgery time within 30 min; 2) do not electroporate the first embryos of each horn adjacent to the cervix, in order to minimize the chances of abortion; 3) manipulate the embryos with care making sure the uterus is hydrated for the whole procedure; keep the mouse warm with the heating pad while being under anesthesia and by using a warming lamp during post-operative recovery; 4) reintroduce the uterine horns into the abdomen respecting their original position, to prevent twisting and tangling of the associated vasculature system which could lead to resorption; 5) preferentially use mice aged two to three months as they show better recovery; 6) make sure the plasmids are produced with an endotoxin-free DNA isolation kit. 7) do not try to inject the same embryo more than twice.

Problem 3

Problem in the detection of organelles/vesicles transport dynamics.

Potential Solution

If no movement of the organelles/vesicles is recorded, this may result from poor slice fitness. Post-natal cortical slices have a short survival rate (about 4 h) and therefore every measure that could endorse it should be followed. We highly recommend performing all steps of the procedure in the shortest time possible, to maintain all reagents and perform all manipulations at 4°C.

RESOURCE AVAILABILITY

Lead Contact

Further information and requests should be addressed to Laurent Nguyen (lnguyen@uliege.be).

Materials Availability

This study did not generate new unique reagents.

Data and Code Availability

This protocol includes all datasets generated or analyzed during this study.

SUPPLEMENTAL INFORMATION

Supplemental Information can be found online at https://doi.org/10.1016/j.xpro.2020.100131.

ACKNOWLEDGMENTS

We thank Romain Le Bail for technical assistance, and Franck Polleux and Xavier Morin for kindly providing DNA plasmids. The graphical abstract was done with the BioRender program. The work in the Nguyen laboratory is supported by the F.R.S.-F.N.R.S. (Synet; EOS 0019118F-RG36), the Fonds Leon Fredericq, the Fondation Médicale Reine Elisabeth, the Fondation Simone et Pierre Clerdent, the Belgian Science Policy (IAP-VII network P7/20), and the ERANET Neuron STEM-MCD and NeuroTalk.

AUTHOR CONTRIBUTIONS

This protocol relies on experiments done by L.B. and S.T. and has been written by S.T., L.B., and L.N.

DECLARATION OF INTERESTS

The authors declare no competing interests.

REFERENCES

Beaudoin, G.M., 3rd, Lee, S.H., Singh, D., Yuan, Y., Ng, Y.G., Reichardt, L.F., and Arikkath, J. (2012). Culturing pyramidal neurons from the early postnatal mouse hippocampus and cortex. Nat. Protoc. *7*, 1741–1754.

Courchet, J., Lewis, T.L., Jr., Lee, S., Courchet, V., Liou, D.Y., Aizawa, S., and Polleux, F. (2013). Terminal axon branching is regulated by the LKB1-NUAK1 kinase pathway via presynaptic mitochondrial capture. Cell *153*, 1510–1525.

Even, A., Morelli, G., Broix, L., Scaramuzzino, C., Turchetto, S., Gladwyn-Ng, I., Le Bail, R., Shilian, M., Freeman, S., Magiera, M.M., et al. (2019). ATAT1-enriched vesicles promote microtubule acetylation via axonal transport. Sci. Adv. *5*, eaax2705. http://advances.sciencemag.org/.

Hinckelmann, M.V., Zala, D., and Saudou, F. (2013). Releasing the brake: restoring fast axonal transport in neurodegenerative disorders. Trends Cell Biol. *23*, 634–643.

Langford, D.J., Bailey, A.L., Chanda, M.L., Clarke, S.E., Drummond, T.E., Echols, S., Glick, S., Ingrao, J., Klassen-Ross, T., Lacroix-Fralish, M.L., et al. (2010). Coding of facial expressions of pain in the laboratory mouse. Nat. Methods *7*, 447–449.

Lewis, T.L., Jr., Turi, G.F., Kwon, S.K., Losonczy, A., and Polleux, F. (2016). Progressive decrease of mitochondrial motility during maturation of cortical axons in vitro and in vivo. Curr. Biol. *26*, 2602–2608.

Matsuda, T., and Cepko, C.L. (2007). Controlled expression of transgenes introduced by in vivo electroporation. Proc. Natl. Acad. Sci. U S A *104*, 1027–1032.

Mattedi, F., and Vagnoni, A. (2019). Temporal control of axonal transport: the extreme case of organismal ageing. Front. Cell. Neurosci. *13*, 1–11.

Polleux, F., Morrow, T., and Ghosh, A. (2000). Semaphorin 3A is a chemoattractant for cortical apical dendrites. Nature *404*, 567–573. www.nature.com.

Schindelin, J., Arganda-Carreras, I., Frise, E., Kaynig, V., Longair, M., Pietzsch, T., Preibisch, S., Rueden, C., Saalfeld, S., Schmid, B., et al. (2012). Fiji: an open-source platform for biological-image analysis. Nat. Methods *9*, 676–682.

Villarin, J.M., McCurdy, E.P., Martínez, J.C., and Hengst, U. (2016). Local synthesis of dynein cofactors matches retrograde transport to acutely changing demands. Nat. Commun. *7*, 13865. www.nature.com/naturecommunications.

Molecular analysis of axonal transport dynamics upon modulation of microtubule acetylation

Chapter 10

Molecular Analysis of Axonal Transport Dynamics upon Modulation of Microtubule Acetylation

Silvia Turchetto, Romain Le Bail, Loïc Broix, and Laurent Nguyen

Abstract

Axonal transport is used by neurons to distribute mRNAs, proteins, and organelles to their peripheral compartments in order to sustain their structural and functional integrity. Cargoes are transported along the microtubule (MT) network whose post-translational modifications influence transport dynamics. Here, we describe methods to modulate MT acetylation and record its impact on axonal transport in cultured mouse cortical projection neurons as well as in motoneurons of *Drosophila melanogaster* third-instar larvae. Specifically, we provide a step-by step procedure to reduce the level of MT acetylation and to record and analyze the transport of dye-labeled organelles in projection neuron axons cultured in microfluidic chambers. In addition, we describe the method to record and analyze GFP-tagged mitochondria transport along the motoneuron axons of transgenic *Drosophila melanogaster* third-instar larvae.

Key words Axonal transport, MT acetylation, Cargo, Organelles, ATAT1, HDAC6

1 Introduction

Neurons are highly polarized cells that transport cargoes along their protracted axons to supply mRNAs, proteins, and organelles to the axoplasm. Intracellular trafficking of cargoes along axons is essential for neuron maturation and homeostasis as well as for their functional integration into neuronal network via synaptic activity. Cargoes are transported along MTs whose structure, properties, and dynamics rely on its constitutive tubulin subtypes as well as their post-translational modifications (PTMs) that can fine-tune the trafficking of cargoes (reviewed in [1]).

While most PTMs, such as glutamylation, glycylation, and detyrosination, occur on the C-terminal tails of α/β-tubulins, acetylation of α-tubulin takes place on intralumenal Lys40 (K40) of MTs. This PTM is catalyzed by the α-tubulin N-acetyltransferase

Silvia Turchetto and Romain Le Bail are Co-first authors. Loïc Broix and Laurent Nguyen are co-senior authors.

Alessio Vagnoni (ed.), *Axonal Transport: Methods and Protocols*,
Methods in Molecular Biology, vol. 2431, https://doi.org/10.1007/978-1-0716-1990-2_10,

1 (ATAT1) and removed by the histone deacetylase 6 (HDAC6) [2]. The acetylation of α-tubulin modulates the mechanical properties of MTs by enhancing their flexibility, thereby protecting them from stress-induced mechanical aging [3]. Additionally, α-tubulin acetylation has been reported to increase the recruitment and processivity of molecular motors on MTs, pinpointing a functional correlation between MT acetylation and axonal transport dynamics [4, 5]. Accordingly, some neurodegenerative diseases exhibit transport defects which correlate with decreased MT acetylation levels. Restoring the balance of K40 acetylation using overexpression of ATAT1 or inhibitors of HDAC6 subsequently rescues axonal transport, therefore strengthening the link between this PTM and the regulation of axonal transport [4, 6, 7]. In accordance with the role that MTs play in neuronal development and activity, mice lacking ATAT1 display dentate gyrus deformation, hypoplasia of the septum and striatum and enlarged lateral ventricles. Moreover, their somatosensory cortical neurons suffer from axon overgrowth and overbranching, further suggesting an important role for MT acetylation during cortical maturation [8–10].

To investigate the role of ATAT1 on axonal transport dynamics and further untangle its regulatory molecular mechanisms, we assessed axonal transport dynamics in mouse cortical neurons and in third-instar larva motoneurons of *Drosophila melanogaster* upon RNA interference (RNAi)-induced knock-down (KD) of ATAT1 and ATAT2 (the *D. melanogaster* orthologs of mouse Atat1) [11]. We reported comparable axonal transport defects of membrane-bound organelles across species upon knock-down of ATAT1 that were rescued by the expression of a mutant α-tubulin (K40Q) mimicking K40 acetylation in mice or by pharmacological inhibition of HDAC6 in third-instar larvae [11].

Here, we provide an experimental paradigm to analyze the axonal transport of organelles in mouse cortical projection neurons cultured in microfluidics chambers as well as in motoneurons of live anaesthetized *D. melanogaster* third-instar larvae. These models are suitable to study the contribution of MTs acetylation to the transport dynamics of organelles and allow a comparison of these molecular parameters across species. More specifically, we provide a step-by-step method to knock down ATAT1 in mouse cortical neurons by in utero electroporation of short hairpin RNA (shRNA) and to record axonal transport dynamics of dye-labeled organelles in neurons cultured in microfluidic devices. As a culturing platform, microfluidics devices enable the physical isolation of axons from cell bodies and dendrites, thus allowing the study of axon biology and its transport dynamics. Moreover, we describe the experimental protocol to record axonal transport of mitochondria along the motoneuron axons from anesthetized third-instar larvae as well as the genetic strategies used to generate simple or compound conditional Atat1/2 and/or Hdac6 knock-down. We

further emphasize the pharmacological strategy used to rescue MT acetylation levels in larvae upon Atat1/2 KD and ultimately provide the detailed procedure to quantify the axonal transport parameters extracted from the time-lapse recordings.

2 Materials

2.1 Axonal Transport Recordings in Mouse Cortical Neurons

2.1.1 In Utero Electroporation

1. Micropipette puller (Sutter Instrument, #P-97).
2. Electroporator (BTX, #ECM 830).
3. Micro-injector (Eppendorf, #5252000013).
4. Isoflurane anesthesia vaporizer (Harvard Apparatus, #34-1041).
5. Heating pad (Beurer, HK 35 Heat pad).
6. Surgical lamp with flexible arm.
7. Endo-free plasmid maxi kit (Macherey-Nagel, #740420).
8. Sterile PBS.
9. Fast green.
10. Isoflurane.
11. Analgesic: Buprecare 0.3 mg/mL injection (Animalcare).
12. Ophthalmic lubrificant: Fucithalmic Vet 10 mg/g (Aventix).
13. 3 mm φ platinum electrodes (Sonidel, # CUY650P3).
14. Borosilicate Glass capillaries (Harvard Apparatus, #30-0016).
15. Syringe 1 mL.
16. Needle 26GA (0.45 × 10 mm).
17. Microloader tips (Eppendorf, #5242956003).
18. Scissors.
19. Spring scissors.
20. Ring forceps.
21. Vicryl suture 4–0.
22. Plasmids: pEGFP α-tubulin WT (Clontech) and pEGFP α-tubulin K40Q (Addgene, #105302).
23. Atat1 short hairpin RNA (shRNA); sequence: 5'- GCAG CAAATCATGACTATTGT -3′ [12]. Scrambled-shRNA; sequence: 5'-TACGCGCATAAGATTAGGG-3′.

2.1.2 Culturing and Plating Mouse Cortical Neurons in Microfluidic Devices

1. Vacuum desiccator.
2. Glass-bottom dish (*Mattek Life Science, #P50G-0-30-F).*
3. Microfluidic chambers, 450μm microgroove barrier (XONA microfluidics, # SND450).

4. 0,1 mg/mL Poly-D-Lysine, resuspended in sterile water, ready to use. Solution can be stored at 4 °C for up to 2 years.
5. Neurobasal medium (ThermoFisher, #21103049), to be supplemented with 1% Penicillin-Streptomycin, 1% Glutamine, and 2% B27 to prepare the culturing medium.
6. 200 mM Glutamine
7. 10,000 units/mL Penicillin-Streptomycin (P/S)
8. B27 (Gibco, Invitrogen, #15140122).
9. Forceps.
10. Perforated spoon.
11. 20μm/mL BDNF, resuspended in culturing medium and aliquoted for long-term storage at −20 °C (Peprotech, #450-02).
12. Mitotracker Red (ThermoFisher, # M7514).
13. Lysotracker Deep red (ThermoFisher, # L12492).
14. Ethanol 70%.
15. 40μm cell strainer.
16. 30% Glucose.
17. HBSS.

2.2 Axonal Transport Recordings *in* Drosophila melanogaster

1. Drosophila culture tubes 25 × 95 mm (MLS, # QD789008).
2. Foam plug, Ø 36 × 40 mm (MLS, # QD330070).
3. Homemade cornmeal medium based on BDSC standard recipe (https://bdsc.indiana.edu/information/recipes/bloomfood.html).
4. Incubators.
5. Fly lines of the appropriate genotype (Table 1).

2.2.1 Fly Lines and Husbandry

2.2.2 Recording of Axonal Transport

1. Ether.
2. 80% glycerol solution in water.
3. 10% Sucrose solution in water.
4. 50 mL conical centrifuge tubes.
5. 12-well plate.
6. Beaker.
7. Parafilm.
8. Forceps.
9. Tissue paper.
10. Standard microscope slides.
11. 32 × 32 mm microscope coverslips.

Table 1
Fly lines used in this protocol with their origin and purpose

Fly line	Origin	Purpose
D42-GAL4 > UAS-*mito*GFP	Bloomington drosophila stock center (BDSC) #42737	Expression of Gal4 in motor neurons [11]
UAS-RNAi HDAC6	BDSC #34072	UAS-dependent expression of interfering RNA (RNAi) against the HDAC6 enzyme to increase acetylation levels [11]
UAS-RNAi ATAT1	VDRC #106247	UAS-dependent expression of RNAi against the ATAT1 enzyme to decrease acetylation levels [11]
UAS-RNAi ATAT2	VDRC #101273	UAS-dependent expression of RNAi against the ATAT2 enzyme to decrease acetylation levels [11]
UAS-RNAi ZPG	VDRC #33277	Control line using UAS-dependent expression of RNAi against ZPG, a protein expressed in gonads [11]

12. Dissection microscope equipped with fluorescent lamp.
13. Confocal microscope.

2.2.3 Treating Third-instar Larvae with Tubastatin A

1. 24-well plates.
2. 10% sucrose solution in water.
3. Tubastatin A powder (Sigma, # SML0044).
4. DMSO.
5. Heating bath.
6. Vortex.

3 Methods

3.1 Axonal Transport Recording of Mouse Cortical Neurons Seeded in Microfluidic Devices

3.1.1 Preparation of the Microfluidic Chambers

1. Coat glass-bottom dishes with 0.1 mg/mL Poly-D-lysine (2 mL/dish) and incubate overnight at 4 °C. Rinse 3 times with sterile water and allow to air dry under a laminar flow hood for 30 min. Dried coated dishes can be stored at 4 °C until use for up to 1 month.
2. Sterilize microfluidics chambers with 70% ethanol for 30 min, making sure microgrooves are facing up. Remove ethanol and allow to dry under laminar flow hood (*see* **Note 1**).
3. Assemble the microfluidic chambers with the microgrooves facing downward on the coated dishes and press gently, either with your fingers or a pipette tip; be gentle on the grooves, to prevent their clogging that would hamper the media flow from somal to axonal compartments. To remove air bubbles that might have formed within the grooves, place microfluidics in a desiccator under vacuum for 30 min.

3.1.2 Irrigation of the Microfluidics

1. Irrigate the main channel of the somal compartment by adding into one of the two adjacent wells 200μL of Neurobasal medium complemented with 1% Glutamine, 1% P/S, and 2% B27 (culturing medium). Wait 5 min for the media to flow through the channel and equilibrate with the other somal well. Fill up both somal wells with further 100μL of media.
2. Wait up to 1 h to allow the media in the somal channel to flow through the microgrooves into the axonal channel, thus filling the adjacent axonal wells. Keep the microfluidics in the incubator until ready to use (*see* **Note 2**).

3.1.3 In Utero Electroporation of Cortical Projection Neurons

1. Prepare a mix of endotoxin-free plasmids in sterile nuclease-free water in a total volume of 10μL by diluting each plasmid at 1μg/μL with 0.1% (w/v) Fast green at 1/10 volume to visualize the injection site. To downregulate Atat1 and decrease MT acetylation level, you can use conditional sh-Atat1-expressing plasmid or sh-scrambled-expressing plasmid, as control, combined with a cre recombinase-expressing plasmid to drive their respective expression. To restore MT acetylation levels, use a plasmid encoding for α-tubulin K40Q which mimics MT acetylation or a WT tubulin-expressing plasmid, as control (*see* **Notes 3** and **4** for details of the plasmids).
2. By using a Needle Pipette Puller, pull glass microcapillaries tubing with inner diameter of 0.58 mm under the following conditions: heat: 634; pull: 92; velocity: 115; time: 210.
3. By using microloader tips, fill pulled microcapillaries with the plasmid mix. Use spring scissors to make progressively deeper diagonal cuts at the microcapillary tip, thus enlarging its diameter, until the plasmid solution passes through. To prevent air drying of the solution, cut the tip of microcapillaries only at the start of the surgery.
4. Anesthetize a pregnant mouse at E14.5 with a flow of 4% isoflurane; once sedated transfer it on a heating pad to quickly apply ophthalmic lubricant (Fucithalmic Vet® 5 mg/g) and inject the analgesic (Buprecare 0.1 mg/kg injection) subcutaneously.
5. Reduce the anesthetic flow to 2% and turn the mouse on its back. Shave the abdomen with depilatory cream and disinfect afterwards with 70% ethanol solution. Place the surgical field with rhomboidal aperture on the shaved area and wet it with warm phosphate-buffered saline (PBS) before performing a first incision of about 1.5 cm along the skin and a second along the midline of the abdominal muscles.
6. Use ring forceps to pull one uterine horn at a time out of the abdomen cavity by holding it at the junction between embryos. Expose the horn on the surgical field and make sure to apply

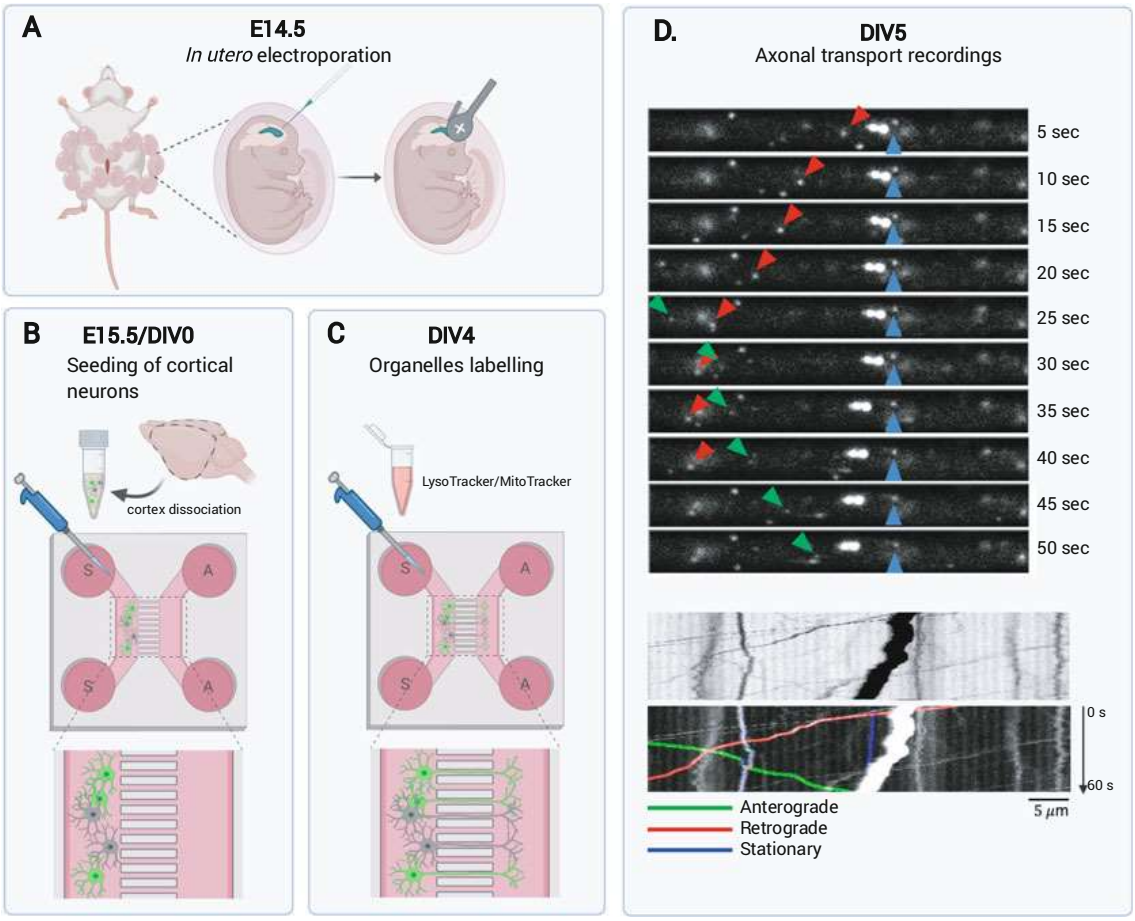

Fig. 1 Axonal transport recordings of mouse cortical neurons seeded in microfluidics chambers. (**a**) In utero electroporation of E14.5 mouse embryos with a solution of DNA plasmids to modulate MT acetylation level. Inject one lateral ventricle with the plasmid mix until the injection site is decorated by the fast green. Electroporate the injected plasmids into the neocortex by positioning the cathode (positively charged electrode) towards the target area and the anode (negatively charged electrode) at the opposite side of the brain. (**b**) Seeding of E15.5 cortical neurons dissociated from electroporated brains. Dissect and dissociate the electroporated hemisphere to prepare a cell suspension to be plated in the somal compartment (S) of the microfluidic chambers. Note that the seeded culture encompass also non-electroporated neuron. (**c**) Labeling of membrane-bound organelles. At DIV4, label seeded neurons with organelle-labeling dyes (e.g., LysoTracker for lysosomes and MitoTracker for mitochondria) for overnight incubation. (**d**) Recording of the axonal transport at DIV5 to follow the movements of labeled organelles. Wash somal (S) and axonal (A) wells with fresh medium and use a confocal microscope to record axonal transport dynamics of labeled organelles along the lower microgrooves segment lining the axonal channel

further warm saline solution during the entire procedure to prevent its drying.

7. Gently, hold an embryo steadily and by using a prepared micro-capillary connected to a mouth-controlled tube or micro-injector, inject 0.1–0.2μL of DNA plasmid mix through the placenta into one of the lateral ventricles. The filling of the ventricles with the Fast-Green dye indicates the success of the injection (*see* **Note 5**) (Fig. 1a).

8. Hold the embryo with electrode-type forceps, placing the anode at the injection site and the cathode at the opposite side of the brain and deliver 5 electric pulses of 40 V at 50-ms intervals for 950 ms (*see* **Note 6**) (Fig. 1a).
9. After performing ventricle injection and electroporation of the remaining embryos, wet the uterine horn before placing it back into the abdominal cavity. Perform the same procedure on the second uterine horn.
10. Suture first the abdominal muscles and then the skin before placing the operated mouse into a cage kept under a warming light. Monitor closely the recovery of the mouse (*see* **Note 7**).

3.1.4 Culture of Electroporated Cortical Projection Neurons in Microfluidic Chambers

1. Prepare primary mouse cortical neurons isolated from electroporated E14.5 mouse embryos. Briefly, 1 day after performing in utero electroporation (E15.5), dissect the brains and check for fluorescence of the co-electroporated reporter plasmid under a binocular fluorescent microscope. Dissect the electroporated cerebral hemisphere in ice-cold Hank's balanced salt solution (HBSS) supplemented with 1.5% glucose. In the case of embryos electroporated with the same plasmid mix, collect the micro-dissected electroporated cortexes in the same tube. Dissociate mechanically in culturing medium by using a P1000 pipette and pipetting up and down very gently for approximately 15–20 times. Filter the cellular suspension through a 40μm strainer, concentrate it by centrifugation at 150 × *g* for 5 min, and finally resuspend the cells in culturing medium at 40×10^3 cells/μL (*see* **Note 8**).
2. Aspirate the medium from all the four wells to leave a thin layer of medium covering the well surface (*see* **Note 9**).
3. Load slowly, by keeping the pipette tip at the entrance of the somal channel, 5μL of cell suspension. To favor high seeding density within the channel, quickly after adding the cells, remove 5μL of media from the opposite somal well and slowly load it back in the same well. This practice allows first the cell transit along the channel and then it's slowing down. Quickly, observe under a microscope the cell flow through the channel until cell positioning; cells should have attached also along microgrooves entrance (*see* **Note 10**) (Fig. 1b).
4. Without adding any additional media to the wells, incubate in a humidifier incubator for 2 h until cells have attached.
5. Fill somal and axonal wells with fresh culture medium supplemented with 20 ng/mL BDNF and 50 ng/mL BDNF, respectively, to promote axon outgrowth. In order to establish a fluidically isolated system ensuring compartment-specific BDNF concentrations, keep a 50μL media volume difference between somal and axonal compartment, with the higher

volume in the somal well. This practice prevents diffusion of the higher BDNF concentrated solution from the axonal to the somal well.

6. Keep the devices in a humidified incubator at 37 °C, 5% CO_2.
7. Check the media volume in the wells every day, and fill up if evaporation occurred. Every 2 days, replace half of the media with fresh BDNF-enriched media.

3.1.5 Labeling of Membrane-Bound Organelles

1. At DIV4, label mitochondria or lysosomes by replacing half of each reservoir media with fresh culturing media containing 200 nM Mitotracker® or Lysotracker®, to reach a final concentration of 100 nM (*see* **Note 11**) (Fig. 1c).
2. Incubate for 60 min at 37 °C.
3. Wash twice the wells with fresh culturing media and incubate overnight. Acquisitions are performed the following day.

3.1.6 Recording and Axonal Transport Analysis

After overnight incubation of the culture upon labeling with organelle-specific dies, the transport dynamics of lysosomes and/or mitochondria can be recorded. Position the glass-bottom dish within a recording chamber controlled at 37 °C and 5% CO_2 of a confocal microscope (for Even et al. [11], we used a Zeiss LSM 880) and use a 63× oil objective with a working distance of 0.14 mm to acquire time-lapse movies. Given the shorter lengths of dendrites, image at the bottom of the microgrooves (approximately 450μm from the somal channel) lining the axonal channel to unambiguously focus on axons. The MitoTracker and LysoTracker label the organelles of all cultured neurons, including the non-electroporated ones. Focus only on the electroporated neurons identified by the fluorescent reporter gene of choice. We recommend to acquire three frames per second for 60 s in total, as mitochondria and lysosomes trafficking follows the dynamics of the fast axonal transport (*see* **Note 12**) (Fig. 1d).

3.2 Axonal Transport Recording upon Modification of MT Acetylation *in* Drosophila Melanogaster

3.2.1 Generation of Third-Instar Larvae

1. The D42-Gal4 > UAS *mito*GFP line is maintained at 20 °C and passed every 15–20 days.
2. To generate third-instar larvae for axonal transport, transfer stock vials in a 25 °C incubator to hasten the life cycle. Adult flies can be passed every 2 days to maximize the amount of eggs that are laid.
3. Transfer the vials with eggs in a 29 °C incubator to maximize the expression of Gal4 and check regularly to monitor the growth of larvae.

3.2.2 Anesthesia and Recording of Axonal Transport in Motoneurons from D42-Gal4 > UAS mitoGFP Larvae

1. Prepare the anesthesia setup by perforating the lid of a 50 mL Falcon to allow ether fumes to penetrate. Place absorbing paper at the bottom of a glass beaker and add 5 mL of ether on the paper. Close the beaker hermetically with parafilm to prevent the evaporation of ether fumes (*see* **Note 13**).
2. When third-instar larvae from the D42-GAL4 > UAS-*mito*GFP line are abundant, collect and place 10 larvae in a 12-well plate filled with 10% sucrose solution (*see* **Note 14**). Larvae should only be kept in sucrose solution for a maximum of 1 h. Proceed immediately with the rest of the protocol.
3. Select the larvae with the brightest GFP expression in motoneurons using a dissection microscope equipped with a fluorescent lamp and discard the other larvae (*see* **Note 15**).
4. Select 3 larvae and place them on absorbing paper to dry them (*see* **Note 16**). Transfer the larvae on the inside of the perforated 50 mL falcon lid and close the falcon, making sure that the larvae rest on the inside of the falcon against the lid. Place the falcon with the lid against the paper soaked with ether to position the larvae directly on top of the ether fumes and seal with parafilm for 8 min (Fig. 2a).
5. Prepare 3 microscope slides and add 300μL glycerol in the center. All the following steps should be performed quickly since the anesthesia lasts about 30 min. After 8 min incubation, transfer one anesthetized larva per microscope slide. The larvae should always be placed with the same orientation (e.g., with the head facing the side of the slide reserved for annotation) to ensure that the orientation of the movies will be consistent. Use a dissection microscope and a pair of forceps to rotate the tracheas against the microscope slide so that the brain is facing up, as shown in Fig. 2b. Place a 32 × 32 mm coverslip on top of the larvae and adjust the position of the larvae by gently moving the coverslip with your finger until the brain and motoneurons are clearly visible on the dissection microscope (*see* **Note 17**).
6. Place the microscope slide with the coverslip facing the objective of the confocal microscope. The slide should be placed consistently so that the head of the larvae is always on the right (Fig. 2c).This will allow the discrimination between anterograde and retrograde transport during the analysis of the movies.
7. Find the brain and the motoneurons emerging from the ventral nerve cord using a small magnification objective and epifluorescent illumination (*see* **Note 18**). Focus on the proximal segment of motor neurons emerging from the ventral nerve cord with a 60× objective, as shown in the red square representing the field of view in Fig. 2c.

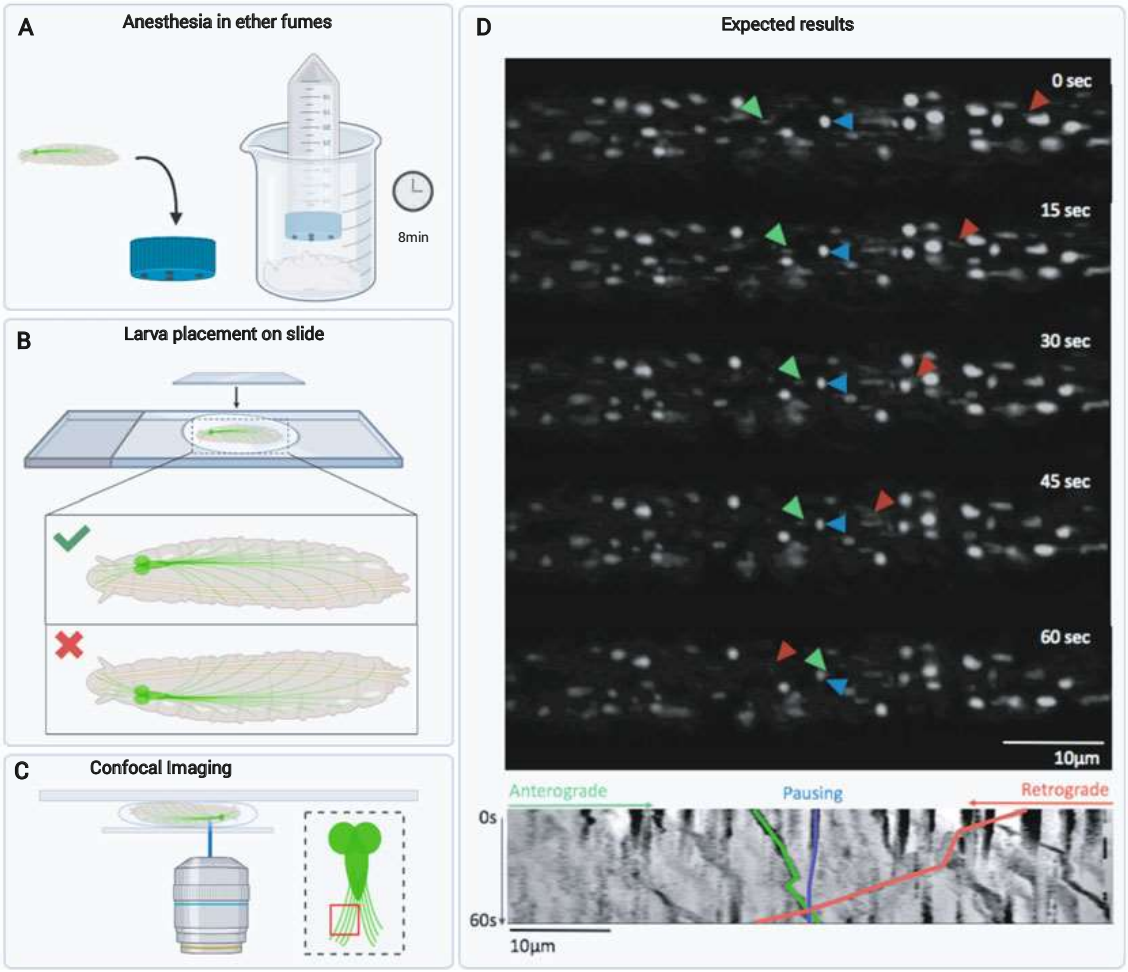

Fig. 2 Axonal transport recording in third-instar larvae. (**a**) The fly larvae are placed on the inside of a perforated 50 mL falcon lid. The falcon is then closed with the larvae on the inside and placed in a beaker with ether-soaker tissue paper for 8 min**.** (**b**) The anesthetized larva is placed in a drop of 80% glycerol on a microscope slide with the ventral side facing up and is then covered by a 32 × 32 mm glass coverslip. (**c**) A confocal microscope is used to record motile mitochondria in the proximal segment of the axon in motoneurons emerging from the ventral nerve cord, as shown in the red square depicting the field of view. (**d**) Motile mitochondria can be visualized as shown in the expected results and the corresponding kymograph. Arrows track moving mitochondria which are highlighted on the kymograph below. (Panel D is adapted from Le Bail et al. with permission [13])

8. Acquire 1-min movies with a maximum of 600 ms between frames. Settings of the laser, gain, and offset should be adjusted based on the setup (*see* **Note 19**). Multiple movies can be acquired in different motoneurons of the same larva to maximize the number of mitochondria that can be tracked. Multiple larvae should also be used for a single experiment to accurately represent inter-individual variability. Expected results and their corresponding kymograph for recordings of GFP-tagged mitochondria are shown in Fig. 2d (*see* **Note 20**).

3.2.3 Treatment with Tubastatin A to Increase MTs Acetylation

1. Prepare the stock solution of Tubastatin A by diluting the powder in DMSO at a concentration of 100 mM (*see* **Note 21**).
2. Select third-instar larvae as in Subheading 3.2.2 and maintain them in 10% sucrose solution.
3. Fill a 24-well plate with 500μL 10% sucrose solution per well and divide it in two halves for the control and treated conditions. For the control group add 5μL of DMSO (*see* **Note 22**) and for the treated group add 5μL of the tubastatin A stock solution to reach a final concentration of 1 mM.
4. Add larvae to the wells of the desired condition for 30 min. The larvae should move and absorb the drug through the feeding reflex. After treatment, immediately prepare the larvae for axonal transport recording, starting from drying the larvae on absorbing paper and following the steps as previously described in Subheading 3.2.2 (*see* **Note 23**).

3.2.4 Transgenic Fly Lines to Modulate MT Acetylation Levels

1. Transgenic fly lines expressing RNAi directed against the main regulators of MT acetylation can be used to modulate MT acetylation levels. To decrease MT acetylation, use a double transgenic line expressing both RNAi ATAT1 and RNAi ATAT2 (*see* **Note 24**), conversely, to increase MT acetylation, use RNAi against HDAC6. To record axonal transport and knock down ATAT1, ATAT2, or HDAC6, cross the D42-GAL4 > UAS-*mito*GFP with either of the RNAi expressing line. The steps to carry out the crossings are detailed below.
2. The flies used to carry out the crossings should be homozygous to ensure that the F1 larvae will all be heterozygous for the transgenic alleles. To generate homozygote flies, make sure that all flies have lost their balancer and the corresponding phenotypic marker (*see* **Note 25**). Males from one line should then be crossed with females from the other line.
3. Segregate males and virgin females based on their morphological characteristics (*see* **Note 26**).
4. Cross males from line 1 (e.g., D42-GAL4 > UAS-*mito*GFP) with females from line 2 (e.g., any RNAi line) to generate larvae expressing mitochondrial GFP and RNAi against the desired target in motoneurons (*see* **Note 27**). As in Subheading 3.2.1, carry out crossings at 25 °C and transfer adult flies every 2 days to a new vial. Transfer the vials with eggs at 29 °C to maximize the expression of mitochondrial GFP and RNAi before recording axonal transport. From this step, follow the protocol as described in Subheading 3.2.2.

3.3 Analysis of Axonal Transport Recordings

1. Open an image series in FIJI/ImageJ provided with the plugin KymoToolBox [14].
2. If necessary, separate stacked channels [Image | Color | Split channels].
3. Invert the values of Slices and Frames in the image properties [Image | Properties] (e.g., if the value in Slices is 1 and the value in Frames is 50, change the value of Slices to 50 and the value of Frames to 1). This step is necessary for the Kymotoolbox plugin.
4. Use the Segmented Line Tool [right-click on the Line icon | Segmented Line] to manually trace the shape of the axon. Make sure to always trace the line following the directionality of anterograde transport (starting from the soma to the tip of the axon) to ensure that the anterograde and retrograde directionality will be maintained in the kymograph.
5. Double-click on the Segmented Line Icon to select a width that encompasses all moving particles within the axon. Take note of the width and change the value back to 1. Click [t] to add the trace to the Region of Interest (ROI) Manager. Export the data set into excel to keep a trace of the axons that were tracked (*see* **Note 28**).
6. Use the KymoToolBox plugin to generate a kymograph [Plugin | KymoToolBox | Draw Kymo], tick [Get Kymo] and set the width to the value determined previously in **step 5**.
7. On the kymograph, draw a segmented line along the length of the particle's trajectories, and, as described in **step 5**, define their ROI and add it to the ROI Manager.
8. Analyze the displacement over time of the particles tracked by the segmented lines [Plugin | KymoToolBox | Analyse Kymo]. Set the directionality of the movement [Outward is... From left to Right] to ensure that the directionality of anterograde and retrograde transport is preserved. Set the minimum speed for movement to 0,10μm/s. Choose [Show colored kymo] to generate a color-coded kymograph for representative purposes where stationary particles are shown in blue, whereas motile particles moving with anterograde or retrograde directionality are shown in green and red, respectively (*see* **Note 2**).
9. Export the Summary data set from the Result panel into Excel. [Mean_speed_Out] is the average velocity in the anterograde direction for a given particle, conversely [Mean_speed_in] is the average velocity in the retrograde direction. A particle moving in the anterograde direction, then changing its course and moving in the retrograde direction would have a value for both these parameters. [Mean_speed] represents the average speed considering both retrograde and anterograde

movements of a given particle. [%_Time_Pause] is the percentage of time during which a given particle has a velocity lower than the threshold set in the previous step (0.10μm/s).

4 Notes

1. For the success of the bonding it is important that the device surface is debris-free. Surface contaminants may favor the formation of suboptimal hydrophobic bonds with the glass dish surface, leading to media leaking and axons growing outside the microgrooves. Before sterilization, tape can be used to gently remove debris and cell contaminants accumulated on the chamber surface from previous usages.
2. We recommend to prepare and irrigate the microfluidic platforms a few days before the plating day. If excessive pressure was exerted on the microgrooves during the bonding procedure, a longer time would be needed for the media to flow through the microgrooves. To improve the flow through the microgrooves, pipette up and down very gently at the entrance of the somal channel, making sure of not exerting an excess of pressure that could induce the detachment of the device from the dish. In case of incomplete filling of the microgrooves, ensure that the axonal wells are irrigated with a lower volume compared to the somal ones, to create a hydrostatic pressure that would force the media to pass through the microgrooves. Keep the microfluidic chamber in the incubator for 24–48 h until microgrooves are filled.
3. In Even et al. (2019) [11] we used a pCX-cre expressing plasmid to drive the expression of the sh-Atat1/scrambled-expressing plasmids. Alternatively, a conditional Cre recombinase, e.g., a CreERT2 Tamoxifen-driven expression plasmid, can be used to modulate in a time-controlled manner the downregulation of the protein of interest, e.g., downregulation of a protein of interest at post-mitotic stages by injecting tamoxifen to drive cre recombination after the neurogenesis window.
4. If possible, use plasmids expressing a fluorescent reporter. For example, in Even et al. (2019) we co-expressed the pair sh-Atat1/scrambled- and Cre-expressing plasmids with a plasmid expressing either pEGFP α-tubulin WT or pEGFP α-tubulin K40Q, to assess the Atat1-driven contribution of tubulin acetylation on axonal transport dynamics. If, on the other hand, the plasmids of interest do not express a fluorescent reporter, we recommend to co-inject a reporter plasmid expressing a fluorescent protein to allow the visualization of the electroporated neurons. Make sure that the fluorophore of the reporter

plasmid does not overlap with the channel of the MitoTracker/LysoTracker as this would interfere with the transport dynamics recording of the fluorescently labeled organelles.

5. A microcapillary tip optimally cut enables a precise and harmless injection into the ventricle. A suboptimal cut could prevent a sharp tissue perforation hampering its integrity and may allow the leakage of amniotic fluid.
6. Electroporation parameters should be adapted to the experimental design, in accordance with the developmental stage of the embryos to electroporate. The parameters described here were used in Even et al. (2019) [11]. The correct position of the positively and negatively charged electrodes with respect to the electroporated area, and their steady placement on the uterus wall are critical for the success of the electroporation. When delivering the electric pulses, pay attention not to touch the heart or the placenta with the electrodes, to prevent administering a shock to the dam. For more practical information, check Turchetto et al. (2020) [15].
7. To increase the survival rate of the operated mouse and electroporated embryos, it is crucial to perform the surgery within 45–50 min.
8. To increase cell survival rates, reduce the time required to prepare the cell suspension by dissociating the tissue mechanically without previous enzymatic digestion. This reduces the risk of cell damage that would induce cell aggregation and heterogeneous seeding along the axonal channel.
9. It is very important that both somal wells contain the same volume of media. As follows, the addition of cells into a somal well would generate a hydrostatic pressure between the two somal wells driving the cell to transit along the axonal channel.
10. If 5μL cell suspension does not ensure 60–70% cell confluency along the somal channel, repeat the loading a second time. Be careful to not load more than three times, as high confluency in the somal compartments would compromise survival of the cells in the channels.
11. Multiple fluorescent organelle dyes can be simultaneously added to a given culture.
12. To prevent neuron photodamages and loss of the fluorescent signal over time, set the lasers of the microscope at a low power to enable the visualization of the labeled cargos for the entire acquisition time.
13. This step should be performed inside a fume hood to prevent the inhalation of ether fumes.
14. Third instar is the last stage of larval growth. At this stage, larvae wander on the edge of the vials before starting pupation.

To collect third-instar larvae, use a pair of forceps to grab motile wandering larvae on the edge of a vial.

15. The D42 driver allows the expression of Gal4 in motoneurons but also in salivary glands. The GFP signal can be strong in the salivary glands bordering the brain but should not be taken into consideration when selecting the larvae. Focus instead on the brightness of the motoneurons emerging form the ventral nerve cord of the brain.
16. Incomplete drying of larvae will result in inconsistent anesthesia by the ether fumes.
17. If the coverslip is moving during transport or imaging, use nail polish on the sides of the coverslip to seal it.
18. The brightest mitochondria tend to remain stationary, whereas the motile mitochondria tend to be smaller and dimmer in fluorescent signal. The settings of the microscope should be adjusted accordingly in order to capture most motile mitochondria.
19. Axonal transport should always be recorded in the same region to ensure consistent results. We typically record in the proximal portion of the motoneurons, close to the ventral nerve cord.
20. We typically use a Nikon A1R confocal microscope in resonant mode.
21. Tubastatin A is a specific HDAC6 inhibitor which can be used to increase MT acetylation in models with reduced MT acetylation [16]. The Tubastatin solution should be clear in DMSO. If some precipitate can be observed, incubate the solution at 37 °C and vortex intermittently until it turns clear.
22. We have observed a slight effect of 1% DMSO solution on axonal transport velocity which explains why when treating with tubastatin A, the control group must be treated with DMSO as well.
23. We usually treat 3 larvae at a time with either the DMSO vehicle or the tubastatin A and anesthetize all 3 after the end of the treatment to record axonal transport. The timing of the experiment has to be followed rigorously and the anesthesia and recording of axonal transport should be carried out as quickly as possible following treatmen,t to minimize experimental variability.
24. ATAT1 is the major enzyme responsible for promoting the acetylation of Lysine 40 of MTs in mammals [17]. In consequence, its loss results in strong reduction of MT acetylation. *Drosophila Melanogaster* has two orthologs of the ATAT1 gene, ATAT1 and ATAT2 which have a redundant function, meaning that downregulation of one or the other will result in partial loss of MT acetylation, whereas combined downregulation will result in an almost complete loss of MT acetylation.

25. Balancer chromosomes are modified chromosomes which prevent homologous recombination, carry a dominant phenotype marker mutation and are recessive lethal. Based on these properties, flies can be identified based on the phenotypic marker associated to their balancer chromosome and cannot carry two copies of the same balancer chromosome. For instance, flies carrying the CyO balancer will exhibit curled wings (Cy marker) while flies carrying the TM6B balancer will be shorter and thicker than wild-type flies at both the larval and pupal stages (Tubby marker).
26. Males have a thin abdomen, slightly curved inwards with visible genitals appearing as a large brown mass in the postero-ventral part of the abdomen, whereas females are bigger than males and their abdomen is round and white. Virgin females are slightly translucent and can be recognized by the meconium, a dark spot in the upper left abdomen persisting up to 3 h after eclosion. The presence of the meconium guarantees that the female is a virgin since female flies are only fertile 8 h after eclosion.
27. Both sexes can be taken from each line for the crossing if the genes of interest are carried on the somatic chromosomes (1, 2, or 3). If a transgenic allele is carried by the X chromosome, only virgin females should be used to ensure that all the progeny will receive one transgenic allele.
28. If an axon harbors a high number of static cargoes which are cluttering the kymograph, it is possible to choose a smaller width which would allow to exclude some static cargoes to focus only on motile ones. We also recommend to trace segmented lines of the same length along all the axons/motoneurons considered for the analysis, for standardized calculations of vesicles run length.
29. By convention, anterograde transport is represented from left to right on representative kymographs and has a positive value for velocity, whereas retrograde transport is represented from right to left and has a negative value for velocity.

Acknowledgments

S.T. and R.L.B are PhD students from F.R.S-F.N.R.S.; L.B. and L.N. are respectively Postdoctoral Researcher and Director from F.R.S-F.N.R.S. The work in the Nguyen laboratory is supported by the F.R.S.-F.N.R.S. (Synet; EOS 0019118F-RG36), the Fonds Leon Fredericq, the Fondation Médicale Reine Elisabeth, the Fondation Simone et Pierre Clerdent, the Belgian Science Policy (IAP-VII network P7/20), and the ERANET Neuron STEM-MCD and NeuroTalk. The figures were made with Biorender (https://biorender.com/).

References

1. Janke C, Magiera MM (2020) The tubulin code and its role in controlling microtubule properties and functions. Nat Rev Mol Cell Biol 21(6):307–326. https://doi.org/10.1038/s41580-020-0214-3
2. Hubbert C, Guardiola A, Shao R et al (2002) HDAC6 is a microtubule-associated deacetylase. Nature 417:455–458. https://doi.org/10.1038/417455a
3. Portran D, Schaedel L, Xu Z et al (2017) Tubulin acetylation protects long-lived microtubules against mechanical ageing. Nat Cell Biol 19:391–398. https://doi.org/10.1038/ncb3481
4. Dompierre JP, Godin JD, Charrin BC et al (2007) Histone deacetylase 6 inhibition compensates for the transport deficit in Huntington's disease by increasing tubulin acetylation. J Neurosci 27:3571–3583. https://doi.org/10.1523/JNEUROSCI.0037-07.2007
5. Reed NA, Cai D, Blasius TL et al (2006) Microtubule acetylation promotes Kinesin-1 binding and transport. Curr Biol 16:2166–2172. https://doi.org/10.1016/j.cub.2006.09.014
6. Godena VK, Brookes-Hocking N, Moller A et al (2014) Increasing microtubule acetylation rescues axonal transport and locomotor deficits caused by LRRK2 Roc-COR domain mutations. Nat Commun 5:5245. https://doi.org/10.1038/ncomms6245
7. D'Ydewalle C, Krishnan J, Chiheb DM et al (2011) HDAC6 inhibitors reverse axonal loss in a mouse model of mutant HSPB1-induced Charcot-Marie-tooth disease. Nat Med 17:968–974. https://doi.org/10.1038/nm.2396
8. Kim GW, Li L, Gorbani M et al (2013) Mice lacking α-tubulin acetyltransferase 1 are viable but display α-tubulin acetylation deficiency and dentate gyrus distortion. J Biol Chem 288:20334–20350. https://doi.org/10.1074/jbc.M113.464792
9. Li L, Jayabal S, Ghorbani M et al (2019) ATAT1 regulates forebrain development and stress-induced tubulin hyperacetylation. Cell Mol Life Sci 76:3621–3640. https://doi.org/10.1007/s00018-019-03088-3
10. Wei D, Gao N, Li L et al (2018) α-Tubulin acetylation restricts axon overbranching by dampening microtubule plus-end dynamics in neurons. Cereb Cortex 28:3332–3346. https://doi.org/10.1093/cercor/bhx225
11. Even A, Morelli G, Broix L et al (2019) ATAT1-enriched vesicles promote microtubule acetylation via axonal transport. Sci Adv 5:eaax2705. https://doi.org/10.1126/sciadv.aax2705
12. Li L, Wei D, Wang Q et al (2012) MEC-17 deficiency leads to reduced α-tubulin acetylation and impaired migration of cortical neurons. J Neurosci 32:12673–12683. https://doi.org/10.1523/JNEUROSCI.0016-12.2012
13. Le Bail R, Morelli G, Gladwyn-ng I (2017) Dacapo regulates axonal transport through the modulation of microtubule acetylation. Master's Thesis, University of Liege, Belgium. https://orbi.uliege.be/handle/2268/235914
14. Zala D, Hinckelmann M-V, Yu H et al (2013) Vesicular glycolysis provides on-board energy for fast axonal transport. Cell 152:479–491. https://doi.org/10.1016/j.cell.2012.12.029
15. Turchetto S, Broix L, Nguyen L (2020) Ex vivo recording of axonal transport dynamics on postnatal organotypic cortical slices. STAR Protoc 1:100131. https://doi.org/10.1016/j.xpro.2020.100131
16. Butler KV, Kalin J, Brochier C, Vistoli G, Langley B, Kozikowski AP (2005) Rational design and simple chemistry yield a superior, neuroprotective HDAC6 inhibitor, tubastatin A. Bone 23:1–7. https://doi.org/10.1021/ja102758v.Rational
17. Kalebic N, Sorrentino S, Perlas E et al (2013) αTAT1 is the major α-tubulin acetyltransferase in mice. Nat Commun 4:1962. https://doi.org/10.1038/ncomms2962